Conference Proceedings of the Society for Experimental Mechanics Series

Julie M. Harvie · Javad Baqersad *Editors*

Shock & Vibration, Aircraft/ Aerospace, Energy Harvesting, Acoustics & Optics, Volume 9

Proceedings of the 35th IMAC, A Conference and Exposition on Structural Dynamics 2017

Springer

Conference Proceedings of the Society for Experimental Mechanics Series

Series Editor

Kristin B. Zimmerman, Ph.D.
Society for Experimental Mechanics, Inc.,
Bethel, CT, USA

More information about this series at http://www.springer.com/series/8922

Julie M. Harvie • Javad Baqersad
Editors

Shock & Vibration, Aircraft/Aerospace, Energy Harvesting, Acoustics & Optics, Volume 9

Proceedings of the 35th IMAC, A Conference and Exposition on Structural Dynamics 2017

Springer

Editors
Julie M. Harvie
Environments Engineering
and Integration Department
Sandia National Laboratories
Albuquerque, NM, USA

Javad Baqersad
Experimental Mechanics and NVH Laboratory
Kettering University
Flint, MI, USA

ISSN 2191-5644 ISSN 2191-5652 (electronic)
Conference Proceedings of the Society for Experimental Mechanics Series
ISBN 978-3-319-54734-3 ISBN 978-3-319-54735-0 (eBook)
DOI 10.1007/978-3-319-54735-0

Library of Congress Control Number: 2017936482

Printed on acid-free paper

This Springer imprint is published by Springer Nature
The registered company is Springer International Publishing AG
The registered company address is: Gewerbestrasse 11, 6330 Cham, Switzerland

Preface

Shock and Vibration, Aircraft/Aerospace, and Energy Harvesting represent one of ten volumes of technical papers presented at the 35th IMAC, A Conference and Exposition on Structural Dynamics, organized by the Society for Experimental Mechanics, and held in Garden Grove, California, January 30–February 2, 2017. The full proceedings also include volumes on *Nonlinear Dynamics*; *Dynamics of Civil Structures*; *Model Validation and Uncertainty Quantification*; *Dynamics of Coupled Structures*; *Sensors and Instrumentation*; *Special Topics in Structural Dynamics*; *Structural Health Monitoring and Damage Detection*; *Rotating Machinery, Hybrid Test Methods, Vibro-Acoustics and Laser Vibrometry*; and *Topics in Modal Analysis and Testing*.

Each collection presents early findings from experimental and computational investigations on an important area within structural dynamics. Topics represent papers on practical issues improving energy harvesting measurements, shock calibration and shock environment synthesis, and applications for aircraft/aerospace structures.

The organizers would like to thank the authors, presenters, session organizers, and session chairs for their participation in this track.

Livermore, CA, USA — Julie M. Harvie
Flint, MI, USA — Javad Baqersad

Contents

Chapter 1
Scaling up of the Impedance-Matched Multi-Axis Test (IMMAT) Technique

P.M. Daborn

Abstract The Impedance-Matched Multi-Axis Test (IMMAT) technique has been shown to offer significant benefits when compared with the conventional single-shaker vibration test. Thus far, IMMAT has only been demonstrated on relatively small and lightweight structures and to moderate vibration severity. This paper describes the activities undertaken to scale-up the IMMAT technique to larger structures and to severe vibration levels.

Keywords Random vibration • Multi-axis testing • Acoustic test • Vibration test • Mechanical impedance

1.1 Introduction

The research described in this paper fits into a long-term strategy to enhance vibration testing methodology. Previous work in this area bore a new vibration test method, entitled the "Impedance-Matched Multi-Axis Test (IMMAT)" technique [1]. IMMAT aims to replicate the in-service boundary conditions (mechanical impedance) and is executed with multiple small shakers, each controlled by a Multi-Input-Multi-Output (MIMO) vibration controller in order to match target PSDs at a number of response locations on the structure.

IMMAT offers far more realistic tests over traditional methods and in much shorter test durations [2–4]. Thus far, IMMAT has only been demonstrated on relatively small and lightweight structures and to moderate vibration severity and the aim of the work presented in this paper is to scale-up the IMMAT technique by applying it to a realistic structure whilst recreating severe vibration levels.

1.2 The Modal Analysis Test Vehicle

The structure selected to scale-up the IMMAT technique was the Modal Analysis Test Vehicle (MATV) and is presented in Fig. 1.1, where it is undergoing a modal test. The mass of the MATV was approximately 60 kg, which is far greater than any previous structure subjected to an IMMAT test (<10 kg). The approximate overall dimensions of the MATV were 0.8 m in length and 0.4 m in diameter. In addition to the mass and dimension characteristics, the MATV also had inherent properties akin to real-world structures such as complicated joints and exotic materials, for example foams and rubbers.

A finite element (FE) model of the MATV was created in Ansys (Fig. 1.2) and was solved for its natural frequencies and modeshapes within the frequency range of 0–2000 Hz. A modal test was conducted on the MATV hardware, the results of which were used to update the FE model such that the significant majority of the correlated natural frequencies were within ±5%.

P.M. Daborn (✉)
Structural Dynamics, AWE Aldermaston, Reading, Berks, RG7 4PR, UK
e-mail: philip.daborn@awe.co.uk

J.M. Harvie, J. Baqersad (eds.), *Shock & Vibration, Aircraft/Aerospace, Energy Harvesting, Acoustics & Optics, Volume 9*,
Conference Proceedings of the Society for Experimental Mechanics Series, DOI 10.1007/978-3-319-54735-0_1

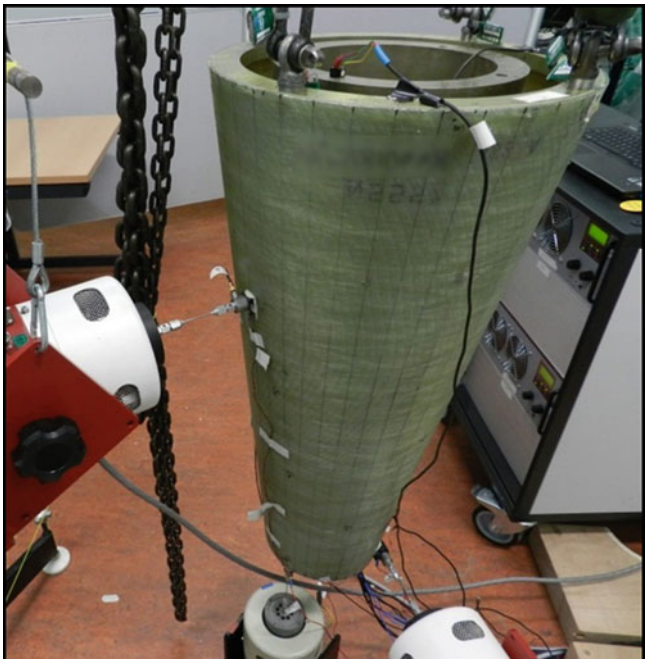

Fig. 1.1 The Modal Analysis Test Vehicle (MATV) subjected to a modal test

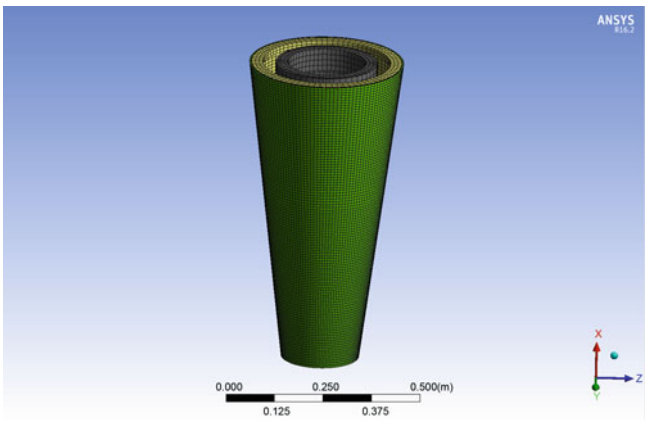

Fig. 1.2 The finite element model of the MATV modelled in Ansys

1.3 Gathering the "Truth Data"

The sole purpose of the MATV structure is to aid research programmes, and as such, it has never been deployed in-service. This means that no in-service vibration data exists for the MATV and it was necessary to self-generate this "truth data" as part of the research. There were a number of requirements associated with this process; (1) the vibration environment needed to be severe, (2) the excitation should be random in nature, (3) the excitation was to be distributed over the outer surface of the MATV, and (4) the MATV structure must be supported in a free-free configuration. The requirements above were to ensure that the "truth data" would be representative of data obtained from freely flying aerospace and defence structures.

The most efficient way to meet the above requirements was to carry out a series of acoustic tests in a reverberant chamber. The Institute of Sound and Vibration Research (ISVR) laboratory at the University of Southampton was selected as the preferred location and is shown in Fig. 1.3. Acoustic excitation was delivered into the reverberant chamber by exhausting high flowrate air through a sound horn. The sound waves then reflected off the walls and ceiling to establish a diffuse acoustic field (i.e. distributed and non-directional), whose magnitude and spectral shape was controlled by a system which utilises microphones situated near the structure as demonstrated in Fig. 1.4. The MATV structure was suspended using slings in one corner of the room. This establishes a smaller "pseudo room" where acoustic sound levels are far higher than in the general room space, whilst still ensuring a diffuse excitation field.

Fig. 1.3 The reverberant chamber at the ISVR in the University of Southampton

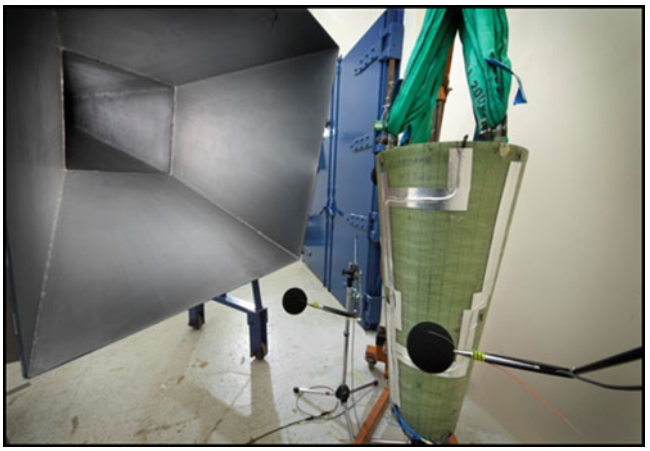

Fig. 1.4 A close-up view of the acoustic test setup showing the outlet of the sound horn and the control microphones

The MATV structure was subjected to diffuse acoustic excitation at "low" (130 dB), "medium" (145 dB) and "high" (155 dB) sound pressure levels for approx. 1 min at each level, with the sound pressure spectrum being controlled to be predominantly flat (i.e. white noise) across a frequency range of 50–2000 Hz. Ten tri-axial accelerometers were mounted throughout the MATV structure and recorded 30 channels of acceleration during the acoustic tests. A sample of three acceleration time-histories recorded by an accelerometer at the large diameter end of MATV is shown in Fig. 1.5. An informative way to view the data is to observe it in the frequency domain in the form of Power Spectral Density (PSD) plots as demonstrated in Fig. 1.6. The PSD plots show that the structure is generally linear (homogeneity) over the excitation levels observed in the acoustic tests, allowing for future interpolation and reasonable extrapolation if required. It should be noted that only the "high" level data (155 dB) is used in the remainder of this paper.

1.4 Deriving a Test Specification (Target Spectra) for an IMMAT Test

A traditional test specification provides a target for the laboratory test which, if achieved, will produce similar damage potential to the test structure as seen in-service. An IMMAT test specification goes one stage further by trying to replicate the actual environment. It does this by utilising high-fidelity data from the in-service environment, in this case the acoustic test data. This is unlike traditional test specifications whose curves are heavily sanitised through a process known as "enveloping". Both traditional and IMMAT test specifications are designed to draw out potential failures in the test laboratory before they are seen in-service.

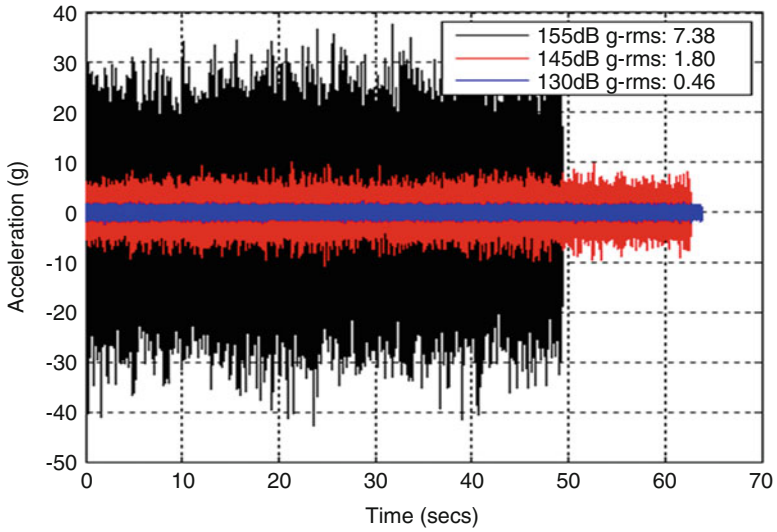

Fig. 1.5 Acceleration time-histories recorded during the acoustic test at the large diameter end of the MATV structure (sensing in a radial direction)

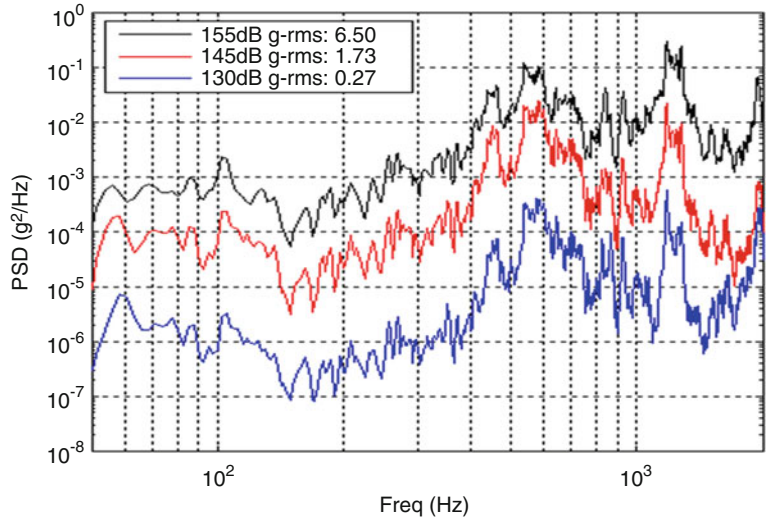

Fig. 1.6 Power spectral density (PSD) plots obtained from the data recorded in the acoustic tests

The first consideration when developing a test specification is to consider the vibration control locations/directions, i.e. the positions at which the test engineer wishes the vibration to be controlled. Previous work has shown that it is beneficial to select control locations which are spread over the outer surface of the structure and sensing in all directions simultaneously [1]. The rationale for this is that if the outer surface is behaving in a representative manner then the internal components will also. Previous work also demonstrated that it is beneficial to select control positions which were not in close proximity to any exciters. All of these factors were considered when selecting control positions.

A high number of vibration control channels leads to a large test specification dataset which, in turn, results in a labour intensive process to input the data into the vibration controller. This is time-consuming and increases the risk of human error and as such a practical limitation of 9–12 control channels is imposed. With this in mind, three locations on the outer surface, each measuring in three orthogonal directions, were selected for the control positions/direction, i.e. nine control channels.

When conducting an IMMAT test with nine control channels, the vibration controller required nine PSDs and 36 Cross Spectral Densities (CSDs). The PSDs were taken directly from the measurements obtained in the 1 min acoustic test at high level at the associated positions, as shown in Fig. 1.7. The test specification covered a frequency range of 50–2000 Hz as this was the main excitation frequency range in the acoustic environment. The test specification also required the 36 unique Cross Spectral Densities (CSDs) which provides information regarding the phase and correlation between all of the control locations. These CSDs were obtained directly in the laboratory prior to the IMMAT test using the “buzz test” developed in earlier work [1].

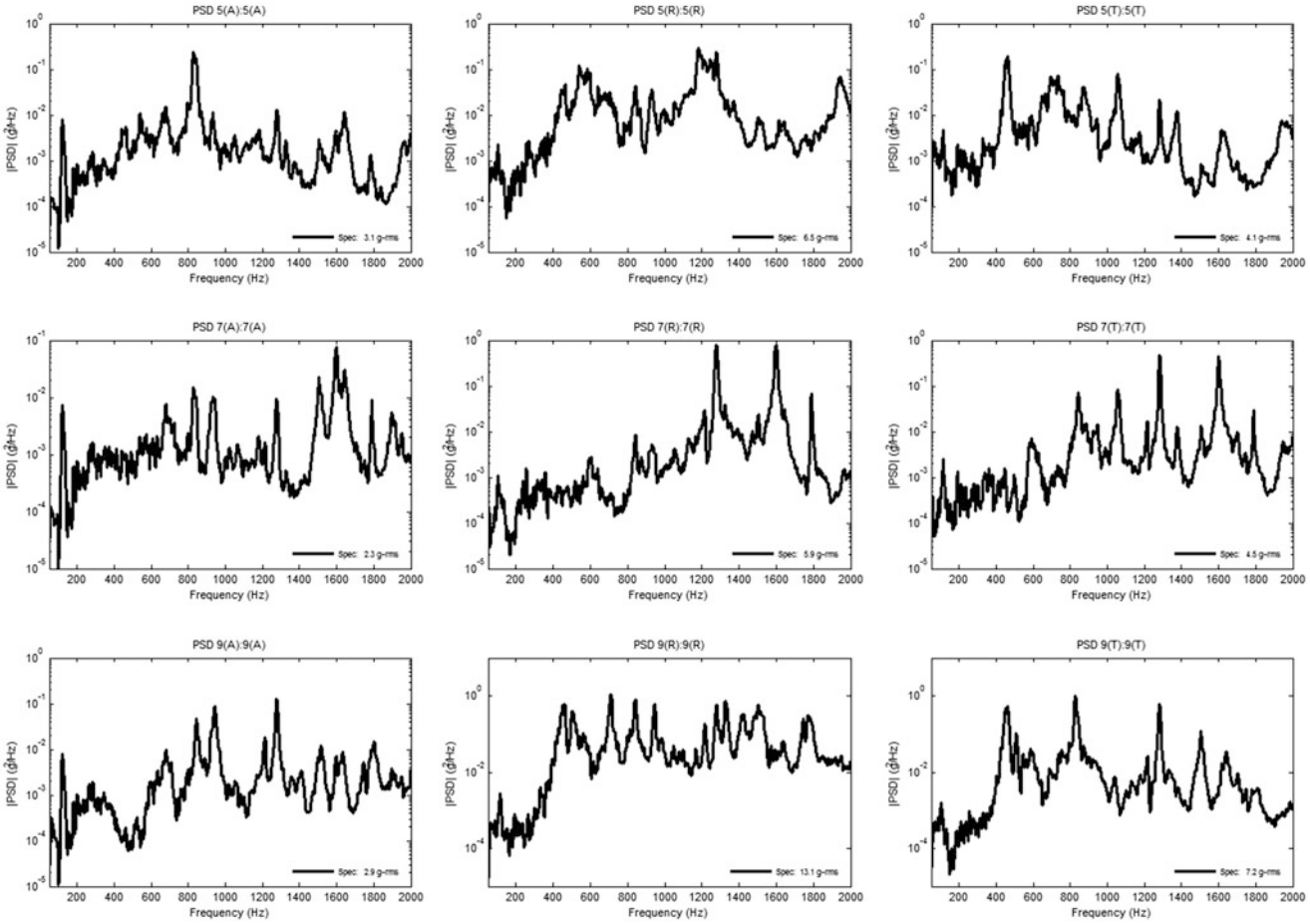

Fig. 1.7 The nine PSDs which form part of the test specification (note, the unique 36 CSDs are not shown)

1.5 Planning the IMMAT Test

It is crucial to the success of an IMMAT test to select adequate locations to excite the structure. These positions must be able to excite specific resonances and to the vibration levels observed in the acoustic test. There were an infinite number of exciter patterns which could have been selected to excite the MATV structure and it was important to make a scientifically informed decision—the FE model provided the means for making such a decision.

It has been shown on numerous occasions that using an FE model to "rehearse" a test, otherwise known as "virtual testing", gives a far greater chance of success than engineering judgement alone. It was decided to use the updated MATV FE model to develop a Virtual IMMAT algorithm, which would allow the test engineer to rehearse the IMMAT test of the MATV structure.

The Virtual IMMAT algorithm was developed in Matlab in order to determine the excitation locations and to predict the expected force levels required to excite MATV to meet the test specification. The code was developed by the author in Matlab and, in order to aid usability, was embedded within a Graphical User Interface (GUI), as shown in Fig. 1.8. The data utilised from the FE model is the geometry, modeshapes and natural frequencies, and as the test planning process need only be applied to regions of the structure which shakers can be physically attached to, only the outer skin of the MATV FE model is required in the Virtual IMMAT algorithm.

The algorithm used in Virtual IMMAT is based off standard multi-input multi-output (MIMO) matrix mathematics which links the vibration response to the forces imparted and the structure transfer functions, further details can be found in references [1, 5]. The algorithm is an iterative process which essentially keeps adding exciter forces until the code predicts that the specification will be met (to be agreed by the user), whilst ensuring low exciter force requirements.

The Virtual IMMAT algorithm was run on the MATV FE model and resulted in the test plan configuration shown in Fig. 1.8. From this screenshot, it is difficult to see the precise location of the exciters, but these will become apparent later

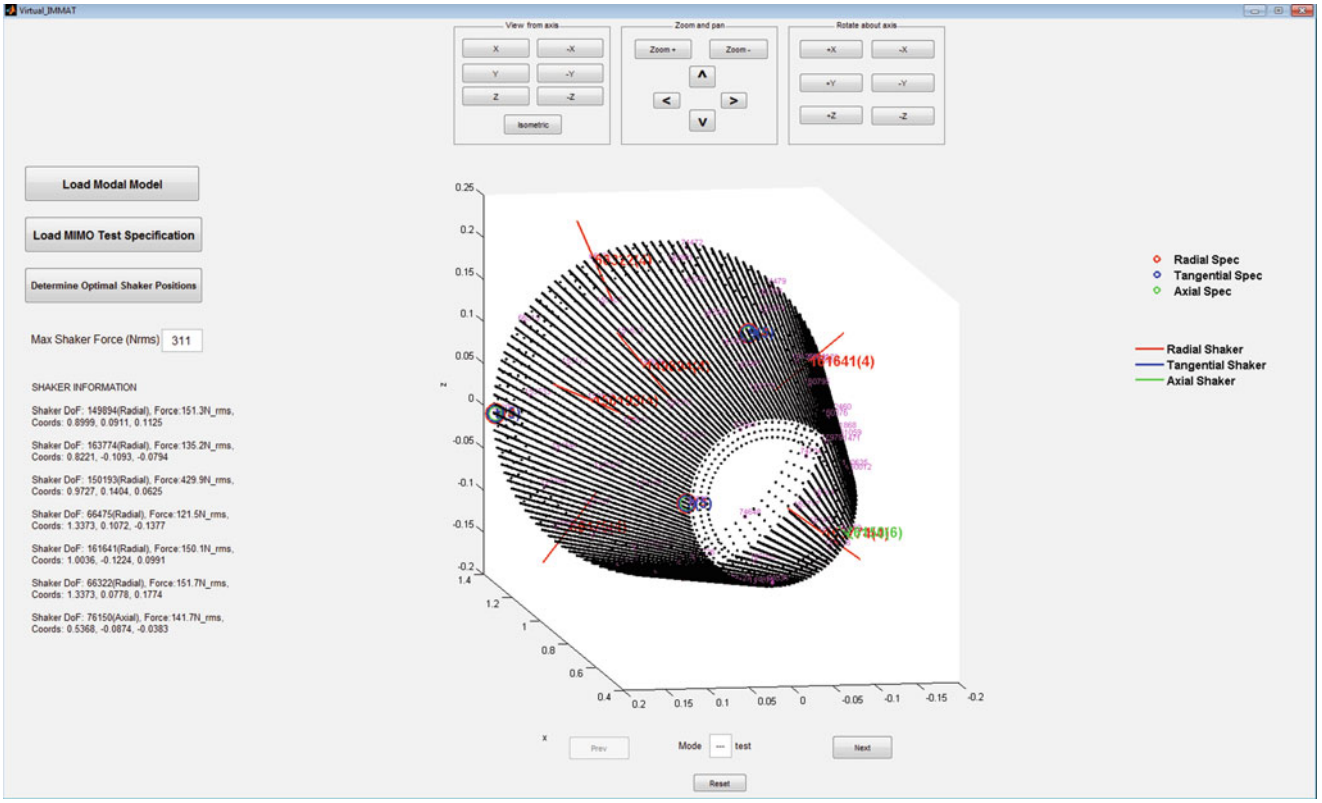

Fig. 1.8 The virtual IMMAT GUI showing the test plan for the IMMAT test of MATV

when viewing the physical test setup. The test plan configuration consisted of seven exciters, six exciting in a radial direction at locations spread over the external surface of the structure and one exciting in an axial direction at the small diameter end. It should be noted that prior to executing this test plan, all options of adding a tangential exciter were removed from the dataset. This is because no obvious torsional excitation occurred during the acoustic test and the addition of any shakers exciting in a tangential direction adds unnecessary complexity.

When arranging shakers around a structure, there is a minimum separation distance between them to allow them to fit. For this reason, the candidate set of exciter positions were reduced prior to test planning activities to ensure that no two exciters could be within a distance of 0.1 m. This reduced candidate set not only ensures this minimum separation of shakers, but also has the added advantage of significantly increasing the speed of the algorithm.

1.6 The IMMAT Test

The test setup followed the configuration that was specified in the Virtual IMMAT algorithm and is shown in Figs. 1.9 and 1.10. The MATV structure was suspended from lifting slings in order to replicate the boundary conditions observed in the acoustic test. Before describing the shaker configuration, it is worth pointing out that considerable time was spent attempting different methods of supporting the shakers and attaching them to the structure. It is not necessary to describe this process in detail, and what is given here is a description of the final setup, and any pertinent learning points.

Some of the initial shaker configurations were designed to make locating and aligning the shakers a simple process. This was done by intuitively placing shakers such that they were aligned to excite in the Y or Z (lateral) axes only. This practice was carried out to investigate whether it was necessary to use a scientific test plan, i.e. the Virtual IMMAT algorithm, or whether engineering judgement would suffice. These initial setups were unsuccessful at either exciting to the necessary levels or controlling the vibration response to match the PSD profiles of the test specification. This showed that it is vital to use some form of scientific test plan method such as the Virtual IMMAT algorithm.

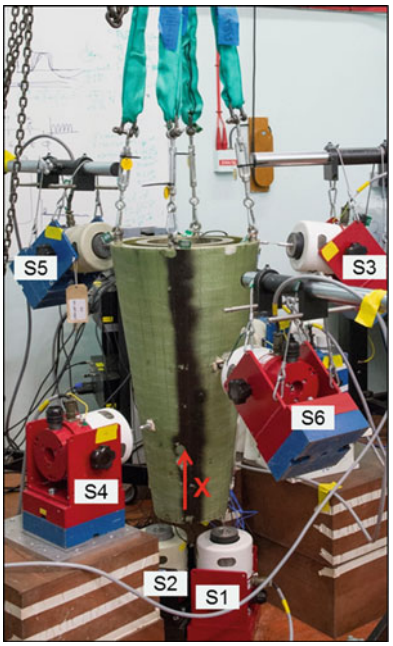

Fig. 1.9 The test setup for IMMAT of MATV showing suspension slings and shakers S1–S6

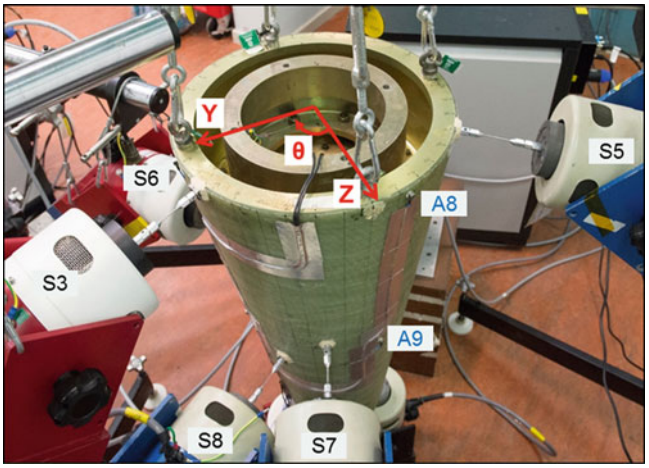

Fig. 1.10 The IMMAT test setup viewed from above showing shakers (S3 and S5–S8) and two control accelerometers (A8 and A9)

The radial shakers were attached to the outer surface of the MATV at the positions specified by the Virtual IMMAT test plan using thin drive rods. The drive rods were relatively short to ensure that their natural frequencies were high and that a high level force (and therefore energy) can be delivered through them within the test frequency range. The drive rods were made of thin (1.57 mm) "piano type" steel wires to reduce moment excitation to the structure.

The test plan specified that only one axial shaker was required for the IMMAT test. However, it was decided that two axial shakers should be used as the axial shakers in the physical setup partially support the mass of the structure. In addition, the axial shakers excite in a direction which is collinear with the centre of mass and there are only a few modes in the axial direction, leading to a high dynamic mass.

The shakers were connected to suitable power amplifiers, which in turn, were supplied by excitation voltages from a Siemens Leuven Measurement Systems (LMS) Supervisory Control and Data Acquisition System (SCADAS) multi-axis vibration controller. All ten tri-axial accelerometers were connected to the same LMS system resulting in 30 data input channels, nine of which were used for vibration control, whilst the remaining 21 were recorded only.

Pre-cursor checks revealed that any attempt to match the full test specification over the entire frequency range risked damaging valuable assets such as shakers and amplifiers. It was decided to carry out two reduced IMMAT tests:

- Test 1—full-level vibration over half the frequency range (50–1100 Hz)
- Test 2—reduced-level vibration over the entire frequency range (50–2000 Hz)

The two IMMAT tests were run for 20 s each as this was similar to durations of severe environments of in-service systems. In order to run Test 2 over the full frequency range, the test specification PSD amplitudes were reduced by a factor of approx. 9:1, which leads to a reduction in the acceleration rms by a factor of approx. 3:1.

1.7 Results and Discussion

1.7.1 Test 1

The acceleration PSDs obtained from IMMAT Test 1 (red) for the nine control channels are shown in Fig. 1.11 and are overlaid against the test specification (black). The plots also show the g-rms values associated with each of the test specification and IMMAT PSDs. It is apparent from the curves that the profile and level of the IMMAT acceleration PSDs generally match those of the test specification with some small frequency portions showing evidence of notable over-testing and under-testing. Eight of the nine graphs show that the IMMAT g-rms values are within −4 to +21% of the test specification value, which indicates that the overall IMMAT vibration levels are very representative and tend to be slightly conservative.

During the execution of Test 1, it was apparent that the shakers, and the associated drive rod apparatus, were approaching their power and strength limits respectively. This is due to the high vibration levels excited (up to 11 g-rms) with relatively small shakers and mechanical connections which are primarily designed for low force-level modal tests. This is likely to be the main cause of regions of deviation between the test specification and IMMAT curves.

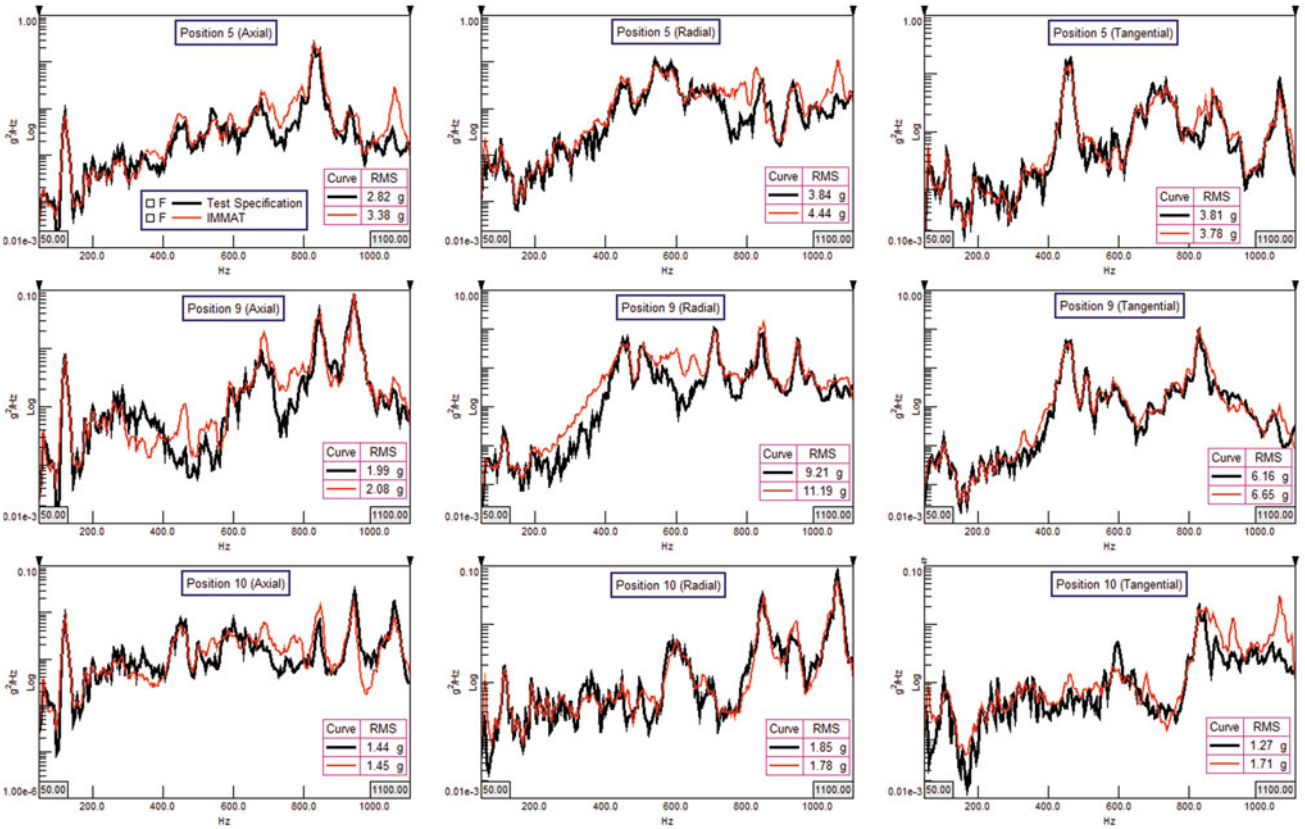

Fig. 1.11 Acceleration PSDs from IMMAT Test 1 (*red*) at the control locations versus the test specification (*black*)

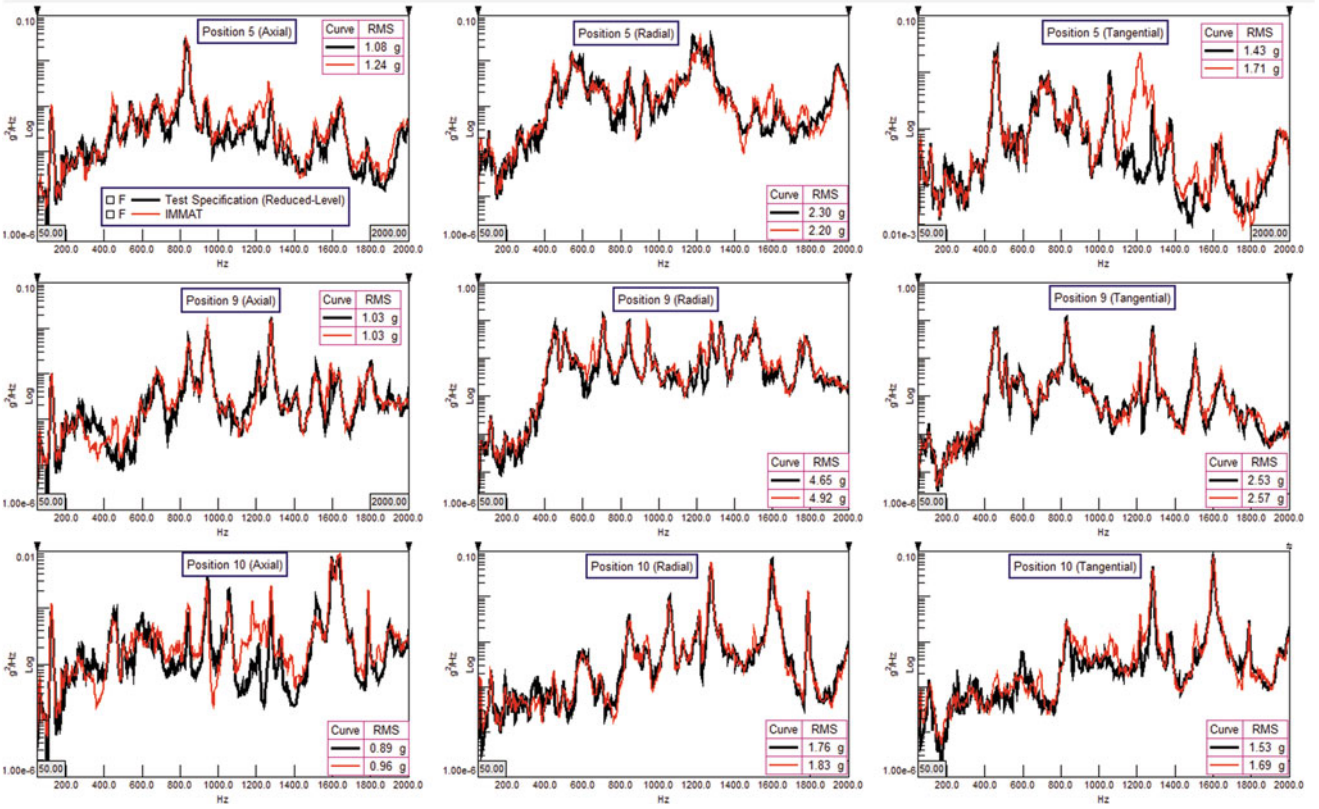

Fig. 1.12 Acceleration PSDs from IMMAT Test 1 (*red*) at the control locations versus the test specification (*black*)

1.7.2 Test 2

The acceleration PSDs obtained from IMMAT Test 2 (red) for the nine control channels are shown in Fig. 1.12 and are overlaid against the test specification (black). It is apparent from the curves that the profile and level of the IMMAT acceleration PSDs are an excellent replication of the test specification, and therefore the acoustic test. In addition, all of the nine graphs show that the IMMAT g-rms values are within −4 to +20% of the test specification value. Again, this shows that the overall IMMAT vibration levels are very representative and tend to be slightly conservative.

At a few small frequency portions there is evidence of over-testing and under-testing. The most notable example is the severe over-testing at 1200 Hz on some of the plots and the reasons for this are unclear.

1.8 Conclusions

This study has shown that the IMMAT technique can be scaled-up to test a relatively large and heavy structure. The technique provided an excellent frequency-domain replication of the acoustic environment at multiple locations and directions on the MATV structure. In addition, the vibration levels achieved were similar to those observed in harsh aerodynamic and acoustic environments, particularly within the aerospace and defence sectors. Furthermore, an IMMAT test excites all directions simultaneously and eliminates the need to carry out sequential X, Y and Z tests which are time consuming and introduces ambiguity in the form of cross-axis excitation. Further areas of development include improved selection of exciter and control locations and increasing the power capabilities of the shaker setup. These will further enhance the IMMAT technique and make it attractive for qualification programmes of real-world structures.

References

1. Daborn, P.M.: Smarter dynamic testing of critical structures PhD Thesis, University of Bristol, Bristol (2014)
2. Daborn, P.M., Ind, P.R., Ewins, D.J.: Replicating aerodynamic excitation in the laboratory. In: Proceedings of IMAC XXXI, Garden Grove, 2013
3. Daborn, P.M., Roberts, C., Ewins, D.J., Ind, P.R.: Next-generation random vibration tests. In: Proceedings of IMAC XXXII, Orlando, 2014
4. Daborn, P.M., Ind, P.R., Ewins, D.J.: Enhanced ground-based vibration testing for aerodynamic environments. Mech. Syst. Signal Process. **49**(1), 165–180 (2014)
5. Ewins, D.J.: Modal Testing-Theory, Practice and Application, 2nd edn. Research Studies Press Ltd, Baldock (2000)

Chapter 2
6-DOF Shaker Test Input Derivation from Field Test

Michael Ross, Laura D. Jacobs, Greg Tipton, Garrett Nelson, Kevin Cross, Norman Hunter, and Julie Harvie

Abstract Six degree of freedom (6-DOF) subsystem/component testing is becoming a desirable method, for field test data and the stress environment can be better replicated with this technology. Unfortunately, it is a rare occasion where a field test can be sufficiently instrumented such that the subsystem/component 6-DOF inputs can be directly derived. However, a recent field test of a Sandia National Laboratory system was instrumented sufficiently such that the input could be directly derived for a particular subsystem. This input is compared to methods for deriving 6-DOF test inputs from field data with limited instrumentation. There are four methods in this study used for deriving 6-DOF input with limited instrumentation. In addition to input comparisons, response measurements during the flight are compared to the predicted response of each input derivation method. All these methods with limited instrumentation suffer from the need to inverse the transmissibility function.

Keywords Multi-input multi-output (MIMO) • 6-DOF vibration • Multi-axis vibration • Environmental test specification • Input derivation

2.1 Introduction

During typical field tests of systems, it is rare to have sufficient instrumentation to measure or derive the six degree of freedom (6-DOF) inputs to either a subsystem or component. These tests are designed to subject an instrumented system to environments such as transportation, handling, and flight as would be seen in its final operating environment. Subsequently, the results of these tests can be used to gain an understanding of the system's behavior during these environments. Multi-axis vibration testing is gaining popularity as a method to simulate these environmental conditions in a lab setting. It has been shown that when compared to other lab test methods, full 6-DOF testing produces a more realistic stress state in the subsystem or component [1].

A key element to the successful simulation of a field environment with multi-axis shaker systems in the laboratory is the input specification which is used to define the desired dynamics of the test. This paper explores four different methods of deriving these inputs for a 6-DOF shaker system given the absence of a direct measurement of the 6-DOF inputs in field data. Each method requires the development of a transmissibility function, which will need to be inverted during the derivation process. In addition to numerical errors caused by this inversion, there may be additional errors encountered due to the use of a different unit in the field and laboratory tests, as well as a change in boundary conditions between the two test environments. By construct, the different derivation methods try to match responses at key locations during the laboratory test to those in the field. Accordingly, the inverse methodologies which were implemented may potentially correct some of these errors.

An accompanying paper discusses the experimental set-up and results of the laboratory tests conducted [2]. Given that the ultimate goal of these tests is to recreate the field environment, the response of the system in the lab is compared to that measured in the field. A close agreement between these two datasets is used as an indication of the performance of each specification derivation method explored. This paper uses the transmissibility function and the derived inputs obtained from each method to make predictions of the dynamic responses of the system under investigation. Subsequently, these responses are compared to those originally obtained in the field. Each method was explored for two distinct test cases: (1) a full 6-DOF input consisting of three translations and three rotations and (2) a 3-DOF input of consisting of only the translations. In the

M. Ross (✉) • L.D. Jacobs • G. Tipton • G. Nelson • K. Cross • N. Hunter
Sandia National Laboratories, P.O. Box 5800, Albuquerque, NM 87185, USA
e-mail: mross@sandia.gov

J. Harvie
Environments Engineering and Integration Department, Sandia National Laboratories, P.O. Box 5800-MS 0840, Albuquerque, NM 87185, USA

J.M. Harvie, J. Baqersad (eds.), *Shock & Vibration, Aircraft/Aerospace, Energy Harvesting, Acoustics & Optics, Volume 9*,
Conference Proceedings of the Society for Experimental Mechanics Series, DOI 10.1007/978-3-319-54735-0_2

results presented, it will be shown that the 3-DOF input under-drives the responses, the Smallwood–Cap method [3] produces the least amount of predicted error, and that scaling has very little effect on the error. The fact that the scaling has little effect on the error is important, because it has been shown that the input spectral density matrix may not be positive semidefinite, and scaling will correct this problem [4].

2.1.1 Overall Concept

Ultimately, in this work, it is desirable to reproduce the response of a system's internal dynamics (as measured at key positions with an accelerometer) during a single field test in the laboratory with the use of 6-DOF shaker table. The following process was used as the framework for this investigation:

1. Provide an estimated flight level input to the system on the 6-DOF shaker table. Using the responses measured to this input, derive a transmissibility function, $\boldsymbol{H}(\omega)$, from the input to the response locations. The details of this step are discussed in Sect. 2.2.
2. Using actual flight test responses and the transmissibility function, $\boldsymbol{H}(\omega)$, develop a set of inputs, $\boldsymbol{S}_{xx}(\omega)$, in terms of the power spectral density matrix that will, as best as possible, replicate internal response from flight if used as input for the 6-DOF shaker table. This is discussed in Sect. 2.3.
3. Perform a forward problem to predict the responses in the lab using the transmissibility functions and the calculated inputs and compare those to the flight data. This comparison is discussed in Sect. 2.4.
4. Perform the 6-DOF shaker test with these inputs and compare the results to actual flight test data. The laboratory results will be discussed in the companion paper [2].

2.2 Deriving the Transmissibility Function

When deriving the transmissibility function from both the input and output responses of the system on a 6-DOF shaker, a mathematical model is constructed. The model derived from this experimental data is known as an experimentally derived model (EDM), $\boldsymbol{H}(\omega)_{EDM}$. For the remainder of this paper, the subscript EDM is assumed on all transmissibility matrices. A bold variable is used to represent either a matrix or a vector. Like all mathematical models, the EDM has certain limitations and assumptions. One assumption is that the system will remain linear. In an effort to reduce the error associated with the linear assumption, it is best to derive the transmissibility function with inputs as close to the environment that is being replicated as possible.

As previously mentioned, all methods used in this work require the use of a transmissibility function. Typically, this frequency dependent function is defined in a simple input/output system as

$$\boldsymbol{Y}(\omega) = \boldsymbol{H}'_{\boldsymbol{xy}}(\omega)\,\boldsymbol{X}(\omega)\,, \tag{2.1}$$

where $\boldsymbol{Y}(\omega)$ is a column vector representing the Fourier transforms of the output responses, $\boldsymbol{H}(\omega)$ is the transmissibility matrix, and $\boldsymbol{X}(\omega)$ is a column vector representing the Fourier transform of the inputs. When using random vibration data, the transmissibility matrix can be found using the following form [5].

$$\boldsymbol{H}_{\boldsymbol{xy}}(\omega) = \boldsymbol{G}_{\boldsymbol{xx}}^{-\dagger}(\omega)\,\boldsymbol{G}_{\boldsymbol{xy}}(\omega)\,, \tag{2.2}$$

where $\boldsymbol{G}_{xx}(\omega)$ is the input spectral density matrix, $\boldsymbol{G}_{xy}(\omega)$ is the input/ouput cross-spectral density matrix, and the superscript $[\,]^{-\dagger}$ represents the Moore-Penrose generalized inverse of the matrix. Equation (2.2) requires an input autospectral density matrix that is found from three translational accelerations $(\ddot{x}, \ddot{y}, \ddot{z})$, and three rotational accelerations$(r\ddot{x}, r\ddot{y}, r\ddot{z})$. The method to determine these six inputs is discussed next.

It has been found that these six inputs can best be replicated by using a set of tri-axial accelerometers located at the corners of the fixture [6], as seen in Fig. 2.1, and referred to as the fixture gages. The six inputs are found at a virtual location by assuming the fixture remains rigid in the frequencies of interest.

The input at the virtual location is found using an inverse method given the responses of the fixture gages. The forward problem is written as seen in Eq. (2.3).

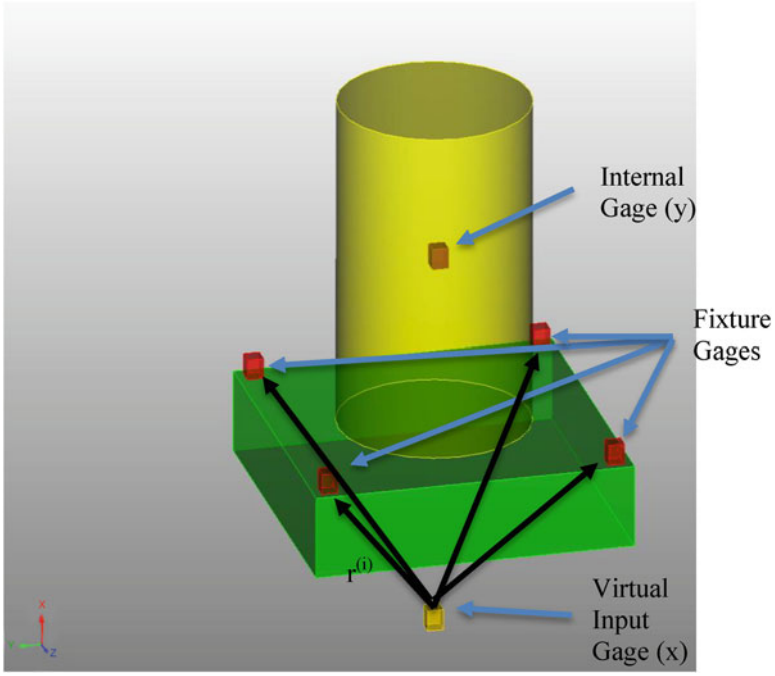

Fig. 2.1 Experimental set-up with fixture gages and a virtual input gage used to derive the transmissibility function

$$\begin{Bmatrix} \ddot{x}_1 \\ \ddot{y}_1 \\ \ddot{z}_1 \\ \vdots \\ \ddot{x}_4 \end{Bmatrix}_{12x1} = \begin{bmatrix} 1\,0\,0 & 0 & r_z^1 & -r_y^1 \\ 0\,1\,0 & -r_z^1 & 0 & r_x^1 \\ 0\,0\,1 & r_y^1 & -r_x^1 & 0 \\ 1\,0\,0 & 0 & r_z^2 & -r_y^2 \\ 0\,1\,0 & -r_z^2 & 0 & r_x^2 \\ 0\,0\,1 & r_y^2 & -r_x^2 & 0 \\ 1\,0\,0 & 0 & r_z^3 & -r_y^3 \\ 0\,1\,0 & -r_z^3 & 0 & r_x^3 \\ 0\,0\,1 & r_y^3 & -r_x^3 & 0 \\ 1\,0\,0 & 0 & r_z^4 & -r_y^4 \\ 0\,1\,0 & -r_z^4 & 0 & r_x^4 \\ 0\,0\,1 & r_y^4 & -r_x^4 & 0 \end{bmatrix} \begin{Bmatrix} \ddot{x} \\ \ddot{y} \\ \ddot{z} \\ r\ddot{x} \\ r\ddot{y} \\ r\ddot{z} \end{Bmatrix}_{6x1} \tag{2.3}$$

Equation (2.3) can be written in compact form as

$$\boldsymbol{a_f} = \boldsymbol{R}\boldsymbol{a}_x, \tag{2.4}$$

where $\boldsymbol{a_f}$ contains the fixture gage responses, $\boldsymbol{R}$ is a geometric relation matrix with r being the moment arm from the virtual location to the fixture gage, and $\boldsymbol{a}_x$ contains the desired translational and rotational inputs to the system. A least squares solution is found for $\boldsymbol{a}_x = \boldsymbol{R}^{-1}\boldsymbol{a}_f$. The virtual input accelerations and rotations in conjunction with internal responses are then used to find $\boldsymbol{G}_{xx}(\omega)$, $\boldsymbol{G}_{xy}(\omega)$, and ultimately $\boldsymbol{H}_{xy}(\omega)$.

In the experimental results reported in this work there were ten internal responses (as depicted in Fig. 2.2). Although an optimal set of internal response gages could have been found for the development of $\boldsymbol{H}_{xy}(\omega)$, all ten responses were used in the current research due to time constraints on the work conducted. Therefore, the transmissibility matrix was $10 \times 6 \times nfreq$, where *nfreq* is the number of discrete frequencies used for analysis. This paper presents $\boldsymbol{H}_{xy}(\omega)$ as a 2D matrix with the knowledge that it is solved at each frequency.

The first step in the verification process is assuring that the $\boldsymbol{H}_{xy}(\omega)$ matrix is of proper rank and well-conditioned. This is performed throughout each derivation method in this study. A large condition number is a good indicator of an ill-conditioned matrix. "As the condition number increases by a factor of ten; it is likely that one less digit of accuracy will be obtained in

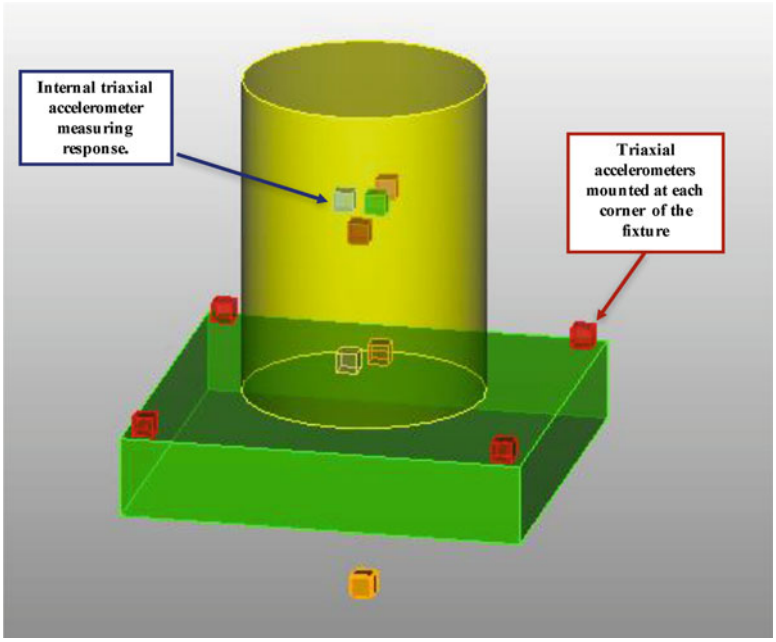

Fig. 2.2 Notional depiction of internal accelerometers

the solution" [7]. Generally, a double precision matrix provides 15 significant decimal digits [8]. Thus, a condition number of 1×10^{15} would indicate a singular matrix. In this study, any condition number below 5×10^{3} is considered appropriate.

2.3 Deriving the 6-DOF Shaker Table Input Given Flight Data

Once a transmissibility function is found for the test hardware (see Sect. 2.2), the various methods can be used to derive a 6-DOF input that is applicable for the test equipment. The 6-DOF input is in the form of an input spectral density matrix, denoted as $\boldsymbol{S}_{xx}(\omega)$, which is specified with coherence and phase for the off diagonal terms. It is imperative that $\boldsymbol{S}_{xx}(\omega)$ remain positive semidefinite, and checks are applied to assure this in each method. The four specific methods explored are discussed in the following subsections.

2.3.1 Method 1: PINV

The PINV method uses the typical input-output relation for linear systems, Eq. (2.1), but solving for the inputs as follows:

$$\boldsymbol{X}(\omega) = \left[\boldsymbol{H}_{xy}^{T}(\boldsymbol{\omega})\right]^{-\dagger} \boldsymbol{Y}_{\boldsymbol{flight}}(\omega), \tag{2.5}$$

where $\boldsymbol{Y}_{flight}(\omega)$ is the Fourier transforms of the acceleration responses from the field test data, $\boldsymbol{X}(\omega)$ is the Fourier transforms of the inputs, $\boldsymbol{a}_x$, and the superscript $[\ ]^T$ is the transpose of the matrix. The frequency spacing of $\boldsymbol{H}_{xy}(\omega)$ was interpolated to be the same as $\boldsymbol{Y}_{flight}(\omega)$, since $\boldsymbol{H}_{xy}(\omega)$ originally had a coarser frequency spacing. Once $\boldsymbol{X}(\omega)$ was found, it was used to calculate $\boldsymbol{S}_{xx}(\omega)$.

2.3.2 Method 2: ZINV

The input spectral density matrix can also be found from the following equation [5]:

$$\boldsymbol{S}_{xx}(\omega) = \boldsymbol{Z}_{xy}^{T*}(\omega)\, \boldsymbol{G}_{yy}(\omega)\, \boldsymbol{Z}_{xy}(\omega), \tag{2.6}$$

where $\boldsymbol{Z}_{xy}(\omega) = \boldsymbol{H}_{xy}^{-\dagger}(\omega)$, and the superscript $[\,]^{T^*}$ is the complex conjugate transpose. As was done with the previous method, the response spectral density matrix of the field data, $\boldsymbol{G}_{yy}(\omega)$, was interpolated to match frequency spacing of $\boldsymbol{H}_{xy}(\omega)$. As seen in the expression for the input spectral density matrix, this method also requires the inverse of the transmissibility function; however, for this particular approach two of such inverses are required.

2.3.3 Method 3: Scaling

This method explores the effect of scaling the results from Method 2: ZINV. Smallwood [4] developed a scaling method that assures the input matrix is positive semidefinite. In this study, all methods found a positive semidefinite input spectral density matrix; however, if straight-line specifications were developed from the inputs then scaling would be necessary. Therefore, scaling by Smallwood's method is explored to understand if there is any additional error introduced.

The scaling concept is done has follows. A new field response spectral density matrix is found by:

$$\boldsymbol{G}_{yy,scaled}(\omega) = \boldsymbol{S}_s(\omega)\,\boldsymbol{G}_{yy}(\omega)\,\boldsymbol{S}_s(\omega)\,, \tag{2.7}$$

with

$$S_{s,ii}(\omega) = \sqrt{\frac{1}{G_{yy,ii}(\omega)}}, \tag{2.8}$$

where $\boldsymbol{S}_s(\omega)$ is the scaling matrix that only has values on the diagonals, $S_{s,ii}(\omega)$, that are found from the diagonal of the original response spectral density matrix of the field data, $\boldsymbol{G}_{yy}(\omega)$. Then a scaled input spectral density matrix, $\boldsymbol{S}_{xx,scaled}(\omega)$, can be found.

$$\boldsymbol{S}_{xx,scaled}(\omega) = \boldsymbol{Z}_{xy}^{T*}(\omega)\,\boldsymbol{G}_{yy,scaled}(\omega)\,\boldsymbol{Z}_{xy}(\omega)\,. \tag{2.9}$$

This now needs to be scaled back to obtain correct values, and this is accomplished as follows:

$$\boldsymbol{S}_{xx}(\omega) = \boldsymbol{Z}_{xy}^{T*}(\omega)\,\boldsymbol{S}_s^{-1}(\omega)\,\boldsymbol{H}_{xy}^{T*}(\omega)\,\boldsymbol{S}_{xx,scaled}(\omega)\,\boldsymbol{H}_{xy}(\omega)\,\boldsymbol{S}_s^{-1}(\omega)\,\boldsymbol{Z}_{xy}(\omega)\,. \tag{2.10}$$

2.3.4 Method 4: Smallwood–Cap

The final method explored in this work is a modified version of the one developed by Cap et al. [3]. This method has two interesting features. First, and most importantly, is the feature that it modifies the response spectral density matrix of the field data, $\boldsymbol{G}_{yy}(\omega)$, such that it does not use the off diagonal terms of the matrix, but it assures that the phase and coherence is compatible with the transmissibility matrix and through an iterative process the input spectral density matrix, $\boldsymbol{S}_{xx}(\omega)$. The second interesting feature is that it uses Tikhonov regularization. Tikhonov regularization is a simple and commonly used method for ill-posed problems.

Typical Tikhonov regularization for solving the equation $\boldsymbol{Ax} = \boldsymbol{b}$, is conducted by solving

$$\widehat{\boldsymbol{x}} = \left[\boldsymbol{A}^T\boldsymbol{A} - \lambda^2\boldsymbol{I}\right]^{-1}\boldsymbol{A}^T\boldsymbol{b}. \tag{2.11}$$

In this work, it is desired to solve $\boldsymbol{H}_{xy}^{T*}(\omega)\,\boldsymbol{S}_{xx}(\omega)\,\boldsymbol{H}_{xy}(\omega) = \boldsymbol{G}_{yy}(\omega)$ for $\boldsymbol{S}_{xx}(\omega)$. This is accomplished with Tikhonov regularization in a two-step process. First in the typical Tikhonov form, Eq. (2.11), set $\boldsymbol{A} = \boldsymbol{H}_{xy}^{T*}(\omega)\,, \boldsymbol{x} = \boldsymbol{S}_{xx}(\omega)\,\boldsymbol{H}_{xy}(\omega)$, and $\boldsymbol{b} = \boldsymbol{G}_{yy}(\omega)$, then solve for $\boldsymbol{S}_{xx}(\omega)\boldsymbol{H}_{xy}(\omega)$

$$\boldsymbol{S}_{xx}(\omega)\,\boldsymbol{H}_{xy}(\omega) = \left[\boldsymbol{H}_{xy}(\omega)\,\boldsymbol{H}_{xy}^{T*}(\omega) - \lambda^2\boldsymbol{I}\right]^{-1}\boldsymbol{H}_{xy}^{*}(\omega)\,\boldsymbol{G}_{yy}(\omega)\,. \tag{2.12}$$

For clarity assign the following:

$$\boldsymbol{D}(\omega) = \left[\boldsymbol{H}_{xy}^{*}(\omega)\boldsymbol{H}_{xy}^{T*}(\omega) - \lambda^2\boldsymbol{I}\right]^{-1}\boldsymbol{H}_{xy}^{*}(\omega)\boldsymbol{G}_{yy}(\omega). \tag{2.13}$$

Thus, Eq. (2.12) can be rewritten as follows:

$$\boldsymbol{S}_{xx}(\omega)\boldsymbol{H}_{xy}(\omega) = \boldsymbol{D}(\omega) \rightarrow \boldsymbol{H}_{xy}^{T*}(\omega)\boldsymbol{S}_{xx}^{T*}(\omega) = \boldsymbol{D}^{T*}(\omega). \tag{2.14}$$

Then the second step is another Tikhonov regularization on $\boldsymbol{H}_{xy}^{T*}(\omega)\boldsymbol{S}_{xx}^{T*}(\omega) = \boldsymbol{D}^{T*}(\omega)$, where $\boldsymbol{A} = \boldsymbol{H}_{xy}^{T}(\omega), \boldsymbol{x} = \boldsymbol{S}_{xx}^{T}(\omega)$, and $\boldsymbol{b} = \boldsymbol{D}^{T}(\omega)$.

$$\widehat{\boldsymbol{S}_{xx}^{T*}(\omega)} = \left[\boldsymbol{H}_{xy}(\omega)\boldsymbol{H}_{xy}^{T*}(\omega) - \lambda^2\boldsymbol{I}\right]^{-1}\boldsymbol{D}^{T*}(\omega). \tag{2.15}$$

Iterations can be performed setting $\boldsymbol{G}_{yy}(\omega) = \boldsymbol{H}_{xy}^{T*}(\omega)\widehat{\boldsymbol{S}_{xx}(\omega)}\boldsymbol{H}_{xy}(\omega)$.

During the Tikhonov regularization, the response spectral density matrix of the field data, $\boldsymbol{G}_{yy}(\omega)$ is modified to $\widehat{\boldsymbol{G}_{yy}(\omega)}$ as follows. First, the diagonals of the original $\boldsymbol{G}_{yy}(\omega)$ are copied: $\widehat{G_{yy,ii}(\omega)} = G_{yy,ii}(\omega)$. Next, the phase and coherence of $\widehat{\boldsymbol{G}_{yy}(\omega)}$ is set to be compatible with the transmissibility matrix, $\boldsymbol{H}_{xy}(\omega)$, and the input spectral density matrix, $\boldsymbol{S}_{xx}(\omega)$. This is done by first setting.

$$\boldsymbol{C}(\omega) = \boldsymbol{H}_{xy}^{T*}(\omega)\boldsymbol{S}_{xx}(\omega)\boldsymbol{H}_{xy}(\omega), \tag{2.16}$$

During the first iteration $\boldsymbol{S}_{xx}(\omega)$ is unknown and set to a diagonal matrix with 1×10^{-6} set on the diagonals. Now the off diagonals of $\boldsymbol{C}(\omega)$ are normalized as

$$C_{ijN}(\omega) = \frac{C_{ij}}{\sqrt{C_{ii}C_{jj}}}, \forall i \neq j. \tag{2.17}$$

Then, the off diagonals of $\widehat{G_{yy,ij}(\omega)} = C_{ijN}(\omega)$. Recall that the diagonal is the same as $\boldsymbol{G}_{yy}(\omega)$. Then, the off diagonals of $\widehat{G_{yy,ij}(\omega)}$ are scaled to values closer to $\boldsymbol{G}_{yy}(\omega)$ in the following manner

$$\widehat{G_{yy,ij}(\omega)} = C_{ijN}(\omega)\sqrt{G_{yy,ii}G_{yy,jj}}, \quad \forall i \neq j. \tag{2.18}$$

2.4 Comparison Metric for Methods

The ultimate assessment of the performance of each derivation method is given by a comparison of how well the methods reproduce the field data during the actual laboratory experiment. As mentioned, these results are presented in an accompanying paper to this work. However, two comparisons can be made at this time. The first is a comparison of the inputs to the field recommended input. However, this might be misleading as the field data is from a different unit. It is possible that these methods might correct for some unit-to-unit variability and the different boundary conditions found in flight and the laboratory. The second comparison is a prediction of the responses from each method.

Each method has a 6-DOF spectral density matrix (SDM) and a 3-DOF SDM. Including the rotational values adds some complexity; therefore, this study evaluated if just using translational (3-DOF) values would be appropriate.

2.4.1 Comparison of Inputs

The autospectral densities of the derived inputs are plotted in Figs. 2.3 and 2.4, for translational and rotational degrees of freedom respectively. It is difficult to make any firm recommendations on these values. It does appear that the 3-DOF predictions would put in less energy than the 6-DOF, because the translational ASD for the 3-DOF are generally of smaller magnitude.

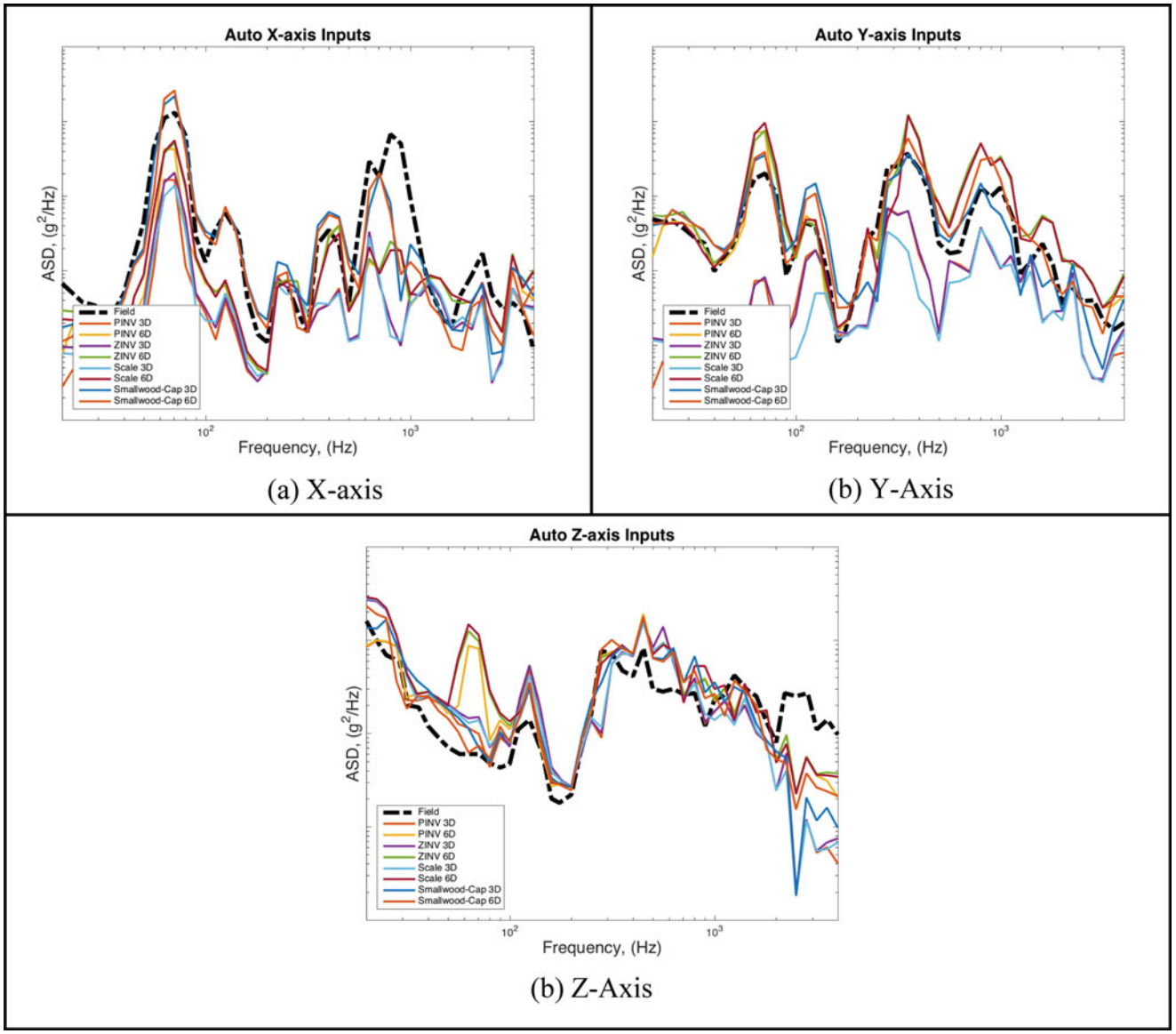

Fig. 2.3 Input comparisons of the different methods to the field data recommended input for translational values

2.4.2 Comparison of Predicted Responses to Actual Field Responses

Once the desired inputs are formed, the forward problem can be run numerically using the following equation from [9].

$$\boldsymbol{S}_{yy}(\omega) = \boldsymbol{H}_{xy}^{T*}(\omega)\,\boldsymbol{S}_{xx}(\omega)\,\boldsymbol{H}_{xy}(\omega)\,. \tag{2.19}$$

The predicted responses are denoted as $\boldsymbol{S}_{yy}(\omega)$ to keep a distinction from the actual response spectral density matrix of the field data, $\boldsymbol{G}_{yy}(\omega)$. This is of interest to see if, numerically, the desired input can be found such that $\boldsymbol{S}_{yy}(\omega)$ is a close approximation of $\boldsymbol{G}_{yy}(\omega)$. There will be some errors, since there are different units used for the field test as the one for the laboratory and that there are more internal gages as compared to inputs. In addition, there will be some numerical error associated with the interpolation done on several of the matrices.

In an effort to compare different methods, an error metric is established. First, the ASDs are filtered into 1/6th octave bands. Sixth octaves are chosen to attempt to accommodate any unit-to-unit variability. Then, an error in terms of decibels is found at each 1/6th octave frequency line, as follows:

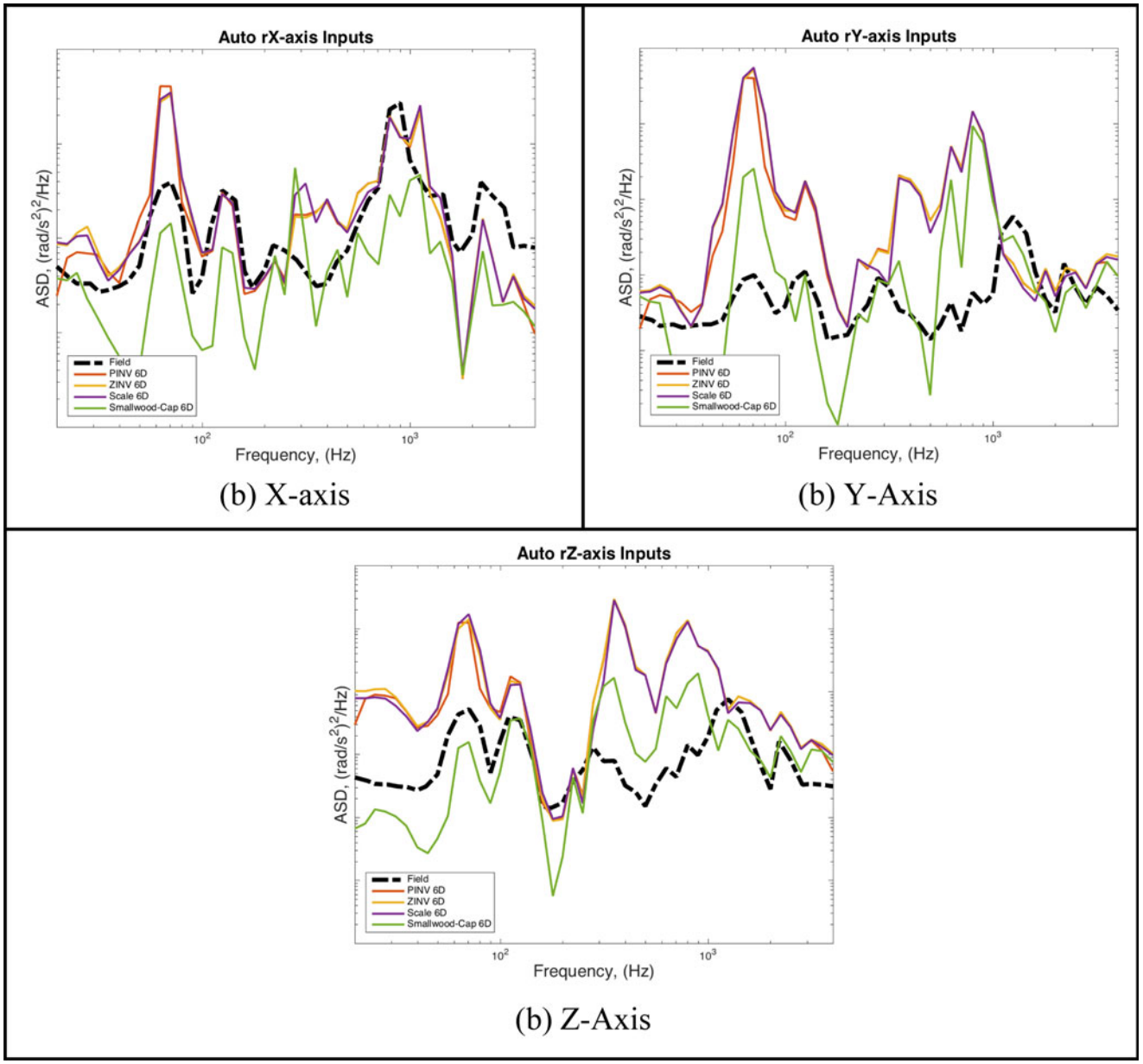

Fig. 2.4 Input comparisons of the different methods to the field data recommended input for rotational values

$$dB_{error}\left(\omega_{6th}\right) = 10 * log_{10} \frac{\boldsymbol{S}_{yy_{method}}\left(\omega_{6th}\right)}{\boldsymbol{G}_{yy}\left(\omega_{6th}\right)}. \tag{2.20}$$

Then, given the error at each frequency line in terms of decibels, three statistics can be generated for each method. The first is the statistics across each gage at each frequency line that is plotted as seen in Fig. 2.5. The second is the statistics across each gage, which is provided in Fig. 2.6. Finally, all error values at each frequency for each gage can be used to determine one mean and standard deviation for each method as seen in Fig. 2.7.

By comparing the predicted responses, some general trends have been noticed. First, the 3-DOF inputs appear to under excite the responses. Second, the Smallwood–Cap method appears to be the best method to choose, because it results in the smallest errors. Third, scaling appears to have very little effect when comparing the Scaling method to the ZINV method. This is useful information for when scaling is needed to keep the input spectral density matrix positive semidefinite.

Fig. 2.5 Error comparisons in terms of decibels at each frequency line for each method

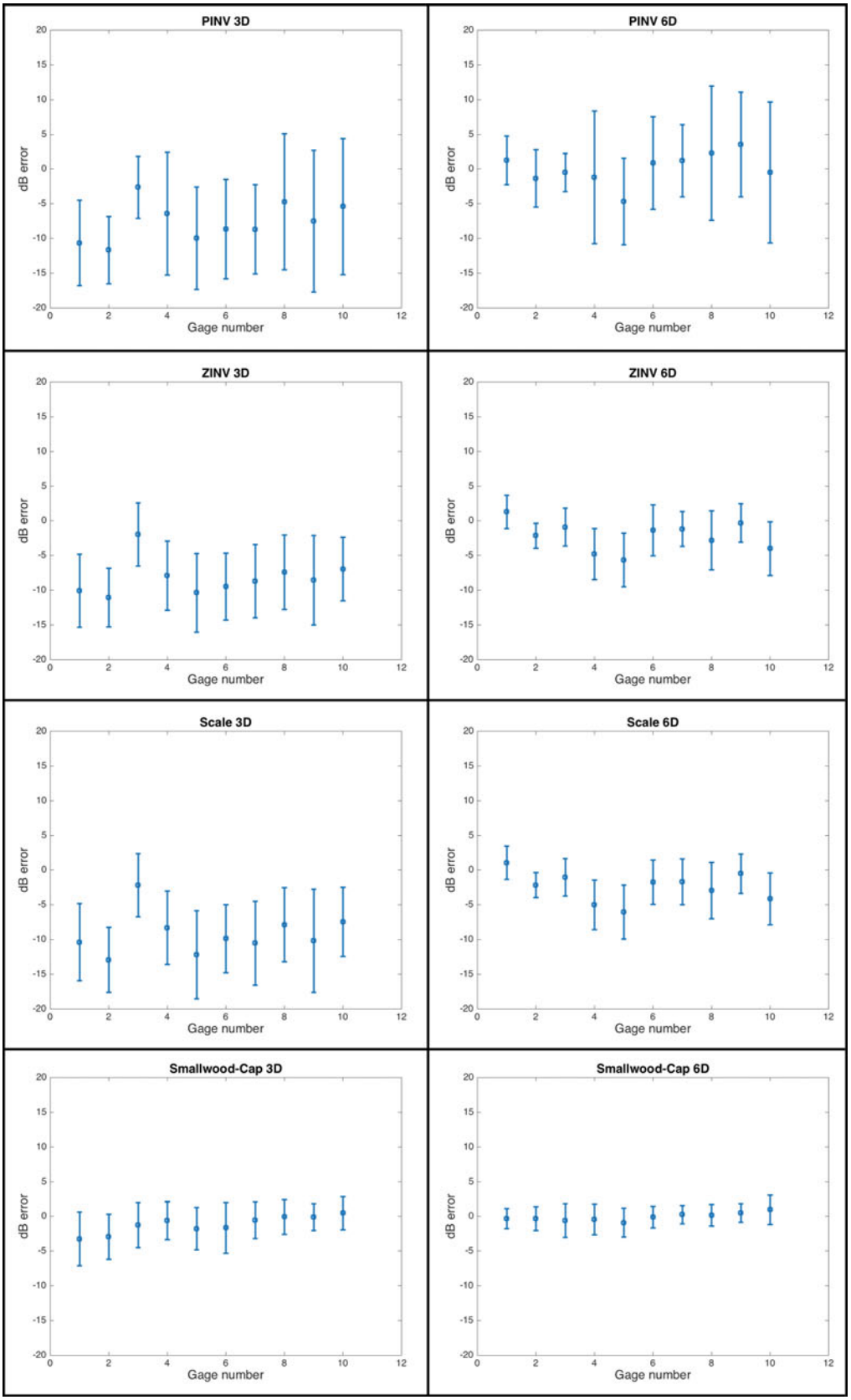

Fig. 2.6 Error comparisons in terms of decibels at each gage for each method

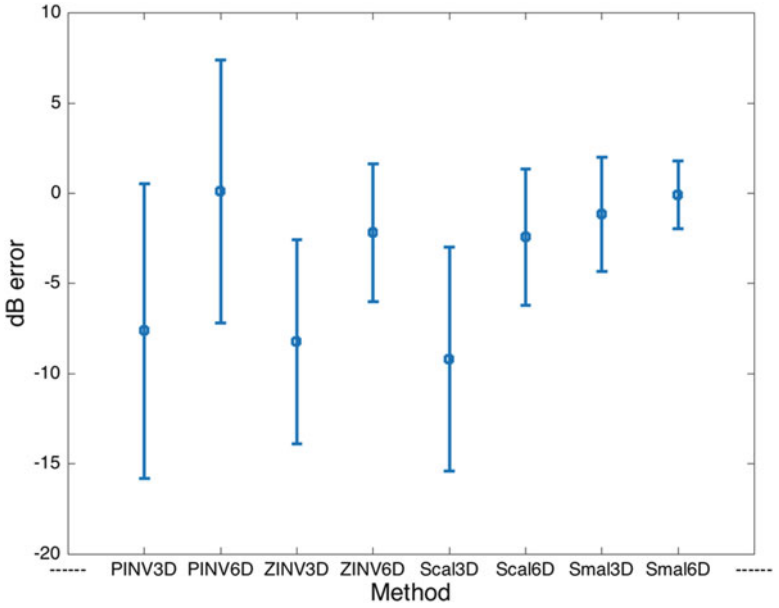

Fig. 2.7 Overall error comparisons among the different methods

2.5 Conclusions

This paper explores four different methods of deriving 6-DOF shaker inputs for a particular subsystem using an inverse methodology. An accompanying paper discusses the experimental set-up and the results of the actual experiment as compared to the flight data. This paper uses the transmissibility function and the recommended inputs to make predictions of the responses and compares those to the flight data. Each method explores using a full 6-DOF input of three translations and three rotations and only a 3-DOF input of just the translations. The predicted responses show that the 3-DOF input under excites the responses, that the Smallwood–Cap method produces the least amount of predicted error, and that scaling has very little effect on the error. Having little effect on the error is desirable for it has been shown that the input spectral density matrix may not be positive semidefinite, and scaling will correct this problem [4].

This work focused on potential methods to replicate an actual field test with a 6-DOF laboratory shaker test. Potential future work would include derivations of straight line specifications for the subsystem/component that is possible on the 6-DOF shaker. Also, the inverse problem could be proposed as an optimization problem and this might potentially derive the best input. Using an optimization algorithm could also have the benefit of assuring certain gages responses do not go below or above a certain amount, and gages could be given a weight to assure that they are met over others. Additional future work would be to explore the sources of error. It would be interesting to note if the inverse methods discussed correct for some of the errors.

Acknowledgements Sandia National Laboratories is a multi-mission laboratory managed and operated by Sandia Corporation, a wholly owned subsidiary of Lockheed Martin Corporation, for the U.S. Department of Energy's National Nuclear Security Administration under contract DE-AC04-94AL85000.

References

1. Tipton, D.G., Bitsie, F., Smallwood, D.O.: Comparison of the response of a simple structure to single axis and multiple axis random vibration inputs. In: 79th Shock Vibration Symposium, Orlando, 2008
2. Jacobs, L., Ross, M., Tipton, G., Cross, K., Hunter, N., Harvie, J., Nelson, G.: Experimental execution of 6DOF tests derived from field/flight tests. In: IMAC-XXXV Conference & Exposition on Structural Dynamics, Orange County, 2016
3. Cap, J., Tipton, D.G., Smallwood, D.O.: The derivation of random vibration specifications from field test data for use with a six degree-of-freedom shaker test. In: 80th Shock and Vibration Symposium, San Diego, October 2009
4. Smallwood, D.O.: A proposed method to generate a spectral density matrix for multiple input, multiple output (MIMO) vibration test. Shock. Vib. **14**(2), 107–132 (2007)

5. Bendat, J.S., Persol, A.G.: Random Data: Analysis and Measurement Procedures, 3rd edn. Wiley-Interscience Publication, New York (2000)
6. Owens, B., Tipton, D.G., McDowell, M.: 6 degree of freedom shock and vibration: testing and analysis. In: 86th shock and vibration symposium, Orlando, 2015
7. Atkinson, K.E.: An Introduction to Numerical Analysis, 2nd edn. John Wiley & Sons, New York (1988)
8. Kincaid, D., Cheney, W.: Numerical Analysis: Mathematics of Scientific Computing, 3rd edn. In: Pirtle, B. (ed.) Brooks/Cole (2002)
9. Wirsching, P.H., Paez, T.L., Ortiz, K.: Random Vibrations: Theory and Practice. Dover Publications, Inc., New York (1995)

Chapter 3
Frequency Based Spatial Damping Identification—Theoretical and Experimental Comparison

Matija Brumat, Janko Slavič, and Miha Boltežar

Abstract This research compares spatial damping identification methods, both theoretically and experimentally. In contrast to the commonly used damping methods (modal, proportional) the spatial damping information improves structural models with a known location of the damping sources. The real case robustness of full FRF matrix and local equation of motion methods were tested against: modal and spatial incompleteness, differences in viscous and hysteretic damping models and the effect of damping treatments. To obtain accurate results, a careful analysis of measurements in terms of reciprocity in the raw measurements, and in terms of how to preserve symmetry has to be done. It was found that full FRF matrix needs to be symmetrisized due to small deviations in reciprocity before the damping identification. Full frequency response function (FRF) matrix methods (e.g.: Lee-Kim) can identify the spatial damping if spatial and modal incompleteness are carefully evaluated, but the measurement effort increases with second order and, consequently, the size of the FRF matrix.

Keywords Spatial damping • Inverse identification • Frequency response • Modal incompleteness • Spatial incompleteness

3.1 Introduction

Numerical and analytical prediction of the structural responses depends on the identified spatial damping throughout the structure. Good damping prediction is important for validation of analytical/numerical models in civil, mechanical and aerospace engineering. Damping in linear mechanical systems is usually identified using one of the methods such as logarithmic decay [1] in time domain, continuous wavelet transform [2], the Morlet wave method [3] or the synchrosqueezed wavelet [4] in time-frequency domain or half-power point [1] and first order perturbation [5] in frequency domain. Damping identification methods form the basis of several model updating methods [6, 7], where accurate damping identification can further improve numerical models [8, 9]. Two other examples where exact damping spatial location is needed are: identification of damping sources on existing structures and precise application of damping treatment. However, typically used damping identification methods [1, 8] do not provide spatial information (damping distribution throughout the structure).

An alternative approach is to use direct damping identification methods that were developed for identification of damping distribution directly from the frequency response functions (FRF) without the transformation to the modal coordinates. One of the typically used direct methods is the Lee and Kim's dynamic stiffness method [10]. The core of the method is a inverse identification of linear damping model from the complex part of the measured data which have been found to be very sensitive to real world problems in most follow-on studies, e.g. phase error [11], noise when the modal overlap is low [5] and leakage [12]. Ozgen and Kim [12] proposed a new experimental procedure with simultaneous excitation of all nodes to overcome described measurement errors, but the procedure is not practical with lots of measurement degrees of freedom because demands as many shakers as there are measurement degrees of freedom. Some direct methods, not considered in this research, are reviewed in [5, 11, 13].

This research focuses on the modal and spatial incompleteness effect on the identification of spatial damping. Modal incompleteness deals with limited frequency span over number of modes whereas spatial incompleteness covers effects of non-measured points on the structure [14]. Modal and spatial incompleteness for spatial damping have been studied numerically [5, 15] and experimentally [11] on low DOF models.

M. Brumat (✉) • J. Slavič • M. Boltežar
Faculty of Mechanical Engineering, University of Ljubljana, Aškerceva cesta 6, 1000 Ljubljana, Slovenia
e-mail: matija.brumat@fs.uni-lj.si

J.M. Harvie, J. Baqersad (eds.), *Shock & Vibration, Aircraft/Aerospace, Energy Harvesting, Acoustics & Optics, Volume 9*,
Conference Proceedings of the Society for Experimental Mechanics Series, DOI 10.1007/978-3-319-54735-0_3

This research is organized as follows. Section 3.2 gives theoretical background to Lee-Kim frequency-domain direct damping identification method. In Sect. 3.3, the experimental research is presented. Analysis and discussion follow in Sect. 3.4 and finally conclusions are drawn in Sect. 3.5.

3.2 Theoretical Background

In this section the background of direct damping identification methods is briefly presented. Lee and Kim method is a matrix method and requires full measured frequency response function (FRF) matrix $[H]$. We begin with the general, second-order, matrix differential equation [1]:

$$[M]\ \{\ddot{x}\}(t) + [C]\ \{\dot{x}\}(t) + [K]\ \{x\}\,(t) = \{f\}\,(t), \tag{3.1}$$

where $[M]$ is the mass matrix, $[C]$ is the viscous damping matrix and $[K]$ is the stiffness matrix, respectively. Remaining parts of (3.1) are the response vector $\{x\}\,(t)$ and the force vector $\{f\}\,(t)$. Assuming a linear system and harmonic excitation/response, Eq. (3.1) can be rewritten in frequency domain as:

$$\left[[K] - \omega^2\ [M] + \mathrm{i}\,\omega\ [C]\right]\ \{X\}\,(\omega) = \{F\}\,(\omega) \tag{3.2}$$

From Eq. (3.2), the FRF matrix $[H]\,(\omega)$ is defined as:

$$\{X\}\,(\omega) = [H]\,(\omega)\ \{F\}\,(\omega) \tag{3.3}$$

and furthermore:

$$[H]\,(\omega) = \left[[K] - \omega^2\ [M] + \mathrm{i}\,\omega\ [C]\right]^{-1} \tag{3.4}$$

The dynamic stiffness matrix $[Z]\,(\omega)$ is defined as the matrix inverse of $[H]\,(\omega)$ for each frequency point ω:

$$[Z]\,(\omega) = [H]\,(\omega)^{-1} = \left[[K] - \omega^2\ [M] + \mathrm{i}\,\omega\ [C]\right] \tag{3.5}$$

Using (3.5) viscous damping matrix might be obtained directly from imaginary part of the dynamic stiffness matrix $[Z]\,(\omega)$ [10]:

$$\mathrm{imag}([Z]\,(\omega)) = \mathrm{imag}([[H]\,(\omega)]^{-1}) = \omega\ [C]\,, \tag{3.6}$$

Rearranging (3.6) to isolate viscous damping matrix $[C]$ gives:

$$[C] = \frac{1}{\omega}\,\mathrm{imag}([[H]\,(\omega)]^{-1}) \tag{3.7}$$

Method (3.7) is not limited to viscous damping [12], for example hysteretic damping matrix version is:

$$[D] = \mathrm{imag}([[H]\,(\omega)]^{-1}) \tag{3.8}$$

3.3 Experiments

An experiment was conducted on the three equal sized free-free beam specimens to compare direct damping identification methods. The specimens are: a) plain beam—beam A, b) with asymmetrically added local viscous damper—beam B and c) with constrained layer damping (CLD)—beam C, see Fig. 3.1. Beam specimens B and C have asymmetrically applied damping treatment over restricted area of the beam in order to know damping spatial location. Three samples were considered to emphasize effect of different damping treatments on the identified spatial location in later discussion. The beam A was

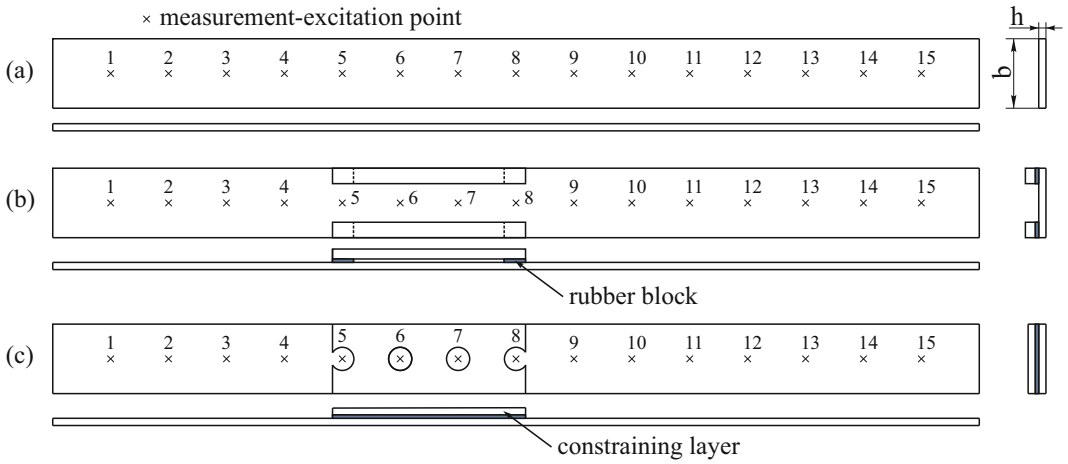

Fig. 3.1 (**a**) plain beam specimen—beam A, (**b**) beam with added discrete viscous damper—beam B, (**c**) beam with added constrained layer damper—beam C

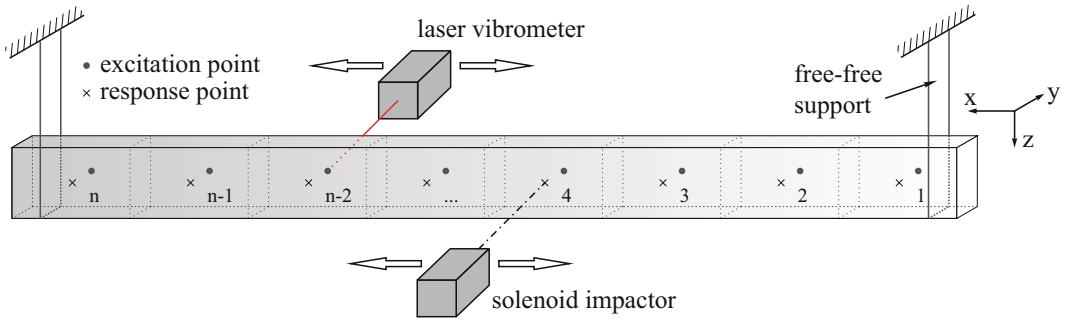

Fig. 3.2 Measurement setup

a plain steel beam with constant cross-section $h \times b = 1\,\text{mm} \times 30\,\text{mm}$, length $l = 400\,\text{mm}$, mass $m = 92.6\,\text{g}$ and Young modulus $E = 210000\,\text{MPa}$. Beam dimensions were selected to have low modal overlap and to have large number of modes in the frequency span up to 3000 Hz. Beam is shown in Fig. 3.1a. Two soft springs (stiffness $\approx 50\,\text{N/m}$) were used at each beam boundary in y-direction to limit rigid body translation after impact. The beam B was a similar steel beam as beam A, but additional viscous damper was added between points 5–8, see Fig. 3.1b. Discrete damper is based on the design by Rijnen et al. [16], each damper is made from two rubber blocks of a size $5 \times 5 \times 1\,\text{mm}$ glued with the cyanoacrylate to the beam and connected with the aluminium struts of the size $80 \times 5 \times 5\,\text{mm}$. The beam C was the steel beam used as beam A, but had attached a constrained layer damper as shown in Fig. 3.1c. The visco-elastic layer for application was 3M 112P02 damping material [17]. Steel constraining layer was of the same material and thickness as the beam to maximize damping [17]. Holes were drilled in constraining layer to measure responses of the beam, only.

3.3.1 Measurement Setup

Measurement setup is shown in the Fig. 3.2. Custom made solenoid impactor with PCB 086E80 force sensor was used for repeatable impulse excitation. Response (velocity) measurements employed Polytec PDV100 laser vibrometer. Impactor/laser based measurement allows for non-contact measurement without structural modification due to added stiffness or mass from sensors or shakers. Data acquisition and signal processing were undertaken in custom python software environment using pyDAQmx library [18] to interface NI 9215 acquisition hardware. Sampling rate was 100 kHz and signal was captured for 10 s.

To obtain full FRF matrix $[H]$ the structure was sequentially excited at 15 points and responses are measured at the same 15 points (15×15 excitation-response pairs, $n = 15$), as shown in Fig. 3.2. Each excitation-response point was measured three times to obtain the averaged H_1 estimator (mobility FRF) and later divided by $\mathrm{i}\,\omega$ in the frequency-domain to obtain receptance FRFs [1].

3.4 Analysis and Discussion

Measured responses (675: 225 points with three averages) were assembled into a full FRF matrix of size 15×15 used by the direct damping identification methods for each beam. Figure 3.3 shows example of the measured receptance magnitude FRF at the pair 15–10 for all three beams; where 15–10 denotes 15th excitation and 10th response point (the designation will be used throughout this paper). From the FRF's it can be seen that the damping treatment of beams B and C affects high-frequency region more than the low-frequency. Further, the added stiffness and mass due to damping treatment barely shifts eigenfrequencies, see Fig. 3.3.

In contrast to damping amplitudes at eigenfrequencies, the damping spatial location is in focus of this research. Before using viscous and hysteretic damping matrix identification methods, the measured FRFs have to be tested for repeatability, linearity and most importantly for FRF reciprocity. For a damping model with a symmetric damping matrix the reciprocity is expected [19]. Nevertheless, the measured FRFs deviate from reciprocity in some details (see Fig. 3.4), which is often the case in experimental measurements [11, 20]. The observed deviations of the reciprocity can be eliminated using FRF matrix symmetrisation at every frequency point using [21]:

$$[H](\omega) = 0.5\left[[H](\omega) + [H]^T(\omega)\right] \tag{3.9}$$

Any non-symmetry in the identified damping matrices after this step is due to the identification procedure only.

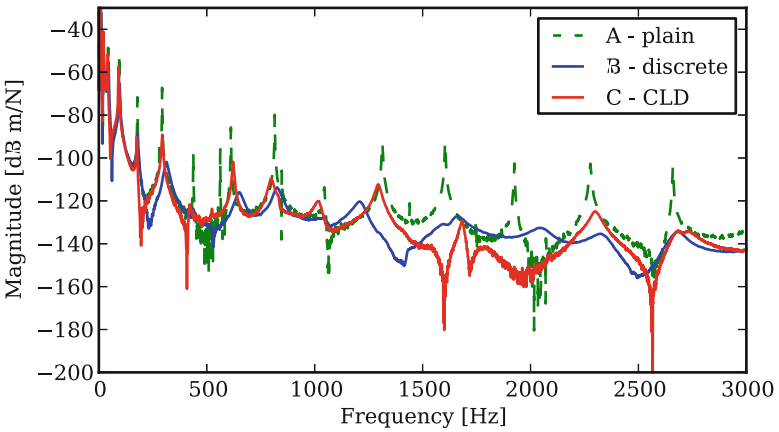

Fig. 3.3 Receptance magnitude FRF plot for point 15–10

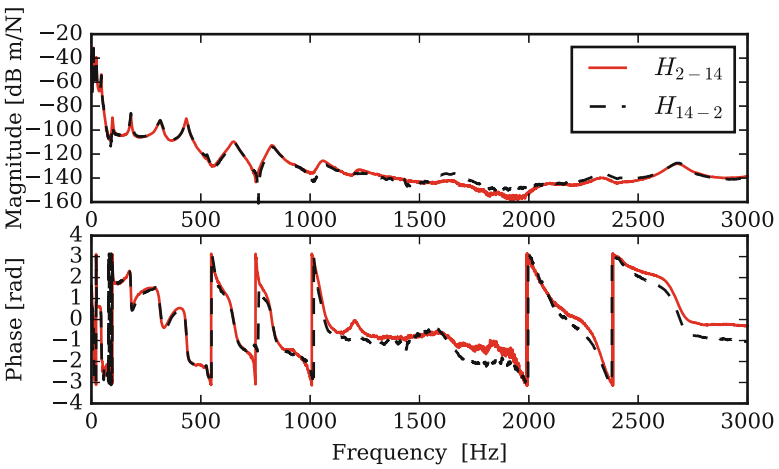

Fig. 3.4 Reciprocity FRF plot for discretely damped beam B

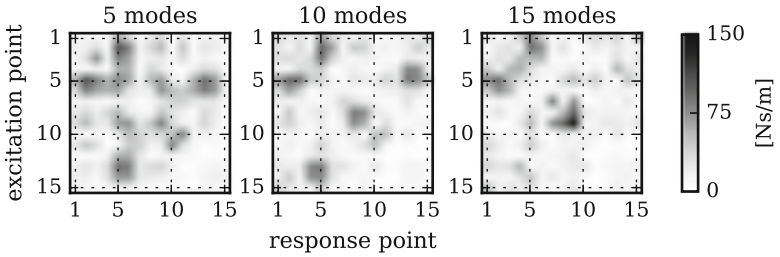

Fig. 3.5 Identified viscous damping matrix for beam B, 5, 10 and 15 modes

3.4.1 Modal Incompleteness

The modal incompleteness is presented in detail using the Lee-Kim method, see Eq. (3.7). Figure 3.5 shows the absolute values of the identified viscous damping matrix $[C]$ for beam B using a frequency range of five (0–200 Hz), ten (0–1100 Hz) and fifteen modes (0–3000 Hz). The larger numerical values (e.g. 150 Ns/m in Fig. 3.5) represent areas of higher damping. The identified matrices are symmetric.

Focusing on the identified values in Fig. 3.5 reveals higher damping values at the points of the applied damping for beam B (left point 4 and right point 9 of the discrete damper).

Comparing the high modal incompleteness with the low incompleteness model it is clear that the spatial location of the damping becomes localised when the modal incompleteness is sufficiently low, see Fig. 3.5. The frequency range of at least ten modes should be used for an accurate viscous damping location—similar conclusions were found in a theoretical study [15].

A theoretical explanation for the modal incompleteness on the identification of the spatial damping matrix $[C]$ seen in Fig. 3.5 is given in [15]. The authors conclude that it is impossible to identify the structural parameters of a real mechanical system from a FRF matrix, measured over a limited frequency range.

Similar theoretical findings were reported by Prandina et al. [15]. Dynamic stiffness matrix $[Z]\,(\mathrm{i}\omega)$ can be partitioned into measured part $[Z_1]$ and other unmeasured ones:

$$[Z]\,(\mathrm{i}\omega) = [H]^{-1}\,(\mathrm{i}\omega) = \begin{bmatrix} [Z]_1 & [Z]_2 \\ [Z]_2^T & [Z]_4 \end{bmatrix} \tag{3.10}$$

where measured part is further composed of r complex modes ψ_r and complex eigenvalues λ_r [15]:

$$[Z]_1\,(\mathrm{i}\,\omega) = \left[\sum_k \left(\psi_k\, \lambda_k^2\, (\mathrm{i}\,\omega - \lambda_k)\, \psi_k^T + \overline{\psi}_k\, \overline{\lambda}_k^2\, (\mathrm{i}\omega - \overline{\lambda_k})\, \overline{\psi}_k^T \right) \right], \tag{3.11}$$

where — denotes complex conjugation, respectively. The influence of higher modes on dynamic stiffness is amplified though λ_k^2 and consequently on identified spatial damping matrix.

3.4.2 Spatial Incompleteness

The spatial incompleteness test was made using the full FRF matrix (15 modes) with deleted rows and columns. These deleted rows and columns can be understood as degrees of freedom (DOF) that were not measured (columns represent response DOFs and rows represent excitation DOFs).

Figure 3.6 shows the identified matrix using the Lee-Kim method for four DOFs (i.e., 1, 5, 10, 15) and eight DOFs (i.e., 1, 3, 5, 7, 9, 11, 13, 15). Comparing the results for the 15 modes shown in Fig. 3.5 with Fig. 3.6 the redistribution of damping over the neighbouring spatial location is observed. The high damping area around the pair 4–9 in Fig. 3.5 (15 modes) is in the spatially incomplete cases redistributed because of the missing information. In the case of 8 DOF the redistribution is to the pair 5–11 and in case of 4 DOF over the complete damping matrix. Low DOF models also tend to have larger damping values because the amount of damping present in the structure is redistributed over fewer DOFs.

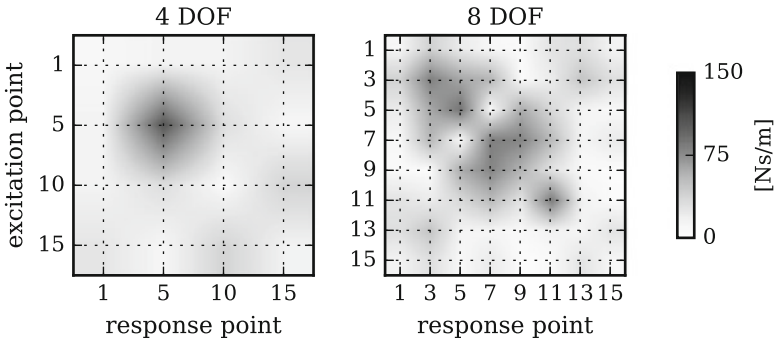

Fig. 3.6 Identified viscous damping matrix for the beam B of the reduced FRF matrix

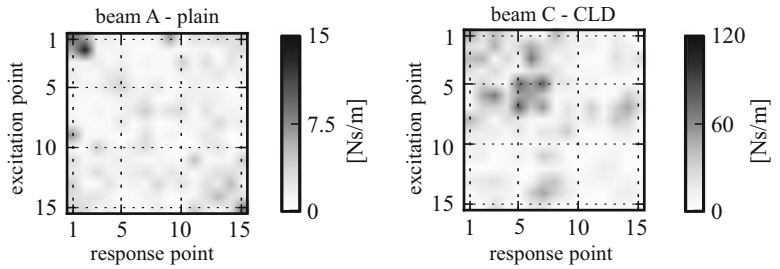

Fig. 3.7 Identified viscous damping matrices for beams A and C. Reader should be aware of different scales

The spatial incompleteness is related to the modal incompleteness [14, 15, 22], e.g., from the experimental modal analysis it is clear that the number of extracted mode shapes depends on the FRF matrix $[H]\,(\omega)$ shape.

3.4.3 Damping Treatment Effect on Spatial Location

In this section the Lee-Kim method for a frequency span of 15 modes is used to evaluate the different damping treatments. The identified viscous damping matrix for beam B was already shown in Fig. 3.5—15 modes. The identified viscous matrices for the remaining two beams are shown in Fig. 3.7. On the plain beam A there are higher damping values identified at the points corresponding to the beam boundaries, where the beam was suspended and an additional soft spring was attached, i.e., at 1–1 and 15–15. The identified damping values of the non-boundary points for beam A are two orders of magnitude lower than for beam C with the CLD treatment. Beam C has more pronounced damping values around points 5–8, which corresponds to the location of the constraining layer damping treatment. The identified damping matrices of beams A and C are also symmetric.

The relationship between the physical location of the damping treatment and the location of the damping values in the identified damping matrix is not always straightforward (example of the identified damping of the beams B and C, see Figs. 3.5 and 3.7). The major damping values occur close to the main matrix diagonal.

3.5 Conclusion

The effectiveness of experimental viscous damping spatial location identification have been analysed. Special measuring setup was made to measure full FRF matrix of size 15×15 for three different beam configurations (plain and with discrete and constrained layer damping treatments). The Lee-Kim method can also identify spatial damping but the numerical and measuring effort raises by square of measuring points. Following conclusions can be drawn:

- In experiment frequency range of 10 modes is sufficient for spatial location identification on the beam, similar to the theoretical findings of Prandina et al. [15].

- Spatial incompleteness can affect identified damping distribution.
- Damping spatial location of CLD treatment (beam C) significantly differs from the discretely damped beam B (even if it was applied at the same locations).

References

1. Ewins, D.: Modal Testing: Theory, Practice and Application, 2nd edn. Research Studies Press, Philadelphia, PA (2000)
2. Slavič, J., Simonovski, I., Boltežar, M.: Damping identification using a continuous wavelet transform: application to real data. J. Sound Vib. **262**(2), 291–307 (2003)
3. Slavič, J., Boltežar, M.: Damping identification with the Morlet-wave. Mech. Syst. Signal Process. **25**(5), 1632–1645 (2011)
4. Mihalec, M., Slavič, J., Boltežar, M.: Synchrosqueezed wavelet transform for damping identification. Mech. Syst. Signal Process. **80**, 324–334 (2016)
5. Srikantha Phani, A., Woodhouse, J.: Viscous damping identification in linear vibration. J. Sound Vib. **303**(3–5), 475–500 (2007)
6. Arora, V., Singh, S., Kundra, T.: Finite element model updating with damping identification. J. Sound Vib. **324**(3–5), 1111–1123 (2009)
7. Pradhan, S., Modak, S.: A method for damping matrix identification using frequency response data. Mech. Syst. Signal Process. **33**, 69–82 (2012)
8. Friswell, M., Mottershead, J.: Finite Element Model Updating in Structural Dynamics. Kluwer, Dordrecht (1995)
9. Mottershead, J., Link, M., Friswell, M.: The sensitivity method in finite element model updating: a tutorial. Mech. Syst. Signal Process. **25**(7), 2275–2296 (2011)
10. Lee, J.-H., Kim, J.: Development and validation of a new experimental method to identify damping matrices of a dynamic system. J. Sound Vib. **246**, 505–524 (2001)
11. Srikantha Phani, A., Woodhouse, J.: Experimental identification of viscous damping in linear vibration. J. Sound Vib. **319**(3–5), 832–849 (2009)
12. Ozgen, G., Kim, J.: Error analysis and feasibility study of dynamic stiffness matrix-based damping matrix identification. J. Sound Vib. **320**, 60–83 (2009)
13. Pilkey, D., Inman, D.: A survey of damping matrix identification. In: 16th International Modal Analysis Conference, SEM (1998)
14. Berman, A., Flannelly, W.: Theory of incomplete models of dynamic structures. AIAA J. **9**(8), 1481–1487 (1971)
15. Prandina, M., Mottershead, J., Bonisoli, E.: An assessment of damping identification methods. J. Sound Vib. **323**(3–5), 662–676 (2009)
16. Rijnen, M., Pasteuning, F., Fey, R., van Schothorst, G., Nijmeijer, H.: A numerical and experimental study on viscoelastic damping of a 3D structure. J. Sound Vib. **349**, 80–98 (2015)
17. 3M^{TM} Viscoelastic Damping Polymeres 112–130 Technical Data (2012)
18. Cladé, P.: pyDAQmx: A Python interface to the National Instruments DAQmx driver (2015)
19. Woodhouse, J.: Linear damping models for structural vibration. J. Sound Vib. **215**(3), 547–569 (1998)
20. Udwadia, F., A note on nonproportional damping. J. Eng. Mech. **135**, 11 (2009). http://ascelibrary.org/doi/10.1061/%28ASCE%290733-9399%282009%29135%3A11%281248%29
21. Bar-Itzhack, I.: Matrix symmetrization. J. Guid. Control. Dyn. **21**(1), 178–179 (1998)
22. Berman, A.: System identification of structural dynamic models theoretical and practical bounds. In: 25th Structures, Structural Dynamics and Materials Conference. American Institute of Aeronautics and Astronautics, Reston, VA (1984)

Chapter 4
Controllability of Aerospace Static Mechanical Loading Coupled with Dynamic Forces

Richard W. Weisenberger and Matthew S. Stefanski

Abstract The objective of this testing activity was to examine and verify the interactions of a hydraulic mechanical load control system loading a thin skinned aerospace structure coupled with applied acoustic vibrations. The goal was to be able to actively control the load of four hydraulic cylinders loading two end plates while an electrodynamic shaker attached to the skin imposed simulated acoustic loading. The objective was to achieve mechanical load control within ±1% of desired static load for each load control channel. The mechanical loads applied ranged from the noise floor to Design Limit Load (DLL) (2000 lbf) using varying ramp rates in conjunction with the random dynamic vibration. The presence of dynamic load introduced an error of 0.4% DLL with traditional PID tuning methods. The testing also quantified the suitability of 2 channel master/slave control vs. 4 channel individual control. It was determined that using a dedicated servo control channel (non-slaved servo channel) per load cylinder drops the maximum difference to 2.2% of full scale applied load (25% DLL), as opposed to 7.8% of full scale applied load (25% DLL) when the top two load cylinders are slaved to one servo and the bottom two load cylinders are slaved to another. This amounted to a 72% reduction in error using non-slaved servos. The test activity's technical approach and test data will be presented.

Keywords Dynamic static mechanical loading structure

4.1 Overview

The testing performed was a risk reduction activity, which supports a larger more complex and sophisticated combined thermo-acoustic static mechanical test. Performing static mechanical loading in conjunction with acoustic/dynamic loading had not been previously accomplished in this manner. With this approach verified, Air Force Research Laboratory's Combined Environment Acoustic Chamber in Building 65, at Wright-Patterson Air Force Base in Dayton Ohio, will be able to impose static mechanical load, acoustic loading, and elevated temperature (excess of 1200 °F) in a combined nature. This allows for a multidisciplinary validation of structural FEM in said environments.

4.2 Objective

The objective of this testing is to verify that static mechanical load and dynamic load can be simultaneously applied and correctly controlled on a representative aerospace vehicle subcomponent structure. Additionally, this test requires multi-channel static load control, and investigates the suitability of 2 channel vs. 4 channel control for future testing requirements. To this end, a large range of loads from low scale (near noise floor) to high scale, as well as very slow mechanical ramp rates were tested.

Distribution Statement Distribution A. Approved for public release: distribution unlimited. Case Number: 88ABW-2016-5380

R.W. Weisenberger (✉) • M.S. Stefanski
Aerospace Vehicles Division, Experimental Validation Branch (AFRL/RQVV), Air Force Research Laboratory,
Aerospace Systems Directorate, 2790 D. St, WPAFB, Columbus, OH 45433, USA
e-mail: richard.weisenberger@us.af.mil

J.M. Harvie, J. Baqersad (eds.), *Shock & Vibration, Aircraft/Aerospace, Energy Harvesting, Acoustics & Optics, Volume 9*,
Conference Proceedings of the Society for Experimental Mechanics Series, DOI 10.1007/978-3-319-54735-0_4

4.3 Success Criteria

This project is considered successful if all static load channels can be controlled to within ±1% of design limit load (DLL) with dynamic loading applied. If ±1% cannot be obtained, further characterization should be done. During the test command (desired applied load) and feedback (actual applied load) will be monitored. Error is determined by subtracting feedback from command.

4.4 Test Article Description

For this test a wing flap was used as a test article, which represents a typical thermal-acoustic thin-skinned test specimen with a built up sub-structure.

4.5 Test Method, Assumptions, and Procedures

The test employed standard approaches to static mechanical load application while including dynamic loading. The test utilized a strong back mounting fixture. Attached to this rig was a reaction frame of double-back C-channels, to which the load cylinders and constraint members were attached. The reaction frame mounted to the test article is shown in Fig. 4.1 with the strong back removed for clarity. The test fixture was designed to apply the desired load conditions while constraining the test article from out of plane deflection. Out of plane deflection is controlled through the use of lateral links. Load cells were installed on each of the lateral links to measure the out of plane mechanical loading experienced during testing. The desired load conditions were applied using four actively controlled hydraulic actuators.

The quasi static mechanical load was applied using hydraulic load cylinders. The load cylinders were attached to the article's fixture frame near the four corners of the panel. Due to the curvature of the test panel, the static loads were not applied on the neutral axis, and bending was induced. Two different methods of controlling the top and bottom actuators

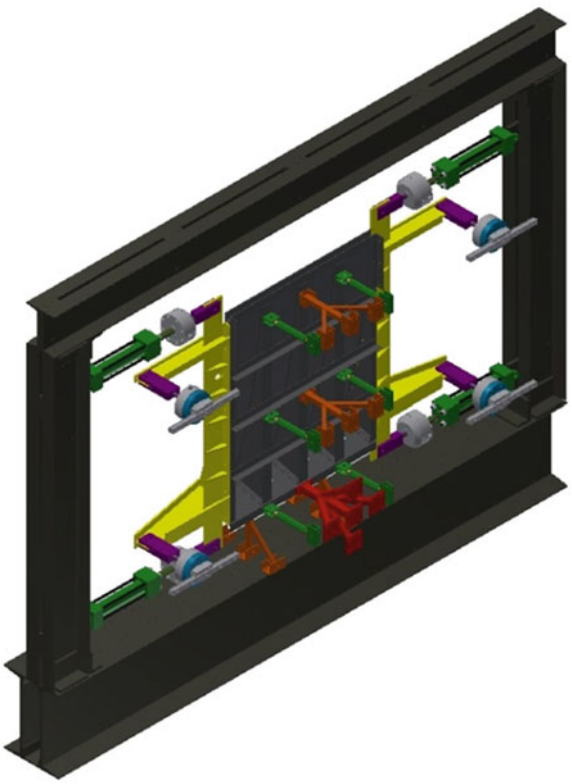

Fig. 4.1 Mechanical loading fixture

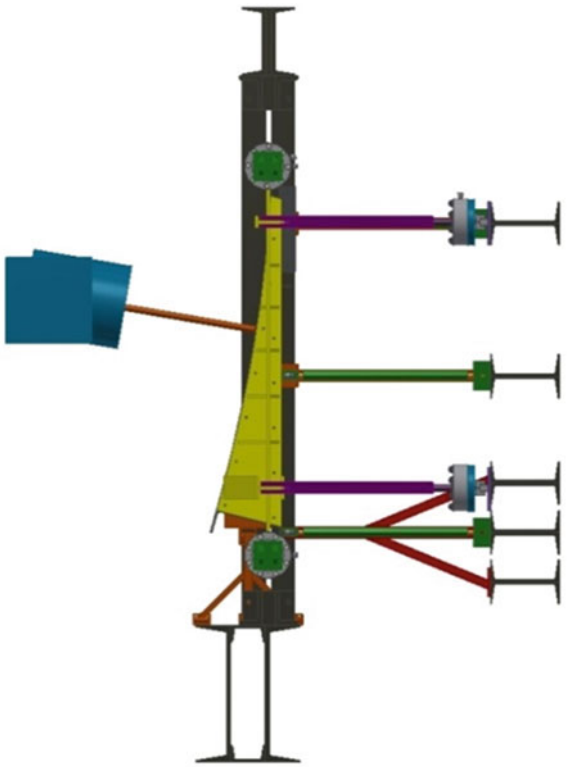

Fig. 4.2 Electrodynamic shaker fixture

were explored. The first method employed was a two servo channel setup, where the top actuators are slaved to one control channel and the bottom actuators are slaved to another channel. The second method used a four servo channel setup, where each actuator has its own channel.

The dynamic load was applied using a 50 pound max force electrodynamic shaker. The shaker was mounted to the frame and attached to the skin of the article using a sting. The sting location was chosen based on previous modal testing to excite a maximum number of structural modes. The shaker was suspended from bungee cords attached to a gantry crane in front of the test article. Figure 4.2 shows how the shaker was attached to the test article. A force gage on the end of the sting provided the input feedback for the magnitude of dynamic energy input into the panel. A signal generator provided a 316 Hz bandwidth white noise centered at 200 Hz as the input spectrum. This was chosen because of the control range of the Air Force Research Labs Combined Environment Acoustic Facility inputs an acoustic spectrum from 50–500 Hz. Different magnitude levels from low to the maximum output of the shaker were tested.

The test run matrix began with a series of static load profiles to provide a baseline, Table 4.1. Test runs were repeated multiple times where the load and loading rate were varied to investigate the controller response. In the next increment, a dynamic load checkout was performed as a baseline using only the shaker. Finally, a series of combined load tests were accomplished. The static load profile is provided in Fig. 4.3. Both bottom actuators had the same applied tension load. Both top actuators had the same applied compression and tension load. The first set of test runs were controlled by using two servos. The top two cylinders as one control channel and similarly, a single control channel for the bottom two load cylinders. The test matrix was re-run with each servo/cylinder operating as an independent control channel.

4.6 Mechanical Load Control

The static load control system employed is a 4 channel MOOG SmarTEST. The MOOG system consists of real time front end controller with a control human machine interface PC and associated software for test setup, operation, and monitoring. Integrated within the SmarTEST system are controllers, signal conditioning, valve drivers, a synchronization computer, and test station controller. Software on the PC provides the interface for entry of channel parameters, channel configuration, load profiles, safeties, actions, and test activation. The system provides closed loop control of the hydraulic actuators through a feedback control loop. Feedback to the control loop is provided by load cell, which is then compared to the desired load command signal; the difference is then acted on by the control loop with the output signal then driving an electro-mechanical

Table 4.1 Desired test run matrix

Test run	# of servos	Static load (DLL)	Dynamic load (V limit)	Description
1.a	2	0–40–0%	N/A	*Static load check-out*; tune controls & check hysteresis; set points at 20% incensements
1.b	2	0–100–0%	N/A	
1.c	2	0–40–0%	N/A	
1.d	2	0–100–0%	Repeat 1.b with asymmetric loads	
2	2	N/A	20–50–100%	*Dynamic load check-out*; flat random spectrum (20–2000 Hz)
3	2	Run profile	N/A	Static only
4	2	Run profile	Determined by run # 2	Combined load
5.a	4	0–40–0%	N/A	*Static load check-out*; tune controls and check hysteresis; set points at 20% incensements
5.b	4	0–100–0%	N/A	
5.c	4	0–40–0%	N/A	
5.d	4	0–100–0%	Repeat 5.b with asymmetric loads	
6	4	Run profile	N/A	Static only
7	4	Run profile	Same as run # 4	Combined load

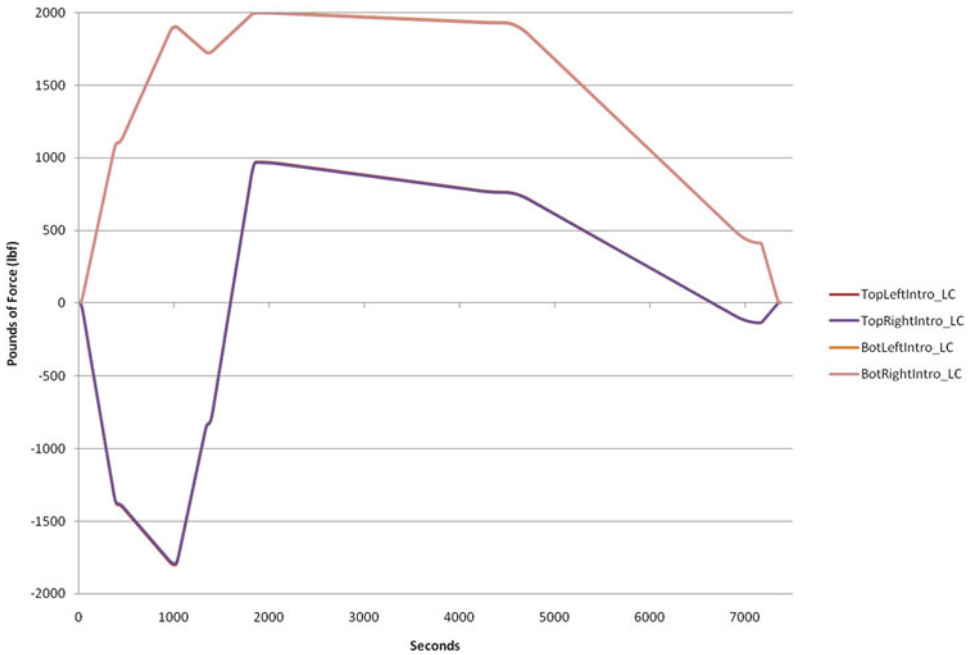

Fig. 4.3 Scaled load profile

hydraulic servo valve. The servo valve then proportions fluid between the tension or compression sides of the actuator and return, resulting in movement in the proper direction until the commanded load is reached.

4.7 Instrumentation and Data Acquisition

A list of instrumentation, capacity and location is given in Table 4.2. The dynamic response of the specimen was recorded with a National Instruments dynamic signal analyzer module with associated embedded rack mounted controller. National Instruments dynamic signal acquisition modules recorded the dynamic force gauge, Moog data, and accelerometers at a sampling rate of 10 kHz. The static response of the specimen was recorded with a National Instruments high speed bridge input modules, recording the load cells data at a sampling rate of 10 Hz. The Moog system sends analog output signals at a rate of 2 kHz for servo drive and load error to the NI of which profile, command, and feedback are passed.

Table 4.2 Test instrumentation

#	Location	Sensor	Manufacturer	Type	Size
1	Top left introduction	Load cell	Interface force	1210CRA-2k	±2k lbf
2	Top right introduction	Load cell	Interface force	1210CRA-2k	±2k lbf
3	Bottom left introduction	Load cell	Interface force	1210CRA-2k	±2k lbf
4	Bottom right introduction	Load cell	Interface force	1210CRA-2k	±2k lbf
5	Shaker sting	Force gage	PCB	208 A03	500 lbf
6	Top right panel	Tri-ax accel	PCB	HT356A24	500 g
7	Mid center skin	Tri-ax accel	PCB	HT356A24	500 g
8	Bottom right panel	Tri-ax accel	PCB	HT356A24	500 g
9	Middle stiffener	Accelerometer	PCB	352C22	500 g
10	Top left reaction	Load cell	Interface force	1210CRA-500-B	±500 lbf
11	Top right reaction	Load cell	Interface force	1210CRA-500-B	±500 lbf
12	Bottom left reaction	Load cell	Interface force	1210CRA-500-B	±500 lbf
13	Bottom right reaction	Load cell	Interface force	1210CRA-500-B	±500 lbf

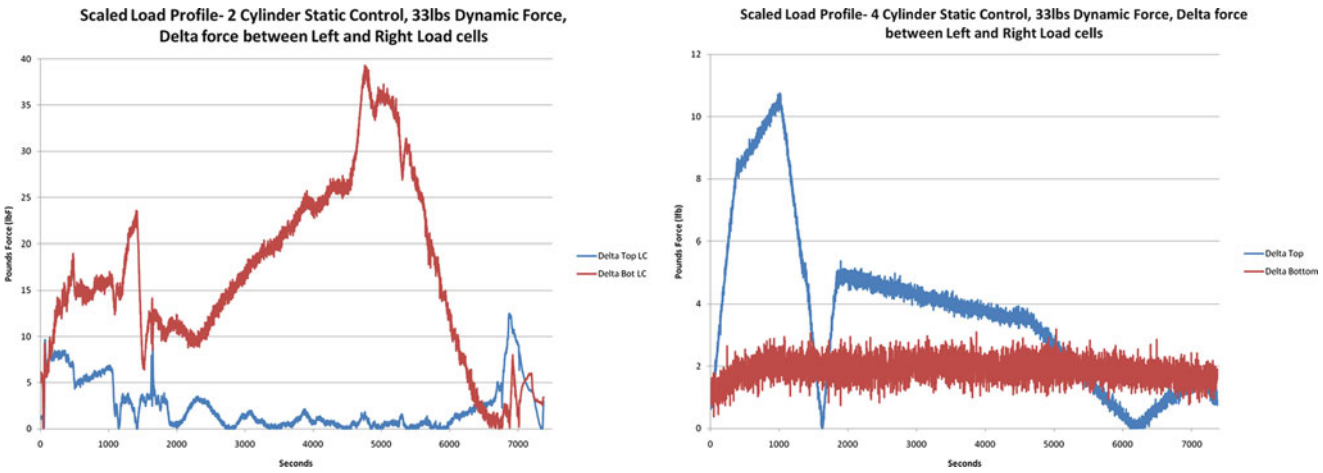

Fig. 4.4 Difference plots (*Right subtract left*) of top and *bottom* servos under dynamic loading

4.8 Results and Discussion

The test data were analyzed both qualitatively and quantitatively. For controllability, success is measured by the error in the static loading signal under varying dynamic input forces. The criterion for passing was established as an error no larger than ±1% DLL. Due to the concern of vibration loads imparted to the load cylinders, the acceleration at the loading points was measured as well. For the secondary objective of simultaneous multi-channel static load control, the 2 and 4 servo configuration data were reviewed.

4.9 2 Servo Versus 4 Servo Response Static only

Based on the loading requirement, this test the test apparatus incorporated four load cylinders and a multi-channel static load control setup. The suitability of 2 channel vs. 4 channel load control was investigated per the requirements due to symmetry of the loading. The desired outcome would a 2 channel setup (lower cost option) if it could give adequate control. Figure 4.4 presents load diffrences between the left and right actuators (for both top and bottem), applied load is a 25% of DLL, or 25% scaled version of profile given in Fig. 4.3 (max 500 lbs in the top cylinders). The left plot in Fig. 4.4 shows the difference derived by subtracting the feedback from the command signal for the 2 servo controlled system. The right plot in Fig. 4.4 shows the same for the 4 channel servo controlled system. Both configurations included a dynamic 33 lbf applied.

The two servo controlled system gave a maximum load difference over the trajectory on a bottom cylinder of 39 lbf (7.8% full scale applied load). In contrast, the four servo controlled system yielded a maximum difference of 11 lbf (2.2% full scale applied load) over the trajectory on a top cylinder. This is a reduction in maximum of 72%. It is interesting to note that the independent control of the bottom cylinders reduced the load error from 39 to 3 lbf of maximum error over the trajectory while independent control of the top cylinders did not alter the maximum error but shifted it to a different location within the trajectory. This may be due to the imparted vibration load as can be seen in Fig. 4.4 where the bottom cylinder is seeing more variation about the mean.

4.10 Static only Load Response

The objective the static only testing was to baseline the error in a mechanical load control on a deflecting structure. To that end the response of the static load control system force required, command, minus feedback or error was measured. If that error was less than 1% with minimal static load control tuning effort the test would be considered successful. An error plot of the static load profile is shown in Fig. 4.5. Notice the error is less than 0.15 lbf which is less than 0.01% DLL.

To address controllability, a stable system that minimizes error is desired. The approach taken uses Moog SmarTEST that employs a PID feedback loop control system. The PID control loop uses the error and applies 3 corrective terms, P gain (Proportional gain), I gain (Integral gain), D gain (Derivative gain). Error is defined as desired load point, command, minus load feedback. To tune the control system in a manner safe to the test specimen, only loads 30% of full scale are employed initially. To tune the control system a square wave with magnitude 30% of full scale and 50% duty cycle square wave. The transitions between zero load and 30% full scale and back to zero again, which is the most challenging method of control the hydroelectric system can operate. Once started, P gain is increased until the system response, load feedback, oscillates. Once this occurs, the P gain is halved, and determined if the response is reasonable, usually response follows closely but feedback may lag behind to achieve 30% load. Once achieved, I gain is increased until response follows command as closely as possible with minimal overshoot. D gain is not used typically in this type of testing application. After a satisfactory response is found at 30% full load, a static load profile going from zero load to 100% full scale with 20% increments is employed. This gives the ability to transition the PID parameters to the higher load. Further tuning is employed by adjusting P gain and I gain as required, using experience of the test engineer to guide in the adjustment process. Afterwards the system should

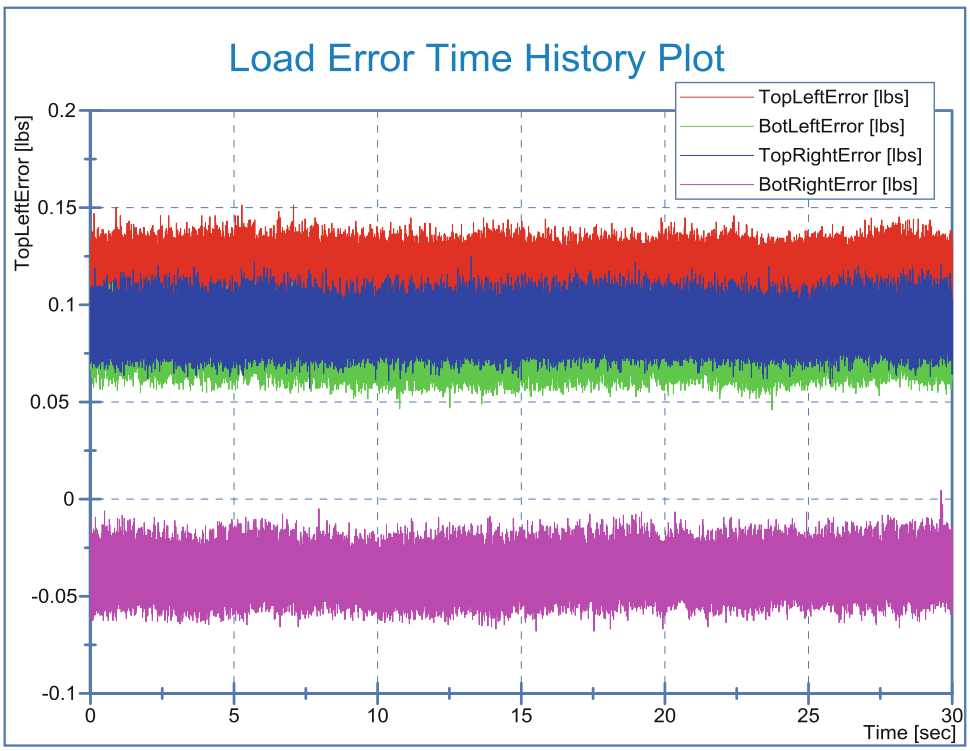

Fig. 4.5 Sample of static loading error time history plot

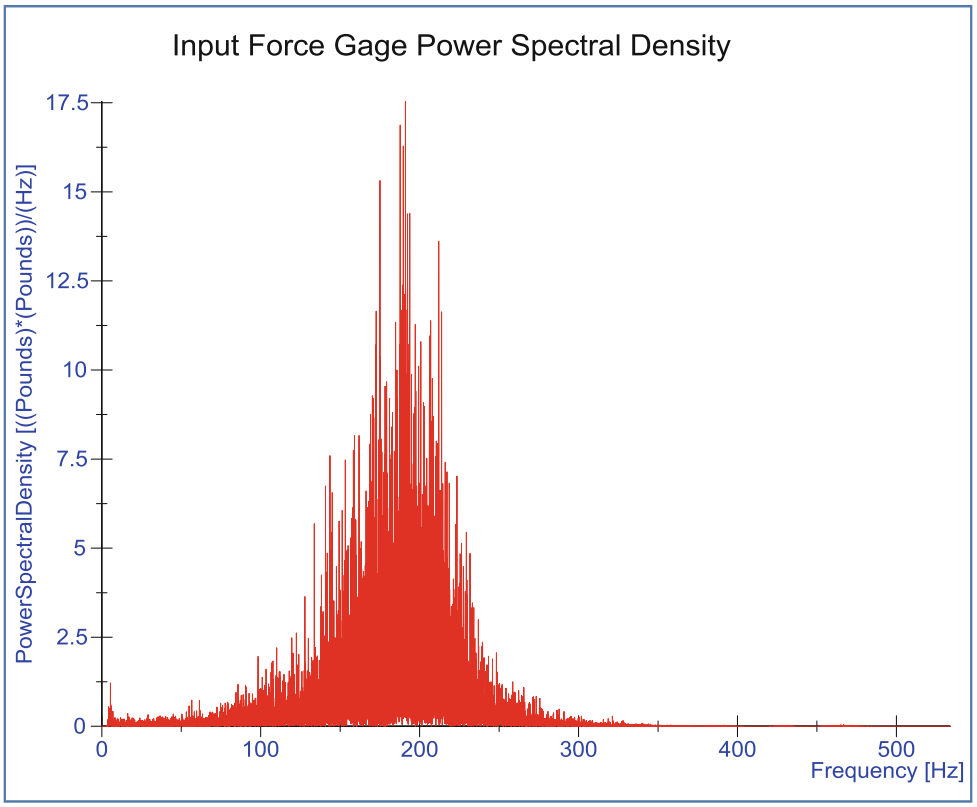

Fig. 4.6 Frequency spectrum power spectral density plot

be ready for all other static and combined experiments. This system was relatively easy to tune due to the stiff nature of the specimen, the design of the load introduction hardware, and supporting fixture.

4.11 Combined Static and Dynamic Load Response

The response of the static load control system, force minus feedback or error with dynamic loads applied was measured. The dynamic loading profile was chosen as a narrow band (316 Hz) noise applied with center frequency of 250 Hz providing 30–33 lb. of dynamic force. The frequency spectrum chosen is based on the acoustic spectrum of frequencies typical to the dynamic laboratory acoustic facility. Figure 4.6 shows a typical Power Spectral Density frequency response of the dynamic load input into the structure. Dynamic response to this article was around 20 g of acceleration seen on the panel skin, and less than 5 g on connection points. Figure 4.7 shows the input dynamic loading at 34 lbf rms, which was the maximum input loading the shaker could provide. A selected error plot of the top and bottom servo actuators of the static load profile with dynamic forces applied presented in Fig. 4.8. For all combined loading test runs, the maximum static error approaches a maximum of 11 lbs peak force or 0.4% DLL (2000 lbs) with no change to static PID parameters (no new tuning was required or performed).

4.12 Conclusion

This experiment performed a twofold objective. To see which configuration of control methods would allow a reasonable amount of error, 2 servo hydraulic channels or 4 servo hydraulic channels. Then to see if adding a dynamic force to a deflecting structure would generate additional error that could not be tuned out via the control system. The 2 servo channel configuration had left and right difference close to 8%, this is usually unacceptable in a quasi-static load test, concluding

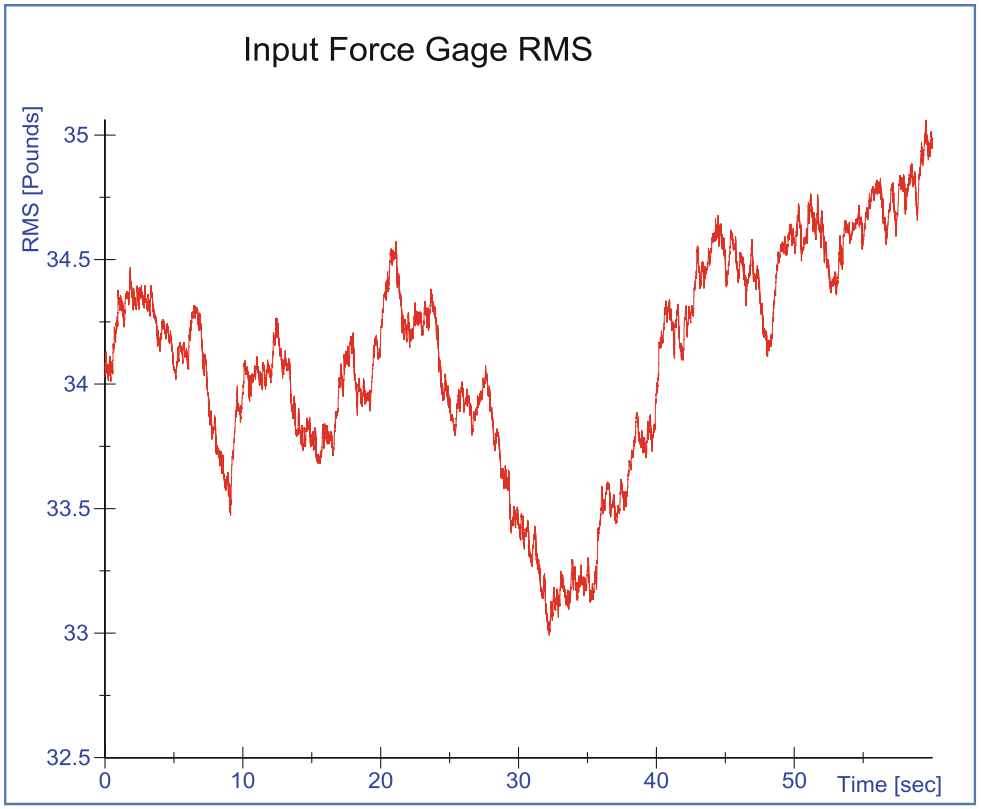

Fig. 4.7 RMS values of the input dynamic loading at maximum shaker output

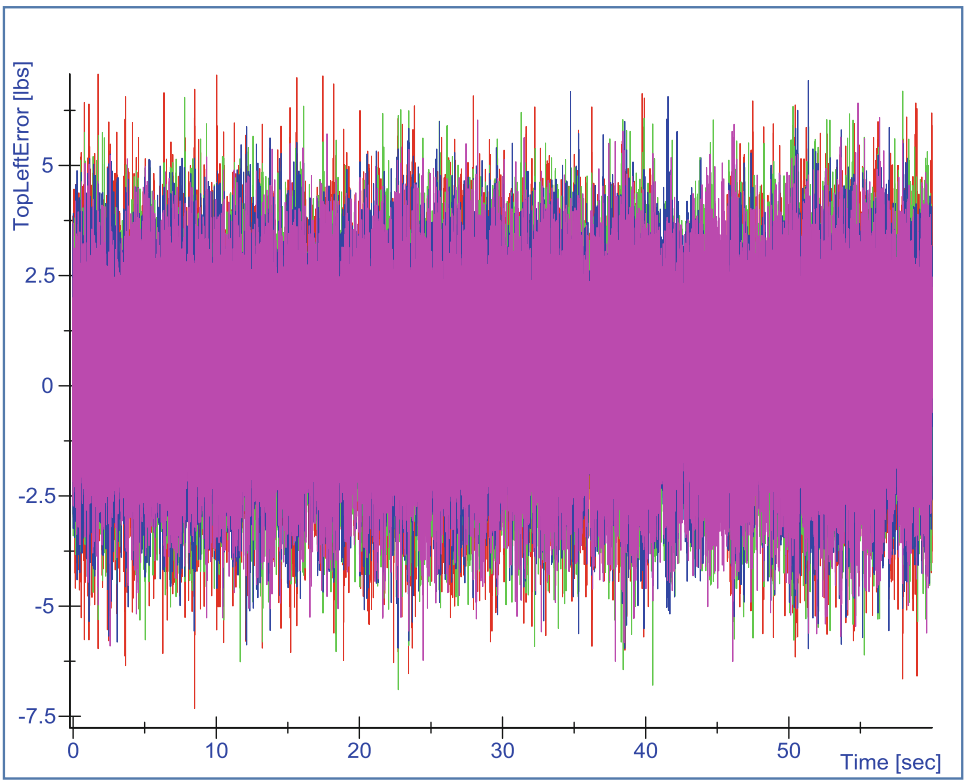

Fig. 4.8 Selected static load error time history with dynamic forces applied

that the 4 channel configuration was more desirable. The 4 channel servo configuration had difference less than 0.1%. Using standard tuning methods from prior mechanical only static load tests produced acceptable controllability and performance factors of the mechanical load control system when dynamic forces were applied to the structure. The load cells used for control feedback saw little variations due to the relative small magnitude disturbances from the shaker and structurally stiff test article. With mechanical loads applied to Design Limit Load (DLL) (2000 lbs) and using varying ramp rates in conjunction with the random dynamic vibration, the dynamic load introduced an error of 0.4% DLL. This is still within the $\pm 1\%$ and is deemed acceptable, and mechanical load tuning resulted in no erroneous aborts due to the dynamic forces applied on the test article. Future considerations may be necessary if there is a significant increase in the magnitude of applied dynamic forces or a less structurally stiff article.

Chapter 5
Identification of Full-Field Dynamic Loads on Structures Using Computer Vision and Unsupervised Machine Learning

Alexander Roeder, Huiying Zhang, Lorenzo Sanchez, Yongchao Yang, Charles Farrar, and David Mascareñas

Abstract Real-world structures, such as civil and aerospace structures, are subjected to various dynamic loads which are spatially local and distributed. Assessment of operational performance, prediction of the dynamic responses, and prognosis of the remaining service life of the structure therefore requires accurate, high-resolution measurements, and modeling of the dynamic loads. This is extremely difficult, if not impossible, with the current state of the art. First, dynamic loads on structures usually come from a wide spectrum of sources, some of which are extremely challenging to accurately measure, such as the traffic loads on a bridge. Also, it is impractical to instrument a dense array of force measurement devices on the structure due to the high cost, the effect of mass-loading, and modification of the structure's surface. On the other hand, digital video cameras are non-contact measurement device that are relatively low-cost, agile, and able to provide high spatial resolution, simultaneous, pixel measurements. This study develops a novel method for identification of the high-resolution, full-field loads on the structure from the video of the operational structures by leveraging advanced computer vision and unsupervised learning techniques. Impact and wind loads were applied on a cable structure to experimentally validate the method. The non-contact, remote, simultaneous sensing capability of the proposed technique should enable truly high-resolution, full-field force estimation that was previously not feasible.

Keywords Load identification • Dynamic model • Regularization methods • Cable dynamics • Video measurement

5.1 Introduction

5.1.1 Motivation

Real-world structures are subjected to various dynamic loads during their lifetime of service. Civil structures, such as buildings and bridges for example, can encounter operational loads (wind, traffic), natural hazards (earthquakes, wave motion, hurricanes) and man-made disasters (blast, impact). Measurements and modeling of these dynamic loads acting on structures are essential to assess operational performance, predict the dynamic response, and estimate the remaining service life of the structure. The loading patterns on such structures are spatially local and distributed. Therefore, load information must be spatially-refined and high-resolution to accurately capture this loading.

A. Roeder
Department of Mechanical Engineering, Georgia Institute of Technology, Atlanta, GA 30332, USA
e-mail: akalex9@gmail.com

H. Zhang
Department of Applied Math, Columbia University, New York, NY 10027, USA
e-mail: hz2315@columbia.edu

L. Sanchez
Department of Mechanical Engineering, Brown University, Providence, RI 02912, USA
e-mail: lorenzo_sanchez@brown.edu

Y. Yang (✉)
Los Alamos National Lab, Engineering Institute, P.O. Box 1663, MS T001, Los Alamos, NM 87545, USA
e-mail: yyang@lanl.gov; yangyongchaohit@gmail.com

C. Farrar • D. Mascareñas
Los Alamos National Lab, Engineering Institute, Los Alamos, NM 87545, USA
e-mail: farrar@lanl.gov; dmascarenas@lanl.gov

J.M. Harvie, J. Baqersad (eds.), *Shock & Vibration, Aircraft/Aerospace, Energy Harvesting, Acoustics & Optics, Volume 9*,
Conference Proceedings of the Society for Experimental Mechanics Series, DOI 10.1007/978-3-319-54735-0_5

5.1.2 Dynamic Model and System Input-Output Theory

The dynamics in any linear physical system can be represented with a dynamic model. This dynamic model can take the form of a frequency response function (FRF). Given the mode shapes and the estimated natural frequencies, a full field and full order dynamic model of the cable can be established via

$$[\mathrm{H}(\omega)]_{\mathrm{N}\times\mathrm{N}} = [\phi]_{\mathrm{N}\times\mathrm{m}}\left[\left(\lambda_{\mathrm{i}}^2 - \omega^2\right)\right]^{-1}_{\mathrm{m}\times\mathrm{m}}[\phi]^{\mathrm{T}}_{\mathrm{m}\times\mathrm{N}} \tag{5.1}$$

where the FRF matrix $[H(\omega)]_{N\times N}$ depends on a mode shape matrix $[\phi]_{N\times m}$ and a diagonal matrix of the difference of squares between each natural frequency λ_i and ω [1]. Furthermore, according to system input-output theory any input to a system can be related to the output by:

$$\mathrm{Y}(\mathrm{x},\mathrm{t}) = \int_0^{\mathrm{t}} \mathrm{H}(\mathrm{x},\mathrm{s})\,\mathrm{F}(\mathrm{x},\mathrm{t}-\mathrm{s})\ \mathrm{ds} \tag{5.2}$$

or alternatively, in the frequency domain:

$$\mathrm{Y}(\mathrm{x},\omega) = \mathrm{H}(\mathrm{x},\omega)\,\mathrm{F}(\mathrm{x},\omega) \tag{5.3}$$

5.2 Background

5.2.1 Video Processing: Automated Video Extraction

A novel algorithm that leverages unsupervised machine learning and computer vision techniques to estimate both the natural frequencies and mode shapes has been developed [2]. Since cable dynamics is well understood [3], the application of this algorithm to the cable structure enables the construction of a full field and full order dynamic model. This algorithm can be broken down into several steps: phase based optical flow magnifies and extracts the time history of phase for every pixels [4, 5], principal component analysis reduces the dimensions of a high dimensional motion matrix by projection onto a smaller number of principal components [6], and blind source separation (BSS) identifies individual modes from the principal components [7]. The BSS model states

$$\mathrm{x}(\mathrm{t}) = \mathrm{As}(\mathrm{t}) = \sum_{\mathrm{i}=1}^{\mathrm{n}} \mathrm{a_i s_i}(\mathrm{t}) \tag{5.4}$$

where $x(t)$ are the observed mixtures, $s_i(t)$ are the unknown sources, and a_i are the respective weights for each source. Under the assumption that the observed mixtures are statistically independent for all t, the sources $s_i(t)$ can be determined from the observed mixtures, $x(t)$ [6]. The application of the video processing algorithm to a video of the vibrating cable structure extracts the modal frequencies and mode shapes (in the video space) of the cable structure.

5.2.2 Regularization Methods

Based on system input-output theory the relationship between the response $Y(x,\omega)$ and the input $F(x,\omega)$ is given by

$$\mathrm{Y}(\mathrm{x},\omega) = \mathrm{H}(\mathrm{x},\omega)\,\mathrm{F}(\mathrm{x},\omega) \tag{5.5}$$

in the frequency domain. To estimate the loading on the system, $F(x,\omega)$, ideally it is possible to solve by inverting the matrix $H(x,\omega)$. Inverse problems are prone to two types of problems, depending on the eigenvalues of the system matrix $H(x,\omega)$ [8]. In cases where there is a gap in the eigenvalues, the matrix H is considered rank deficient. In cases where there is gradual decay in the eigenvalues, the matrix is considered ill posed. There are many well-established methods to solve inverse problems. Two of these techniques are Tikhonov regularization and LASSO regression.

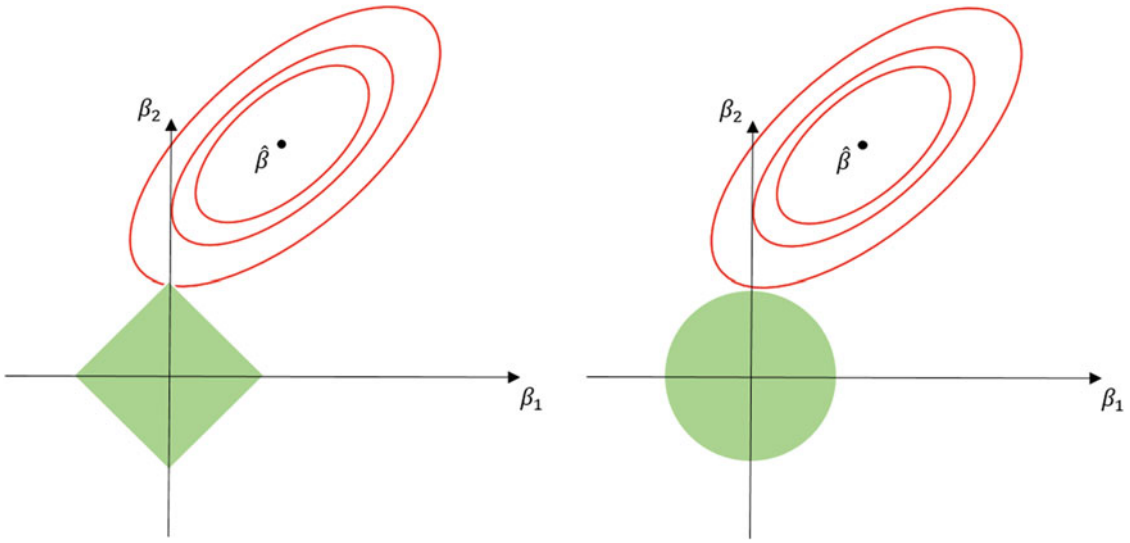

Fig. 5.1 Constraint regions and contours for LASSO and Tikhonov regularization [9]

The basic formulation of Tikhonov regularization is as a minimization problem:

$$\min_{\mathrm{F}} \left[\|\mathrm{HF} - \mathrm{Y}\|_2^2 - \lambda^2 \|\mathrm{LF}\|_2^2 \right] \tag{5.6}$$

where λ is a regularization parameter, $\|HF - Y\|^2$ is the squared residual and LF is a size function with L as either the identity matrix or first/second derivative operators. The choice of L depends on the type of smoothing expected in the solution F and the regularization parameter λ can be chosen with several methods, including an L-curve, generalized cross validation, and Lagrange multipliers.

LASSO is one of several penalized models, alternatively called shrinkage models in regression [9]. Several other penalized models are elastic net and ridge regression, which is very closely related to Tikhonov regularization. The formulation of LASSO regression is very similar to the one of Tikhonov regularization but differs in one main point.

$$\min_{\mathrm{F}} \left[\|\mathrm{HF} - \mathrm{Y}\|_2^2 - \lambda |\mathrm{F}|_1 \right] \tag{5.7}$$

The size function is minimized with respect to the L1 norm, instead of the L2 norm. This change in norms gives LASSO an added capability of performing dimension reduction of F. The selection of F can be thought of as the intersection between contours of the constraint region and the contours of the error function [9].

As can be seen above in Fig. 5.1, if the contours intersect at a corner of the constraint region then some of the elements in vector F could potentially be set to zero, thus performing dimension reduction. The difference in the constraint regions in LASSO and Tikhonov determines which situations each method will be applied in.

5.3 Experimental Setup

5.3.1 Laboratory Setup

To test the technique, a 1.75 m long braided, stainless steel cable with a diameter of 2.38 mm (3/32 in.) held in place within a Unistrut frame was recorded using a standard Sony digital video camera recording at 480 fps (Fig. 5.2). The cable was excited by either impacting it at a point with a modal hammer (spatially local) or using a commercial air blower for wind excitation (distributed). For a more detailed description of the complete setup, see [10].

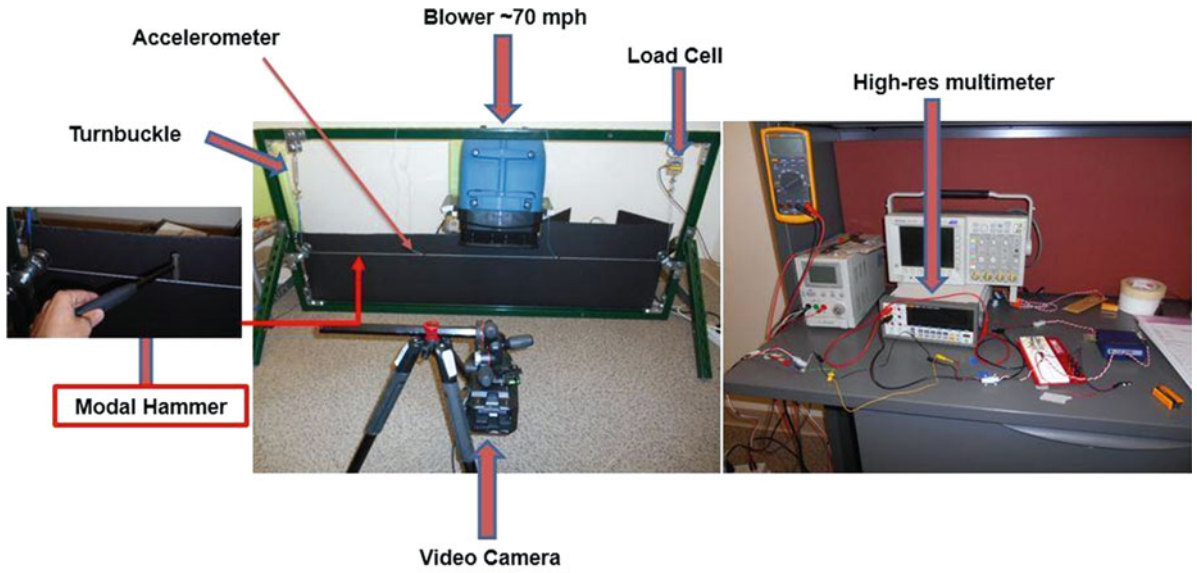

Fig. 5.2 Experimental setup

5.3.2 Establishing Dynamic Model

As mentioned previously, the FRF matrix will take the form of

$$[\mathrm{H}(\omega)]_{\mathrm{N}\times\mathrm{N}} = [\phi]_{\mathrm{N}\times\mathrm{m}}\left[\left(\lambda_{\mathrm{i}}^2 - \omega^2\right)\right]^{-1}_{\mathrm{m}\times\mathrm{m}}[\phi]^{\mathrm{T}}_{\mathrm{m}\times\mathrm{N}} \tag{5.8}$$

where the FRF matrix $[H(\omega)]_{N\times N}$ depends on a mode shape matrix $[\phi]_{N\times m}$ and a diagonal matrix of the difference of squares between each natural frequency λ_i and ω [1]. From prior work, both the mode shape matrix and the natural frequencies can be estimated from the video [10].

5.3.3 Inverse Load ID

By examining the singular values from the SVD decomposition of the dynamic model, $H(x,\omega)$, it can be confirmed that this matrix is rank deficient since, as seen in Fig. 5.3, there is a significant gap between the first seven singular values and the rest.

To solve the inverse load ID problem, specific regularization and penalized models can be used such as Tikhonov regularization and LASSO.

5.4 Results

First it is important to verify the natural frequencies estimated from the video since they directly feed into the frequency response function, $H(x,\omega)$, that is used in the system input-output model. Two ways to verify the estimated natural frequencies include comparing the cable tension calculated using the estimated natural frequencies to the cable tension calculated using the natural frequencies measured by PCB accelerometers and comparing the cable tension calculated using the estimated natural frequencies to the measured tension by a Futek load cell [10]. This paper presents a third method of verification, the construction of a finite element model.

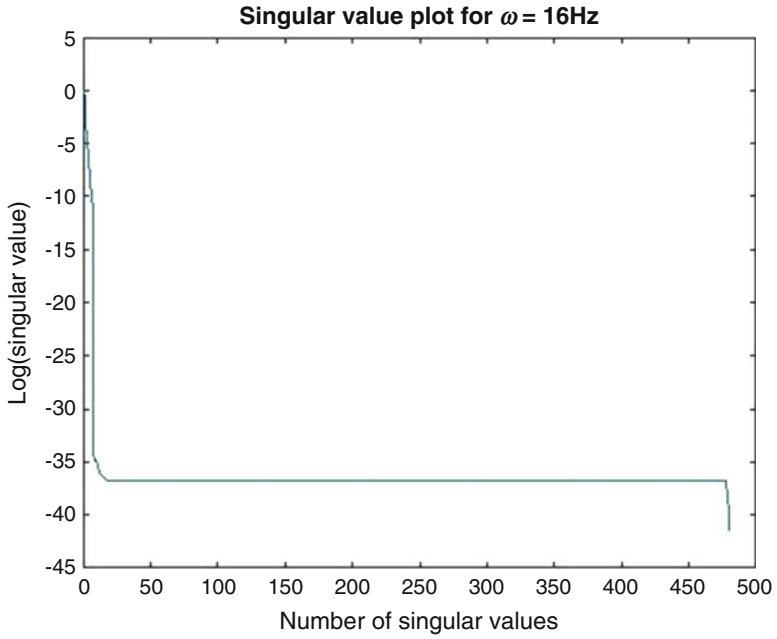

Fig. 5.3 Singular value plot of frequency response function H

5.4.1 FEA Model

A finite element model of the taut-cable structure was created using ANSYS Workbench to aid in verification of the video measured response of the cable and the predicted loading. The method consisted of five main steps: (1) geometry creation (2) static tensioning of the structure (3) modal analysis (useful for initial validation) (4) dynamic modeling to impact loading, and (5) export of displacement and response frequency decomposition. By approximating the cable as a solid cylinder with equivalent area to the braided wire cross-section and including damping in the modal analysis, the modal frequencies of the cable and its response to an experimentally-measured impact loading were predicted with reasonable accuracy in comparison to the video measurements and the accelerometer data. The results of the analysis can be seen in Figs. 5.4 and 5.5. This FEA modeling technique could be used in the future as a method to test the predicted loading from the video technique.

5.4.2 Inverse Load ID

After verifying the video estimated natural frequencies and establishing the frequency response function, $H(x, \omega)$, the problem of inverse load identification can be addressed. The algorithm to solve the inverse load ID problem applies the Tikhonov regularization and LASSO methods discussed before to the system input-output relation

$$\mathrm{Y}\,(\mathrm{x}, \omega) = \mathrm{H}\,(\mathrm{x}, \omega)\,\mathrm{F}\,(\mathrm{x}, \omega) \tag{5.9}$$

where now $H(x, \omega)$, the frequency response function, and $Y(x, \omega)$, the displacement from the video, are both known. The two types of excitation focused on are impact and wind loading. Impact loading is sparse in space, thus the LASSO method is suitable while wind loading is distributed, thus the Tikhonov regularization method is suitable. Two approaches are undertaken to solve the inverse load identification problem. The first approach is to apply the algorithm to experimental frequency response functions, but simulated excitations and confirm that the developed algorithm is able to identify the excitation. The second approach is to use both experimental frequency response functions and the displacement from video to back out the excitation applied in the lab.

Two plots were developed for each trial due to the fact that the excitation and response were distributed in time and in space (i.e. along the cable). For impact loads, both the distribution in time and in space is sparse while wind loading is well distributed in both time and space. As can be seen below in Figs. 5.6 and 5.7, the simulated impact and wind loads closely

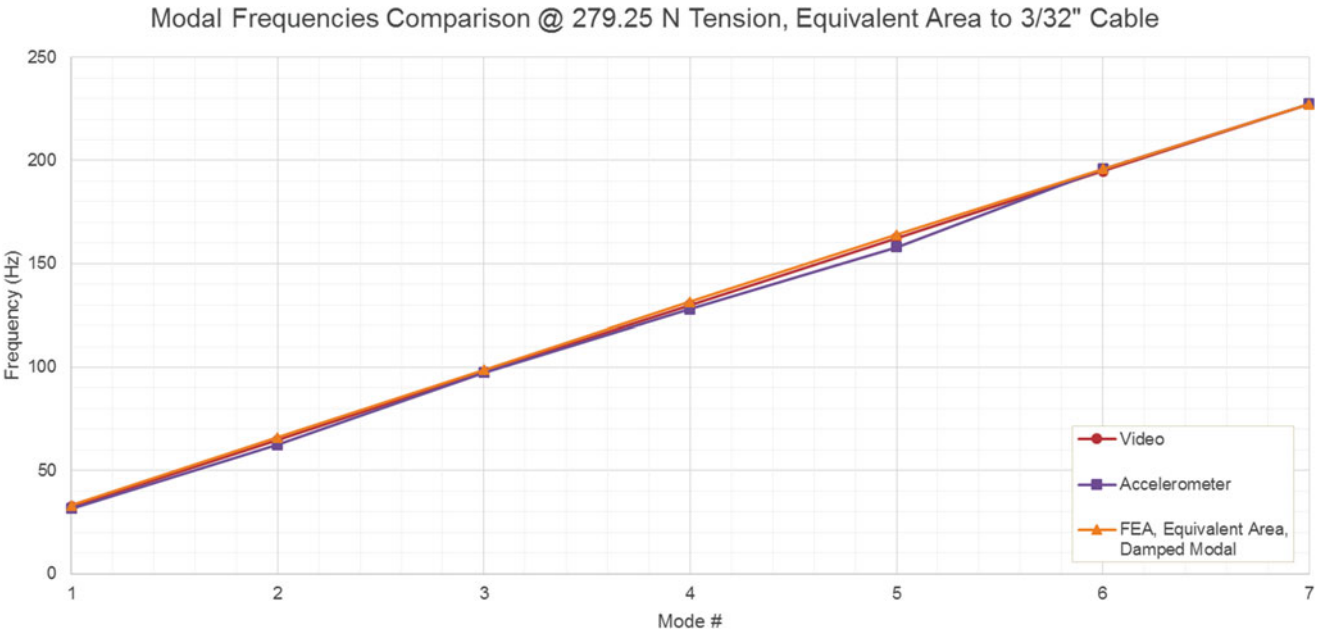

Fig. 5.4 Comparison of the modal frequencies estimated by the video measurement algorithm, accelerometer data, and the FEA simulation

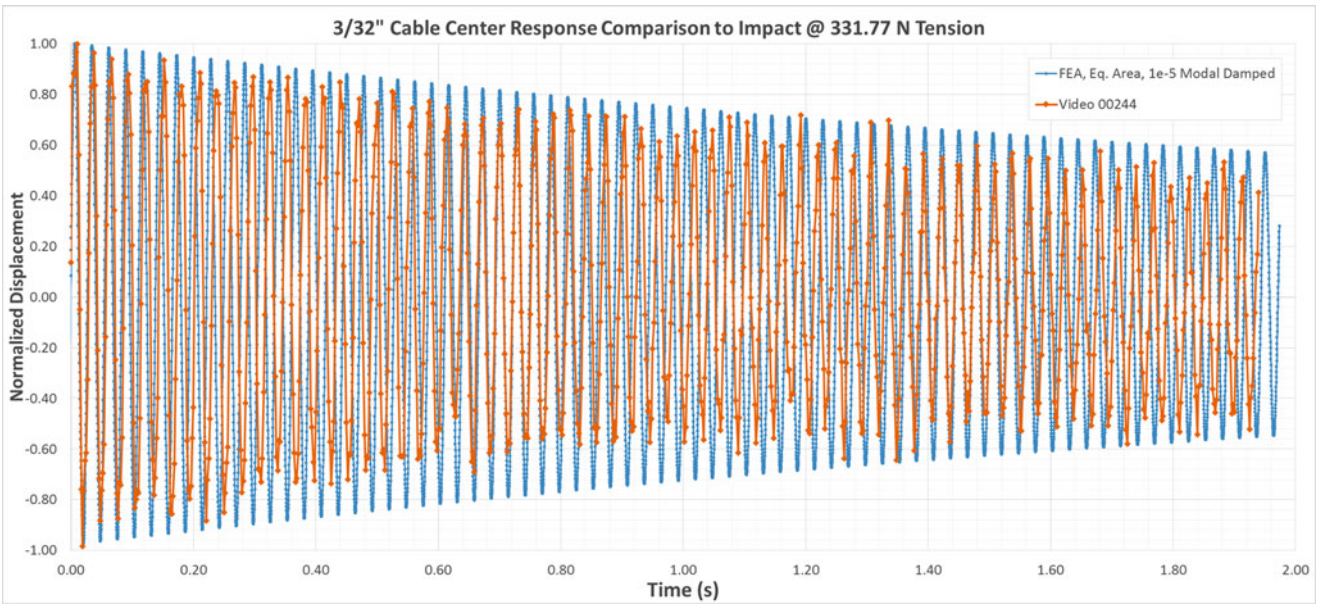

Fig. 5.5 Comparison of the measured displacement of the taut-cable to the ideal response estimated by the FEA simulation. Damping ratio compares well, but there are some other transient effects that need to be further investigated

match the estimated loading from the algorithm in both time (up to a small delay) and space. The L2 error was calculated for both types of excitations in time and space. The error for the impact estimated loading was 2.51 and 1.41 in space and time, respectively and the error for the wind estimated loading was 6.74 and 11.7 in space and time, respectively. The estimated wind distribution is expected to be much noisier in both time and space since wind loading is distributed in space. Thus, gaussian white noise was used to simulate wind excitation on a section of the cable.

The second approach used the experimentally determined frequency response function and the video response (i.e. cable displacement and motion) to solve the inverse load identification problem for impact loading. As seen below in Fig. 5.8, the algorithm was able to identify the location of the impact with reasonable accuracy. There were additional interesting points to identify in the figure. First, there was significant noise in the results which could be improved in the future work by some denoising algorithm. Second, besides the location of the impact, the reaction forces at the ends of the cable were also visible

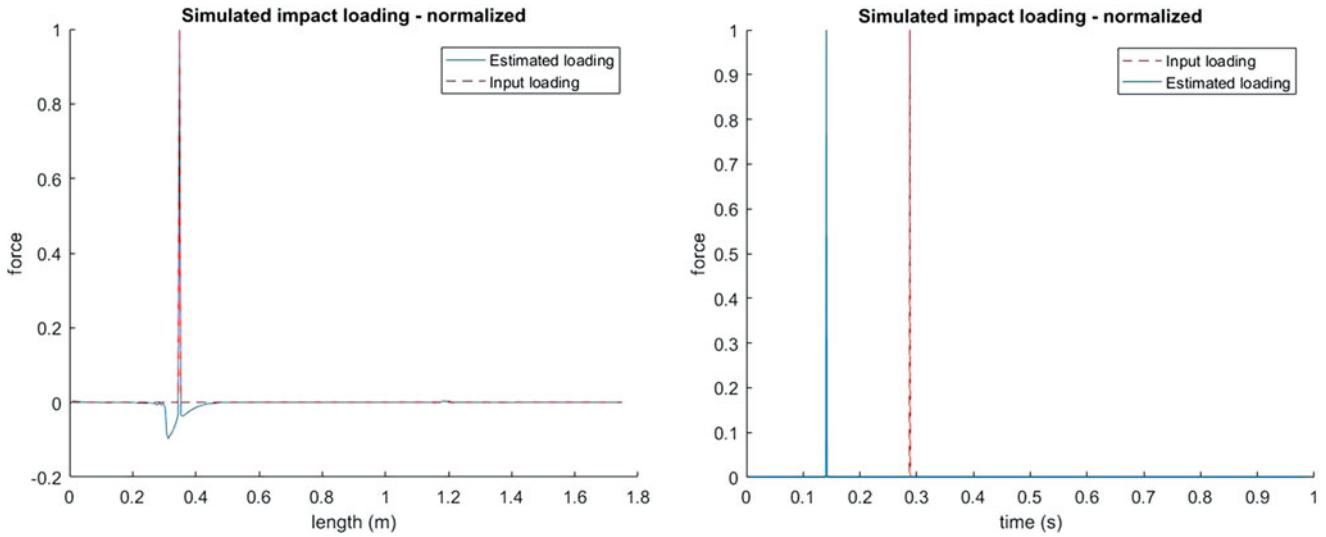

Fig. 5.6 Comparing simulated impact loading to estimated impact from algorithm in both time and space (along cable)

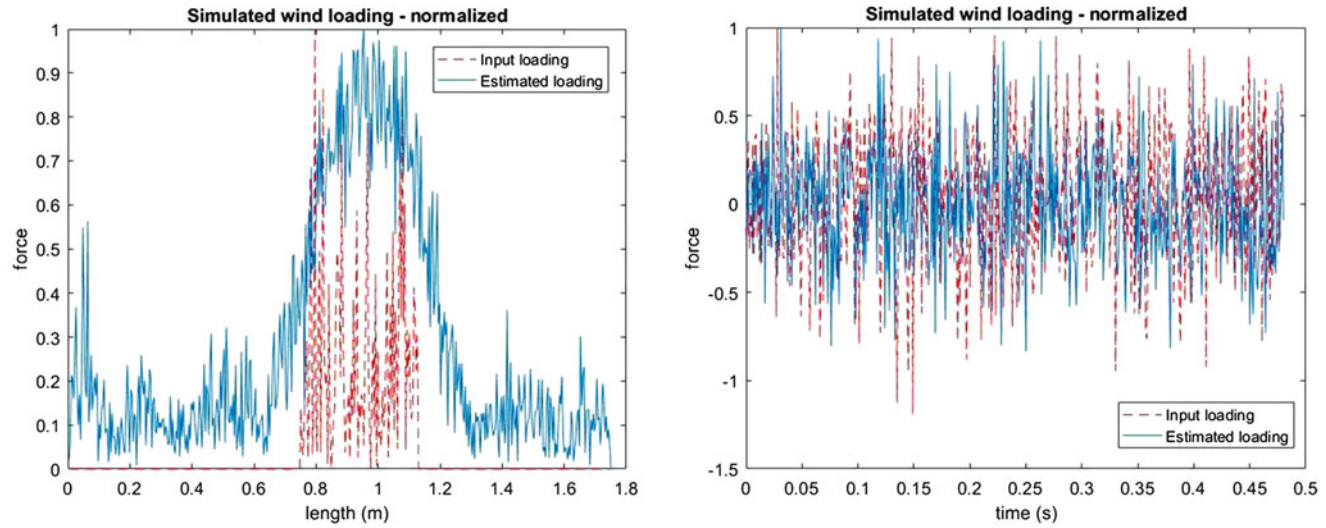

Fig. 5.7 Comparing simulated wind loading to estimated impact from algorithm in both time and space (along cable)

and opposite of the impact. This matches our expectations since the cable is held in place in the lab within a Unistrut frame and during impacts there should be opposing forces at the ends.

All the figures presented have been normalized with respect to the max force, as is typical in output-only analysis.

5.5 Conclusion

This paper presents a novel technique for identification of dynamic loading on a structure using non-contact video measurement with a pixel-level resolution. Load estimation is achieved by displacement extraction from video data, mode shape matrix construction which informs a dynamic model, and load extraction using regularization techniques for matrix inversion. Using a cable, it was shown that high-resolution measurements for dynamic loading could be reasonably determined both in time and space for spatially local and distributed loading schemes. Further work should be undertook to refine the loading identification algorithm magnitude accuracy and reduce noise likely caused by distortion in the creation of the frequency response function, leading to application of the technique to real-world structures.

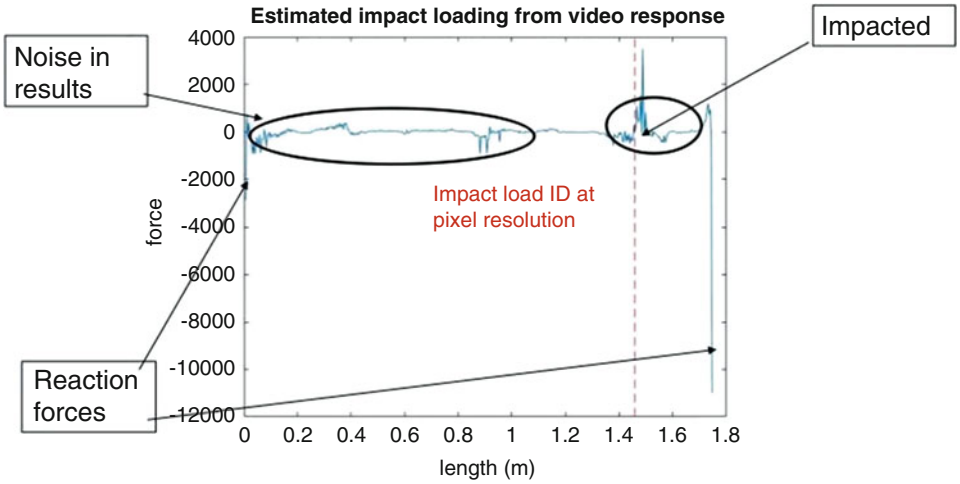

Fig. 5.8 Comparing location of impact from algorithm (*blue spike*) to location of impact in lab (*red dashed line*)

References

1. Ewins, D.: Modal Testing. Research Studies Press Ltd, Philadelphia (2000)
2. Yang, Y., Dorn, C., Mancini, T., Talken, Z., Kenyon, G., Farrar, C., Mascarenas, D.: Blind identification of full-field vibration modes from video measurements with phase-based video motion magnification. Mech. Syst. Signal Process. **85**, 567–590 (2017)
3. Warnitchai, P., Fujino, Y., Susumpow, T.: A non-linear dynamic model for cables and its application to a cable-structure system. J. Sound Vib. **187**(4), 695–712 (1995)
4. Fleet, D.J., Jepson, A.D.: Computation of component image velocity from local phase information. Int. J. Comput. Vis. **5**(1), 77–104 (1990)
5. Wadhwa, N., Rubinstein, M., Durand, F., Wadhwa, N.: Phase-based video motion processing. ACM Trans. Graph. **32**(4), 1 (2013)
6. Hyvarinen, A., Oja, E.: Independent component analysis: algorithms and applications. Neural Netw. **13**(4), 411–430 (2000)
7. Antoni, J.: Blind separation of vibration components: principles and demonstrations. Mech. Syst. Signal Process. **19**(6), 1166–1180 (2005)
8. Hansen, P.C.: Rank-Deficient and Discrete Ill-Posed Problems. Society for Industrial and Applied Mathematics, Philadelphia (1998)
9. Hastie, T., Tibshirani, R., Friedman, J.: The Elements of Statistical Learning. Springer, New York (2009)
10. Sanchez, L., Zhang, H., Roeder, A., Bowlan, J., Crochet, J., Yang, Y., et al.. Establishment of full-field, full-order dynamic model of cable vibration by video motion manipulations. 35th IMAC, Orange County (2017)

Chapter 6
Research of Under-Sampling Technique for Digital Image Correlation in Vibration Measurement

Yihao Liu, Hongjian Gao, James Zhuge, and Jeff Zhao

Abstract In the field of vibration test including modal analysis, the completion of a traditional test requires many devices and takes several days due to its complex process. The development of digital image technology makes the application of the image sensor to complete vibration test and modal test possible, which is known for collecting a large amount of data within several hours. This paper developed a new testing method that targeting at operating deflecting shape vibration test based on stereo vision. Normally, it is required that the image sensor can be triggered at a very high frequency to oversample a high frequency vibration. With the application of undersampling technology, the method proposed in this paper breaks through this limitation and the camera can be triggered at less than 3 Hz to analyze structure that vibrates at more than 30 Hz. Furthermore, a timestamp-based optimization method is proposed and developed to address Jitter problem in the process of undersampling. More than two hundred test results validate the accuracy and reliability of this new method, which can satisfy the needs of operating deflecting shape modal analysis.

Keywords Digital image correlation • Stereo vision • Undersampling • Modal analysis • Timestamps

6.1 Introduction

The Digital image correlation and stereo vision have not been applied in the field of vibration test and model analysis until recently years. Studies have shown that Digital image correlation can be applied to study dynamic properties of structures [1, 2]. However, almost all the experiments that have been done use an extremely high speed camera to oversample a high frequency vibration signal [3–5]. Since the price of a camera with speed higher than 10,000 fps is typically more than 100 k dollars, it is nearly impossible to implement this approach for industrial usage. By applying the approach proposed in this paper, samples per period can be determined manually. As a result, the vibration can always be oversampled regardless of the sample frequency. For this reason, a stereo camera with regular frame rate 30, or 60 fps, can be used and yield almost the same result in operating deflecting shape measurement. The cost of the stereo camera will be typically about a few thousand dollars, which allows this approach being applied in many industrial occasions. This paper first briefly introduce the stereo vision and digital image correlation, then brings in the principle of undersampling technique and timestamp optimization. Two test examples are presented to demonstrate and verify the feasibility of this approach.

6.2 Estimate Depth of Workpiece with a Stereo Camera

A stereo camera refers to a camera with two or more lenses. This structure allows three dimensional information be obtained by examines side-by-side image taken by each lens at the same instant. To calculated the distance between the surface of the workpiece and the camera, a stereo camera with two lenses is placed directly at the workpiece as shown in Fig. 6.1.

Once triggered, stereo camera will take a side-by-side image from both lenses simultaneously. After perform digital image correlation between the two images, a one on one correlate relationship can be established between most of the pixels in both images. Suppose a measurement point P_0 is mapped to one pixel in left and right images respectively, and the coordinates

Y. Liu • H. Gao
Zhejiang University, Hangzhou, China
e-mail: lyh593657236@gmail.com

J. Zhuge • J. Zhao
Crystal Instruments, Santa Clara, CA, USA

J.M. Harvie, J. Baqersad (eds.), *Shock & Vibration, Aircraft/Aerospace, Energy Harvesting, Acoustics & Optics, Volume 9*,
Conference Proceedings of the Society for Experimental Mechanics Series, DOI 10.1007/978-3-319-54735-0_6

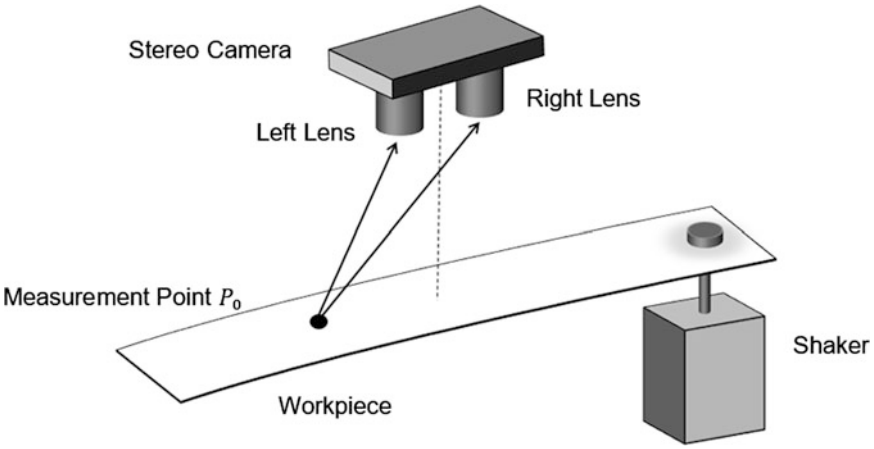

Fig. 6.1 Outline for measuring structural vibration using a camera

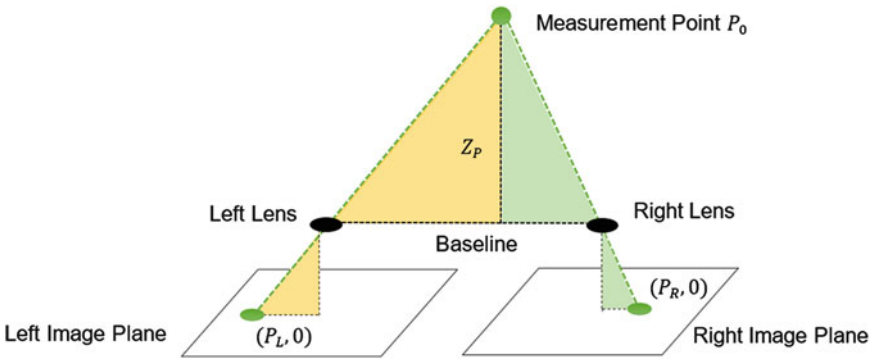

Fig. 6.2 How the depth information is obtained by disparity value

of the pixels are $(P_L, 0)$ in left image plane and $(P_R, 0)$ in right image plane. After a successful image correlation, these two coordinates will be identified as the same structure. The difference between these two coordinates is denoted as Disparity [6]. Under appropriate light conditions and corresponding camera configuration, most of the pixels in left image can be correlated to a certain pixel in right image. Hence, every correlated pair of pixels will have a disparity value.

From a disparity value, the distance of the object to the center of camera can be obtained. As shown in Fig. 6.2, it is obvious that two pair of shaded triangle in Fig. 6.2 are similar to each other.

$$\frac{Z_p \times |P_L|}{Focus\ \ Length} + \frac{Z_p \times |P_R|}{Focus\ \ Length} = Baseline \quad \overset{yields}{\rightarrow} \quad \frac{Z_p \times (-P_L) + Z_p \times P_R}{Focus\ \ Length} = Baseline \tag{6.1}$$

Thus, the depth of P_0 relative to the camera can be computed as:

$$Z_P = \frac{Baseline \times (Focus\ \ Length)}{Disparity} \tag{6.2}$$

Since every correlated pair of pixels can be related to a disparity value, given that the Baseline and Focus Length of the camera already known, the depth of the workpiece surface can be determined. During the test, for a 2048×768 resolution stereo camera, one side-by-side images can generate more than 4 K pair of correlated pixels belong to the workpiece, which means more than 4 K depth information of the workpiece can be collected by a single trigger of the stereo camera, from which the deflecting shape of the workpiece at that instant can be determined. The correlation process has been well documented in [4, 5].

6.3 Undersampling Technique

Generally speaking, oversampling is required for signal processing. Particular in operating deflecting shape analysis, an extremely high frequency camera is recommended. It is possible for a stereo camera to be trigger at a very high frequency. With Undersampling technique, a camera that triggered at a very low frequency can output the same result given enough time. With the frequency of the trigger known, discrete signal by undersampling can be remap to the correct time. Denote the frequency of trigger by f_t and the frequency of shaker by f_s, the *nth* sample which is triggered at $t_n = \frac{1}{f_t} \times n$ is actually the same as it is triggered at

$$t_n = \frac{1}{f_t} \times n - \frac{1}{f_s} \times k \tag{6.3}$$

where k is any non-negative integer that makes expression (6.2) non-negative. More specifically, suppose the *nth* sample samples the value of signal at signal's *mth* period, we can shift it by k times the signal's period and have the same value. The Based on this, if we find the biggest k value for t'_n to be non-negative, the sequence of discrete values which was sampled at a very low frequency within several minutes can be remapped into first one period of vibration signal, that is $\frac{1}{f_s}$. It is essential to trigger the camera at an appropriate frequency so that two samples will not be shifted to a same time.

It is obvious that the accuracy of both trigger frequency and vibration frequency is essential for correctly remapping. Any slight shift in both frequencies will be accumulated and result in a significant deviation. For this reason, a close loop control system is applied to excite the shaker with less than 2.5×10^{-6} error.

6.4 Timestamp Optimization

Ideally, undersampling technique can be applied in any condition as long as both trigger signal frequency and vibration frequency is known. Suppose that the frequency of trigger signal has an inaccuracy of af_t. From (6.3) we know that in worst situation, the different between the true time and assumed time is:

$$\Delta \mathrm{t} = t_2 - t'_2 = \frac{n\left(1 - \frac{1}{1+a}\right)}{f_t} \tag{6.4}$$

It proves that a tiny disturbance at the beginning of undersampling will be accumulates. Suppose that p% error of the time will result in a fail analysis, it requires that:

$$\frac{f_s \times n\left(1 - \frac{1}{1+a}\right)}{f_t} < 0.01 \times p \tag{6.5}$$

$$\mathrm{a} < \frac{0.01p \times f_t}{f_s \times n - 0.01p \times f_t} \tag{6.6}$$

If $\mathrm{p} = 1$ and we want to sample a 20 Hz vibration with 5 Hz trigger signal and have at least 50 valid data, the inaccuracy of the trigger signal should be less than 5×10^{-5}, which is a condition that hard to accomplish without close loop control. To overcome this issue that limits the application of undersampling technique, this paper introduces a timestamps correction method.

We program the camera to generate a timestamp every time the shutter is closed. The timestamp is accuracy to 1 μs and is generated based on 1394 cycle timer, its error should be less than 100 ns [7–9]. By using the timestamp correction, we can modify the expression (6.3) to:

$$t_n = (ts_n - ts_1) - \frac{1}{f_s} \times k \tag{6.7}$$

In which ts_n is the *nth* timestamp, indicating the time of the shutter's *nth* close. ts_1 is the timestamp of the first timestamp, indicating the time of the shutter's first close. From observing (6.7), we can conclude that by introducing timestamp optimization in undersampling technique, the error in trigger signal that needed to be concerned is replaced by the error in 1394 clock timer. More importantly, the sample index n is not in (6.7), meaning that error in this method will not accumulate as it previously did. It makes possible for us to sample more than 200 data within one period using a low triggered camera.

6.5 Experimental Verification

To verify the feasibility of above contents and test its performance. We performed a test with aluminum plate. For correlation to work successfully, we apply certain pattern on the plate.

Figure 6.3 show the setup for stereo camera and the workpiece. Figure 6.4 show the outline of our experimental setup. The shutter speed of camera is set to 2.030 μs to avoid possible blur in images. The trigger signal from the generator is 2.17 Hz. Aluminum plate is excited by the shaker which is operating at 5 Hz, and its amplitude is 1 mm.

We operated the whole system for 46 s and captured 100 side-by-side images. A typical side-by-side image is shown in Fig. 6.5. The offset of the two lenses result in a slight difference about the field of view between the left image and the right image.

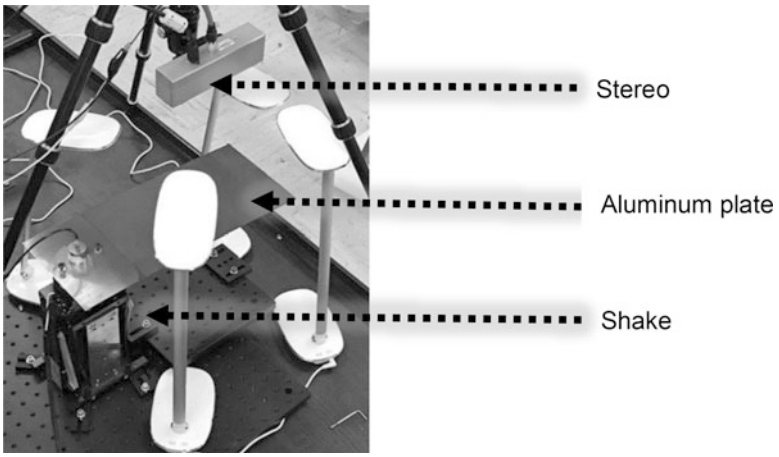

Fig. 6.3 Setup of stereo camera and workpiece

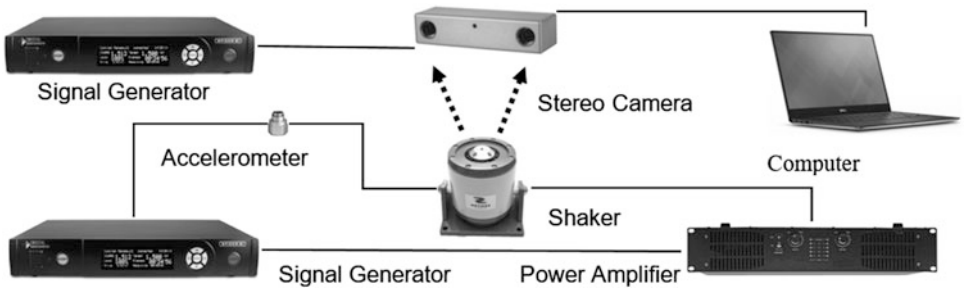

Fig. 6.4 Outline of experimental setup

Fig. 6.5 Typical captured side-by-side image

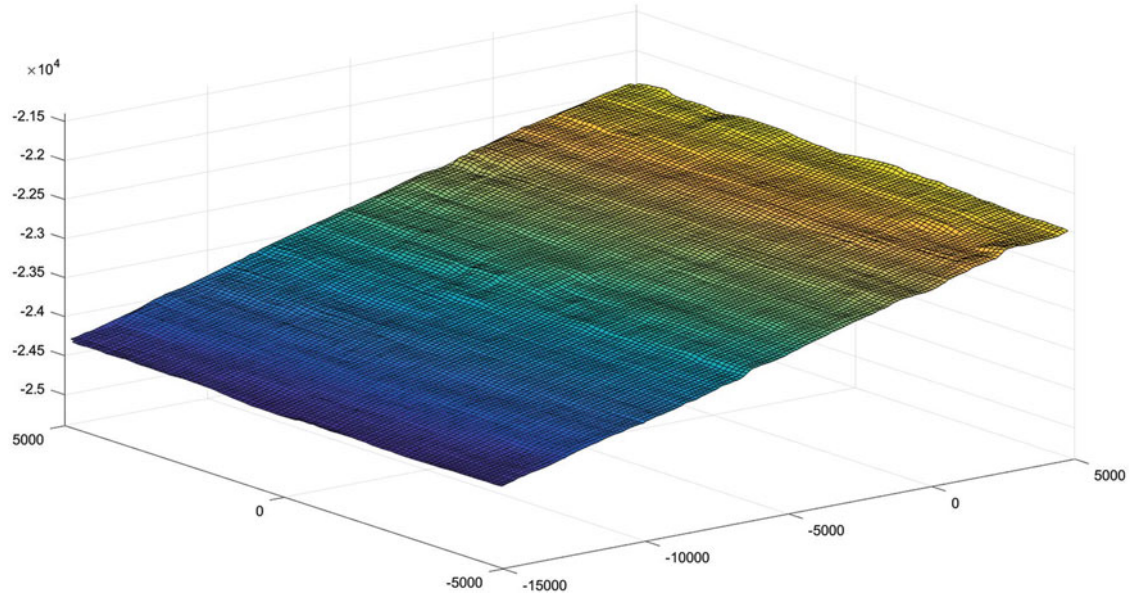

Fig. 6.6 Surface of the aluminum plate plots from interpolated coordinates

More than 14 K pairs of correlated pixels are generated from Fig. 6.5 by digital image correlation. Since the edge of the Aluminum plate will produce many incorrect correlation results, we set the range of X to −150 to 50 mm and Y to −50 to 50 mm to eliminate the edges, the origin is the center of stereo camera. 44,419 pair of correlated pixels are obtained and thus, 44,419 three dimensional coordinates are generated. For demonstrate purpose, we interpolation those coordinates and plot the surface of the Aluminum plate as shown in Fig. 6.6 (in 0.01 mm).

We can verify the correctness of undersampling technique by exam the change of depth of a measurement point over time. Since the camera is placed directly at the Aluminum plate and the shaker is operating at 1 mm and 5 Hz, we can simplify the calculation by assume that deflection will not cause a significant change in XY coordinates. Hence, we assume that the same XY coordinates in different images represent the same structure. To reduce the Gauss noise in the image that produce incorrect correlation, we exam the average depth value of a region of 0.5×4 mm, which contains about 40 coordinates. Figure 6.7 shows the change of depth over time of the region selected and its fourier transform. Totally 100 samples were collected in this experiment. Even though the sample frequency is 2.17 Hz, through undersampling technique, all 100 samples have been shifted into one period, makes it equivalent to sample at 500 Hz. Apparently, most of its frequency is at 5 Hz.

Figure 6.8 shows the change of depth in time domain and its Fourier transform after applying the timestamp optimization. There is a slight difference between these two results, the signal after timestamp optimization is obviously better from observing the time domain signal.

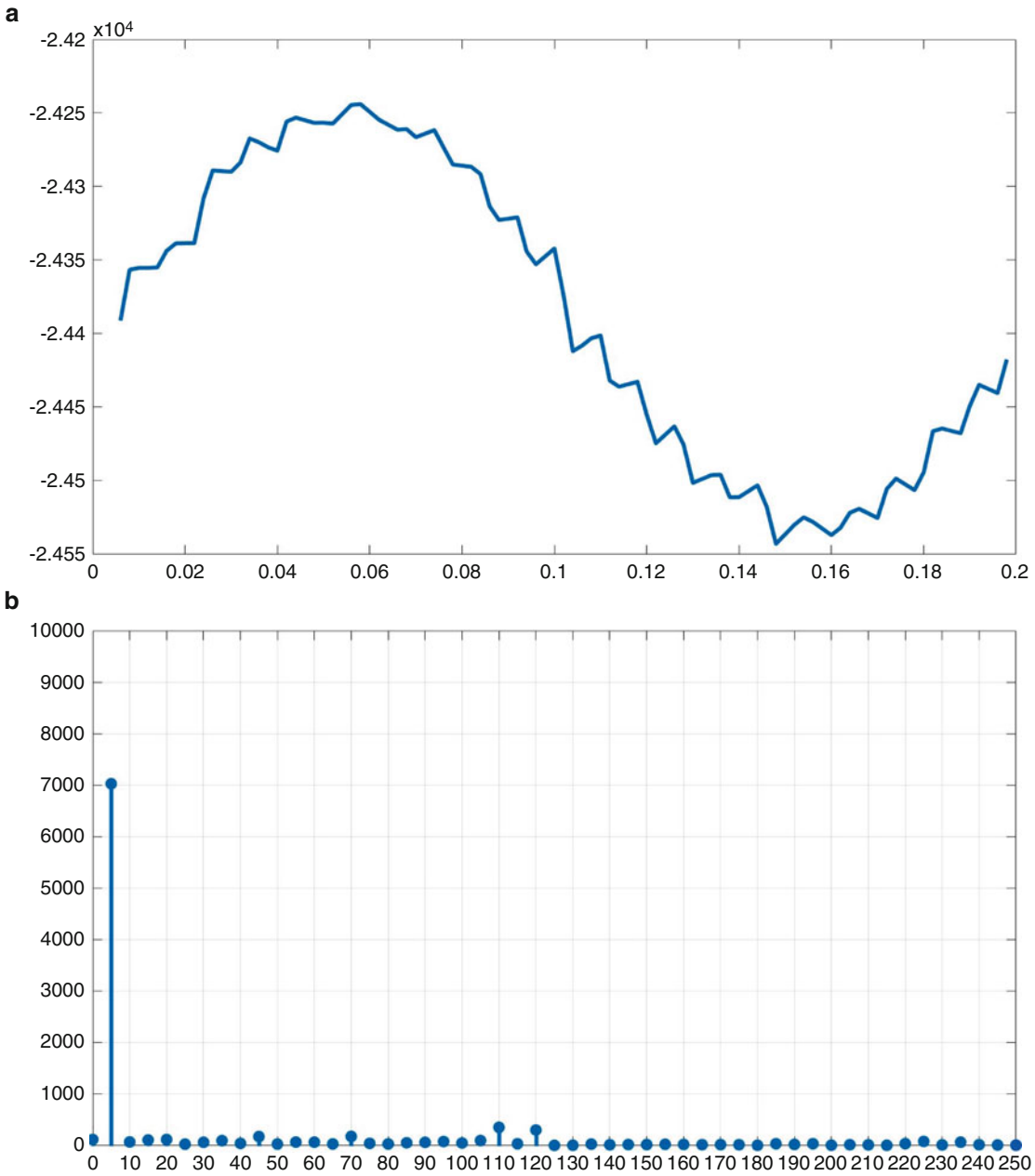

Fig. 6.7 (**a**) Depth information in time domain. (**b**) Spectrum magnitudes of depth

Due to the experiment equipment limitation, the highest frequency we test is 35 Hz. The trigger signal to the stereo camera remain to be 2.17 Hz, and the shaker's amplitude is set to 0.4 mm. Since 100 images were taken in one period of vibration frequency, it equivalent to sample the signal at 3500 Hz. Figs. 6.9 and 6.10 show the depth information in time domain and its fourier transform without timestamp optimization and with timestamp optimization.

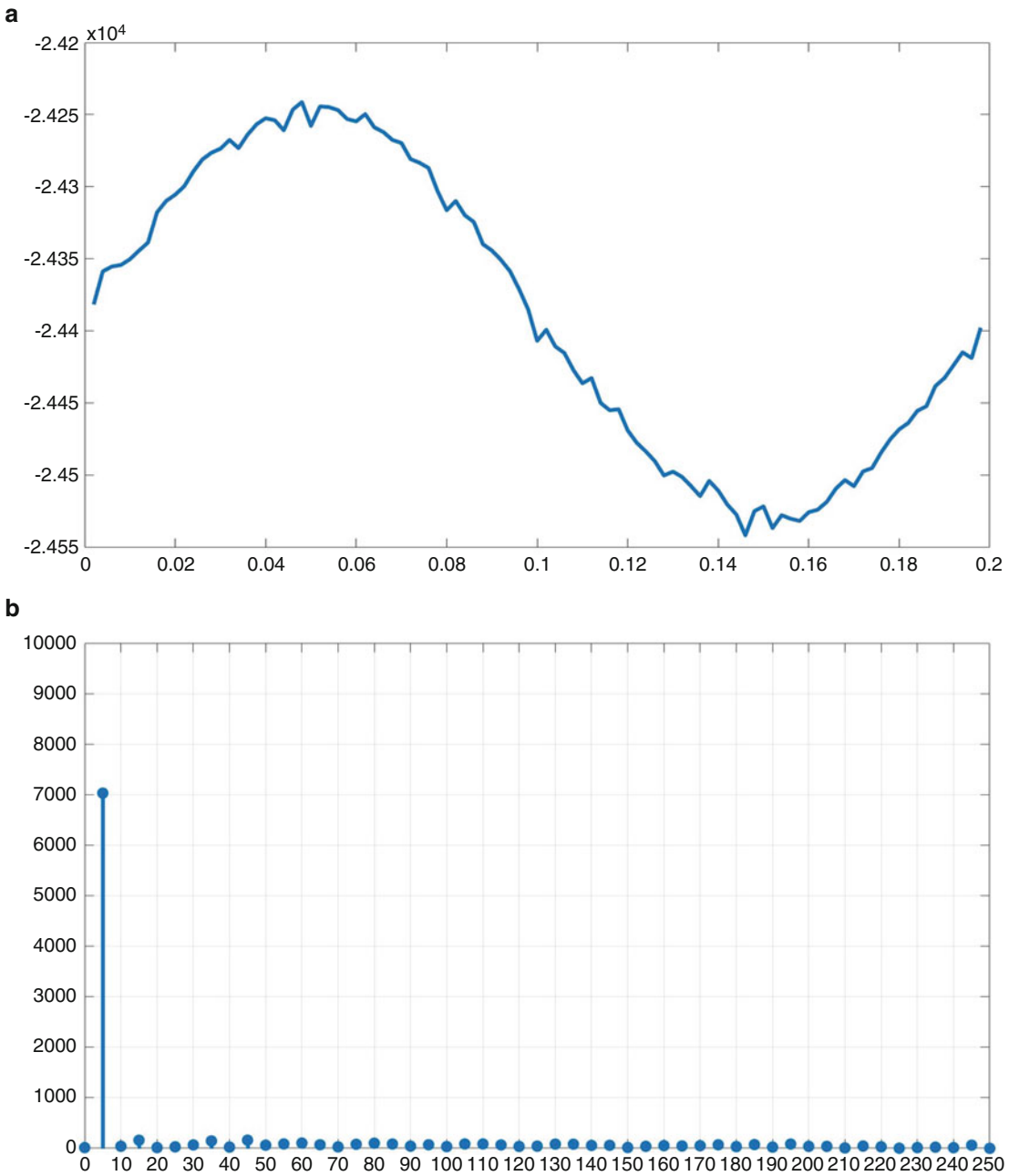

Fig. 6.8 (**a**) Depth information in time domain after timestamp optimization. (**b**) Spectrum magnitudes of depth after timestamp optimization

As shown in Figs. 6.9 and 6.10, timestamp optimization will produce an exceedingly better result compared to which without timestamp optimization. Since as shaker operates at a higher frequency, the error in trigger frequency which does not change, will become more significant relative to the shaker's frequency.

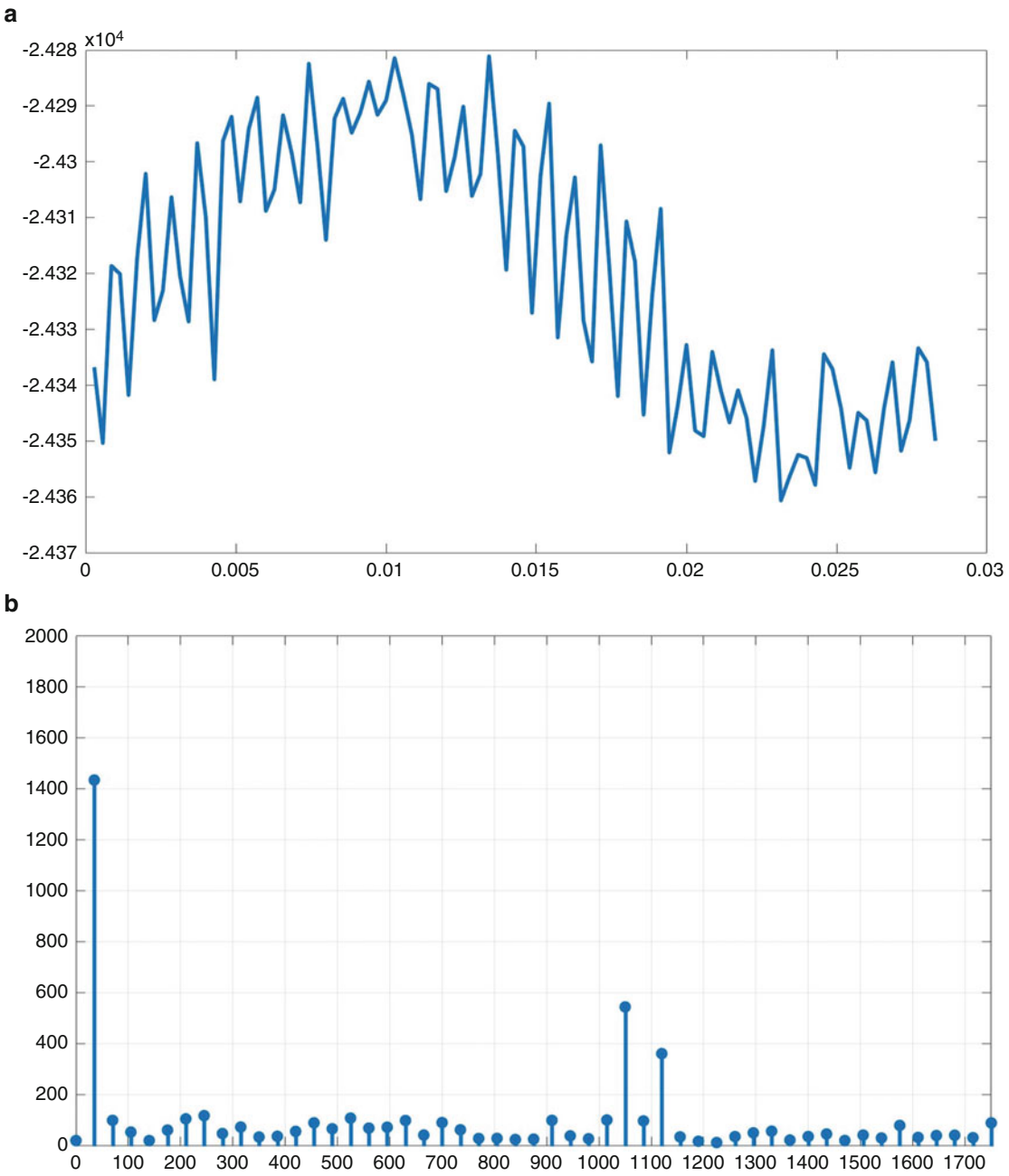

Fig. 6.9 (**a**) Depth information in time domain without timestamp optimization. (**b**) Spectrum magnitudes of depth without timestamp optimization

6.6 Conclusion

The results of this study show that undersampling technique can be used in digital image correlation to measure operating deflecting shape. Moreover, the experiments proved that undersampling can be optimized by timestamp, which significantly increase the accuracy in frequency more than 35 Hz. Due to the limitation of experimental equipment, we did not perform a test with frequency higher than 35 Hz. Technically this approach would be capable of measuring vibration with frequency higher than a few hundred Hz.

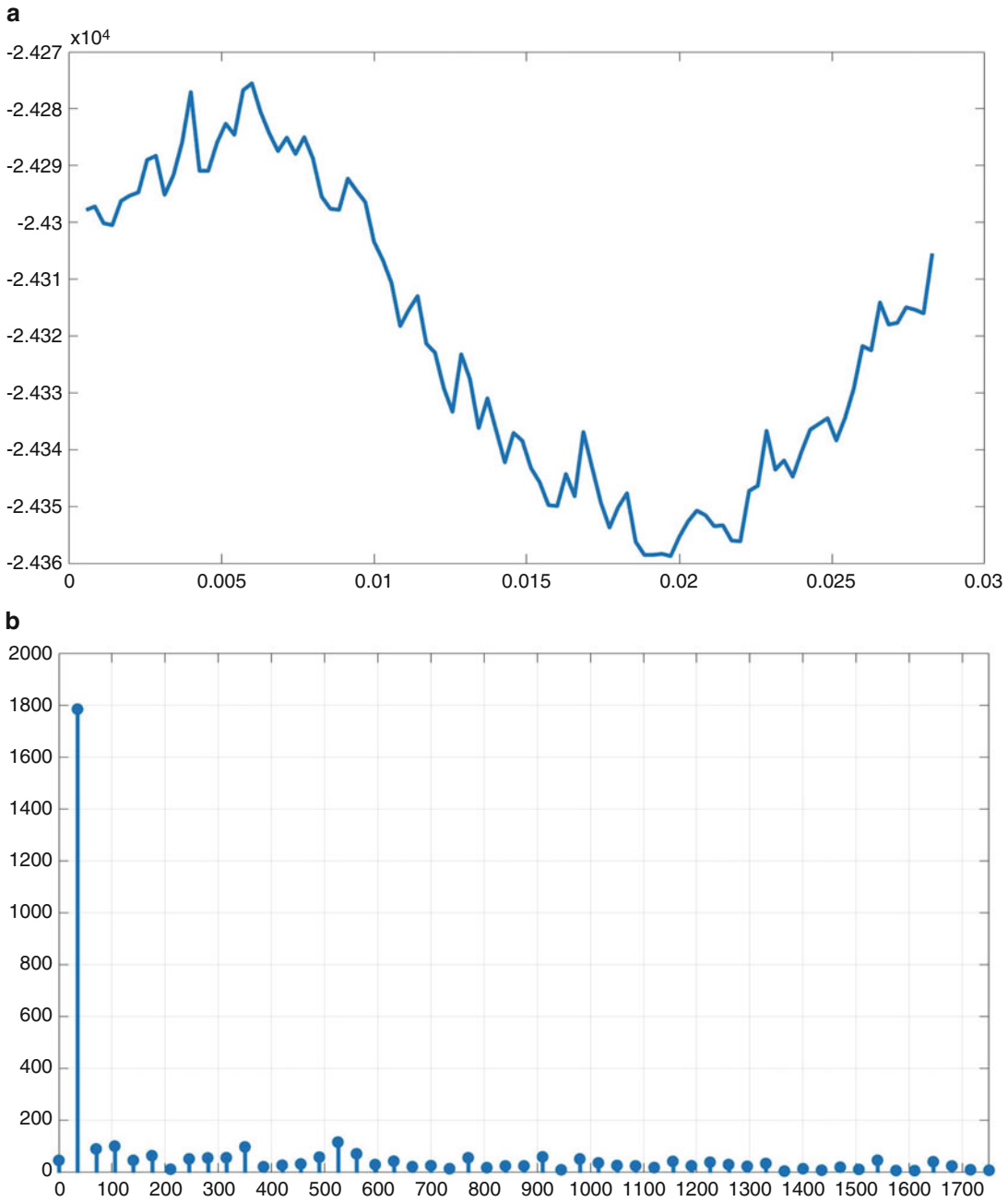

Fig. 6.10 (**a**) Depth information in time domain after timestamp optimization. (**b**) Spectrum magnitudes of depth after timestamp optimization

References

1. Warren, C., Niezrecki, C., Avitabile, P.: 3D digital image correlation methods for full-field vibration measurement. Proceedings of the twenty sixth international modal analysis conference (2008)
2. Avitabile, P., Helfrick, M., Warren, C., Pingle, P., Niezrecki, C.: Noncontact measurement techniques for model correlation. Sound Vib. **44**(1), 8 (2010)
3. Helfrick, M.N., Niezrecki, C., Avitabile, P., Schmidt, T.: 3D digital image correlation methods for full-field vibration measurement. Mech. Syst. Signal Process. **25**(3), 917–927 (2011)
4. Peters, W.H., Ranson, W.F., Sutton, M.A., Chu, T.C., Anderson, J.: Application of digital image correlation methods to rigid body mechanics. Opt. Eng. **22**(6), 738–742 (1983)
5. Chu, T.C., Ranson, W.F., Sutton, M.A.: Applications of digital-image correlation techniques to experimental mechanics. Exp. Mech. **25**(3), 232–244 (1985)

6. Point Grey Research: How is depth determined from a disparity image? Point Grey Research Knowledge Base (2014)
7. Norimatsua, T., Takagi, H., Gail, H.R.: Performance analysis of the IEEE 1394 serial bus (2002)
8. Dunn, J.: Sample clock jitter and real-time audio over the IEEE-1394 high performance serial bus. Nanophon Limited Cambridge, England (1999)
9. IEC-PAS 61883-6:1998: Consumer audio/video equipment–digital interface–part 6: audio and music data transmission protocol, 1394 Trade Association, Austin, 1997 and IEC, Geneva (1998)
10. Point Grey Research: Triclops stereo vision SDK manual (2003)
11. Point Grey Research: Imaging products timestamping and different timestamp mechanisms. Point Grey Knowledge Base (2014)

Chapter 7
Nonlinear Dynamic Analysis of a Thermally Buckled Aircraft Panel Using NNMs

Lucas M. Jarman, Chris VanDamme, and Mathew S. Allen

Abstract Many thin walled structures experience a combination of static thermal stress and large amplitude dynamic loads. From a dynamic perspective, the heating can change both the linear and nonlinear properties of the system so that completely different responses may be obtained (e.g. they may snap through rather than exhibiting a simple hardening nonlinearity). This work uses the "cold modes" approach to create various reduced order models of one panel from a concept hypersonic vehicle; heating is assumed to change only the linear natural frequencies of the panel, but not the mode shapes or geometrically nonlinear effects. The resulting reduced order models are studied by computing their nonlinear normal modes and their response subject to a random dynamic pressure. The comparisons reveal that much can be inferred about the response from the nonlinear modes.

Keywords Reduced order modeling • Geometric nonlinearity • Nonlinear normal modes • Implicit condensation and expansion • Thermal expansion

7.1 Introduction

Geometric nonlinearity is important for thin plates and shells when deformations approach the thickness of the material, especially when the deformation shape or constraints are such that bending deformation induces membrane stretching, as shown in Fig. 7.1 for a clamped-clamped beam. If the boundary conditions are rigid and the structure is initially flat, then small changes in temperature can induce significant membrane stresses, changing the behavior significantly. This work has been motivated by the efforts of the United States Air Force (USAF) and the National Aeronautics and Space Administration (NASA) to model and design reusable hypersonic aircraft. At hypersonic speeds (Mach >5) the aerodynamic pressure is sufficient to cause thin panels to vibrate nonlinearly and thermal loads are also of utmost importance because of the residual stress that they induce and because they can lead to buckling and highly nonlinear vibration of the panel between two buckled states. Similar issues are encountered in stealth aircraft where the engines are buried within the structure to minimize their thermal signature, so that hot exhaust gasses impinge on structural panels.

While the response of a thermally loaded panel could, in principle, be computed using commercial FE codes, the computational cost can measure into the weeks even for relatively simple shell structures with only a few hundred thousand DOF [1]. While much progress has been made in recent years on creating and validating reduced order models (ROM) for geometrically nonlinear structures (e.g. see [2–4] and the review [5]), relatively few works have explored the effect of temperature on the ROM, and on the dynamics of the underlying system. Gordon and Hollkamp [2] created ROMs for a curved panel subjected to a random load and showed how the power spectrum of the response evolved with temperature. They used two approaches, a "cold modes" approach where the linear modes of the structure at room temperature (i.e. no thermal expansion) were used to create the ROM and a "hot modes" approach where the modes at the temperature of interest were used to create the ROM and showed that the two approaches gave almost identical results. Przekop and Rizzi [6] and Spottswood et al. [7] also explored the use of reduced order models under thermal loads, and Mignolet et al. have explored various modeling strategies [8–10].

This work further explores these issues using a section of the "ramp panel," similar to that which was studied by Culler and McNamara [11]. In order to obtain moreinsight into the nonlinear dynamic response, the authors employ Nonlinear Modal analysis, using the definition of a Nonlinear Normal Mode (NNM) pioneered by Rosenberg [12] and refined by Vakakis and Kerschen [13, 14]. The ramp panel model is flat, and while it may not have the thermal relief needed for high temperature

L.M. Jarman (✉) • C. VanDamme • M.S. Allen
Department of Engineering Physics, University of Wisconsin, Madison, WI 53706, USA
e-mail: ljarman@wisc.edu; cvandamme@wisc.edu; msallen@engr.wisc.edu

J.M. Harvie, J. Baqersad (eds.), *Shock & Vibration, Aircraft/Aerospace, Energy Harvesting, Acoustics & Optics, Volume 9*,
Conference Proceedings of the Society for Experimental Mechanics Series, DOI 10.1007/978-3-319-54735-0_7

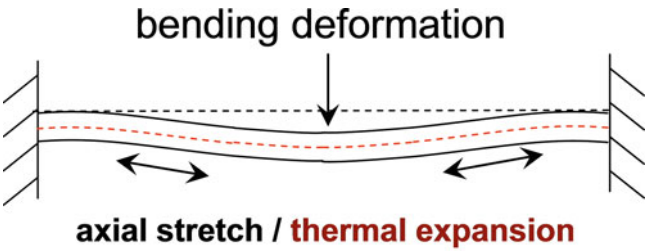

Fig. 7.1 Schematic of clamped-clamped beam subject to bending and thermal loads. When the deformations are small axial stretching can be neglected, but for large deformations the total stiffness increases as the beam must both bend and stretch axially to accommodate the deformation. If the structure is heated then thermal expansion provides additional axial stretching, possibly relaxing the effect due to bending

applications, it does provide an excellent test case since a relatively small temperature change can cause the panel to buckle so that the dynamics change significantly. The linear and nonlinear modal parameters are computed using a "cold modes" reduced order model [7, 15], in which the modes of the room temperature structure are presumed to form an adequate basis for a reduced model. The reduced model is also subjected to random loading and the connection between the nonlinear modes and the random response is explored. The results show that the NNMs give considerable insight into the dynamics. An increase in temperature causes the linear natural frequencies to reduce while leaving the mode shapes largely unchanged. The cold modes approach assumes that the nonlinearity remains unchanged with temperature, and so this reduction in linear stiffness leads to a more strongly nonlinear response and increased interactions between the underlying linear modes.

The paper is outlined as follows. Section 7.2 briefly reviews the ROM modeling strategy and the definition of nonlinear normal modes used in this work. In Sect. 7.3 the methods are applied to the ramp panel using a Titanium material model that includes variation of the modulus and thermal expansion coefficient with temperature. The NNMs and random response are evaluated at various temperatures and conclusions are presented in Sect. 7.4.

7.2 Theoretical Development

After discretization by the finite element method, a nonlinear structure can be represented as,

$$\mathbf{M}\ddot{\mathbf{x}} + \mathbf{K}\mathbf{x} + \mathbf{f}_{NL}(\mathbf{x}) = \mathbf{f}(t) \tag{7.1}$$

where $\mathbf{M}$ and $\mathbf{K}$ are the $N \times N$ linear mass and stiffness matrices and the geometric nonlinearity exerts a nonlinear restoring force through the $N \times 1$ vector, $\mathbf{f}_{NL}(\mathbf{x})$. External loads are accounted for with the $N \times 1$ vector $\mathbf{f}(t)$, and the $N \times 1$ vectors $\mathbf{x}(t)$ and $\ddot{\mathbf{x}}(t)$ are the displacement and acceleration, respectively.

7.2.1 Review of Reduced Order Modeling

A reduced order model is obtained by presuming that the response can be well represented using a small set of mode shapes$(\mathbf{K} - {\omega_r}^2\mathbf{M})\varphi_r = 0$ so that

$$\mathbf{x}(t) = \mathbf{\Phi}_m \mathbf{q}(t) \tag{7.2}$$

Each column in the $N \times m$ mode shape matrix, $\mathbf{\Phi}_m$, is a mass normalized mode shape vector, φ, and $\mathbf{q}(t)$ is a vector of time-dependent modal displacements. The vectors in $\mathbf{\Phi}_m$ are truncated to a small set of m mode shapes, with $m << N$. After applying the modal transformation to the full order Eq. (7.1), the equation of motion for each modal degree of freedom becomes

$$\ddot{q}_r + \omega_r^2 q_r + \theta_r(q_1, q_2, \ldots, q_m) = \boldsymbol{\varphi}_r^{\mathrm{T}} \mathbf{f}(t) \tag{7.3}$$

where ω_r is the linear natural frequency, $()^{\mathrm{T}}$ is the transpose operator and q_r is the rth modal displacement. The nonlinearity couples the modal degrees of freedom so the nonlinear modal restoring force is generally a function of all of the modal displacements $\theta_r(\mathbf{q}) = \boldsymbol{\varphi}_r^{\mathrm{T}} \mathbf{f}_{NL}(\boldsymbol{\Phi}_m \mathbf{q})$. The response of the modes that are excluded from the modal basis is hoped to be negligible. The theory for geometric nonlinearity reveals that the nonlinear modal restoring force can be modeled with second and third order polynomials, which are shown to be

$$\theta_r(q_1, q_2, \ldots, q_m) = \sum_{i=1}^{m} \sum_{j=i}^{m} B_r(i,j)\, q_i q_j + \sum_{i=1}^{m} \sum_{j=i}^{m} \sum_{k=j}^{m} A_r(i,j,k)\, q_i q_j q_k \tag{7.4}$$

The scalars B_r and A_r are the coefficients of the quadratic and cubic nonlinear stiffness terms, respectively, for the rth equation of motion. The two approaches commonly used to determine these coefficients are the Implicit Condensation and Expansion (ICE) method [16] and the Enforced Displacement (ED) method [1, 17]). In the former, a series of load cases are applied to the model and the resulting displacements are used to form a least squares problem in the nonlinear stiffness coefficients. In the latter, the converse procedure is performed, with displacements enforced on the full order model and constraint forces extracted to solve a set of algebraic equations in B_r and A_r. In some works the ED method has seemed to be more numerically stable, but does not implicitly capture the axial stretching effects, so several axial modes of the structure must be included to obtain accurate results. ICE, on the other hand, requires only dominant bending modes of the structure in the basis, and so the basis tends to be approximately half or one third as large.

7.2.2 *Review of Nonlinear Normal Modes*

The nonlinear normal mode definition used throughout this work is based on the definition by Vakakis, Kerschen and others [13, 14], where an NNM is a *not necessarily synchronous periodic solution to the conservative, nonlinear equations of motion*. Nonlinear modes are typically depicted on a frequency versus energy plot, or FEP, which shows how the natural frequency evolves as the response amplitude changes, revealing many qualitative insights into the amplitude dependent dynamics. NNMs are used here to validate the dynamics of NLROMs against those of the original full-order model in a load-independent fashion, as was done in [4].

A pseudo-arclength continuation algorithm, developed originally by Peeters et al. [18], is used throughout this work to compute the NNMs of each of the undamped reduced order models. There exist at least m nonlinear normal mode branches that each initiate at a linear mode at low response amplitude. The continuation algorithm uses the shooting technique to find a set of initial conditions and an integration period that satisfy periodicity as the amplitude in the response changes. A shooting function is defined as,

$$\mathbf{H}(T, \mathbf{q}_0, \dot{\mathbf{q}}_0) = \begin{Bmatrix} \mathbf{q}(T, \mathbf{q}_0, \dot{\mathbf{q}}_0) \\ \dot{\mathbf{q}}(T, \mathbf{q}_0, \dot{\mathbf{q}}_0) \end{Bmatrix} - \begin{Bmatrix} \mathbf{q}_0 \\ \dot{\mathbf{q}}_0 \end{Bmatrix} = \{0\}, \tag{7.5}$$

where T is the period of integration, and $\mathbf{q}_0$ and $\dot{\mathbf{q}}_0$ are the initial modal displacements and velocities for a candidate NNM. The NLROM equations must be integrated over a period T subject to the initial conditions; $\mathbf{q}_0$, $\dot{\mathbf{q}}_0$ and T are modified until the magnitude of the shooting function drops below a numerical tolerance and periodicity is satisfied. The NNM solution is then uniquely defined by $\mathbf{q}_0$, $\dot{\mathbf{q}}_0$, and T. These quantities are used by the continuation algorithm to predict a new periodic solution at a slightly different energy level, eventually forming the full locus of NNMs in frequency-energy space.

7.3 Application to FE of an Aircraft Ramp Panel

The structure modeled was a geometrically nonlinear a ramp panel for a concept hypersonic vehicle. The ramp panel skin is 12 in. (0.3048 m) long, and 10 in. (0.254 m) wide. The skin of the panel has a thickness of 0.065 in. (1.651 mm). Two stiffeners run along the entire length of the skin at the left and right edges. The stiffeners have a depth of 1.25 in. (31.75 mm) and a section thickness of 0.0325 in. (0.8255 mm). The entire panel is composed of Titanium 6AL-4 V, with a Poisson's ratio of 0.31 and temperature dependent elastic modulus and coefficient of thermal expansion shown in Table 7.1.

Table 7.1 Elastic modulus and coefficient of thermal expansion for titanium-6AL-4 V at different temperatures [MIL-HDBK-5H 1998, pp. 5–62 to 5–65]

Temperature (K)	Elastic modulus (GPa)	Temperature (K)	Coefficient of thermal expansion (K^{-1})
264.26	110	294.26	8.82×10^{-6}
699.82	82.7	477.59	9.36×10^{-6}
755.37	73.9	810.93	10.3×10^{-6}
810.93	57.4	1144.26	10.3×10^{-6}

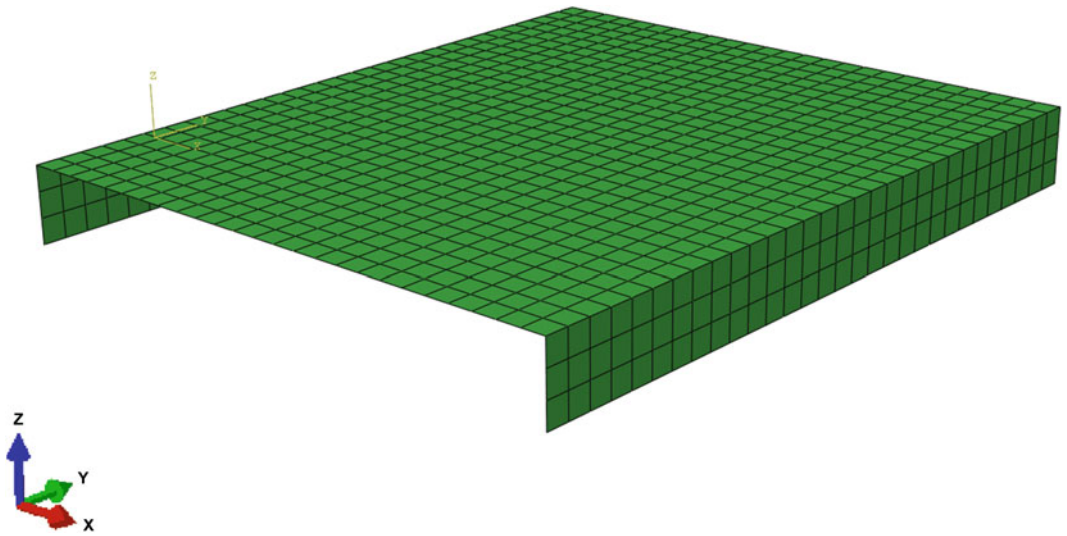

Fig. 7.2 Finite element model of geometrically nonlinear aircraft ramp panel

The finite element model was created in Abaqus®, meshed with 992 S4RT elements, and is shown in Fig. 7.2. The model was initially created and analyzed at room temperature (294.26 K), and then the temperature was varied and modal analysis was repeated to understand how the modal properties change as the material properties change with temperature and the pre-stress in the model changes. This was done in Abaqus® by defining a coupled temperature-displacement step, followed by a linear frequency step. Fixed boundary conditions were applied at all edges to prevent bending motion but allow thermal expansion. Specifically, the bottom edges of the stiffeners were constrained in x and z displacements, but allowed axial extension in the y-direction and rotation. The leading edge of the panel skin was fully constrained in all six DOF. The trailing edge of the panel skin was constrained in every DOF except y-displacement.

The linear natural frequencies of the first three modes computed at various temperatures using this approach are shown in Fig. 7.3. All frequencies initially decreased with increasing temperature, but then they each individually reach a point where the frequency begins to increase, presumably as the buckled shape induces enough curvature so that the flat panel becomes arched. Interestingly, the second and third natural frequencies cross at about 545 K. An investigation of the mode shapes, shown in Fig. 7.4 reveals that the mode shapes switch, so this would need to be accounted for in the cold modes ROM approach.

The mode shapes shown in Fig. 7.4 reveal that that, except for the changing order of the modes, the mode shapes seem to remain relatively constant. As a result one would expect the cold modes ROM approach to remain valid.

The ICE method was then used to create a ROM at room temperature. Various combinations of modes were used to generate static load cases, and then static analysis was performed in Abaqus and the resulting force displacement data was used to compute the nonlinear terms in the reduced equations of motion. In all of these cases the load levels were chosen so that the linear structure would deform the average of the skin thickness and stiffener thickness. Figure 7.5 shows the FEP of the first NNM for a few candidate ROMs.

Initially, a ROM that used only mode 1 was created, and modes were continually added to the basis in the order of their dominance in the static responses used to create the previous ROM. This seemed reasonable since the first NNM was expected to dominate the response and the others were expected to be important only if they were statically coupled to NNM 1. The shapes of the other modes that were added to the ROM are shown in Fig. 7.6. NNM 1 was found to change very little as higher modes were added to the ROM, however for the five mode ROM the first NNM comes to an internal

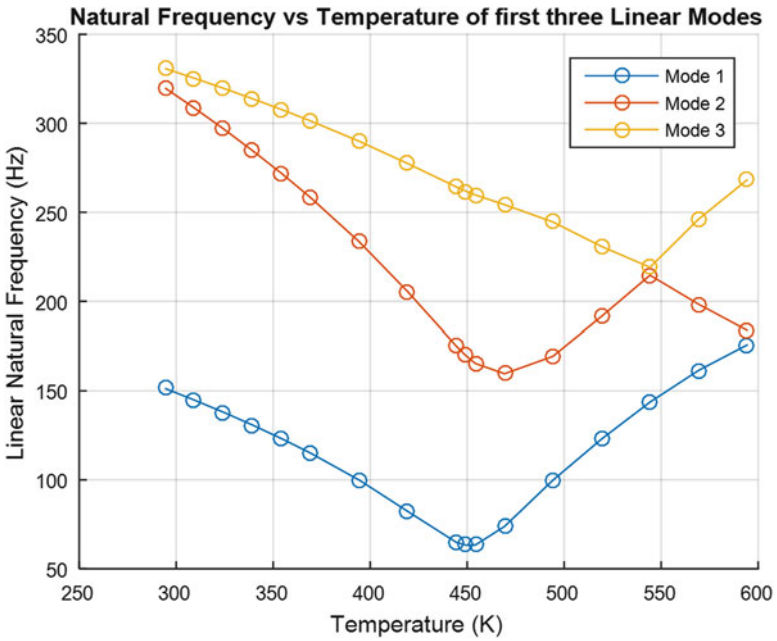

Fig. 7.3 Natural frequencies of the first three linear modes vs. temperature for the panel

resonance at 225 Hz and is not able to compute the rest of the backbone. The four mode ROM (containing modes 1, 2, 5 and 6) appeared to agree very well with the five mode ROM (containing modes 1, 2, 5, 6 and 19) and so NNMs were computed at increased temperature for both of these ROMs. As mentioned previously, this was done using a "cold modes" approach [7, 15, 19]. The FEPs for a few temperatures, found using both the four and five mode ROMs, are shown in Fig. 7.7.

The FEPs for both cases agreed very well, although we were not able to compute the NNM of the five mode ROM to as high of temperatures to internal resonance. Hence, the first NNM from the five mode ROM ran into internal resonance at 170 Hz for the 309.26 K case, 165 Hz for the 339.26 K case, and around 200 Hz for the 369.26 K case. The 369.26 K continuation continued for a while after resonance, but with heavy interaction from other modes affecting reliability of the result. The four mode case ran uninterrupted to at least 260 Hz for all cases, and so it was used from here forward. The FEPs for the four mode ICE 1-2-5-6 ROM are shown in Fig. 7.8 for a variety of temperatures.

The FEP shows that first linear natural frequency of the ROMs decreased with increasing temperature, as expected. However, because the nonlinearity remains the same as the stiffness goes down, the high temperature ROMs also began to diverge from linearity at lower energies. The NNMs at the two higher temperatures were not computed to as high of energies as the others because the algorithm encountered some internal resonance branches and was not able to continue, and the publication schedule of this paper did not allow us to explore this further.

The power balance algorithm in [20, 21] was used to compute how large of a force would be needed to drive the system to various points on the NNM curves. In all cases the force was uniformly distributed in space in the z-direction and sinusoidal at the NNM frequency. The forces computed at 294 and 394 K, shown in Fig. 7.8 are nearly the same, and drive the system to almost the same energy, suggesting that the same level of force is needed to drive the system to a certain energy level, even though the linear stiffness has decreased significantly. This suggests that the random response may reach similar levels as the temperature varies, but that the level of nonlinearity excited (as evidenced by the shift or smearing of the resonance frequency) would be much greater at higher temperature. This inference will now be checked by computing the true random response of these NLROMs.

The environment of interest for the panel is a random pressure loading. To evaluate the ROM's performance in this environment, the response of the ROM was found subject to a uniform (over the panel area) pressure that varied randomly in time. The spectrum of the input was white and constant from 0 to 800 Hz, encompassing the first several modes of the panel. The power spectrum of the resulting time response and the power spectral density (PSD) for each case is shown in Fig. 7.9.

Although the nonlinear terms in the EOM were the same in each of these ROMs, the panel's linear stiffness decreased with heating and so it diverged from linearity earlier. Perhaps most revealing of the PSDs is the first, and lowest amplitude case shown in Fig. 7.9. In this case the room temperature ROM still looks very linear and has a peak corresponding to the first linear frequency. For the same amplitude the 394 K ROM underwent a frequency shift of about 5 Hz, and the 454 K ROM experienced a shift of 10 Hz, corresponding to a point far up the frequency-energy curve for that temperature. Increasing the

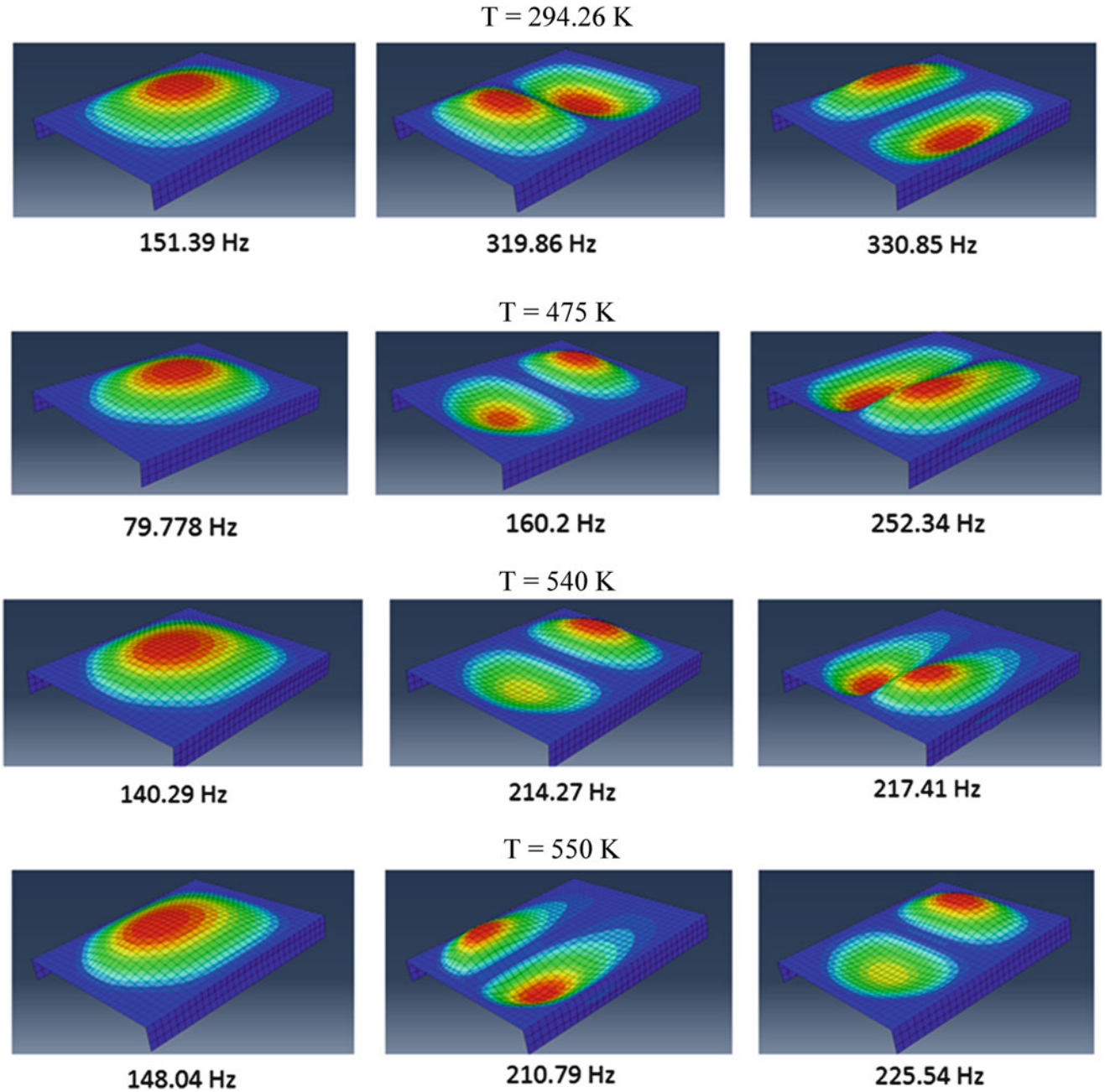

Fig. 7.4 Shapes of the first three linear modes at various temperatures. Note that between 540 and 550 K, the second and third mode shapes switch order

amplitude of the pressure made the responses all nonlinear. For reference, at 294 K the RMS displacement at the center of the panel was 0.09, 0.27 and 0.57 mm at the three load levels, while at 454 K it increased to 0.2, 0.4 and 0.7 mm. Clearly the nonlinearity sets in at lower amplitudes as the temperature increased, just as one would have expected based on the NNMs. It is also interesting to note that the RMS displacement increased by only about a factor of two for every order of magnitude increase in the pressure amplitude. This highlights the value in exploiting nonlinearity in a design such as this.

The modal interactions are also evident in the PSDs; these can be seen more clearly in modal coordinates. Shown in Fig. 7.10 is the PSD of Modes 1 and 2 at the intermediate amplitude. As the temperature increases and the response becomes more nonlinear, mode 2 is more strongly excited. Mode 2 would not be excited in a linear response due to its anti-symmetric shape, so presumably it is excited due to an interaction with mode 1.

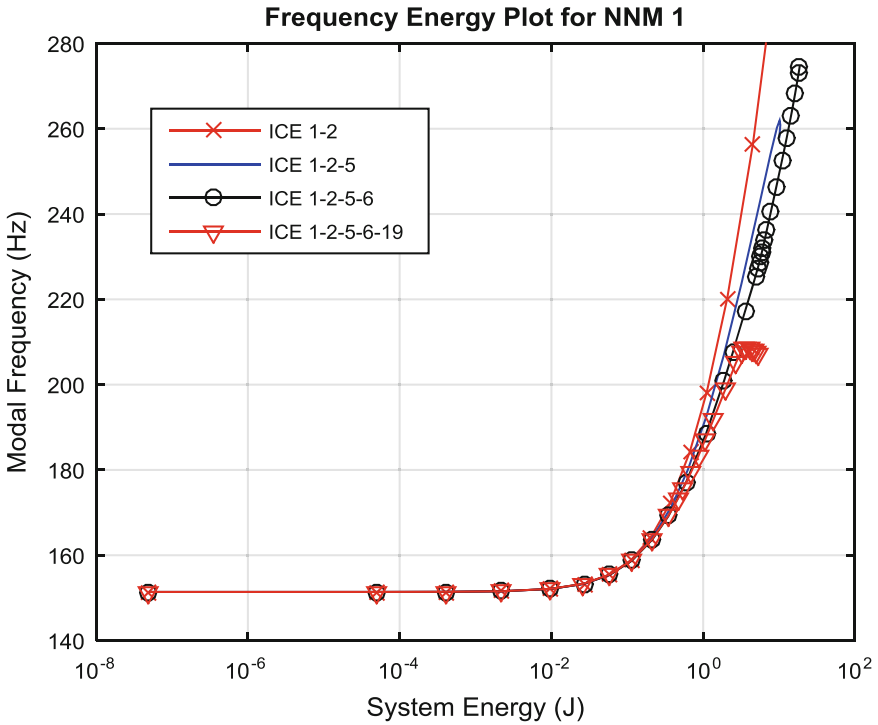

Fig. 7.5 Frequency-energy plot of the first nonlinear normal mode of the ramp panel at room temperature for various candidate ROMs

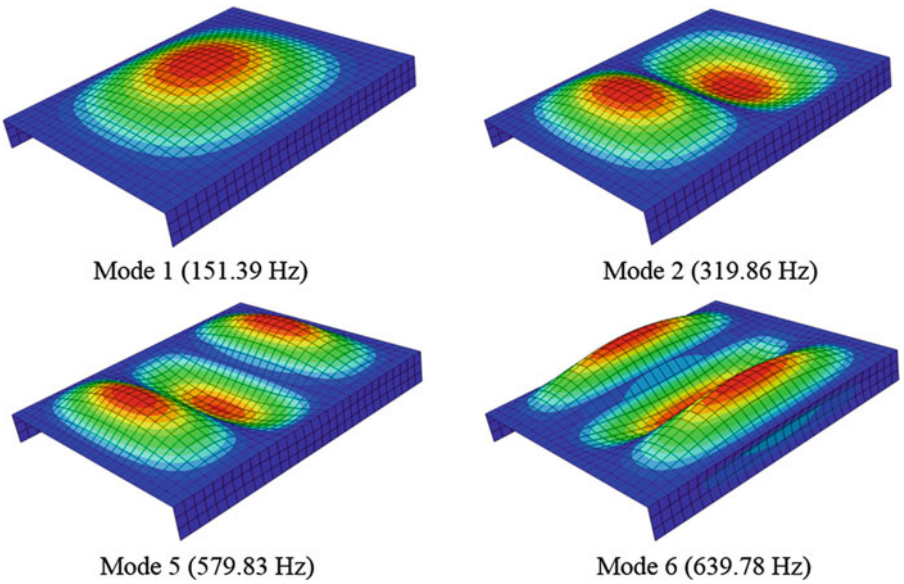

Fig. 7.6 Modes 1, 2, 5 and 6 used to generate the four mode ROM

7.4 Conclusions

This work investigated an approach to generate reduced order models for dynamic analysis of a structure that experiences thermal deformation. The ROMs enabled us to compute the nonlinear frequency-energy dependence and dynamic response of the heated FE model at a dramatically lower computational cost than would have been required on the full order model. The temperature dependence of the behavior of a ramp panel was clearly revealed. Temperature was shown to have a significant effect on the dynamics of the system. As the panel was heated it became more compliant due to residual stress,and this

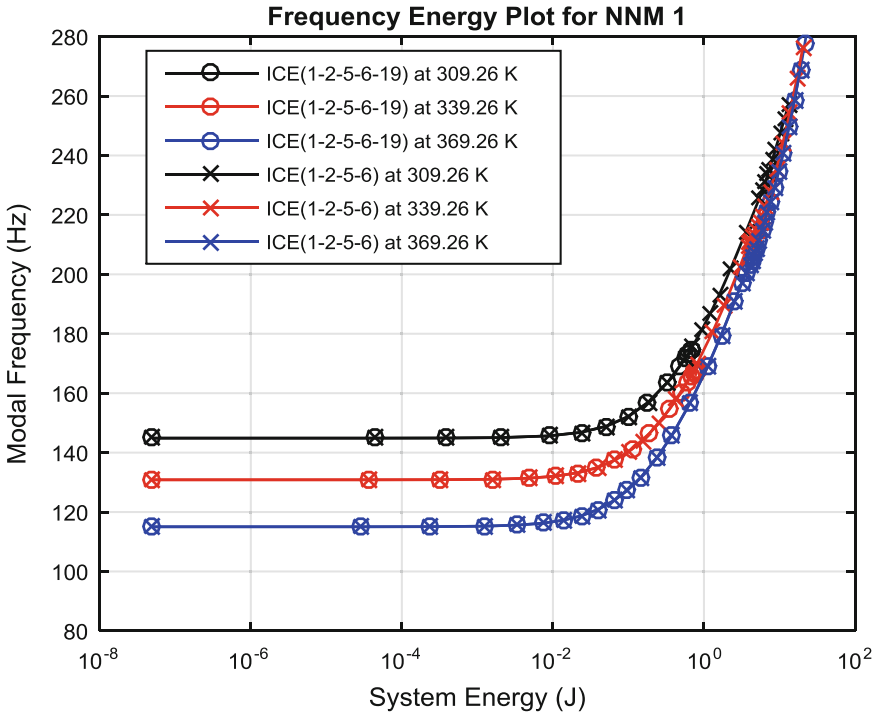

Fig. 7.7 Frequency-energy plot of the first NNM for three temperatures, comparing the four and five mode ICE ROMs

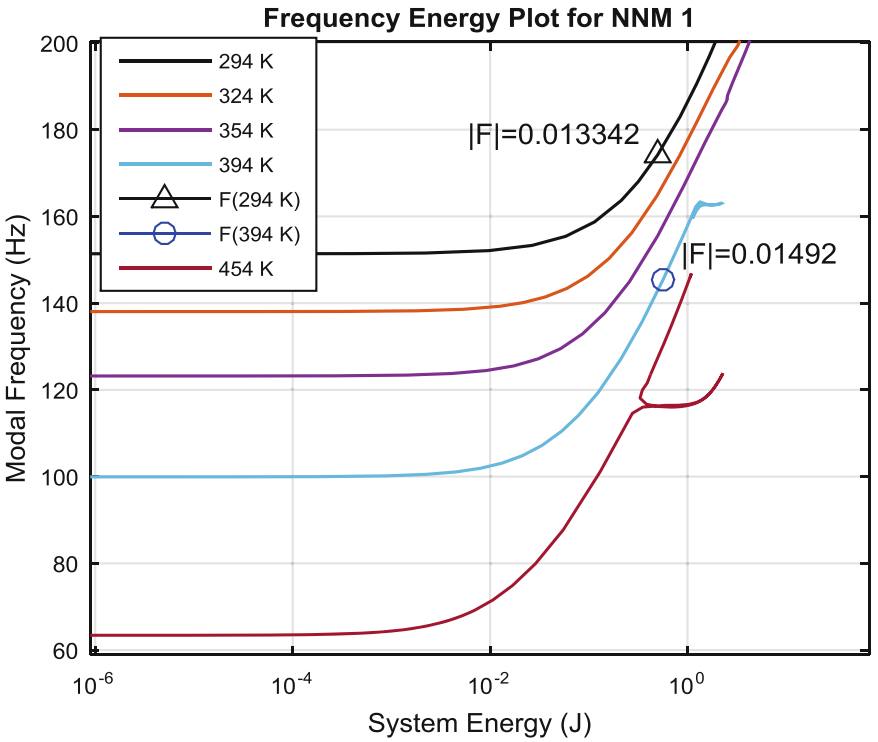

Fig. 7.8 Frequency -energy plots for the first NNM of the panel at various temperatures

caused the linear natural frequencies to decrease while the nonlinearity in the model (for the cold modes approach) remained unchanged. This increased compliance caused the system to behave more nonlinearly for the same forcing amplitude, leading to smearing of the resonance in the PSD and enhanced modal interactions.

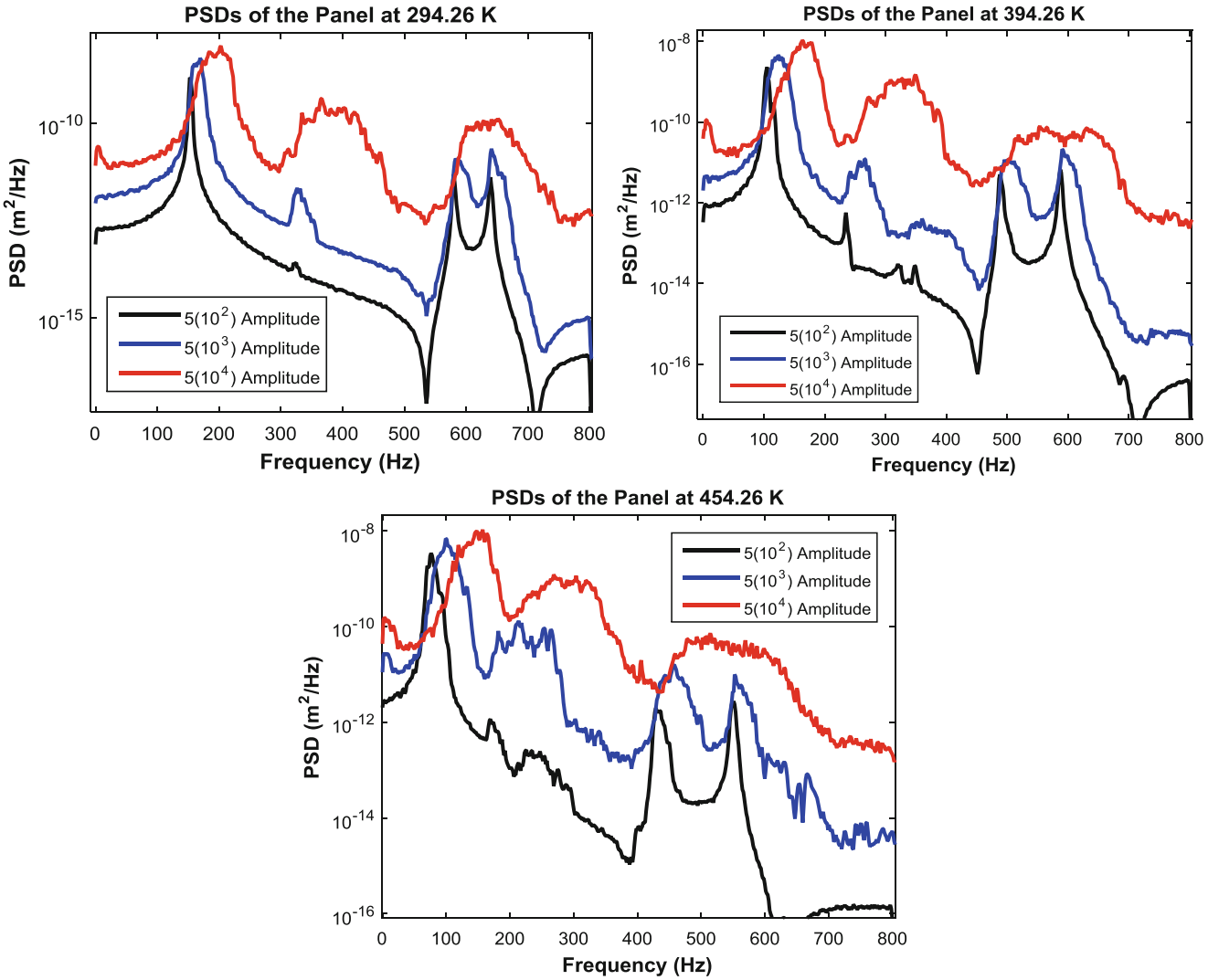

Fig. 7.9 Power spectral density at a point near the *center* of the panel. Each plot shows the panel at three amplitude levels for a different temperature. In each case the pressure was applied in the z-direction on every node on the panel skin with amplitude that varied randomly in time

7.5 Future Work

A few things are notably absent from this paper due to the tight publication schedule. First, the ROMs have not been validated other than checking that they converge as modes are added to the basis. Perhaps we could argue that this mimics a realistic case in which a model is too large to compute the truth NNMs. However, even with a large model we expect that it would be possible to at least peform a periodicity check by integrating the full FEM with the initial condition from the ROM, as done in [22]. It would also be useful to validate the PSDs that were obtained using the ROM by integrating the full order model. However, even with this simple model it took about 1 day to complete full order time integration over a long enough window to allow the PSD to be computed, and so in the time that was required to perform all of the analyses here it was not possible to finish debugging even one integration of the full order Abaqus model. Finally, the cold modes approach does make a significant assumption about the modal basis of the ROM, and for the large displacements observed here it would seem wise to also explore the "hot modes" approach. This will certainly be pursued in future works.

Acknowledgements The authors wish to thank Joseph D. Schoneman from ATA Engineering, Huntsville, AL for providing the impetus for the work and for help implementing the thermal models and Dr. Joseph Hollkamp from the Structural Sciences Center at the Air Force Research Laboratory for helpful suggestions and discussions regarding the ROM modeling.

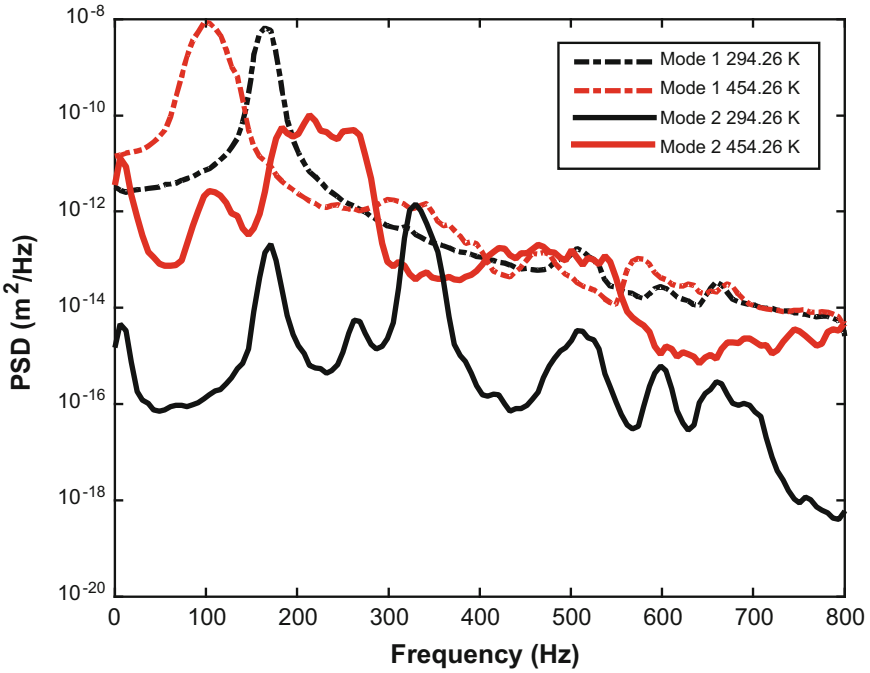

Fig. 7.10 Power spectral density of linear modal amplitudes of modes 1 and 2 at room temperature, and 454.26 K for a forcing amplitude of 5×10^3 (the intermediate forcing case)

References

1. Perez, R., Wang, X.Q., Mignolet, M.P.: Nonintrusive structural dynamic reduced order modeling for large deformations: enhancements for complex structures. J. Comput. Nonlinear Dyn. **9**, 031008 (2014)
2. Gordon, R.W., Hollkamp, J.J.: Reduced-order models for acoustic response prediction. AFRL-RB-WP-TR-2011-3040 (2011)
3. Hollkamp, J.J., Gordon, R.W., Spottswood, S.M.: Nonlinear modal models for sonic fatigue response prediction: a comparison of methods. J. Sound Vib. **284**, 1145–1163 (2005)
4. Kuether, R.J., Deaner, B., Allen, M.S., Hollkamp, J.J.: Evaluation of geometrically nonlinear reduced order models with nonlinear normal modes. AIAA J. **53**, 3273–3285 (2015)
5. Mignolet, M.P., Przekop, A., Rizzi, S.A., Spottswood, S.M.: A review of indirect/non-intrusive reduced order modeling of nonlinear geometric structures. J. Sound Vib. **332**, 2437–2460 (2013)
6. Przekop, A., Rizzi, S.A.: Dynamic snap-through of thin-walled structures by a reduced-order method. AIAA J. **45**, 2510–2519 (2007)
7. Spottswood, S.M., Hollkamp, J.J., Eason, T.G.: Reduced-order models for a shallow curved beam under combined loading. AIAA J. **48**, 47–55 (2010)
8. Matney M., Perez R.A., Spottswood S.M., Wang X.Q., Mignolet A.M.P.: Nonlinear structural reduced order modeling methods for hypersonic structures. In: 53rd AIAA/ASME/ASCE/AHS/ASC structures, structural dynamics and materials conference, Honolulu, HI, United States, 23–26 April 2012
9. Radu A.G., Yang B., Kim K., Mignolet M.P.: Prediction of the dynamic response and fatigue life of panels subjected to thermo-acoustic loading. In: Collection of Technical Papers – 45th AIAA/ASME/ASCE/AHS/ASC structures, structural dynamics, and materials conference; 12th AIAA/ASME/AHS Adapt. Struct. Conf.; 6th AIAA Non-Deterministic Approaches Forum; 5th AIAA Gossamer Spacecraft Forum, 19–22 April 2004, Palm Springs, CA, USA, pp. 520–528 (2004)
10. Kim K., Yang B., Mignolet M.P., Spottswood S.M.: Fatigue life prediction of panels subjected to thermo-acoustic loading. In: 44th AIAA/ASME/ASCE/AHS/ASC Structures, Structural Dynamics, and Materials Conference, 7–10 April 10, 2003, Norfolk, VA, USA, pp. 3430–3438 (2003)
11. Culler A.J., McNamara J.J.: Coupled flow-thermal-structural analysis for response prediction of hypersonic vehicle skin panels. Paper presented at the 51st AIAA/ASME/ASCE/AHS/ASC structures, structural dynamics, and materials conference, Orlando, FL (2010)
12. Rosenberg, R.M.: Normal modes of nonlinear dual-mode systems. J. Appl. Mech. **27**, 263–268 (1960)
13. Vakakis, A.F.: Non-linear normal modes (NNMs) and their applications in vibration theory: an overview. Mech. Syst. Signal Process. **11**, 3–22 (1997)
14. Kerschen, G., Peeters, M., Golinval, J.C., Vakakis, A.F.: Nonlinear normal modes. Part I. A useful framework for the structural dynamicist. Mech. Syst. Signal Process. **23**, 170–194 (2009)
15. Gordon R.W., Hollkamp J.J.: Reduced-order models for acoustic response prediction. Air Force Research Laboratory, AFRL-RB-WP-TR-2011-3040, Dayton, OH (2011)
16. Hollkamp, J.J., Gordon, R.W.: Reduced-order models for nonlinear response prediction: implicit condensation and expansion. J. Sound Vib. **318**, 1139–1153 (2008)

17. Muravyov, A.A., Rizzi, S.A.: Determination of nonlinear stiffness with application to random vibration of geometrically nonlinear structures. Comput. Struct. **81**, 1513–1523 (2003)
18. Peeters, M., Viguie, R., Serandour, G., Kerschen, G., Golinval, J.C.: Nonlinear normal modes, part II: toward a practical computation using numerical continuation techniques. Mech. Syst. Signal Process. **23**, 195–216 (2009)
19. Przekop A., Stover M.A., Rizzi S.A.: Nonlinear reduced-order simulation using stress-free and pre-stressed modal bases. In: 50th AIAA/ASME/ASCE/AHS/ASC structures, structural dynamics and materials conference, Palm Springs, CA, United States, 4–7 May 2009
20. Kuether, R.J., Renson, L., Detroux, T., Grappasonni, C., Kerschen, G., Allen, M.S.: Nonlinear normal modes, modal interactions and isolated resonance curves. J. Sound Vib. **351**, 299–310 (2015)
21. Hill, T.L., Cammarano, A., Neild, S.A., Wagg, D.J.: Interpreting the forced responses of a two-degree-of-freedom nonlinear oscillator using backbone curves. J. Sound Vib. **349**, 276–288 (2015)
22. Kuether R.J., Allen M.S.: Validation of nonlinear reduced order models with time integration targeted at nonlinear normal modes. Paper presented at the 33rd International Modal Analysis Conference (IMAC XXXIII), Orlando, FL (2015)

Chapter 8
Empirically-Derived, Constitutive Damping Model for Cellular Silicone

Jonathan B. Russ and Benjamin R. Pacini

Abstract One of the more common forms of passive vibration isolation in mechanical systems has been the use of elastomeric or foam pads. Cellular silicone foam is one such example which has been used for vibration isolation and mitigating the effects of mechanical shock. There are many desirable properties of cellular silicone, including its resilience and relative insensitivity to environmental extremes. However, there is very little test data that is useful for understanding its dynamic characteristics or for the development of a predictive finite element model. The problem becomes increasingly difficult since foam materials typically exhibit nonlinear damping and stiffness characteristics. In this paper we present a test fixture design and method for extraction of a few dynamic properties of one type of cellular silicone foam pad. The nonlinear damping characteristics derived from the experimental testing are then used to attempt to improve the predictive capability of a linear finite element model of the system. Difficulties and lessons learned are also presented.

Keywords Cellular silicone • Nonlinear damping • Foam • Strain energy • Modal analysis

Nomenclature

ω_i	Natural frequency of mode i
ζ_i	Damping ratio for mode i
$\underline{\underline{M}}$	System mass matrix
$\underline{\underline{C}}$	System damping matrix
$\underline{\underline{K}}$	System stiffness matrix
$\underline{\underline{\Phi}}$	Mode shape matrix
$\underline{\ddot{q}}$	Modal acceleration vector
$\underline{F}$	System external force vector
SE_{CS}	Strain energy in the cellular silicone material
$\underline{\underline{K}}_{CS}$	Cellular silicone stiffness matrix
FEM	Finite element model

8.1 Background

Cellular silicone pads have been commonly used between mechanical components in order to mitigate the effects of vibration and mechanical shock. Typically, the material is also compressed to some extent, either by gravity, bolt loads, or some combination of external loads. As a consequence of the underlying structure of the material and the preload, the material typically exhibits highly nonlinear stiffness and damping characteristics which may significantly impact the dynamics of the overall assembly.

J.B. Russ (✉)
Analytical Structural Dynamics, Sandia National Laboratories, P.O. Box 5800, Albuquerque, NM 87123-0840, USA
e-mail: jbruss@sandia.gov

B.R. Pacini
Experimental Structural Dynamics, Sandia National Laboratories, P.O. Box 5800, Albuquerque, NM 87123-0557, USA
e-mail: brpacin@sandia.gov

J.M. Harvie, J. Baqersad (eds.), *Shock & Vibration, Aircraft/Aerospace, Energy Harvesting, Acoustics & Optics, Volume 9*,
Conference Proceedings of the Society for Experimental Mechanics Series, DOI 10.1007/978-3-319-54735-0_8

Often it is desirable to be able to predict the response of an assembly to some set of external loads via the use of a finite element model (FEM). Performing testing on real components for all given load cases may be cost prohibitive or perhaps the testing is not currently achievable, either due to lack of knowledge, time, or other constraints. In these cases, development of a mathematical model of the system may be the only option to gain insight into the potential response of a given system.

In an effort to reduce the epistemic uncertainty associated with the development of any model of a physical system, the properties and constitutive models of the materials should be as representative of the physical system as possible. However, this requires sufficient test data that is relevant to and representative of the physics in one's particular system. For common elastic, isotropic materials this is usually not an issue. However, for a material with a more complex behavior, the experimental data in the literature is commonly sparse. This motivates the need for additional material testing.

We will attempt to use experimental modal techniques in conjunction with finite element modeling to derive a constitutive model for the nonlinear damping for cellular silicone pads as a function of strain energy resulting primarily from shear deformation (hereafter referred to as shear strain energy). A test fixture was designed such that the silicone pads were the only medium for energy dissipation within a specified frequency bandwidth. Two sets of impact modal tests were then conducted on this fixture. The first utilized low excitation forces to establish a linear model which was used to initially calibrate a linear FEM of the hardware. The second exercised the nonlinearities in the cellular silicone via high excitation forces. A modal filtering approach similar to that from [1] was used to then extract a time-varying damping function of a specific target mode from this high level excitation data. This nonlinear damping data was then incorporated into a FEM in order to create a constitutive damping model for the cellular silicone material undergoing primarily shear deformation. Note that this constitutive model would only be applicable for determining the damping associated with shear deformation in the silicone. A separate constitutive model would need to be developed to account for the damping associated with compressive/tensile deformation and is included in the plans for future work section of this paper.

Section 8.2, the test hardware, instrumentation, and test approach are described along with the results of the low level impact modal test. Section 8.3 discusses the post-processing of the high level impact data and the method for extracting the time-varying damping. The calibration of the linear FEM for the test hardware to the linear modal results is contained in Sect. 8.4. The nonlinear, time-varying damping extracted from the high level experimental data is then incorporated into the FEM as described in Sect. 8.5. Using results from the FEM, the damping is then fit in terms of the shear strain energy in the cellular silicone pads. This function is then used to predict the response to different hammer impacts that were conducted on the hardware. Sections 8.6 and 8.7 summarize our conclusions and plans for future work.

8.2 Experiment

8.2.1 Test Fixture Design

In an effort to obtain some insight into the dissipative capacity (damping) of the material, a simple test fixture was designed with the intention of isolating the properties of the cellular silicone pad while appropriately representing the base state in which a 50% compression preload is applied. A diagram illustrating the different components of the simple fixture is provided in Fig. 8.1. The steel block in the center of the fixture is held between the two outer aluminum plates with four rectangular strips of the cellular silicone pads in between. Four bolts pass through the outer aluminum plates allowing the cellular silicone pads to be compressed. In addition, the surfaces of the steel block and aluminum plates that are in contact with the cellular silicone pads were machined to a precise level of surface flatness. In order to accurately control the level of compression of the cellular silicone pads, four steel spacers (hollow cylinders which allow the bolts to pass through) were machined to a precise length. This ensures that when the bolts are sufficiently tightened, the pads will assume the desired level of compression.

The main intent of the test fixture design is to ensure that there will only be strain energy in the cellular silicone material for the first few flexible mode shapes of the system. A "rectangular" shape (i.e. the length of the fixture is longer than its width) was chosen in an effort to better separate the modal frequencies of the first six modes of the system so that extraction of the modal parameters could be performed with higher confidence. The first six mode shapes of the system reflect the rigid body motion of the steel block with respect to the aluminum plates, developing strain energy only in the cellular silicone pads.

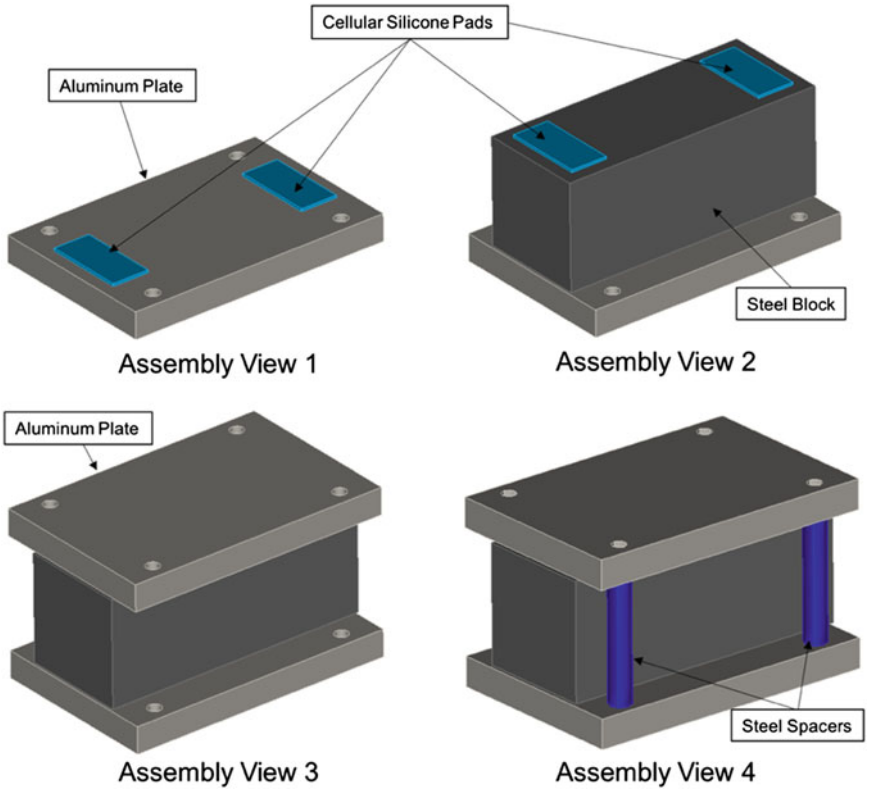

Fig. 8.1 Test fixture assembly views

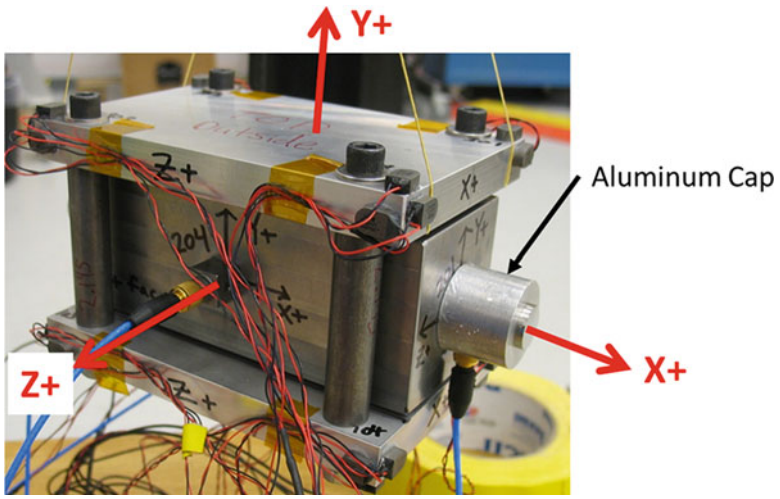

Fig. 8.2 Test hardware and coordinate system

8.2.2 Test Set-Up

The test hardware shown in Fig. 8.2 was softly suspended using bungee cords to approximate a free-free boundary condition and instrumented with 10 mV/g accelerometers. The accelerometers were located on the block and two plates such that their six degree of freedom (DOF) rigid body modes would be accurately captured: one triaxial accelerometer was placed on each exposed face of the steel block and three uniaxial accelerometers were placed on three orthogonal faces at each corner of each aluminum plate. Additionally, an aluminum cap was placed over the accelerometer on both square faces of the block. These caps allowed for good alignment of the excitation and response when impacting at these locations.

Table 8.1 Excitation information

Input DOF	Description	Low level peak force (N)	High level peak force (N)
101Z	Lateral input at corner of lower plate	2	N/A
201X	Lateral input on square face of steel block	2	44, 178, 311
303Y	Vertical input at corner of upper plate	2	N/A
304Y	Vertical input at corner of upper plate	2	N/A

Table 8.2 Linear modal parameters[a,b]

Mode	Frequency (Hz)	Damping (%cr)	Reference	Description
7	93	6.37	101Z	Block translation in global Z with rotation in Y–Z plane (roll mode)
8	*106*	*5.98*	*201X*	*Block translation in global X*
9	116	6.24	101Z	Block rotation in X–Z plane (yaw mode)
10	127	6.12	101Z	Block rotation in Y–Z plane (roll mode) with translation in global Z
11	190	11.91	304Y	Block translation in global Y
12	209	10.28	303Y	Block rotation in X–Y plane (pitch mode)

[a]Rigid body modes not shown
[b]Italicised mode is the target mode for nonlinear analysis

Two series of hammer impact tests were conducted on this hardware. The first minimized nonlinear response by applying low level inputs with peak forces of approximately 2 N at the locations shown in Table 8.1. The data from these tests were used to extract the linear model of the hardware. The second set of tests excited nonlinear response of the X-translation mode of the steel block by impacting DOF 201X at 44, 178, and 311 N. The 311 N data was used to extract the nonlinear damping function while the 44 and 178 N data was used to validate the accuracy of this damping function via interpolation using a finite element model. Note that the hammer tip was selected to ensure that the excitation bandwidth only included the rigid modes of the steel block with respect to the fixture and not the elastic fixture modes. This ensures that all strain energy is contained in the silicone pads.

8.2.3 Linear Modal Analysis Results

The Synthesize Modes And Correlate (SMAC) program by Mayes and Hensley [2] was used to extract the modal parameters from the low level impact data using a real modes approximation in Table 8.2. Rigid body mode shapes were calculated from the measured physical properties of the hardware.

These data were used to create the mode shape matrix that is utilized later in this report. The X-translation mode of the block (mode 8) is the target mode for the nonlinear analysis as it deforms the silicone pads purely in shear. Additionally, it is the mode that is able to be most purely excited given the test fixture and instrumentation.

8.3 Post-Processing of High Level Impact Data

The objective for this work is to develop a nonlinear damping function in terms of cellular silicone shear strain energy. Simple shear in the pads is achieved when the steel block rigidly translates in the X-direction (mode 8 from Table 8.2). The next step is to extract the nonlinear, time-varying damping of this mode. This is accomplished in two phases. The first phase is to extract the motion of mode 8 from the responses measured by the accelerometers during the 311 N impact test. This is accomplished using a modal filter. The second task is the calculate the time-varying damping of this mode. The following two subsections discuss these processes in further detail.

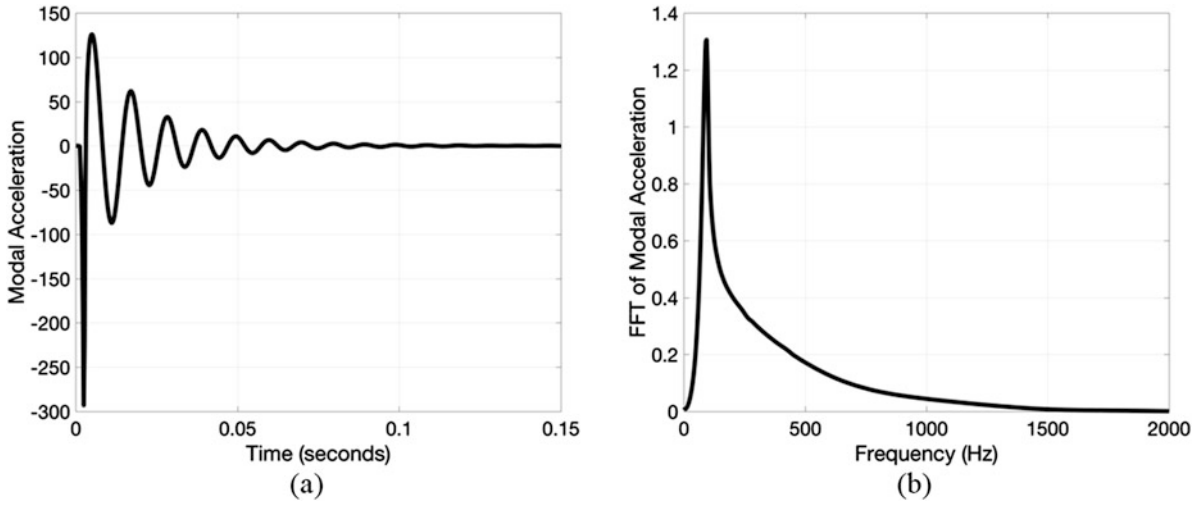

Fig. 8.3 Modal acceleration of mode 8 extracted from 311 N impact experiment in (**a**) time domain and (**b**) frequency domain

8.3.1 Modal Filter

The use of a modal filter in nonlinear system identification was successfully employed in [1] where a pseudo modal model was used to capture the nonlinear characteristics of a complex structure. The success of this method is directly dependent on the ability of the modal filter to eliminate all other modal responses except for the single mode of interest. Reference [1] offers multiple methods for modal filtering the measured responses. One of those options, the Full Modal Filter (FMF), is utilized for this work. The FMF is derived from the modal substitution equation:

$$\underline{\ddot{u}} = \underline{\underline{\Phi}} \cdot \underline{\ddot{q}} \tag{8.1}$$

where $\underline{\underline{\Phi}}$ is the matrix of all rigid body and elastic extracted mode shapes in the frequency band of interest. By pre-multiplying (8.1) by the pseudo-inverse of the mode shape matrix, one obtains

$$\underline{\underline{\Phi}}^{+} \cdot \underline{\ddot{u}} = \underline{\ddot{q}} \tag{8.2}$$

The desired modal response is then selected from the corresponding row (or column) of $\underline{\ddot{q}}$. The $\underline{\underline{\Phi}}$ matrix for this work was extracted from the low level impact testing described in Sect. 8.2.3. Figure 8.3 shows the response of the X translation mode of the steel block extracted from the 311 N impact test. Now that this mode has been isolated, its associated time-varying damping can now be extracted.

8.3.2 Nonlinear Damping from Ring-Down Data

Once we have obtained a single degree of freedom response of mode 8 from modal filtering as described above, we can quantify the damping as a function of time. The method for accomplishing this is described in [1] which closely follows the procedure from [3, 4]. In this work, the Hilbert Transform is computed and a cubic polynomial is fit to the time varying amplitude and phase. This approach fits the modal response of mode 8, $\ddot{q}(t)$, to the following functional form,

$$\ddot{q}(t) = e^{d(t)} \cos\left[\theta(t)\right] \tag{8.3}$$

where $d(t)$ and $\theta(t)$ are each cubic polynomials in time and are, respectively, the decay and phase of the time varying response model. In order to calculate the time-varying damping, the analytic signal, $\ddot{Q}(t)$, is used:

$$\ddot{Q}(t) = \ddot{q}(t) + i\,\mathscr{H}\left(\ddot{q}(t)\right) \tag{8.4}$$

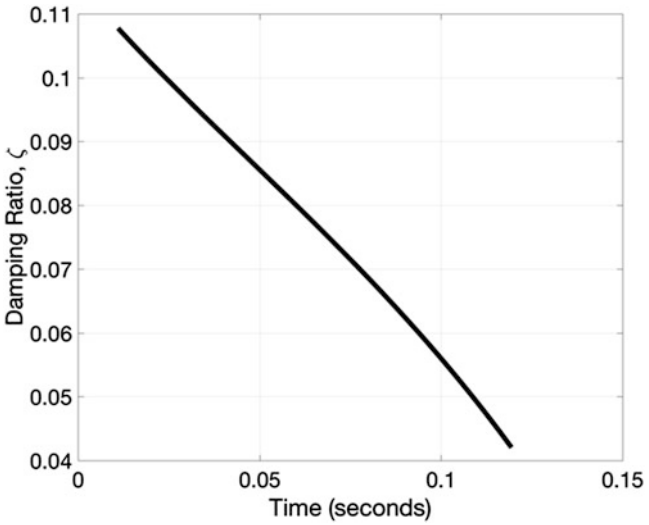

Fig. 8.4 Time-varying damping for mode 8 extracted from 311 N hammer hit

where $\mathscr{H}$ represents a Hilbert Transform. The decay, $d(t)$, is fit to the natural log of the amplitude of the analytic signal, $d(t) = \ln\left|\ddot{Q}(t)\right|$, and the phase, $\theta(t)$, is fit to the unwrapped angle, $\theta(t) = \arg\left[\ddot{Q}(t)\right]$.

The phase of the analytic signal gives the oscillation frequency, so the damped natural frequency was defined as its derivative in [3],

$$\omega_d(t) \triangleq \dot{\theta}(t) \tag{8.5}$$

which one can readily show gives the desired result for a linear time invariant system. Similar expressions can be found for ω_n and ζ.

$$\omega_n(t) \triangleq \left(\omega_d(t)^2 + \dot{d}^2(t)\right)^{\frac{1}{2}} \tag{8.6}$$

$$\zeta(t) \triangleq \frac{\dot{d}(t)}{\omega_n(t)} \tag{8.7}$$

The above process was completed for the ring-down response of mode 8 extracted from the 311 N impact data and the time varying damping is plotted in Fig. 8.4. As a high level verification of this curve, an estimate of the linear damping for this mode was extracted from the 311 N impact data using SMAC and was determined to be 11%. From Table 8.2, the linear damping for this mode as extracted from a 2 N impact was determined to be 6%. Comparing the achieved damping values from Fig. 8.4 to the linear approximations of damping at high and low level excitation gives confidence that the time-varying damping extracted from the 311 N is reasonable.

8.4 Calibration of Linear FEM

Before the nonlinear damping from Sect. 8.3.2 can be incorporated into a FEM, an accurate FEM must first be created for the linear model. The finite element mesh is illustrated in Fig. 8.5. The mesh consists of 110,938 8-node hexahedral elements and 127,039 nodes. The bolts are represented by beam elements which are connected to the volumetric hexahedral elements through kinematic constraint equations (rigid pseudo-elements) [5]. The mass of the bolts, washers, nuts, and compression sleeves was accounted for by updating the density of the beam element material and the stiffness of the beam element material was increased to reflect the addition of the compression sleeves and the preloaded state of the system. The stiffness properties of the bolts and compression sleeves are not important in this instance since the stiffness need only be high enough to ensure that no strain energy develops in the bolts for the first six modes of the system (i.e. that the first six elastic modes of the

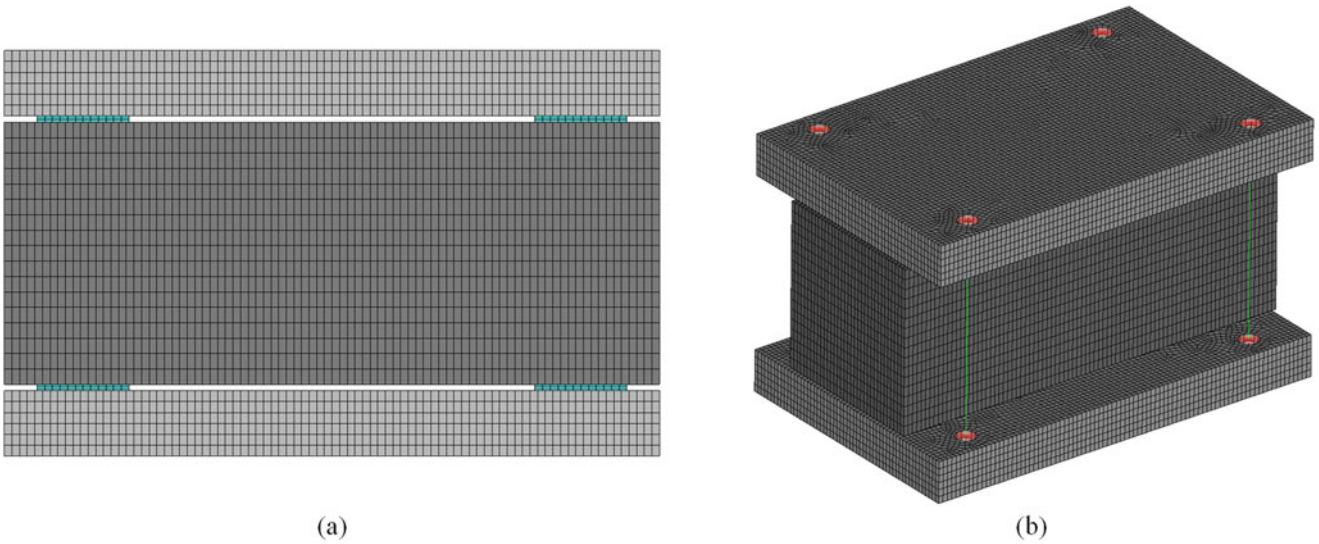

Fig. 8.5 (**a**) Side view and (**b**) isometric view of the finite element mesh of the system

Table 8.3 Results from calibration of FEM to experimentally extracted modal data

Experimental mode number	Calibrated FEM modal frequency (Hz)	Experimentally determined modal frequency (Hz)	Percent error (%)
7	104.3	93	12.15
8	*104.3*	*106*	*−1.60*
9	114.8	116	−1.03
10	113.5	127	−10.63
11	190.5	190	0.26
12	208.5	209	−0.24

assembly are strictly rigid body motion of the steel block, assuring that all strain energy is contained in the silicone pads). The mass properties, however, are very important. Therefore, each component of the experimental system was individually weighed and the density of the corresponding component was appropriately updated in the finite element model.

The corresponding mode shapes and modal frequencies of the system were then estimated using Sierra SD (Structural Dynamics), a massively parallel finite element code developed and maintained by Sandia National Laboratories [6]. If we assume that the cellular silicone material behaves in an elastic, isotropic manner then we have two stiffness parameters with which to calibrate the FEM (the elastic modulus and Poisson's ratio). The calibration was performed with respect to the experimentally obtained mode shapes and modal frequencies from Table 8.2, and the results are shown in Table 8.3.

Note that for modes 7 and 10 there is significant error between the experimentally extracted frequency and that obtained from the FEM. We believe the cause of this discrepancy is the asymmetric pre-loading in the experiment created by additional compression of the lower silicone pads due to gravitational effects; during testing, the bottom pads were visibly more compressed than the top pads due to the weight of the block. This effect was not replicated in the model. However, this work focuses on the motion associated with mode 8 since it deforms the silicone pads solely in shear and was able to be most purely excited in the experiment (see Fig. 8.6). Therefore, the experiment-FEM discrepancies for modes 7 and 10 do not significantly influence the results presented herein.

8.5 Development of Constitutive Damping Model

Once the linear FEM was calibrated to the low level impact data, the time-varying damping extracted from the high level experiment was incorporated into the FEM where a simulation of the 311 N impact was conducted. The results from the FEM were then used to derive the constitutive damping model for cellular silicone as a function of shear strain energy. Strain energy was selected since it is a general quantity that is also decaying in time similar to the calculated level of damping. The amplitude of the peaks in strain energy also increases with increases in excitation forces, which is qualitatively consistent with the experimental data. The following two subsections describe the constitutive damping model development process in greater detail.

Fig. 8.6 Shape of mode 8

8.5.1 Shear Strain-Based Damping Model

In this section we propose allowing the damping ratio for mode 8 to be a function of the current level of strain energy in the cellular silicone material, defined in Eq. (8.8). The classical, coupled equations of motion may be written as shown in Eq. (8.9).

$$SE_{CS} = \frac{1}{2}\,\underline{u}^{T}(x,t)\cdot\underline{\underline{K}}_{CS}\cdot\underline{u}(x,t) \tag{8.8}$$

$$\underline{\underline{M}}\,\underline{\ddot{u}}(x,t) + \underline{\underline{C}}\,\underline{\dot{u}}(x,t) + \underline{\underline{K}}\,\underline{u}(x,t) = \underline{F}(x,t) \tag{8.9}$$

Let $\underline{u}(x,t) = \sum_{i=1}^{N} q_i(t)\cdot\underline{\varphi}_i$ where $q_i(t)$ is the *ith* modal coordinate and $\underline{\varphi}_i$ is the *ith* mass-normalized mode shape. If we employ modal damping and allow the damping ratio to be a function of strain energy in the cellular silicone for a particular shear deformation mode (say mode k), the damping matrix takes on the following form:

$$\underline{\underline{C}} = 2\cdot\zeta_k(SE_{CS})\cdot\omega_k\cdot\left(\underline{\underline{M}}\,\underline{\varphi}_k\right)\cdot\left(\underline{\underline{M}}\,\underline{\varphi}_k\right) + \sum_{\substack{i=1\\ i\neq k}}^{N} 2\cdot\zeta_i\cdot\omega_i\cdot\left(\underline{\underline{M}}\,\underline{\varphi}_i\right)\cdot\left(\underline{\underline{M}}\,\underline{\varphi}_i\right) \tag{8.10}$$

Substituting the expression for $\underline{u}(x,t)$ and Eq. (8.10) into Eq. (8.9) and pre-multiplying the equation by $\underline{\varphi}_j^{\,T}$ we obtain the following set of uncoupled modal equations as a result of orthogonality of the modal vectors with respect to $\underline{\underline{M}}$ and $\underline{\underline{K}}$:

$$\ddot{q}_i(t) + 2\cdot\zeta_i\cdot\omega_i\cdot\dot{q}_i(t) + \omega_i{}^2 q_i(t) = \underline{\varphi}_i{}^{T}\,\underline{F}(x,t)\cdots, \quad i = 1\ldots N,\ \ i\neq k$$

$$\ddot{q}_i(t) + 2\cdot\zeta_i(SE_{CS})\cdot\omega_i\cdot\dot{q}_i(t) + \omega_i{}^2 q_i(t) = \underline{\varphi}_i{}^{T}\,\underline{F}(x,t)\cdots, \quad i = k \tag{8.11}$$

where the strain dependency of damping is indicated for mode k. Note that for this work, ζ_i is constant and is equal to the corresponding value in Table 8.2 for all modes except for mode 8. This is an approximation since other modes of the system exercise the silicone pads in shear. However, the 311 N impact primarily excited mode 8, and therefore the responses of the other modes are relatively insignificant.

It is noted that there is also a stiffness nonlinearity; when subjected to the 311-N impact load, the frequency of mode 8 changes from approximately 84 Hz at high amplitude response (early time) to 103 Hz at low amplitude response (late time). However, damping is the focus of this work and as such the natural frequency was assumed constant throughout each simulation and was chosen to match the response frequency in early time for each load level (see Table 8.4). In order to realize these frequencies in the FEM, the elastic modulus of the cellular silicone was appropriately altered for each load level.

Table 8.4 Mode 8 simulation natural frequencies

Experimental input load level (N)	FEM simulation natural frequency (Hz)
44	94
178	92
311	88

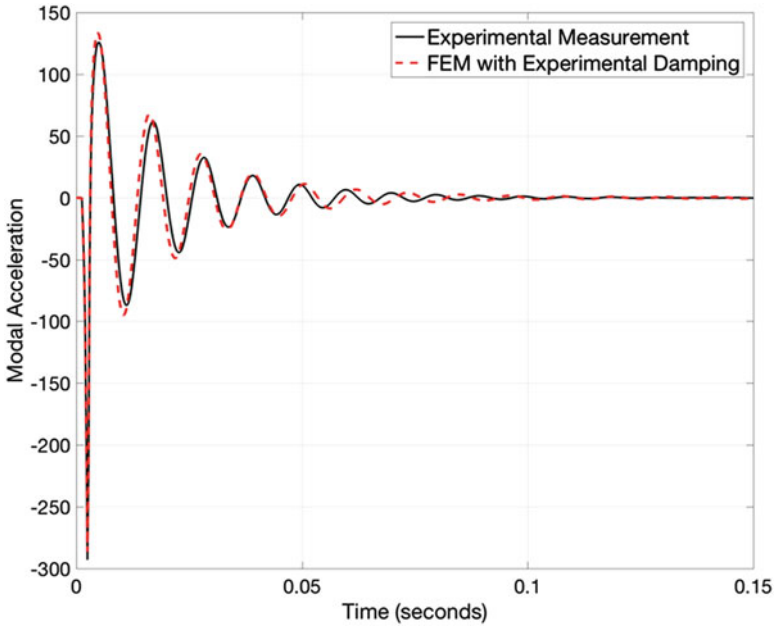

Fig. 8.7 Measured modal acceleration vs. prediction using measured damping ratio versus time data for mode 8 (311 N load)

8.5.2 FEM Simulation

Since strain energy is not easily extracted from nonlinear experimental data, the relationship between shear strain energy and damping was developed using the FEM by simulating the response of mode 8 to the equivalent modal force produced by the 311 N impact where the natural frequency was held constant at 88 Hz and the modal damping versus time data from Fig. 8.4 was used directly. The results are presented in Fig. 8.7. It is clear that the modal acceleration amplitude prediction shows very good agreement with the experimental measurement. This provides additional confidence in the measured damping ratio versus time data.

The FEM-computed shear strain energy versus time for this same simulation run is shown in Fig. 8.8. By plotting the measured damping ratio versus the amplitude of each peak in shear strain energy and applying a curve fit to the data we arrive at the empirically-derived, constitutive damping model for damping as a function of strain energy in the cellular silicone material. The data and curve fit are shown in Fig. 8.9 and the curve fit equation is provided in (8.12). This equation was obtained by applying a simple fourth order polynomial fit of the base 10 logarithm of the data. The equation form was selected so that the damping ratio would remain positive and approach zero as the strain energy approaches zero.

$$\zeta\left(SE_{CS}\right) = 10^{\left(-0.0034234\cdot\log_{10}(SE_{CS})^4 - 0.042199\cdot\log_{10}(SE_{CS})^3 - 0.19624\cdot\log_{10}(SE_{CS})^2 - 0.3451\cdot\log_{10}(SE_{CS})^1 - 1.1678\right)} \tag{8.12}$$

As an initial check on the efficacy of this developed constitutive damping property, (8.12) was used to predict the response of mode 8 to the equivalent modal force from the 44-N and 178-N impacts. In order to incorporate (8.12) into the solution (which depends on the calculation of the strain energy in only the cellular silicone at every time step) the C++ finite element library, deal.II [7] and the SLEPc eigensolver [8] were used. The former was utilized to assemble the mass and stiffness matrices from which the SLEPc eigensolver then extracted the corresponding modal frequencies and mode shapes. Note that these modal frequencies were within 1–2 Hz of those calculated by Sierra SD as described in Sect. 8.4. The mode shapes were used to obtain the modal force that was applied in each simulation.

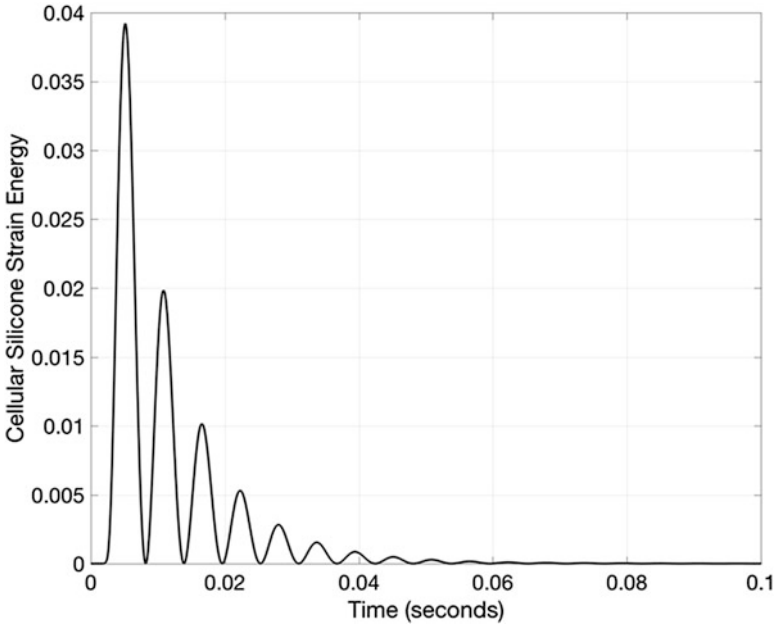

Fig. 8.8 Computed strain energy vs. time in the cellular silicone material when subjected to the 311 N load

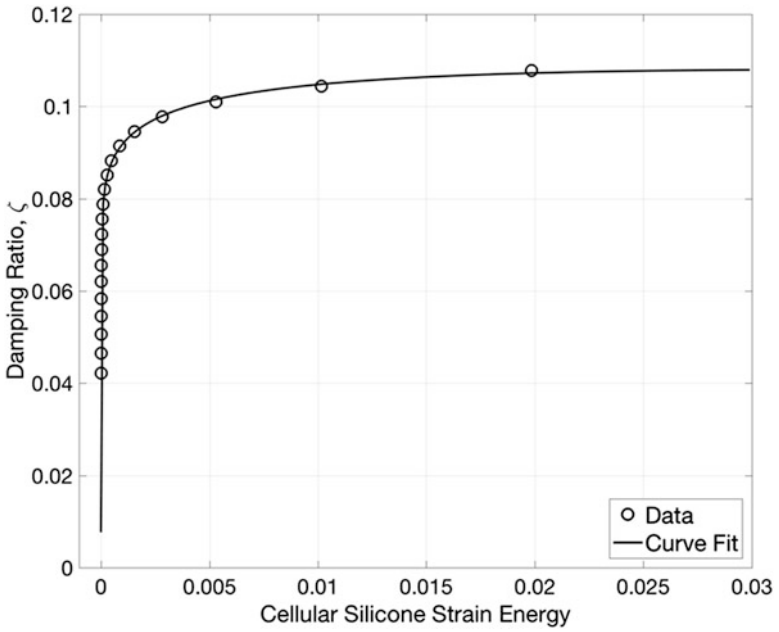

Fig. 8.9 Damping ratio for mode 8 versus strain energy amplitude in the cellular silicone material

There were two strategies employed for updating the damping ratio while numerically integrating the single modal equation for comparison to the test data. The first strategy involved continuously updating the damping ratio by computing the current strain energy in the cellular silicone at every time step. The second involved only updating the damping ratio at peaks in strain energy. This latter method was studied since the original damping ratio versus strain energy data was really damping ratio versus the *peaks* in the computed strain energy. Thus, it seems reasonable to only update the damping ratio at peaks in the strain energy. The modal acceleration response prediction results obtained for the 178-N and 44-N loads are illustrated in Figs. 8.10 and 8.11, respectively.

Relative to the results from the linear, experimentally extracted damping estimate from mode 8, the results from the continuously-updated and peak-updated damping values are encouraging. Figures 8.10b and 8.11b illustrate approximately the same character of the response. Since the amplitude of the strain energy in the pads is decreasing in time, the peak-updated

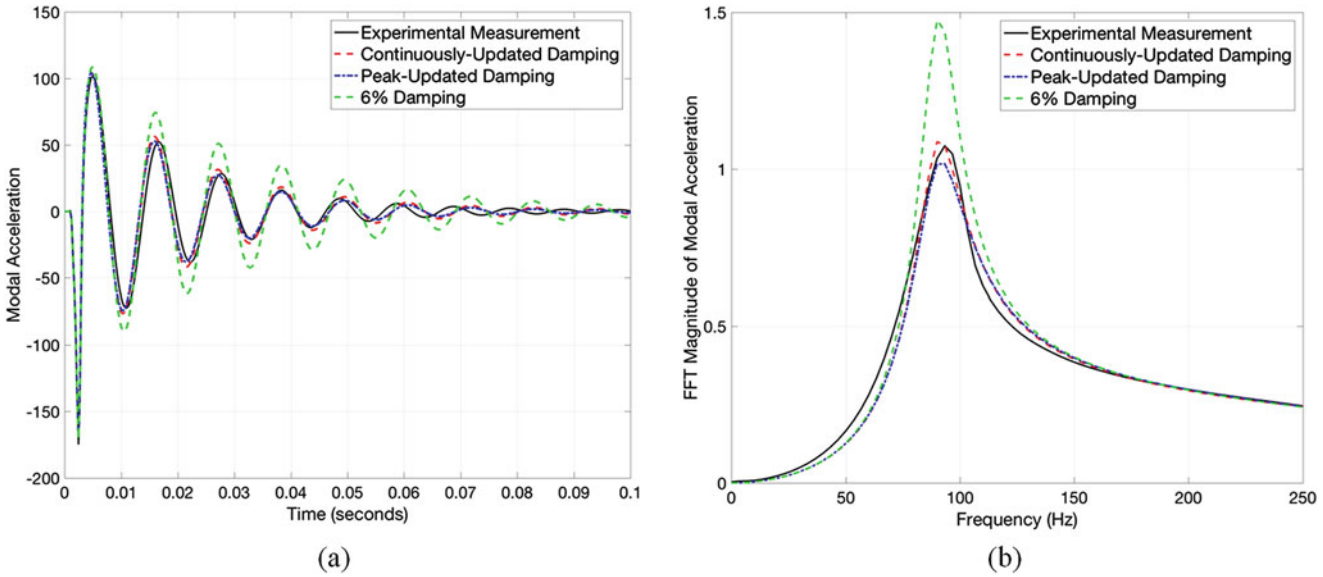

Fig. 8.10 (**a**) Modal acceleration prediction vs. experimental data in the time domain and (**b**) frequency domain, 178 N hit

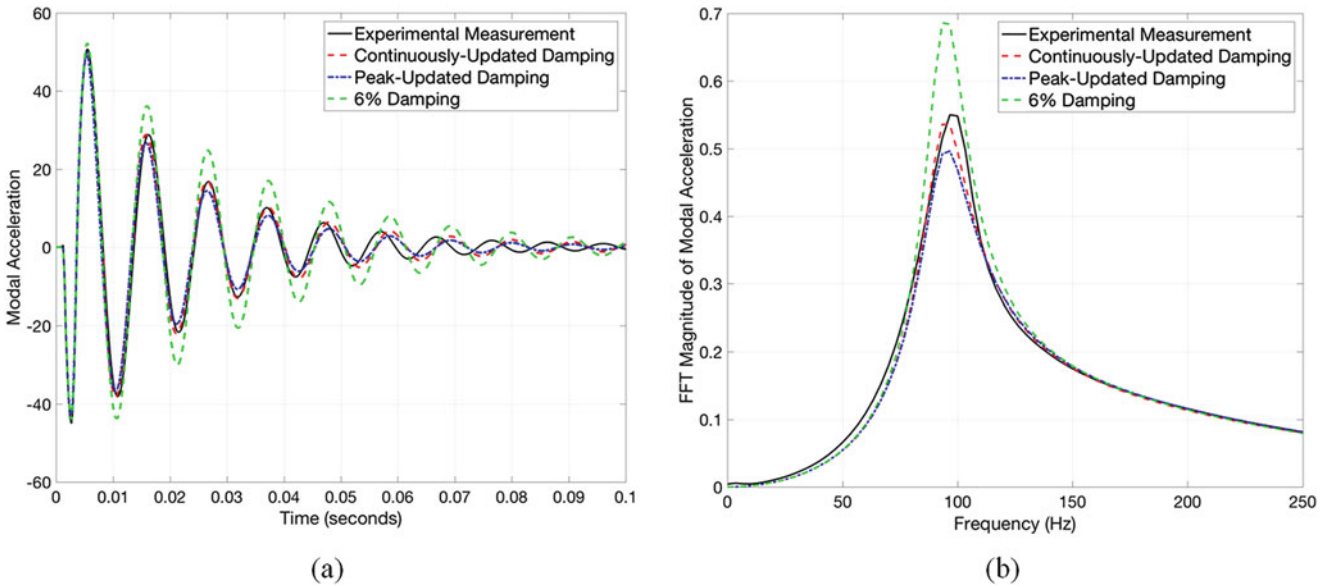

Fig. 8.11 (**a**) Modal acceleration prediction vs. experimental data in the time domain and (**b**) frequency domain, 44 N hit

damping removes slightly more energy in each cycle since it keeps the damping constant over the cycle. Consequently, the amplitude of the modal acceleration response in this case is slightly under-predictive. In contrast, the predicted response using continuously-updated damping appears to result in significantly more accurate energy dissipation characteristics as evidenced by the improved response amplitude prediction. For reference, the maximum strain energy produced by the 311, 178, and 44 N loads correspond to values of 0.02, 0.01, and 0.003, respectively (refer to Fig. 8.9).

8.6 Conclusions

The results from experimental testing were used in order to derive a constitutive damping model for cellular silicone as a function of strain energy for deformations primarily involving shear. It was demonstrated that the results for the same system subjected to two different levels of load are encouraging. However, additional testing is necessary in order to confirm whether the method can be generalized to improve the predictive accuracy of a system with mode shapes containing strain energy in multiple components in addition to shear strain in the cellular silicone.

8.7 Plans for Future Work

The presented development in this paper may only be applicable for mode shapes in which shear is the primary deformation mode in the cellular silicone. This is evidenced by the linear damping extraction for each of the first six flexible modes provided in Table 8.2. The modes involving primarily tensile/compressive deformation are associated with much higher levels of damping than the those associated with primarily shear deformation. Thus, we plan to develop a similar damping constitutive model for modes involving primarily deformation along the axis of preload by applying the same process to mode 11.

Since we were not able to complete additional testing with a different system, it is still uncertain whether this approach to apply modal damping would improve accuracy in a general setting. Currently, we plan to modify the test fixture geometry in order to determine whether this method improves the predictive capability of a linear FEM for a different assembly and input load. Furthermore, if we are successful, we would like to try to incorporate a modified version of this approach into a model of an assembly in which multiple modes with significant strain energy in numerous components in addition to the cellular silicone are excited by a single input load.

References

1. Mayes, R.L., Pacini, B.R., Roettgen, D.R.: A modal model to simulate typical structural dynamic nonlinearity. Presented at the 34th international modal analysis conference Orlando, Florida, 2016
2. Hensley, D.P., Mayes, R.L.: Extending SMAC to multiple references. In: Proceedings of the 24th International Modal Analysis Conference. The Printing House, Inc. Stoughton, WI, pp. 220–230 (2006)
3. Deaner, B., Allen, M.S., Starr, M.J., Segalman, D.J., Sumali, H.: Application of viscous and iwan modal damping models to experimental measurements from bolted structures. ASME J. Vib. Acoust. **137**(2), 021012 (2015)
4. Sracic, M.W., et al.: Identifying the modal properties of nonlinear structures using measured free response time histories from a scanning laser Doppler vibrometer. Presented at the 30th International Modal Analysis Conference Jacksonville, Florida, 2012
5. Reese, G., Bhardwaj, M., Walsh, T.: Sierra Structural Dynamics—Theory Manual. Technical Report SAND2009–0748. Sandia National Laboratories, Albuquerque (2011)
6. Sierra Structural Dynamics Development Team: Sierra Structural Dynamics—User's Notes. Technical Report SAND2015–9132. Sandia National Laboratories, Albuquerque (2015)
7. Bangerth, W., Davydov, D., Heister, T., Heltai, L., Kanschat, G., Kronbichler, M., Maier, M., Turcksin, B., Wells, D.: The deal.II library, version 8.4. J. Numer. Math. **24**(3), 135–141 (2016)
8. Hernandez, V., Roman, J., Vidal, V.: SLEPc: a scalable and flexible toolkit for the solution of eigenvalue problems. ACM Trans. Math. Software. **31**(3), 351–362 (2005)

Chapter 9
Simultaneous Qualification Testing of Multiple Components and the Influence of Closely Spaced Vibration Modes

Carl Sisemore and Julie Harvie

Abstract Vibration and shock qualification testing of components can be an expensive and time-consuming process. If the component is small, often two or more units can be mounted on a fixture and tested simultaneously to reduce test time. There is an inherent danger in simultaneously testing two or more identical components as the fundamental natural frequencies and mode shapes of the individual components will be nearly identical with some slight variation due to manufacturing variability. Testing in this manner can create a situation where closely spaced vibration modes produce unwanted interference between the two units under test. This phenomenon could result in a case where one unit is over-tested while the other is under-tested. This paper presents some experimental results from simultaneously testing pairs of components which show distinct interference between the units. Some analysis will also be presented showing how variations in the components can alter the intended test response, potentially impacting component qualification.

Keywords Vibration • Shock • Multiple components • Tuned absorber • Beating

9.1 Introduction

Laboratory testing time is often expensive and difficult to obtain. One popular solution to this problem is to try and test as many components as possible in the limited time available. A common solution for small components is to install multiple components on the shaker table or shock machine simultaneously when the tests specifications are the same. This is an obvious time saver since two, four, or more components can be tested in the same time as it would normally take to test one component. However, given that each identical component is likely not truly identical due to slight manufacturing variability, the situation can easily arise with several closely spaced resonant frequencies in a test. Exciting multiple components with nearly the same resonant frequency can create unwanted interference between the individual units under test. This could result in a situation where one unit is over-tested while others are under-tested.

The situation described in this work was discovered while analyzing test data from shock and vibration tests of two identical test articles mounted on the same fixture, as depicted in Fig. 9.1. The test data clearly shows that at some points during the test series the two component responses interfered in a way significantly different from what was expected. Experimental evidence of beating was recorded as well as the appearance of responses analogous to a tuned vibration absorber in the frequency response functions.

A common method for protecting a system from a steady-state harmonic disturbance is with a tuned vibration absorber. Vibration absorbers are designed with a second spring-mass system added to the primary device which protects it from vibrating. The effect is to change the original single-degree-of-freedom system into a two-degree-of-freedom system. The stiffness and mass of the absorber system are chosen to minimize the motion of the original system at the expense of substantial absorber mass motion [1].

The theoretical developments for a tuned vibration absorber are always based on the fundamental premise of a steady-state sinusoidal excitation at constant frequency. Their application is usually limited to machinery running at a constant speed. Inman presents a mathematical development for deriving the appropriate absorber mass and stiffness to eliminate motion of the primary system [1]. To generate the optimum response, it is necessary to design the mass and stiffness such that the natural frequency of the vibration absorber equals the natural frequency of the system to be controlled. This in turn is the exact definition of closely spaced modes.

C. Sisemore • J. Harvie (✉)
Environments Engineering and Integration, Sandia National Laboratories, P.O. Box 5800–MS 0840, Albuquerque, NM 87185, USA
e-mail: clsisem@sandia.gov; jharvie@sandia.gov

J.M. Harvie, J. Baqersad (eds.), *Shock & Vibration, Aircraft/Aerospace, Energy Harvesting, Acoustics & Optics, Volume 9*,
Conference Proceedings of the Society for Experimental Mechanics Series, DOI 10.1007/978-3-319-54735-0_9

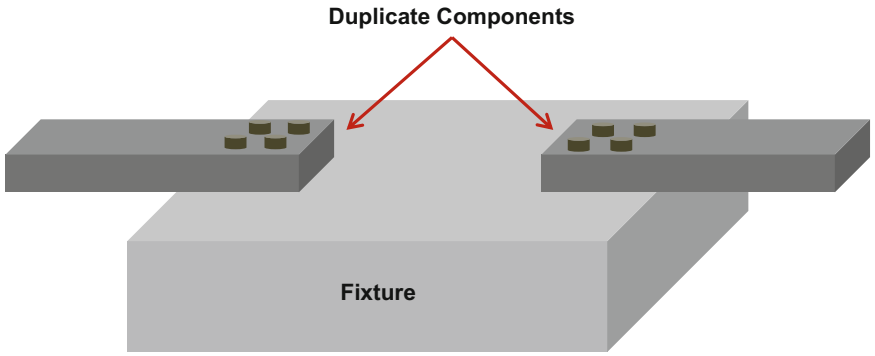

Fig. 9.1 Schematic of multiple component test setup for shock and vibration testing

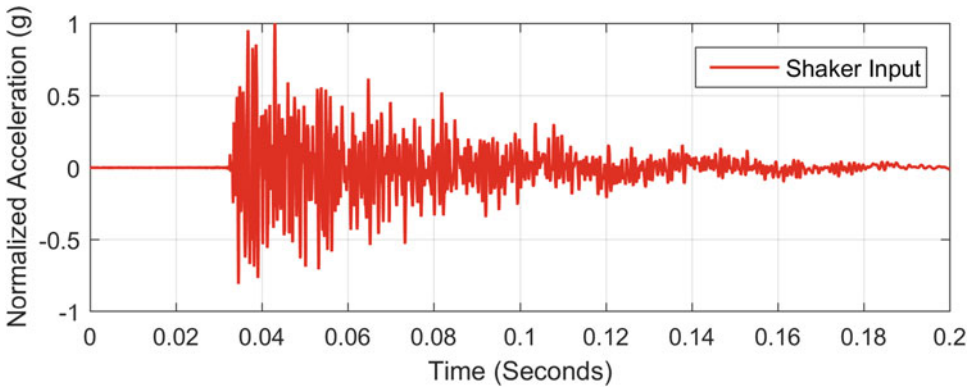

Fig. 9.2 Normalized shaker shock input time history

Closely spaced modes are defined as two vibration modes whose frequencies are close to a common mean. Typically, the modes are within about 10% of a common mean. Closely spaced modes can become especially problematic when their modal effective masses are significant and approximately the same order of magnitude [2]. If the modal effective mass is not significant then there is usually no notably different response. However, if the modal mass is significant in both of the closely spaced modes, beating can occur and the component responses can be significantly altered.

9.2 Shock Test Results

Shaker shock testing on the two component set-up was performed in each of the three axes at increasing severity levels. Figure 9.2 shows a plot of the normalized acceleration input to the fixture base. The input appears to be a straightforward, rapidly decaying shock event.

Figures 9.3 and 9.4 present the response on the cantilever part of test articles A and B, respectively. Since the test articles are cantilevered in the fixture, it would be reasonable to expect a response profile to be similar to the input with some amplification. Component B shows a time history plot similar to what is expected with a normalized peak response of approximately 2.83 g. In contrast, Component A shows a time history plot with an obvious 0.03 s beat period. The peak normalized acceleration from the Component A time history is also 3.18 g, approximately 12.4% greater than the Component B response, although both parts were tested side-by-side.

Figures 9.5 and 9.6 present the responses on the cantilever part of test articles C and D, respectively. For this second test, components A and B were replaced with components C and D and a nearly identical input time history was applied. However, for this test, the beating response was not apparent in either component. Also of note is that the maximum normalized peak acceleration of Component C was 3.11 and 2.90 g for Component D, a difference of about 7%. This is a more reasonable difference than the previous test where beating occurred.

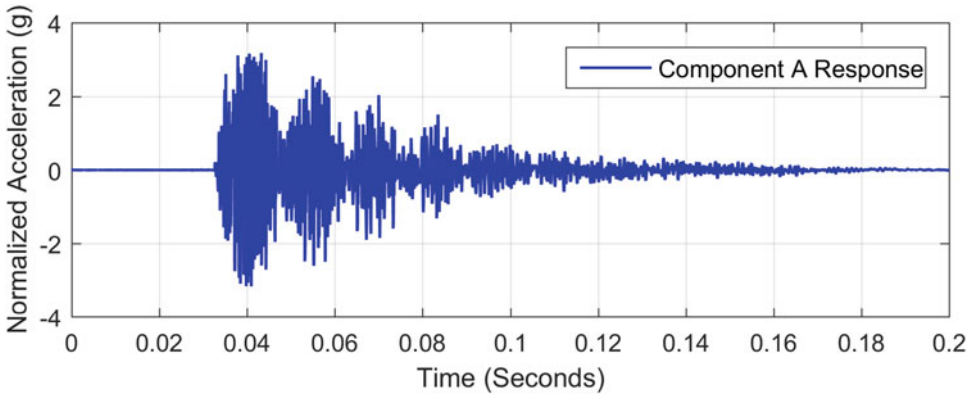

Fig. 9.3 Component A normalized shaker shock response time history

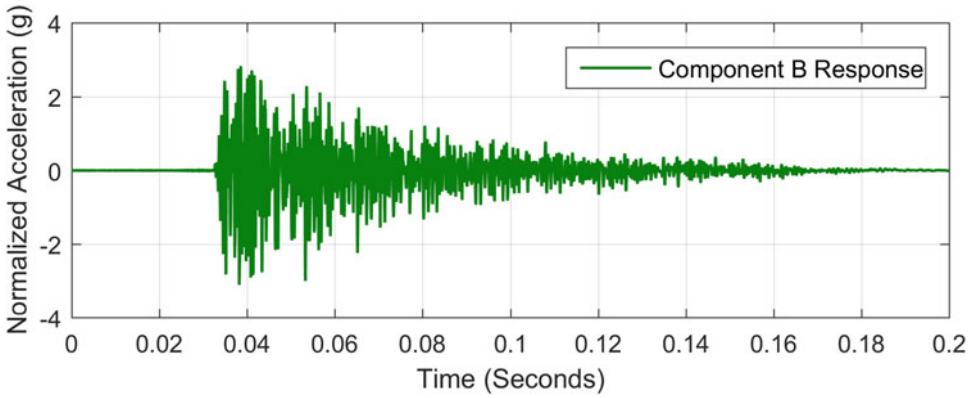

Fig. 9.4 Component B normalized shaker shock response time history

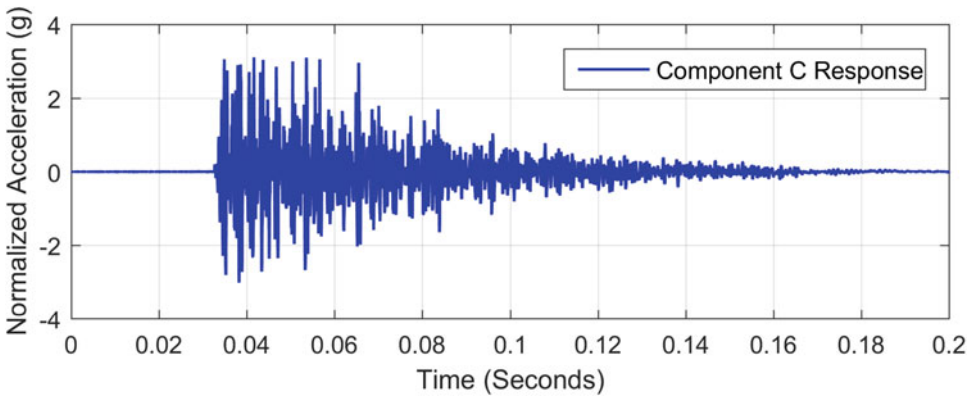

Fig. 9.5 Component C normalized shaker shock response time history

The results of the two shaker shock tests, which were intended to be identical, were actually quite different from a time history perspective. Figure 9.7 shows the corresponding acceleration Shock Response Spectra (SRS) plots for the four components overlaid. The SRS plot shows that the response of components B, C, and D only differ slightly. However, the response of component A shows significantly increased energy in the 60–350 Hz range as well as somewhat higher energy above 5 kHz. Since the inputs to the two test were essentially identical and each test consisted of two identical components mounted side-by-side, the resulting difference in the SRS must be attributed to the beating response measured on component A.

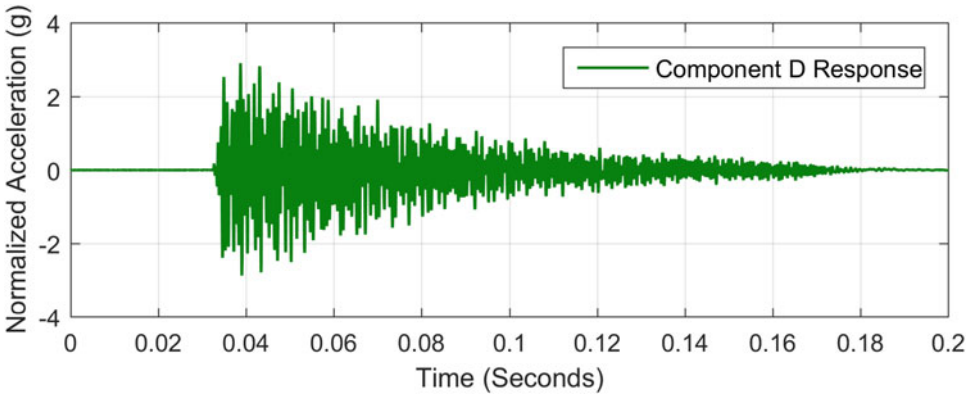

Fig. 9.6 Component D normalized shaker shock response time history

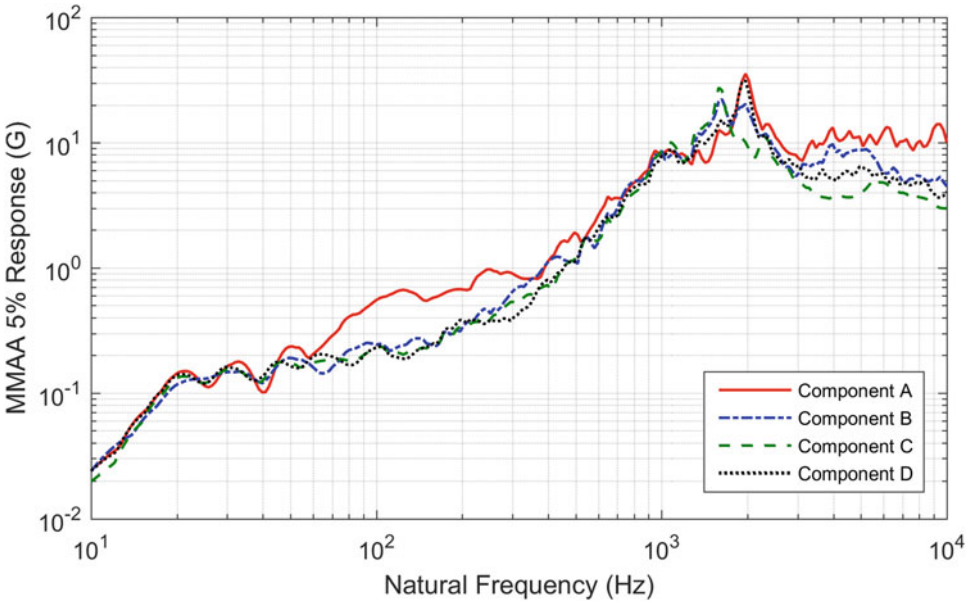

Fig. 9.7 Comparison of response SRS for components A, B, C, and D

9.3 Vibration Test Results

In addition to the shaker shock testing discussed previously, random vibration testing was also conducted on the components mounted side-by-side in the test fixture. Figure 9.8 shows the resulting Frequency Response Functions (FRF) from the single-axis random vibration testing of Components A and B mounted side-by-side in the same test fixture. As can be seen here, the FRFs from the accelerometers mounted on the cantilever portion of the component show that the natural frequency of Component A is about 2050 Hz where the natural frequency of Component B is around 1900 Hz. The difference between these modes is about 7.5% which is less than the approximate 10% threshold for closely spaced modes discussed earlier. As a result, Component B shows a significantly higher response than Component A and this difference in natural frequency is likely the reason that the beating response showed up so clearly in the shaker shock testing.

Figure 9.9 shows the FRFs calculated from the testing of Components C and D in the same side-by-side configuration. The results shown here are strikingly different than those shown in Fig. 9.8. These results show a strong natural frequency at 1900 Hz for component C, basically identical to that shown previously for Component A. However, Component D shows what appears to be resonant frequencies at 1610 and 2300 Hz which is almost evenly split left and right of the Component C 1900 Hz frequency. Since Components C and D are physically the same, within normal manufacturing tolerances, the results here are highly suspicious. It appears from the FRF that at 1900 Hz, Component C is vibrating significantly while Component D is essentially behaving as a rigid body. This is precisely the desired outcome of the tuned vibration absorber described previously. Likewise, the consequence of adding a tuned vibration absorber is the addition of frequencies to the left and right of the desired operating frequency. This is readily apparent in the FRF shown here.

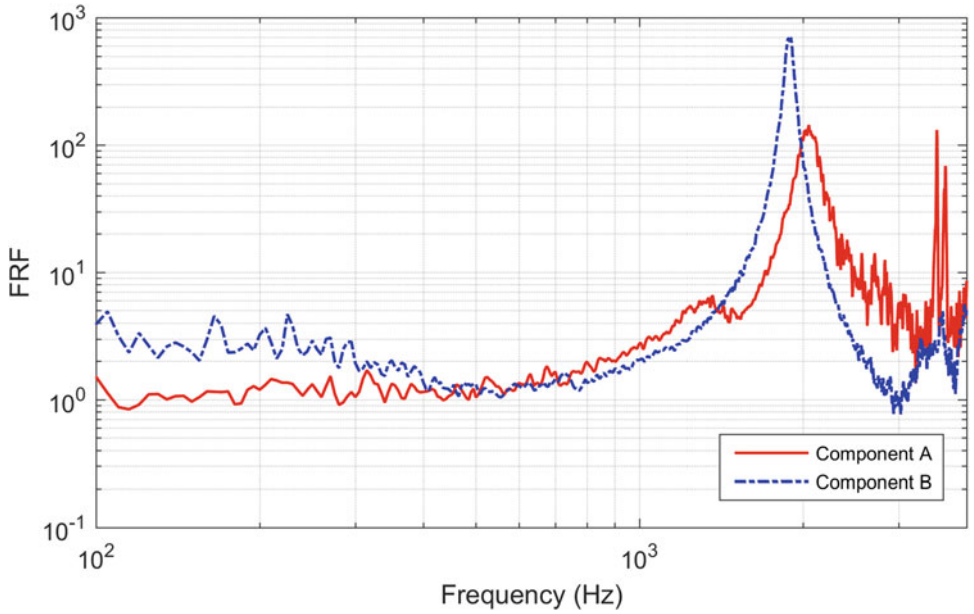

Fig. 9.8 Components A and B frequency response functions to random vibration input

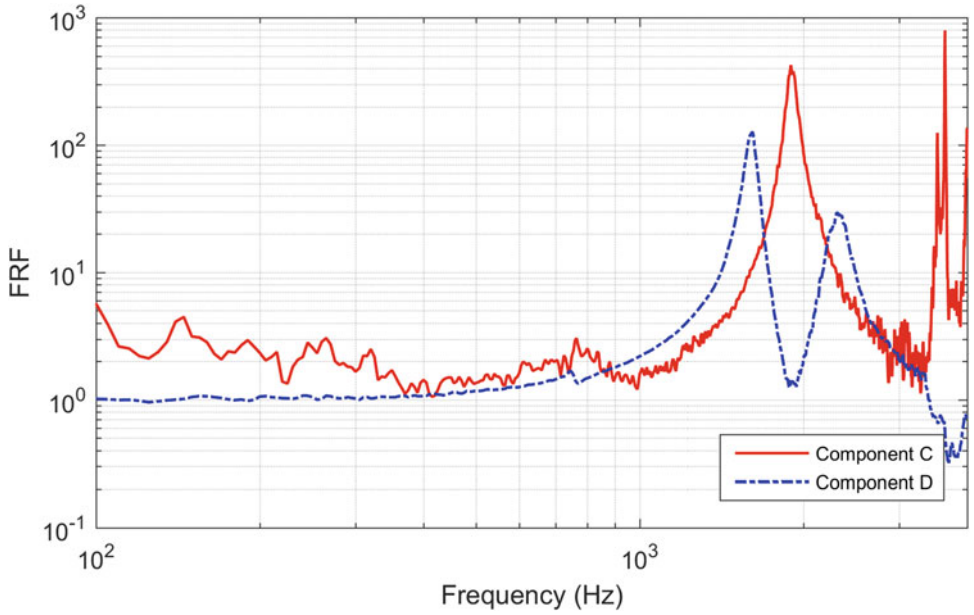

Fig. 9.9 Components C and D frequency response functions to random vibration input

These results are most unusual in that the theory of tune vibration absorbers always assumes a steady state sinusoidal input motion, not a random vibration input.

9.4 Simulation Results

To gain insight into the phenomena seen in the laboratory, a simple finite element analysis was performed. The finite element model used 18 beam elements, eight elements for each of the two identical cantilever beam components and two elements connecting the two components and simulating a stiff fixture. The element cross-sectional properties were arbitrarily chosen such that the two components would have a nominal first resonant frequency in the 2.2–2.3 kHz range using aluminum

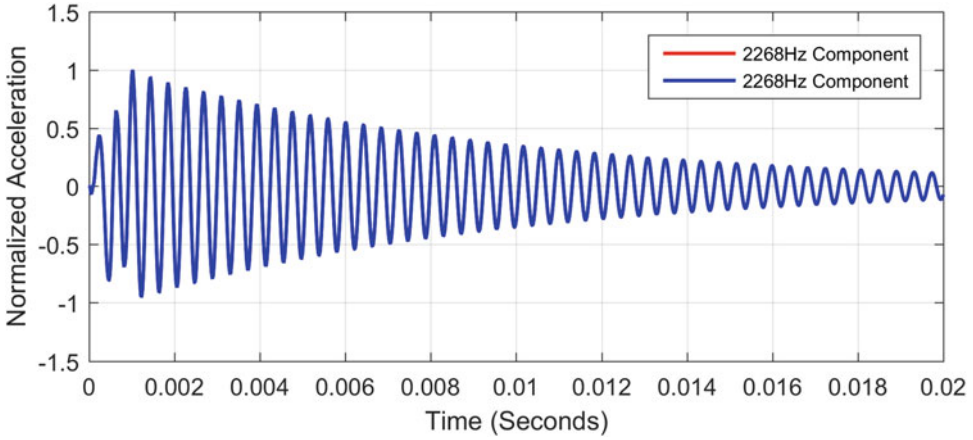

Fig. 9.10 Simulated two component free end responses with identical material properties

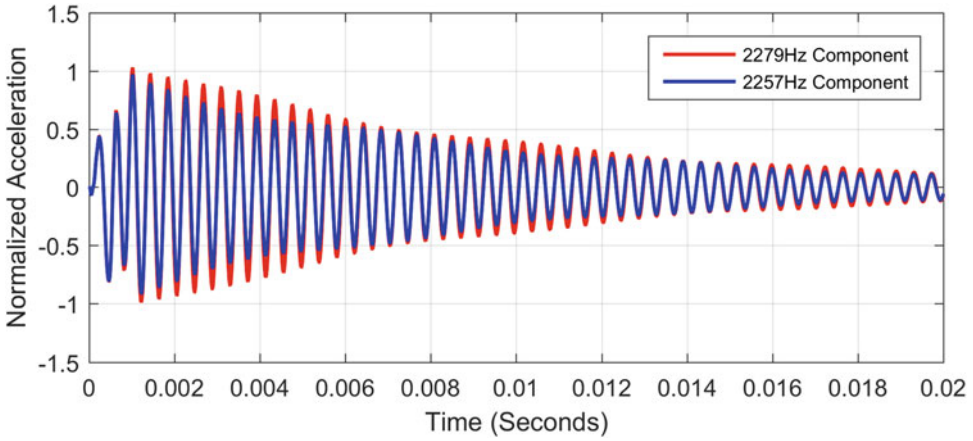

Fig. 9.11 Simulated two component free end responses with ±0.5% first mode variation

material properties. The two elements representing the fixture were modeled as steel with section properties substantially greater than the component properties. This was done so that the fixture would be extremely stiff compared to the components but not mathematically rigid.

For this finite element study, a simple half-sine high-frequency shock type displacement was simulated at the center of the test fixture and a transient simulation was performed to predict the responses at the free ends of the cantilevered components. Several simulations were performed by varying the modulus of elasticity for the two cantilever components.

The first simulation, as shown in Fig. 9.10, used identical material properties for the two components. The next three simulations, shown in Figs. 9.11, 9.12, and 9.13, represent variations in the modulus of elasticity of 1, 5, and 10%, respectively. The resulting frequency shifts, noted in the legends, are all well within normal tolerance ranges for components; however, the variation in response is dramatic due to the development of a closely spaced mode response phenomena.

When the components were completely identical, the responses were also identical. However, as the variation in fundamental frequency increased, the responses of the two components became dramatically different. The beating phenomenon became more prevalent, and the difference in peak response also increased. The peak response and fundamental frequency details for all cases are outlined in Table 9.1.

It is also interesting to note that the component with the higher peak response was always the component with the higher frequency. This observation aligns with the tuned absorber theory. Higher frequencies are attributed to increased stiffness and/or decreased mass, and tuned absorbers are typically designed to be much smaller and lighter than the primary structures they are attached to.

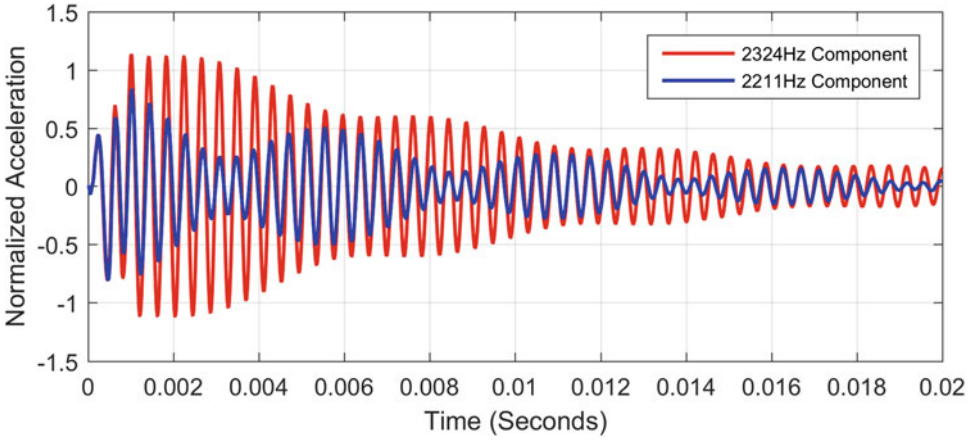

Fig. 9.12 Simulated two component free end responses with ±2.5% first mode variation

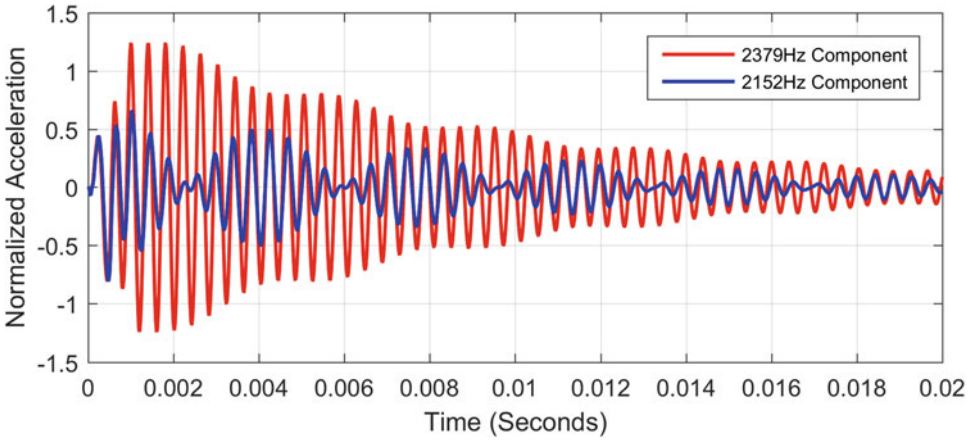

Fig. 9.13 Simulated two component free end responses with ±5.0% first mode variation

Table 9.1 Comparison of peak response for components with varying fundamental frequency

Variation in fundamental frequency (%)	Component 1 fundamental frequency (Hz)	Component 1 peak normalized response (g)	Component 2 fundamental frequency (Hz)	Component 2 peak normalized response (g)
0	2268	1.000	2268	1.000
0.5	2279	1.030	2257	0.969
2.5	2324	1.137	2211	0.836
5.0	2379	1.244	2152	0.805

9.5 Conclusions

When components are fabricated, there will inherently be some variation in the dynamic characteristics due to manufacturing variability. The amount of frequency variation can have a substantial effect on the response of the components when multiple components are tested simultaneously for qualification testing. It is almost inevitable that some components will be over-tested and others will be under-tested relative to the intended environment exposure. The actual component responses will vary from test to test, as seen in the experimental results, because the dynamic characteristics are slightly different for each unit. If multiple components must be tested simultaneously, it is recommended to fully analyze the test setup and responses and potentially alter the inputs to ensure that all components are seeing the required exposure at a minimum.

Additionally, while these studies were focused on simultaneous testing of only two components, the complexity of response is expected to increase as more components are added. It is not unusual to simultaneously test four or more components. The addition of more components may be investigated in future work.

Acknowledgments Sandia National Laboratories is a multi-mission laboratory managed and operated by Sandia Corporation, a wholly owned subsidiary of Lockheed Martin Corporation, for the U.S. Department of Energy's National Nuclear Security Administration under contract No. DE-AC04-94AL85000.

References

1. Inman, D.J.: Engineering Vibration, pp. 250–257. Prentice-Hall, Inc., New Jersey (1994)
2. Scavuzzo, R.J., Pusey, H.C.: Naval shock analysis and design, SVM-17. In: The Shock and Vibration Information Analysis. Center/Booz-Allen and Hamilton, Inc., Falls Church (2000)

Chapter 10
Extraction of Full-Field Structural Dynamics from Digital Video Measurements in Presence of Large Rigid Body Motion

Sudeep Dasari, Charles Dorn, Yongchao Yang, Charles Farrar, Amy Larson, and David Mascareñas

Abstract Video cameras offer a versatile high resolution alternative to traditional sensor apparatuses for full field structural dynamics analysis. Previous work has extended phase based motion magnification techniques to achieve state of the art results in vibrational and structural analysis. One limitation on the current approach is that it does not work very well in situations where substantial rigid body motion is present in the scene. The large rigid motion drowns out the tiny vibrations that are relevant for a full-field structural analysis. This work extends upon previous phase based motion algorithms in order to allow them to work even in cases with large rigid body motion present. Through a keypoint tracking and video cropping scheme rigid body motion is subtracted from video streams, while preserving the smaller motions of interest. After this preprocessing step, the new video stream can be passed into the full-field analysis scheme as usual, in order to get a full-field modal decomposition.

Keywords Operational modal analysis • Video processing • Blind source separation • Motion magnification • Rigid motion

10.1 Introduction

Extracting full-field, high-resolution vibration measurements and structural dynamics parameters is beneficial for a variety of structural dynamics and health monitoring applications [1]. Previous techniques are usually insufficient for high-resolution vibration measurements. Instrumenting structures with accelerometers and strain gauges makes for a relatively low resolution solution, and are sometimes heavy enough to change the dynamics of the target structure significantly. Alternatively, digital video cameras can fill in as versatile and inexpensive tools to extract full-field dynamics and build high-resolution dynamics models of structures.

While using video cameras for this task is not in itself a new idea, previous methods have limitations that restrict their possible use cases. For example, some previous methods require coating structures with fragile (and visually unappealing) coating. Previous work by Yang et al. [1], has been able to develop alternative techniques to extract the desired motion information from raw video streams. This technique manages to capture high resolution motion information at every pixel of the video sequence. Once captured, these local motion signals are then fed into a dimensionality reduction and machine

S. Dasari
Department of Electrical Engineering and Computer Science, University of California Berkeley, 253 Cory Hall, Berkeley, Berkeley, CA 94720, USA
e-mail: sdasari@berkeley.edu

C. Dorn
Graduate Aerospace Laboratories, California Institute of Technology, Pasadena, 1200 East California Blvd, Pasadena, CA 91125, USA
e-mail: cdorn@caltech.edu

Y. Yang (✉)
Los Alamos National Lab, Engineering Institute, P.O. Box 1663, MS T001, Los Alamos, NM 87545, USA
e-mail: yyang@lanl.gov; yangyongchaohit@gmail.com

C. Farrar
Los Alamos National Lab, Engineering Institute, P.O. Box 1663, MS D454, Los Alamos, NM 87545, USA
e-mail: farrar@lanl.gov

A. Larson • D. Mascareñas
Los Alamos National Lab, Engineering Institute, Los Alamos, NM 87545, USA
e-mail: amylarson@lanl.gov; dmascarenas@lanl.gov

J.M. Harvie, J. Baqersad (eds.), *Shock & Vibration, Aircraft/Aerospace, Energy Harvesting, Acoustics & Optics, Volume 9*,
Conference Proceedings of the Society for Experimental Mechanics Series, DOI 10.1007/978-3-319-54735-0_10

learning powered post processing step. The final step generates a full field dynamic model and modal decomposition of the target structure. This technique achieves state of the art results, and manages to extract dynamics information that was simply not recoverable previously.

Often times, real life situations will involve the presence of rigid body motion, or other forms of background noise in the video stream. Imagine a video of a car crossing an intersection at 20 miles/h. The relevant vibrations in the car would be drowned out by the larger rigid motion (in this case the car moving) as well as by background movement. Even in turbulent real life scenarios like this, it would be extremely useful to still recover useful structural dynamic information. This work seeks to adapt the previously described technique to be applicable to noisy real life situations—with substantial rigid body present—through a series of pre-processing steps.

10.2 Background

10.2.1 Extracting Full-Field Dynamics Through Phase Based Motion Analysis

Relevant vibrational data is present in video streams even if it is not necessarily detectable by the human eye. The previously described technique recovers this information using phase based motion processing as described in [2]. Video sequences can be considered as a sequence of image frames of uniform size (with height h and width w) and (in the case of RGB color images) three channels containing color specific intensity information. This amounts to a total of hw pixels in each frame, and t frames (depending on video length). These frames are first transformed into the frequency domain using the two-dimensional discrete Fourier transform. Post transform, the frames are fed one by one into a complex steerable pyramid of Gabor filters at various orientations. The phase response of this filter scheme encodes the local motion information for each pixel at every time step. Changes in the phase signals over time correspond to motion at that location. Thus, analyzing how this signal changes over time will yield insight into the vibration.

Once phase signals are generated for each pixel, the contextually relevant motion information needs to be extracted from the sea of data points. Remember that the dimensionality of the video stream has not been reduced at all, rather, it has been transformed from pixel intensity data to motion encoding phase data. In order to reduce the size of the problem PCA is applied on the raw phase signals. This reduces the number of phase signals from hw to just a few principle components. At this point a blind source separation algorithm, called Complexity Pursuit, is used to recover the modal coordinates and power spectrum of the target structure. From end to end this procedure is entirely automated. Further reading can be found in [1].

10.2.2 Frame Stabilization Using Keypoint Tracking

The phase based motion processing model does a wonderful job pulling dynamics from vibrating structures. The first primary goal is to extend the algorithm to work well with objects undergoing large rigid motion in the video stream. One solution—described previously by [3]—is to stabilize the video sequence frame by frame and then feed the stabilized video into the phase based algorithm. As previously described, a video frame can be considered as an ordered sequence of frames:

$$V = \{F_1, F_2, \ldots, F_n\} \tag{10.1}$$

In order to perform stabilization, the primary goal is to find a new video stream V^* such that:

$$V^* = \{F_1,\ f_1(F_2), \ldots, f_n(F_n)\} \tag{10.2}$$

where $f_i(F_i)$ is a warping function applied on each original frame. The overall goal is to find a warping function which preserves the relevant structural vibrations, while subtracting out the noisy rigid body motion. This warping function—$f_i(F_i)$—is modelled as an affine transformation.

Identifying the correct parameters for $f_i(F_i)$ is crucial for effective warping. At each frame after F_1 the object of interest is assumed to have undergone a transformation such that its position at time $t - \sigma_t$—is a transformed version of its position at time $t - 1$. This transform T, is modelled as two separate transforms, such that:

$$T_t = T_{rigid,t} + T_{dynamic,t} \tag{10.3}$$

$T_{rigid,t}$ is a rigid affine transform which models the object's motion due to the rigid body motion, and $T_{dynamic,t}$ is the small vibrations that are relevant to a dynamics study. If $T_{rigid,t}$ can be solved for every frame, then every frame can be transformed by $-T_{rigid,t}$ in order to get rid of the object's overall rigid body motion. As a result, all $f(F)$ has to do to compute V^* is transform every frame by the corresponding$-T_{rigid,t}$.

Under this interpretation of the problem, all that is left to do is calculate the correct transformation for $T_{rigid,t}$ at each frame. As shown in Eq. (10.3), once $T_{rigid,t}$ is subtracted all that is left in V^* are the "dynamic motions", or vibrations relevant to modal analysis. Once these values are known the new sequence can be calculated iteratively. In order to assist in this calculation, the CMT keypoint tracker [4] is employed. CMT tracks a set of specific keypoints in an image—usually corresponding to distinctive corners - across multiple frames of a video. The points are found using SIFT [5] or a similar algorithm. A user gives the tracker a bounding box which entirely contains the object of interest in the first frame. CMT finds the object in the next frame by looking for the telltale keypoints in the next frame and then applying a series of corrections. After finding the object in the next frame, CMT returns a series of points that describe the bounding box in the next frame. $T_{rigid,t}$ can then be estimated by using simple least squares to fit an affine transformation that best transforms the bounding box in frame F_{t-1} to its new position in frame F_t. Of significant concern is the quality of the estimation made by CMT. If its estimate for rigid motion in the scene was off, the estimation for $T_{rigid,t}$ would erroneously include parts of $T_{dynamic,t}$ or could perhaps be entirely wrong. Fortunately, since CMT operates on a set of sparse keypoints, it does a pretty good job of detecting larger rigid motion without also detecting the smaller vibrations of interest to us. Furthermore, CMT attempts to track the object's center of mass as it rotates, moves, and possible even deforms over time. This makes CMT's tracking estimates far more robust, and as a result allows the final estimates for transformation to be far less noisy.

10.3 Rigid Body Motion Subtraction and Extracting Vibration Modes

The overall process for extracting full field dynamics in the presence of rigid body motion has two distinct steps: first stabilizing and cropping the input video, and then analyzing the processed video stream with the usual phase based motion algorithm. The user must provide the system a video stream as well as a bounding box around the object of interest. The warping code—written in Python and OpenCV—will then use the CMT tracking scheme to estimate the object's rigid body motion and then subtract it from the stabilized video output. At this point the object of interest will look still in time, in the sense that no rigid motion will be present in the object but relevant vibrations will still be present. Any motion in the background will still be present, however. Cropping the video stream with an off the shelf program like Avidemux is a simple solution to this problem. Post crop all that is left is a video of the object of interest vibrating in the same position over time. This final video stream can then be fed to the phase based motion processing algorithm, which will perform a full-field modal analysis as previously described.

10.4 Experimental Results

The project's overall goal was to enable modal analysis using raw video streams, even in situations where plenty of rigid body motion is present. A common example of this in real life would be structures floating on offshore rigs or boats. One could imagine the observer camera or target structure bobbing up and down or rotating slightly due to—even slight—turbulence in the ocean. Nonetheless, a structural engineer would still like to perform meaningful structural analysis on the offshore platform. An experimental mockup of this situation was designed in lab to test the effectiveness of the rigid body motion subtraction algorithm (Fig. 10.1).

A cantilever beam was mounted atop a heavy steel block, and then placed in a pool of water. In this setup, the beam is entirely visible above water, but the block is mostly submerged. An observer boat was built using Styrofoam, and a Samsung Galaxy phone was attached to it to act as an onboard camera. While a seemingly strange choice, the Galaxy smartphone is relatively compact and is also equipped with a slow motion 120 frames per second (fps).

Once the boat was placed in water, waves were manually generated to simulate a boat rolling back and forth in the ocean. The motion was restricted to mostly in-plane rigid body motion, by attaching the boat to the sides of the pool. The boat could sway back and forth and move rigidly, but could not rotate around the body of interest. The cantilever beam was repeatedly excited, and the smartphone filmed its vibrations for a set amount of time. As seen below in Figs. 10.2 and 10.3, a stabilized video was first obtained and the 10 Hz mode was successfully extracted by applying the rigid body subtraction and modal analysis technique to the recorded video data.

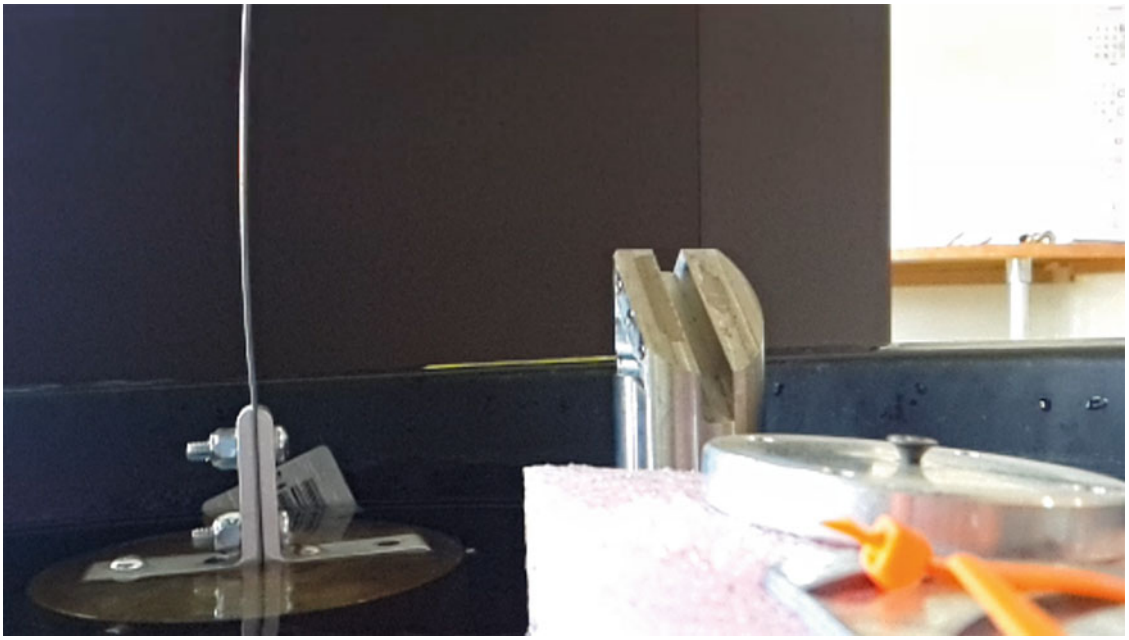

Fig. 10.1 The experimental setup of the cantilever beam floating on the water

Fig. 10.2 One frame of the obtained stabilized video

10.5 Conclusions and Future Plans

This work adapted previous phased based full-field vibrational analysis techniques to work in situations where plenty of rigid body motion is present. Without handling this motion, the large rigid motion would drown out the smaller vibrations of interest. Through a keypoint detection and tracking scheme, objects are tracked over time and their rigid body motion is subtracted in the output video stream. The video stream is then cropped to reduce background noise, and fed into the normal phase based motion processing algorithm.

This technique was able to reliable remove rigid motion in a variety of video streams. While requiring some user input, in particular a bounding box for the first frame of the video sequence, the proposed algorithm manages to be almost as autonomous as the original full field vibrational analysis technique. The proposed technique works as a natural extension of previous work in the field, in order to make it more applicable in a variety of real life situations.

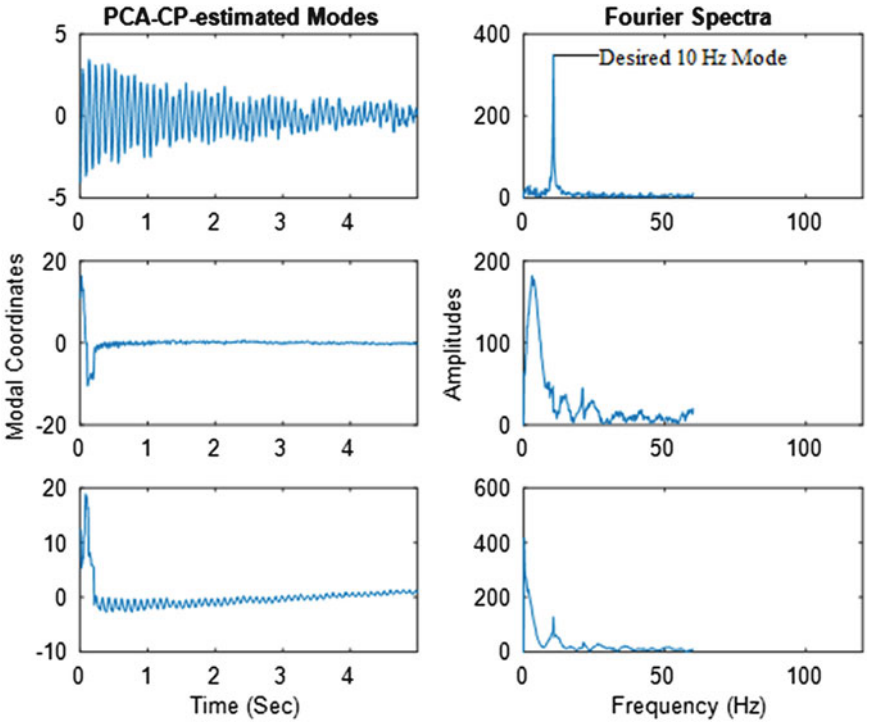

Fig. 10.3 The vibration modes blindly extracted from the obtained stabilized video

The current rigid motion subtraction algorithm assumes that objects are undergoing affine transformations. As a result, it works well in situations where objects are rigidly moving, but it does not work as well in situations where objects are deforming rapidly or undergoing out of plane motion. For example, imagine a drone flying around a deforming object while observing said object with a camera. The object would appear to the camera to be undergoing significant out of plane rotation, while also deforming. Relaxing the current assumption of affine transformation, would allow us to further extend our algorithm to work in these more difficult cases. Exploring state of the art machine learning and computer vision algorithms to attack this task, would be the next step in making phase based methods even more versatile and applicable to real life scenarios.

Acknowledgements The authors would like to thank the Los Alamos National Laboratory (LANL) Engineering Institute, as well as LANL's Lab Directed Research and Development (LDRD) program. In particular, the LDRD program has supported Yongchao Yang's Director's Postdoctoral Fellowship and David Mascareñas' Early Career Award.

References

1. Yang, Y., Dorn, C., Mancini, T., Talken, Z., Kenyon, G., Farrar, C., Mascareñas, D.: Blind identification of full-field vibration modes from video measurements with phase-based video motion magnification. Mech. Syst. Signal Process. **85**, 567–590 (2017)
2. Wadhwa, N., Rubinstein, M., Durand, F., Freeman, W.: Phase-based video motion processing. In: Proceedings SIGGRAPH 2013. ACM Trans. Graph, 2013
3. Elgharib, M., Hefeeda, M., Durand, F., Freeman, W.: Video magnification in presence of large motion. In: CVPR, pp. 4119–4127, 2015
4. Nebehay, G., Pflugfelder, R.: Clustering of static-adaptive correspondences for deformable object tracking. In: CVPR, pp. 2784–2791, 2015
5. Lowe, D.: Distinctive image features from scale-invariant keypoints. Int. J. Comput. Vis. **60**, 91–110 (2004)

Chapter 11
Efficient Full-Field Operational Modal Analysis Using Neuromorphic Event-Based Imaging

Charles Dorn, Sudeep Dasari, Yongchao Yang, Garrett Kenyon, Paul Welch, and David Mascareñas

Abstract As an alternative to traditional sensing methods, video camera measurements offer a non-contact, cost-efficient, and full-field platform for operational modal analysis. However, video cameras record large amounts of redundant background data causing video processing to be computationally inefficient. This work explores the use of a silicon retina imager to perform operational modal analysis. The silicon retina provides an efficient alternative to standard frame-based video cameras. Modeling the biological retina, each silicon retina pixel independently and asynchronously records changes in intensity. By only recording intensity change events, all motion information is captured without recording redundant background information. This asynchronous event-based data representation allows motion to be captured on the microsecond scale, equivalent to traditional cameras operating at thousands of frames per second. With minimal data storage and processing requirements, the silicon retina shows promise for real-time vibration measurement and structural control applications. This study takes the first step toward these applications by adapting existing video frame-based modal analysis techniques to operate on event-based silicon retina measurements. Specifically, blind source separation and video motion processing techniques are used to automatically output vibration parameters from silicon retina data. The developed method is demonstrated on a cantilever beam.

Keywords Operational modal analysis • Video processing • Blind source separation • Silicon retina • Event-based sampling

11.1 Introduction

Structural dynamics parameters such as modal parameters (modal frequencies, damping ratios, and mode shapes) are crucial to the characterization of structures [1]. Traditionally, physically attached sensors such as accelerometers or strain gauges are used for modal analysis. While they offer reliable measurements, these sensors only record the response at discrete points on a structure, foregoing potentially vital local vibration characteristics and introducing mass-loading effects on lightweight structures. Laser vibrometers produce dependable vibration response measurements, but they collect sequential measurements and are expensive. Video cameras have recently been demonstrated as a reliable tool for vibration sensing, offering cost-efficient, full-field, and simultaneous measurements. Digital image correlation can be used for modal analysis [2, 3], but requires a speckle pattern to be prepared on the structure's surface. Recent methods have demonstrated local phase based video processing techniques to perform discrete-point modal analysis without the need for a speckle pattern on the structure [4]. Full-field video-based operational modal analysis is developed in [5] by performing unsupervised machine learning on local phase signals. In this work, the video-based full-field operational modal analysis technique developed in

C. Dorn
Graduate Aerospace Laboratories, California Institute of Technology, 1200 East California Blvd, Pasadena, CA 91125, USA
e-mail: cdorn@caltech.edu

S. Dasari
Department of Electrical Engineering and Computer Science, University of California Berkeley, 253 Cory Hall, Berkeley, CA 94720, USA
e-mail: sdasari@berkeley.edu

Y. Yang (✉) • P. Welch • D. Mascareñas
Los Alamos National Lab, Engineering Institute, P.O. Box 1663, MS T001, Los Alamos, NM 87545, USA
e-mail: yyang@lanl.gov; yangyongchaohit@gmail.com; pwelch@lanl.gov; dmascarenas@lanl.gov

G. Kenyon
Los Alamos National Lab, Applied Modern Physics Group, P.O. Box 1663, MS D454, Los Alamos, NM 87545, USA
e-mail: gkenyon@lanl.gov

J.M. Harvie, J. Baqersad (eds.), *Shock & Vibration, Aircraft/Aerospace, Energy Harvesting, Acoustics & Optics, Volume 9*,
Conference Proceedings of the Society for Experimental Mechanics Series, DOI 10.1007/978-3-319-54735-0_11

[5] is adapted for a data-efficient event-based neuromorphic imaging framework. The use of a silicon retina, an event-based imager, to extract full-field structural dynamics parameters is proposed.

Traditional video cameras record too much data for real-time calculation of full-field vibration parameters. Neuromorphic cameras offer an efficient alternative to traditional video cameras. By emulating the efficient biological vision process, neuromorphic imaging sensors eliminate the large amounts of background data by only measuring changes in image intensity. The silicon retina imager, originally developed by Mead and Mahowald [6], is an event-based neuromorphic imager that dramatically reduces the amount of data required to capture a video. Avoiding uniformly spaced frames, each silicon retina pixel independently reports asynchronous events corresponding to intensity changes. With this event-based format, all useful motion information is recorded while omitting any redundant background information. The asynchronous data output offers the unique advantages of low data rates and extremely high temporal latency. The silicon retina has shown potential for short time-scale control applications [7, 8]. In this work the Dynamic Vision Sensor (DVS) is used, a 128×128 pixel silicon retina with a maximum temporal resolution of 15 μs [9]. The DVS128 records temporal difference video at speeds equivalent to thousands of frames per second, which can be processed quickly. However, existing image processing methods are based on uniform, sequential frame-based video measurements, requiring adaption of existing video processing techniques to an event-based format and the development of novel event-based video processing methods. This work adapts a previously developed video frame-based modal analysis process [5] to an efficient event-based framework, which has the potential to open doors to real-time characterization of structural dynamics and vibration control of structures.

11.2 Background

11.2.1 Extracting Full-Field Vibration Motion from Traditional Video

High spatial resolution vibration motion is encoded in video of a vibrating structure. The authors' previous work shows how this information can be extracted in a fully automated, output-only fashion with no knowledge of the loading or characteristics of the structure [5]. Video measurements track intensity through time at each pixel. A video of a vibrating structure can be represented as a displaced and temporally translated intensity $I(x + \delta(x,t))$ where x locates a pixel in space and $\delta(x,t)$ is the temporally varying local vibration motion. With only knowledge of the measured intensity signal at each pixel, $\delta(x,t)$ can be extracted by analyzing the local phase $\psi(x,t)$. Local phase is defined as the argument of a complex bandpass filter response [10]

$$G_{\omega_o}(x) * I\left(x + \delta\left(x,t\right)\right) = \rho_{\omega_o}\left(x,t\right)\exp\left(j\psi\left(x,t\right)\right) = \rho_{\omega_o}\left(x,t\right)\exp\left(j\omega_o\left(x + \delta\left(x,t\right)\right)\right) \tag{11.1}$$

where j is the imaginary number, ρ_{ω_o} is the local amplitude. The complex bandpass filter is typically a Gabor filter with some fixed spatial scale ω_o. The symbol "$*$" denotes the two-dimensional discrete convolution operator. Measuring the local phase throughout each video frame is equivalent to measuring a scaled structural response at each pixel. Once the temporal local phase signals are calculated, a modal model of the structure can be created. For linear structures, modal superposition can be employed to represent the response as a linear combination of vibration modes

$$\delta\left(x,t\right) = \Phi(x)q(t) = \sum_{i=1}^{n}\varphi_i(x)q_i(t) \tag{11.2}$$

where $\Phi \in \mathbb{R}^{N\times n}$, is comprised of mode shapes $\varphi_i(x)$ and $q \in \mathbb{R}^{n\times T}$,is comprised of the corresponding modal coordinates $q_i(t)$. Since the response is measured at each pixel on the structure, this is a very over-complete problem; there are phase measurements at up to millions of pixels while structural dynamics is typically low-dimensional with only a handful of active modes. Machine learning techniques can be used to solve this over-complete problem, estimating the mode shapes and modal responses based on measured response δ at each pixel. Principal component analysis (PCA) is used to reduce the dimensionality of the data, followed by blind source separation (BSS) to uncouple the modal coordinates. In this study, the complexity pursuit (CP) algorithm is used for blind source separation [11].

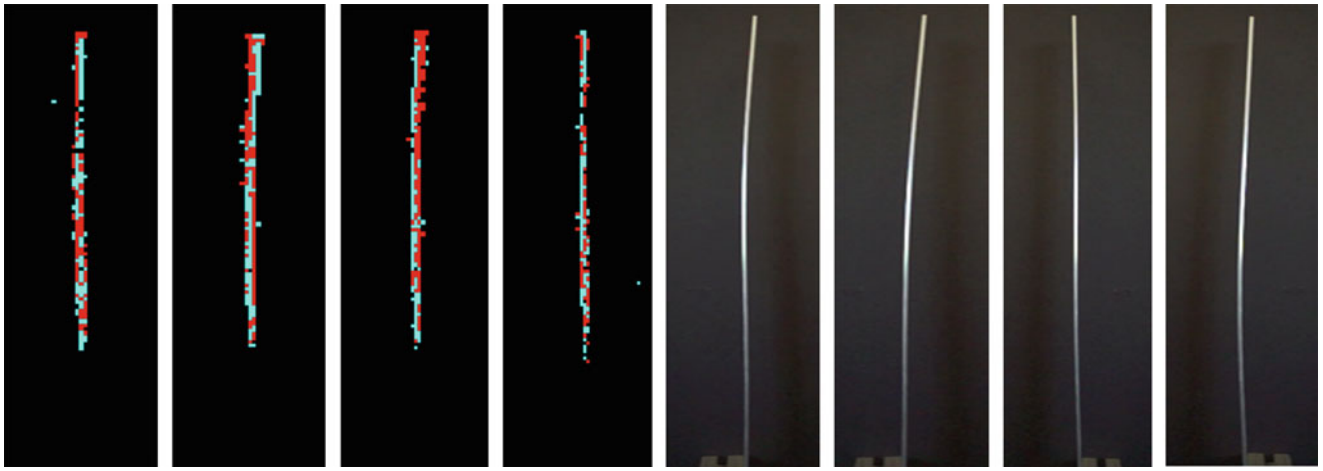

Fig. 11.1 Silicon retina events over brief time windows for a vibrating cantilever beam (*left*). *Red* represents off events, *blue* represents on events. Video frames for the same vibrating cantilever (*right*)

11.2.2 Frameless Event-Based Imaging

Conventional frame-based cameras record intensity in uniform frames where each pixel provides synchronized intensity measurements. Alternatively, event-based imagers record only differences in intensity, with each pixel acting independently in an asynchronous fashion. This allows extremely fast temporal latency, equivalent of thousands of frames per second [9], where fast moving objects can be captured without blur. Events are produced when the intensity changes by some threshold, producing an extremely efficient data stream to represent motion in a video. To allow for a high dynamic range, the DVS 128 [9] measures differences in log intensity rather than raw intensity. Events are triggered when the log of intensity at a pixel changes by more than a fixed on or off threshold θ

$$\left|\Delta\Big(\log\left(I\left(x,y,t\right)\right)\Big|\right| > \theta \tag{11.3}$$

Events are stored in address-event representation; each event is recorded as a tuple containing the x and y coordinate address of the active pixel along with the event timestamp and polarity. When the condition in Eq. (11.3) is met, an event (x, y, t, p) is recorded where p is the polarity of the event (-1 for off, 1 for on). Videos are stored as a chronological list of event tuples. Silicon retina events in a few brief time windows are displayed next to traditional video frames in Fig. 11.1 capturing the flexural vibration of a cantilever beam.

11.3 Extracting Vibration Motion from Silicon Retina Measurements

To take advantage of the efficiency of event-based sampling, processing should be done in the asynchronous event domain. However, traditional video processing techniques rely on uniformly recorded frames, so methods must be adapted to an event-based format or new video processing methods must be developed. This study adapts the methods in [5], to be efficiently implemented on event-based silicon retina data for real-time applications.

In event-based video, there is no grayscale intensity value to be processed. Instead of processing intensity, we define a function $S(x, y, t)$ for pixel coordinates (x, y), similar to that defined in [12], that represents the signal of accumulated events at each pixel over a small backward time window

$$S\left(x,y,t\right) = \sum_{t-\Delta t}^{t} e\left(x,y,t\right) \tag{11.4}$$

where $e(x, y, t) = 1$ at the time and location of an event and is zero elsewhere. Since events are generated along moving edges, the function $S(x, y, t)$ allows edges to be located throughout the video.

The first step the vibration mode extraction process is to determine local phase. In contrast to [5], a single complex Gabor filter is applied locally in the spatial domain to the spatial neighborhood of each event instead of a multiscale pyramid of filters applied to an entire frame. For each event,

$$R = G_{\omega_o} * \widehat{S} \tag{11.5}$$

where $\widehat{S} \in \mathbb{R}^{n \times n}$ is the function defined in Eq. (11.4) evaluated in the $n \times n$ spatial neighborhood centered at the location of the event at the time of the event. The filter response $R \in \mathbb{R}^{n \times n}$ is complex valued, whose angles are the local phase values near the event. The occurrence of an event only effects the local phase in the $n \times n$ spatial neighborhood centered at the event. Updating local phases near each event allows for construction of event-based temporal local phase signals at each pixel. An amplitude weighted Gaussian blur is applied to the filter response to reduce noise in the local phase signal, as defined in [13]. Once phase signals are calculated, PCA is used for dimension reduction followed by BSS to isolate modal contributions to the phase signals. Since PCA and BSS enforce decorrelation and independence of the phase signals at a given instance in time, local phase signals must be reconstructed onto a common time vector. In this study, linear interpolation was used to reconstruct the signal. Once uniformly spaced phase signals are constructed, the PCA-BSS routine outlined in [5] can be applied to extract full-field mode shapes and natural frequencies.

It was heuristically determined that the backward time increment Δt used in Eq. (11.4) can be reduced to contain only a single event. This results in a major reduction in computational complexity. The local phase due to a single event can be pre-calculated; obtaining time series phase signals for each pixel becomes a simple problem of indexing the pre-calculated phase matrix at each event.

11.4 Experimental Results

The proposed method has been verified on a cantilever beam. The DVS128 was used to record video of a cantilever subject to hammer excitation near its base. A traditional video of the same hammer impact was recorded for comparison. The experimental setup is shown in Fig. 11.2.

The first step in extracting the vibration motion is to calculate local phase at each pixel. A spatial neighborhood of 9×9 pixels was used to calculate local phase signals. The local phase signals calculated from silicon retina video are noisy, as shown in Fig. 11.3 for arbitrary pixels on the beam.

The DVS128 is lower resolution than the video camera used and also outputs noise events that can disrupt the phase signal reconstruction. However, the PCA-BSS process is robust enough to sensor noise to estimate mode shapes and natural

Fig. 11.2 Experimental setup for recording both silicon retina and frame-based video of cantilever beam vibration due to hammer impact

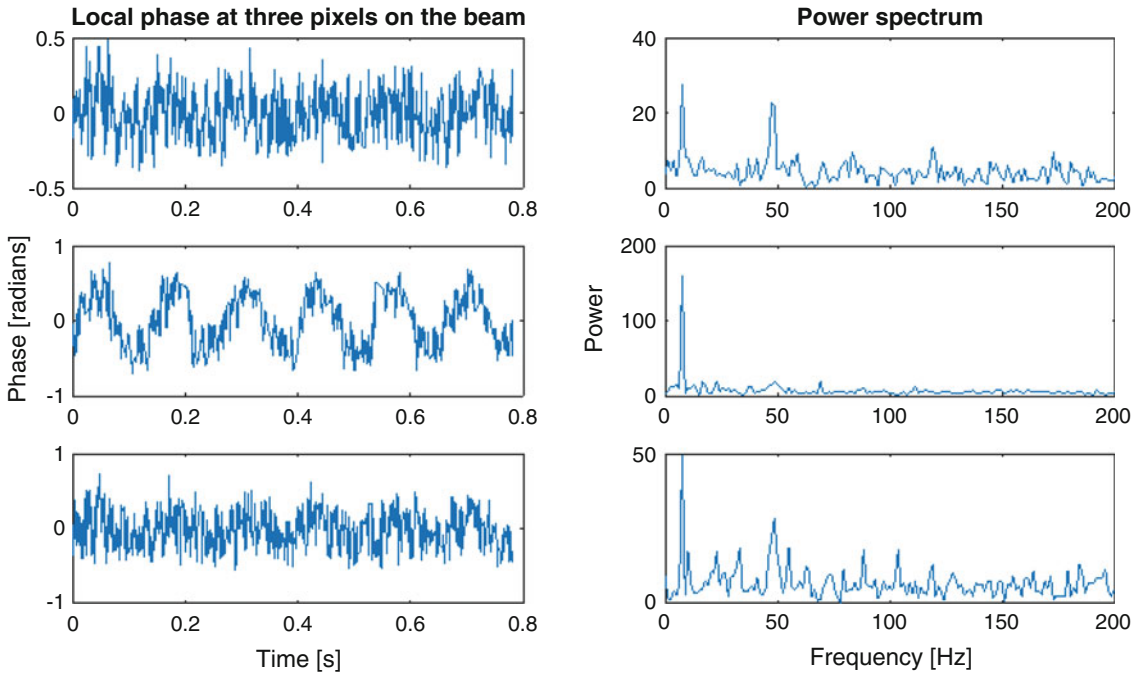

Fig. 11.3 Local phase signals at three pixels on the beam from the silicon retina measurement

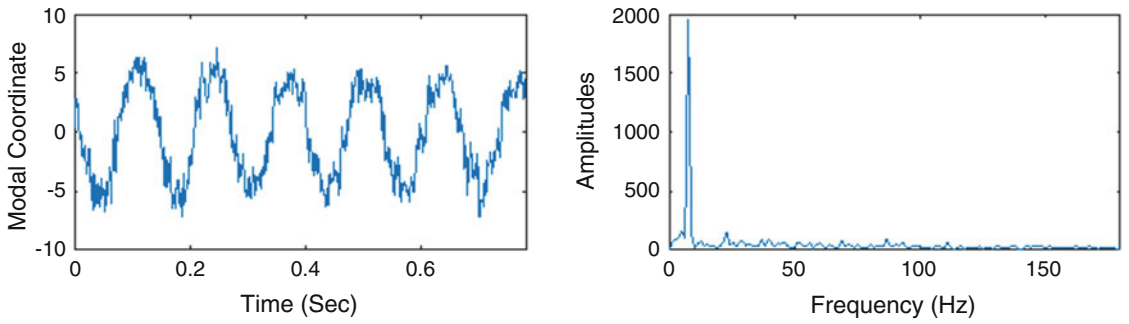

Fig. 11.4 The first modal coordinate estimated by the complexity pursuit (CP) algorithm for the silicon retina measurement

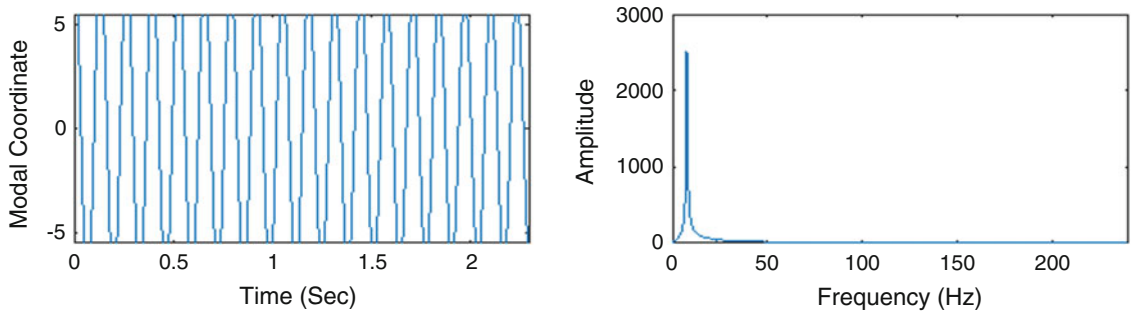

Fig. 11.5 The first modal coordinate estimated by the complexity pursuit (CP) algorithm for the frame-based video measurement

frequencies since the motion signal and sensor noise are independent. Estimated modal coordinates from silicon retina data and traditional video are shown in Figs. 11.4 and 11.5, respectively (the dominant mode 1 is shown here for demonstration).

The frequencies of the estimated modal coordinates are verified in Table 11.1. The analytical natural frequencies for the flexure of a cantilever beam are taken from [14]. The modal coordinate responses were too noisy to measure accurate damping values. Full-field mode shapes for the first bending mode estimated from traditional video and silicon retina video data are shown in Fig. 11.6.

Table 11.1 Cantilever bending natural frequencies

	Silicon retina measurement	Frame-based video	Analytical
Mode 1 frequency (Hz)	7.66	7.41	7.59
Mode 2 frequency (Hz)	48.53	47.96	47.58

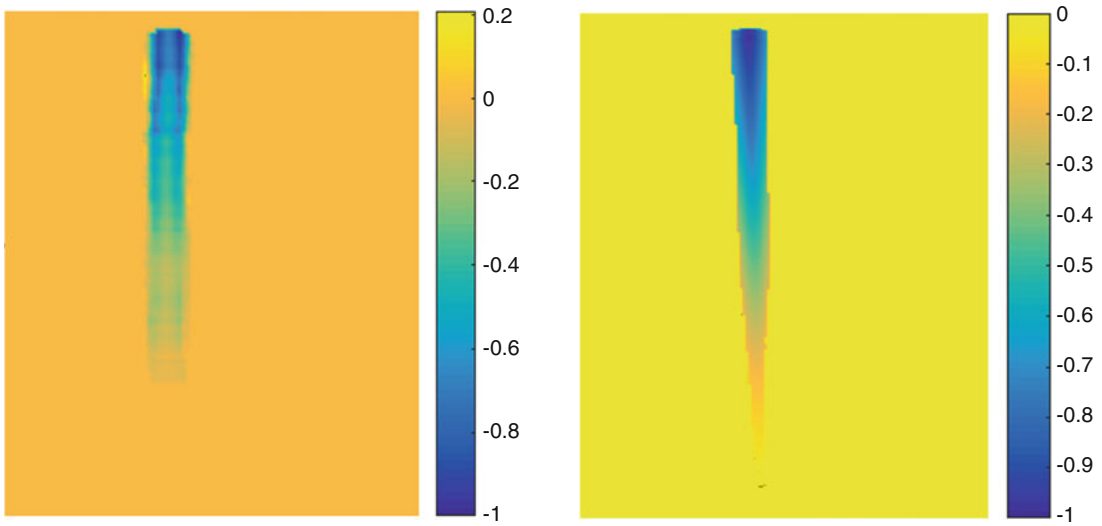

Fig. 11.6 First full-field cantilever bending mode shape identified by the silicon retina (*left*) and a traditional camera (*right*)

Only the first two bending modes were distinguishable in this study. Higher vibration modes were disrupted by harmonic noise introduced event-based sampling. Spurious harmonic peaks can be seen in the bottom row of silicon retina local phase signals in Fig. 11.3. Event-based sampling inherently introduces spurious harmonic noise when sampling periodic signals [15]. Few events are generated at the peaks and troughs of the signal which leads to harmonic noise. The harmonic disturbance could be mitigated by using a more robust event-based signal reconstruction method than linear interpolation. Also, a lower event threshold would decrease harmonic noise, leading to more events as the signal changes directions [15]. However, current silicon retina hardware limits how small the event threshold can be for accurate measurements.

11.5 Conclusions and Future Work

The outcome of this study is an operational modal analysis measurement tool capable of detecting full-field mode shapes and natural frequencies extremely efficiently based on silicon retina video. Event-based silicon retina video contains much less data than traditional frame-based video by only capturing essential motion information and disregarding redundant background data. While event-based video is extremely data-efficient, the field of computer vision is based on the processing of video frames. This work adapts an existing automated video-based modal analysis technique [5], that uses phase-based motion extraction and unsupervised machine learning, to an efficient event-based format.

Results show that the proposed method is capable of extracting the frequency and full-field mode shape for the first two bending modes of a cantilever beam. Higher modes were not captured due to spurious harmonic noise resulting from event-sampling periodic signals. Thus, immediate future work could focus on robust reconstruction of asynchronous event-sampled periodic signals to allow for higher modes to be extracted. Nevertheless, dominant modes can efficiently be measured by the proposed method, which could have significant applications in vibration-based structural analysis. For example, a single full-field mode shape can be used to detect and locate minute local damage in a structure [16]. The capability to obtain full-field vibration information in real-time could also open the door to new structural vibration control applications.

Acknowledgements The authors would like to acknowledge the support of the Los Alamos National Laboratory Institute for Materials Science and the Lab Directed Research and Development (LDRD) program. This program has supported this work in the form of a Director's funded postdoctoral fellowship for Yongchao Yang and an Early Career Award for David Mascareñas. We would also like to acknowledge the Los Alamos National Laboratory—Chonbuk National University Engineering Institute—Korea for supporting Charles Dorn over part of the duration of this work.

References

1. Ewins, D.: Modal Testing: Theory, Practice, and Application. Research Studies Press, Baldock, Hertfordshire, England (2000)
2. Warren, C., Niezrecki, C., Avitabile, P., Pingle, P.: Comparison of FRF measurements and mode shapes determined using optically image based, laser, and accelerometer measurements. Mech. Syst. Signal Process. **25**(6), 2191–2202 (2011)
3. Wang, W., Mottershead, J., Siebert, T., Pipino, A.: Frequency response functions of shape features from full-field vibration measurements using digital image correlation. Mech. Syst. Signal Process. **28**, 333–347 (2012)
4. Chen, J., Wadhwa, N., Cha, Y., Durand, F., Freeman, W., Buyukozturk, O.: Modal identification of simple structures with high-speed video using motion magnification. J. Sound Vib. **345**, 58–71 (2015)
5. Yang, Y., Dorn, C., Mancini, T., Talken, Z., Kenyon, G., Farrar, C., Mascarenas, D.: Blind identification of full-field vibration modes from video measurements with phase-based video motion magnification. Mech. Syst. Signal Process. **85**, 557–590 (2017)
6. Mead, C., Mahowald, M.: A silicon model of early visual processing. Neural Netw. **1**(1), 91–97 (1988)
7. Conradt J., Berner R., Cook M., Delbruck T.: An embedded aer dynamic vision sensor for low-latency pole balancing. In: Computer vision workshops (ICCV Workshops), 2009 IEEE 12th International conference (2009)
8. Delbruck, T., Lang, M.: Robotic goalie with 3 ms reaction time at 4% CPU load using event-based dynamic vision sensor. Front. Neurosci. **7**, 223 (2015)
9. Lichtsteiner, P., Posch, C., Delbruck, T.: A 128 × 128 120 dB 15 μs latency asynchronous temporal contrast vision sensor. IEEE J. Solid State Circuits. **43**(2), 566–576 (2008)
10. Fleet, D., Jepson, A.: Computation of component image velocity from local phase information. Int. J. Comput. Vis. **5**(1), 77–104 (1990)
11. Yang, Y., Nagarajaiah, S.: Blind modal identification of output-only structures in time-domain based on complexity pursuit. Earthq. Eng. Struct. Dyn. **42**(13), 1885–1905 (2013)
12. Barranco F., Fermuller C., Aloimonos Y.: Bio-inspired motion estimation. In: International Work-Conference on Artificial Neural Networks (2015)
13. Wadhwa, N., Rubinstein, M., Durand, F., Wadhwa, N.: Phase-based video motion processing. ACM Trans. Graph. **32**(4), 80 (2013)
14. Ginsberg J.: Appendix C. In: Mechanical and Structural Vibrations. Wiley, New York (2001)
15. Aeschlimann F., Allier E., Fesquet L., Renaudin M.: Spectral analysis of level-crossing sampling scheme. In: International Conference on Sampling Theory and Application, Samsun, Turkey (2005)
16. Yang, Y., Dorn, C., Mancini, T., Talken, Z., Kenyon, G., Farrar, C., Mascarenas, D.: Reference-free detection of minute, non-visible, damage using full-field, high-resolution mode shapes output-only identified from digital videos of structures. Struct. Health Monit. (2017) (Under review)

Chapter 12
Hydro-Mechanical Coupling in Unstable Aircraft Braking Systems

Antoine Gatt, Aurélien Durel, Sébastien Besset, Abdelbasset Hamdi, Jean-Frédéric Diebold, and Louis Jezequel

Abstract Aircraft braking systems may be subjected to friction-induced vibrations, during which the brake is unstable and behaves as a source of mechanical vibrations. This is an issue for aircraft brake manufacturers as it may jeopardize structural integrity due to accelerated fatigue life, or generate discomfort for the aircraft crew and passengers. The important cost associated to the occurrence of this phenomenon motivates the development of instability simulation and prediction methods that can be used as early as the design stage.

Here, the self-excited vibrations are induced by a coupling of two structure modes by friction. It appears that modifications of the brake hydraulic command system configuration have important consequences on the vibration levels monitored during the tests. It is therefore necessary, when developing a vibration level simulation methods, to consider the hydro-mechanical coupling of the unstable brake structure with the brake hydraulic fluid.

This paper presents a simulation methodology associating a structural reduced model with a unidimensional model of the hydraulic control system, including both passive and active components. Both submodels are validated against experimental data.

The influence of several hydraulic system configurations on the coupled system vibration levels and on the braking performances is evaluated. It is shown that a compromise between vibration reduction and braking performance can be found through simulation. It is the first time that the interaction of self-excited brake structure with a heavy fluid is studied. The present method offers important industrial opportunities and gives an insight into the brake mode-coupling dynamics.

Keywords Mode-coupling instability • Brake system • Fluid-structure interaction • Modal reduction • Non-linear dynamics

12.1 Introduction

12.1.1 Aircraft Braking Systems

The system under study is an aircraft wheel and brake assembly as shown in Fig. 12.1. Modern commercial aircraft brakes are composed of a stack of Carbon/Carbon composite discs called “heat sink”. During braking, hydraulic fluid is sent in the pistons through the hydraulic command system. Pressure is then applied on the heat sink, which generates the braking torque. In order to have a better view of the concerned parts, the landing gear and the tire are not shown here. For more details, see [1].

A. Gatt (✉)
Ecole Centrale de Lyon, LTDS, 36 avenue Guy de Collongue, 69134 Ecully, France

Safran Landing Systems, 7 rue général Valérie André, 78140, Vélizy-Villacoublay, France
e-mail: antoine.gatt@doctorant.ec-lyon.fr

A. Durel • A. Hamdi • J.-F. Diebold
Safran Landing Systems, 7 rue général Valérie André, 78140, Vélizy-Villacoublay, France

S. Besset • L. Jezequel
Ecole Centrale de Lyon, LTDS, 36 avenue Guy de Collongue, 69134 Ecully, France

J.M. Harvie, J. Baqersad (eds.), *Shock & Vibration, Aircraft/Aerospace, Energy Harvesting, Acoustics & Optics, Volume 9*,
Conference Proceedings of the Society for Experimental Mechanics Series, DOI 10.1007/978-3-319-54735-0_12

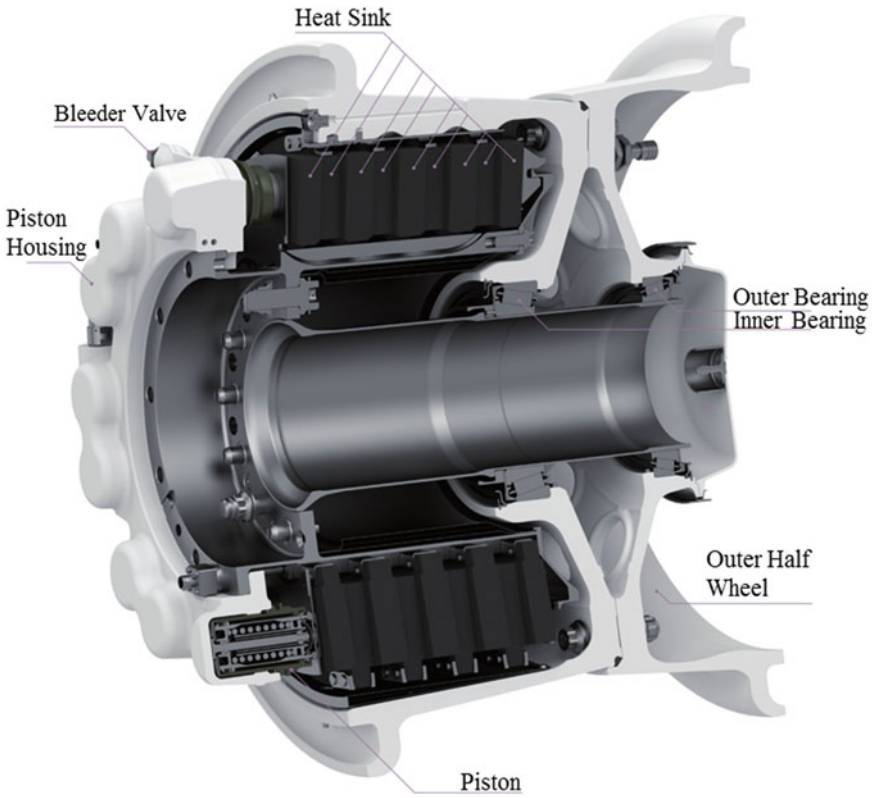

Fig. 12.1 Aircraft wheel and brake assembly

12.1.2 Methodology

Concerning NVH, most of the qualification and part of the development process of an aircraft brake rely on testing, which is costly. It is thus important to minimize the number of brake configurations to be tested by using accurate simulation methods. Braking systems self-excited vibrations have been extensively studied for decades [2] but no complete methodology leading to a robust brake design has yet been developed [3].

The structural dynamic behavior of the aircraft brake is modelled using the finite element method. However a small model is required to perform Transient Dynamic Analyses (TDA), which would otherwise be too computationally intensive. A modal reduction method based on Component Mode Synthesis (CMS) is then used to reduce the model size. This structural model is unstable, which means that it behaves as a source of vibration. The interest of performing non-linear TDA in this context is presented in [4].

A unidimensional model of the hydraulic circuit is built, including an electrohydraulic servo valve, channels and pistons. It is a common practice to use orifices (diameter restriction) in the hydraulic channels as vibration reduction devices. Those devices are also modelled. It appears that the presence of orifices in the brake channels tends to increase the piston filling time, and thus increase the braking distance. It is obvious that an increase of the braking distance is not desired and corresponds to a deterioration of the braking performances. The filling time is simulated.

Both hydraulic and structural models are validated against experimental data. Finally, the coupling of the two subsystems is studied. The influence of several hydraulic system configurations on the coupled system vibration levels is evaluated. It is shown that the hydraulic circuit can advantageously be tuned to perform as an unstable vibration reduction device. A compromise between braking performances and vibration reduction can be found, which drastically facilitates decision making and allows reducing the number of test to be performed.

The original scientific contributions of this paper are multiple. To the author's knowledge, the study of the non-linear hydro-mechanical coupling in an unstable braking system with such a level of fidelity does not exist in the literature. Also, it is often considered that contact losses between the frictional interfaces is the only non-linear phenomenon accounting for brake squeal vibration level saturation. It is demonstrated here that the hydraulic command system has also to be taken into

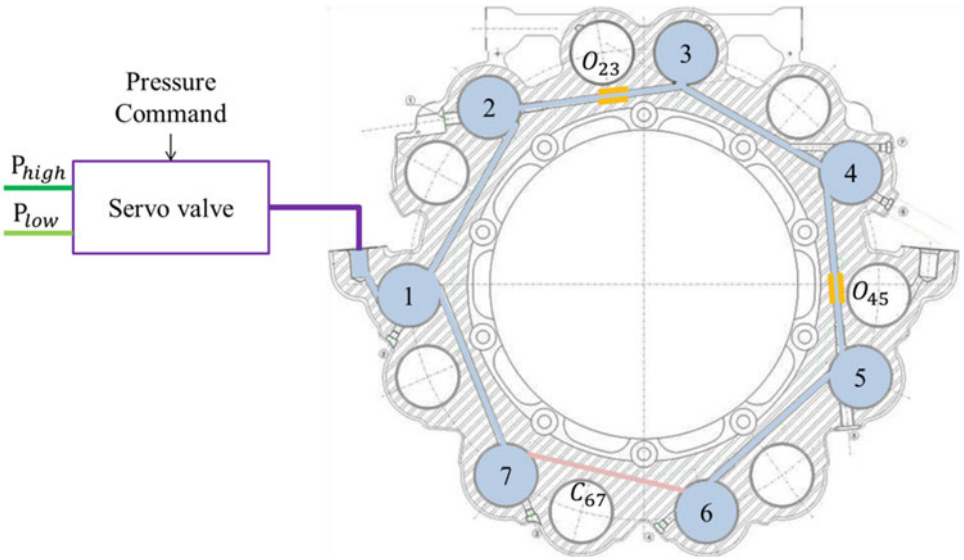

Fig. 12.2 Schema of the hydraulic circuit

account. More generally, for industrial systems with hydraulic circuits, the identification of the dynamic contribution of the hydraulic system is a common issue. The linearity and the damping contribution are discussed in the present paper.

12.2 Experimental Set Up

A typical hydraulic system is represented bellow in Fig. 12.2. It is a double circuit, so only half of the piston cavities (PC) are used for braking. They are numbered from 1 to 7. Two orifices O_{23} and O_{45} are represented between cavities 2 and 3 and cavities 4 and 5 respectively. A servo valve controls the downstream pressure by feedback to match the pressure command. This pressure command is issued by the pilot or the automated braking system in operating conditions, or by the test engineer during tests. The servo-valve is connected to a high pressure tank at pressure P_{high} and to a low pressure tank at pressure P_{low}. The pressure in the piston cavities is then applied by the pistons on the heat-sink.

During the braking test, the piston cavities are equipped with pressure transducers and accelerometers to monitor both pressure variation and acceleration. At some point during the braking phase, the whole wheel and brake assembly may be subjected to self-excited vibrations. It then appears that that the pressure in the hydraulic circuit oscillates with the same frequency as the structure.

The brake filling time is defined as the duration between the setting of the pressure command and the application of the braking pressure on the heat sink. It is the time required to fill the piston cavity. It depends on the pressure losses in the circuit, especially on the pressure losses introduced by the orifices.

It has been known for years that the presence of orifices in the hydraulic circuit tends to lower brake vibration levels [5]. Different configurations have to be selected for qualification or development tests. Orifices number, size and position may be tuned. It is also possible to close the hydraulic circuit with an additional channel, labelled here C_{67}. It is obvious that the number of possible configurations for the hydraulic circuit is very high. Without the help of simulation, the brake manufacturer has to perform many costly tests to characterize the behavior of the system and cannot ensure that the best configuration has been chosen.

12.3 Modelling

The chosen numerical approach is to couple a structural model which represents the mode coupling instability with a hydraulic model. The latter takes into account both passive components, as channels or orifices, and active components, such as the servo-valve.

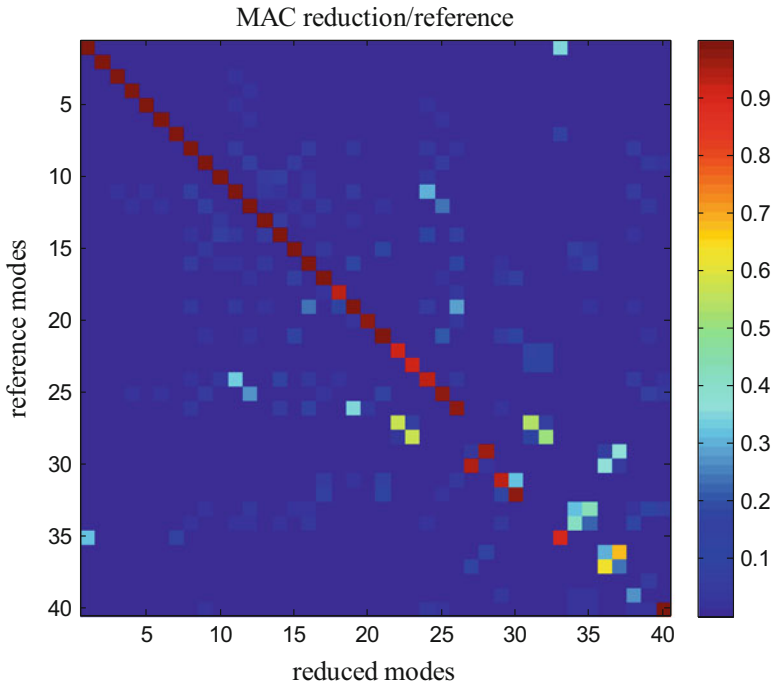

Fig. 12.3 MAC reduction/reference

12.3.1 Structure

The wheel and brake structure is modeled using the finite element method. The fidelity of the FEM model with respect to the test is evaluated using the Operational Deflection Shape (ODS) and the Modal Assurance Criterion (MAC) [6].

However, in order to perform TDA, it is necessary to reduce the FEM model size. This can be achieved through modal reduction as in [7]. The resulting simplified model has less than 300 degrees of freedom (DOF). It does not reduce the DOF corresponding to the pistons, as they will be used at the interface between the structural and the hydraulic models. The structure modes are changed significantly by the hydraulic circuit and the pistons behavior. The consequence is that a reduction on a modal basis would not be a satisfying representation of the structure.

To ensure fidelity between the reference FEM and the reduced model, and thus between the experimentally identified ODS and the reduced model, the MAC is evaluated on the real modes (see Fig. 12.3). It appears that the diagonal is close to unity up to mode 26, which guarantees the dynamic fidelity above the 3rd harmonic of the brake unstable mode.

12.3.2 Hydraulic

The hydraulic circuit presented in Fig. 12.2 is modelled in Matlab-Simulink, using the Simscape toolbox. The hydraulic fluid used in the simulation is Skydrol LD-4. It is represented as heavy, viscous and compressible. Local pressure losses, due to the turbulent flow behavior at the orifices, are accounted for as described in [8].

Among the limitations of the model, we should note that the flow/pressure relationships are based on coefficients identified for stationary flow configurations, however flow is not stationary in practice. However, calculation checks were performed to ensure the error introduced by this hypothesis was reasonable. A higher level of fidelity would require a more complex Computational Fluid Dynamics approach based on co-simulation. Such a strategy would be far more computationally intensive, thus without any real industrial interest.

12.3.3 Simulations

Here, two types of simulation are of interest. On the one hand, the brake filling time indicates how the use of small size orifices deteriorates braking performances. For these calculations, an equivalent stiffness is sufficient to model the brake structure. Compared to experimental results, the relative error on the brake filling time is below 5%, which validates the hydraulic model.

On the other hand, the non-linear TDA outputs the stationary self-excited vibration levels. The coupling of the two submodels described above is ensured by assuming continuity of the pistons velocity at the interface. A realistic braking pressure of 60 bar is applied.

12.4 Results

12.4.1 Brake Filling Time

The filling time, as it impacts directly the braking distance, is critical for brake performances. The typical result from a brake filling time computation is shown below in Fig. 12.4. The pressure is recorded in every piston cavity (PC). The chosen configuration is two 1.6 mm orifices in O_{23} and O_{45}, without the connection channel C_{67}.

The pressure command is a step function of 31 bar starting at t_1. The first piston cavities to be filled are PC1, PC2 and PC7 at t_2, then PC3 and PC4 at t_3 and finally PC5 and PC6 at t_4. At t_4 the last pistons encounter the first braking disk, pressure rises rapidly in all the piston cavities and the full braking pressure is applied a few milliseconds later. The brake filling time is by convention:

$$t_b = t_4 - t_1$$

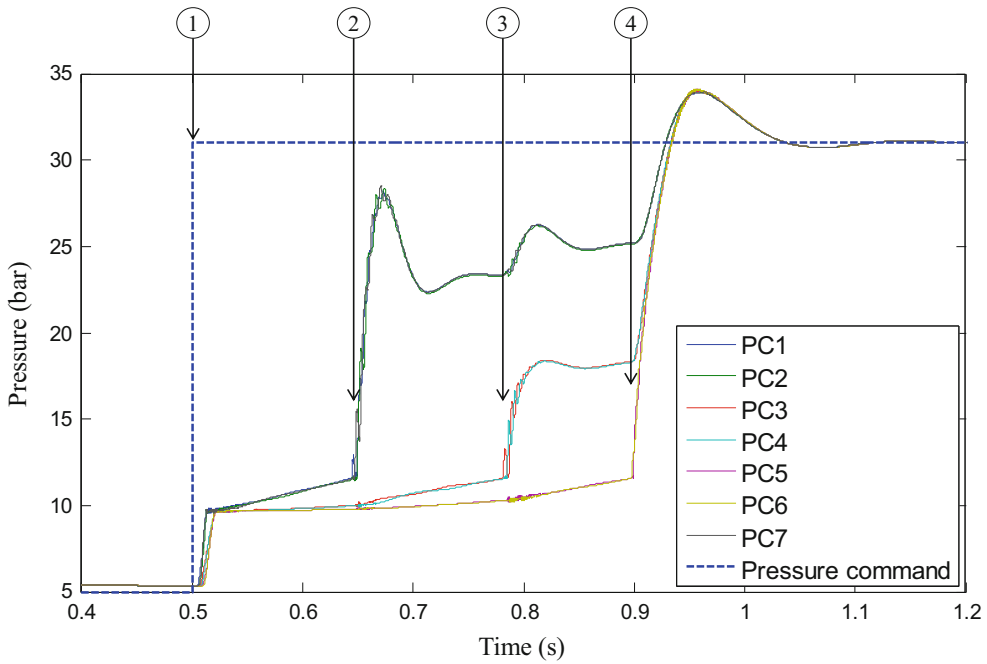

Fig. 12.4 Brake filling time

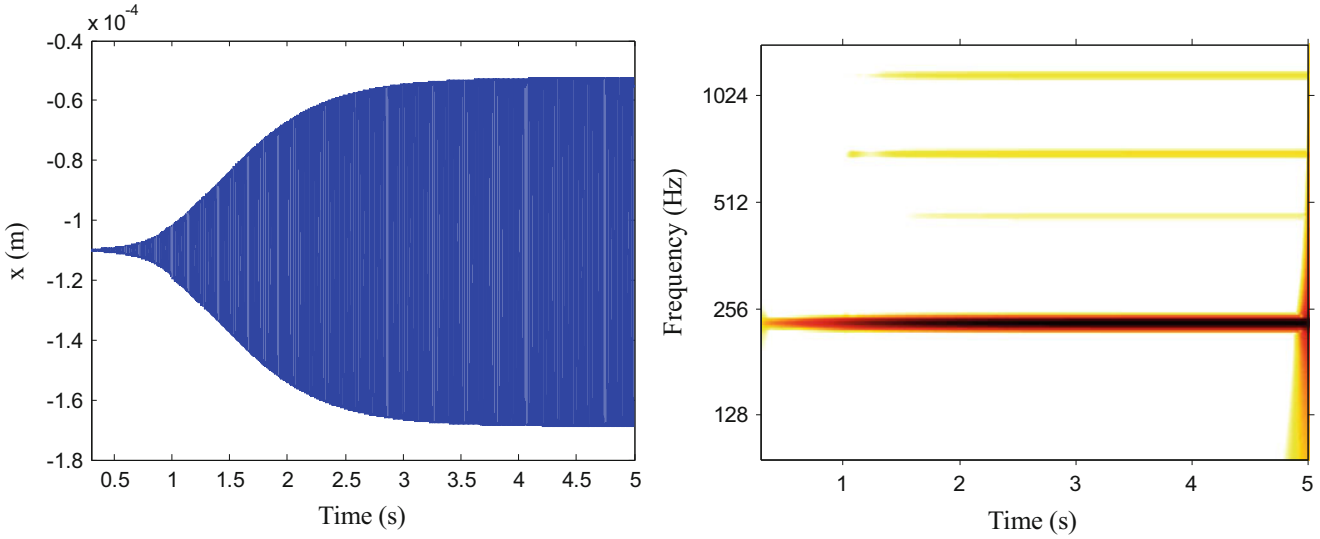

Fig. 12.5 Out-of-plane piston housing displacement (*left*) and wavelet transform (*right*)

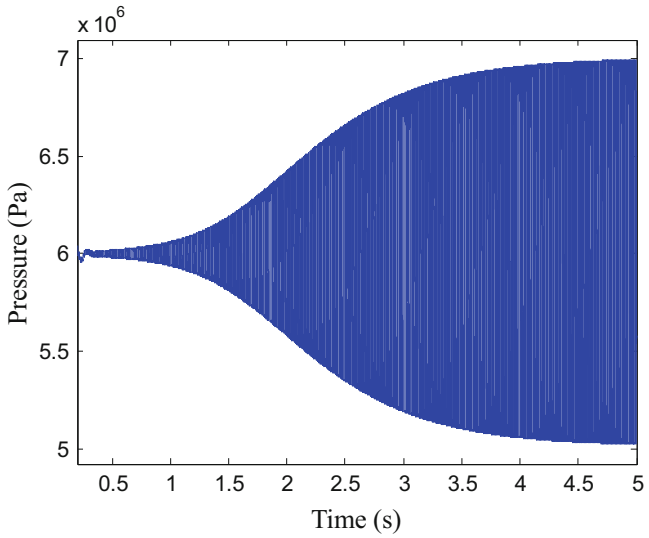

Fig. 12.6 Pressure PC6 vs time

12.4.2 Non-linear Dynamic Simulations

12.4.2.1 Non-linear TDA

Typical results of non-linear TDA are presented in Figs. 12.5 and 12.6. We observe that similar behaviors can be observed for pressure and displacement. The time history can classically be divided into three parts:

- From $t = 0$ to $t = 1$ s the system behavior is self-excited and linear, which results in an exponential increase of the vibration levels. It can be seen on the Continuous Wavelet Transform (CWT) that the fundamental frequency appears, but without any harmonic component.
- From $t = 1$ to $t = 4$ s the vibration levels continue to increase, but non-linearities enter into play. Vibration increase is not exponential anymore and the harmonic components appear in the CWT.
- After $t = 4$ s limit cycles are reached.

It appears here that the non-linear hydraulic system, when coupled to a self-excited linear structure model, enables vibration level stabilization. Therefore, the hydraulic system contribution cannot be seen as a simple linear damping.

12.5 Discussion

We can isolate three main dynamic contributions to the coupled system dynamic. First, the most obvious is the energy dissipation in the hydraulic circuit. Vibrations in the structure are transmitted to the hydraulic circuit and translate in pressure difference between cavities, inducing a flow through the orifices. This results in a local pressure loss causing energy dissipation. The description of this phenomenon is based on fluid mechanic equations; it involves flow regime transition and turbulent flow behavior, and is therefore essentially non-linear.

Secondly, in real hydraulic systems, the air content of the fluid is not negligible. As it can be seen in Fig. 12.7, the fluid's homogenized bulk modulus decreases rapidly for low pressure. It implies that, for a typical air content $\alpha = 2\%$, as the pressure variation amplitudes increase as in Fig. 12.6, the fluid modulus is going to vary of about $\pm 5\%$. The hydraulic circuit can then be thought of as a non-linear stiffness.

Finally, the aforementioned stiffness variations have an influence on the system stability and thus on the self-excited vibrations. Indeed, the mode-coupling instability at the origin of brake squeal might be affected in the sense that the real part of the eigenvalues of the linearized system might be modified.

It would be a complex task to design a hydraulic system based on the understanding on those competing physical phenomena. Hopefully, the proposed model outputs limit cycle's amplitudes, facilitating interpretation. A hydraulic circuit configuration can be evaluated in terms of both braking and vibration performances. We are now interested in reducing the limit cycle's amplitudes by tuning orifices size in the hydraulic circuit, while maintaining acceptable braking performance.

12.5.1 Unstable Vibration Reduction

12.5.1.1 Connection Channel C_{67}

A non-linear TDA is performed with two orifices $O_{23}$and O_{45} both 1.6 mm in diameter. As it may be seen in Fig. 12.8, deleting the channel C_{67}, resulting in a U shaped circuit, improves the vibration performances of the system from 9.2 to 6.3 g.

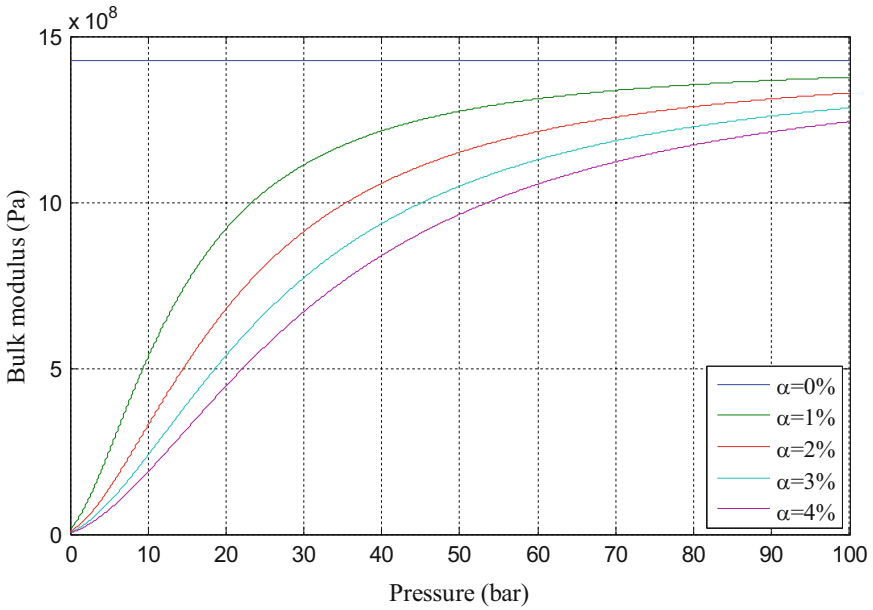

Fig. 12.7 Skydrol bulk modulus vs pressure

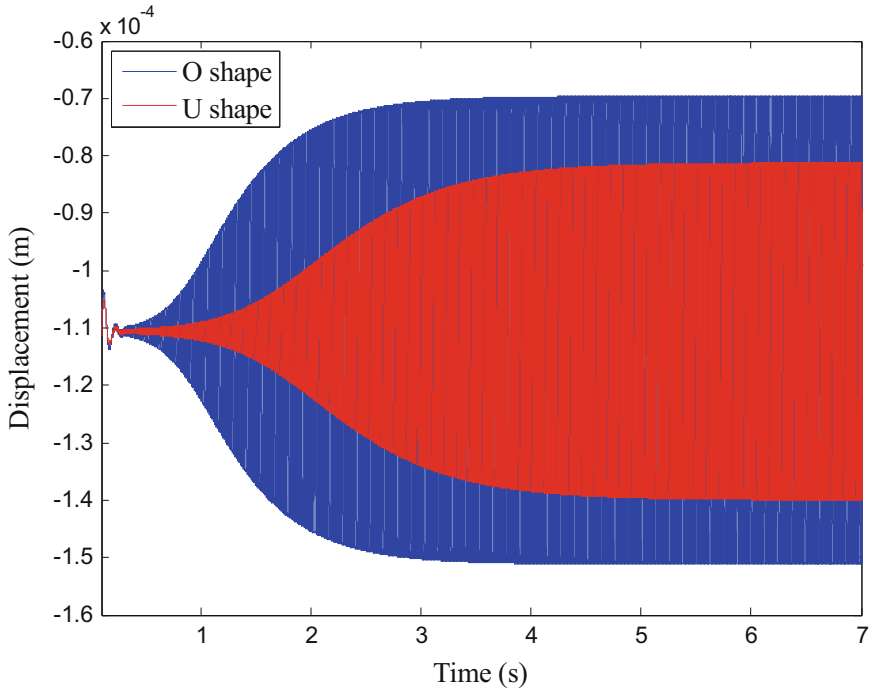

Fig. 12.8 Comparison between the *U* and *O* shape

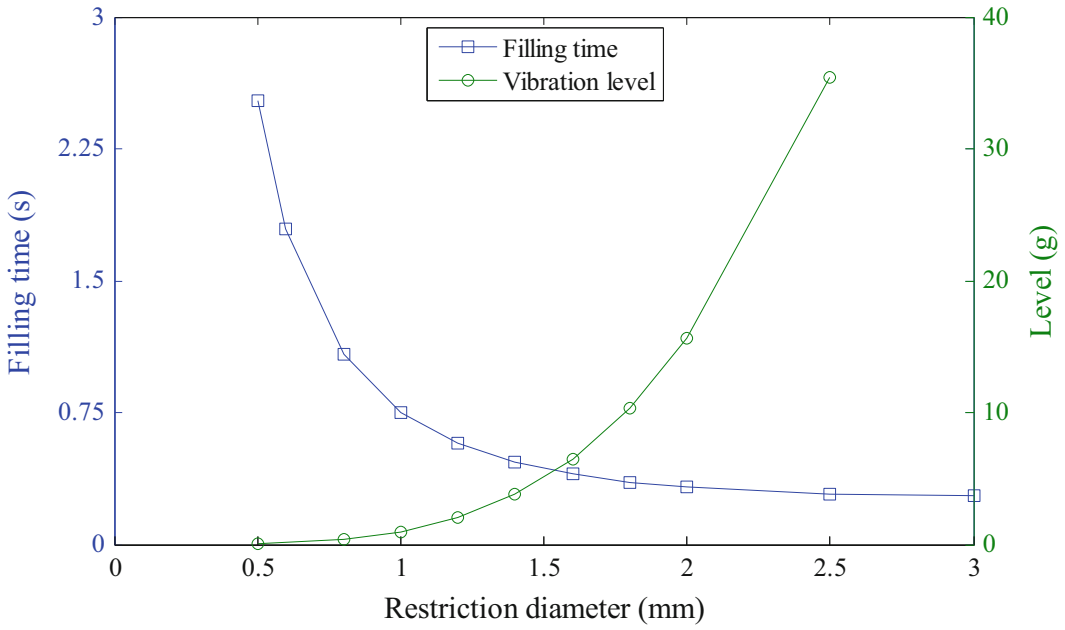

Fig. 12.9 Dynamic performance and filling time versus orifices' size

12.5.1.2 Orifices' Size

On a U shaped circuit, the size of the orifices O_{23} and O_{45} is varied from 2.5 to 0.5 mm in diameter. In parallel, the brake filling time is evaluated for the same configurations. It appears in Fig. 12.9 that, while reducing orifices' size diminishes the vibration levels, it results in an increase of the brake filling time.

It can be seen here that a compromise has to be made between brake performances and self-excited vibration reduction. The use of the presented model allows exploring a wide design space without performing costly tests.

12.6 Conclusion

The coupling of an unstable brake structure with a nonlinear model of the hydraulic command system is presented in this paper. The structural model is obtained using a reduction method on a full-scale finite element model. A unidimensional model of the hydraulic circuit is built, including both active and passive components. Two types of simulation are performed. Limit cycles' amplitudes are calculated using non-linear transient analysis and brake filling time, which is an indicator of braking performance, is evaluated.

It is shown that the hydraulic command circuit can be tuned, using orifices, to lower the self-excited vibrations' amplitudes. The impact of this tuning on the brake filling time is monitored, so that a good compromise between vibration reduction and braking performances can be found. Interesting configurations can be found using simulation, thus diminishing the number of tests that have to be performed.

The fluid-structure interaction modeling presented here is a key step for the non-linear vibration level simulation of aircraft braking systems. Such a tool has a high industrial value as it can be used early in the design process and eases the decision making. It also gives an insight into the heavy fluid dynamic behavior in vibrating structures.

The next step is to use discrete optimization tools to study a very wide design space, using multiple orifices of different size in various locations of the circuit.

References

1. Safran: Landing and braking systems [online]. Available: http://www.safran-group.com/video/8986. Accessed 14 Oct 2016
2. Kinkaid, N.M., O'Reilly, O.M., Papadopoulos, P.: Automotive disc brake squeal. J. Sound Vib. **267**(1), 105–166 (2003)
3. Ouyang, H., Nack, W., Yuan, Y., Chen, F.: Numerical analysis of automotive disc brake squeal: a review. Int. J. Veh. Noise Vib. **1**(3–4), 207–231 (2005)
4. Sinou, J.-J.: Transient non-linear dynamic analysis of automotive disc brake squeal–on the need to consider both stability and non-linear analysis. Mech. Res. Commun. **37**, 96–105 (2010)
5. Sinou, J.-J.: Synthèse non-linéaire des systèmes vibrants. Application aux systèmes de freinage. PhD thesis, Ecole Centrale de Lyon, 2002
6. Allemang, R.J.: The modal assurance criterion–twenty years of use and abuse. J. Sound Vib. **37**(8), 14–21 (2003)
7. Gatt A. et al., Double modal synthesis applied to aircraft brake squeal prediction and simulation. AIAA. J. Aircr. (2017), in press
8. Idel'chik, I.E., Steinberg, M.O.: Handbook of Hydraulic Resistance. Begell House, Danbury (1996)

Chapter 13
Energy Based Representation of 6-DOF Shaker Shock Low-Cycle Fatigue Tests

Carl Sisemore, Vit Babuska, and Jason Booher

Abstract Materials subject to cyclic loading have been studied extensively and experimentally determined comparisons of stress to number of cycles are used to estimate fatigue life under various loading scenarios. Fatigue data are traditionally presented in the form of S-N curves. Normally, S-N data are derived from cyclic loading but the S-N results are also applicable to random vibration loading and, to some extent, shock. This paper presents an alternate presentation of fatigue data in terms of input energy and number of cycles to failure. In conjunction with this study, a series of shock tests was conducted on 3D printed cantilever beams using a 6-DOF shaker table. All of the beams were tested to failure at shock levels in the low-cycle fatigue regime. From these data, a nominal fatigue curve in terms of input energy and number of shocks to failure was generated and compared with the theoretical developments.

Keywords Fatigue • Shock testing • 6-DOF • Energy spectra • Shock response spectra

13.1 Introduction

Energy response spectra, along with the shock response spectrum (SRS), are both valid methods for quantifying the severity of single mechanical shock events. The SRS was introduced in the 1930s and is currently the standard method for describing mechanical shock events. Energy spectra methods for the analysis of mechanical shock are nearly as old as the SRS, being introduced in the 1950s. The seismic and civil engineering community has long used the energy methods, including energy response spectra, for describing damage potential to structures from earthquakes. Energy response spectra are generally analogous to the SRS but are based on other quantities such as potential, kinetic, and total energy.

In the seismic community the shock loading is typically a single earthquake event and the structure either passes or fails accordingly. However, many shock scenarios in other disciplines are based on events related to transportation: ground or air transport. As such, the number of shock events could be quite high as the component of interest is transported from one location to another. This leads to the concept of low or high-cycle fatigue shock loading. SRS methods are only applicable to single shocks in which the failure mechanism is an overstress. In contrast, energy quantities seem better suited to capturing the cumulative effects of multiple shocks.

The purpose of this investigation was first to determine how 6-DOF shock testing related back to single degree-of-freedom shock testing. The 6-DOF testing used herein applied shocks simultaneously in all three translational directions as well as three rotational shocks. The second goal of this investigation was to better understand how energy quantities apply to repetitive shock events and to develop a theoretical framework for their application. Do energy metrics follow a similar framework as more traditional fatigue life estimation methods?

This paper describes the results of a series of 6-DOF shaker shock tests performed on ABS plastic cantilever beams manufactured with a 3D printer. Over three thousand 6-DOF shocks were applied to 68 different cantilever beams during the course of this study. The general test approach was to test several beams simultaneously at a level below that known to cause failure with one shock and repeat that test until all beams failed. The test was then repeated with a new set of beams and a different low-level shock input. The test specifics, data processing, and results are described in this paper along with an appropriate failure theory based on input energy.

C. Sisemore • V. Babuska (✉) • J. Booher
Environments Engineering and Integration Department, Sandia National Laboratories, P.O. Box 5800–MS 0840, Albuquerque, NM 87185, USA
e-mail: vbabusk@sandia.gov

J.M. Harvie, J. Baqersad (eds.), *Shock & Vibration, Aircraft/Aerospace, Energy Harvesting, Acoustics & Optics, Volume 9*, Conference Proceedings of the Society for Experimental Mechanics Series, DOI 10.1007/978-3-319-54735-0_13

13.2 Basquin's Equation for Shock

Endurance of materials subject to cyclic loading has been extensively studied since the 1800s. The endurance life or fatigue life, defined as the number of cycles to failure or the ability of a machine part to resist fatigue, is dependent on the developed stress in the part. The data from these tests characterizing the endurance of the material are displayed as S-N curves. The S-N curve in the high-cycle fatigue region can be represented analytically. The most popular representation is the Basquin relation:

$$NS^b = C. \tag{13.1}$$

In the above equation, N is the number of cycles to failure, S is the cyclical stress amplitude, b is the fatigue strength coefficient, and C is an empirically determined constant. The fatigue strength coefficient is determined from S-N data where $-1/b$ is the slope of the S-N line in log-log space.

Basquin's equation is a model based on test data. Fatigue strength coefficients typically range from 3 to 25 with the most common values falling between 3 and 10. Lalanne [1] has compiled typical fatigue strength coefficient values for a variety of materials (aluminum, steel, solder) and components (resistors, capacitors, circuit boards, and other complex electronic items) measured from numerous tests. The spacecraft community has settled on a fatigue strength coefficient of 4.0 for electronic and electrical equipment, 6.4 for load carrying structures under sinusoidal vibration, and 8.0 for load carrying structures under random vibration [2, 3].

Basquin's equation is popular and has been used for more than 60 years for several reasons: it fits measured data well; it is consistent with fracture mechanics models; and it can be adjusted to account for factors such as surface finish, corrosion, stress concentration factors, stress ratios, and others as needed.

It has been postulated previously that a power law relationship like Basquin's equation applies to shock environments and energy spectra comparisons [4]. In this context, the Basquin equation would be defined in terms of some energy quantity and number of cycles to failures.

13.3 Input Energy and Fatigue Life

In the energy framework, fatigue life is a function of the input energy, which can be calculated for any dynamic system as:

$$E_I = \int_{t=0}^{t=T} \boldsymbol{p}(t)\dot{\boldsymbol{x}}(t)dt \tag{13.2}$$

where $\boldsymbol{p}(t)$ is an external load vector and $\dot{\boldsymbol{x}}(t)$ is the response velocity vector. Note that input energy includes a response term. This means that the input energy can vary across a structure depending on the response location. In the subsequent development, there is an implicit assumption that the input energy is calculated for the component of interest.

The S-N plot is the experimentally determined relationship between zero mean, constant cyclic stress amplitude and number of cycles to failure. To create a similar E_I-N curve from an S-N curve, consider the case of constant amplitude cyclic loading. In this case $p(t) = A\sin(\Omega t)$, and any environment is characterized by $[p(t),T]$ or $[A,\Omega,T]$. For steady state cyclic loading, the input energy can be written as:

$$E_I = \int_{t=0}^{N/\Omega} \boldsymbol{p}(t)\dot{\boldsymbol{x}}(t)dt = N\int_{t=0}^{1/\Omega} \boldsymbol{p}(t)\dot{\boldsymbol{x}}(t)dt = N\overline{E_I} \tag{13.3}$$

where N is the number of cycles and $\overline{E_I}$ is the input energy per cycle.

Input energy per cycle has another interpretation—as the energy dissipated per cycle. If a dissipative system starts and ends at rest, with no permanent deformation, the total input energy is equal to the total dissipated energy, $E_I = E_D$. So it follows by extension that $\overline{E}_I = \overline{E}_D$.

This relationship can be used to generate the E_I-N curve. Damping energy is proportional to the square of the stress amplitude, S, in linear dynamical systems with viscous damping [5]. Thus, it is apparent that

$$\overline{E}_D \propto S^2 \tag{13.4}$$

Substituting Eq. 13.4 into Eq. 13.1 implies that dissipated energy also follows a power law relationship with the number of cycles.

$$N\bar{E}_D^{\frac{b}{2}} = C_D \tag{13.5}$$

where C_D is an empirically determined constant, not necessarily the same as C from Eq. 13.1. Rearranging this equation gives:

$$\bar{E}_I = \bar{E}_D = C_D{}^{\frac{2}{b}} N^{-\frac{2}{b}} \tag{13.6}$$

This form of the equation is consistent with the way S-N curves are shown graphically whereas the original form of Eq. 13.1 is consistent with fracture mechanics models. The slope of the S-N curve is $-1/b$, so the slope of a corresponding $\bar{E}_I$-N curve is twice the slope of the S-N curve. Thus, in terms of total input energy or total dissipated energy, Eq. 13.6 becomes

$$E_I = E_D = N\bar{E}_I = C_D{}^{\frac{2}{b}} N^{\left(1-\frac{2}{b}\right)} \tag{13.7}$$

While damping energy is approximately proportional to the square of stress amplitude as shown in Eq. 13.4, Dowling provides a more realistic relationship between stress and damping energy as a non-linear function of stress amplitude [5]. For metals, this relationship is given as

$$\bar{E}_D \propto S^{\beta} \begin{cases} \beta \sim 2.4, S < 0.8S_{yield} \\ \beta \sim 8, S \geq 0.8S_{yield} \end{cases} \tag{13.8}$$

Thus, the more general form of Eq. 13.6 is:

$$\bar{E}_I = C_D{}^{\frac{\beta}{b}} N^{-\frac{\beta}{b}} \tag{13.9}$$

For high-cycle fatigue, generally, $S < 0.8S_{yield}$ suggesting that $\beta = 2.4$ is appropriate and slightly more conservative than $\beta = 2$. A common average value for the fatigue strength coefficient for general structural members is $b = 6.67$ which is consistent with References [2, 3] and. The slope of the S-N curve is then $-1/b \cong -0.15$, so a typical slope of the $\bar{E}_I$-N curve is about -0.36 and the slope of the corresponding E_I-N curve would be 0.64.

The main implication of the similarity between the S-N curve and the $\bar{E}_I$-N curve is that all of the machinery developed for high-cycle fatigue analysis is applicable when the quantity of interest is input energy instead of stress—specifically Miner's rule.

13.4 Test Article Description

The test article of interest in this study are ABS plastic 3D printed cantilever beams printed by the Sandia National Laboratories Additive Manufacturing group. The beams were printed with crosswise rastering. Crosswise raster printing produces brittle beams with inhomogeneous material properties. Figure 13.1 shows the brittle nature of the beams in stress strain curves measured during static testing of crosswise raster printed cylindrical coupons. The elastic properties were measured at slow strain rates. At higher strain rates, typical of shock loading, the material may be more brittle. Figure 13.2 is a micrograph of a cross section of one of the coupons. The printing orientation is clearly visible as is the inhomogeneity of the material.

The S-N and E_I-N relationships were derived using characteristics of high-cycle fatigue behavior. The source of high cycle fatigue failure is usually a flaw such as a microcrack or void that is irritated by even low levels of strain so that a crack initiates. Low cycle fatigue is usually characterized by cyclic loading that induces plastic deformation. The slope of the S-N curve in this region is smaller than the slope in the high cycle region. Once the yield stress is exceeded, strain based fatigue models must be used because stress and strain are no longer linearly related, but an S-N curve can be approximated using empirically deduced models (e.g., Coffin model). However, brittle materials, by their very nature, do not tolerate large strains well. Inhomogeneous materials such as the 3D printed plastic have intrinsic microstructural (and macrostructural)

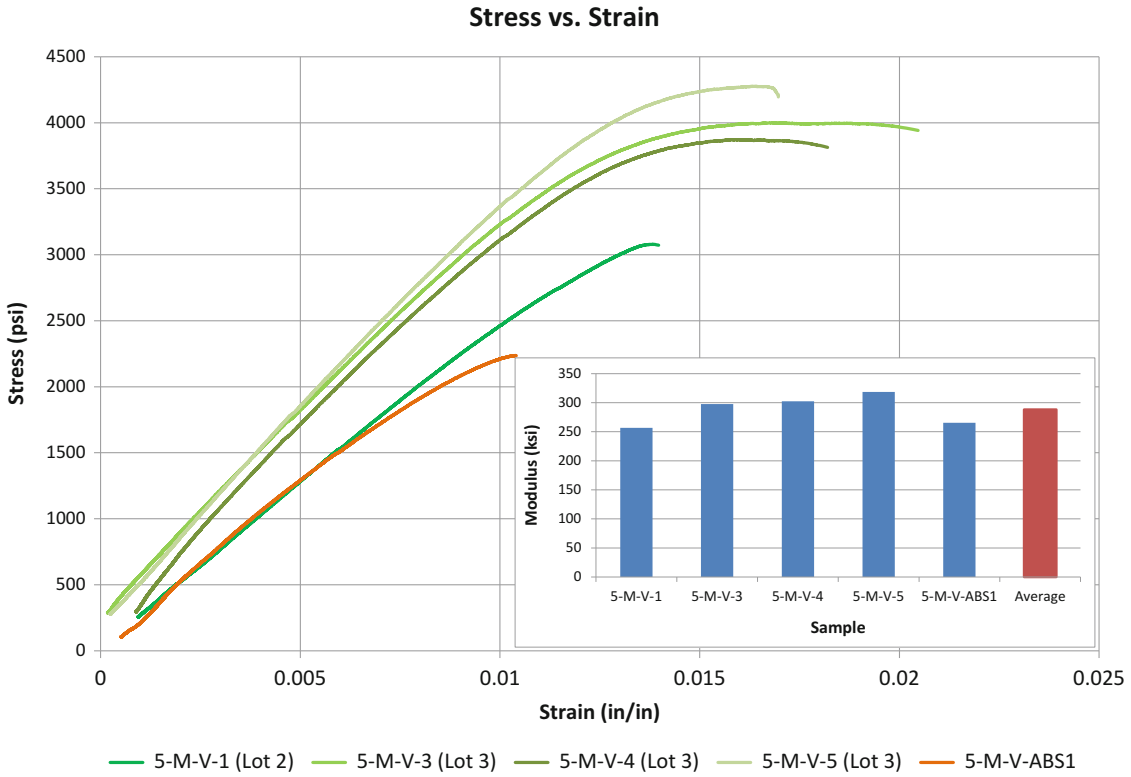

Fig. 13.1 Modulus of ABS plastic beams

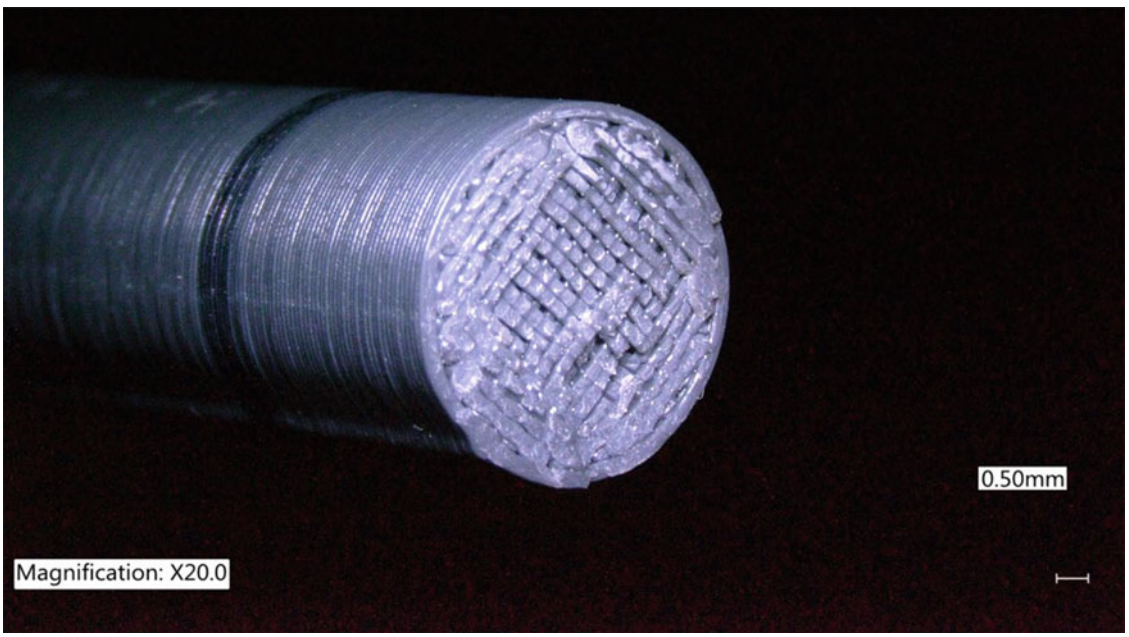

Fig. 13.2 Micrograph of ABS beam cross-section

failure initiation mechanisms. Therefore, a high-cycle fatigue model may apply to the 3D printed beams in that there is no low-cycle fatigue region because they are brittle; i.e., the S-N curve has a constant slope down to a very low number of cycles. Furthermore, the macroscopic flaws are analogous to the microscopic flaws in metals, so the slope of the S-N curve of the 3D printed beams curve may be in-family with typical published values.

13.5 6-DOF Shock Testing Overview

For the experimental portion of this study, the 68 ABS plastic 3D printed cantilever beams were tested on the Sandia National Laboratories large 6-DOF shaker table. A photograph of the test setup is shown in Fig. 13.3. The tests were conducted in 17 sets with four beams per tests. The first test sets were performed by incrementally stepping up the input shock load until all four beams failed. Typically, most beams failed after a few shocks. The second round of testing was performed to quantify fatigue failures for cantilever beams of the same design. For the fatigue tests, a test level less than the failure level was selected and that test was repeated until all beams failed. The test was then repeated with new beams and a different shock input level.

Figure 13.4 shows a close-up photograph of a set of 3 in. long cantilever beams installed in the test fixture. Testing was performed on both three inch and 5 in. long cantilever beams in this study. Also shown in this figure are a set of steel clamp-on collar weights and the stress concentration notch near the cantilever beam's base.

A total of 3424 shocks were performed on the 6-DOF shaker table divided among the 17 test series. All failures were brittle failures by design due to the crosswise raster orientation of the 3D printed beams. It was noted that many beams developed obvious cracks prior to failure; however, the cracks were not always readily propagated through the cross-section. It appeared that some of the cracks caused the fundamental beam frequency to shift to a region outside of the shaker excitation frequency band, thus slowing crack growth significantly.

Instrumentation for these tests consisted of five tri-axial accelerometers, one mounted at the base of the upright beam fixture and the other four mounted near each of the four corners of the table as shown in Fig. 13.3. These five measurements allowed for determination of the table translations and rotations.

Figure 13.5 shows a plot of a typical translational acceleration time history from a 6-DOF shock event. The acceleration shown here is the average table acceleration input in each direction. Figure 13.6 shows a similar plot of the typical rotational acceleration time histories from the same shaker shock event. The rotational acceleration time histories had to be derived from the tri-axial accelerometers at the table corners. For this analysis it was assumed that the table's center of rotation was coincident with the table's geometric center. The resulting calculations indicated that there was a slight difference between the table's geometric center and the center of rotation. The difference was very small and thus it was ignored for this analysis, consistent with previous researchers [6].

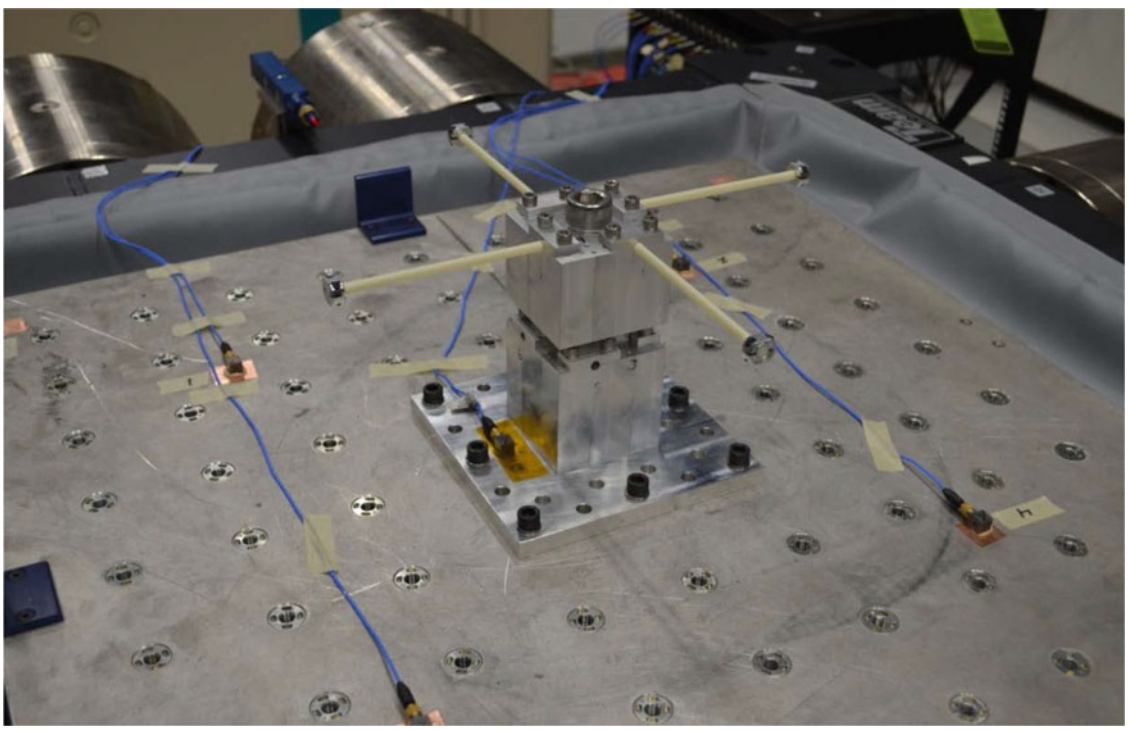

Fig. 13.3 Cantilever beam test fixture and test specimen installed on 6-DOF shaker table

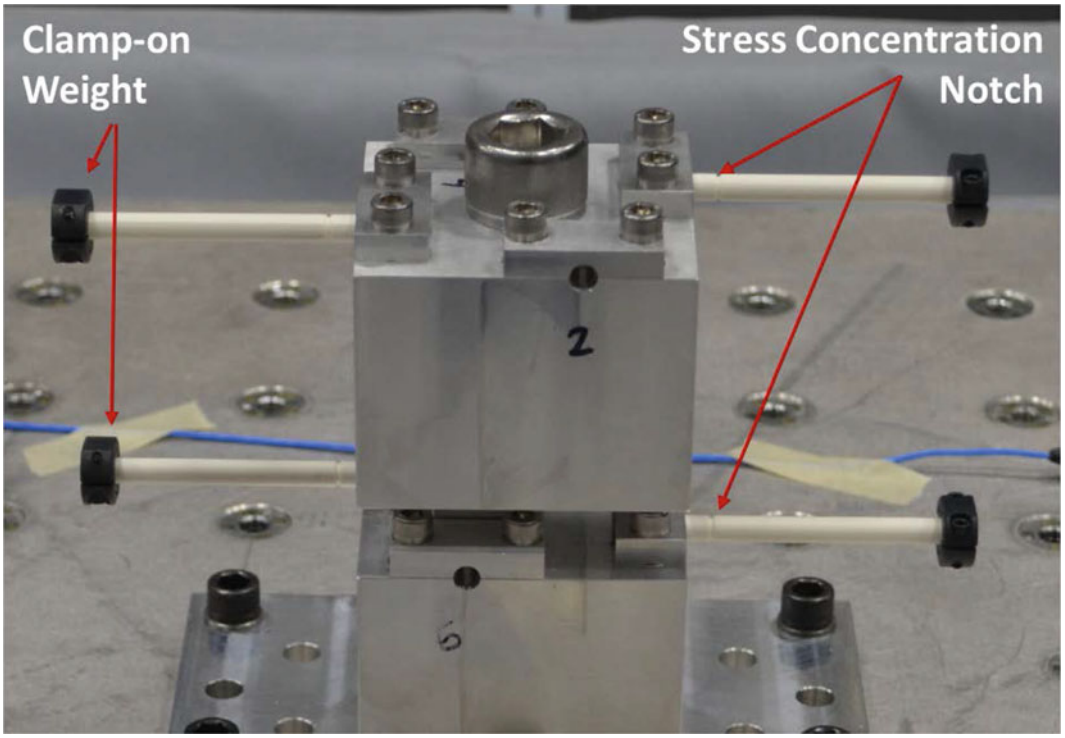

Fig. 13.4 Photograph of the test fixture with 3-D printed cantilever beams installed showing the clamp-on collar weights and the stress concentration notch

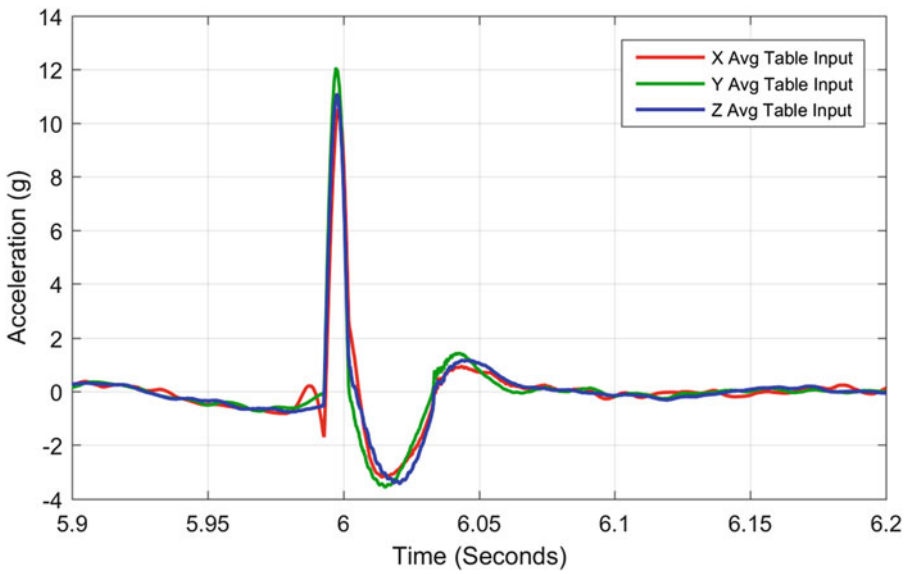

Fig. 13.5 Typical translational acceleration profile from 6-DOF shaker shock tests

13.6 Derivation of 6-DOF Composite Energy Spectra

Calculating an energy spectrum from a single translational input is a relatively simple task. However, to evaluate the failure results from 6-DOF testing it is necessary to extend the energy spectrum concept to account for simultaneous rotational and translational shocks. This extension is necessary to generate comparisons with analytical single-axis failure predictions and single-axis test to failure results.

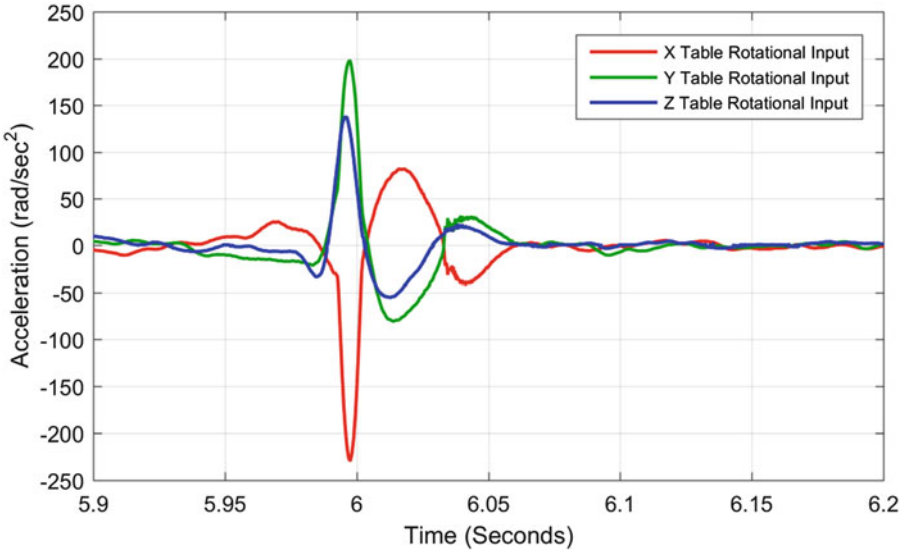

Fig. 13.6 Typical rotational acceleration profile from 6-dof shaker shock tests

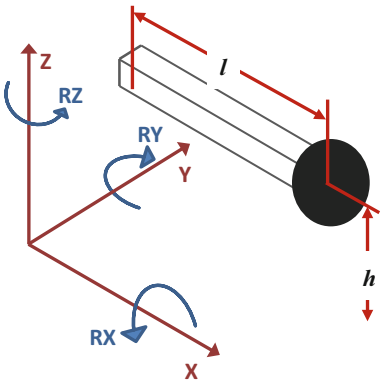

Fig. 13.7 Cantilever beam and coordinate system for 6-DOF tests

Since the energy spectrum formulations all have a component of velocity, as seen in Eq. 13.2, and there is a direct relationship between velocity, or pseudo-velocity SRS (PVSRS) and stress, a composite 6-DOF SRS based on PVSRS is appropriate. The details of this 6-DOF composite SRS derivation are presented in [7] and are summarized here. Figure 13.7 shows a hypothetical cantilever beam oriented with respect to the 6-DOF coordinate system. Here, the x-axis is oriented parallel to the cantilever beam's long axis but offset by a distance h. This coordinate system corresponds well with the actual 6-DOF shaker coordinate system where it is assumed that the table's center of rotation is at the geometric center of the table face but the part under test will of necessity be mounted some distance above the table face.

The concept of a composite pseudo-velocity SRS is needed to relate the three translational SRS and three rotational SRS from the 6-DOF shock input to failure of the test article. It is obvious that failure should not be equal to any single axis response individually but to the combination of all inputs loading the structure. Each of the six shocks induces normal stresses in the structure—bending stress from transverse shocks and axial stress from axial shocks. Figure 13.7 shows the coordinate system assumed for the composite SRS calculations with axial shocks occurring along the x-axis and transverse shocks occurring in the y- or z-axes.

There are several methodologies for combining multi-axis stress such as the von Mises or maximum distortional energy theory, maximum principal stress theory, or the Tresca or maximum shear stress theory for example. However, in this case, the derivation is performed in terms of pseudo-velocity SRS since actual stress was not measured. In the derivation presented in [7], an effective axial and bending PVSRS for each of the three directions was presented as:

$$PV_{xeff} = PV_x$$

$$PV_{yeff} = PV_y + PV_{rz}l + PV_{rx}h$$

$$PV_{zeff} = PV_z + PV_{ry}l \tag{13.10}$$

where l and h are the distances shown in Fig. 13.7. Equation 13.10 reduces the original six shock relations to three and is the first step in creating a single, composite spectrum. It is based on the kinematic velocity equation:

$$V = v_T + \omega xr \tag{13.11}$$

where V is the total velocity, v_T is the translational velocity ω is the rotational velocity. For the cantilever beam shown in Fig. 13.7, a composite pseudo-velocity SRS from the 6-DOF shock input is given by the relationship:

$$PV_{composite} = \frac{r}{4l}PV_{xeff} + \sqrt{\left(PV_{yeff}\right)^2 + \left(PV_{zeff}\right)^2}. \tag{13.12}$$

This relationship was derived and demonstrated by testing documented in [7] for the cantilever beams tested here. From the pseudo-velocity, a composite expression for the absorbed energy spectrum can be directly calculated as given by Hudson [8] from:

$$E_{Am} = \frac{1}{2}PV^2. \tag{13.13}$$

Thus, it is apparent that the absorbed energy can also be calculated by:

$$E_{Am} = \frac{1}{2}PV^2_{composite} = \frac{1}{2}\left[\frac{r}{4l}PV_{xeff} + \sqrt{\left(PV_{yeff}\right)^2 + \left(PV_{zeff}\right)^2}\right]^2. \tag{13.14}$$

It has been shown previously that a similar relationship exists for input energy [7]. Input energy can be calculated for each of the six shocks, converted to an analogous velocity spectrum using the inverse of Eq. 13.13 and combined in a similar fashion as Eq. 13.14 to yield a composite input energy spectrum. It is this resulting composite input energy spectrum that is used to derive the low-cycle fatigue results from the testing described here.

13.7 6-DOF Shock Test Results

The 6-DOF shock tests applied a similar shock load simultaneously in all 6 degrees of freedom as shown previously. For the initial tests, the shock loads were applied once and then incrementally increased for subsequent shocks until all beams failed. Most beams in a set failed at the same shock level or at consecutive shock levels indicating that the failure levels were reasonably consistent for parts of the same design. Following the initial testing, low-cycle fatigue testing was performed by selecting a shock test level less than the determined failure load and repeating that shock until all beams in the set failed. A different shock input level was then selected and the test repeated. From the data collected, a composite input energy spectrum was calculated for each shock as detailed previously and the sum of the input energy from all shocks experienced by a given cantilever beam was calculated. Figure 13.8 shows a plot of the total input energy compared to the number of shocks to failure from the elliptic cantilever beam tests. The slope of the least squares fit straight line through the data is 0.65 which is nearly identical to the predicted slope of 0.64 for common structural materials. While this is very interesting that the measured slope and the theoretical slope are very close, it may be a coincidence since the theoretical slope is derived from a nominal value for common structural materials. However, it is significant that the slope is in family with structural materials and not substantially different from the basic theory.

Figure 13.9 shows a plot of the same elliptic beam 6-DOF fatigue test data, this time formatted to show the number of shocks to failure compared to the average input energy per shock. Since all of the shock events for a single test series were nominally the same, the input energy from all the shocks was averaged. The slope of the least squares fit straight line through the data is −0.35 which is again nearly equal to the predicted slope of −0.36 for common structural materials. Here again, the significance is not in the closeness of the result exactly but rather that the result is in family with general structural materials which confirms that the fatigue relationships derived here for input energy are similar to the more common S-N curve results with similar Basquin equation exponents.

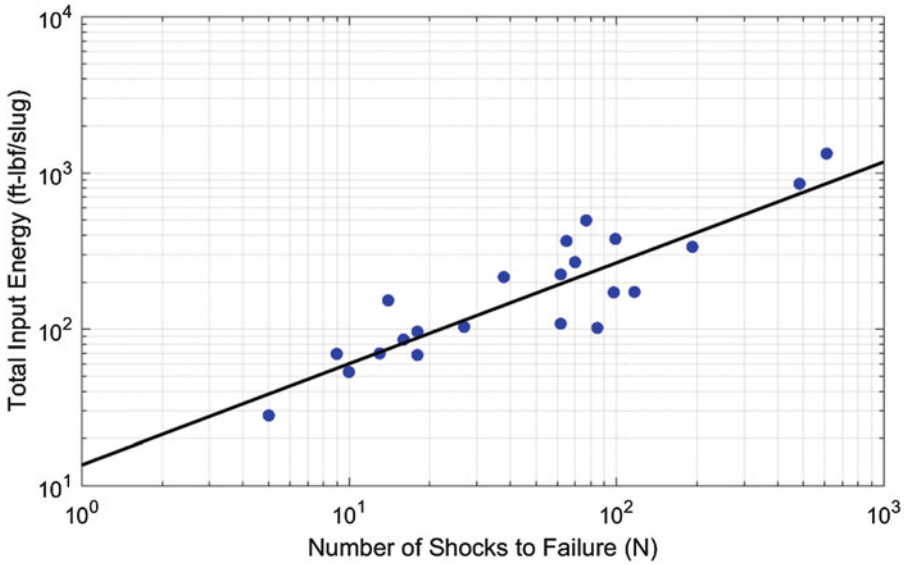

Fig. 13.8 Plot of number of shocks to failure versus total input energy from 6-DOF cantilever beam tests

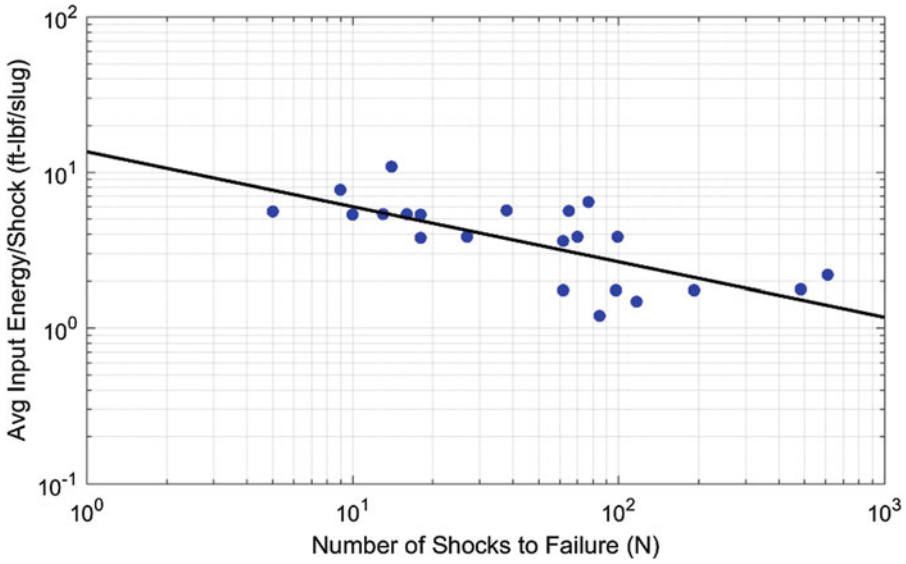

Fig. 13.9 Plot of number of shocks to failure versus average input energy from 6-DOF cantilever beam tests

13.8 Conclusions

A power-law relationship between input energy and number of cycles was derived for high and low-cycle fatigue. This relationship was extended to low-cycle fatigue from the application of multiple low level shocks.

The equation, like the traditional S-N relationship, depends on experimental data to define empirical coefficients. Experiments with cantilever beams on a 6-DOF shaker were performed to estimate the coefficients for ABS plastic. The 6-DOF shaker introduced a multi-axial stress state in the beams and a technique for accounting for the complex excitation was developed and applied to the test data.

The empirically determined coefficients were in family with those determined for most metals and general structural materials.

Acknowledgement Sandia National Laboratories is a multi-mission laboratory managed and operated by Sandia Corporation, a wholly owned subsidiary of Lockheed Martin Corporation, for the U.S. Department of Energy's National Nuclear Security Administration under contract DE-AC04-94AL85000.

References

1. Lalanne, C.: Fatigue Damage, Mechanical Vibration and Shock Analysis, vol 4, 3rd Edn. Wiley, NJ (2014)
2. NASA: Dynamic Environmental Criteria. Technical Handbook, NASA-HDBK-7005, National Aeronautics and Space Administration, 13 March 2001
3. SMC Standard SMC-S-16, Test Requirements for Launch, Upper Stage and Space Vehicles, 13 June 2008, Section 10.2.2, p 109
4. Babuška, V., Sisemore, C., Booher, J.: Energy based representations of mechanical shock for failure characterization. In: Proceedings of the AIAA SciTech 2016 Conference, San Diego, California, January 2016
5. Dowling, N.E.: Mechanical Behavior of Materials, Engineering Methods for Deformation, Fracture, and Fatigue, 3rd edn, pp. 827–832. Pearson, Prentice Hall (2007)
6. Smallwood, D. O., Gregory, D.: Evaluation of a Six-DOF electrodynamic shaker system. In: Proceedings of the 79th Shock and Vibration Symposium, Orlando, Florida, October 2008
7. Sisemore, C., Babuška, V., Booher, J.: 6-DOF mechanical shock failure predictions of a cantilever structure using energy response spectra methods. In: Proceedings of the 87th Shock and Vibration Symposium, New Orleans, Louisiana, October 2016
8. Hudson, D. E.: Response spectrum techniques in engineering seismology. In: Proceedings of the World Conference on Earthquake Engineering, Berkeley, California, 1956, pp 4.1–4.12

Chapter 14
Experimental Execution of 6DOF Tests Derived from Field Tests

Laura D. Jacobs, Michael Ross, Gregory Tipton, Kevin Cross, Norman Hunter Jr., Julie Harvie, and Garrett Nelson

Abstract Recent advances in 6DOF testing has made 6DOF subsystem/component testing a preferred method because field environments are inherently multidimensional and can be better replicated with this technology. Unfortunately, it is rare that there is sufficient instrumentation in a field test to derive 6DOF inputs. One of the most challenging aspects of the test inputs to derive is the cross spectra. Unfortunately, if cross spectra are poorly defined, it makes executing the tests on a shaker difficult. In this study, tests were carried out using the inputs derived by four different inverse methods, as described in a companion paper. The tests were run with all 6DOF as well with just the three translational degrees of freedom. To evaluate the best way to handle the cross spectra, three different sets of tests were run: with no cross terms defined, with only the coherence defined, and with the coherence and phase defined. All of the different tests were compared using a variety of metrics to assess the efficacy of the specification methods. The drive requirements for the different methods are also compared to evaluate how the specifications affect the shaker performance. A number of the inverse methods show great promise for being able to derive inputs to a 6DOF shaker to replicate the flight environments.

Keywords Multi-axis • Vibration • Experimental • Structural response • Dynamics

14.1 Introduction

The vast majority of product life-cycle and environmental vibration tests are currently conducted on uniaxial vibration test platforms. These tests have been established as a method to detect part failures and predict the effects of service loads without the need of costly and time consuming field testing [1]. The most widely referenced standard for these tests, MIL-STD-810G, specifies the use of sequential single axis tests in each of three orthogonal axes to characterize and validate the performance of both components and assemblies [2]. Comparable methods are provided by the U.S. Navy in NAVMAT P-9492 and the electronics industry's JESD22-B103B [3, 4]. Per the guidance given by these standards, the device is first tested along a single axis and then rotated 90° about the appropriate axis, with a test conducted after each rotation.

In the past few decades, advances in multi-axis testing hardware and software solutions have increased the application of multi-axis testing at both the system and component level. Vibration systems capable of multi-axis simulation have been successfully incorporated in both research and development labs across the U.S. in universities, government labs, and industry alike [5–10]. Their increased prevalence is motivated by a growing body of evidence which indicates shortcomings in conventional single axis testing [11]. In many environments, the effects of cross-axis excitation can have large impacts on the resulting dynamics of a structure [12]. Accordingly, it has been found that the combined loading effects caused by these multi-axis excitations can result in different stress states [13–15], failure modes [16], and rates of damage accumulation [17–19]. Thus, it is no surprise that multi-axis testing has been shown to produce loading conditions that more closely simulate real world environments [20, 21]. This has motivated a dramatic increase in research on multi-axis test methods and the tools and analysis techniques necessary to make this testing possible. One key research area, and the focus of the present discussion, is the development of specifications for multi-axis testing.

In general, multi-axis vibration test specifications require the definition of a desired energy level and distribution for each axis as well as a definition for the relationship between each pair of axes. For random vibration tests, the specification for each independent axis is most commonly defined by an auto spectral density (ASD). As a function of frequency, the ASD

L.D. Jacobs (✉) • M. Ross • G. Tipton • K. Cross • N. Hunter Jr. • G. Nelson
Vibration/Acoustics Simulation, Sandia National Laboratories, P.O. Box 5800, MS 0557, Albuquerque, NM 87185, USA
e-mail: ldjacob@sandia.gov

J. Harvie
Environments Engineering and Integration Department, Sandia National Laboratories, P.O. Box 5800-MS 0840, Albuquerque, NM 87185, USA

J.M. Harvie, J. Baqersad (eds.), *Shock & Vibration, Aircraft/Aerospace, Energy Harvesting, Acoustics & Optics, Volume 9*,
Conference Proceedings of the Society for Experimental Mechanics Series, DOI 10.1007/978-3-319-54735-0_14

specifies the level of energy in units of g^2/Hz. For a multi-axis specification, the relationship between each axis can be defined by the cross power spectral density (CPSD). For convenience and increased physical understanding, this relationship is often presented as a frequency dependent coherence and phase. Collectively, the ASDs and CPSDs fully define the desired input conditions for the test.

Traditional multi-axis testing is conducted by developing a control scheme based on rigid body acceleration at the base of a component, assembly, or fixture [22]. Unfortunately, due to limits on the number of channels available for data acquisition during field tests, it is rare to have sufficient instrumentation such that six degree of freedom (6-DOF) inputs can be directly derived at either the system or sub-system level. Specifically, the coherence and phase between axes is not adequately quantified and little to no data is available for rotational acceleration measurements. This has led to the development of various methods to derive test specifications and inputs by pairing field data with analysis on a dynamic model of the system of interest. Depending on the availability of a high fidelity finite element model of the unit under investigation, alternate experimental model techniques may be employed.

A recent field test conducted by Sandia National Laboratories on a system level assembly was instrumented specifically such that these multi-axis inputs could be directly measured. In addition to providing an input signal which could be used directly for multi-axis testing, this set of field data also provided the unique opportunity to benchmark the performance of other methods for deriving 6-DOF test inputs from field data with limited instrumentation. This was possible by comparing the results of tests conducted with input signals derived from only response channels which would have been available during a standard field test to those conducted with the "true" input signals which were directly measured. Specifically, four different multi-axis input specification derivation methods were explored: (1) using the pseudo-inverse of the transmissibility function (PINV), (2) the output spectral density method (ZINV), (3) a scaled output spectral density method (Scaling), and (4) an iterative spectral density method with Tikhonov regularization (Smallwood-Cap). These methods are discussed further in the companion paper [24]. In addition to comparing the estimate of input signal obtained from each method, the dynamic response of the test article to these derived inputs were experimentally obtained on a shaker system and compared to measurement response data from the original field test. Comparisons were made with a set of seven measurement locations which were consistent between the lab and field tests. Objective measures of the performance of each method were based on both time and frequency domain characteristics of the data.

14.2 Test Setup

14.2.1 Instrumentation

The test article was equipped with an array of triaxial accelerometers for control. Additional accelerometers were placed in key locations internally to the system. The four control accelerometers were positioned symmetrically about both lateral axes at the mid-plane of the test article's base for testing on the multi-axis system. The locations of the control gauges and internal gauges are shown notionally in Fig. 14.1.

14.2.2 Test Equipment

For physical testing conducted on the system, Team Corporation's Tensor 18 kN (TE6-18 kN) multi-axis high frequency vibration test system was employed (see Fig. 14.2). Due to the test equipment's configuration of twelve independent electrodynamic shakers, by controlling the relative amplitude and phase of the various shakers, it is capable of full six degree of freedom (6DOF) vibration testing.

14.2.3 Test Specifications

Several different tests were specified. In addition to conducting tests that were specified using the different input derivation methods described in the companion paper [24], different methods for determining the cross spectra were also explored: no cross spectra, coherence only, and coherence with phase. Additionally, the tests were performed using the three translational degrees of freedom (3DOF tests) only and the three translational degrees of freedom with the addition of the three rotational degrees of freedom (6DOF tests).

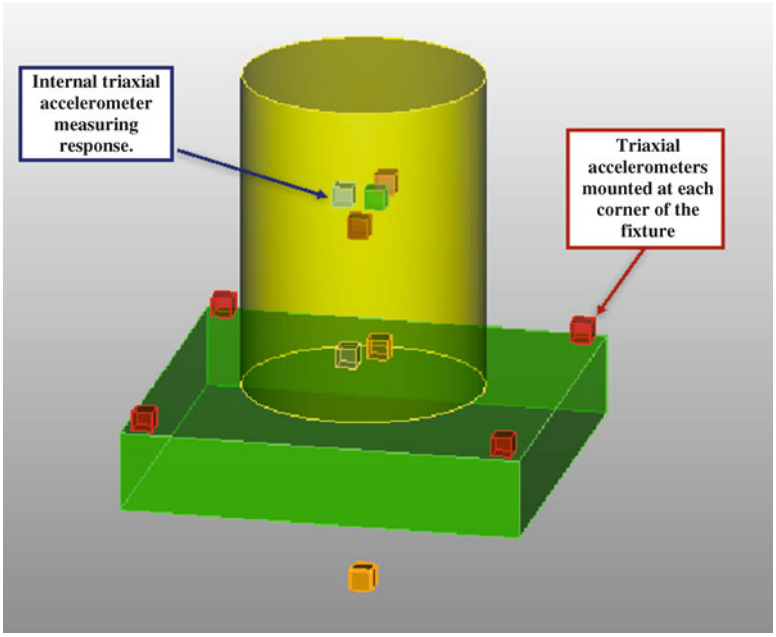

Fig. 14.1 Notional depiction of test article and accelerometers

Fig. 14.2 Tensor 18 kN multi-axis vibration test system [23]

14.3 Experimental Results

14.3.1 Visual Comparison

Doing a visual inspection of the response of the system to the various inputs provides some valuable insight into some general trends of the behavior of the system in the lab versus what was seen in the field. The visual inspection shows some clear differences between the 3DOF testing (Fig. 14.3a) and the 6DoF testing (Fig. 14.3b).

One general trend of the 3DOF testing (Fig. 14.3a) is that, with the exception of the Smallwood–Cap input, the 3DOF inputs led to responses on the test article that contained significantly less energy from 20 to 200 Hz and 300 to 600 Hz. At higher frequencies, with exception of a few shifts in the peaks and valleys, the responses of each 3DOF test were reasonably similar to those in field testing. The low frequency peaks line up well, even though they are a lower amplitude. In other words, the shapes of the PSDs at lower frequencies are similar. The PSDs at higher frequencies differ from those measured in the field test. This result is unsurprising because the unit to unit variability in the dynamics were more pronounced at the higher frequencies. Many of the modes appear to have less damping than they did during field testing, because they have higher amplitudes and sharper peaks than the ones in field testing. It is possible that the change in boundary condition affects the apparent damping of the system.

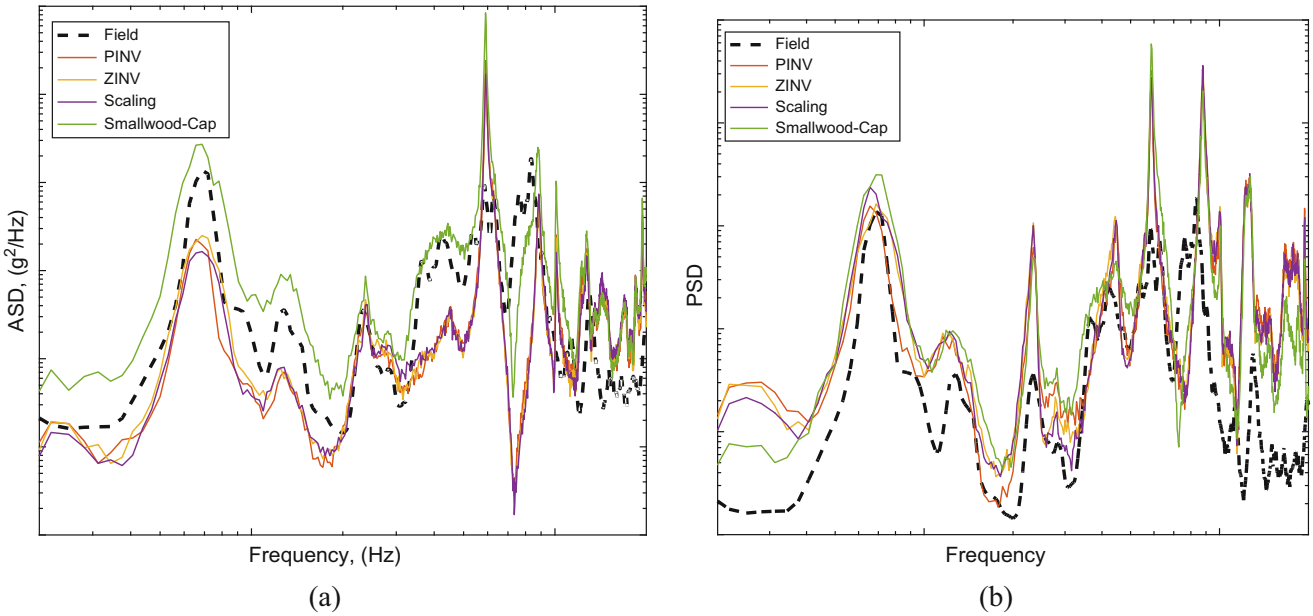

Fig. 14.3 Response of the system to (**a**) 3DOF inputs (**b**) 6DOF inputs

One of the interesting trends in the 6DOF data (Fig. 14.3b) is that the responses are higher across the entire frequency range. This result suggests that adding the rotations makes certain modes more pronounced. It was also easier to recreate one of the rigid body modes that is transferred into the system when rotations were included. Although the shapes of the PSDs demonstrate close agreement at frequencies below 1000 Hz, the peaks are somewhat shifted and are a higher amplitude than those found in the field test. Above 1000 Hz, the response of the system in the laboratory test was significantly higher than the response in the field test. The rotations appear to have a significant effect on the higher frequencies.

Although a visual inspection of the various responses can be used to gain valuable insight about the different methods employed, it is challenging to determine which of the methods of defining the specifications leads to the closest match to what was seen in the field test. Therefore, quantitative metrics should be used to make a clear determination of the best method.

14.3.2 Methods for Comparison

One of the goals of this study is to evaluate how well each of the methods of defining the inputs did at replicating the response measured during the field test and determine which one is most promising. In order to do that, a variety of metrics were calculated and compared to one another. The metrics were combined using equal weighting.

A few different features are of interest when comparing the laboratory response to that measured in the field test. The first feature is the shape of the PSD curve, which gives information about the frequency content of the response. One of the things to consider in comparing the shape, is that small differences in the natural frequencies between the field test and laboratory units could show up in the PSD, so having some leeway in the exact locations of the peaks in the PSD would be valuable in a metric, so small shifts are not heavily penalized. The second feature is the overall energy in the response.

The first step in calculating the metrics is to convert the data to sixth octave spacing. This means that there are six frequency lines per octave, with their corresponding amplitudes of the PSD. Since octaves represent a doubling of frequency, more frequency lines are averaged at the higher frequencies than the lower frequencies. This technique helps to remove some of the jitter seen at the higher frequencies as well as smooth out some of the slight shifts in frequency due to unit to unit variability.

The first metric is the error in the rms, which is a way to compare the energy levels from the laboratory test and the field test. The rms for both the field test and laboratory data were calculated by finding the area under the PSD curve. Calculating the error for each gauge can be done by using the following equation:

$$error_{rms} = 20log\left(\frac{rms_{test}}{rms_{flight}}\right) \tag{14.1}$$

Summing the error of each gauge gives the total error in the rms across the system.

In order to be able to weight each metric equally, the error in the rms needed to be converted to a number between 0 and 1, where 1 is the value associated with the smallest error in the rms. This was accomplished by first using the following equation:

$$\boldsymbol{normalized_{rms}} = \mathbf{1} - \frac{\boldsymbol{TotalRmsError}}{\boldsymbol{MaxRmsError}} \tag{14.2}$$

which gives a set of metrics where now the largest one is associated with the test that had the smallest error in the rms. Then, to make the one with the smallest error have a value of 1, the following equation is applied

$$\boldsymbol{metric_{rms}} = \frac{\boldsymbol{normalized_{rms}}}{\boldsymbol{max}\left(\boldsymbol{normalized_{rms}}\right)} \tag{14.3}$$

The next metric is the mean dB error, which is another way to compare the energy between the laboratory test and the field test. This metric calculates the dB error at each frequency line and then performs an average over all frequencies. This metric can be sensitive to small shifts in the natural frequencies inherent to unit to unit variability. The mean dB error is calculated as follows:

$$\boldsymbol{error_{dB}} = \frac{1}{\boldsymbol{N}} \sum_{\boldsymbol{f_{min}}}^{\boldsymbol{f_{max}}} \mathbf{10}\left(\log\left(\frac{\boldsymbol{test}\left(\boldsymbol{f}\right)}{\boldsymbol{flight}\left(\boldsymbol{f}\right)}\right)\right) \tag{14.4}$$

The mean dB error can then be summed across all the gauges to get a single metric for each test method. The normalization is calculated in the same manner as the error in the rms, using the following equation

$$\boldsymbol{normalized_{dB}} = \mathbf{1} - \frac{\boldsymbol{TotaldBError}}{\boldsymbol{MaxdBError}} \tag{14.5}$$

which gives a set of metrics where now the largest one is associated with the test that had the smallest error in the rms. Then, to make the one with the smallest error have a metric of 1, the following equation is applied

$$\boldsymbol{metric_{dB}} = \frac{\boldsymbol{normalized_{dB}}}{\boldsymbol{max}\left(\boldsymbol{normalized_{dB}}\right)} \tag{14.6}$$

The next metric is the correlation coefficient, which is a way to compare the shapes of the PSDs. This gives an indication of how well the two PSDs match in terms of amplitudes at each frequency line. One disadvantage to this metric is that small shifts in the natural frequencies can be heavily penalized because peaks can line up with valleys in more than one place. The correlation coefficient is calculated using the corrcoef function in Matlab to compare the PSDs of each location during the test to the PSD of the same locations in the field test. The correlation coefficient is a number between -1 and 1, where 1 is perfect correlation, 0 is completely uncorrelated, and -1 is perfectly negatively correlated. To get a number between 0 and 1, the following equation is used:

$$\boldsymbol{normalized_{corr}} = \mathbf{10}\left(\boldsymbol{corr} + \mathbf{1}\right) \tag{14.7}$$

Then, to make the one with the smallest error have a value of 1, the following equation is applied

$$\boldsymbol{metric_{corr}} = \frac{\boldsymbol{normalized_{corr}}}{\boldsymbol{max}\left(\boldsymbol{normalized_{corr}}\right)} \tag{14.8}$$

One way to get around the problem of small shifts in the natural frequencies is to calculate the cross correlation. Like the correlation it can give an indication the two PSDs match, but the cross correlation is a measure of similarity when there is a lag present, which means that it is more forgiving of small shifts in the natural frequencies. The cross-correlation coefficient is calculated using the xcorr function in Matlab to compare the PSDs of each location during the test to the PSD of the same locations in the field test. The cross-correlation coefficient is a number between -1 and 1, where 1 is perfect correlation, 0 is completely uncorrelated, and -1 is perfectly negatively correlated. To get a number between 0 and 1, the following equation is used:

$$\boldsymbol{normalized_{xcorr}} = \mathbf{10}\left(\boldsymbol{xcorr} + \mathbf{1}\right) \tag{14.9}$$

Table 14.1 Comparison metrics between laboratory tests and field tests

	No cross products		Coherence only		Coherence and phase	
Method	Metric	Rank	Metric	Rank	Metric	Rank
6th octave 3DoF	2.710	14	[a]	[a]	[a]	[a]
6th octave 6DoF	1.935	25	[a]	[a]	[a]	[a]
PINV 3DoF	3.139	8	2.938	12	3.253	5
PINV 6DoF	2.707	15	2.457	17	2.187	23
ZINV 3DoF	3.140	7	2.934	13	3.324	4
ZINV 6DoF	2.411	19	2.278	21	2.444	18
Scaling 3DoF	3.032	9	2.681	16	3.025	10
Scaling 6DoF	2.220	22	2.323	20	2.034	24
Smallwood-cap 3DOF	3.152	6	3.723	2	3.763	1
Smallwood-cap 6DOF	[b]	[b]	3.005	11	3.372	3

[a]Not specified
[b]No data available

Then, to make the one with the smallest error have a value of 1, the following equation is applied

$$\boldsymbol{metric}_{xcorr} = \frac{\boldsymbol{normalized}_{xcorr}}{\boldsymbol{max}\left(\boldsymbol{normalized}_{xcorr}\right)} \tag{14.10}$$

14.3.3 Results

In addition to the different methods for deriving the inputs that were described in the companion paper [24], different methods for determining the cross spectra were used: no cross spectra, coherence only, and coherence with phase. Additionally, the tests were performed using the three translational degrees of freedom (3DOF tests) as well as the three translational degrees of freedom with the three rotational degrees of freedom (6DOF tests). Table 14.1 summarizes the results of the comparison between the different methods of deriving specifications for this set of tests.

The response of the system in the lab did not exactly match the response of the system in the field. In fact, using the full 6DOF inputs measured in the field yielded responses that were least like those in the field. This result can be understood in lieu of the fact that the boundary conditions in the field and the laboratory are different. In general, a change in boundary conditions will lead to differing dynamic responses. Additionally, the unit tested in the laboratory was different than the one used in the field test, and the unit to unit variability is going to lead to differences in the dynamic response. However, using an inverse method that accounts for the response of the structure on the shaker allowed for the laboratory response to be closer to that measured in the field test.

Another interesting trend is that, across the board, the metrics indicate that 3DOF tests matched the field data better than their 6DOF counterparts that were derived using the same methods. One possible explanation for this difference is that the rotations are more susceptible to both the variations in the parts and the change in boundary conditions than are the translations.

The Smallwood–Cap 3DOF method gave the best match to the field test data, no matter how the cross spectra were defined. Including the coherence and phase in the Smallwood–Cap method yielded the responses that matched the most closely to those measured in the field. In fact, for five out of the eight inverse methods, including the coherence and phase yielded the closest match with the field data. This is unsurprising as the dynamic response of the system is coupled between axes. Additionally, the vibration input into the system in the field test has coupling between axes, so including that in the specifications in the laboratory would be expected to yield responses that are closer to those in the field test. Of the remaining three, two of the methods yielded the closest match to the field test when both coherence and phase were not specified.

From the initial look at the data for the tests run to 2 kHz, the laboratory inputs should be derived using an inverse method, they should be 3DOF inputs, and the spectral density matrix should include both the coherence and phase. It is also recommended that the Smallwood–Cap method be used.

14.4 Conclusions

Recent field tests at Sandia National Laboratories had sufficient instrumentation to derive the full 6DOF base inputs to a system using a variety of methods. Testing in the laboratory implemented the different inputs and the response at seven key locations were measured. The responses at the seven key locations were compared to those measured in the field testing and a few key trends were apparent in the data.

With the exception of the Smallwood–Cap method, the 3DOF input produced a response that was lower than that of the field data. Conversely, the 6DOF input produced a response that matched well at low frequencies, but was too high at the higher frequencies.

Using an inverse method, rather than the inputs directly calculated from the field data seemed to yield internal responses that were closer to those measured in the field. Performing an inverse calculation based on transfer functions of the system on the shaker seems to remove some of the effects of the different boundary condition as well as the unit to unit variability.

It was very difficult to use a visual inspection of the data to draw any conclusions about which of the methods performed best. Therefore, it was necessary to use quantitative metrics to objectively assess how well the various input derivations performed. The metrics quantified how well the energy input as well as how well the shape of the PSDs matched between the field data and the laboratory simulations. Multiple metrics were necessary to capture both of these quantities.

In every instance, the metrics indicate that 3DOF tests matched the field data better than their 6DOF counterparts that were derived using the same methods. The Smallwood–Cap 3DOF method gave the best match to the field test data, no matter how the cross spectra were defined. However, including the coherence and phase in the Smallwood–Cap method yielded the responses that matched the most closely to those measured in the field. In general, including both the coherence and phase improved the response of the system.

Based on the results, it is recommended to use an inverse method to derive the inputs rather than relying on the measured field data. Also, the inputs should be 3DOF inputs rather than 6DOF inputs and the spectral density matrix should include the coherence and phase. Finally, it is recommended that the Smallwood–Cap method be used.

Acknowledgments Sandia is a multi-program laboratory operated by Sandia Corporation, a Lockheed Martin Company, for the United States Department of Energy under contract DE-AC04-94AL85000.

References

1. Sater, J.M., Crowe, C.R., Antcliff, R., Das, A.: An Assessment of Smart Air and Space Structures: Demonstrations and Technology. Institute for Defense Analyses, Alexandria (2000)
2. U.S. Department of Defense: Environmental Engineering Considerations and Laboratory Tests (2008)
3. U.S. Navy: Manufacturing Screening Test Standards (1979)
4. Joint Electron Device Engineering Council: JEDEC Standard: Vibration Variable Frequency (2006)
5. Choi, C., Al-Bassyiouni, M., Dasgupta, A., Osterman, M.: PoF issues in multi-dof vibration testing: ED shakers and RS shakersq. In: IEEE Accelerated Stress Testing and Reliability Conference, New Jersey (2009)
6. Shafer, M.J., Wilson, D.R., Johnson, R.V.: New ICBM shock and vibration test capabilities at OOALC's survivability and vulnerability integration center. In: Proceedings of the Joint Services Data Exchange Conference (1994)
7. Chen, M., Wilson, D.: The new triaxial shock and vibration test system at Hill Air Force Base. J. IEST. **41**(2), 27–32 (1998)
8. Smallwood, D.O., Gregory, D.: Evaluation of a six-DOF electrodynamic shaker system. In: Proceedings of the 79th Shock Vibration Symposium, Orlando, FL (2008)
9. McIntosh, K., Davis, J.: Multi-axis testing of under wing and ground vehicle weapons systems. Aerospace Testing International (2002)
10. Füllekrug, U., Sinapius, M.: Simulation of multi-axis vibration in the qualification process of space structures. In: International Symposium Environmental Testing for Space Programmes, Noordwijk, Netherlands (1993)
11. Whiteman, W.E., Berman, M.S.: Fatigue failure results for multi-axial versus uniaxial stress screen vibration testing. Shock Vib. **9**(6), 319–328 (2002)
12. Habtour, E., Connon, W., Pohland, M.F., Stanton, S.C., Paulus, M., Dasgupta, A.: Review of response and damage of linear and nonlinear systems under multiaxial vibraiton. Shock. Vib. **21**(4), (2014)
13. Gregory, D., Bitsie, F., Smallwood, D.O.: Comparison of the response of a simple structure to single axis and multiple axis random vibration inputs. In: Proceedings of the 79th Shock Vibration Symposium, Orlando, FL (2008)
14. Loychik, N.E., Pan, J.: Achieving reliability goals for an EFV LRU through laboratory testing. In: Proceedings of the Annual Reliability Maintainability Symposium, Lake Buena Vista, FL (2011)
15. Ling, H., Shichao, F., Yaoqi, F.: Effect of multi-axis versus single-axis vibration test on the dynamic responses of typical spacecraft structure. In: Proceedings of the 25th International Conference. Noise Vibration Engineering, Leuven, Belgium (2012)
16. French, R.M., Handy, R., Cooper, H.L.: A comparison of simultaneous and sequential single-axis durability testing. Exp. Tech. **30**(5), 32–37 (2006)

17. Himelblau, H., Hine, M.J., Frydman, A.M., Barrett, P.A.: Effects of triaxial and uniaxial random excitation on the vibration response and fatigue damage of typical spacecraft hardware. In: Proceedings of the 66th Shock Vibration Symposium, Biloxi, MS (1995)
18. Ernst, M., Habtour, E., Dasgupta, A., Pohland, M., Robeson, M., Paulus, M.: Comparison of electronic component durability under uniaxial and multiaxial random vibrations. J. Electron. Packag. **137**(1), 011009 (2015)
19. Peterson, C.: Time-to-failure testing using single- and multi-axis vibraiton. Sound Vib. **47**(3), 13–16 (2013)
20. Harman, C., Pickel, M.B.: Multi-axis vibration reduces test time. Eval. Eng. **45**(6), 44 (2006)
21. Aykan, M., Celik, M.: Vibration fatigue analysis and multi-axial effect in testing of aerospace structures. Mech. Syst. Signal Process. **23**(3), 897–907 (2009)
22. Underwood, M.A., Hale, M.: MIMO testing methodologies. In: Proceedings of the 79th Shock Vibration Symposium, Orlando, FL (2008)
23. Team Corporation: Tensor 18kN multi-axis high frequency vibration test system (2004). Available: http://www.teamcorporation.com/images/brochures_A4/Tensor18kN_a4.pdf
24. Jacobs, L.D., Ross, M., Tipton, G., Cross, K., Hunter, N., Harvie, J., Nelson, G.: 6-DOF shaker test input derivation from field test. In: Proceedings of the XXXV IMAC (2017)

Chapter 15
Vibration of Cracked Timoshenko Beam Made of Functionally Graded Material

Nguyen Tien Khiem, Nguyen Ngoc Huyen, and Nguyen Tien Long

Abstract Functionally Graded Material (FGM) is an advanced composite that finds increasing application in high-tech industries such as mechatronics, space technology, bio-materials etc. In the application of FGM, dynamics of structures such as beams, plates or shells made of the material is of a great importance. This report is devoted to develop general theory of vibration of cracked FGM beams based on the power law of material grading and Timoshenko beam theory. Crack is modeled by an equivalent spring of stiffness calculated from its depth. First, governing equations of motion of the beam are constructed in the frequency domain taking into account the actual position of beam neutral plane. This enables to obtain general solution of free vibration of the beam and condition for uncoupling of axial and flexural vibration modes. Using the solution natural frequencies and mode shapes of cracked FGM beam are examined in dependence upon material properties and crack parameters.

Keywords FGM • Timoshenko beam • Cracked beam • Modal analysis

15.1 Introduction

Due to advantage properties compared to the laminate composites the functionally graded material (FGM) has been intensively studied recently and got wide application in the high-tech industries. An overview of the problems for manufacturing, modelling and testing FGM was given in [1]. Numerous methods such as the Finite Element Method (FEM) [2]; Spectral Element Method (SEM) [3]; Dynamic Stiffness Method (DSM) [4] or Rayleigh-Ritz method [5] have been developed for analysis of structures made of FGM. Nevertheless, the analytical methods are still the most accurate and efficient for dynamic analysis of functionally graded beam-like structures [6–9]. While the most of the aforementioned studies investigated undamaged beam, the crack problem in FGM has been recently studied in [10, 11]. The most important result of the studies is that a crack in FGM beam can be modeled by an equivalent spring of stiffness calculated from the crack depth. Based on the rotational spring model of crack, Yang and Chen [12] studied free vibration and buckling of Euler-Bernoulli FGM beam with edge cracks. They found that natural frequencies of FGM beam with smaller slenderness and lower ratio of the bottom Young's modulus to the top one are more sensitive to cracks. The transfer matrix method was employed by Wei et al. [13] for obtaining frequency equation of FGM beam with arbitrary number of cracks in the form of third-order determinant. This simplifies significantly the modal analysis of multiple cracked FGM beam. Aydin [14] has conducted an expression for mode shape of FGM beam with multiple cracks and used it for constructing the frequency equation in the form of an explicit determinant of third-order also. Forced vibration and nonlinear free vibration of cracked FGM beam are investigated in Ref. [15, 16]. Based on the exponential law of FGM and rotational spring model of crack, Yu and Chu [17] and Banerjee et al. [18] have applied the FEM and the Frequency Contour Method (FCM) for detecting a crack in Euler-Bernoulli and Timoshenko FGM beams respectively.

N.T. Khiem (✉)
Vietnam Academy of Science and Technology, 18, Hoang Quoc Viet, Cau Giay, Hanoi, Vietnam
e-mail: ntkhiem@imech.ac.vn; khiemvch@gmail.com

N.N. Huyen
Thuy Loi University, 175, Tay Son, Dong Da, Hanoi, Vietnam
e-mail: nnhuyen@tlu.edu.vn

N.T. Long
Institute of Mechanics and Environment Engineering, VUSTA, 264, Doi Can, Ba Dinh, Hanoi, Vietnam
e-mail: nguyentienlongntl@gmail.com

J.M. Harvie, J. Baqersad (eds.), *Shock & Vibration, Aircraft/Aerospace, Energy Harvesting, Acoustics & Optics, Volume 9*,
Conference Proceedings of the Society for Experimental Mechanics Series, DOI 10.1007/978-3-319-54735-0_15

In the present paper, an analytical approach in frequency domain is proposed to study free vibration of functionally graded Timoshenko beam with an open crack modeled by a pair of translational and rotational springs. This is a novelty of present paper in comparison with the previous ones where only rotational spring model of crack was adopted. Using the proposed model of crack, frequency equation of a cracked cantilever is conducted and used for sensitivity analysis of natural frequencies to crack parameters. Numerical results of natural frequencies as functions of crack positions and depths are obtained by MATLAB code.

15.2 Governing Equations

15.2.1 Model of FGM Beam

Consider a beam of length L, cross-section area $A = b \times h$ made of FGM with material parameters varying along thickness by the power law

$$\begin{Bmatrix} E(z) \\ G(z) \\ \rho(z) \end{Bmatrix} = \begin{Bmatrix} E_b \\ G_b \\ \rho_b \end{Bmatrix} + \begin{Bmatrix} E_t - E_b \\ G_t - G_b \\ \rho_t - \rho_b \end{Bmatrix} \left(\frac{z}{h} + \frac{1}{2} \right)^n, -h/2 \le z \le h/2, \tag{15.1}$$

where E, G and ρ with indexes t and b stand for elasticity, shear modulus and material density at the top and bottom respectively; z is ordinate from the central axis at high $h/2$. Assuming linear theory of shear deformation, the displacement fields in the cross-section at x are

$$u(x,z,t) = u_0(x,t) - (z - h_0)\,\theta(x,t)\,; w(x,z,t) = w_0(x,t)\,, \tag{15.2}$$

with $u_0(x,t)$,$w_0(x,t)$ being the displacements of neutral axis that is located at the high h_0 from the central axis; θ is slope of the cross-section. Therefore, constituting equations get the form

$$\varepsilon_x = \partial u_0/\partial x - (z - h_0)\,\partial\theta/\partial x; \gamma_{xz} = \partial w_0/\partial x - \theta \tag{15.3}$$

and

$$\sigma_x = E(z)\varepsilon_x; \tau_{xz} = \kappa G(z)\gamma_{xz}. \tag{15.4}$$

In the latter equation κ is a coefficient introduced to account for the geometry-dependent distribution of shear stress. Hamilton principle allows one to obtain equations of motion in the time domain as

$$I_{11}\ddot{u} - A_{11}u'' - I_{12}\ddot{\theta} = 0;\;\; I_{12}\ddot{u} - I_{22}\ddot{\theta} + A_{22}\theta'' + A_{33}\left(w' - \theta\right) = 0;\;\; I_{11}\ddot{w} - A_{33}\left(w'' - \theta'\right) = 0, \tag{15.5}$$

where

$$A_{11} = \frac{2E_0A\,(R_e + n)}{(R_e + 1)\,(1 + n)};\;\; I_{11} = \frac{2\rho_0A\left(R_\rho + n\right)}{\left(R_\rho + 1\right)(1 + n)};\;\; I_{12} = \frac{2\rho_0Ah}{\left(R_\rho + 1\right)}\left[\frac{2R_\rho + n}{2\,(2 + n)} - \frac{R_\rho + n}{(1 + n)}\alpha\right];\;\; A_{33} = \frac{2\kappa G_0A\,(R_G + n)}{(R_G + 1)\,(1 + n)}; \tag{15.6}$$

$$A_{22} = \frac{24E_0I_0}{(R_e + 1)}\left[\frac{3R_e + n}{3\,(3 + n)} - \frac{2R_e + n}{(2 + n)}\alpha + \frac{R_e + n}{(1 + n)}\alpha^2\right];\;\; I_{22} = \frac{24\rho_0I_0}{\left(R_\rho + 1\right)}\left[\frac{3R_\rho + n}{3\,(3 + n)} - \frac{2R_\rho + n}{(2 + n)}\alpha + \frac{R_\rho + n}{(1 + n)}\alpha^2\right];\;\; \alpha = 1/2 + h_0/h;$$

$$h_0 = \frac{n\,(R_e - 1)\,h}{2\,(n + 2)\,(n + R_e)}, R_e = \frac{E_t}{E_b}, R_\rho = \frac{\rho_t}{\rho_b}; E_0 = \frac{E_b + E_t}{2}; \rho_0 = \frac{\rho_b + \rho_t}{2}; G_0 = \frac{G_b + G_t}{2}; I_0 = bh^3/12; A = bh.$$

Introducing the displacement amplitudes

$$\{U, \Theta, W\} = \int_{-\infty}^{\infty} \{u_0(x,t), \theta(x,t), w_0(x,t)\} e^{-i\omega t} dt \tag{15.7}$$

Equation (15.5) get to be

$$\left(\omega^2 I_{11} U + A_{11} U''\right) - \omega^2 I_{12} \Theta = 0;\ \left(\omega^2 I_{22} \Theta + A_{22} \Theta''\right) - \omega^2 I_{12} U + A_{33}\left(W' - \Theta\right) = 0;\ \omega^2 I_{11} W + A_{33}\left(W'' - \Theta'\right) = 0. \tag{15.8}$$

Using the following matrix and vector notations

$$\mathbf{A} = \begin{bmatrix} A_{11} & 0 & 0 \\ 0 & A_{22} & 0 \\ 0 & 0 & A_{33} \end{bmatrix};\ \mathbf{\Pi} = \begin{bmatrix} 0 & 0 & 0 \\ 0 & 0 & A_{33} \\ 0 & -A_{33} & 0 \end{bmatrix};\ \mathbf{C}(\omega) = \begin{bmatrix} \omega^2 I_{11} & -\omega^2 I_{12} & 0 \\ -\omega^2 I_{12} & \omega^2 I_{22} - A_{33} & 0 \\ 0 & 0 & \omega^2 I_{11} \end{bmatrix};\ \mathbf{z} = \{U, \Theta, W\}^T,$$

Equation (15.8) are rewritten in the form [19]

$$\mathbf{A}\mathbf{z}'' + \mathbf{\Pi}\mathbf{z}' + \mathbf{C}\mathbf{z} = 0. \tag{15.9}$$

15.2.2 Crack Modeling

Assume that the beam has been cracked at the position e measured from the left end of beam and the crack is modeled by a pair of equivalent springs of stiffness T for translational spring and R for rotational one. Therefore, conditions that must be satisfied at the crack are

$$U(e+0) - U(e-0) = N(e)/T;\ \ \Theta(e+0) - \Theta(e-0) = M(e)/R;\ \ W(e+0) = W(e-0);$$

$$N(e) = N(e+0) = N(e-0); Q(e+0) = Q(e-0); M(e+0) = M(e-0) = M(e), \tag{15.10a,b}$$

where N, Q, M are respectively internal axial, shear forces and bending moment at section x

$$N = A_{11} U_x'; M = A_{22} \Theta_x'; Q = A_{33}\left(W_x' - \Theta\right). \tag{15.11}$$

Substituting (15.11) into (15.10a,b) one can rewrite the latter conditions as.

$$U(e+0) = U(e-0) + \gamma_1 U_x'(e);\ \ \Theta(e+0) = \Theta(e-0) + \gamma_2 \Theta_x'(e);\ \ W(e+0) = W(e-0);$$

$$U_x'(e+0) = U_x'(e-0); \Theta_x'(e+0) = \Theta_x'(e-0); W_x'(e+0) = W_x'(e-0) + \gamma_2 \Theta_x'(e), \tag{15.12}$$

$$\gamma_1 = A_{11}/T; \gamma_2 = A_{22}/R. \tag{15.13}$$

The so-called crack magnitudes γ_1, γ_2 introduced in (15.13) are function of the material parameters such as elastic modulus and they should be those of homogeneous beam when $E_t = E_b = E_0$. On the other hand, using expressions (15.6) the crack magnitudes (15.13) can be rewritten as

$$\gamma_1 = \gamma_a \theta_1(R_E, n); \gamma_2 = \gamma_b \theta_2(R_E, n), \tag{15.14}$$

where

$$\gamma_a = E_0 A/T; \gamma_b = E_0 I_0/R; \theta_1 = \frac{2(R_e + n)}{(R_e + 1)(1 + n)}; \theta_2 = \frac{24}{(R_e + 1)}\left[\frac{3R_e + n}{3(3 + n)} - \frac{2R_e + n}{(2 + n)}\alpha + \frac{R_e + n}{(1 + n)}\alpha^2\right]. \tag{15.15}$$

In case of homogeneous beam when $R_e = 1$ the crack magnitudes must be equal to γ_{10},γ_{20}, that are calculated from crack depth a for axial [20] and flexural [21] vibrations as

$$\gamma_{10} = E_0 A/T_0 = 2\pi\left(1-\nu_0^2\right) hf_1(z), z = a/h; \tag{15.16}$$

$$f_1(z) = z^2\Big(0.6272 - 0.17248z + 5.92134z^2 - 10.7054z^3 + 31.5685z^4 - 67.47z^5 + \\ + 139.123z^6 - 146.682z^7 + 92.3552z^8\Big);$$

$$\gamma_{20} = E_0 I/R_0 = 6\pi\left(1-\nu_0^2\right) hf_2(z); \tag{15.17}$$

$$f_2(z) = z^2\Big(0.6272 - 1.04533z + 4.5948z^2 - 9.9736z^3 + 20.2948z^4 - 33.0351z^5 + \\ + 47.1063z^6 - 40.7556z^7 + 19.6z^8\Big).$$

For modal analysis of cracked FGM beam crack magnitudes are proposed herein to be approximately calculated using expressions (15.16–15.17) with $\gamma_a = \gamma_{10}\,, \gamma_b = \gamma_{20}$, i.e.

$$\gamma_1 = F_1(a); \gamma_2 = F_2(a); \tag{15.18}$$

$$F_1(a) = 2\pi\left(1-\nu_0^2\right) h\theta_1 f_1(a); F_2(a) = 6\pi\left(1-\nu_0^2\right) h\sigma_2 f_2(a). \tag{15.19}$$

These functions would be used for calculating the crack magnitudes from given crack depth.

15.2.3 Characteristic Equation

Continuous solution of Eq. (15.9) sought in the form $\mathbf{z}_0 = \mathbf{d}e^{\lambda x}$ yields the equation

$$\left[\lambda^2\mathbf{A} + \lambda\mathbf{\Pi} + \mathbf{C}\right]\mathbf{d} = 0. \tag{15.20}$$

The latter equation would have nontrivial solution with respect to constant vector $\mathbf{d}$ under the condition $\det[\lambda^2\mathbf{A} + \lambda\mathbf{\Pi} + \mathbf{C}] = 0$, that can be in turn expressed in the form

$$\left(\lambda^2 A_{11} + \omega^2 I_{11}\right)\left[\left(\lambda^2 A_{33} + \omega^2 I_{11}\right)\left(\lambda^2 A_{22} + \omega^2 I_{22}\right) - \omega^2 I_{11} A_{33}\right] - \left(\lambda^2 A_{33} + \omega^2 I_{11}\right)\omega^4 I_{12}^2 = 0.$$

This is in fact a cubic equation with respect to $\eta = \lambda^2$ that could be elementarily solved and results in three roots $\eta_1\,, \eta_2\,, \eta_3$. Introducing the notations

$$\lambda_{1,4} = \pm k_1 = \pm\sqrt{\eta_1}; \lambda_{2,5} = \pm k_2 = \pm\sqrt{\eta_2}; \lambda_{3,6} = \pm k_3 = \pm\sqrt{\eta_3}, \tag{15.21}$$

general continuous solution of Eq. (15.9) is represented as

$$\mathbf{z}_0\,(x,\omega) = \mathbf{G}\,(x,\omega)\,\mathbf{C}, \tag{15.22}$$

with $\mathbf{C} = (C_1\,, \ldots\,, C_6)^T = (d_{11}\,, \ldots\,, d_{16})^T$ and

$$\mathbf{G}\,(x,\omega) = [\mathbf{G}_1\,(x,\omega)\;\; \mathbf{G}_2\,(x,\omega)]\,; \tag{15.23}$$

$$\mathbf{G}_1\,(x,\omega) = \begin{bmatrix} \alpha_1 e^{k_1 x} & \alpha_2 e^{k_2 x} & \alpha_3 e^{k_3 x} \\ e^{k_1 x} & e^{k_2 x} & e^{k_3 x} \\ \beta_1 e^{k_1 x} & \beta_2 e^{k_2 x} & \beta_3 e^{k_3 x} \end{bmatrix}; \mathbf{G}_2\,(x,\omega) = \begin{bmatrix} \alpha_1 e^{-k_1 x} & \alpha_2 e^{-k_2 x} & \alpha_3 e^{-k_3 x} \\ e^{-k_1 x} & e^{-k_2 x} & e^{-k_3 x} \\ -\beta_1 e^{-k_1 x} & -\beta_2 e^{-k_2 x} & -\beta_3 e^{-k_3 x} \end{bmatrix},$$

$$\alpha_j = \omega^2 I_{12}/\left(\omega^2 I_{11} + \lambda_j^2 A_{11}\right); \beta_j = \lambda_j A_{33}/\left(\omega^2 I_{11} + \lambda_j^2 A_{33}\right); j = 1, 2, 3.$$

Using (15.22), it can be found that solution of Eq. (15.9) denoted by $\mathbf{S}(x)$ satisfying the conditions

$$\mathbf{S}(0) = \left(S_1^0, S_2^0, 0\right)^T; \mathbf{S}'(0) = \left(0, 0, S_3^0\right)^T. \tag{15.24}$$

is represented as

$$\mathbf{S}(x) = [\mathbf{\Phi}(x)] \left\{\mathbf{S}^0\right\}, \tag{15.25}$$

where $\mathbf{S}^0 = \left\{S_1^0, S_2^0, S_3^0\right\}^T$ and matrix

$$[\mathbf{\Phi}(x)] = \begin{bmatrix} \alpha_1 \cosh k_1 x & \alpha_2 \cosh k_2 x & \alpha_3 \cosh k_3 x \\ \cosh k_1 x & \cosh k_2 x & \cosh k_3 x \\ \beta_1 \sinh k_1 x & \beta_2 \sinh k_2 x & \beta_3 \sinh k_3 x \end{bmatrix} \cdot \begin{bmatrix} \delta_{11} & \delta_{12} & \delta_{13} \\ \delta_{21} & \delta_{22} & \delta_{23} \\ \delta_{31} & \delta_{32} & \delta_{33} \end{bmatrix}; \tag{15.26}$$

$$\Delta_1 = \left(\delta_{11} S_1^0 + \delta_{12} S_2^0 + \delta_{13} S_3^0\right) / \Delta; \Delta_2 = \left(\delta_{21} S_1^0 + \delta_{22} S_2^0 + \delta_{23} S_3^0\right) / \Delta;$$

$$\Delta_3 = \left(\delta_{31} S_1^0 + \delta_{32} S_2^0 + \delta_{33} S_3^0\right) / \Delta; \quad \Delta = k_1 \beta_1 (\alpha_2 - \alpha_3) + k_2 \beta_2 (\alpha_3 - \alpha_1) + k_3 \beta_3 (\alpha_1 - \alpha_2);$$

Assuming furthermore that $S_1^0 = \gamma_1 U_x'(e), S_2^0 = S_3^0 = \gamma_2 \Theta_x'(e)$ or $\mathbf{S}^0 = [\mathbf{\Sigma}] \left\{\mathbf{z}_0'(e)\right\}$ with

$$\mathbf{\Sigma} = \begin{bmatrix} \gamma_1 & 0 & 0 \\ 0 & \gamma_2 & 0 \\ 0 & \gamma_2 & 0 \end{bmatrix}, \tag{15.27}$$

a particular solution $\mathbf{z}_c(x)$ of Eq. (15.9) that satisfies initial conditions

$$\mathbf{z}_c(0) = \left\{\gamma_1 U_x'(e), \gamma_2 \Theta_x'(e), 0\right\}^T; \mathbf{z}_c'(0) = \left(0, 0, \gamma_2 \Theta_x'(e)\right)^T, \tag{15.28}$$

is

$$\mathbf{z}_c(x) = [\mathbf{\Phi}(x)] [\mathbf{\Sigma}] \left\{\mathbf{z}_0'(e)\right\} = [\mathbf{G}_c(x)] \left\{\mathbf{z}_0'(e)\right\}. \tag{15.29}$$

Using the matrix-function notation

$$\mathbf{K}(x) = \begin{cases} \mathbf{G}_c(x) : x > 0; \\ 0 \quad : x \le 0; \end{cases} \quad \mathbf{K}'(x) = \begin{cases} \mathbf{G}_c'(x) : x > 0; \\ 0 \quad : x \le 0; \end{cases} \tag{15.30}$$

one is able to prove that the function

$$\mathbf{z}(x) = \mathbf{z}_0(x) + \mathbf{K}(x - e) \mathbf{z}_0'(e) \tag{15.31}$$

is general solution of Eq. (15.9) satisfying conditions (15.12) at the cracked section.

It can be easily to verify that boundary conditions for cantilever beam are

$$u(0, t) = w(0, t) = \theta(0, t) = 0; \quad N(L, t) = M(L, t) = Q(L, t) = 0. \tag{15.32a,b}$$

Applying conditions (15.32a) for solution (15.31) leads to

$$\mathbf{B}_{01} \mathbf{C}_1 + \mathbf{B}_{02} \mathbf{C}_2 = 0, \tag{15.33}$$

$$\mathbf{C}_1 = \{C_1, C_2, C_3\}^T; \mathbf{C}_2 = \{C_4, C_5, C_6\}^T; \quad \mathbf{B}_{01} = \begin{bmatrix} \alpha_1 & \alpha_2 & \alpha_3 \\ 1 & 1 & 1 \\ \beta_1 & \beta_2 & \beta_3 \end{bmatrix}; \quad \mathbf{B}_{02} = \begin{bmatrix} \alpha_1 & \alpha_2 & \alpha_3 \\ 1 & 1 & 1 \\ -\beta_1 & -\beta_2 & -\beta_3 \end{bmatrix}.$$

Obviously, the above equation allows the vectors $\mathbf{C}_1$, $\mathbf{C}_2$ to be expressed as

$$\mathbf{C}_1 = [\mathbf{B}_{01}]^{-1}\mathbf{D}, \mathbf{C}_2 = -[\mathbf{B}_{02}]^{-1}\mathbf{D}$$

with an arbitrary constant vector $\mathbf{D}$, so that solution $\mathbf{z}_0(x)$ can be rewritten in the form

$$\mathbf{z}_0(x,\omega) = \mathbf{G}_0(x,\omega)\,\mathbf{D}, \tag{15.34}$$

where

$$\mathbf{G}_0(x,\omega) = \mathbf{G}_1(x,\omega)\,\mathbf{B}_{01}^{-1} - \mathbf{G}_2(x,\omega)\,\mathbf{B}_{02}^{-1}.$$

Consequently, one obtains

$$\mathbf{z}(x) = \left[\mathbf{G}_0(x,\omega) + \mathbf{K}(x-e)\,\mathbf{G}_0'(e,\omega)\right]\{\mathbf{D}\} = [\mathbf{G}_{\mathrm{L}}(x,\omega)]\{\mathbf{D}\}. \tag{15.35}$$

Applying boundary condition (15.32b) for solution (15.34) one gets

$$\left[\mathbf{B}_{\mathrm{LL}}\omega\right)\Big]\{\mathbf{D}\} = 0,\ \ \mathbf{B}_{\mathrm{LL}}(\omega) = \mathbf{B}_{\mathrm{L}}\{\mathbf{G}_{\mathrm{L}}(x,\omega)\}|_{x=L}\ ; \tag{15.36}$$

$$\mathbf{B}_L = \begin{bmatrix} A_{11}\partial_x & 0 & 0 \\ 0 & A_{22}\partial_x & 0 \\ 0 & -A_{33} & A_{33}\partial_x \end{bmatrix}.$$

So that characteristic or frequency equation of the cracked FGM beam is obtained as

$$\Lambda(\omega) = \det[\mathbf{B}_{\mathrm{LL}}(\omega)] = 0. \tag{15.37}$$

Positive root ω_j of this equation provide desired natural frequency of the beam. In the case of intact beam the frequency Eq. (15.37) is reduced to

$$\Lambda_0(\omega) = \det[\mathbf{B}_{\mathrm{L0}}(\omega)] = 0;\ \ \mathbf{B}_{\mathrm{L0}}(\omega) = \mathbf{B}_{\mathrm{L}}\{\mathbf{G}_0(x,\omega)\}|_{x=L}\ . \tag{15.38}$$

Thus, forward problem is to calculate natural frequencies of cracked or uncracked FGM beam by solving Eqs. (15.37) or (15.38).

15.3 Numerical Results and Discussion

15.3.1 Comparative Study

To investigate effect of actual position of neutral axis on natural frequencies of Timoshenko FGM cantilevered beam, it is examined an undamaged beam studied in [4] that is composed from steel: $E_b = 210\,\mathrm{GPa}$, $\rho_b = 7800\,\mathrm{kg/m^3}$, $\mu_1 = 0.3$ at the bottom and Aluminum Oxide (Al_2O_3): $E_t = 390\,\mathrm{GPa}$, $\rho_t = 3960\,\mathrm{kg/m^3}$, $\mu_t = 0.25$ at the top surface.

Table 15.1 show first five natural frequencies computed in the present paper for various slenderness ratio *L/h*, and power law index *n*. Comparison with those obtained in [4] where neutral axis is assumed coincident with the middle one shows that effect of actual position of neutral axis on the lower natural frequencies is clearly observed in the case of small slenderness, L/h = 5, and n = 2. In this case natural frequencies calculated with actual position of neutral axis are lower than those computed by the centroid axis theory. However, higher natural frequencies of FGM beam with greater slenderness and power law index are not very much changed by the correcting position of neutral axis.

Table 15.1 Comparison of frequency parameters, $\lambda = \left(\omega L^2/h\right)\sqrt{\rho_b/E_b}$, for undamaged FGM cantilever beam: Present—actual and Ref. [4]—centroid position of neutral axis

L/h		5		10		20		30	
n	Fr. No.	Present	Ref. [4]	Present	Ref. [4]	Present	Ref. [4]	Present	Ref. [4]
0.1	1	1.7377	1.7574	1.7854	1.7966	1.8020	1.8070	1.8060	1.8089
	2	9.3254	9.0511	10.6630	10.782	11.1116	11.196	11.2359	11.278
	3	14.1039	14.095	28.0582	28.190	30.4454	30.800	31.1476	31.325
	4	22.3755	22.682	28.3600	28.404	56.3576	56.379	60.2240	60.681
	5	37.5464	37.747	51.8239	51.618	58.0334	58.897	84.5711	84.569
0.2	1	1.6294	1.6638	1.6804	1.7010	1.7011	1.7107	1.7061	1.7126
	2	8.6806	8.9969	9.9804	10.208	10.4534	10.600	10.5981	10.678
	3	13.4167	13.390	26.3172	26.781	28.5635	29.161	29.3406	29.657
	4	20.9419	21.482	26.9510	26.895	53.4530	53.562	56.6568	57.449
	5	35.5698	35.754	48.9926	48.878	54.4140	55.762	80.3494	80.343
0.5	1	1.4308	1.4911	1.4852	1.5244	1.5118	1.5332	1.5183	1.5348
	2	7.5158	8.0609	8.7058	9.1477	9.2390	9.4992	9.4075	9.5691
	3	12.0814	12.012	22.8654	24.024	25.1327	26.130	25.9870	26.576
	4	18.3974	19.243	24.5762	24.098	47.3355	48.048	50.0731	51.475
	5	32.0833	32.022	43.5626	43.787	48.3416	49.962	72.0863	72.072
1.0	1	1.2809	1.3557	1.3345	1.3864	1.3636	1.3945	1.3705	1.3960
	2	6.6597	7.3164	7.7397	8.3146	8.3071	8.6383	8.4791	8.7027
	3	10.9037	10.811	20.3079	21.623	22.5403	23.755	23.3925	24.165
	4	16.4188	17.441	22.1864	21.886	42.3703	43.246	45.0165	46.795
	5	28.9477	28.989	38.7308	39.732	43.5214	45.402	64.8906	64.870
2.0	1	1.1757	1.2471	1.2252	1.2762	1.2519	1.2839	1.2583	1.2853
	2	6.1047	6.7053	7.1063	7.6440	7.6240	7.9501	7.7835	8.0112
	3	9.8238	9.7403	18.6028	19.481	20.6777	21.851	21.4688	22.239
	4	15.0301	15.937	20.0358	20.088	38.6088	38.961	41.3021	43.049
	5	26.4566	26.428	35.5854	36.403	39.4505	41.733	58.4651	58.442
5.0	1	1.1030	1.1446	1.1405	1.1722	1.1604	1.1795	1.1651	1.1809
	2	5.8414	6.1274	6.6706	7.0111	7.0955	7.3014	7.2209	7.3594
	3	8.8103	8.7633	17.3374	17.527	19.2998	20.057	19.9462	20.425
	4	14.3168	14.516	17.7729	18.391	35.0124	35.053	38.4225	39.525
	5	24.9321	24.009	32.4530	33.2625	36.5838	38.278	52.5932	52.580
10	1	1.0629	1.0867	1.0962	1.1130	1.1105	1.1199	1.1138	1.1212
	2	5.6345	5.8159	6.4753	6.6562	6.8192	6.9324	6.9167	6.9876
	3	8.3591	8.3430	16.6488	16.686	18.6108	19.394	19.1378	19.394
	4	13.5189	13.776	17.0828	17.459	33.3597	33.372	36.9246	37.532
	5	22.8182	22.783	31.2177	31.575	35.3365	36.345	50.0635	50.058

15.3.2 Sensitivity of Natural Frequencies to Crack

The change in natural frequencies caused by a crack is usually called sensitivity of the natural frequencies to crack. The natural frequency sensitivity is represented in this paper by a ratio of the damaged to undamaged frequencies as function of crack location along the beam length. The natural frequency ratios of cracked the beams are examined as function of crack position for various scenarios of crack depth $\overline{a} = a/h$, elasticity modulus ratio $r = E_t/E_b$ and fraction index n in the boundary conditions: simple supports (SS), clamped ends (CC) and cantilever. Results of computation are presented in Figs. 15.1, 15.2, and 15.3 respectively for the cases of boundary conditions in combination with the parameters $\overline{a}, n, r$.

Observing graphics given in the figures allows one to make the following concluding remarks. Likely to the homogeneous beam, all natural frequencies of FGM beam are reduced when a crack occurred in the beam except some positions where crack makes no effect on natural frequency of certain mode. Such the locations of crack on beam can be termed by natural frequency node and they have been determined numerically for first three modes of beam with conventional boundary conditions (see Table 15.2). The figures show that frequency nodes are almost independent on the material properties such as volume fraction index n and elasticity modulus ratio $r = E_t/E_b$ of FGM beam. Nevertheless, reduction of natural frequencies

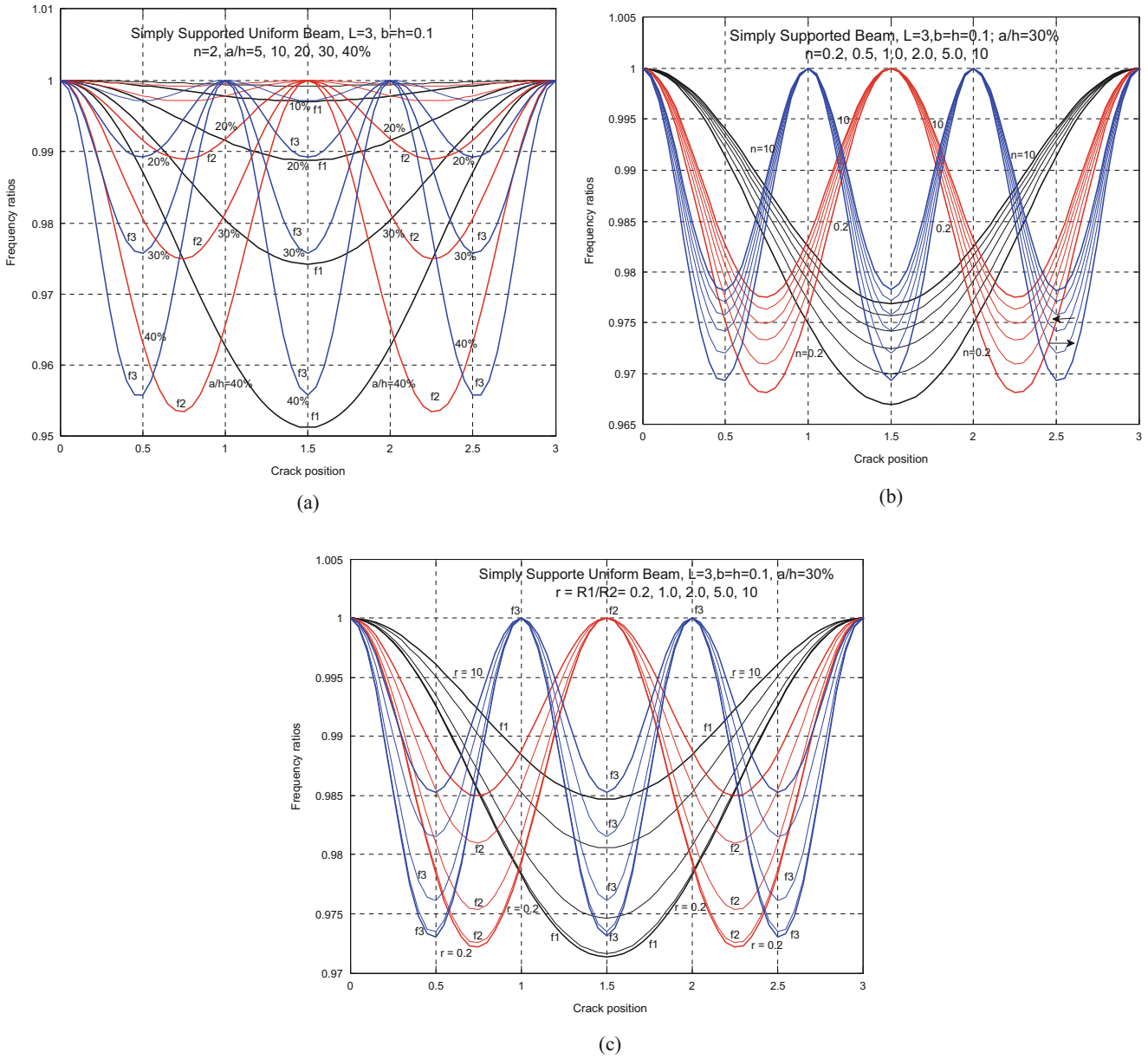

Fig. 15.1 Normalized three lowest natural frequencies of uniform FGM SS-beam in dependence on the crack depth (**a**), fraction index n (**b**) and elasticity modulus ratio r (**c**)

due to crack is strongly dependent on the material parameters. Graphs given in Figs. 15.1, 15.2, and 15.3 show that the natural frequencies are monotonically reducing with growing crack depth and it is dependent also on the material and geometry of the beam. Namely, the natural frequency reduction is growing with elasticity modulus ratio $r = E_t/E_b$ for $n < 1$ and decreasing when $n > 1$. The latter implies that increase of elasticity modulus from bottom to top of Timoshenko beam makes the natural frequencies more or less sensitive to crack dependently on that $n < 1$ or $n > 1$. Similarly, it is observed that natural frequency sensitivity is increasing with n for a fixed $r < 1$ and would be decreasing if $r > 1$. It is observed also that natural frequencies of flexural vibration modes become less sensitive to crack for increasing slenderness ratio and it is independent on whatever material the beam is made of but the axial mode frequencies show to be most sensitive to crack when L/h = 10.

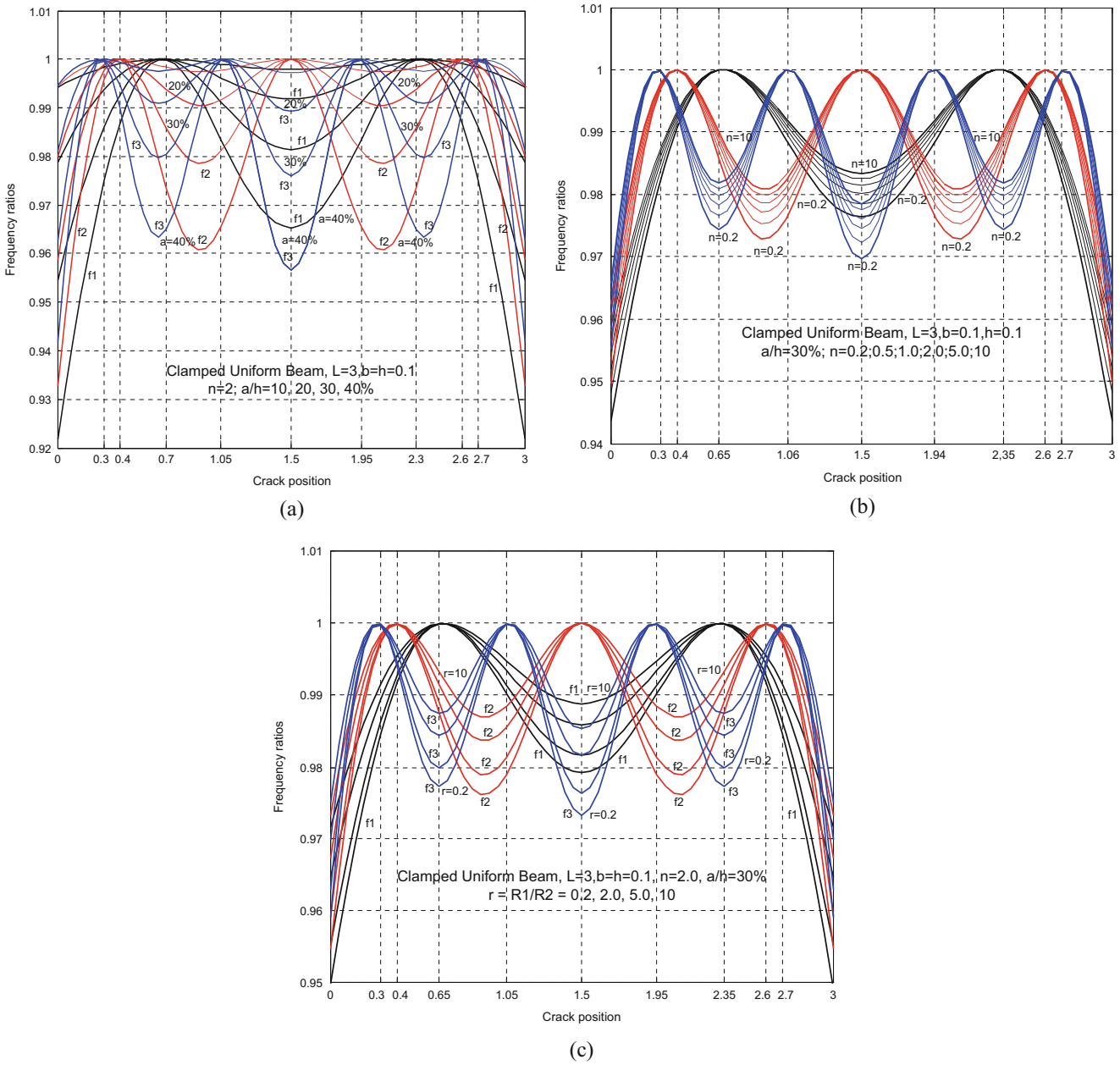

Fig. 15.2 Normalized three lowest natural frequencies of uniform FGM CC-beam in dependence on the crack depth (**a**), fraction index n (**b**) and elasticity modulus ratio (**c**)

15.4 Conclusion

Main results obtained in the present paper are as follows:

1. A consistent theory of vibration beam has been formulated in the frequency domain for functionally graded Timoshenko beam that can be used for analysis of either free or forced vibrations in the beam.
2. Frequency equation for functionally graded Timoshenko beam with single crack modeled by coupled translation and rotation springs was constructed in a form that is applicable straightforward to frequency analysis of the beam. Application of the equation for natural frequency analysis of FGM beam demonstrates that natural frequencies of flexural vibration modes are more sensitive to crack than those of axial vibration modes and the natural frequency sensitivity is strongly dependent on both material and geometry parameters of functionally graded Timoshenko beam.
3. The theory proposed in the present work can be further developed for analysis and identification of FGM beam with multiple cracks.

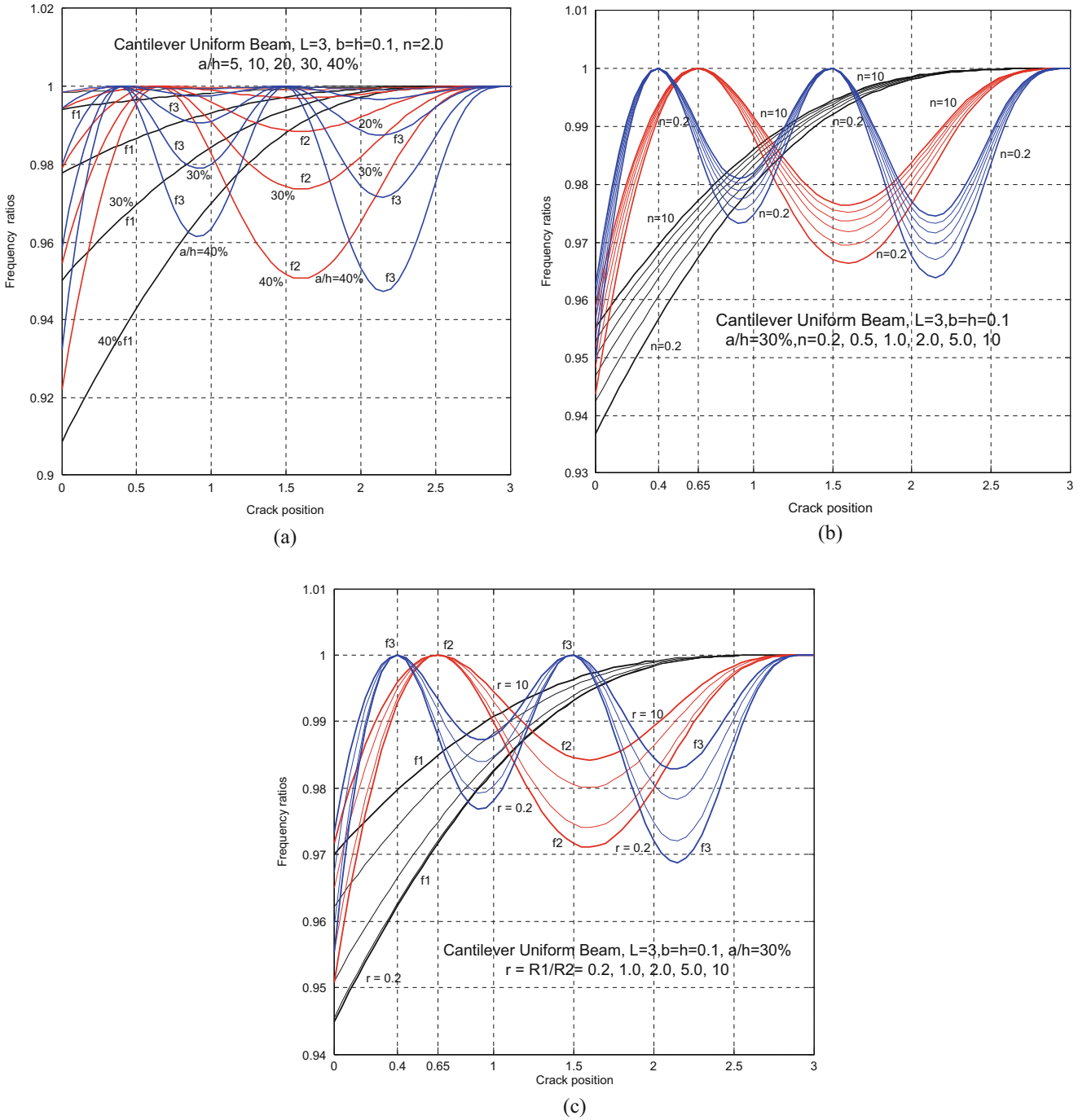

Fig. 15.3 Normalized three lowest natural frequencies of uniform FGM CF-beam in dependence on the crack depth (**a**), fraction index n (**b**) and elasticity modulus ratio (**c**)

Table 15.2 Natural frequency nodes of uniform FGM beam in different boundary conditions

Mode	Clamp-free ends		Simple supports		Clamped ends			
1	n/a		n/a			0.66	2.34	
2	0.65		1.5		0.39	1.50		2.61
3	0.4	1.49	1.0	2.0	0.28	1.06	1.94	2.72

E1 = 390; E2 = 210 GPa, $\rho_1 = 3960$; $\rho_2 = 7850$ kg/m^3; $\mu_1 = 0.25$; $\mu_2 = 0.30$, $n = 2$, $L = 3$ m

Acknowledgement The first author is sincerely thankful to the NAFOSTED of Vietnam for financial support under Grant of Number:107.01-2015.20.

References

1. Birman, V., Byrd, L.W.: Modeling and analysis of functional graded materials and structures. Appl. Mech. Rev. **60**, 195–215 (2007)
2. Chakraborty, A., Gopalakrishnan, S., Reddy, J.N.: A new beam finite element for the analysis of functional graded materials. Int. J. Mech. Sci. **45**, 519–539 (2003)
3. Chakraborty, A., Gopalakrishnan, S.: A spectrally formulated finite element for wave propagation analysis in functionally graded beams. Int. J. Solids Struct. **40**, 2421–2448 (2003)
4. Su, H., Banerjee, J.R.: Development of dynamic stiffness method for free vibration of functionally graded Timoshenko beams. Comput. Struct. **147**, 107–116 (2015)
5. Pradhan, K.K., Chakraverty, S.: Free vibration of Euler and Timoshenko functionally graded beams by Rayleigh-Ritz method. Compos. Part B. **51**, 175–184 (2013)
6. Zhong, Z., Yu, T.: Analytical solution of a cantilever functionally graded beam. Comput. Sci. Technol. **67**, 481–488 (2007)
7. Sina, S.A., Navazi, H.M., Haddadpour, H.: An analytical method for free vibration analysis of functionally graded beams. Mater. Des. **30**, 741–747 (2009)
8. Li, X.F.: A unified approach for analyzing static and dynamic behaviors of functionally graded Timoshenko and Euler-Bernoulli beams. J. Sound Vib. **318**, 1210–1229 (2008)
9. Simsek, M., Kocatuk, T.: Free and forced vibration of a functionally graded beam subjected a concentrated moving harmonic load. Compos. Struct. **90**(4), 465–473 (2009)
10. Jin, Z.H., Batra, R.C.: Some basic fracture mechanics concepts in functionally graded materials. J. Mech. Phys. Solids. **44**(8), 1221–1235 (1996)
11. Erdogan, F., Wu, B.H.: The surface crack problem for a plate with functionally graded properties. J. Appl. Mech. **64**, 448–456 (1997)
12. Yang, J., Chen, Y.: Free vibration and buckling analysis of functionally graded beams with edge cracks. Compos. Struct. **83**, 48–60 (2008)
13. Wei, D., Liu, Y.H., Xiang, Z.H.: An analytical method for free vibration analysis of functionally graded beams with edge cracks. J. Sound Vib. **331**, 1685–1700 (2012)
14. Aydin, K.: Free vibration of functional graded beams with arbitrary number of cracks. Eur. J. Mech. A Solid. **42**, 112–124 (2013)
15. Kitipornchai, S., Ke, L.L., Yang, J., Xiang, Y.: Nonlinear vibration of edge cracked functionally graded Timoshenko beams. J. Sound Vib. **324**, 962–982 (2009)
16. Yan, T., Kitipornchai, S., Yang, J., He, X.Q.: Dynamic behavior of edge-cracked shear deformable functionally graded beams on an elastic foundation under a moving load. Compos. Struct. **93**, 2992–3001 (2011)
17. Yu, Z., Chu, F.: Identification of crack in functionally graded material beams using the p-version of finite element method. J. Sound Vib. **325**, 69–85 (2009)
18. Banerjee, A., Panigrahi, B., Pohit, G.: Crack modelling and detection in Timoshenko FGM beam under transverse vibration using frequency contour and response surface model with GA. Nondestr. Test. Eval. (2015). doi:10.1080/10589759.2015.1071812
19. Khiem, N.T., Kien, N.D., Huyen, N.N.: Vibration theory of FGM beam in the frequency domain. In: Proceedings of National Conference on Engineering Mechanics celebrating 35th Anniversary of the Institute of Mechanics, VAST, April 9, 2014, vol. 1, pp. 93–98 (in Vietnamese)
20. Chondros, T.G., Dimarogonas, A.D., Yao, J.: Longitudinal vibration of a continous cracked bar. Eng. Fract. Mech. **61**, 593–606 (1998)
21. Chondros, T.G., Dimarogonas, A.D., Yao, J.: A continuous cracked beam theory. J. Sound Vib. **215**, 17–34 (1998)

Chapter 16
Eliminating Blur in Small Unmanned Aircraft Imaging Systems

Weston J. Swetich and William H. Semke

Abstract A novel procedure to eliminate blur in imagery captured by small unmanned aircraft is demonstrated. The whirling props and airflows often cause unwanted image blur due to the unstable platform from which they are captured. In multirotor aircraft these image artifacts often produce remote sensing data that is inferior to the imaging system capability. By eliminating the vibration of the host vehicle, the full potential of the instruments can be obtained, as demonstrated in imaging studies presented. To accomplish this an attachment system has been developed so that the props can be shut off in a perched configuration and the unwanted vibration will cease. This concept not only reduces the vibration levels, but also greatly prolongs the effective use of imaging or robotic systems. Typically, most of the power usage is for propulsion and not for payloads, therefore without the need for lift and maneuvering, the payload systems can operate for periods many times the flight operation duration. The dynamic performance of two aircraft is presented; first is a highly modified remote control helicopter clearly illustrating the concept and the second a custom built system in a small footprint enclosure with increased payload capacities for remote sensing and robotic equipment.

Keywords Unmanned aircraft • Remote sensing • Camera stability • Robotic operations • Perching attachment

16.1 Introduction

Large multirotor vehicles that operate in uncluttered, open-air spaces have few restrictions in terms of their construction; the weight of a payload is spread across many, sometimes redundant, exposed spinning rotors and vibration dampening systems can be built-in with minimal concern about how that additional mass will affect final flight performance. While these luxuries have allowed multirotor UAVs to transform and disrupt a number of different industries and recreational activities, there are still many areas where payload-capable systems are either poorly matched to the working environment or application specific platforms remain entirely undeveloped.

Previous work focusing on smaller-scale UAVs performing specific tasks in alternative environments has been very successful [1–3], and research exploring different attachment methodologies has also shown promise [4–6]. The two prototype platforms developed for this design project seek to expand upon these efforts in two ways. First, the configuration and construction of these two systems will be geared toward operations occurring in industrial spaces and close-proximity situations. Mazes of pipe, tangles of wire, and other local infrastructure are common features in areas where relevant engineering data usually resides. As such, a minimized and enclosed propulsive footprint is required in order to ease flight access at remote sites and mitigate physical safety concerns. Second, a magnetic-based "perching" capability is implemented and demonstrated using off-the-shelf components. This attachment mechanism will be able to leverage ferromagnetic structures and surfaces already in place, as well as enable stable, longer-term measurement objectives spanning from real-time visual surface inspections to sensor installation using onboard robotic actuation [7].

W.J. Swetich • W.H. Semke (✉)
Department of Mechanical Engineering, College of Engineering and Mines, University of North Dakota, Grand Forks, ND58202, USA
e-mail: william.semke@engr.und.edu

J.M. Harvie, J. Baqersad (eds.), *Shock & Vibration, Aircraft/Aerospace, Energy Harvesting, Acoustics & Optics, Volume 9*, Conference Proceedings of the Society for Experimental Mechanics Series, DOI 10.1007/978-3-319-54735-0_16

16.2 Design Specifications

The Phase I platform, shown in Fig. 16.1, utilizes an upgraded propulsion unit from a 500-size 4-channel RC coaxial helicopter. Unlike a multirotor system, the control characteristics rely more on that of helicopter flight mechanics: the bottom blade set, spun in one direction on the outer shaft, is connected to a cyclic swashplate that is manipulated by two servos. The upper blade set, spun in the opposite direction on the inner shaft, is connected to a weighted flybar. Yaw is kept in check via a head-holding gyro with adjustable gain and delay settings, along with a separate motor mixing component with its own adjustable gain setting. A 3D-printed adapter hub serves as an interface for both the frame standoffs of the propulsion unit and the free of ends of the carbon fiber rods that comprise the spheroid protective enclosure, assembling everything into a single unit. Additionally, the camera used with this platform—a GoPro HERO3—was mounted within the open form factor of the adapter hub. The perching functionality is enabled by the adhesion force of a single holding magnet; a centrally located, outward-facing permanent magnet surrounded by a compact electromagnet all of which is contained in a cylindrical housing. This holding magnet is placed in a separate 3D-printed holder suspended at the top of the protective enclosure, held in place by the crossover of the carbon fiber rods and further secured at the intersections of the rods.

For Phase I, the passive holding force of a single permanent magnet is more than sufficient to support the weight of the platform while attached to a surface. No additional power input, beyond what is required to maintain radio control, is needed to maintain secure magnetic adhesion. There are instances, however, where temporary activations of the built-in electromagnet help supplement the overall operation of the system. Utilizing an open transmitter channel and reverse polarity, the holding force of the permanent magnet can be momentarily increased, aiding in positive surface acquisition and preventing premature detachment. Inversely, the holding force of the permanent magnet can be almost entirely negated when energized using normal polarity. This allows the platform to effortlessly disengage from its "perching" position, as well as avoid unwanted surface attachment while in transit.

The Phase II platform, shown in Fig. 16.2, employs two motors and two linked flap-servo pairs (2M 2S) in a configuration colloquially termed CoaxCopter. The brushless motors are stacked vertically on a centrally located axis with the flap-servos oriented in an "x" configuration about that same axis; the coordination of these control elements is handled by the PI-tunable firmware of a miniature consumer-grade flight controller. A one-piece frame fabricated from ¼″ carbon fiber sandwich panel serves as the foundation upon which all onboard systems are built and attached. A radial arrangement of through-holes and hub mounting patterns allows the same diameter of carbon fiber rod that was used on the Phase I platform to be arranged in a variety of different protective enclosures; the first design emulated a sphere using six carefully interlaced carbon fiber rods and later iterations formed an elongated, pill-shaped enclosure using only three carbon fiber rods.

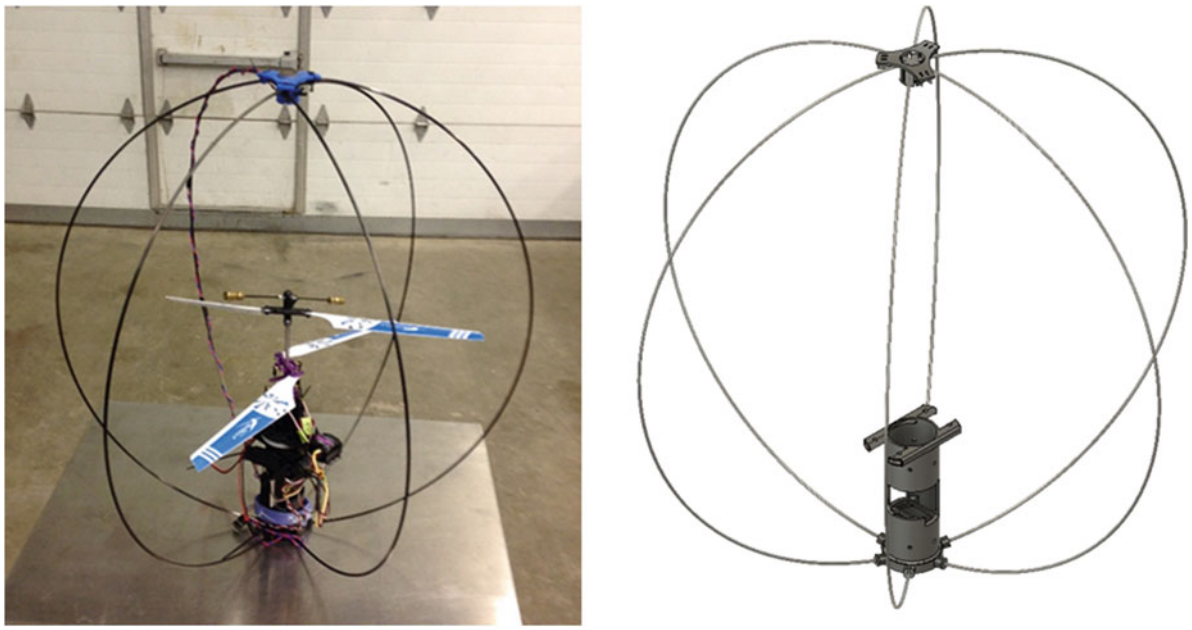

Fig. 16.1 Assembled Phase I Platform and CAD Model. The holding magnet is suspended by the carbon fiber rods at the point of mutual crossover. The carbon fiber rods extend out into the spheroid enclosure around the original propulsion unit. The rapid-prototyped adapter hub, with room for an onboard camera, couples the propulsion unit and the carbon fiber rods into a single assembled unit

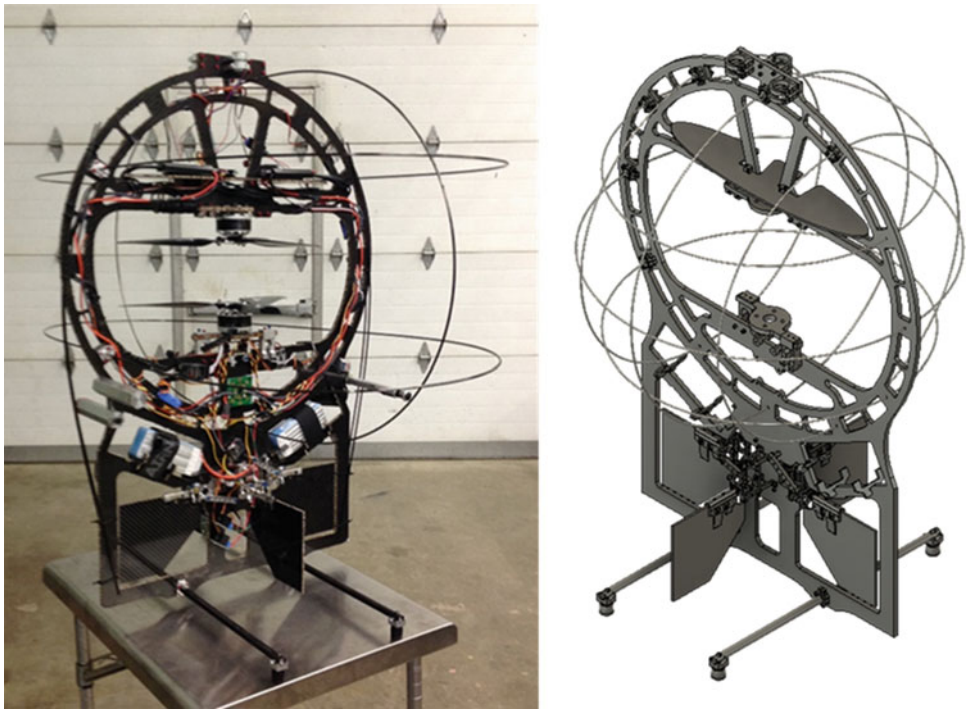

Fig. 16.2 Assembled Phase II platform and CAD model. This platform employs two motors and two linked flap-servo pairs in a CoaxCopter configuration. A one-piece frame fabricated from ¼″ carbon fiber sandwich panel serves as the foundation upon which all onboard systems are attached inside of the carbon fiber rod enclosure

Table 16.1 Dimension specifications for Phases I and II platforms

	Phase I	Phase II
Length (cm)	53	56–102
Width (cm)	53	61
Height (cm)	53	91
Weight (kg)	0.68	5.6
Propulsion	370 kV brushless	435 kV brushless
Maximum RPM	427	10,962
Rotor diameter (cm)	48	39
Hover duration (min)	5–10	7–12

For Phase II, a constellation of three slightly larger holding magnets provides needed improvements over the limitations of the Phase I platform. For example, a single holding magnet acts as a point of rotation while attached to a surface, allowing the platform to yaw during both motor shutdown and startup; three holding magnets eliminates this effect entirely. Additionally, the circuitry that enabled the manipulation of the adhesion force of the permanent magnet for the Phase I platform was restricted to a single polarity. While an adhesion-increasing polarity was initially used to ensure secure surface attachment on the way up to the test fixture, the wiring leads had to be switched by hand while the platform was perched to allow for adhesion-decreasing polarity and the capability to detach. The Phase II platform overcomes this constraint by using three compact onboard SPDT relays; in this way, the polarity of the three holding magnets can be changed and activated by the operator as needed during any mode of operation using two separate transmitter channels.

Further specifications for the Phases I and II platforms are shown in Table 16.1.

16.3 Perching Advantage 1: Extended Mission Time

The ideal flight profile for a given mission can be divided into three basic stages; transition to the target area, completion of tasks within the target area, and transition back to the user. For multirotor platforms, it is necessary to reduce the length of the bookending transitory stages in order to maximize the amount of time a payload can be effectively deployed in the

Table 16.2 Low-power amperage for Phases I and II platforms in perched configuration

	Measured amperage (motors shutdown)			
	4.2 V/cell		3.2 V/cell	
	Magnet inactive (mA)	Magnet energized	Magnet inactive (mA)	Magnet energized
Phase I	∼200	∼720 mA	∼180	∼580 mA
Phase II	∼190 to 230	∼1.1 A	∼210 to ∼260	∼1.4 A

Table 16.3 Usage of battery capacity based on stages of flight activity

	Potential flight profiles					
	Phase I			Phase II		
	Launch/Landing (mAh)	"Perching" (mAh)	Attach (h)	Launch/Landing (mAh)	"Perching" (mAh)	Attach (h)
Profile 1	533	237	1.3	2773	1387	5.3
Profile 2	400	400	2	3120	1040	4

target area. Even with optimized launches and landings, the rapid expenditure of energy needed for maneuvering and simply staying aloft greatly impacts not only the amount of data that can be collected, but also the quality of that data. With the ability to perch, however, battery capacity that is essentially wasted while the payload is active can instead be consumed at a significantly slower, much more consistent rate over a considerably longer period of time. The best way to illustrate this advantage is to construct several hypothetical flight profiles based on battery capacity using known performance values from the Phases I and II platforms.

The low-power state of the Phase I platform, described here as a complete shutdown of the brushless motors and no power being used by the holding magnet, draws ∼200 mA at a full charge voltage of 4.2 V/battery cell and ∼180 mA at a low charge voltage of 3.2 V/battery cell; the largest capacity battery used for this platform is a 1000 mAh 3-cell lithium polymer chemistry from Turnigy. The usable charge is around 80% of the total capacity, leaving only 800 mAh for continuous operation. Dividing that capacity into thirds results in 533 mAh for transition to and from a target surface and only 267 mAh for the reduced amperage while magnetically attached. At a rate of ∼200 mA, the Phase I platform could remain perched for up to 1.3 h. For optimized launch and landing, it may be possible to commit only half the usable capacity for flight purposes; with this profile, up to 2 h of attachment is possible. The GoPro HERO3 camera—powered by its own battery—carried by the Phase I platform can record video for 2–3 h depending on quality and wireless settings and other environmental factors.

The low-power state of the Phase II platform, described here as a complete shutdown of the brushless motors, no activated onboard relays, and no power being used by the holding magnets, draws ∼190 to ∼230 mA at a full charge voltage of 4.2 V/battery cell and ∼210 to ∼260 mA at a low charge voltage of 3.2 V/battery cell. For this platform, two 2600 mAh 6-cell lithium polymer batteries from BuddyRC were wired in parallel resulting in a capacity of 5200 mAh. As mentioned previously, the usable charge is around 80% of the total capacity, leaving 4160 mAh for sustained operation. Dividing that capacity into thirds results in 2773 mAh for transition to and from a target surface and 1387 mAh for the reduced amperage while magnetically attached. At a rate of ∼260 mA, the Phase II platform could remain perched for up to 5.3 h. With the greater payload capability offered by this platform, it is likely that launch and landing will account for a greater proportion of available capacity, potentially 75% or more. With this increased demand, 3120 mAh would be used for transitory flight with 1040 mAh remaining for perching purposes; with this profile, up to 4 h of attachment is possible. The GoPro HERO4 Session camera—powered by its own battery—carried by the Phase II platform can record video for 1.5–2 h depending on quality and wireless settings and other environmental factors.

A summary of amperage values and flight profiles is compiled in Tables 16.2 and 16.3, respectively.

16.4 Perching Advantage 2: Increased Measurement Fidelity

There are a number of different vibratory sources beyond imbalanced spinning rotors that can plague multirotor platforms; loose screws, misaligned bearings, and improper tuning of flight-controlling components are just a few examples of problems whose resolution, while not trivial, can often be handled with patience and the occasional application of strategically-placed double-sided foam tape. Operation in confined spaces and close-proximity situations, which is inherent to many engineering applications, introduces a new vibration-inducing dynamic in the form of turbulent airflows. While mechanical and structural issues can be anticipated and accounted for from a design standpoint, the effect of random air currents on data collection and

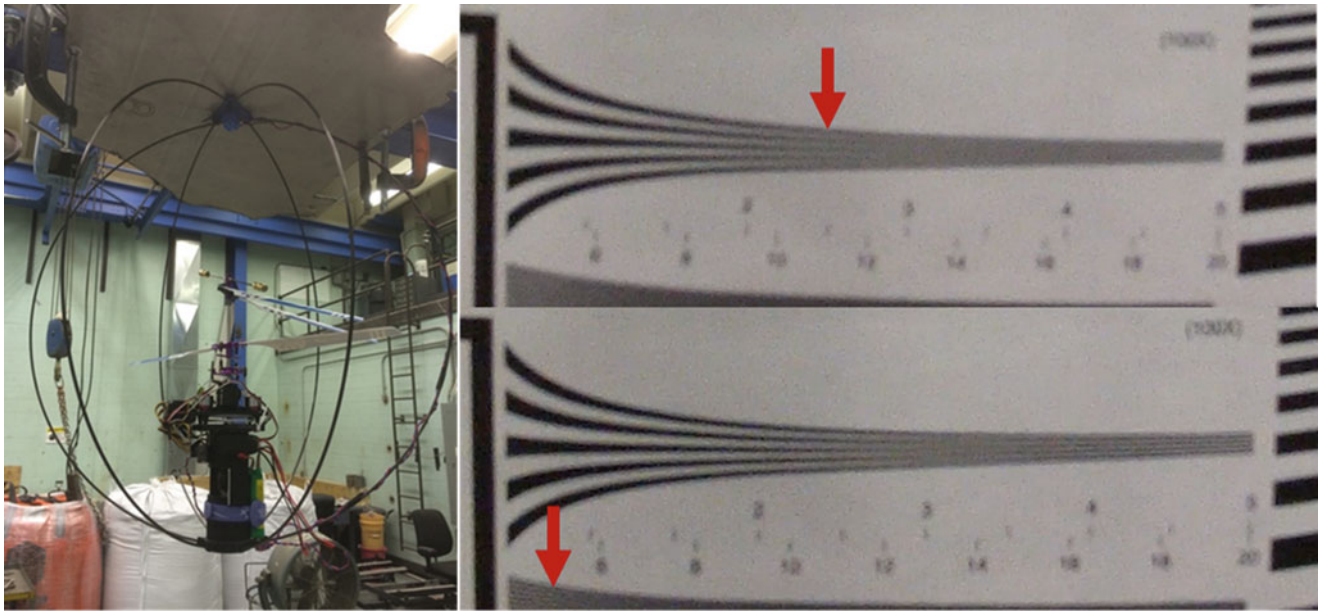

Fig. 16.3 Perched Phase I platform with unattached (*top right*) and attached (*bottom right*) visual resolutions. The *top right* shows a magnified portion of the resolution target as captured while in-flight; the *red arrow* indicates the region where the alternating *black* and *white* lines become individually indistinguishable around 250 LW/PH. The *bottom right* image show a magnified portion of the resolution target as captured while perched; the *red arrow* falls around 500 LW/PH

multirotor performance is not so easily mitigated. Additionally, the physical impacts of propwash on the process or surface that is being so closely observed and measured must also be taken into consideration. Stable attachment to a ferromagnetic surface addresses all of these concerns; the ability to completely shut off onboard motors eliminates the generation of disruptive, swirling air and removes the prevailing origin of induced platform vibrations.

In order to determine the difference in image quality between the attached and unattached configurations, a reference target (http://www.bealecorner.org/red/test-patterns/Square-wedges-80grey.pdf) was utilized to allow for simple visual analysis of the resolution of any recorded images by way of line widths per picture height (LW/PH); 10 s of video for both arrangements for each platform was captured at an image size of 1920 × 1080 at 30 frames/s. For the perched configuration, the target and the platform were positioned such that the vertical extent of the resolution pattern just spanned the height of the camera's perspective. For the "in-flight" configuration, the target was lowered and the platform was hovered so as to achieve a similar ratio of the target's size and orientation within the camera's field of view. The best single frame from each video was isolated and magnified for inspection and comparison.

For the Phase I platform, using the GoPro HERO3 camera, the results shown in Fig. 16.3 display that ∼500 LW/PH could be observed in the attached configuration while only ∼250 LW/PH could be seen during hover. This corresponds to roughly twice the available fidelity while perched compared to images captured when unattached with the motors running. Another comparative metric that can be derived from these numbers is that of the smallest resolvable feature. The resolution chart was printed on a piece of standard US Letter sized paper; setting the picture height equal to 21.6 cm and inverting, the smallest resolvable feature at ∼500 LW/PH would measure 0.43 mm high. At ∼250 LW/PH, the smallest resolvable feature would be two times bigger at 0.86 mm high.

For the Phase II platform, using the GoPro HERO4 Session camera, the results shown in Fig. 16.4 depict that ∼950 LW/PH could be observed in the attached configuration while only ∼625 LW/PH could be seen during hover. While the difference—an increase of only 52%—is not as substantial as seen with the Phase I platform, the outcome is no less compelling. What is also notable is the overall higher resolution captured by the Phase II platform, a disparity which is most likely attributable to both a newer camera model and better target lighting. The smallest resolvable feature at ∼950 LW/PH would measure 0.23 mm high; at ∼625 LW/PH, the smallest resolvable feature would measure 0.35 mm high. Table 16.4 is a summary of these resolution results.

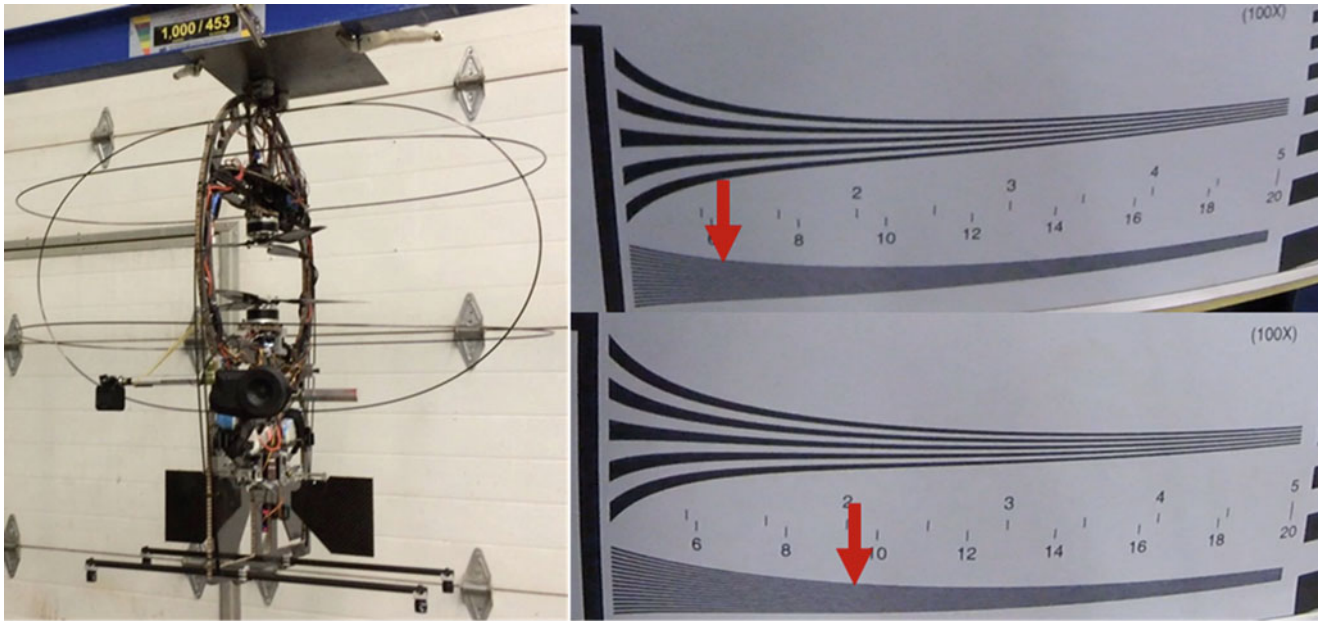

Fig. 16.4 Perched Phase II platform with unattached (*top right*) and attached (*bottom right*) visual resolutions

Table 16.4 Comparison of attached and unattached visual resolution

	Visual measurement resolution	
	Phase I	Phase II
	Resolution (LW/PH)	Resolution (LW/PH)
Attached	~500	~950
Unattached	~250	~625

16.5 Perching Advantage 3: Robotic Payload Actuation

For the majority of multirotor platforms, the flight characteristics for a given rotor layout are largely predetermined by the location of the center of gravity (CoG) relative to a fixed center of thrust (CoT); a high CoG arrangement, while more reactive to control inputs in general, lacks stability in maintaining stationary flight; a low CoG design gains corrective, pendulum-like reactions to disruptions in hovering flight, yet responds lethargically to small commanded maneuvers. The underslung and static position of most current payload systems imparts the operational benefits of the latter condition. However, as more robotic, or otherwise less static, payloads begin to be developed and deployed, either flight controllers will need to more flexible in adapting to a dynamic CoG/CoT relationship or a variety of different strategies will need to be realized. One such strategy being presented here is the methodology of perching attachment, which will be demonstrated in Figs. 16.5 and 16.6. In this case, a deploying robotic arm moves a camera closer to a target for inspection. Orders of magnitude improvements can be realized using the robotic operation where details otherwise indistinguishable can be easily seen. This is just one example of the multitude of applications robotics operations enable and enhance.

16.6 Accelerometer Data

A PCB Model 333B30 single-axis accelerometer was placed on the frame of the propulsion unit of the Phase I platform as shown in Fig. 16.7; the axis being measured is perpendicular to the horizontal mounting surface. Data was recorded at 10 kS/s for 12.1 s of hovering flight, generating 121,000 points of data. The mean, standard deviation, minimum, and maximum for the entirety of the recorded accelerations are shown in Table 16.5. While these numbers give a good generalization for the totality of what was measured, examining statistical metrics at the timescale of a frame of recorded video (1 frame = 0.0333 s) helps better visualize vibratory trends that can influence video quality as flight performance changes due to decreasing battery charge. Thus, for every 0.0333 s of recorded data, a new mean, minimum, and maximum

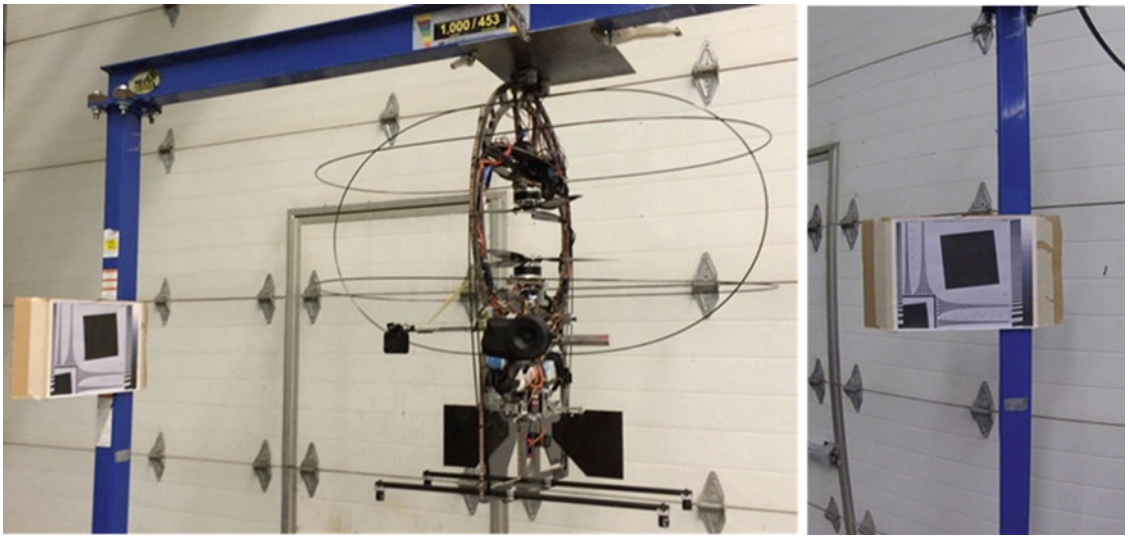

Fig. 16.5 To perform close inspections and provide the ability to interact with the environment, a telescoping robotic arm was added to the Phase II design. This image shows the robotic arm in the retracted position and imagery from the camera

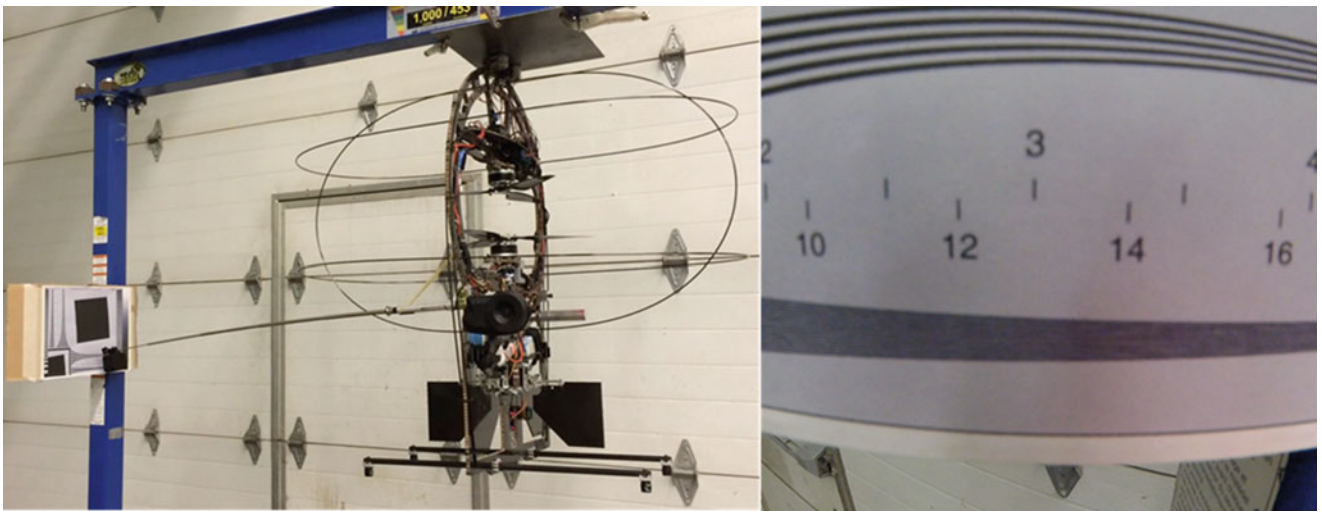

Fig. 16.6 The Phase II telescoping robotic arm can be extended up to 0.8 m toward an area of interest and retracted back to the platform. This allows for greater ability to obtain higher resolution imagery, as shown in the imagery from the deployed camera

value was determined; these calculated results, plotted alongside the raw accelerometer data, is also shown in Fig. 16.7. Focusing first on the calculated means, the introductory values start off around -11.24 to -11.26 m/s^2, slowly trending upward toward -11.30 m/s^2 near the end. Although the size of the change may be slight, this transition likely coincides with decreasing rotor speed over time as battery capacity is depleted. Regarding the arrangement of minimum and maximum values, there appears to be no clear trend or pattern over this period of time. However, their unequal range distribution about the mean values provides insight into the mechanical response of the protective enclosure for the Phase I platform. The minimum values—the most negative accelerations—occur during an upward vertical contraction of the spheroid enclosure; the maximum values—the least negative accelerations—occur during a downward vertical expansion of the spheroid enclosure. With a skewing of calculated means closer to minimum acceleration values, the majority of vibratory accelerations occur within a much smaller interval than the range of extreme values would indicate. Additionally, the presence of larger, more varied spikes of acceleration values in expansion along the measured axis coupled with a smaller, more uniform deviations of acceleration values in contraction along the measured axis signals a non-linear stiffness characteristic for the spheroid orientation of carbon fiber rods for the Phase I platform.

For the Phase II platform, a PCB Model 333B30 single-axis accelerometer was placed on the electrical component plate as shown in Fig. 16.8; the axis being measured is perpendicular to the horizontal mounting surface. Data was recorded at 10 kS/s

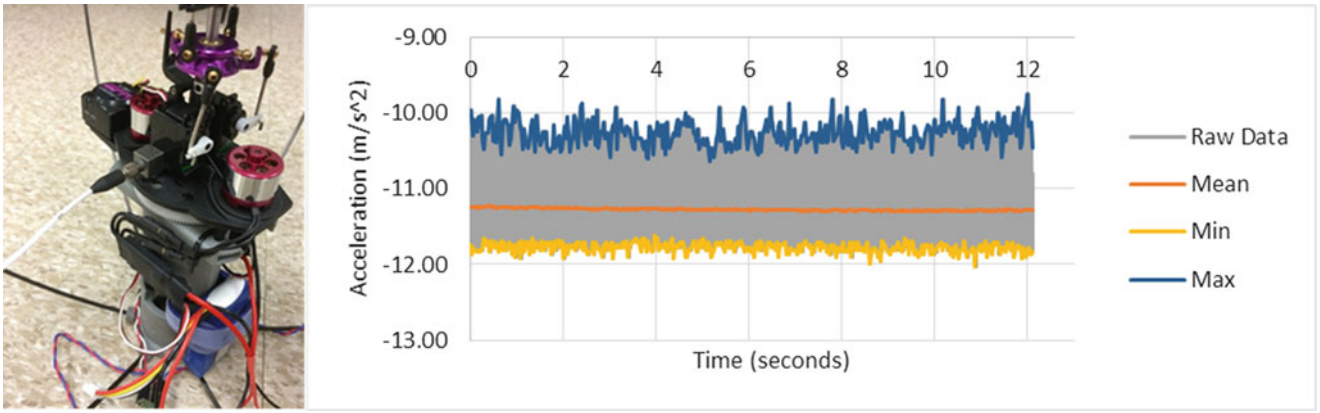

Fig. 16.7 Accelerometer placement on Phase I platform and data captured showing the raw, mean, maximum, and minimum values from the experimental testing

Table 16.5 Statistical metrics for Phases I and II accelerometer data

	Accelerometer data statistical metrics			
	Mean (m/s^2)	Standard deviation	Minimum (m/s^2)	Maximum (m/s^2)
Phase I	−11.27	0.24	−12.02	−9.75
Phase II	−10.69	0.44	−12.20	−9.33

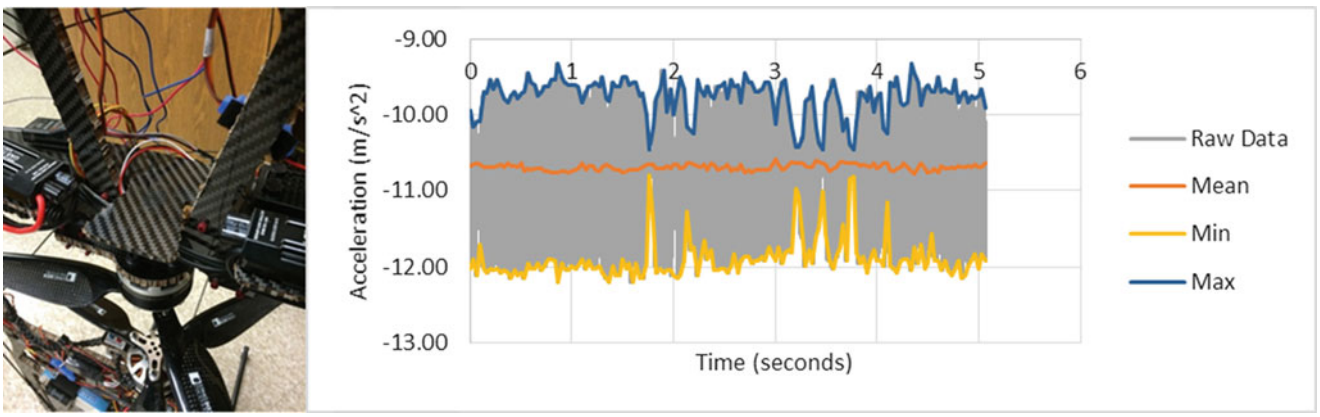

Fig. 16.8 Accelerometer placement on Phase II platform and data captured showing the raw, mean, maximum, and minimum values from the experimental testing

and approximately 5 s, or 50,670 points of data, worth of hovering flight was used. The mean, standard deviation, minimum, and maximum for the sum total of recorded accelerations are also shown in Table 16.5. Following the same regimen as Phase I, the means, minimums, and maximums for the video frame timescale are plotted overtop the raw accelerometer data, also shown in Fig. 16.8. The calculated means seems to vary random around the longer-range mean of −10.69 m/s^2, however, the minimum and maximum values appear to be more symmetrically disbursed around those plotted means. The greater and more sustained range of extreme acceleration values speaks to the amount of thrust being developed by the Phase II platform, as well as abrupt corrective flap-servo control inputs generated by the PI-values of the flight controller.

In furtherance of a more thorough vibration analysis, a series of Fast-Fourier Transforms were completed for both the Phases I and II platforms. The determination of major constituent frequencies for each set of accelerometer data was achieved through the use of four randomly-placed non-overlapping samples of 2^{12} data points. By comparing the resulting graphs against each other, fundamental frequencies could be identified. For Phase I, shown first in Fig. 16.9, the primary frequencies occur near 320, 630, 960, and 1280 Hz. For Phase II, shown second in Fig. 16.9, the dominant frequency is around 650 Hz.

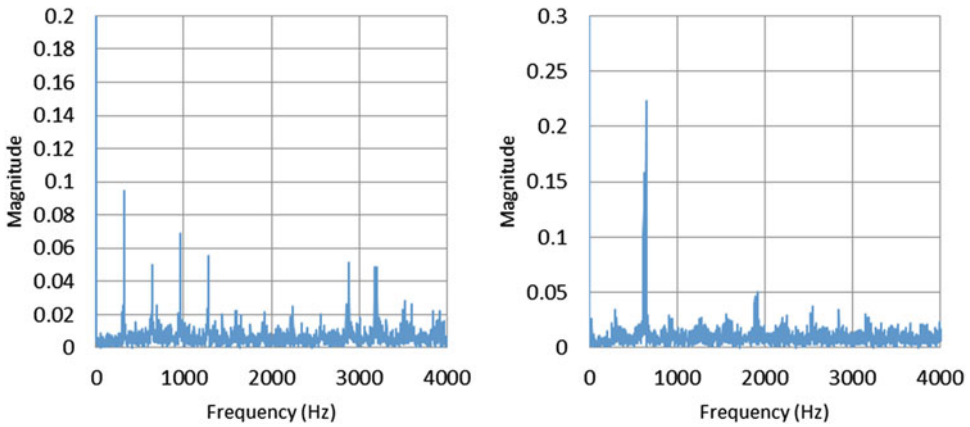

Fig. 16.9 Fast-Fourier transforms for Phases I and II accelerometer data

16.7 Conclusions

The ability for an unmanned platform to attached to a target surface and perch for an extended period of times is a necessary evolution in order to not only open new venues of operation, but also overcome the limitations of current battery chemistries. It has been shown that attachment via holding magnet greatly increases potential task duration and has the ability to effectively double measurement fidelity for onboard payloads. Both of these improvements are possible due to the lack of vibrations intrinsic to spinning props and turbulent airflows. Increased on-station time will benefit missions focusing on fixed-point and mobile surveillance, as well as longer-term monitoring and inspection applications with sensor payloads. The small and enclosed propulsive footprint emphasized by both of the presented platforms allows for close-proximity flying that is safer for indoor spaces and industrial environments. This combination of characteristics in an easy to deploy platform could also greatly reduce downtime by easing logistical requirements and enabling operation in harsher and traditionally inaccessible areas. Work still remains in refining magnetic-based perching and developing other attachment methodologies that can further accommodate unmanned platforms in more varied perching environments.

Acknowledgements Filing and processing of the patent application pertaining to this project was provided by the UND Office of Intellectual Property Commercialization and Economic Development (IPCED). This design project was further funded by IPCED through the ND Experimental Program to Stimulate Competitive Research (ND EPSCoR).

References

1. Briod, A., Kornatowski, P.M., Zufferey, J.-C., Floreano, D.: A collision resilient flying robot. J. Field Rob. **31**(4), 469–509 (2014)
2. Klaptocz, A., Briod, A., Daler, L., Zufferey, J.-C., Floreano, D.: Euler spring collision protection for flying robots. In: International Conference on Intelligent Robots and Systems (IROS), Tokyo, Japan, 2013
3. Briod, A., Klaptocz, A., Zufferey, J.-C., Floreano, D.: The AirBurr: a flying robot that can exploit collisions. In: International Conference on Complex Medical Engineering (CME), 2012 ICME, Kobe, Japan, 2012
4. Daler, L., Klaptocz, A., Briod, A., Sittie, M., Floreano, D.: A perching mechanism for flying robots using a fibre-based adhesive. In: ICRA 13, Karlsruhe, 2013
5. Kovac, M., Germann, J.M., Hürzeler, C., Siegwart, R., Floreano, D.: A perching mechanism for micro aerial vehicles. J. Micro-Nano Mechatron. **5**(3–4), 77–91 (2010)
6. Roberts, J.F., Zufferey, J.-C., Floreano, D.: Energy management for indoor hovering robots. In: IEEE/RSJ International Conference on Intelligent Robots and Systems (IROS), Nice, France, 2008
7. Semke, W.H., Swetich, W.J.: Attachment for robotic operations using unmanned aircraft. US Provisional Patent Application 62/138,702, filed with the US Patent & Trademark Office and foreign patent offices, 26 March 2015

Chapter 17
Experimental Modal Analysis of an Aircraft Fuselage Panel

Travis A. Wyen, Joshua J. Schoettelkotte, Ricardo A. Perez, and Thomas G. Eason

Abstract Hypersonic aircraft structures must operate in complex loading conditions and very high temperatures, making the design of a robust and reusable platform very challenging. An analytical and experimental test program was developed by the Air Force Research Laboratory (AFRL) and industry. The objective of the program is to review the design process of a thin skinned aircraft panel subjected to combined thermal-acoustic-mechanical loading, through a series of laboratory experiments at the AFRL's Structural Dynamics Laboratory.

This paper presents the results from a series of modal tests, performed to estimate the modal parameters of a hat-stiffened fuselage panel designed by industry. A comparison of the modal parameters of the panel, estimated from roving impact and a multiple input multiple output (MIMO) shaker test data of the panel is presented. Also, the variation in the natural frequencies and damping through various stages prior to the combined environment test is discussed.

Keywords Experimental modal analysis • Structural dynamics • Aircraft structure

17.1 Introduction

Typical modelling approaches superpose the worst possible loading conditions to obtain a conservative design. The use of this design paradigm to structures operating in extreme environments can lead to an extremely high structural mass, which could severely shorten the duration of a mission. On the other hand, less conservative approaches could lead to unacceptable uncertainties in the life prediction of the aircraft structure [1]. In order to develop modeling techniques that can lead to accurate predictions of the aircraft structure with a reduced structural mass, an analytical and experimental test program was developed by the Air Force Research Laboratory (AFRL) and industry. The objective of the program is to review the design process of a thin skinned aircraft panel subjected to combined thermal-acoustic-mechanical loading, through a series of laboratory experiments at the AFRL's Structural Dynamics Laboratory.

The focus of this paper is on a series of modal tests conducted to determine and characterize the natural frequencies, mode shapes, and damping of the panel. The modal parameters were obtained in the frequency band from 50 to 562 Hz, which is the frequency range of the acoustic loads that will be applied to the structure in the combined environment test.

A significant amount of instrumentation was installed on the panel. Modal tests of the article were conducted before and after the installation of instrumentation to assess the effect on the modal parameters of the specimen. Furthermore, the tests were performed with and without the load introduction fittings, shown attached to the panel in Fig. 17.1. All of these different tests were performed to help in the updating of the finite element model (FEM) of the panel. Although not included in this paper, another modal test was conducted after the panel was installed in the thermo-acoustic-mechanical test chamber. This data will be used as a baseline to evaluate the health of the panel as combined environment testing is conducted.

Two approaches were used to conduct the modal tests. An impact test using a roving hammer measurement method was initially used for preliminary damping estimates, to identify mode shapes of interest, and to determine excitation locations for shaker placement. The other approach was a shaker based multiple-input multiple-output (MIMO) method using a scanning laser Doppler vibrometer system. A detailed description of these tests will be provided in the following section.

T.A. Wyen (✉)
Experimental Validation Branch, Aerospace Systems Directorate, Air Force Research Laboratory, Wright-Patterson AFB, OH 45433, USA
e-mail: Travis.Wyen@us.af.mil

J.J. Schoettelkotte • R.A. Perez
Universal Technology Corporation, 1270 North Fairfield Road, Dayton, OH 45432, USA

T.G. Eason
Structural Sciences Center, Aerospace Systems Directorate, Air Force Research Laboratory, Wright-Patterson AFB, OH 45433, USA

J.M. Harvie, J. Baqersad (eds.), *Shock & Vibration, Aircraft/Aerospace, Energy Harvesting, Acoustics & Optics, Volume 9*,
Conference Proceedings of the Society for Experimental Mechanics Series, DOI 10.1007/978-3-319-54735-0_17

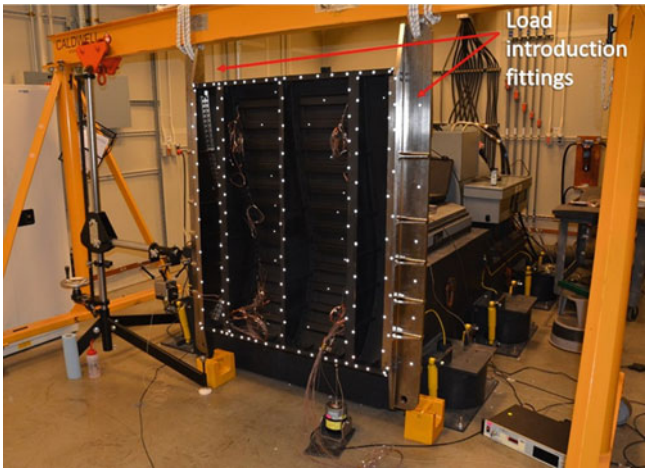

Fig. 17.1 Test specimen with load introduction fittings

The outline of this paper is as follows. Section 17.2 describes the test setup and modal parameter estimation procedures for the following four tests:

1. Impact hammer test of uninstrumented panel with load introduction fittings
2. Multiple-input-multiple-output (MIMO) test of uninstrumented panel with load introduction fittings
3. Multiple-input-multiple-output (MIMO) test of uninstrumented panel without load introduction fittings
4. Impact hammer test of instrumented panel with load introduction fittings

A discussion of the results, with a focus on changes in the modal parameters from test to test, is also presented in Sect. 17.2. Finally, a summary of the work presented will be provided in Sect. 17.3.

17.2 Test Setup and Modal Parameter Estimation

The objectives of this section is to describe the setup and procedure followed to conduct the tests listed in the Introduction. Information on the instrumentation, data acquisition, and other details are presented along with a description of the modal parameter estimation and some results.

The Vibrant Technology ME'ScopeVES® software package was used for data collection and to curve fit the FRFs to estimate the modal parameters of the panel. A brief description of the tools and procedure followed for the modal parameter estimation is included in this section. The following subsections follow the same order of the test list provided in the previous section.

17.2.1 Impact Hammer Test of Uninstrumented Panel with Load Introduction Fittings (Test I)

Initial impulse modal testing was conducted for the purpose of collecting response data from the as-delivered test article. The test data assisted in determining mode shapes, damping, modal frequencies, and determining excitation locations for shaker placement during the proceeding MIMO using the 3-D laser vibrometer system. Mode shapes computed from the finite element model (FEM) of the test article, built using Abaqus®, were also used as a guide for the selection of the location of the reference and response degrees-of-freedom (DOF) in the MIMO shaker test.

The test panel assembly was received with a minimal amount of instrumentation installed on surfaces inaccessible once the panel was assembled. Impulse testing using a roving impact method, with multiple stationary reference triaxial accelerometers, was chosen for initial testing to provide modal parameters of the first 20 structural modes. This information was used to check analytical prediction and complete preliminary model updates to be used for environmental (i.e., thermal, acoustic, and mechanical load) test predictions before any modifications to the structure were completed.

Table 17.1 Data acquisition parameters used for Test I

Number of samples	16,384
Time resolution	0.000488 s
Time block	8 s
Number of lines	8192
Frequency resolution	0.125 Hz
Frequency span	1020 Hz

The fully assembled aircraft fuselage panel with the load introduction end fittings was suspended from 5/8" diameter bungee cord from the crossbeam of a gantry crane as seen in Fig. 17.1. The bungee cord provides a "soft" mount that gives a near free-free boundary condition. The layout of the measurement grid on the outer mold line (OML) or skin of the test panel was determined from the FEM predicted mode shapes, as were the longeron, bulkhead, hat-stiffener, and load introduction structures. A total of 286 impact locations were chosen. From the impact locations, three reference DOF were chosen, one on the upper portion of the OML, another on the center bulkhead, and the third on the outboard bulkhead. A wire frame model was created in 3-D space using Nikon's MCAx II portable measurement system using the reference and impact locations. This model was imported into Vibrant Technologies ME'ScopeVES® software.

The data collection was performed using ME'ScopeVES® software with a National Instruments front end. The front end consisted of a PXI-1031 chassis, PXI-8109 embedded computer, and PXI-4472 dynamic signal acquisition modules. Three low-mass PCB 356A15 triaxial accelerometers were mounted at each of the reference locations. The nominal sensitivity of the accelerometers was 100 mV/g. A PCB 086C03 impact hammer was used to provide the impulse excitation, the hammer sensitivity was 9.82 mV/lbF. The hard nylon tip used provided a flat frequency output to approximately 1000 Hz. All sensors were powered using the PXI-4472 on-board IEPE output.

The data acquisition parameters shown in Table 17.1 were used throughout this particular test series.

Initially, driving point measurements and several preliminary measurements were acquired to check the input, the frequency response, to ensure that the reciprocity criteria was met, to check measurement coherence, and collect data for model scaling. The frequency response function and coherence measurement were recorded at each impact location. A total of three impact measurements were linearly averaged per point. The measurement was triggered using the impact hammer using a pre-trigger set at 100 samples. An exponential window was used on the accelerometer measurement to reduce leakage in the response transform, and a force window was used on the impact hammer measurement. The panel response for impacts on the skin tended to decay more quickly than for impact points on the bulkheads. The exponential window coefficient was modified during the data acquisition process on particular sections of the structure. A total of 2574 frequency response functions were successfully acquired. At the conclusion of the test, the first impact measurement point was reacquired for comparison purposes and the initial room temperature was compared to the end of test temperature.

The multi-reference curve fitting tools in ME'ScopeVES® were used: the Complex Mode Indicator Function (CMIF) was used to count resonance peaks, a multi-reference polynomial function was used to curve fit the portion of the FRFs up to 415 Hz, and the multi-reference complex exponential and stability diagram were used for modes at higher frequencies.

Shown in Fig. 17.2 are a few of the mode shapes obtained, representative of the different types of deformation over different frequencies. For instance, the mode shown in Fig. 17.2a is the first bending mode of the center bulkhead. As shown in Fig. 17.2b, the next mode shape features bending of the outer bulkheads, which are nominally equal, however, they are stiffer than the center bulkhead. Figure 17.2c shows a mode with bending of the top longeron as its dominant feature. At higher frequencies, the deformation ceases to be localized to a group of substructural members, instead, all substructures tend to have a similar contribution to the overall deformation. It is interesting to note that for the modes analyzed, the skin did not have a localized deformation, but seemed to be mostly driven by the deflections of the bulkheads and longerons.

It is well known that the use of an exponential window on the measurement data changes the apparent damping of the system [2]. ME'ScopeVES® accounts for this change to obtain the correct damping estimate. However, since the exponential window time constant was changed during the test, the modal estimation procedure was repeated using local curve fitting tools to obtain the correct damping values. Shown in Fig. 17.2 are estimates of the damping values obtained with the multi-reference curve fitter and the local polynomial fit. It should be noted that errors are expected in the multi-reference damping results since the exponential window varied among the data points. However, the error in the multi-reference results are well within the one and a half significant figures reported, and thus the multi-reference results agree with the local results. Since the impact results were mainly used for preliminary estimates of modal parameters, the effects of windowing the data were noted in the test data and not used for analytical model verification. The shape table with natural frequencies and damping estimates of all the modes extracted from the data is shown in Table A.1 in the Appendix.

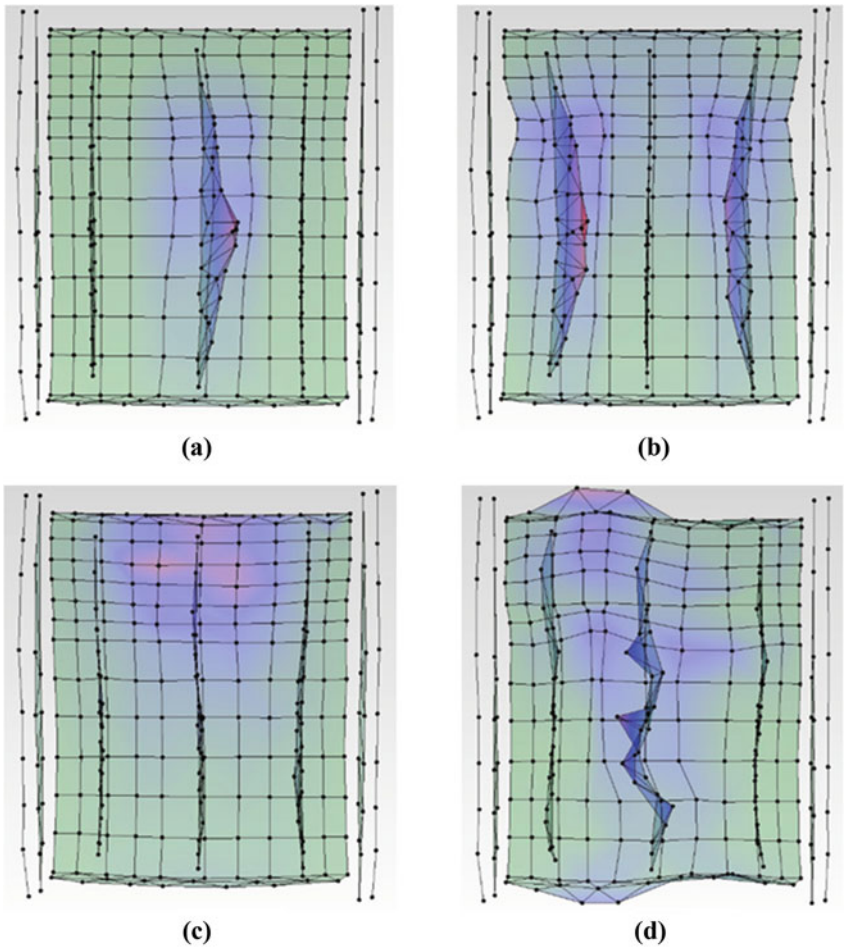

Fig. 17.2 Representative mode shapes of the uninstrumented panel with load introduction fittings estimated using impact hammer measurements. (**a**) $f = 89$ Hz, $\zeta = 0.20\%$, $\zeta_{local} = 0.20\%$; (**b**) $f = 103$ Hz, $\zeta = 0.25\%$, $\zeta_{local} = 0.25\%$; (**c**) $f = 127$ Hz, $\zeta = 0.45\%$, $\zeta_{local} = 0.45\%$; (**d**) $f = 410$ Hz, $\zeta = 0.30\%$, $\zeta_{local} = 0.30\%$

17.2.2 MIMO Test of Uninstrumented Panel with Load Introduction Fittings (Test II)

An additional modal test was conducted in the same condition (i.e., uninstrumented with load fittings installed) using shaker induced excitation and collecting response measurement via a 3-D scanning laser vibrometer system. The system used for this and all other shaker based modal testing was the Polytec® PSV-500-3D vibrometer. This system is able to measure both in-plane and out-of-plane motion of complicated parts using three separate scanning laser vibrometer sensor heads. Three measurements are made simultaneously from three different directions. From the known geometry of the test article, the x, y, and z velocity components are calculated from the angles of incidence of the three sensor heads. The system was also used to generated the random signal supplied to the shaker amplifiers, acquire the reference and response measurements, and create the geometric modal model of the test article. Three electrodynamic shakers were used to excite the modes of interest and acquire all data needed in a single scan.

Using data collected from the impact test, the laser system was arranged to acquire data on the backside of the test article since all areas of interest were in the line of sight of each laser. The FEM mesh was imported into the Polytec software and used to guide the selection of the scanning points. This feature was useful not only for model updating purposes, but also in the alignment of the scanning heads. A total of 323 points were determined to be sufficient to capture all modes of interest. Each point was marked with a retroflective "dot" to improve the return signal from the laser reflection of the test article surface. The scanning points and shaker location are shown in Fig. 17.3. The shakers were coupled to dynamic force sensors connected to the structure by a stinger. The skin shaker used was a Bruel & Kjaer (B&K) 4810 mini shaker powered with a B&K 2706 power amplifier. The outer bulkhead shaker used to excite the outer bulkhead was a Labworks ET-132 powered by

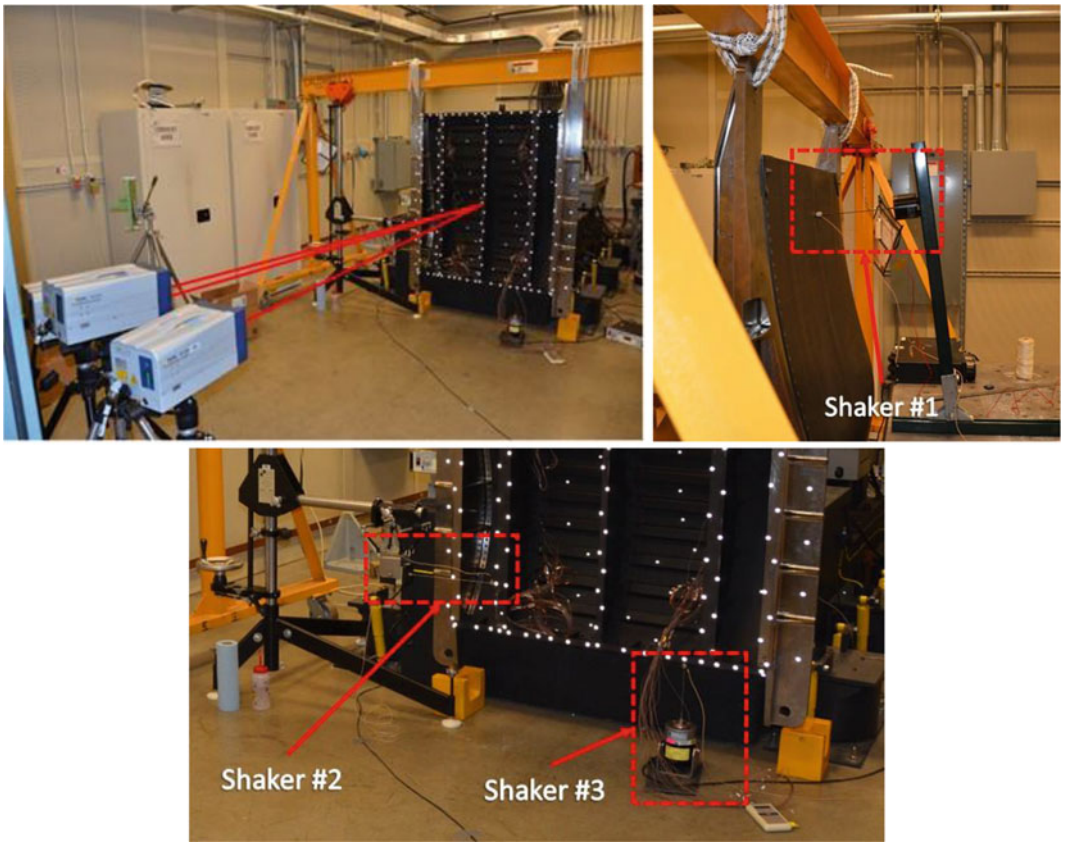

Fig. 17.3 3D-scanning laser vibrometer and panel with scanning points

Table 17.2 Data acquisition parameters for Test II

Excitation	White Noise
Window	Hanning
Number of Averages	30
FFT Lines	6400
Sample time	6.4 s
Bandwidth	50–1000 Hz
Resolution	156.25 mHz

a Labworks PA-138 amplifier. The lower longeron shaker used to excite the outer bulkhead was a Labworks ET-126 powered by a Labworks PA-138 amplifier. All of the dynamic force sensors used were PCB model 208B with a nominal sensitivity of 500 mV/lbF.

The acquisition parameters that were used to collect data are shown in Table 17.2. White noise excitation was used to allow the software to compare the individual inputs from the individual shakers. The modal test scan took over seventeen hours. The temperature was tracked using a standalone thermometer near the test article. The room temperature ranged from 68°F to 71°F during the test.

Most of the modal parameter estimation was performed using the multi-reference AF polynomial method with stability diagram. The modal parameters of modes with natural frequencies above 450 Hz were estimated using the local polynomial, as both multi-reference polynomial and multi-reference AF polynomial approaches failed to produce a good curve fitting of the FRFs in this frequency range. Shown in Fig. 17.4a are some representative modes shapes with their natural frequencies and damping estimates, obtained from Test I (left column) and Test II (right column). Clearly, the discrepancy in the natural frequencies and damping values between Tests I and II is small. The maximum relative difference is of 4.8% for the data shown in Fig. 17.4. The qualitative agreement between the mode shapes is also very good. A quantitative comparison of the mode shapes (e.g., MAC number computation) was not possible since the impact points from Test I and the scanned locations from Test II were not exactly the same. Interpolation from one response grid to another was not judged appropriate since both were relatively coarse. The shape table for the Test II data is shown in Table A.2(a) in the Appendix.

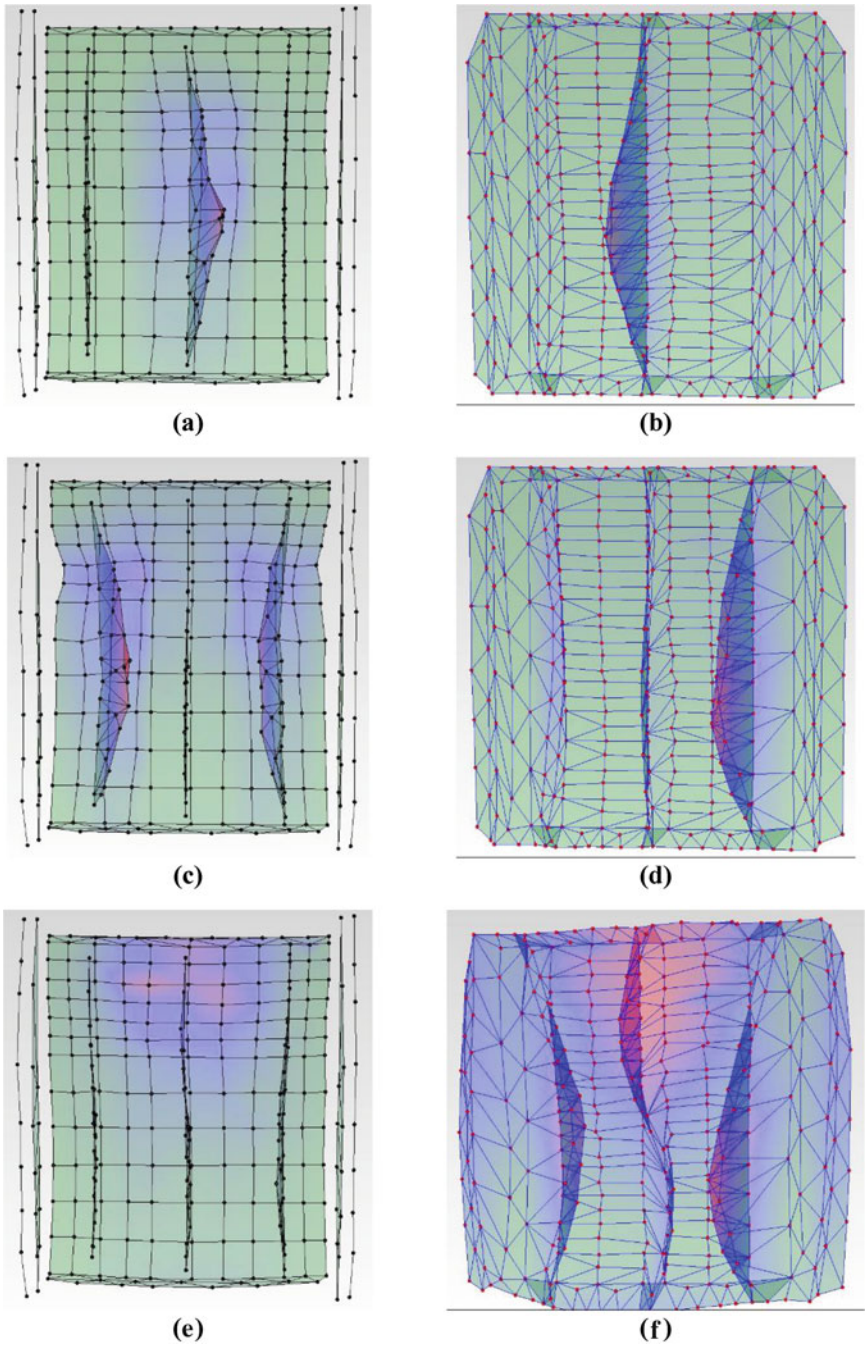

Fig. 17.4 Comparison between representative modes obtained from Test I (*left column*) and Test II (*right column*). (**a**) $f = 89$ Hz, $\zeta = 0.20\%$; (**b**) $f = 90$ Hz, $\zeta = 0.10\%$; (**c**); $f = 103$ Hz, $\zeta = 0.25\%$; (**d**) $f = 105$ Hz, $\zeta = 0.15\%$; (**e**) $f = 127$ Hz, $\zeta = 0.45\%$; (**f**) $f = 127$ Hz, $\zeta = 0.45\%$

17.2.3 MIMO Test of Uninstrumented Panel Without Load Introduction Fittings (Test III)

Following the removal of the load introduction fittings, a MIMO shaker test was conducted to evaluate the response of the panel. The panel was flipped in orientation from the first MIMO test and suspended with elastic cables. Cords were tied to fifty pound weights to prevent the article from swaying, and to square the back face of the panel with the scanning lasers.

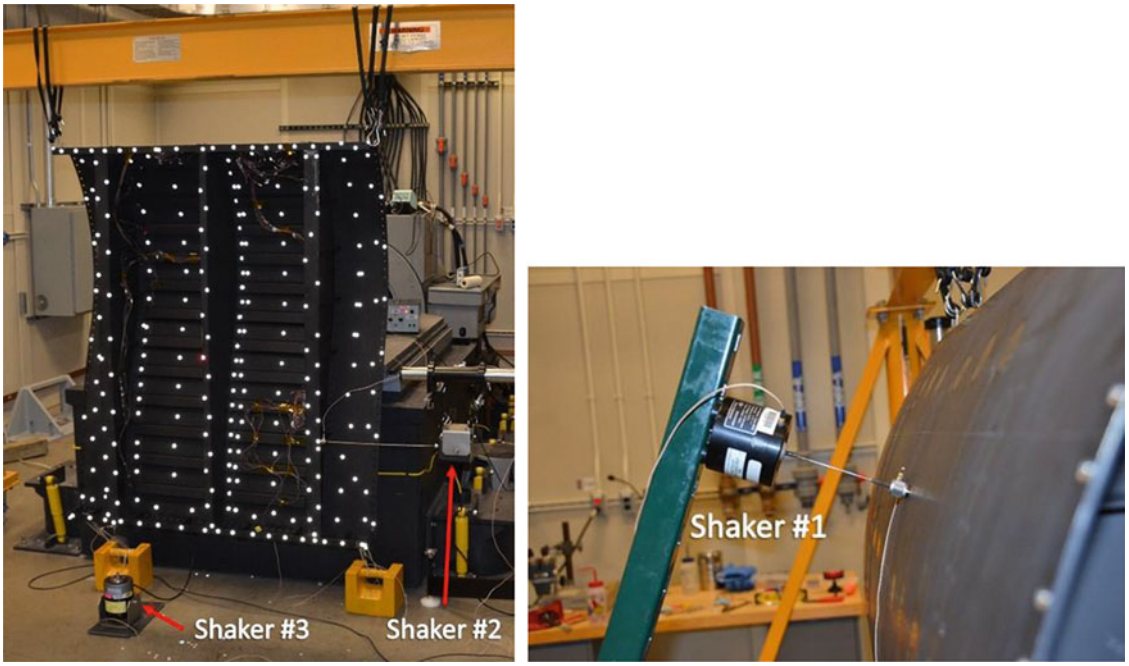

Fig. 17.5 Scanning points used for Test III

A 3-D alignment was performed with the Polytec scanning laser using the Nikon MCAx measurement arm. The precise alignment allowed for the same finite element model to be imported into the acquisition system again. Starting with the same scan points as in Test II, additional points were chosen to obtain more data on the thin skin and on the transition section, since a stiffness reduction in these sections was expected due to the absence of the load introduction fittings. A total of 256 points were scanned during this test. Following the procedure of Test II, three shakers were fixed to the article. Because the article was flipped, new reference points were added. Reference one was driven in the +Z direction. Reference two excited the upstream bulkhead in the –X direction. Finally, reference three excited in the +Y direction on the top longeron of the panel. The same shakers and amplifiers were used from the first MIMO test. Three PCB 208B force gauges with a nominal sensitivity of 500 mV/lbF were fixed to the reference points using M200 bond. Internal IEPE excitation was powered to each of the gauges from the Polytec data acquisition system. The nominal range of the PSV-500-3D scanning vibrometer was 10 mm/s. A Hanning window was applied to the linearly averaged data from the force gauges and 3-D vibrometer. The scan points and shaker locations are shown in Fig. 17.5.

The data sampling settings that were used on Test III are the same as Test II, shown in Table 17.2. White noise excitation was used with thirty averages per point. The test was run for a total time of fourteen hours. The temperature was tracked near the test article using a standalone thermometer, and it ranged from 65 to 68°F during the test.

Shown in Fig. 17.6 are some of the mode shapes estimated. The modal parameters were obtained using the multi-reference AF polynomial with stability diagram, except for the mode shown in Fig. 17.6d, which was obtained using the local polynomial. A satisfactory curve fit was not possible using the multi-reference AF polynomial for this mode. The modes shown in Fig. 17.6 illustrate the stiffening effect that the load introduction fittings have on the transition sections (i.e., skin sections between the outer bulkheads and the load introduction fittings). In the absence of the load introduction fittings the transition section has several localized modes, as the one shown in Fig. 17.6d. The natural frequency of the first bending mode of the center bulkhead, shown in Fig. 17.6a, was essentially unchanged. However, the natural frequency of the first bending mode of the outer bulkheads, shown in Fig. 17.6b decreased by 5%. This is explained by the loss of stiffness in the transition section when the load introduction fittings are not present. The shape table with the natural frequencies and damping of the modes extracted using the Test III data is shown in Table A.2(b) in the Appendix.

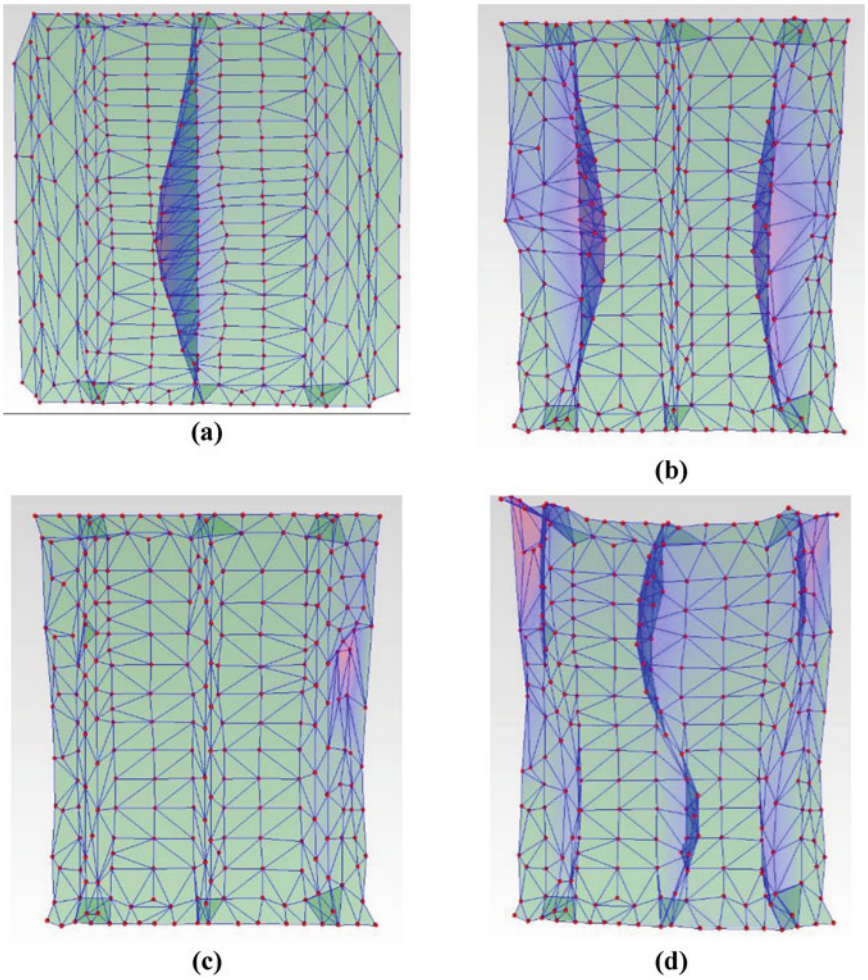

Fig. 17.6 Representative modes of uninstrumented panel without load introduction fittings. (**a**) $f = 90$ Hz, $\zeta = 0.15\%$; (**b**) $f = 100$ Hz, $\zeta = 0.15\%$; (**c**) $f = 146$ Hz, $\zeta = 0.10\%$; (**d**) $f = 158$ Hz, $\zeta = 0.35\%$

17.2.4 Impact Hammer Test of Instrumented Panel with Load Introduction Fittings (Test IV)

In preparation for the combined environment test, the panel was fitted with over 300 channels of instrumentation in the form of thermocouples and various types of strain gauges. In addition to the instrumentation, silicone heaters were installed on the end fittings to counter the thermal expansion of the panel during the combined environment testing. After the additional instrumentation was installed, a roving impact hammer test was conducted on the panel to estimate the frequency and damping shifts. The test article was suspended by the end fittings to create a free-free boundary condition using the same high strength bungee cord as in Test I. All of the instrumentation was hung on a frame built around the test article to characterize how the instrumentation is to be distributed in the combined environment testing. This is shown in Fig. 17.7. Approximately half of the original impact test points were obstructed by the instrumentation, this led to a total of 140 impact points being used instead of the original 286 points from Test I. The same three reference locations were found using the Nikon MCAx measurement arm and the original structure coordinates. The impact points that could be found on the panel were relabeled with the same numbering scheme according to the structure file. Specific points were disregarded to prevent damage to the instrumentation from impact testing.

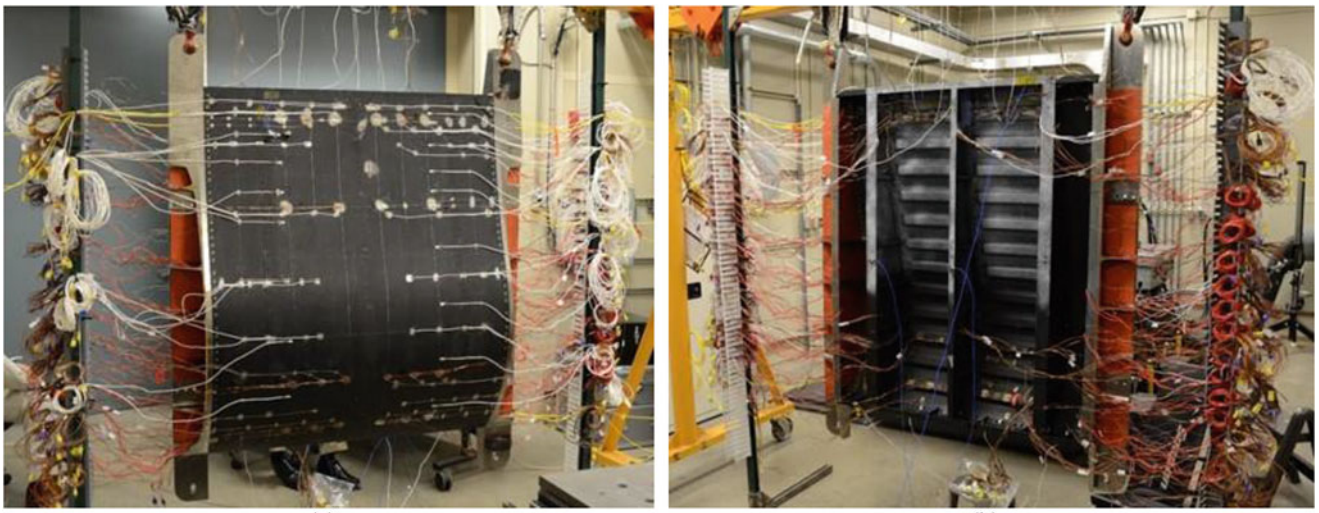

Fig. 17.7 Front and back views of the instrumented panel (**a**) Outer Mold Line of Test Panel, and (**b**) Inner Mold Line of Test Panel

Table 17.3 Data acquisition parameters for Test IV

Number of samples	16,384
Time resolution	0.000488 s
Time block	8 s
Number of lines	8192
Frequency resolution	0.122 Hz
Frequency span	1020 Hz

To conduct the roving impact test, all data acquisition was performed in the ME'ScopeVES software. A National Instruments PXIe-1062Q hybrid chassis was used in conjunction with a PXIe-4499 data acquisition card. Three low mass, triaxial (X, Y, Z) PCB accelerometers were placed at the reference locations. The nominal sensitivity of the accelerometers was 100 mV/g. Following the original impact test, the same degree of freedoms were kept. A PCB Hammer was used with a hard nylon tip to perform the impacts.

The test parameters are shown in Table 17.3. A total of four averages per point were measured. A pre-trigger of 20 samples was set after the impact was detected. A force window was applied to the impact signal after 15 samples and no window was used on the response measurement. A DC current offset removal option within the software was used to zero the response signal of the accelerometers before testing began. Each accelerometer sensitivity range was adjusted to 3.4 or 10 V depending on the impact direction to provide better resolution. This was performed manually based on the response of each point. The frequency response function (FRF), coherence, Fourier spectrum, and auto spectrum were all saved to the data block for each impact point. The time history was viewed after each average for any noise spikes, leakage, or double impacts; but, the time history was not saved.

The modal parameter estimation from the data obtained in Test IV was done with the local polynomial approach. A successful curve fitting of the FRFs was not possible with the multi-reference polynomial. A possible explanation is shifts in the natural frequencies due to the large variation in the room temperature (73–77.7°F) during the test. The natural frequencies, damping, and mode shapes, of a selected group of modes are shown in Fig. 17.8. The left column shows the modal parameters of the uninstrumented panel (Test II) and the modal parameters of the instrumented panel are shown in the right column. As expected, the instrumentation increased the damping values. The increase in damping was particularly large for the mode shown in Fig. 17.8f, which increased by 40%. The natural frequency of this mode decreased as well. The maximum deformation of this mode occurs near the top of the panel, which is also where a large percentage of the instrumentation was added, as seen in Fig. 17.7b. The shape table with the natural frequencies and damping estimated from the data of Test IV can be found in Table A.2(c) in the Appendix.

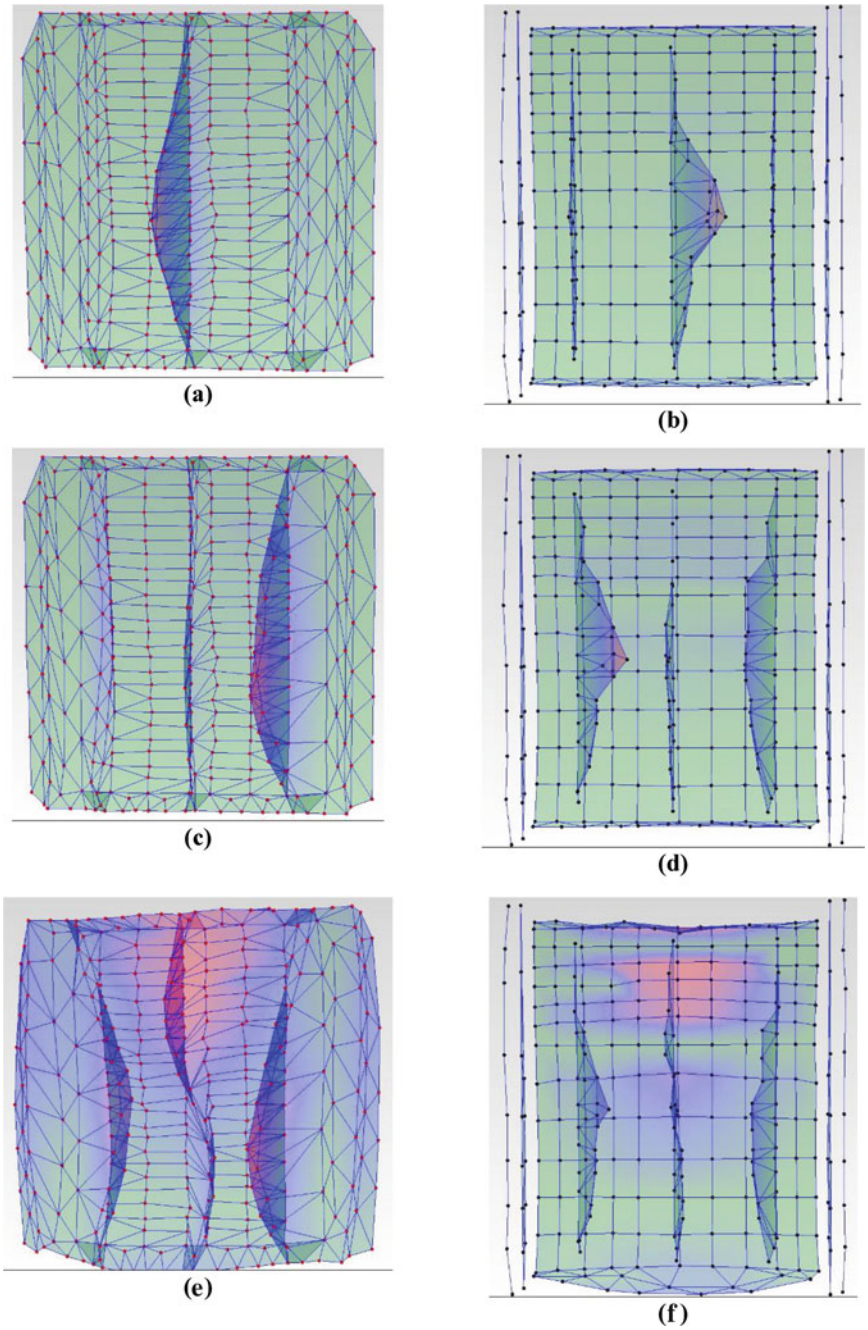

Fig. 17.8 Comparison between representative modes from Test II (*left column*) and Test IV (*right column*). (**a**) $f = 90$ Hz, $\zeta = 0.10\%$; (**b**) $f = 89$ Hz, $\zeta = 0.25\%$; (**c**) $f = 105$ Hz, $\zeta = 0.15\%$; (**d**) $f = 103$ Hz, $\zeta = 0.35\%$; (**e**) $f = 127$ Hz, $\zeta = 0.45\%$; (**f**) $f = 122$ Hz, $\zeta = 0.80\%$

17.3 Summary

A series of modal tests were performed on a hat-stiffened fuselage panel. Four modal tests were performed. The first was an impact hammer test of the fully assembled uninstrumented panel. The second test consisted of a MIMO shaker test of the article in the same conditions. For the third test, the load introduction fittings were removed and a MIMO shaker test performed to assess the effect of the load introduction fittings on the panel response. Finally, an impact hammer test of the fully assembled, instrumented panel was performed. As expected, the instrumentation increased the damping of most of the mode shapes. This information will be used to update a FEM of the article and to assess the state of the panel throughout the various stages of a combined environment test.

Acknowledgements The authors gratefully acknowledge the support of Dr. David Stargel, James Fillerup, and Dr. Jean-Luc Cambier of the Air Force Office of Scientific Research (AFOSR), LRIR numbers 12RB04COR and 15RQCOR244.

Appendix

Table A.1 Natural frequencies and damping from Test I obtained with, (a) the multi-reference polynomial curve fitter and (b) a local polynomial curve fitter

(a)				(b)			
Shape	Frequency (Hz)	Damping (%)	MPC	Shape	Frequency (Hz)	Damping (%)	MPC
1	23	3.50	0.15	1	24	0.90	0.41
2	89	0.20	0.75	2	89	0.20	0.94
3	103	0.25	0.72	3	103	0.25	0.99
4	107	0.25	0.62	4	107	0.20	0.99
5	127	0.45	0.83	5	127	0.45	0.98
6	165	0.15	0.84	6	165	0.10	0.98
7	184	0.20	0.51	7	184	0.15	0.96
8	187	0.20	0.48	8	187	0.30	0.83
9	197	0.10	0.70	9	197	0.10	0.97
10	203	0.30	0.21	10	203	0.30	0.92
11	213	0.40	0.81	11	213	0.40	0.95
12	254	0.90	0.53	12	255	0.85	0.56
13	273	0.10	0.76	13	273	0.10	0.94
14	274	0.40	0.88	14	276	0.35	0.76
15	296	0.20	0.50	15	296	0.20	0.79
16	301	0.25	0.60	16	301	0.30	0.26
17	334	0.10	0.77	17	334	0.10	0.91
18	345	0.45	0.84	18	345	0.50	0.87
19	364	1.20	0.80	19	364	0.60	0.76
20	381	0.15	0.67	20	381	0.15	0.96
21	390	0.15	0.42	21	390	0.15	0.94
22	394	0.10	0.13	22	395	0.15	0.41
23	410	0.30	0.68	23	410	0.30	0.84
24	415	0.15	0.50	24	415	0.15	0.67
25	419	0.30	0.27	25	419	0.30	0.06
26	425	0.30	0.45	26	425	0.30	0.21

Table A.2 Natural frequencies and damping from, (a) Test II, (b) Test III, and (c) Test IV

(a)				(b)				(c)			
Shape	Frequency (Hz)	Damping (%)	MPC	Shape	Frequency (Hz)	Damping (%)	MPC	Shape	Frequency (Hz)	Damping (%)	MPC
1	90	0.10	0.99	1	90	0.15	0.99	1	19.4	0.25	0.99
2	105	0.15	0.99	2	99.5	0.15	0.99	2	89	0.25	0.99
3	112	0.15	0.99	3	110	0.20	0.99	3	103	0.35	0.99
4	127	0.45	0.99	4	146	0.10	0.98	4	108	0.30	0.99
5	165	0.05	0.99	5	158	0.35	0.98	5	122	0.80	0.99
6	185	0.15	0.99	6	167	0.10	0.99	6	165	0.15	0.99
7	195	0.01	0.97	7	183	0.20	0.99	7	181	0.95	0.97
8	197	0.05	0.97	8	191	0.15	0.99	8	188	1.10	0.70
9	199	0.10	0.99	9	196	0.10	0.99	9	198	0.30	0.99
10	207	0.25	0.99	10	203	0.01	0.97	10	207	0.50	0.93
11	214	0.35	0.95	11	210	0.20	0.98	11	273	0.30	0.97
12	274	0.15	0.99	12	213	0.25	0.99	12	294	0.50	0.89
13	296	0.15	0.95	13	248	0.15	0.99	13	300	0.70	0.77
14	328	0.25	0.99	14	255	0.01	0.99	14	323	0.55	0.86
15	336	0.05	0.99	15	256	0.10	0.99	15	333	0.30	0.96
16	346	0.30	0.94					16	343	0.80	0.20
17	391	0.15	0.88					17	368	0.85	0.97
18	402	0.15	0.78					18	395	0.85	0.40
19	420	0.20	0.60					19	411	0.45	0.65

References

1. Zuchowski, B.: Predictive capability for hypersonic structural response and life prediction: phase II—detailed design of hypersonic cruise vehicle hot-structure. Technical Report, AFRL-RB-WP-TR-2012-0280, (2012)
2. Brown, D.L., Allemang, R.J., Phillips, A.W.: Forty years of use and abuse of impact testing: a practical guide to making good frf measurements. In: Proceedings from the Thirty-Forth International Modal Analysis Conference, Orlando, Florida, January (2015)

Chapter 18
Nonlinear Vibrations of a Functionally Graded Material Microbeam with Geometric Nonlinearity

Canan Uz and Ender Cigeroglu

Abstract In this paper, nonlinear vibration analysis of micro scale functionally graded material (FGM) beams with geometric nonlinearity due to large deflection is studied using modified couple stress theory (MCST). MCST is a nonlocal elasticity theory which includes a material length scale parameter since the size of an atomic microstructure becomes comparable to the length of the microbeam. Equations of motion of the micro scale FGM beam are obtained by using Hamilton's principle. Nonlinear free vibrations of the FGM microbeam with simply supported boundary conditions is investigated where the effect of the length scale parameter on the nonlinear natural frequencies of the microbeam is studied. The nonlinear partial differential equations of motion are converted into nonlinear ordinary differential equations by using Galerkin's Method. By using describing function method (DFM), a set of nonlinear algebraic equations are obtained which are solved by an iterative eigenvalue solver.

Keywords Functionally graded material microbeam • Modified couple stress theory • Euler–Bernoulli beam • Describing function method • Nonlinear natural frequency

18.1 Introduction

Use of FGM microbeams has been increasing in microelectromechanical and biomechanical devices, micro sensors and actuators, and atomic force microscopes [1–3]. Gradual spatial change of the mechanical and thermal properties of the microbeam is provided with composite FGM structure along a certain direction, especially thickness direction [4]. Deformation of FGM microbeams is studied by several researchers to obtain high performance and sensitivity in micro scale applications. Experiments exhibit that in micro scale, atomic and molecular forces become comparable with static and vibration behavior of the beams [5]. The size dependent behavior can be modeled properly by applying nonlocal elasticity and continuum theories [6]. Atomic bonds highly resist to deformation which act as a material parameter called length scale parameter in literature. Strong atomic forces and interactions increase stiffness of the beam. The stiffness increase leads to raise of nonlinear natural frequency of the FGM microbeams considering large deformations. Nonlocal elasticity is applied in many studies for the vibration analysis of microbeams where classical continuum theories underestimate the stiffness of the microbeam, since actual size scale is disregarded in derivations [6]. It should be noted that since wavelength is smaller at high frequencies, small scale effect becomes more significant at high frequencies of vibration. The natural frequency of the beam can be captured correctly, if equations of motion are derived utilizing nonlocal continuum theories which can be exemplified as nonlocal elasticity [7], strain gradient theory [5] and modified couple stress theory [8, 9]. Modified couple stress theory (MCST), on which the current study is based, relates the couple stress tensor to the symmetric rotational gradient with a micro length scale parameter [9]. In [10], linear vibration of FGM microbeams is studied with a variable length scale parameter based on MCST and authors predicted static deformation, natural frequencies and mode shapes of the microbeam by using three different beam theories in. Linear dynamics of microbeams is also analyzed in [11–13]. Nonlinear vibration of FGM beams based on EBBT is presented in [14]. The studies analyzing nonlinear vibration of microbeams based on Timoshenko beam theory can be found in [15, 16].

In this paper, nonlinear free vibrations of a functionally graded material (FGM) microbeam is studied considering the effect of geometric nonlinearity. The present work is based on Euler–Bernoulli beam theory (EBBT), von Karman geometric nonlinearity, and modified couple stress theory (MCST). FGM beam is not isotropic and homogeneous, where material properties (i.e. elastic modulus, mass density, Poisson's ratio) are defined with power law distribution through thickness.

C. Uz • E. Cigeroglu (✉)
Department of Mechanical Engineering, Middle East Technical University, Ankara 06800, Turkey
e-mail: ender@metu.edu.tr

J.M. Harvie, J. Baqersad (eds.), *Shock & Vibration, Aircraft/Aerospace, Energy Harvesting, Acoustics & Optics, Volume 9*,
Conference Proceedings of the Society for Experimental Mechanics Series, DOI 10.1007/978-3-319-54735-0_18

The governing partial differential equation of motion is derived by using Hamilton's principle. Galerkin's method is used to discretize the partial differential equations of motion into a set of ordinary differential equations. Describing function method (DFM) is applied with multiple trial functions to convert the nonlinear differential equations of motion into a set of nonlinear algebraic equations, which is solved by using an iterative eigenvalue solver. Using DFM, nonlinear force can be defined as a nonlinear stiffness matrix multiplied by displacement vector which allows to identify the coupling between trial functions [17]. The effects of material property distribution index and micro length scale parameter on the nonlinear natural frequencies of the FGM microbeam are studied.

18.2 Mathematical Modeling

An FGM microbeam of length L, thickness h, cross-section A, Young's modulus $E(z)$, density $\rho(z)$, Poisson's ratio $\nu(z)$ is shown in Fig. 18.1. Since material properties vary in thickness direction, Young's modulus, density and Poisson's ratio are functions of z axis. The cross-section is rectangular and the width is denoted by b. The beam is 100% metal at upper surface ($z = h/2$) and 100% ceramic at lower surface ($z = -h/2$). Material property distribution according to power law distribution can be defined as follows

$$E(z) = (E_m - E_c)\left(\frac{z}{h} + \frac{1}{2}\right)^k + E_c, \tag{18.1}$$

$$\nu(z) = (\nu_m - \nu_c)\left(\frac{z}{h} + \frac{1}{2}\right)^k + \nu_c, \tag{18.2}$$

$$\rho(z) = (\rho_m - \rho_c)\left(\frac{z}{h} + \frac{1}{2}\right)^k + \rho_c, \tag{18.3}$$

where, subscripts m and c denote metal and ceramic phases, respectively. Distribution of metal and ceramic volume fraction is denoted by exponent k.

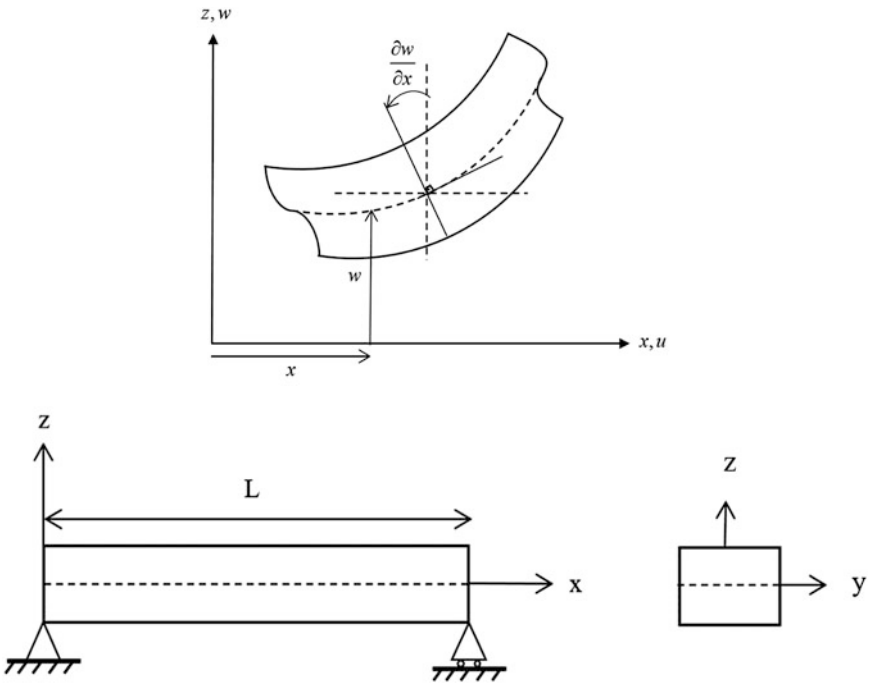

Fig. 18.1 Model of FGM Euler–Bernoulli microbeam and deformed shape

Strain energy based on MCST is given as [10]

$$U = \frac{1}{2}\int_V \left(\sigma_{ij}\varepsilon_{ij} + m_{ij}\chi_{ij}\right) dV, \tag{18.4}$$

where, V is volume, σ_{ij} represents Cauchy stress tensor, ε_{ij} is strain tensor, m_{ij} represents deviatoric couple stress tensor, and χ_{ij} stands for symmetric curvature tensor. Strain tensor is defined as follows

$$\varepsilon_{ij} = \frac{1}{2}\left(u_{i,j} + u_{j,i}\right), \tag{18.5}$$

$$\varepsilon_{ij} = \frac{1}{2}\left(e_{ipq}\varepsilon_{qj,p} + e_{jpq}\varepsilon_{qi,p}\right), \tag{18.6}$$

where, u in Eq. (18.5) represents the displacement vector, e_{ipq} stands for alternating tensor, and comma is used for differentiation notation. Constitutive relations in terms of material properties for linear isotropic material can be expressed as

$$\sigma_{ij} = 2\mu\varepsilon_{ij} + \lambda\delta_{ij}\varepsilon_{kk}, \tag{18.7}$$

$$m_{ij} = 2\mu l^2\chi_{ij}, \tag{18.8}$$

λ and μ are Lame's parameters defined as

$$\lambda = \frac{E\nu}{(1+\nu)(1-2\nu)}, \quad \mu = \frac{E}{2(1+\nu)}, \tag{18.9}$$

where, E is Young's modulus and ν is Poisson's ratio. l in Eq. (18.8) is the material length scale parameter related with symmetric curvature tensor and to denote the couple stress in microbeams and it is assumed as constant through thickness in the present study.

Displacement field of a beam based on EBBT can be expressed as follows

$$\begin{aligned} u_1(x,z,t) &= u(x,t) - z\tfrac{\partial w}{\partial x}, \\ u_2(x,z,t) &= 0, \\ u_3(x,z,t) &= w(x,t), \end{aligned} \tag{18.10}$$

where, $u(x,t)$ and $w(x,t)$ are axial and transverse displacements of location x at the mid-plane at time t, in x and z directions, respectively. Strain tensor, utilizing Von Karman nonlinear strain-displacement relation, and symmetric curvature tensor, can be defined as

$$\varepsilon_{xx} = \frac{\partial u_1}{\partial x} + \frac{1}{2}\left(\frac{\partial u_3}{\partial x}\right)^2 = \frac{\partial u}{\partial x} - z\frac{\partial^2 w}{\partial x^2} + \frac{1}{2}\left(\frac{\partial w}{\partial x}\right)^2, \tag{18.11}$$

$$\chi_{xy} = -\frac{1}{2}\left(\frac{\partial^2 w}{\partial x^2}\right). \tag{18.12}$$

Then, by substituting Eqs. (18.11) and (18.12) into Eqs. (18.7) and (18.8), respectively, stress tensors can be expressed as follows

$$\sigma_{xx} = (2\mu + \lambda)\left(\frac{\partial u}{\partial x} - z\frac{\partial^2 w}{\partial x^2} + \frac{1}{2}\left(\frac{\partial w}{\partial x}\right)^2\right), \tag{18.13}$$

$$m_{xy} = -\mu l^2\left(\frac{\partial^2 w}{\partial x^2}\right). \tag{18.14}$$

Strain energy, U, and kinetic energy, T, by inserting stress and strain tensors can be obtained as

$$U = \frac{1}{2}\int_0^L \int_A \left(\sigma_{ij}\varepsilon_{ij} + m_{ij}\chi_{ij}\right) dAdx = \frac{1}{2}\int_0^L \int_A \left\{\sigma_{xx}\left(\frac{\partial u}{\partial x} - z\frac{\partial^2 w}{\partial x^2} + \frac{1}{2}\left(\frac{\partial w}{\partial x}\right)^2\right) + m_{xy}\left(\frac{\partial^2 w}{\partial x^2}\right)\right\} dAdx, \tag{18.15}$$

$$T = \frac{1}{2}\int_0^L \int_A \rho\left\{\left(\frac{\partial u}{\partial t} - z\frac{\partial^2 w}{\partial x \partial t}\right)^2 + \left(\frac{\partial w}{\partial t}\right)^2\right\} dAdx = \frac{1}{2}\int_0^L \int_A \left\{I_1\left(\frac{\partial u}{\partial t}\right)^2 + I_1\left(\frac{\partial w}{\partial t}\right)^2 - 2I_2\frac{\partial u}{\partial t}\frac{\partial^2 w}{\partial x \partial t} + I_3\left(\frac{\partial^2 w}{\partial x \partial t}\right)^2\right\}, \tag{18.16}$$

where, ρ is mass density. I_1, I_2 and I_3 stand for mass inertia terms and they are given as follows

$$\{I_1, I_2, I_3,\} = \int_{-h/2}^{h/2} \rho(z)\left\{1, z, z^2\right\} bdz. \tag{18.17}$$

$$N_x = \int_A \sigma_{xx} dA = A_{11}\left[\frac{\partial u}{\partial x} + \frac{1}{2}\left(\frac{\partial w}{\partial x}\right)^2\right] - B_{11}\frac{\partial^2 w}{\partial x^2}, \tag{18.18}$$

$$M_x = \int_A \sigma_{xx} z dA = B_{11}\left[\frac{\partial u}{\partial x} + \frac{1}{2}\left(\frac{\partial w}{\partial x}\right)^2\right] - D_{11}\frac{\partial^2 w}{\partial x^2}, \tag{18.19}$$

$$Y_{xy} = \int_A m_{xy} dA = -l^2 A_{55}\left(\frac{\partial^2 w}{\partial x^2}\right), \tag{18.20}$$

where, A_{11}, B_{11}, D_{11}, and A_{55} are elasticity related terms and given by

$$\{A_{11}, B_{11}, D_{11},\} = \int_{-h/2}^{h/2} \frac{E(z)\left(1 - \nu(z)\right)}{\left(1 + \nu(z)\right)\left(1 - 2\nu(z)\right)}\left\{1, z, z^2\right\} bdz, \tag{18.21}$$

$$A_{55} = \int_{-h/2}^{h/2} \frac{E(z)}{2\left(1 + \nu(z)\right)} bdz. \tag{18.22}$$

The strain energy can be expressed in terms of N_x, M_x, and Y_{xy} as

$$U = \frac{1}{2}\int_0^L \left\{N_x\left(\frac{\partial u}{\partial x} + \frac{1}{2}\left(\frac{\partial w}{\partial x}\right)^2\right) + M_x\left(\frac{\partial^2 w}{\partial x^2}\right) - Y_{xy}\left(\frac{\partial^2 w}{\partial x^2}\right)\right\}. \tag{18.23}$$

Hamilton's principle is defined by the integral below

$$\delta\int_{t_0}^{t_1} (T - U + W_{ext})\, dt = 0. \tag{18.24}$$

Determining variation of u and w, applying integration by parts and setting the terms multiplied by δu and δw equal to zero, governing partial differential equations of motion are derived as

$$\frac{\partial N_x}{\partial x} = I_1\frac{\partial^2 u}{\partial t^2} - I_2\frac{\partial^3 w}{\partial x \partial t^2}, \tag{18.25}$$

$$\frac{\partial}{\partial x}\left(N_x\frac{\partial w}{\partial x}\right) + \frac{\partial^2 M_x}{\partial x^2} + \frac{\partial^2 Y_{xy}}{\partial x^2} = I_1\frac{\partial^2 w}{\partial t^2} - I_2\frac{\partial^2 u}{\partial x \partial t^2} + I_3\frac{\partial^4 w}{\partial x^2 \partial t^2}. \tag{18.26}$$

Neglecting axial inertia in Eqs. (18.25) and (18.26), one gets the following expression

$$\frac{\partial u}{\partial x} = \frac{1}{A_{11}}\left[B_{11}\frac{\partial^2 w}{\partial x^2} - A_{11}\left(\frac{1}{2}\left(\frac{\partial w}{\partial x}\right)^2\right) - I_2\frac{\partial^2 w}{\partial t^2}\right], \tag{18.27}$$

Integrating (Eq. 18.27) with respect to x and applying the simply supported geometric boundary conditions; $u(0) = 0$ and $u(L) = 0$ gives

$$u|_{x=0,L} = \int_0^L \left[\frac{B_{11}}{A_{11}}\frac{\partial^2 w}{\partial x^2} - \left(\frac{1}{2}\left(\frac{\partial w}{\partial x}\right)^2\right) - \frac{I_2}{A_{11}}\frac{\partial^2 w}{\partial t^2}\right] = 0. \tag{18.28}$$

Substituting Eq. (18.27) into Eq. (18.19) gives

$$M_x = \frac{{B_{11}}^2}{A_{11}}\frac{\partial^2 w}{\partial x^2} - \frac{B_{11}}{A_{11}}I_2\frac{\partial^2 w}{\partial t^2} - D_{11}\frac{\partial^2 w}{\partial x^2}. \tag{18.29}$$

Finally, the governing equation of motion for free vibration of an FGM microbeam considering geometric nonlinearity is obtained as

$$\left(l^2 A_{55} - \left(\frac{{B_{11}}^2}{A_{11}} - D_{11}\right)\right)\frac{\partial^4 w}{\partial x^4} + I_1\frac{\partial^2 w}{\partial t^2} + I_3\frac{\partial^4 w}{\partial x^2 \partial t^2} = \left\{\frac{A_{11}+B_{11}}{L}\int_0^L \left(\frac{1}{2}\left(\frac{\partial w}{\partial x}\right)^2 - \frac{B_{11}}{A_{11}}\frac{\partial^2 w}{\partial x^2}\right)dx\right\}\frac{\partial^2 w}{\partial x^2}. \tag{18.30}$$

18.3 Solution Method

Using expansion theorem, displacement of the beam can be obtained as follows

$$w(x,t) = \sum_{j=1}^{n} W_j(t)\phi_j(x), \tag{18.31}$$

where, $W_j(t)$ is the j^{th} generalized coordinate and $\phi_j(x)$ is the j^{th} trial function and in this study eigenfunctions of a simply supported linear beam are used and they are given as

$$\phi_j(x) = \sin\left(\frac{j\pi x}{L}\right), \quad j = 1, ..., n. \tag{18.32}$$

Substituting this into Eq. (18.30), multiplying both sides by $\phi_r(x)$ and integrating over the domain, the following nonlinear ordinary differential equations of motion in terms of $W_j(t)$ are obtained for $j = 1, \ldots, n$

$$\begin{aligned}&\left(I_1 + \frac{I_3\pi^2 j^2}{L^2}\right)\frac{d^2 W_j(t)}{dt^2} + \left[l^2 A_{55} - \left(\frac{{B_{11}}^2}{A_{11}} - D_{11}\right)\right]\frac{\pi^4 j^4}{L^4}W_j(t)\\ &+ \frac{(A_{11}+B_{11})\pi^4 j^2}{4L^4}W_j(t)\left(\sum_{r=1}^{n} r^2 {W_r}^2(t)\right) + \frac{2(A_{11}+B_{11})\pi^4 B_{11} j^2}{\pi A_{11} L^4}W_j(t)\left(\sum_{r=1}^{n} r W_r(t)\right) = 0\end{aligned} \tag{18.33}$$

The number of differential equations of motion is n and the last two terms are the nonlinear terms. Boundary conditions for a simply supported beam (hinged-hinged, H–H ends) can be written as follows

$$W(0) = W(L) = 0, \tag{18.34}$$

$$\left.\frac{d^2 W}{dx^2}\right|_{x=0} = \left.\frac{d^2 W}{dx^2}\right|_{x=L} = 0, \tag{18.35}$$

Assuming a single harmonic solution, $W(t)$ can be written as follows using a single harmonic representation

$$W_j(t) = a_j \sin(\omega t), \tag{18.36}$$

where a_j is the modal coefficient of the j^{th} mode. Substituting this into Eq. (18.33), the following discretized nonlinear algebraic equations are obtained

$$\left[l^2 A_{55} - \left(\frac{{B_{11}}^2}{A_{11}} - D_{11}\right)\right]\frac{\pi^4 j^4}{L^4} a_j - \omega^2\left(I_1 + \frac{I_3 \pi^2 j^2}{L^2}\right) a_j + \frac{(A_{11}+B_{11})\,\pi^4 j^2}{4L^4}{a_j}^3 + \frac{2\,(A_{11}+B_{11})\,\pi^4 B_{11} j^2}{\pi A_{11} L^4}{a_j}^2 = 0. \tag{18.37}$$

In Eq. (18.37), coefficient of a_j in the third term denotes geometric nonlinearity and the coefficient of a_j in the fourth term represents the nonlinear effect due to FGM which results in quadratic nonlinearity. Substituting this into Eq. (18.33), and applying DFM, which is developed by Tanrikulu et al. [17], the following set of nonlinear algebraic equations are obtained

$$\left(\mathbf{K} + \mathbf{K_{nl}} - \omega^2 \mathbf{M}\right) \cdot \mathbf{x} = 0, \tag{18.38}$$

where $\mathbf{M}$, $\mathbf{K}$, and $\mathbf{K_{nl}}$ represent the mass matrix, linear stiffness matrix and the displacement dependent nonlinear stiffness matrix associated with geometric and material nonlinearities, respectively and $\mathbf{x}$ is the vector of modal coefficients. In explicit form, matrices can be expressed as

$$\mathbf{M}_{n\times n} = \begin{bmatrix} I_1 + \frac{I_3\pi^2}{L^2} & & 0 \\ & \ddots & \\ 0 & & I_1 + n^2\frac{I_3\pi^2}{L^2} \end{bmatrix}, \tag{18.39}$$

$$\mathbf{K}_{n\times n} = \begin{bmatrix} \left[l^2 A_{55} - \left(\frac{{B_{11}}^2}{A_{11}} - D_{11}\right)\right]\frac{\pi^4}{L^4} & & 0 \\ & \ddots & \\ 0 & & n^4\left[l^2 A_{55} - \left(\frac{{B_{11}}^2}{A_{11}} - D_{11}\right)\right]\frac{\pi^4}{L^4} \end{bmatrix}. \tag{18.40}$$

Both mass and stiffness matrices given by Eqs. (18.39) and (18.40) are diagonal. Using describing function method, details of which can be found in [17], nonlinear internal forcing vector can be written as a displacement dependent matrix multiplied by a displacement vector. This displacement dependent matrix is the nonlinear stiffness matrix which can be obtained easily due to the use of DFM instead of the harmonic balance method (HBM). By using DFM, nonlinearity matrix can be obtained as follows

$$\mathbf{K_{nl}} = \frac{3\,(A_{11}+B_{11})\,\pi^4}{16L^4}\sum_{j=1}^{n}\begin{bmatrix} j^2|a_j|^2 & & 0 \\ & \ddots & \\ 0 & & n^2 j^2 |a_j|^2 \end{bmatrix}. \tag{18.41}$$

The nonlinearity matrix is a diagonal matrix; hence, there is no coupling between the trial functions. As a result of this, each nonlinear algebraic equation can be solved separately and in case one is after only a single mode of vibrations a single trial function is sufficient which is also observed in [18]. Nonlinear equations are uncoupled for each trial function and each one of them can be solved independent of the other equations. Hence, an expression for the variation of nonlinear fundamental natural frequency of FGM microbeam is derived analytically. The nonlinear algebraic equation using a single trial function can be obtained as

$$-{\omega_n}^2 + 1 + \frac{3}{16}\overline{a}_1^2 = 0, \tag{18.42}$$

$${\overline{a}_1}^2 = \frac{(A_{11}+B_{11})}{l^2 A_{55} - \left(\frac{{B_{11}}^2}{A_{11}} - D_{11}\right)}{a_1}^2, \tag{18.43}$$

which can be solved analytically for the normalized modal coefficient $\overline{a}_1$ and the expression for the nonlinear natural frequency as a function of the maximum vibration amplitude is obtained as

$$\omega_n = \sqrt{1 + \frac{3}{16}\overline{a}_1^2}, \tag{18.44}$$

where a_1 is the normalized maximum vibration amplitude. However, it should be noted that even an analytical solution for the nonlinear natural frequency is obtained, due to the application of DFM this result is not exact and it can be considered as an approximate analytical solution.

18.4 Results

In order to study nonlinear free vibration of the FGM microbeam, metallic and ceramic components of composite structure is assigned using aluminum (Al) and ceramic (SiC) and the following material properties are used in the solution: $E_m = 70$ GPa, $\nu_m = 0.3$, $\rho_m = 2700$ kg/m^3 for aluminum and $E_c = 427$ GPa, $\nu_m = 0.17$, $\rho_m = 3100$ kg/m^3 for ceramic. Experimental value of the length scale parameter is determined by Lam et al. as 17.6 μm [5]. In this paper, length scale parameter is set to 15 μm in the calculations.

Table 18.1 shows comparisons of the dimensionless linear frequencies obtained from the current analysis with the results given in [10]. Dimensionless linear natural frequency is obtained as $\omega_l = \Omega L\sqrt{I_{10}/A_{110}}$; where, Ω is the linear natural frequency, I_{10} and A_{110} are values of I_1 and A_{11} calculated by considering a homogeneous metal beam, respectively. The results given are close to each other and the difference in the present study is due to the fact that Timoshenko beam theory is used in [10, 11]. In Fig. 18.2, variation of dimensionless linear natural frequency with respect to h/l, dimensionless length scale parameter, is compared to the result available in [10] for $L/h = 10$, $k = 2$, $l = 15$ μm. Results obtained are very similar to the ones given in [10], the slight difference is due to the beam theory used.

In Fig. 18.3, the variation of the nonlinear natural frequency normalized with respect to the linear one as a function of the normalized maximum vibration amplitude (i.e. normalized modal coefficient) for different values of dimensionless length scale parameter, h/l, is given for $k = 2$ and $L/h = 20$. In the results presented, CBT represents classical beam theory obtained by neglecting length scale parameter. It is observed that increase in dimensionless length scale parameter leads to increase in the normalized nonlinear natural frequency at a given vibration amplitude.

Figure 18.4 shows the variation of normalized nonlinear natural frequency as a function of normalized maximum vibration amplitude for different values of material property distribution index, k. It is seen that, normalized nonlinear natural frequency increases as the material property distribution index increases at a given vibration amplitude. This is an expected result, since the composition of metal increases in the FGM microbeam, effective elastic modulus also increases which results in an increase in the natural frequency.

In Fig. 18.5, the variation of normalized nonlinear natural frequency as a function of normalized maximum vibration amplitude is compared with the results by digitizing the figure given in [16] for $h/l = 3$, $k = 2$ and $L/h = 20$. It can be observed that, the results are close to each other for $L/h = 20$; since Euler–Bernoulli and Timoshenko beam theory are in good agreement for the assumed beam length to thickness ratio.

18.5 Conclusion

In this paper, nonlinear free vibrations of an FGM microbeam based on MCST is studied. EBBT is used as the beam theory and the nonlinear partial differential equations of motion due to von Karman geometric nonlinearity are derived by utilizing Hamilton's principle. The nonlinear partial differential equations are converted into a set of nonlinear ordinary

Table 18.1 Comparison of the dimensionless natural frequencies of FGM microbeam with $L/h = 10$, $l = 15$ μm, $h/l = 2$, $b/h = 2$ based on EBBT and MCST for different, k, material property distribution index

Mode		Ceramic	$k = 0.6$	$k = 1.2$	$k = 2$	Metal
First	[10]	0.8538	0.6084	0.5469	0.5099	0.3797
	[11]	0.8538	0.6084	0.5470	0.5100	0.3863
	Present study	0.8531	0.5987	0.5348	0.4931	0.3361

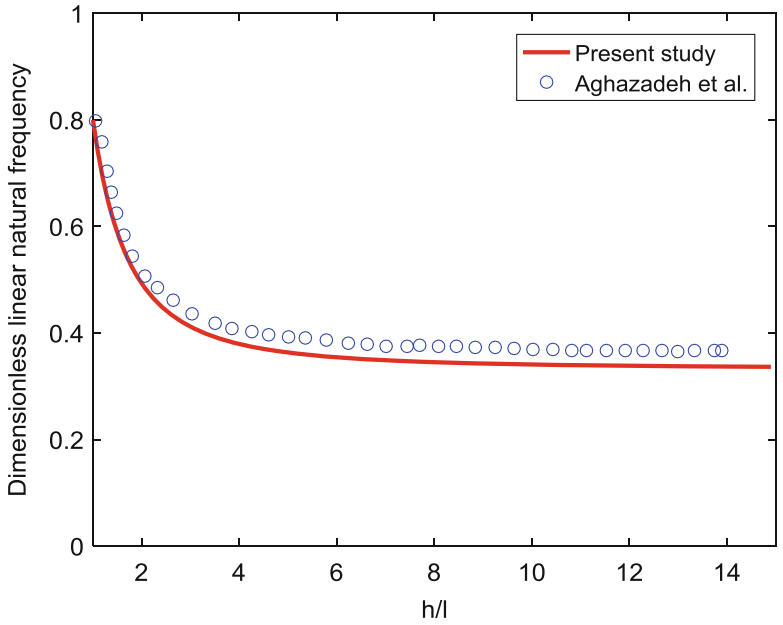

Fig. 18.2 Variation of the dimensionless linear natural frequency with dimesionless length scale parameter, h/l, based on EBBT and MCST; $L/h = 10$, $l = 15$ μm, $b/h = 2$, $k = 2$

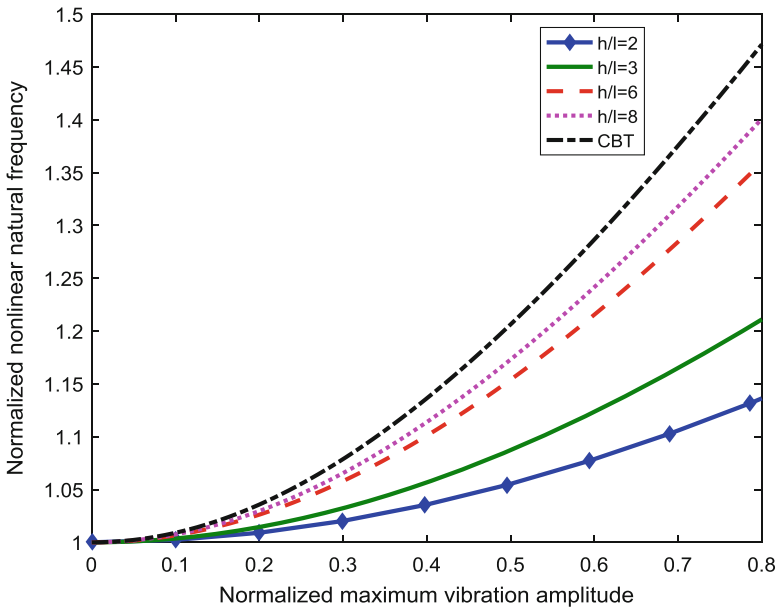

Fig. 18.3 Variation of normalized nonlinear natural frequency for a H–H FGM microbeam vibrating in the first mode for different values of h/l ($k = 2$ and $L/h = 20$)

differential equations by using Galerkin's method. Application of DFM makes it possible to obtain the nonlinear stiffness matrix directly and it is observed that a single trial function is sufficient to obtain nonlinear natural frequencies. The resulting uncoupled nonlinear equations can be solved one by one and as a result of this, an analytical expression for the nonlinear natural frequency is obtained. This approach is computationally very cheap compared to the solution method utilizing spectral methods or differential quadrature method which results in several coupled nonlinear equations need to be solved simultaneously. From the results obtained, variation of length scale parameter significantly changes the normalized nonlinear natural frequency of the FGM microbeam which increases with increasing dimensionless length scale parameter at predefined vibration amplitude. Similarly, as the material property index increases, normalized nonlinear natural frequency at a given vibration amplitude increases.

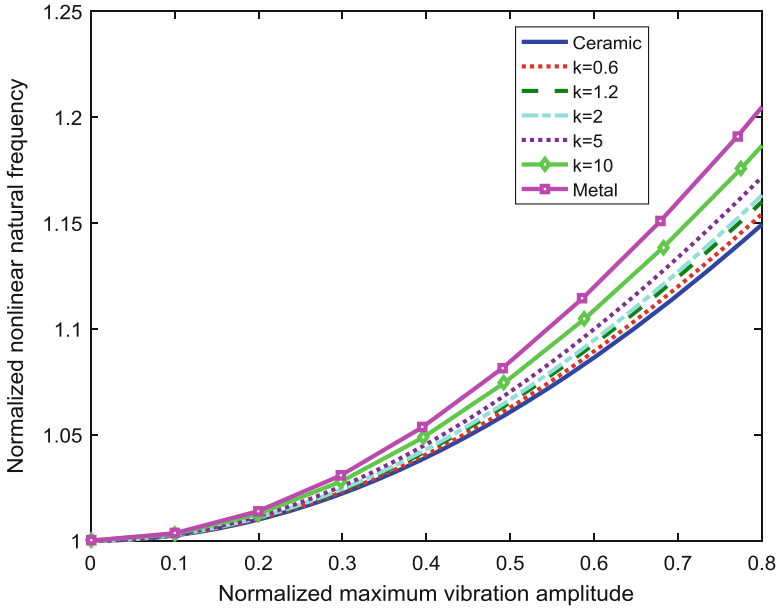

Fig. 18.4 Variation of normalized nonlinear natural frequency for a H–H FGM microbeam vibrating in the first mode for different values of material property gradient index ($h/l = 2$ and $L/h = 20$)

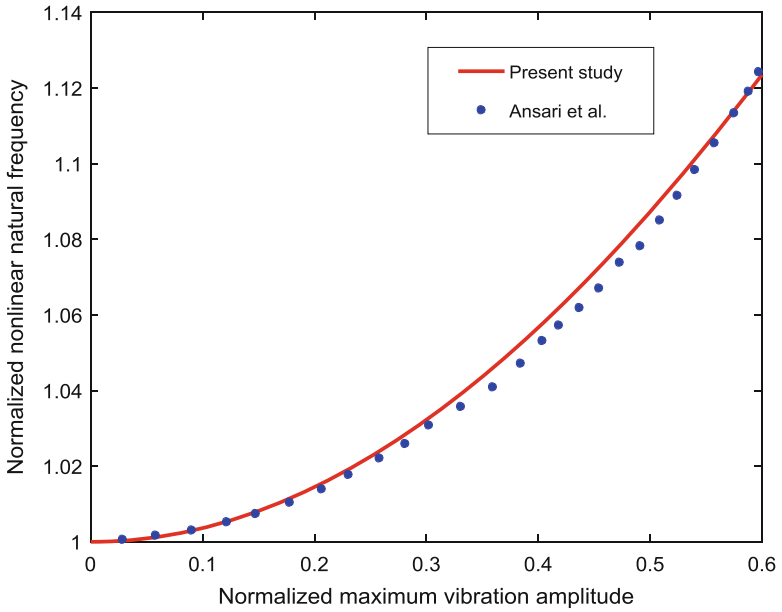

Fig. 18.5 Comparison of variation of normalized nonlinear natural frequency for a H-H FGM microbeam vibrating in the first mode ($h/l = 3$, $k = 2$ and $L/h = 20$)

References

1. Ouakada, H.M., Younis, M.I.: On using the dynamic snap-through motion of MEMS initially curved microbeams for filtering applications. J. Sound Vib. **333**(2), 555–568 (2014)
2. Abdel-Rahman, E.M., Younis, M.I., Nayfeh, A.H.: Characterization of the mechanical behavior of an electrically actuated microbeam. J. Micromech. Microeng. **12**, 759–766 (2002)
3. Sun W., He X.-Y., Li M, Fu Y., Experimental analysis of nano and engineering materials and structures, Proceedings of the 13th International Conference on Experimental Mechanics, pp. C557–C558. Springer, Netherlands (2007)
4. Li, Y., Meguid, S.A., Fu, Y., Xu, D.: Nonlinear analysis of thermally and electrically actuated functionally graded material microbeam. Proc. Math. Phy. Eng. Sci. **470**(2162), 20130473–20130473 (2014)

5. Lam, D.C.C., Yang, F., Chong, A.C.M., Wang, J., Tong, P.: Experiments and theory in strain gradient elasticity. J. Mech. Phys. Solids. **51**(8), 1477–1508 (2003)
6. Eringen, A.C.: Microcontinuum Field Theories. Springer, New York (1998)
7. Eringen, A.C.: On differential-equations of nonlocal elasticity and solutions of screw dislocation and surface-waves. J. Appl. Phys. **54**, 4703–4710 (1983)
8. Mindlin, R.D., Tiersten, H.F.: Effects of couple-stresses in linear elasticity. Arch. Ration. Mech. Anal. **11**, 415–448 (1962)
9. Yang, F., Chong, A.C.M., Lam, D.C.C., Tong, P.: Couple stress based strain gradient theory for elasticity. Int. J. Solids Struct. **39**(10), 2731–2743 (2002)
10. Aghazadeh, R., Cigeroglu, E., Dag, S.: Static and free vibration analyses of small-scale functionally graded beams possessing a variable length scale parameter using different beam theories. Eur. J. Mech. A.Solids. **46**, 1–11 (2014)
11. Ansari, R., Gholami, R., Sahmani, S.: Free vibration analysis of size-dependent functionally graded microbeams based on the strain gradient Timoshenko beam theory. Compos. Struct. **94**, 221–228 (2011)
12. Asghari, M., Rahaeifard, M., Kahrobaiyan, M.H., Ahmadian, M.T.: The modified couple stress functionally graded Timoshenko beam formulation. Mater. Des. **32**, 1435–1443 (2011)
13. Ma, H.M., Gao, X.-L., Reddy, J.N.: A microstructure-dependent Timoshenko beam model based on a modified couple stress theory. J. Mech. Phys. Solids. **56**, 3379–3391 (2008)
14. Ke, L.-L., Yang, J., Kitipornchai, S.: An analytical study on the nonlinear vibration of functionally graded beams. Meccanica. **45**, 743–752 (2010)
15. Ke, L.-L., Yang, J., Kitipornchai, S.: Nonlinear free vibration of size-dependent functionally graded microbeams. Int. J. Eng. Sci. **50**, 256–267 (2012)
16. Ansari, R., Gholami, R., Sahmani, S.: Study of small scale effects on the nonlinear vibration response of functionally graded Timoshenko microbeams based on the strain gradient theory. J. Comput. Nonlinear Dyn. **7**, 031009 (2012)
17. Tanrikulu, O., Kuran, B., Ozguven, H.N., Imregun, M.: Forced harmonic response analysis of nonlinear structures using describing functions. AIAA J. **31**, 1313–1320 (1993)
18. Cigeroglu, E., Samandari, H.: Nonlinear free vibration of double walled carbon nanotubes by using describing function method with multiple trial functions. Phys. E **46**, 160–173 (2012)

Chapter 19
Method to Predict the Shock Response Spectrum Shape from Frequency Response Functions

Jason R. Blough, James DeClerck, Charles VanKarsen, and David E. Soine

Abstract In an effort to understand the details of why a Shock Response Spectrum (SRS) has a particular shape, a method was designed to predict the shape of the SRS based on Frequency Response Functions (FRFs). Gaining a full understand of the relationship between the FRF of a structure and the SRS shape should prove to be very useful in reducing SRS test time and allow the general shape of an SRS response to be predicted more efficiently using finite element methods or experimentally obtained data. To allow comparisons of different shock response plates and fixtures through the use of FRFs a normalized Shock Response Spectrum (nSRS) was developed. The nSRS is derived directly from the FRF of a structure and when coupled with a library of characterized impactor input spectrums allows an SRS to be predicted without performing any testing. This approach allows modifications to the shock response plate/fixture to be evaluated efficiently and the effect of different impactors to be studied without performing a large number of experimental tests. It is hoped that this approach to understanding and predicting SRSs improves the understanding of how the structural dynamics effects an SRS and efficiency of testing.

Keywords Shock • SRS • Experimental

19.1 Introduction

The purpose of this work is to streamline Shock Response Spectrum (SRS) testing. One of the difficulties in performing SRS tests is predicting or understanding what the necessary fixtures and impactors are to achieve an SRS which falls within the required limits. This paper outlines an approach based on initial Frequency Response Function (FRF) measurements, a library of estimated input power spectrums from various impactors, and the standard SRS calculations.

Experimental data along with FEA modeling was done to understand what aspects of a shock response plate and fixture can be important in the shape of the SRS curve.

19.1.1 Normalized SRS Calculation

To allow more consistent comparisons of experimentally acquired SRS measurements the concept of the normalized SRS (nSRS) was developed. The nSRS was developed because each time that the resonant shock plate was excited the excitation level was of a different amplitude, this led to SRSs that were of different amplitudes. Having different level SRSs made them difficult to compare, when what was of interest was the knee frequencies and the shape of the SRS above the knee frequency. The concept of the nSRS allowed SRS functions to be overlaid such that these comparisons could easily be made.

The nSRS is calculated following the flow chart shown in Fig. 19.1.

David E. Soine: The Department of Energy's Kansas City National Security Campus is operated and managed by Honeywell Federal Manufacturing & Technologies, LLC under contract number DE-NA0002839.

J.R. Blough (✉) • J. DeClerck • C. VanKarsen
Michigan Technological University, Houghton, MI 49931, USA
e-mail: jrblough@mtu.edu

D.E. Soine
Honeywell Federal Manufacturing and Technologies, LLC, Kansas City, MO 64147, USA

J.M. Harvie, J. Baqersad (eds.), *Shock & Vibration, Aircraft/Aerospace, Energy Harvesting, Acoustics & Optics, Volume 9*,
Conference Proceedings of the Society for Experimental Mechanics Series, DOI 10.1007/978-3-319-54735-0_19

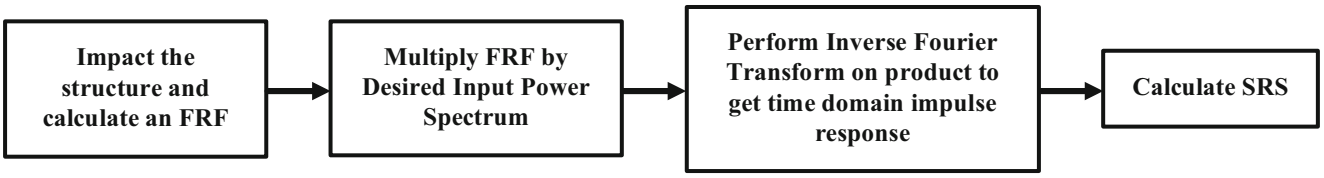

Fig. 19.1 Process to compute normalized SRS

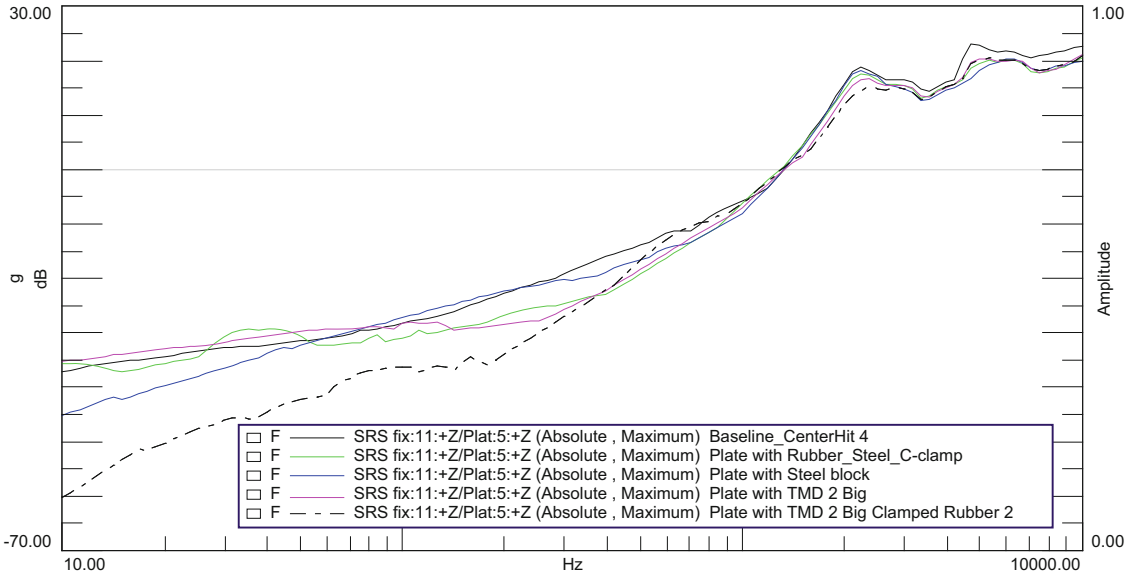

Fig. 19.2 nSRS functions for different structural modifications

The FRF is typically measured using an instrumented modal impact hammer which measures the force input into the structure. The level of excitation provided by the impact hammer can cause system non-linearity's to be excited if the impact force is high enough. These non-linearity's will be apparent in the FRF but unless severe do not appear to have a large impact on the shape of the SRS. The FRF could be measured using other impact devices or a modal shaker as well.

The input power spectrum is the autopower spectrum that would be generated by the impactor of interest. The shape of the input power spectrum controls which modes of the resonant plate are excited, modes which are above the frequency where the excitation energy of the impactor has rolled off will not be excited with an equal amount of energy as the lower frequency modes. The roll-off of the impactor's power spectrum has a significant impact on the shape of the SRS at the higher frequencies and is the reason that most SRS functions end with a flat or negative slope instead of an increasing amplitude. To assess the effect that a different impactor might have on a measured SRS, various input power spectrums can be used with the measured FRF.

Once the product of the FRF and the desired impactor input spectrum is calculated, it is inverse Fourier transformed to a resulting time domain impulse response. This time domain impulse response is then used as the input to the SRS calculation.

The advantage of the nSRS over a standard SRS is observed when comparing multiple test cases to more accurately understand the effect of structure and impactor changes. An example of overlaid nSRS functions can be seen in Fig. 19.2.

If a standard SRS is used, the SRS functions cannot be easily overlaid as shown in Fig. 19.3 which shows multiple SRS functions from the same structure but with slightly different force inputs. Note how difficult it would be to assess small changes in the SRS even without changes to the structure in this case.

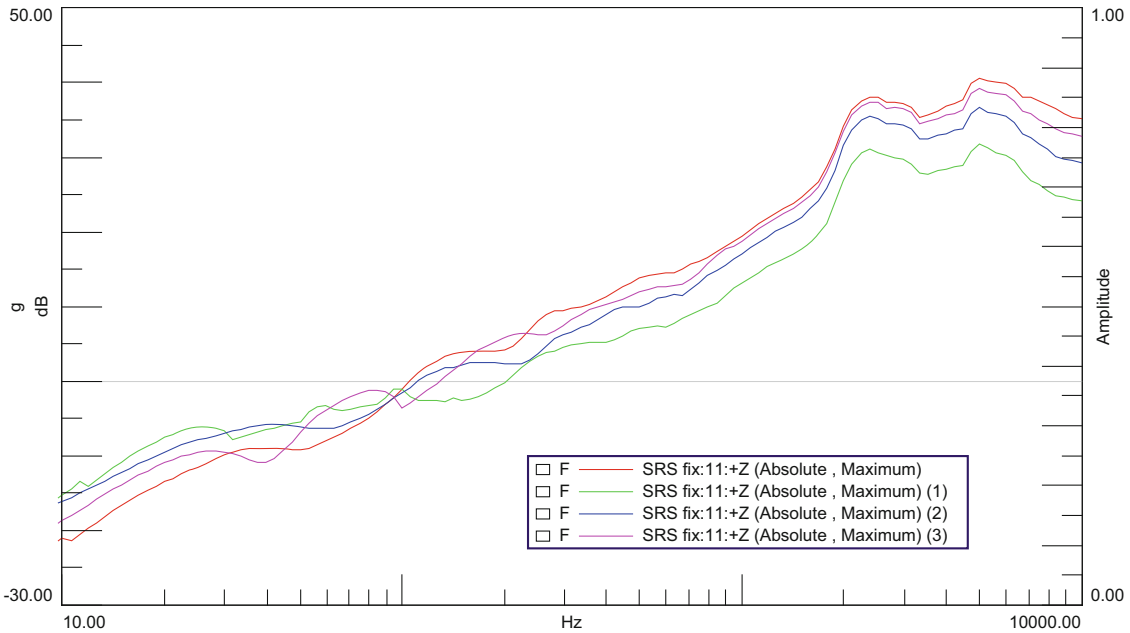

Fig. 19.3 Overlayed SRS functions for different structural modifications

19.1.2 Correlation Between FRF Shape and SRS Shape

Having developed a procedure which allows experimental SRS measurements to be compared by normalizing relative to the input spectrum several test cases were evaluated to understand how well the FRF of a system correlated to the estimated SRS.

The resonant plate systems tested, include the following variations which are all based off of the same resonant plate and fixture. Structural modifications were made to the resonant plate to assess the changes in the SRS. The modifications are listed below:

1. Baseline resonant plate and fixture.
2. Baseline resonant plate and fixture with two large tuned mass dampers attached on one side.
3. Baseline resonant plate and fixture clamped to ground on one side through rubber material.
4. Baseline resonant plate and fixture with steel mass bolted to one side of plate.
5. Baseline resonant plate and fixture with steel block clamped to plate through rubber material.

Pictures of the modified resonant plate are shown in Fig. 19.4.

FRFs were measured on the baseline plate/fixture along with each of the modified resonant plate setups and are shown in Fig. 19.5.

Figure 19.6 left shows a zoomed in view of the first natural frequency while Fig. 19.6 right shows a zoomed in view of the second natural frequency. In both cases, it can be seen that the differences in the FRFs are very significant.

The estimated SRS functions related to the systems with these FRFs are shown in Fig. 19.7. Note that the SRS does not roll-off or decrease in amplitude at the very high frequencies due to an impact input autopower spectrum which does not roll off. In most cases, it is expected that the impactor would produce an input autopower spectrum with roll-off at these very high frequencies and hence the SRS would roll off as well.

Figure 19.8 shows a zoomed in view of the SRS curves near the knee frequency and above. While there are very apparent differences in the SRS curves, they do not exactly track the differences which the FRF's might suggest.

In understanding how the FRF's and SRS's correlate to one another several analyses were performed. While no perfect correlation was discovered, when comparing the energy summation in the FRF around a natural frequency and the amplitude of the corresponding peak in the SRS there was quite good correlation. It is believed that a perfect correlation was not achieved because of the nature of the SRS being a peak hold type estimate as well as the differences in the damping in the FRF, this can have a sizable effect on the SRS amplitude.

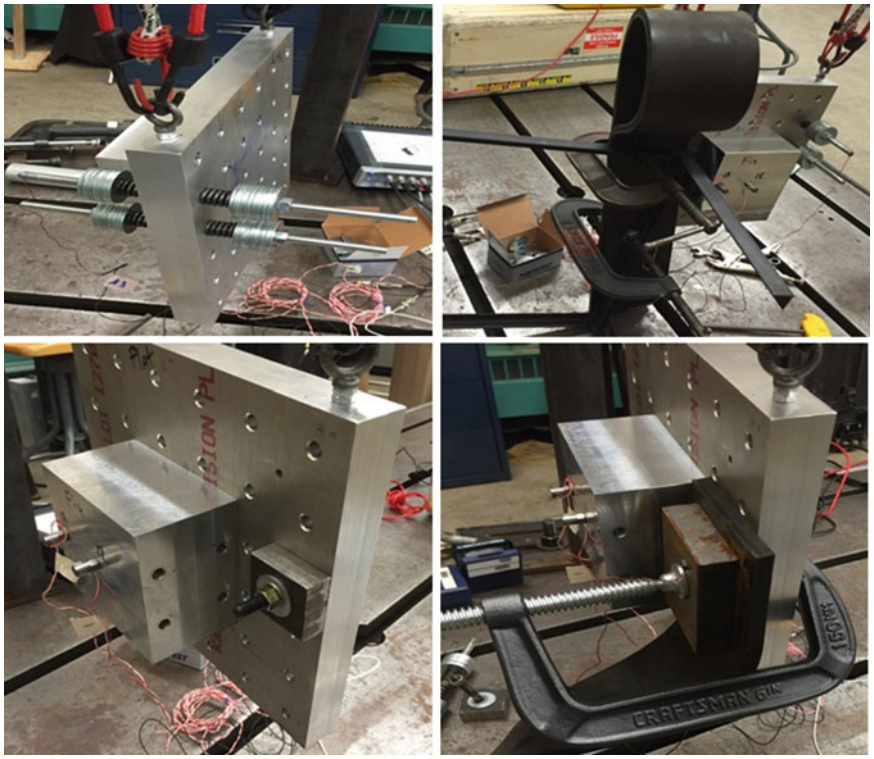

Fig. 19.4 Resonant plate test configurations

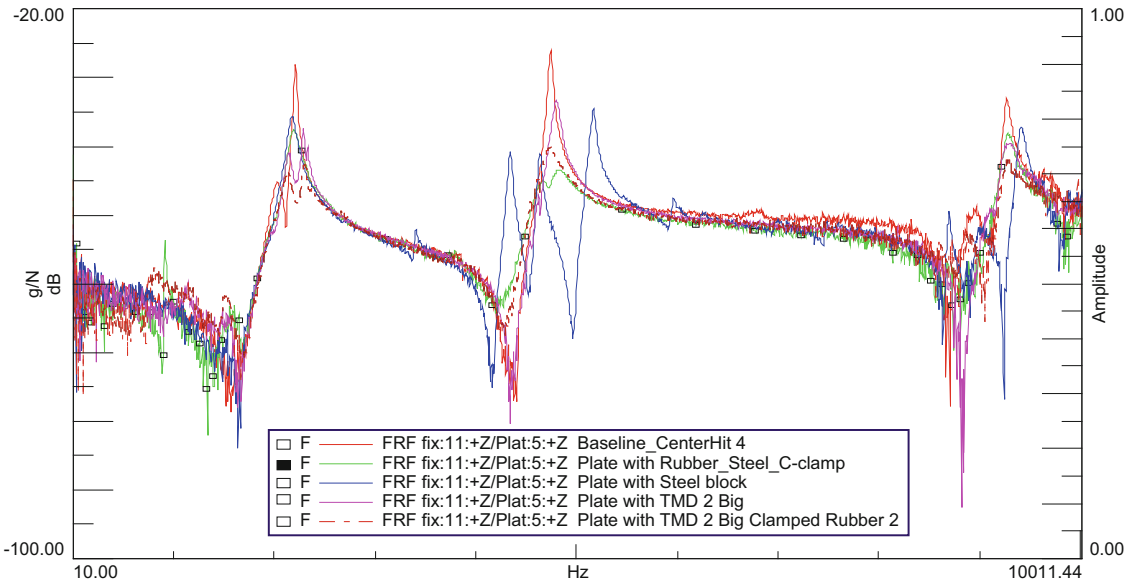

Fig. 19.5 FRFs of resonant plate configurations

19.1.3 Effects of Measurement Quality on the SRS Shape

In an attempt to understand more about how measurement quality affects the computation of an SRS, a study was done with experimental data. The study involved striking the resonant plate and fixture with different hammers with different intensities.

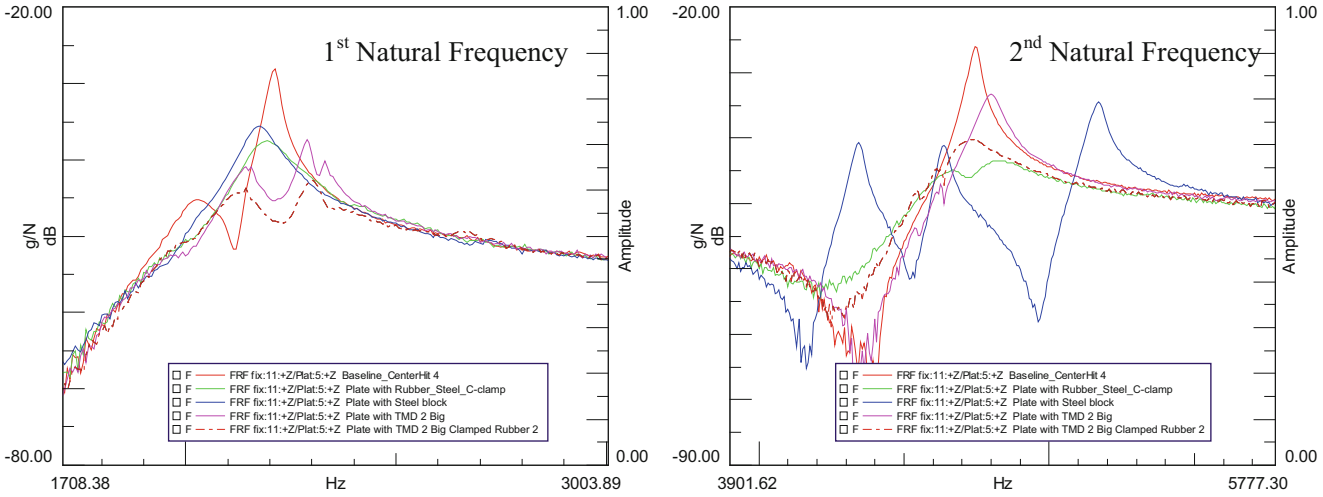

Fig. 19.6 Zoomed in view of the first natural frequency (*left*) and second natural frequency (*right*) of the resonant plate

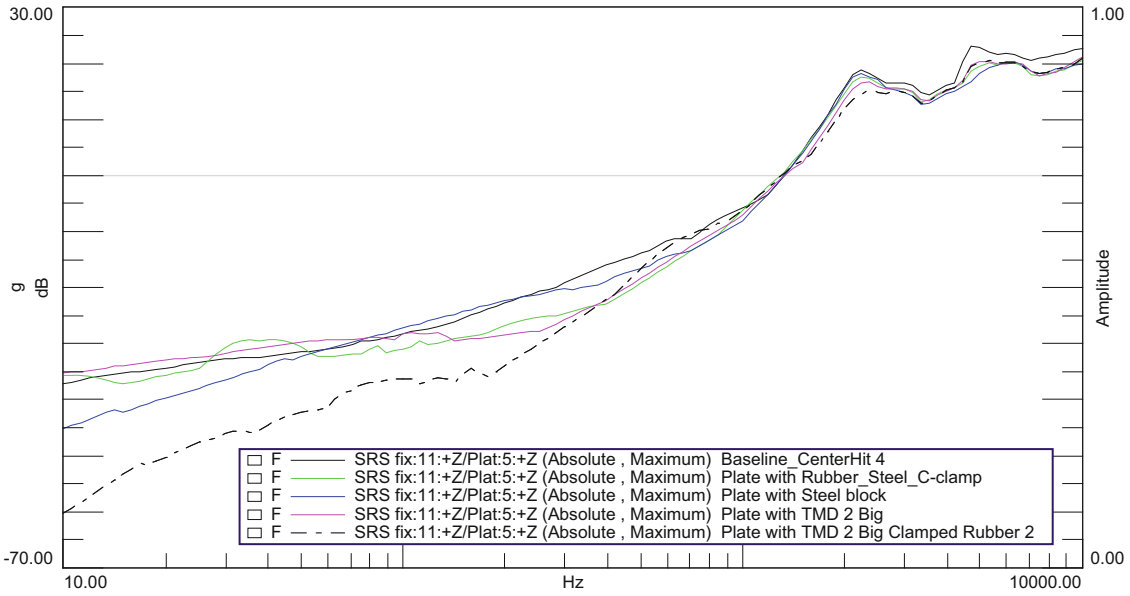

Fig. 19.7 SRS's of the resonant plate configurations

Figure 19.9 shows that as the intensity of the impact and the energy imparted into the plate increases the SRS amplitude also increases. Figure 19.9 also show a relationship between the input autopower spectrum and the SRS shape. When the input spectrum rolls off at lower frequencies the amplitude of the SRS also decreases at frequencies above the input spectrum roll off as would be expected.

In the extreme cases, the resonant plate was struck with enough force to cause a non-linear response as shown in the FRF's of Fig. 19.10. The non-linearity's are evident due to the non-symmetric shape of the peak in the FRF.

Figure 19.11 shows the SRS functions which result from the impacts used to measure the FRF's in Fig. 19.10. Note, all of these functions were measured using the same impactor with different intensities of impact. The shapes of the SRS functions change with the intensity of the impact considerably. An interesting observation is that it is not easy to tell from an SRS whether a structure has been impacted hard enough to drive it to a non-linear response.

A group of tests were also performed where several different impact hammer/hammer tip/impact intensities were collected. The FRF's from these tests are shown overlaid in Fig. 19.12. Note that many of the FRF's from this testing have a high amount of noise at the higher frequencies. These high noise measurements would typically be rejected due to the level of noise and efforts made to acquire measurements with less noise made.

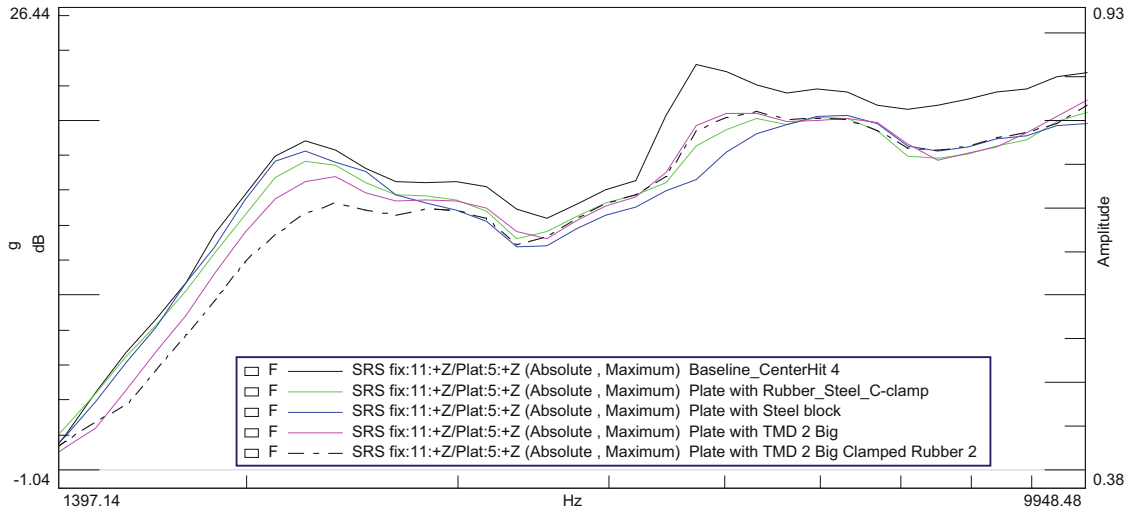

Fig. 19.8 Zoomed in view of SRS functions for resonant plate

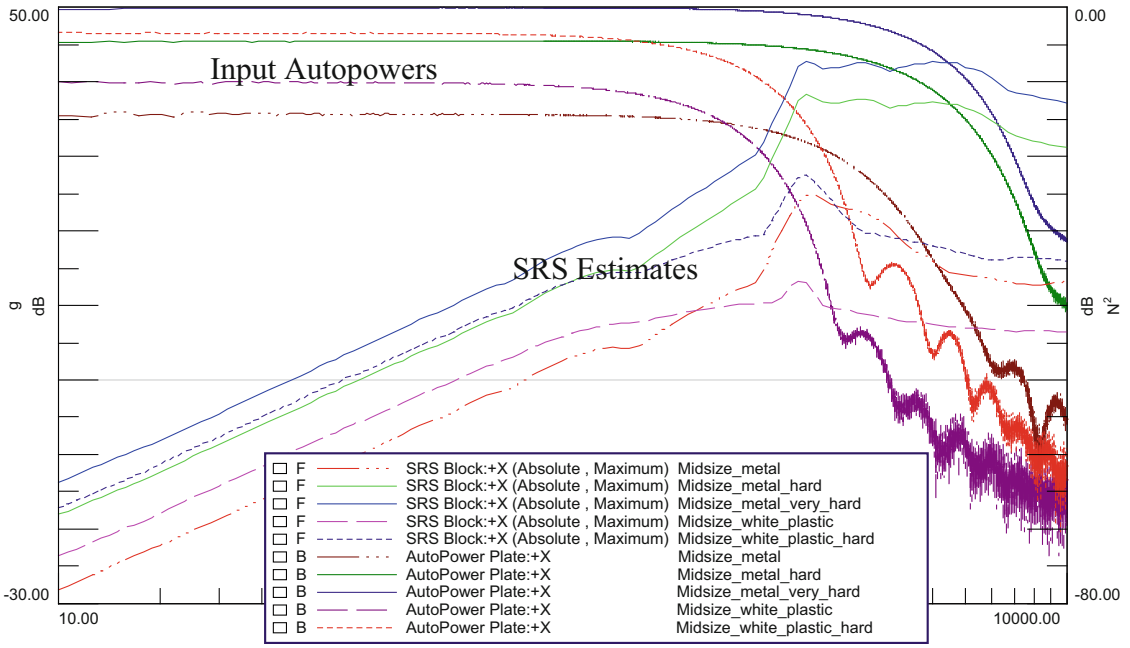

Fig. 19.9 Input autopower spectrum and SRS overlaid to show relationship

Even with the high levels of noise on some of the measurements it is very apparent that there are differences in the response of the structure, both linear and non-linear, around the peaks of the natural frequencies. Calculating SRS functions from these same tests results in the SRS's shown in Fig. 19.13.

An interesting aspect of the SRS's in Fig. 19.13 is that while some of the input measurements contained a very high level of noise as evidenced by the noisy looking FRFs, the SRS functions do not indicate the input to the SRS calculation was noisy. This is due to the fact that the SRS is a peak hold type of function and is not sensitive to noise. This would imply that no matter the quality of the original measurement made, the SRS will look acceptable. Additionally, the differences in the SRS's in Fig. 19.13 are completely from the differences in the inputs to the resonant plate and fixture, no other changes were made. This indicates that there is great potential to shape an SRS by changing only the input used to excite the resonant plate. Another conclusion that can be drawn from these SRS's is that an input which does not excite to as high a frequency will typically have a flatter SRS response at the higher frequencies.

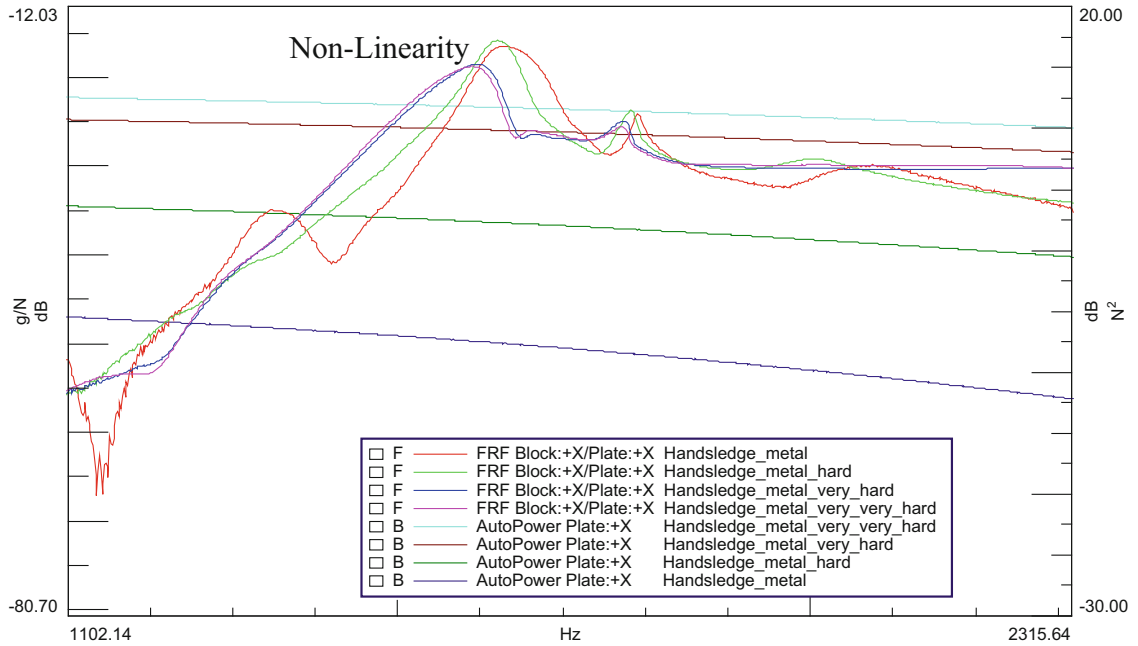

Fig. 19.10 FRF showing non-linearity due to very hard impact

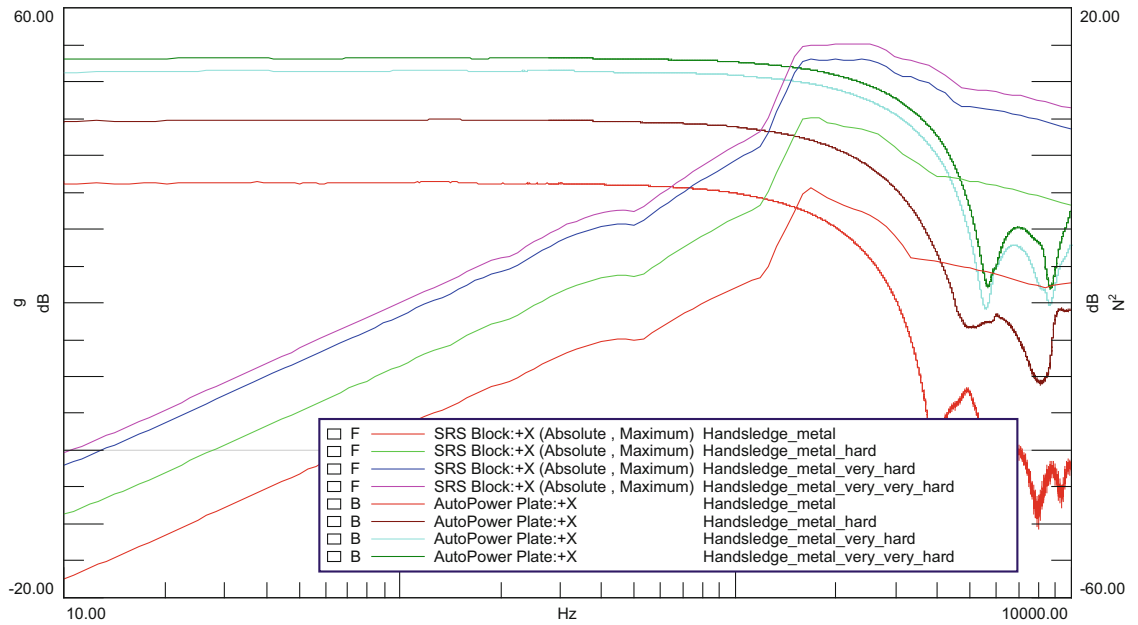

Fig. 19.11 SRS functions due to varying intensity impacts

19.2 Summary

The *normalized SRS* (nSRS) was developed which allowed several different experimental studies to very easily be evaluated to explore the structural response aspects of an SRS. The nSRS is calculated by estimating the Frequency Response Function (FRF) of a structure, multiplying this FRF by the input autopower spectrum of a particular impactor, and then taking the Inverse Fast Fourier Transform (IFFT) of this product and calculating an SRS from the resulting time domain impulse response.

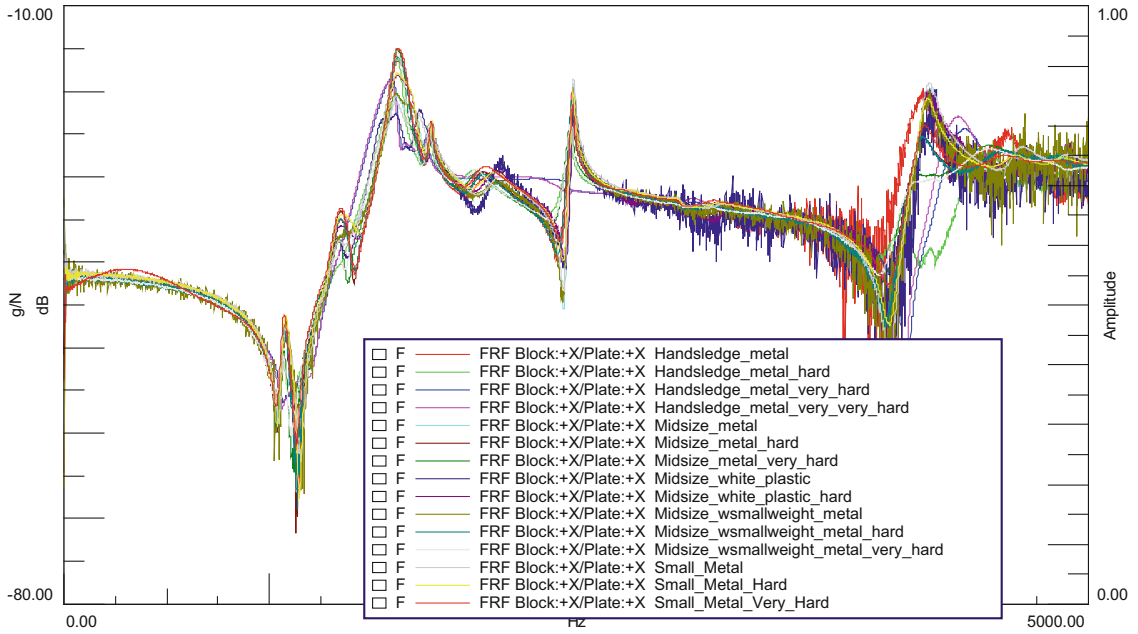

Fig. 19.12 FRFs overlaid from many different input functions

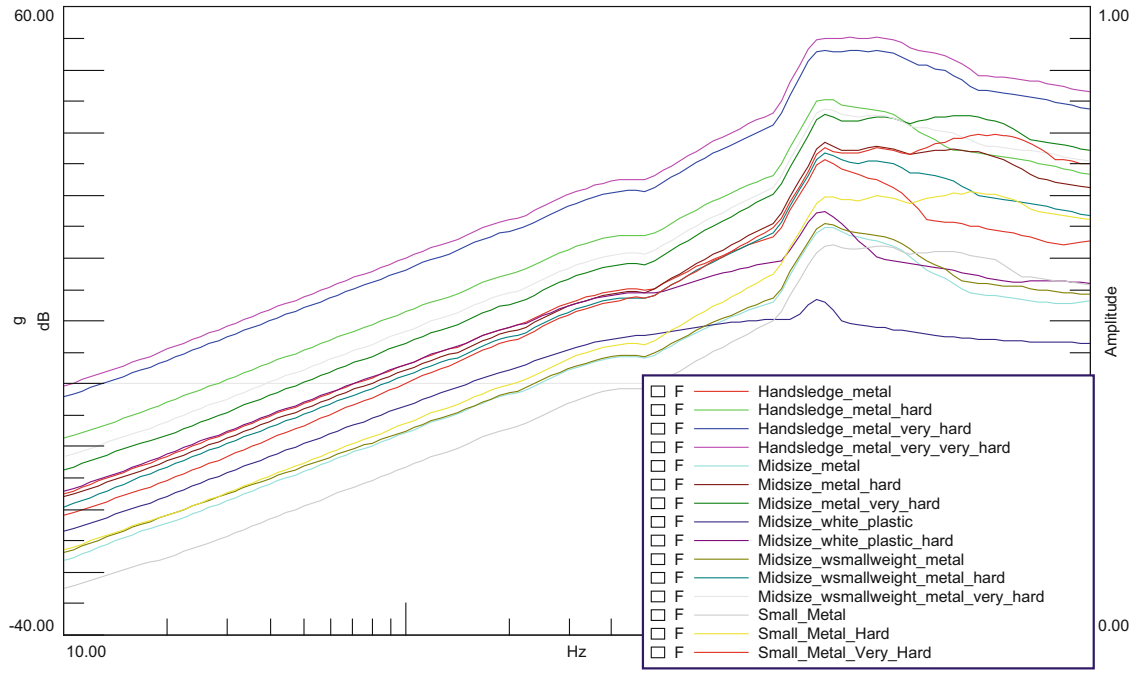

Fig. 19.13 SRS functions calculated from many different input functions

Modifications were made to the shock response plate and both FRFs and SRS functions estimated. The modifications included clamping to ground through heavy rubber, adding tuned mass dampers, bolting on mass, and clamping rubber with added mass. These structural modifications produced very large changes in the FRFs at all natural frequencies as well as changes in the SRS functions. While the changes in the SRS functions were significant they did not appear to track the changes in the FRFs directly. The best correlation between the FRFs and the SRS functions was achieved by comparing overall energy in bands around the natural frequencies but was not an ideal correlation.

To assess the effect that different impactors have on the shape of the SRS the same shock plate/fixture assembly was impacted with many different hammer/tip combinations and with different impact intensities. While the FRFs were unchanged, except when the impact was hard enough to excite non-linearities, the SRS functions showed large differences due to the roll-off in energy at the higher frequencies related to the measured input autopower spectrums from the different hammers. If the input autopower spectrum rolled off at a lower frequency the corresponding SRS also began to decrease in amplitude at a lower frequency.

The last study performed was to assess the appearance of the SRS due to different levels of quality of the measurement process. It was shown that using a very noisy FRF measurement in the nSRS calculation still resulted in a smooth SRS function. Additionally, FRFs clear non-linearity's in them did not significantly change the shape of the SRS function in a way that the non-linearity was apparent. One disconcerting fact that arose from the study of different FRF measurement qualities and the SRS relationship is that by only looking at the SRS it is not obvious whether it is a valid measurement or based on a very noisy input, which for any other reason would be considered of insufficient quality to make engineering decisions.

Chapter 20
Investigation and Application of Digital Image Correlation Technology in Vibration Measurement Based on Two Cameras

Hugo Gao, Yihao Liu, James Zhuge, and Jeff Zhao

Abstract There are many methods for vibration and modal testing. With the development of digital technology and 3-D imaging technology, the development and application of digital image correlation (DIC) technology becomes possible. Now we can use stereo digital image correlation and dynamic photography to obtain data on the structure mode. It should be noted that this is a noncontact measurement technique, meaning there will be a wide range of applications. In addition, the visualization of vibration modes provides the intuitive pictures. This paper focuses on how to build a test environment. The project uses BUMBLEBEE binocular stereo cameras to shoot the images of test object. The images then are transferred, stored, and processed to get the relative coordinates of each pixel. After that, a MATLAB program is developed to revert the coordinates of every pixel, reduce noise, and generate stereo images. The stereo images can be animated based on the timestamps they were acquired. As for data processing, this paper studies the effects of various parameters, such as shutter speed, exposure, gain, vibration frequency and amplitude. The relationship between these parameters and the accuracy of pixel coordinates is studied.

Keywords DIC processing • Stereo camera • Vibration measurement • Stereo image processing • Vibration analysis

20.1 Introduction

There are many mature technologies in vibration measurement, and they can be categorized into contacting measurements and non-contacting measurements, including hammer/accelerometer testing, laser Doppler vibration measurement, stereo photogrammetry and some other methods. However, in actual production work, people still more often in the use of traditional contacting measurement methods, with accelerometers and other sensors. Although this method is the most widely used, allowing more wideband measurements, it has three obvious limitations: The first point is that the operation is time-consuming and labor-intensive, because the testing method requires many manual placements. The second point is that the effects of mass loading needs to be considered due to the use of accelerometers, which will affect the quality of the measurement results. Because the accelerometer measuring method is a contact measurement, the accelerometer characteristics will result in obvious limitations in the case of high-frequency vibration. The third point is that for the points far away from the excitation points in the large complex structures and in the large damping structure, the response signal can be weak and the signal-to-noise ratio can be low, which would require multiple excitations. Laser Doppler vibration measurement is a non-contact, wide-band measurement method, but it can deal only with one point at a time, and it costs much more compared to the regular accelerometers. While stereo camera photography method can overcome these shortcomings. One Stereo camera photography shot may contain up to 100,000 data points. Furth more, the measurement of large displacement vibration using stereo camera can be of high accuracy [1]. Within certain range, the greater the vibration displacement, the more accurate measurement can be obtained from the stereo camera photography shots.

H. Gao (✉) • Y. Liu
Zhejiang University, Hangzhou, China
e-mail: 418232126@qq.com

J. Zhuge • J. Zhao
Crystal Instruments, Santa Clara, CA, USA

J.M. Harvie, J. Baqersad (eds.), *Shock & Vibration, Aircraft/Aerospace, Energy Harvesting, Acoustics & Optics, Volume 9*,
Conference Proceedings of the Society for Experimental Mechanics Series, DOI 10.1007/978-3-319-54735-0_20

20.2 Digital Image Correlation (DIC) Technology

20.2.1 How the Camera Works

As shown in Fig. 20.1, Point A is the center point of the left camera aperture. Point B is the center point of the right camera aperture. Point C is the imaging point of the measured pixel in the left camera imaging plane. Point D is the imaging point of the measured pixel in the right camera imaging plane. Point E is the measured pixels.

The working principle of binocular stereo cameras is basically the same as the working principle of human eyes. Binocular stereo camera observes the same pixel through the left and right camera perspective. We can get the pixel in the left and right of the two different cameras in the image. And then through the calculation, analysis and transformation of spatial coordinates, the spatial coordinate information of the pixel can be obtained. The distance between point A and point B is determined, and the distance from point A to the left camera imaging plane and from point B to the right camera imaging plane are determined as the focal length of the cameras. If we can confirm that point C and point D are the imaging points of the measured pixel points in the left and right camera imaging planes respectively, then by the intersection of the straight line AC and the straight line BD, we can determine the E point in the left and right camera coordinate system position.

The specific mathematical geometry is illustrated in Fig. 20.2.

Assuming that the two camera axes are parallel, B is the distance from the projection center of the two cameras, and the focal length is f.

If the left and right cameras take the same point in the same object at the same time, P (X_c, Y_c, Z_c), and then get the image of point P on the left and right cameras respectively, the coordinates are P_{left} (X_{left}, Y_{left}), P_{right} (X_{right}, Y_{right}).

Now P_{left} and P_{right} shot by the binocular camera are in a plane, thus the Y coordinates of P_{left} and P_{right} are the same, $Y_{left} = Y_{right}$, then

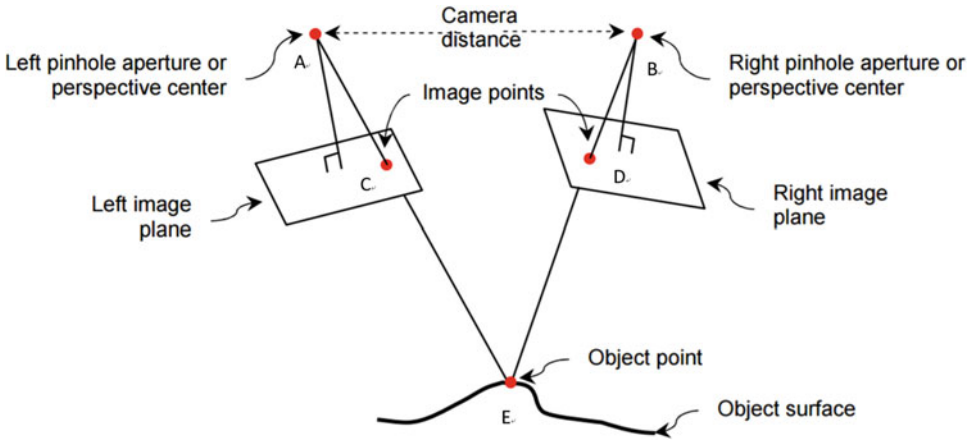

Fig. 20.1 Stereo camera pair [2]

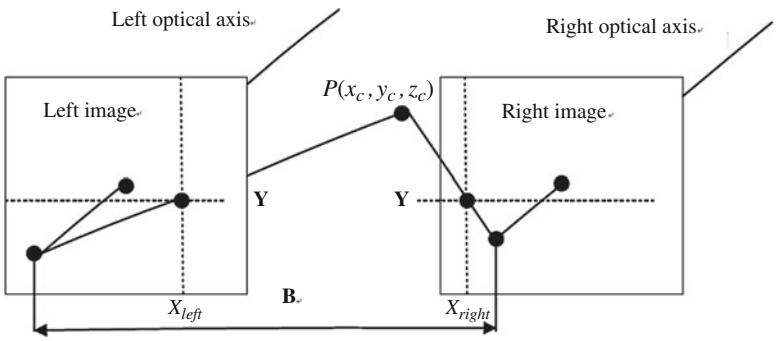

Fig. 20.2 Geometric model of binocular camera [3]

$$\begin{cases} X_{left} = f\frac{x_c}{z_c} \\ X_{right} = f\frac{(x_c - B)}{z_c} \\ Y = f\frac{y_c}{z_c} \end{cases} \tag{20.1}$$

Their disparity is equal to $X_{left} - X_{right.}$ From this, in the camera's coordinate system, the three-dimensional coordinates of point P are

$$\begin{cases} x_c = \frac{B \cdot X_{left}}{Disparity} \\ y_c = \frac{B \cdot Y}{Disparity} \\ z_c = \frac{B \cdot f}{Disparity} \end{cases} \tag{20.2}$$

Therefore, if a point on the image plane of the left camera can be matched to the corresponding point on the image plane of the right camera, we can get the three-dimensional space coordinates of the point.

Now we figure out the coordinates of the point E in the camera coordinate system. Suppose that in the left camera coordinate system, the coordinate of the point E is (x, y, z). Finally, we need to do matrix transformation to get the coordinates of the point E in the global coordinate system. Suppose that point E (x, y, z) becomes E′(x′, y′, z′) after transformation. Dimensional coordinate transformation:

$$\left[x', y', z', 1\right] = [x, y, z, 1]$$

Translational transformation

$$T = [1\ 0\ 0\ 0; 0\ 1\ 0\ 0; 0\ 0\ 1\ 0; Tx\ \ Ty\ \ Tz\ \ 1]$$

Tx, Ty, Tz are the translation distance of point E in x, y and z directions, respectively.

Proportional transformation

$$T = [a\ 0\ 0\ 0; 0\ e\ 0\ 0; 0\ 0\ 0\ j; 0\ 0\ 0\ 1]$$

a, e, j are the scaling ratio of point E in x, y and z directions, respectively.

Rotating transformation

$$T = [\cos\theta\ \sin\theta\ 0\ 0; -\sin\theta\ \cos\theta\ 0\ 0; 0\ 0\ 1\ 0; 0\ 0\ 0\ 1]$$

θ is the rotation angle around the X axis.

$$T = [1\ 0\ 0\ 0; 0\ \ \cos\theta\ \sin\theta\ 0; 0 - \sin\theta\ \cos\theta\ 0; 0\ 0\ 0\ 1]$$

θ is the rotation angle around the Y axis.

$$T = [\cos\theta\ 0 - \sin\theta\ 0; 0\ 1\ 0\ 0; \sin\theta\ 0\ \ \cos\theta\ 0; 0\ 0\ 0\ 1]$$

θ is the rotation angle around the Z axis.

After this series of transformations, the three-dimensional coordinates of E point in the global coordinate system can be gotten [4].

20.2.2 How the Two Images Match Each Other

In practice, to obtain the three-dimensional coordinates of point E in the global coordinate system, the key issue in stereo vision is to confirm in the left and right plane which two pixels are the image points of point E of. This is DIC matching problem. To do so, the initial image is taken through the binocular stereo camera, and preprocessed. Because this image needs to be corrected first, it is important to smooth it ahead of time. To correct this image, set the low-pass filter in advance

Fig. 20.3 Initial image [5]

and turn it on. In case no low-pass filter is applied, we can still correct the image. However, after image correction, it is prone to aliasing. Of course, if faster processing speed is desired over a smoother image, the low-pass filter may be turned off.

The initial image is shown in Fig. 20.3.

For a lens with barrel distortion, the line will curve in the image. Correction is to repair the distortion caused by the lens. In the original image, it is easy to find the image distortion caused by the lens, especially along the edge of the object. In short, a straight line in the initial image turns into a curve, especially exaggerated along the sides and corners. Correction is to remove the distortion in this case. By correcting the image, the barrel distortion will be removed, and the lines that would turn into curves become straight. If the image is not properly corrected, the digital image correlation search in the horizontal or vertical direction will result in error.

The camera's internal parameters include the camera coordinate origin, focal length f, and lens distortion. Lens distortion including radial distortion, centrifugal distortion and thin prism distortion. Taking all the possible distortion into account, the resulting distortion model is:

$$d_x = A_1 x r^2 + A_2 x r^4 + A_3 x r^6 + B_{1-} \left(r^2 + 2x^2\right) + 2xyB_2 + E_1 x + E_2 y, \tag{20.3}$$

$$d_y = A_1 y r^2 + A_2 y r^4 + A_3 y r^6 + B_{2-} \left(r^2 + 2y^2\right) + 2xyB_1, \tag{20.4}$$

where A_1, A_2, A_3 are radial distortion parameters, B_1, B_2 are tangential distortion parameters, E_1, E_2 are thin prism distortion parameters [6].

After correction, Fig. 20.4 is obtained.

Then, Laplace-Gaussian filtering is applied to the corrected image to obtain the edge image. Why do we need edge images? Edge detection a process to search for edge based on the change in brightness along the edge. The edge image obtained by the edge detection can improve image detection results, but on the other hand, the edge detection is equivalent to the introduction of additional processing steps which will inevitably slow down the processing. Therefore, we must consider the compromise between improvement of the results and the extra processing time, to determine whether to use edge image processing (Fig. 20.5).

Now it is time to calculate the sum of absolute difference for each pixel of edge image to find the digital image correlation between two images.

In this way it can be determined which pixels are corresponding to each other in the pictures captured by the left and right cameras, and get the space coordinates of each point in image. From this the depth of the image can be obtained, as shown in Fig. 20.6.

Fig. 20.4 Corrected image [5]

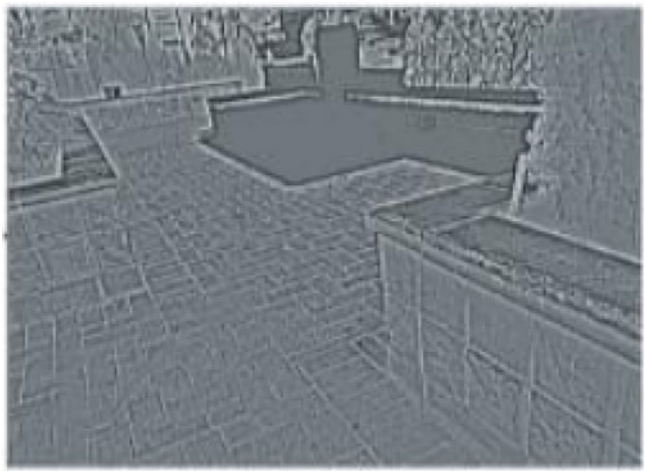

Fig. 20.5 Edge image [5]

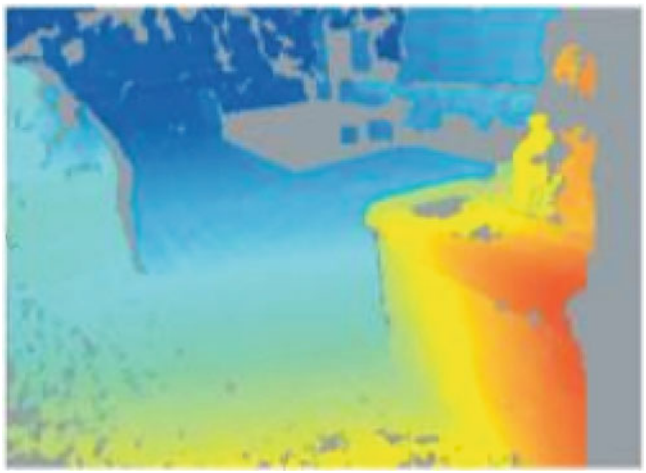

Fig. 20.6 Depth image [5]

20.2.3 How the Stereo Parameters Work

There are two types of errors in three-dimensional stereo cameras: matching error and estimation errors. A matching error is where the disparity is simply wrong. The estimation error refers to that the digital image correlation match is correct, but certain error occurs when the subpixel disparity value is estimated.

There are several methods to remove these errors. They are limited range of disparity, verification, stereo mask, edge mask, etc.

The disparity range is defined when we are searching in the image captured by the right camera to find the digital images correlated pixels in the image captured by the left camera, as the range of pixels that we will search. If it is 0 pixel disparity, it represents the pixel at infinity distance. This is easy to understand, when we use our eyes to observe objects, the nearby objects are prone to two images, and very distant objects are often overlapping. The maximum disparity range defines the closest object that can be observed from the cameras. We also need to adjust the disparity range based on actual testing requirements. The larger the disparity range is, the longer the calculation time is, and more likely the matching error may occur. On the other hand, the smaller the disparity range, the faster the calculation but less likely to find matching points.

The purpose of verification is purely to remove the matching error. And verification doesn't affect the accuracy of the pixels of the effective stereoscopic disparity. It just throws away the pixels that mismatch. In some cases, such as the measured object is internally closed and lack of texture change, then the DIC processing cannot produce a suitable edge image, or find the appropriate correlated point. Because there is no texture change, each point appears to be correlated. In this case, wrong correlation will be established. Since the correlation is not established correctly, the measurement results will definitely be wrong. Therefore, to avoid this situation, following verification scheme are designed.

Texture verification—This is based on the degree of change of the texture. If the matching feature between images does not have enough contrast or texture, texture validation considers them to be insufficient to generate a correct match, and the pixel is discarded.

Back and forth verification—This verification is to match the image in the right image when the left image is used as the reference image, and to perform an inverse validation to match the image in the left image when the right image is the reference image. Although the two matching processes greatly increased the cost of verification of resources, but the results are very good.

Uniqueness verification—This verification means that for a certain pixel, we rely on a template to find a matching pixel. It is necessary to analyze the best match between two pixels, by comparing the matching degree of other adjacent pixels which rely on the same template in order to find a matching pixel. It is possible the previous matching pixel found is not good enough. Because even if the texture of the relevant template is changing and meeting the requirements, due to the closure of the measured object, there may be no suitable match. If two pixels are not correlated enough, they will be discarded [7].

Stereo mask is defined as a square pixel area around a certain pixel. With this small area of pixels, it is possible to find the matching pixels in another image. The size of the stereo mask needs to be defined. In simple terms, a stereo mask with larger pixel range provides better accuracy while producing denser, smoother depth images. It's suitable for continuous surfaces. However, an obvious shortcoming is that for the object whose depth is not continuous, the recognition accuracy of large pixel range of stereo mask will cause problem. On the other hand, the stereo mask with small pixel range is more suitable for non-continuous objects. The problem is that the resulting images are sparse, some pixels may not be matched, and the signal-to-noise ratio is not high enough.

An experiment to test the effect of the stereo mask on the estimation error is performed. The results are shown as standard deviations.

As can be seen from Table 20.1, for different resolutions, the correlation accuracy is of little change. But we need to consider that if the distance between measured object and the space position of camera lens is unchanged, then the surface area on the measured object to which a low-resolution pixel corresponding is greater than the surface area on the measured object to which a high-resolution pixel correspondingly. Assuming one pixel corresponds to 0.16 mm^2 at 160×120 resolution, then under same circumstances, one pixel corresponds to 0.01 mm^2 at the resolution of 640×480. Although it seems the accuracy of the correlation between the two is the same, in fact there is still a large difference in their absolute accuracies.

Table 20.1 Correlation accuracy results, stereo mask 11, edge mask 9 [8]

Resolution	Correlated accuracy (pixel)
160×120	0.10
320×240	0.11
640×480	0.10

Table 20.2 Correlation accuracy results at 320 × 240 resolution (edge mask = stereo mask-2) [8]

Stereo mask	Correlation accuracy (pixel)
5	0.18
7	0.18
9	0.14
11	0.11
13	0.10
15	0.10

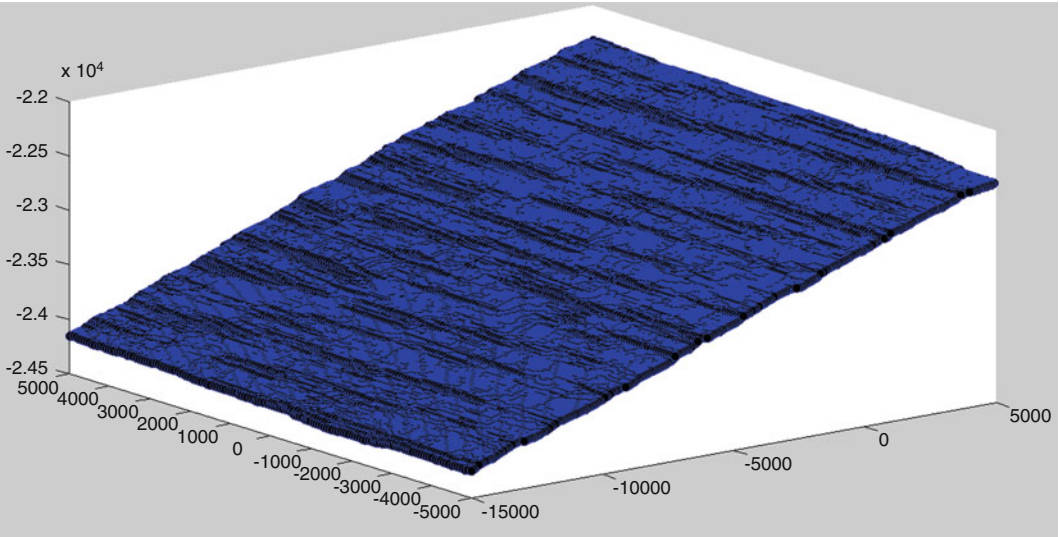

Fig. 20.7 Fit all points in an image to generate the surface

As can be seen from Table 20.2, for the same resolution conditions, in a certain range, if we adopt a larger pixel range of the stereo mask, then the correlation accuracy will be improved.

20.2.4 Image Processing

After such a series of DIC processing, the spatial coordinates of each pixel in the image captured by the binocular camera can be derived. And it is time to re-generate the image using the MATLAB program developed on the PC. Following are the processing steps:

Import the point coordinate file

Display and observe the point coordinate file in the three-dimensional graph (Figs. 20.7 and 20.8).

20.3 Error Analysis

Stereo cameras used for DIC analysis have two types of errors: matching error and estimation error. These errors, for the time being, are inevitable and limited by hardware as well as depth analysis algorithms.

From the results of image fitting and fitting analysis of points, it can be seen that there are several causes that affects the validity of the data. They are,

Shutter time: As the shutter time increases, the fitting degree becomes higher and higher.

Gain: the relationship between gain and fitting degree is more like an inverted U-shaped relationship. The fitting degree will be high and then low in a certain range. The fitting degree increases because more valid points are obtained and the data is more reliable. Then the fit decreases after a peak, because too much gain leads to too much noise, polluting the signal.

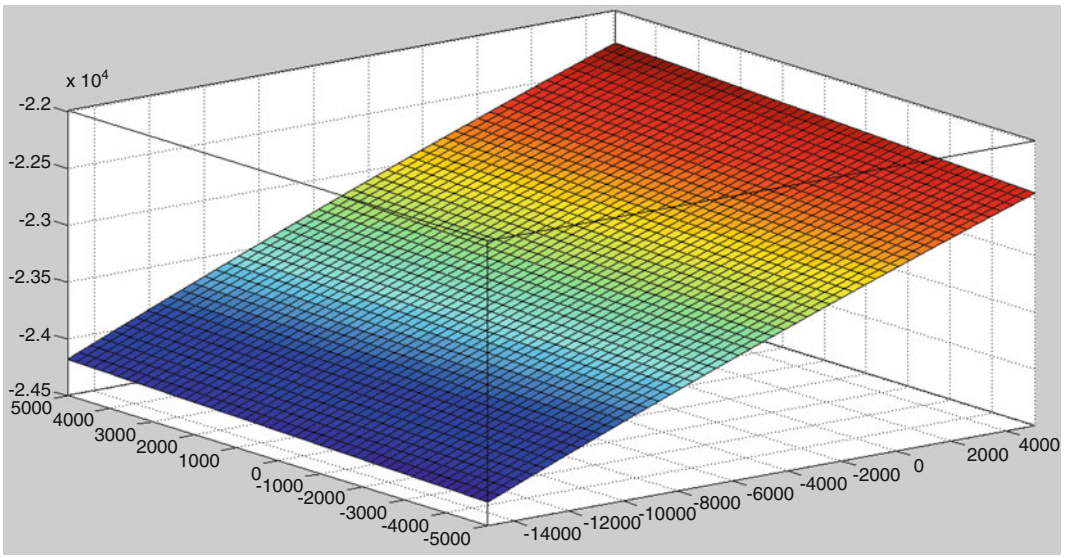

Fig. 20.8 Generate a continuous surface, resulting in vibration animation

Vibration frequency: in the fixed amplitude, shutter and gain circumstances, in the 5–20 Hz range, with the vibration frequency increases, the fitting degree gradually reduced, this situation is more apparent in the case of a longer shutter time than in a shorter shutter time. This is because the long shutter time will lead to continuous exposure, so that the image is blurred, and the data validity is reduced.

In order to reduce the error, there are several concerns can be done from the following aspects.

Camera side:

First, consider the vibration frequency. If the vibration frequency is too high, in order to avoid the residual image, we need to reduce the shutter time appropriately to improve the coordinates of the effectiveness of the pixel. If the vibration frequency is too low, then we need to try to use a longer shutter time to improve the resulting pixel for digital image correlation processing accuracy.

If we use a longer shutter time, we can refer to more comprehensive statistics and records to find the most suitable gain for the current shutter time.

If we have to use a lower shutter time, such as less than 1ms, then we should try to use a relatively high gain. If the gain is too low, then the result is that we are not able to get pixels, let alone whether it is effective.

DIC processing side:

We need to select the appropriate object to be measured, including the following characteristics: First, the object is preferably a continuous, flat plane. Second, the edge of the object to be measured to should be photographed. Finally, the surface of the object to be measured is preferably of a recognized texture, facilitating DIC detection.

Because we use a continuous plane for testing, taking into account the accuracy of larger pixel range of the stereo mask is higher, and this kind of stereo mask is more suitable for measuring continuous and smooth object. So we use the largest 15×15 stereo mask to get denser and smoother depth images.

We need to adjust the distance between the camera and the plane, try to limit disparity range. Because if the disparity range is too large, a mismatch may occur. While the disparity range is too small, it's hard to find the matching object. This requires constant adjustment.

We need to adjust the verification strength. Because validation is more like a remedy for removing invalid points. However, it is best to generate as few invalid points as possible. In general, we can use to back and forth verification.

Processing program side:

The processing program developed in MATLAB is the last remedy to reduce the error.

Some obvious points of error can be removed according to the shape of the test object. For example, if the test object is a flat plane, then if some of the data points protrude or deviate from the surrounding data points, they should be deleted or be forced to be close to the surrounding points.

For a relatively simple test object, the appropriate fitting equation can be used. Because the vibration of a simple object has vibration equation to follow, the vibration of the object can be fitted.

20.4 Conclusion

This paper studies the application of DIC technology in the vibration measurement. It makes it possible to visualize the vibration object. The key of the success of this method relies on how to reduce the errors from all aspects and the major aspects of errors are discussed in details. In the case of the noncontiguous objects, further study can be done.

References

1. Avitabile, P., et al.: Noncontact measurement. Techniques for model correlation. Sound Vib. **44**(1), 8 (2010)
2. Helfrick, M.N., et al.: Optical non-contacting vibration measurement of rotating turbine blades. In: Proceedings of the IMAC-XXVII, pp. 1–5 (2009)
3. Lucas, B.D., Kanade, T.: An iterative image registration technique with an application to stereo vision. IJCAI, vol. 81, No. 1 (1981)
4. Changlin, L., Benrong, C., et al.: On nonlinear 3D rectangular coordinate transformation method based on improved Gauss-Newton method. J. Geod. Geodyn. **27**(1), 50–54 (2007)
5. Point Grey Knowledge Base. Stereo vision introduction and applications, https://www.ptgrey.com/support/downloads/10353, 2015
6. Woods, A.J., Docherty, T., Koch, R.: Image distortions in stereoscopic video systems. In: IS&T/SPIE's Symposium on Electronic Imaging: Science and Technology. International Society for Optics and Photonics, 1993
7. McKeown, D.M., McVay, C.A., Lucas, B.D.: Stereo verification in aerial image analysis. Opt. Eng. **25**(3), 253333 (1986)
8. Point Grey Knowledge Base. Stereo accuracy and error modeling, https://www.ptgrey.com/support/downloads/10403, 2012

Chapter 21
A Mission Synthesis Procedure for Sine-on-Random Excitations in a Helicopter Application

Bram Cornelis, Simone Manzato, Bart Peeters, Raphael Van der Vorst, and John Hiatt

Abstract This paper considers a so-called "Mission Synthesis" procedure where a qualification test specification is derived for an electronic component (i.e., a VHF radio) mounted on a console inside a helicopter cockpit. The environmental vibrations, which are measured during various flight maneuvers, consist of deterministic sine tones superimposed on Gaussian random excitations, i.e. so-called "Sine-on-Random" (SoR) vibration. The Fatigue Damage Spectrum (FDS) model is utilized for analyzing the fatigue damage potential of these SoR excitations. A particular objective in this application example is to assess the induced fatigue damage for two design alternatives of the radio console, which is achieved by means of an FDS comparison. Furthermore, it is demonstrated that experimental modal analysis can provide valuable insights on the physical root causes for large induced fatigue damage, such that appropriate design modifications can be prescribed. Finally, the Mission Synthesis procedure enables the derivation of an accelerated but damage-equivalent shaker qualification test. For the component considered in this example it is demonstrated that the derived test specification is more severe than a MIL-STD standardized SoR test specification.

Keywords Mission synthesis • Sine-on-random • Fatigue damage spectrum • Experimental modal analysis • Helicopter

21.1 Introduction

In many engineering applications (e.g. in automotive or aerospace and defense), equipment and components are exposed to dynamic loads that may induce failures due to fatigue phenomena. To validate whether the hardware components will remain operational during their service life, they are subjected to extensive vibration tests on electrodynamic shakers, i.e. so-called qualification tests [1–5]. It has become standard practice to develop a qualification test specification based on the actual environmental conditions where these components (also referred to as Devices-Under-Test, DUT) will be mounted, instead of using a generic test specification from a standard (e.g. [4]). This procedure is referred to as "Test Tailoring" or "Mission Synthesis", and was originally proposed in French military standards [3]. The derived test should be "damage-equivalent", i.e. it should induce the same fatigue damage compared to the fatigue damage accumulated over the service life of the component, induced by the real-life environmental excitations [1, 2]. A particular challenge however is that the test should also be "accelerated", i.e. typically the shaker test duration should be significantly shorter than the service life of the component [5].

This paper considers a particular application example, where a qualification test specification has to be derived for an electronic component (i.e., a VHF radio) which is mounted on a console inside a helicopter cockpit. Helicopters and their subsystems/components are exposed to high vibration levels, because of the combination of a lightweight airframe structure and the presence of strong excitation sources, e.g. the rotor(s) [6–8]. The vibrations measured on helicopter structures and/or on helicopter subsystems/components therefore typically consist of strong deterministic sine tones, i.e. originating from the helicopter rotor(s), superimposed on Gaussian random excitations so that this "combined" vibration environment is commonly referred to as "Sine-on-Random" (SoR) vibration [4]. In structural dynamics testing, the presence of the (strong) deterministic sine tones typically makes the analysis more difficult. For example, as traditional (response-only) operational modal analysis techniques rely on a white noise assumption for the unknown input loads, the sine tones have to be filtered out of the operational data in a pre-processing step [6, 7]. For qualification testing of components mounted inside/onto

B. Cornelis • S. Manzato (✉) • B. Peeters • R.V. der Vorst
Siemens Industry Software NV, Interleuvenlaan 68, 3001, Leuven, Belgium
e-mail: simone.manzato@siemens.com

J. Hiatt
Siemens Industry Software North America, Detroit, MI, USA

J.M. Harvie, J. Baqersad (eds.), *Shock & Vibration, Aircraft/Aerospace, Energy Harvesting, Acoustics & Optics, Volume 9*,
Conference Proceedings of the Society for Experimental Mechanics Series, DOI 10.1007/978-3-319-54735-0_21

an helicopter, special efforts have similarly been made to account for the specific SoR vibration environment. Standards such as MIL-STD [4] already prescribe SoR shaker profiles, which can be applied in most modern shaker control systems. Furthermore, Mission Synthesis procedures for SoR environments have been developed [9–12].

The contributions of this paper are the following. First, it is demonstrated how the Mission Synthesis procedure allows assessing the (fatigue) damage potential of several SoR environments. In particular, it is explained how the damage potential can be quantified by the Maximum Response Spectrum (MRS) and Fatigue Damage Spectrum (FDS) functions [1, 2]. A particular objective in this work is to compare the induced (fatigue) damage for two design alternatives of the console onto which the DUT (i.e., a VHF radio) is mounted. This is achieved by means of a comparison of the aforementioned MRS and FDS functions. When comparing the two console designs, significant differences in the induced (fatigue) damage can be observed. In order to determine the root causes for this difference, an experimental modal analysis of the consoles is therefore performed. The results demonstrate that the combination of the MRS/FDS analysis with the experimental modal analysis leads to valuable insights which can improve the radio console design. Finally, an accelerated but damage-equivalent shaker profile is derived based on the Mission Synthesis results. For the component considered in this example it is demonstrated that the derived test specification is more severe than a MIL-STD standardized SoR test specification, highlighting the value of the Mission Synthesis procedure.

The remainder of the paper is organized as follows. Section 21.2 presents a theoretical review of the Mission Synthesis procedure, including a mathematical treatment of the MRS and FDS calculation. Section 21.3 describes the measurement campaign on an MD902 helicopter, which triggered this work. Section 21.4, 21.5, and 21.6 present the results of the MRS/FDS comparisons, experimental modal analysis and derivation of the test profile, respectively. Finally, Section 21.7 reports the conclusions of the work.

21.2 Mission Synthesis: Theoretical Background

Figure 21.1 presents a schematic overview of the different steps in the Mission Synthesis procedure, which will be further elaborated in this section.

A first crucial phase, referred to as "Mission Profiling" [2], consists of steps 1 and 2 in Fig. 21.1. It entails a definition of the "missions", i.e. a description of the different vibration environments which will be encountered by the DUT during its intended service life. The majority of the service life is typically spent while the DUT in operation at the end user, i.e. during customer usage, but also other phases during the product lifecycle can be important (e.g. a transport phase where the DUT is transported from a component supplier to the OEM). As part of the definition, also a quantification of the exposure time (i.e. time spent in each environment) has to be made. In order to characterize the vibrations in each encountered mission, dedicated operational measurements have to be performed, whereby an accelerometer is placed on the vibrating "host structure" onto

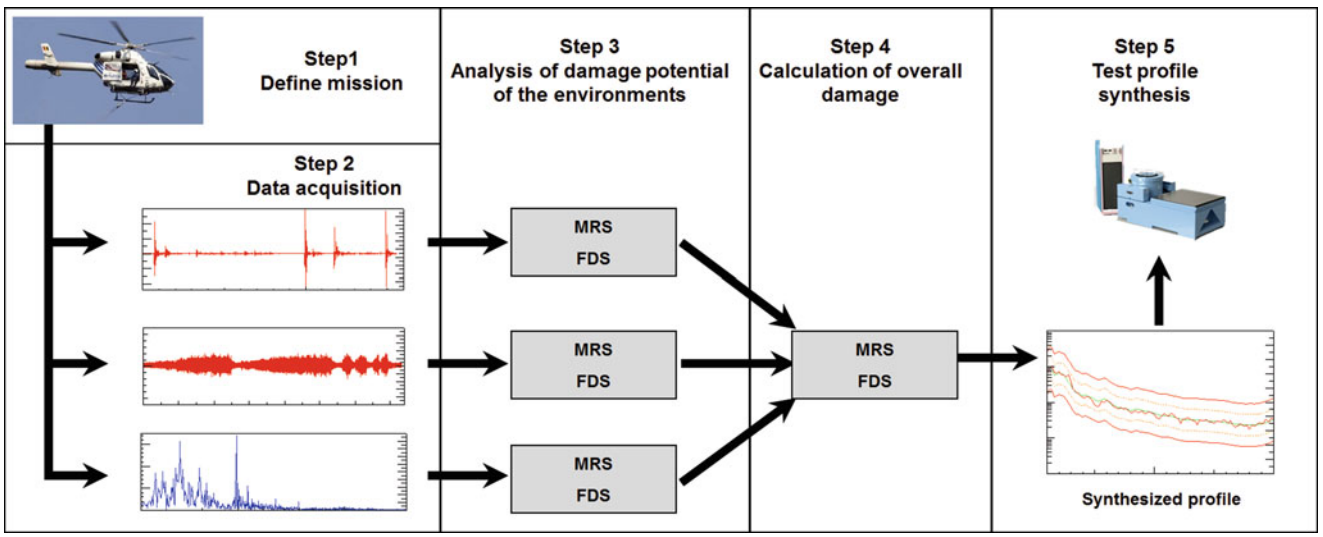

Fig. 21.1 Schematic overview of mission synthesis procedure

which the DUT will be mounted. These recorded vibration signals should be viewed as the "input" vibrations which are seen by the DUT. An example of "Mission Profiling" will be discussed in Sect. 21.4.

After the Mission Profiling stage, the damage potential of each identified environment has to be quantified, cf. steps 3 and 4 in Fig. 21.1. In principle, a (fatigue) damage assessment would require a calculation or a measurement of the stress responses at all possible critical locations on the DUT. In practice it is often too time-consuming and too costly to indeed perform such assessment, especially so for complex electronic components. The considered procedure therefore makes a simplified working assumption, such that a relatively straightforward measurement of the "input" vibrations are sufficient for a quantification of the damage potential of each environment. Similar to the determination of the classic Shock Response Spectrum (SRS) [13], a fictitious single-degree-of-freedom (SDOF) reference system with a variable resonance frequency is assumed. The SDOF reference system allows for an assessment and comparison of the different environmental "input" excitations, independently from the actual characteristics of the DUT. The damage potential of different input excitations can then be quantified by two functions, namely the so-called Maximum Response Spectrum (MRS) and the so-called Fatigue Damage Spectrum (FDS) [1, 2].

The MRS is calculated as the maximum of the mass acceleration response, for a given input acceleration which is applied to the base of an SDOF system with resonance frequency f_n and damping factor ζ. The resonance frequency is hereby varied, so that a result in function of f_n is obtained ("a spectrum"). The damping factor is typically chosen as $\zeta = 0.05$ (cf. [1]), which is equivalent to a Q-factor equal to 10 (i.e., $Q = 1/(2\zeta)$). The MRS is thus very similar to the classic SRS, the difference being that the SRS is usually only calculated for shock input excitations [13]. The MRS is sometimes used to study low cycle fatigue phenomena, where the stress is high enough for plastic deformations to occur [14].

The FDS is calculated similarly as the MRS (i.e. calculate the SDOF response for a given base input excitation and for different SDOF resonance frequencies, yielding a "spectrum"). However, in this case the complete response timeseries (in this case, the relative displacements of the mass) are subsequently processed by a cycle counting algorithm (e.g. the rainflow counting method [15]). The high-cycle fatigue damage (which is a failure phenomenon driven by cyclic loading) can then be calculated based on three main assumptions [14]. First, it is assumed that the stress response timeseries $\sigma(t,f_n)$ is proportional to the calculated relative displacement timeseries $z(t,f_n)$, i.e.

$$\boldsymbol{\sigma}\,(\boldsymbol{t},\boldsymbol{f_n}) = \boldsymbol{K}.\boldsymbol{z}\,(\boldsymbol{t},\boldsymbol{f_n}) \tag{21.1}$$

where K is the linear stiffness constant relating relative displacement to stress, and where the second variable f_n is explicitly included to indicate that a separate time history is calculated for each chosen SDOF resonance frequency f_n. Furthermore, it is assumed that the fatigue life of the component can be described by a Wöhler curve (without endurance limit), which follows Basquin's law [16], i.e.

$$\boldsymbol{N_{f,i}}.\boldsymbol{S_{a,i}^{b}} = \boldsymbol{A^{b}} \tag{21.2}$$

In Eq. (21.2), the values $N_{f,i}$ represent the fatigue life, i.e. the maximum number of cycles that the component can endure when subjected to a sinusoidal load with corresponding stress amplitude $S_{a,i}$. The parameters A and b are material parameters which determine the intercept and slope of the Wöhler curve, respectively. The final assumption is that the fatigue damage accumulation follows the Palmgren-Miner linear damage accumulation rule [17, 18], i.e.

$$\boldsymbol{D} = \sum_{\boldsymbol{i}} \boldsymbol{d_i} = \sum_{\boldsymbol{i}} \frac{\boldsymbol{n_i}}{\boldsymbol{N_{f,i}}} \tag{21.3}$$

In Eq. (21.3), the values n_i are the actual number of cycles at stress amplitude $S_{a,i}$ that the component experiences. If $n_i = N_{f,i}$, the damage is equal to 1 and the component will fail. The values n_i are obtained by applying the rainflow counting algorithm on the stress response timeseries of Eq. (21.1). By combining Eqs. (21.1, 21.2, and 21.3), and by defining $Z_{a,i} = (1/K)\, S_{a,i}$, it can easily be seen that the FDS is given by:

$$\mathbf{FDS}\,(\boldsymbol{f_n}) = \frac{\boldsymbol{K^{b}}}{\boldsymbol{A^{b}}} \sum_{\boldsymbol{i}} \boldsymbol{n_i}\,(\boldsymbol{f_n})\,.\boldsymbol{Z_{a,i}^{b}}\,(\boldsymbol{f_n}) \tag{21.4}$$

From Eq. (21.4) it can be observed that the parameters K and A merely scale the FDS, independently of the actual cycles and amplitudes that are induced by the input excitation. As our goal is only to make relative comparisons of the potential damage induced by different excitations (rather than making accurate fatigue life estimations), these parameters can therefore be treated as normalization constants. The absolute value of the FDS then no longer has a physical meaning (sometimes the

term "pseudo-damage" is used), but it can still be used in relative comparisons so that the outcome of the procedure is not affected. In contrast, the parameter b (which determines the slope of the Wöhler curve) may have a more significant impact on the result, especially when the synthesized test is highly accelerated [5, 14]. An accurate determination of the b parameter may be difficult (especially for electronic components which consist of multiple different materials), so that standards are usually consulted to select an appropriate parameter.

The aforementioned MRS/FDS calculations allow to quantify the damage potential of each environment. These MRS and FDS functions however have to be combined into a "lifetime" MRS and FDS, which represent the total intended lifetime of the DUT (referring back to Fig. 21.1, "step 4" of the Mission Synthesis procedure). The most straightforward situation is the case where the DUT undergoes a series of different, independent environmental conditions. In this case, the lifetime MRS can be obtained by enveloping the individual environmental MRS functions, as this represents the worst case situation (important e.g. for strength failures). The lifetime FDS can be obtained as the sum of the individual environmental FDS functions, which is again motivated by the Palmgren-Miner linear damage accumulation, cf. Eq. (21.3).

Finally, the lifetime MRS and FDS functions can now be utilized to synthesize an accelerated but damage-equivalent shaker test profile (referring back to Fig. 21.1, "step 5" of the Mission Synthesis procedure). Depending on the failure mode that needs to be tested, either the lifetime MRS or the lifetime FDS can be used as starting point, but only the FDS-based synthesis will be considered here as we are mainly interested in failures due to high cycle fatigue phenomena. Similar to [9], we here only consider the most common approach where a Power Spectral Density (PSD) profile is derived, implying a Gaussian random shaker test. In this case, the input acceleration PSD ($W_{\ddot{x}}$), which has to be set as target profile in the shaker test, can be obtained by a closed-form analytical expression [1, 2], i.e.

$$W_{\ddot{x}}(f_n) = \frac{2.(2\pi f_n)^3}{Q} \left(\frac{FDS(f_n).A^b}{f_n.T.K^b.\Gamma\left(1+\frac{b}{2}\right)} \right)^{\frac{2}{b}} \tag{21.5}$$

In Eq. (21.5), Q is the assumed Q-factor of the SDOF system, T is the duration of the shaker test, and $\Gamma(.)$ is the Gamma function, i.e. $\Gamma(t) = \int_0^\infty x^{t-1} e^{-x}\, dx$.

The test duration factor T has to be chosen with care. In order to check that a proper value is selected, the MRS of the obtained test profile is usually calculated and compared to the overall lifetime MRS. In order to avoid undertesting, it is advisable that the MRS of the obtained test profile slightly exceeds the lifetime MRS [1]. However, if the test MRS greatly exceeds the lifetime MRS, there is a risk that the excitation levels may become too high so that the DUT fails due to exceeding the ultimate stress limit (instead of failure due to accumulated fatigue damage) [5]. In this case, the specified test duration needs to be increased to avoid testing the wrong failure mode.

21.3 Measurement Campaign: MD 902 Helicopter

An extensive measurement campaign was performed on a twin-engine light utility helicopter (i.e. MD 902, cf. Fig.21.2). The helicopter is part of a fleet of a law enforcement agency (Belgian Federal Police), and is mainly used in support and patrol

Fig. 21.2 MD 902 Helicopter with NOTAR *("NO TAil Rotor")* system

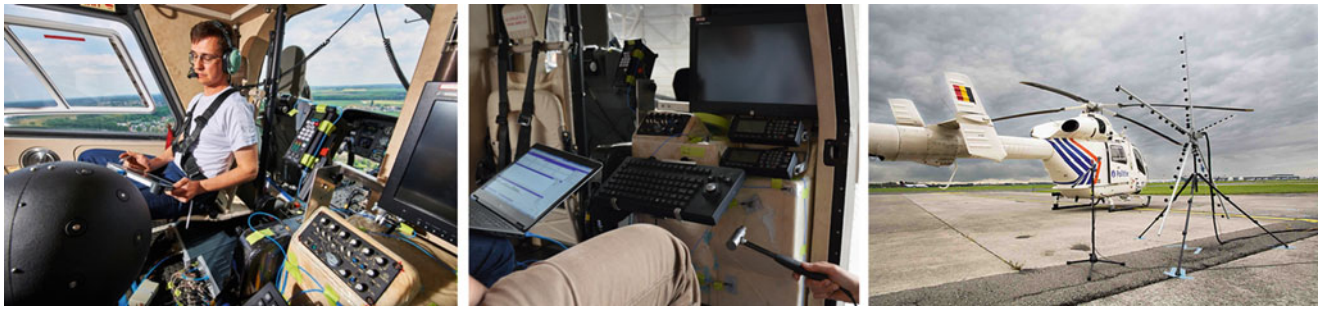

Fig. 21.3 In-Flight Noise and Vibration Measurements (*Left*), Impact Testing of Radio Console (*Middle*), Exterior Sound Source Localization (*Right*)

missions (e.g. air support in law enforcement missions, traffic regulation, air surveillance during large public events, ...). The main characteristics of the helicopter are the following:

- The main rotor has a fundamental frequency at 392 RPM (6.53 Hz), with blade passing frequency at 32.65 Hz (i.e., rotor with 5 blades).
- The helicopter employs a NOTAR anti-torque system, i.e. it does not have a tail rotor.

The measurement campaign consisted of various types of noise and vibration measurements. The measurements were conducted both during flight maneuvers and in non-flight conditions where the helicopter is on the ground.

To characterize the noise emissions, both exterior and interior sound source localization measurements were performed using star-shaped (exterior) and spherical (indoor) microphone arrays (cf. Fig. 21.3). By analyzing the time delays between the recorded microphone signals, it is possible to identify and display the dominant noise sources with their corresponding acoustic power [19].

The main focus of this paper is however on the vibration measurements. Accelerometers were instrumented in various locations inside the helicopter cockpit (cf. Fig. 21.3). In particular, it is important to characterize the vibrations which are experienced by the various electronic devices inside the cockpit (instrument panel, camera control system, radio communication equipment, ...), as long-term exposure to these vibrations may lead to component failure due to accumulated fatigue damage. In this work, we focus on the vibrations which are experienced by the VHF radio equipment. The VHF radio is mounted on a console (cf. Sect. 21.4), whereby the console thus acts as transfer path between the helicopter vibrations and the VHF radio. To measure the "input vibration" seen by the VHF radio (required for Mission Synthesis), an accelerometer is instrumented on the console close to the radio mounting point, i.e. the radio support bracket. Various accelerometers were also instrumented at other points on the console, in order to perform a modal analysis of the structure. All accelerometer channels were recorded both during operational (in-flight) measurements (cf. Sect. 21.4), and during impact testing (cf. Sect. 21.5).

21.4 Mission Synthesis Application: Comparison of Radio Console Designs

This section describes how the Mission Synthesis procedure was applied to this helicopter application example. A particular objective of the work was to make a comparison between two designs for the radio console. The console is the vibrating "host" structure onto which the VHF radio is mounted. It is therefore crucial that the console does not vibrate excessively such that no large excitations are imposed on the radio, as these may lead to (fatigue) failures in the radio circuitry. Fig. 21.4 shows a picture of the "old" console design, i.e. the console which was used in previous helicopter missions, and a virtual mock-up of the "new" console design, which will be used in future missions. For the "old" console, there is the additional information that no radio equipment failures ever occurred during the previous missions. If it could be proven that the "new" console design imposes the same (or lower) excitations on the radio equipment (in terms of induced fatigue damage), then the new design can also be considered safe such that a new qualification test would not be required.

As discussed in Sect. 21.2, the first steps of the Mission Synthesis procedure comprise the definition of the missions (i.e. the vibration environments that will be encountered during the lifetime of the DUT) and the data acquisition where operational vibrations are measured in the identified environments. All operational measurements were performed for two configurations, i.e. one configuration where the old console is installed and another configuration where the new console is installed inside the cockpit, hence resulting in two independent datasets. The operational conditions encountered by the

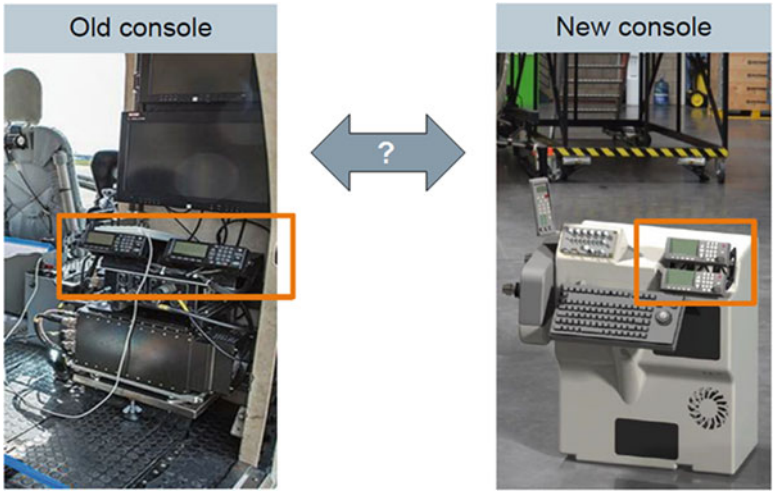

Fig. 21.4 Old (*Left*) and New (*Right*) console designs; VHF radio equipment is indicated

Table 21.1 Mission definition

Mission name	Usage % of total lifetime	# Hours in service
Power up	1%	300 h
Hover On Ground	5%	1500 h
Take Off	5%	1500 h
Hover Off ground	18%	5400 h
Flying at 80 knot = 92 mph	40%	12,000 h
Flying at 120 knot = 138 mph	25%	7500 h
Landing + Power down	6%	1800 h

helicopter were roughly classified into seven categories, as listed in Table 21.1. Each of these conditions was hence defined as a mission, and representative operational vibration measurements were acquired in each mission. Based on the experience of the flight crew, it was furthermore estimated which proportion of the total lifetime is spent in each mission (cf. middle column in Table 21.1). For the further analyses in this work, it was assumed that the DUT should remain in service for a total of 30.000 flight hours. Under this assumption, the amount of service hours for each mission can be readily calculated, cf. the last column of Table 21.1.

Using the acquired operational data, the damage potentials of the seven identified missions can now be quantified by the MRS and FDS functions, as previously explained in Sect. 21.2. The two datasets (old console and new console) were independently processed, assuming however the same parameters settings. The calculations assumed $Q = 10$, $K = A = 1$, and a Basquin slope coefficient $b = 5$. The value of b was selected based on a NATO standard [20], which recommends this value for electronic components. Other references however recommend a value $b = 6.4$, cf. [9, 21]. This alternative choice of the b value however does not have an impact on the main conclusions of this work.

Figure 21.5 illustrates the obtained MRS and FDS results for the different missions (new console dataset). The estimated service hours for each environment (cf. last column Table 21.1) have been taken into account in this comparison. For example, although the mission "flying at 80 knots" does not lead to the largest expected maximum response amplitude (cf. MRS), it accounts for the largest contribution in the consumed fatigue life (cf. FDS), due to the fact that 40% of the lifetime (12.000 hours) is spent in this condition. Both the MRS and FDS contain distinct peaks which are related to the main rotor harmonics (cf. fundamental frequency around 6.5 Hz, blade passing frequency around 33 Hz, and higher orders). As previously noted, the considered helicopter does not have a tail rotor, such that only main rotor harmonics are visible. For most environments, these peaks appear at the same frequencies, which is typical for helicopter vibration (rotor operates at fixed rotational speed). The only exception is the "Power Up" mission, which is the start-up phase before take-off where the rotor is ramping up its speed.

As expected, especially around the blade passing frequency (indicated in Fig. 21.5) large values can be observed in both the MRS and FDS. We recall that the figures should be interpreted as "damage potential" figures. Namely, if a DUT with structural resonance around 33 Hz would be mounted on the point where the vibration was measured, a large induced (fatigue) damage can be expected. Conversely, if the DUT has a resonance at another frequency (e.g. 100 Hz), the induced

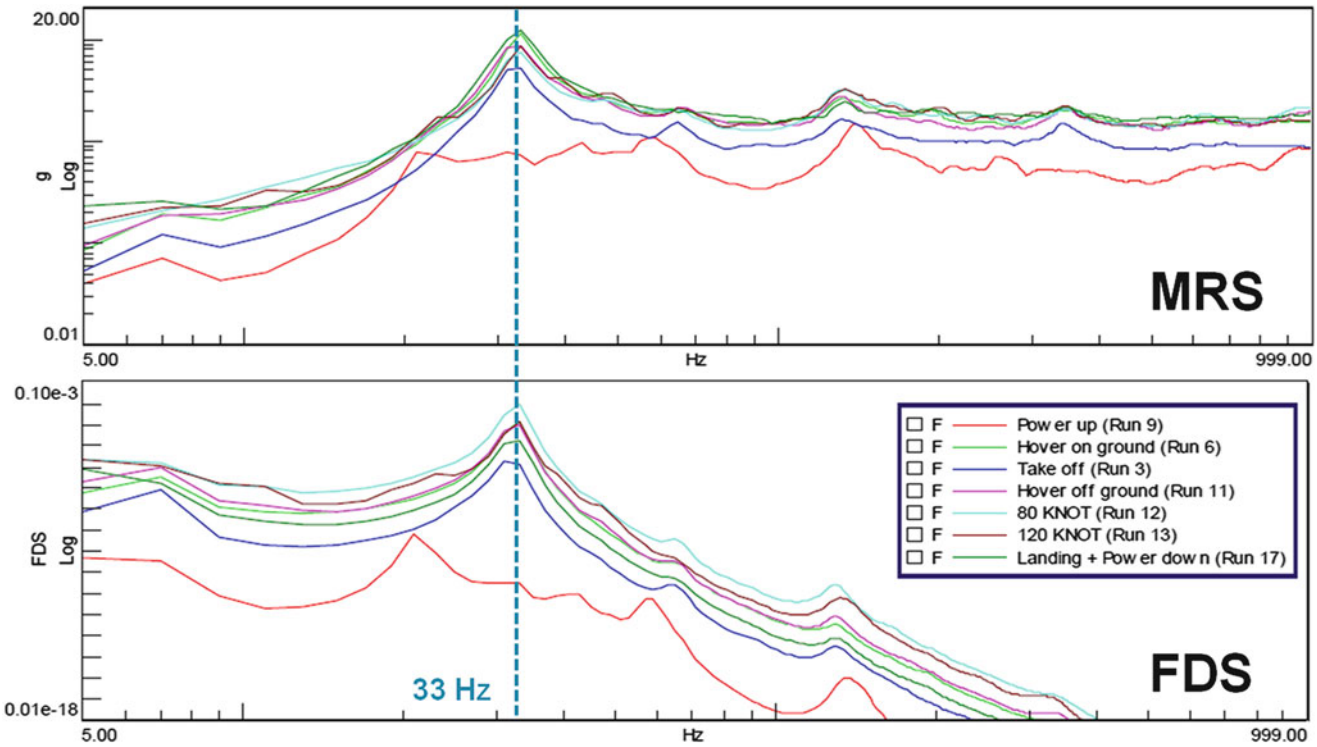

Fig. 21.5 Analysis of the damage potential (MRS and FDS) for 7 identified missions; "New" console data

damage would be much lower. However, as we need to treat the DUT as an unknown "black box" system, we cannot make such assumptions and instead need to synthesize a "safe" shaker qualification test (irrespective of the system characteristics of the DUT).

The seven mission MRS and FDS functions can now be combined into one "lifetime MRS" and "lifetime FDS", which represent the total potential damage induced over the intended lifetime of the DUT (30.000 flight hours). As explained in Sect. 21.2, this calculation is rather straightforward in this example: the lifetime MRS is obtained by enveloping the MRS functions, while the lifetime FDS is obtained by summing the FDS functions. The results are shown in Fig. 21.6, where the data for the old and new console are now displayed together, thus allowing for a comparison. It is clearly observed that the new console design does not always lead to lower damage values, especially so for the frequency region around the blade passing frequency (33 Hz). From previous experience it was known that the old console design never caused failures of the DUT. Given these analysis results, we cannot conclude whether this will still be the case for the new console design: if the DUT presents a natural frequency around 33 Hz, the new console design causes significantly more induced fatigue damage, which may lead to failures. There are now several options to resolve the situation:

- Characterization of the DUT, to understand whether the excitation around 33 Hz is problematic or not. However, as indicated in the motivation for Mission Synthesis, such assessment is typically too time-consuming and too costly, as the DUT is a complex electronic component with unknown failure locations, and should thus be treated as an unknown "black box".
- Perform a root cause analysis which explains "why" the new console design induces higher damage to the DUT. As will be demonstrated in Sect. 21.5, a relatively straightforward experimental modal analysis through impact testing allows to characterize the console. This analysis reveals the physical root causes which cause the higher MRS/FDS values, which can furthermore be used to make appropriate design modifications. It should be noted that the difference with previous bullet is that in this case, the "host structure" which causes the vibration environment is characterized, rather than the DUT itself.
- If the console is not modified, a new qualification test for the DUT can be performed, in order to certify the DUT for the "new" vibration environment. The qualification test profile is hereby synthesized from the lifetime FDS, as will be elaborated in Sect. 21.6.

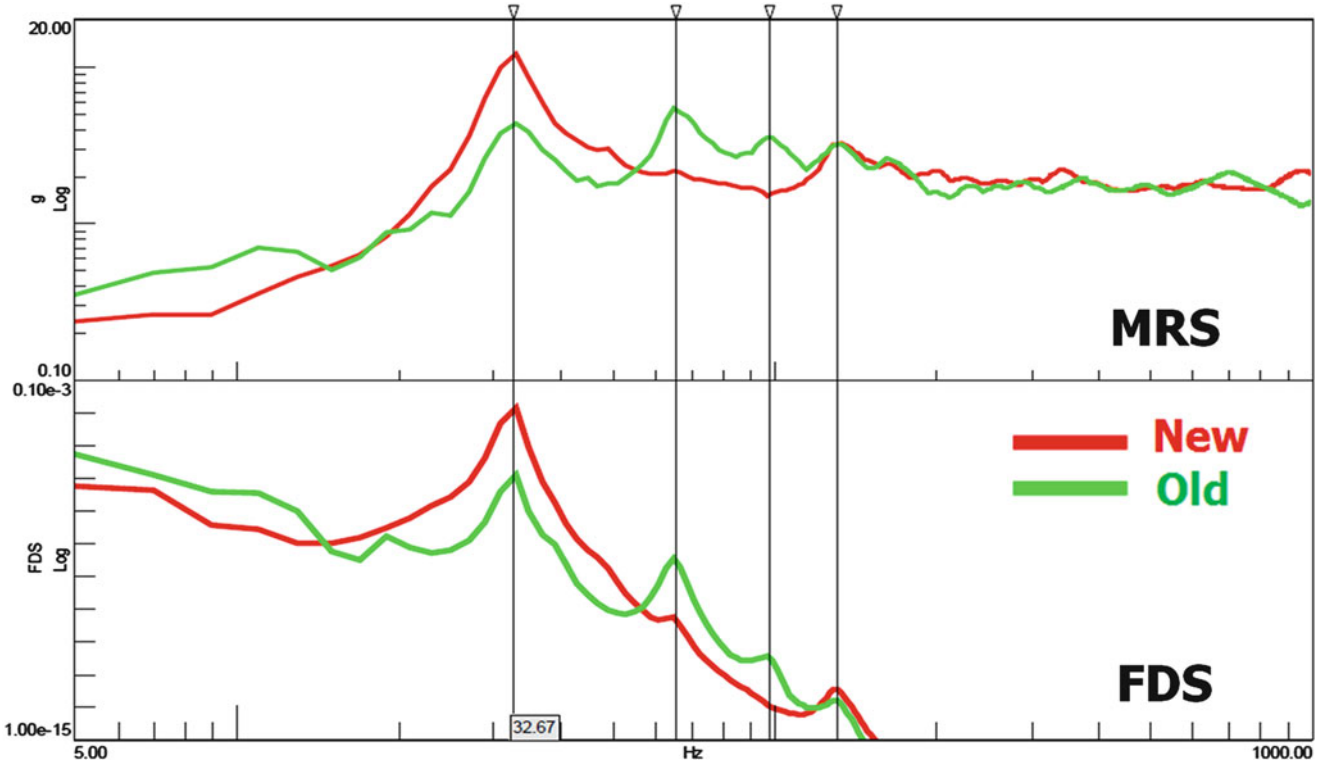

Fig. 21.6 Lifetime MRS and FDS for "Old" and "New" console data

21.5 Experimental Modal Analysis: Root Cause Analysis

In order to understand and justify the observed differences in the MRS/FDS functions between the two console designs, Frequency Response Functions (FRFs) were measured on both consoles using impact testing. Impact testing represents a handy, practical and efficient solution in combination with Mission Synthesis: it provides insights in the dynamic response of the structure of interest (in this case, the radio console) directly in operational configuration, while requiring a limited instrumentation for the measurements.

In this particular case, an impact test was performed on each of the two console designs using a standard modal hammer and a few accelerometers (both triaxial and single axis) distributed over the structure. Fig. 21.7 shows the different setups used. In the old console, because of the simpler design, fewer sensors are required to capture the overall dynamics. On the other hand, the new console is designed to neatly accommodate as many components as possible. As a result, the shape is more complex and more sensors/measurement locations are required to describe the dynamic response.

The colored arrows represent the locations and directions where impacts are applied; additionally, the target points for the MRS/FDS analysis, i.e. the radio support brackets, are also indicated. Because of the completely different designs, replicating the same experimental setup in both cases was not possible. However, FRFs can be viewed as inherent system characteristics which are independent from the applied excitation (under the assumption that the system behaves linearly). Consequently, a qualitative comparison of the FRFs at the point of interest can already yield some insights on the differences between the two designs.

The measured FRFs between the acceleration on the target point of interest and the excitation locations are shown in Fig. 21.8. In Sect. 21.4, the most critical peaks for both FDS and MRS were identified at a frequency of approximately 33 Hz, which was thought to be caused (only) by the blade passage. The FRFs however also show a clear peak in the vicinity of this frequency for both consoles, so that it can already be concluded that whatever excitation applied at that frequency will be significantly amplified and will result in a very strong response. By qualitatively comparing the FRFs for the two designs, it can moreover be observed that the peak is generally wider for the old console, which indicates a higher damping and thus a better dissipation of energy. Consequently, as discussed in the previous section, the operational excitation imposed by the older console design is expected to be less critical for the radio equipment, in case the radio equipment presents a natural frequency in this frequency region.

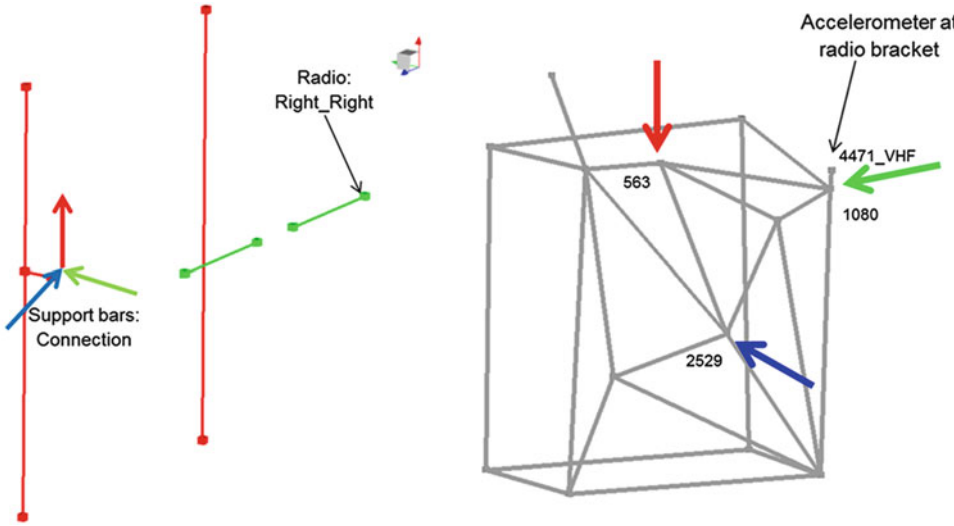

Fig. 21.7 Test geometries for impact testing of "Old" console (*Left*) and "New" console (*Right*)

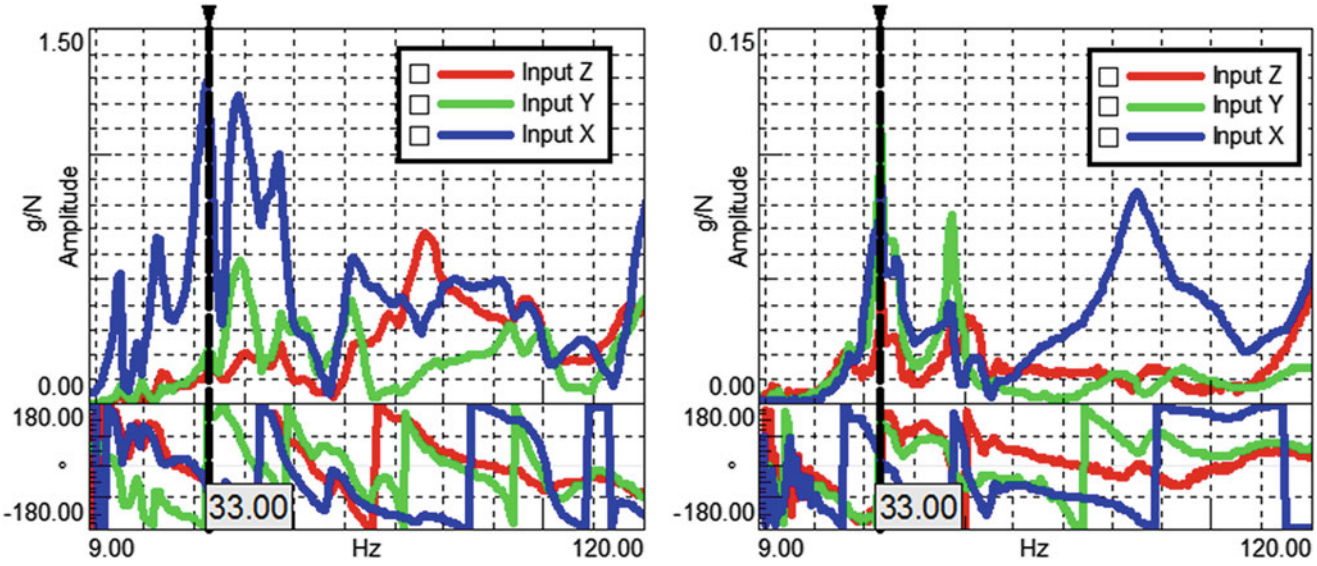

Fig. 21.8 Measured FRF between impact location and target point (vertical acceleration on radio support bracket), for "Old" console (*Left)* and "New" console (*Right)*

A more effective and complete way of analyzing the problem and derive conclusions is to process the measured FRFs using modal analysis. Rather than qualitatively analyzing the FRFs, modal parameter estimation allows to derive natural frequencies, damping ratios and mode shapes to quantitatively and objectively analyze the dynamic behavior of the structure [22]. A key advantage of performing modal analysis is that it processes all data at the same time, thus providing global results. Also, by comparing the measured and synthesized FRFs, one can easily get an idea of the quality of the process and gain confidence in the analysis. The results for the old console are reported in Fig. 21.9, while Fig. 21.10 summarizes the findings for the new console.

The excellent matching between the measured and synthesized FRFs in the considered frequency band gives high confidence in the identified modal parameters. By looking at the mode shapes, it is clear how for both designs the mode around 33 Hz is extremely local on the point of interest (radio support bracket). Finally, as confirmation to the previous qualitative considerations, the modal damping in the new console is indeed almost four times lower than in the old one. As a consequence, since the excitation acting on the components in the operating conditions will be the same, the much lower damping will cause the excitation to be much more critical as less energy is dissipated. From a fatigue analysis point of view, this can directly justify and explain the higher MRS/FDS values observed for the new console design around 33 Hz. Furthermore, a recommendation for a design modification can also be made by virtue of this analysis. Namely, the console design could be modified such that the local mode around 33 Hz is avoided.

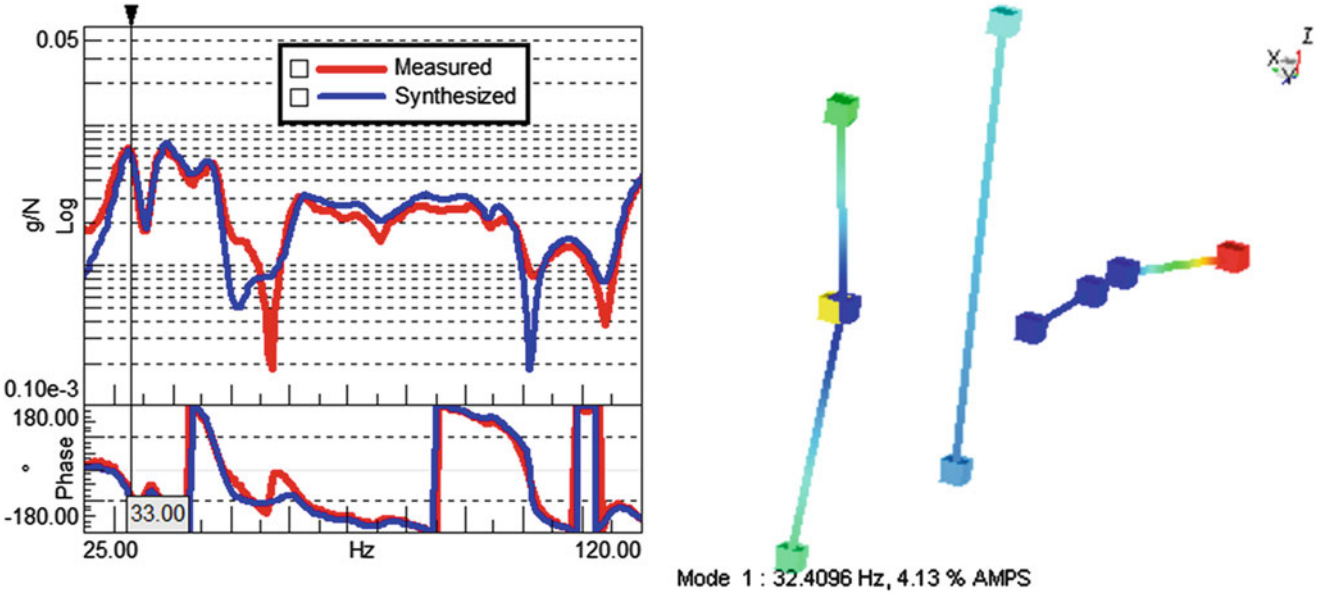

Fig. 21.9 Modal analysis results for the "Old" console; (*Left)*: Synthesized vs. Measured FRF; (*Right)*: modal parameters (frequency, damping, deformation) for the mode of interest

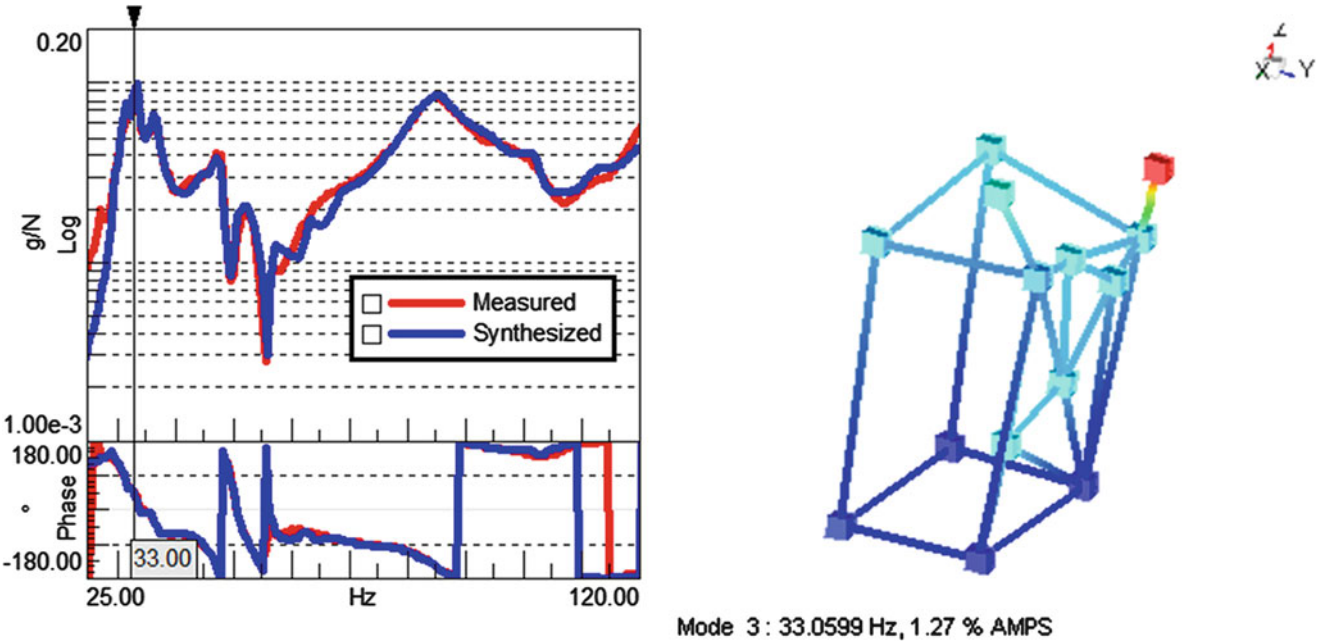

Fig. 21.10 Modal analysis results for the "New" console; (*Left*): Synthesized vs. Measured FRF; (*Right*): modal parameters (frequency, damping, deformation) for the mode of interest

21.6 Derivation of Shaker Test Profile and Comparison with Standard Profile

In this section, it will be demonstrated how a shaker test profile can be synthesized based on the previously calculated "lifetime FDS". It could however be questioned whether a standardized test profile would also lead to a "safe" qualification test. To investigate this, a MIL-STD standard SoR test profile was used as reference, cf. Fig. 21.11.

For this SoR profile, a direct "analytical" calculation of the MRS and FDS is possible [1, 12]. Based on the description in the standard, a test duration time of 48 h was assumed, as the test should then be representative of 30.000 operational flight hours. The obtained MRS/FDS results can then be directly compared to the lifetime MRS and lifetime FDS for the new console, cf. Fig. 21.12. The comparison shows that the standard SoR profile does not completely cover the lifetime

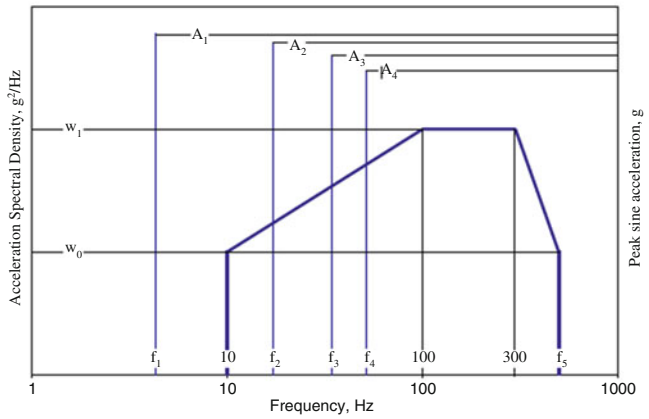

Parameters:

- Rotation speed main rotor = 392 rpm = 6.53 Hz
- #blades = 5
- Note: no tail rotor (NOTAR)

f1 = 6,53 Hz	A1 = 0,168 g
f2 = 32,67 Hz	A2 = 1,75 g
f3 = 65,33 Hz	A3 = 1,05 g
f4 = 98 Hz	A4 = 1,05 g

Fig. 21.11 MIL-STD SoR profile ([4], pg. 326/2.3 Category 14 – Rotary wing aircraft – helicopter)

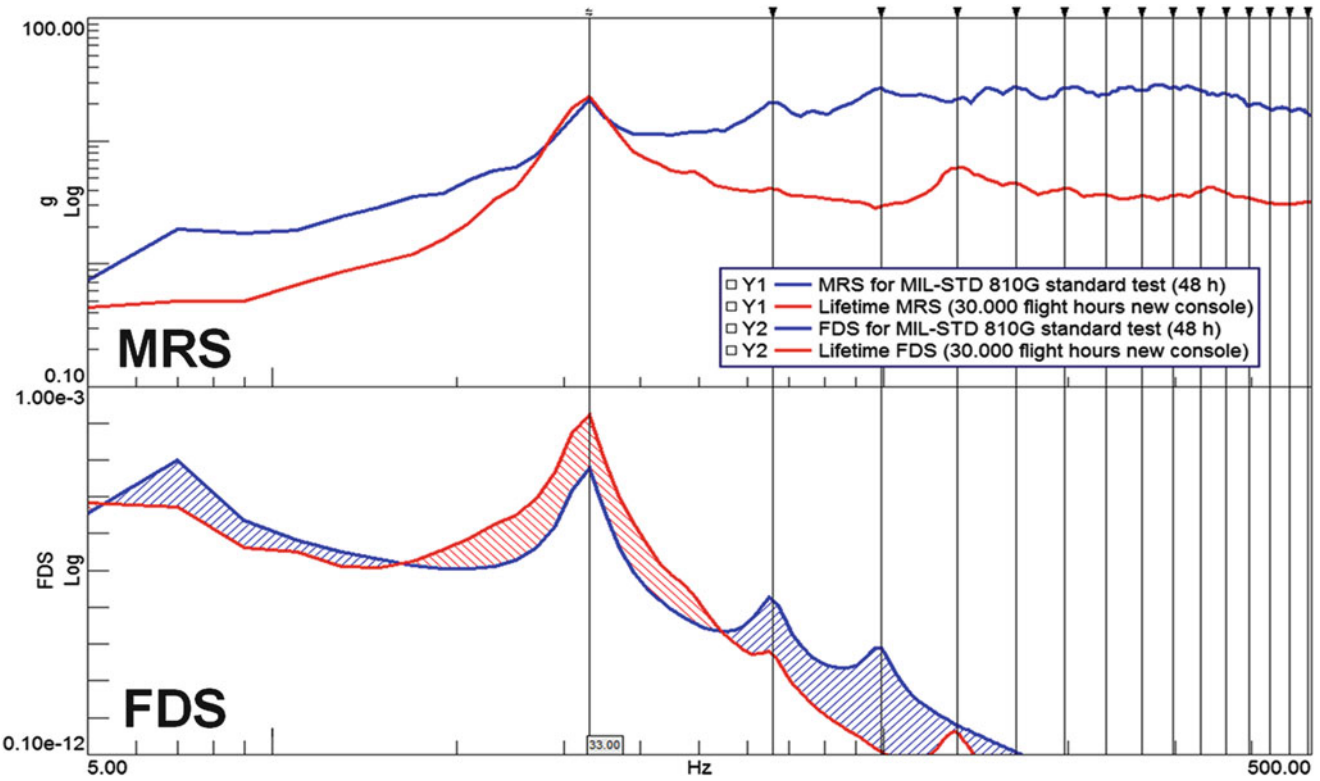

Fig. 21.12 MRS/FDS for MIL-STD SoR profile vs. lifetime MRS/FDS (new console) from Mission Synthesis

mission, in particular in the frequency region around the blade passing frequency (33 Hz). If a component has been qualified using this test specification, we thus cannot guarantee safe operation (in absence of more detailed information about the component).

The previous discussion now motivates a derivation of a "tailored" qualification test profile, i.e. a test profile which is synthesized from the lifetime FDS and is thus better matched to the real-life operational conditions which are encountered by the DUT. As a means of demonstration, we here follow the most common approach where a PSD profile is derived from the lifetime FDS. In this case, the PSD can be obtained by Eq. (21.5), whereby a test duration of 48 h is specified. To check whether this is an appropriate choice, the Root Mean Square (RMS) of the profile is calculated. The RMS should be reasonable, e.g. it should be producible within the shaker's limitations, which is the case in this example (See Fig. 21.13).

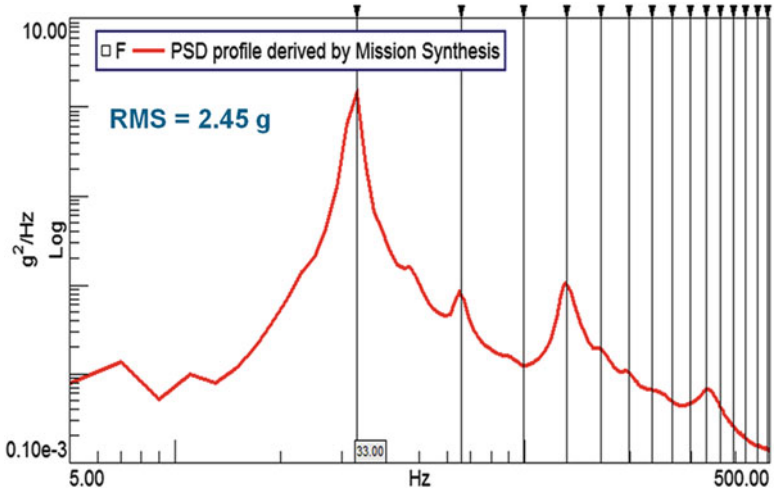

Fig. 21.13 PSD profile synthesized from lifetime FDS

21.7 Conclusions and Outlook

This paper gave an overview of the so-called "Mission Synthesis" procedure, which is used for the derivation of a "tailored" shaker test profile that is used to qualify a DUT. An application example was presented where the procedure is applied to a VHF radio which is mounted on a console inside a helicopter cockpit. A particular point-of-interest is that two different designs for the console were studied. Using the MRS and FDS functions, which are calculated during the Mission Synthesis procedure, it was demonstrated that these consoles (which act as the vibrating "host" structures on which the DUT is mounted) would induce a significantly different (fatigue) damage to the radio. Furthermore, it was demonstrated that an experimental modal analysis (conducted through an impact test) can provide valuable insights into the physical root causes for these observed differences. Finally, it is demonstrated that a standard SoR test profile was not sufficient to cover the lifetime mission in this example, which motivates the derivation of a test profile based on the Mission Synthesis procedure.

In other ongoing research work [12], efforts are focused on the latter aspect, i.e. the derivation of the test profile for SoR excitations. In the current state-of-the-art, it is only possible to synthesize a PSD profile (i.e. Gaussian random excitations) or a sine sweep profile (i.e. purely deterministic sine tone excitations). These are poor approximations of the real-life helicopter environment, which is rather a combination of both types (i.e. sine-on-random). Therefore, it has been proposed [12] to instead synthesize a true SoR profile, and future investigations are planned to assess the benefits of this new approach.

Acknowledgements The authors would like to thank the Belgian Federal Police Air Support Unit for enabling the measurement campaign. The research was conducted in the frame of the project IWT 130936 ADVENT (Advanced Vibration Environmental Testing). The financial support of VLAIO (Flanders Innovation & Entrepreneurship) is gratefully acknowledged.

References

1. Lalanne, C.: Mechanical Vibration and Shock Analysis – Volume 5: Specification Development, 3rd edn. Wiley – ISTE, London (2014)
2. Lee, Y.-L., Kang, H.-T.: Vibration fatigue testing and analysis, Ch. 9. In: Lee, Y.-L., Barkey, M.E., Kang, H.-T. (eds.) Metal Fatigue Analysis Handbook: Practical Problem-Solving Techniques for Computer-Aided Engineering. Butterworth-Heinemann/Elsevier, Waltham, MA, USA (2011)
3. de la Defense, M.: GAM EG-13, Essais generaux en environment des Materials (General Tests of Materials in Environment). Delegation Generale pour l'armement, France (1986)
4. US Department of Defense. MIL-STD-810G, Department of Defense Test Method Standard for Environmental Engineering Considerations and Laboratory Tests, USA, (2008).
5. A.G. Piersol. Accelerated Vibration Testing-Proceed With Caution, Tustin Training News, (1993).
6. Grappasonni, C., Ameri, N., Coppotelli, G., Ewins, D.J., Colombo, A., Bianchi, E., Barraco, V.: Dynamic identification of helicopter structures using operational modal analysis methods in the presence of harmonic loading. In: Proceedings of the ISMA 2012, Leuven, Belgium, (2012)
7. Peeters, B., Cornelis, B., Janssens, K., Van der Auweraer, H.: Removing disturbing harmonics in operational modal analysis. In: Proceedings of the International Operational Modal Analysis Conference (IOMAC), Copenhagen, Denmark, (2007).
8. Johnson, W.: Helicopter Theory. Dover Publications, Inc., New York, (1980)

9. Irvine, T.: Derivation of equivalent power spectral density specifications for swept sine-on-random environments via fatigue damage spectra. In: Proceedings of the International Conference on Engineering Vibration (ICOEV), Ljubljana, Slovenia, September 2015, (2015).
10. Marques, V., Meola, T., Duarte, M.: Development of sine-on-random accelerated tests applied to turbocharger electronics actuators. In: Proceedings of the 22nd International Congress of Mechanical Engineering, (2013).
11. Cho, D.: Evaluation of vibration test severity by FDS and ERS. In: Proceedings of the ISMA 2010, pp. 1725–1736, (2010).
12. Angeli, A., Cornelis, B., Troncossi, M.: Fatigue damage spectrum calculation in a mission synthesis procedure for sine-on-random excitations. J. Phys. **744**(1), 012089 (2016)
13. Rubin, S., Ahlin, K.: Shock data analysis, Ch. 20. In: Piersol, A.G., Paez, T. (eds.) Harris' Shock and Vibration Handbook, 6th edn. McGraw-Hill Inc., New York, (2010)
14. Troncossi, M., Cipollini, R., Rivola, A.. Experimental evaluation of the FDS-based equivalence approach for the mission synthesis in accelerated life tests, In: Proceedings of the International Congress on Sound & Vibration (ICSV), Bangkok, Thailand, 2013 July 7–11, Bangkok (2013).
15. Matsuishi, M., Endo, T.. Fatigue of metals subjected to varying stress, In: Proceedings of the Japan Society of Mechanical Engineers, Fukuoka, Japan, (1968).
16. Basquin, O.H.: The exponential law of endurance tests. In: Proceedings of the American Society for Testing and Materials, vol. 10, pp. 625–630 (1910)
17. Palmgren, A., von Kugellagern, D.L.: (The service life of ball bearings), Zeitschrift des Vereins Deutscher Ingenieure. VDI J. **68**(14), 339–341 (1924)
18. Miner, M.A.: Cumulative Damage in Fatigue. J. Appl. Mech. **67**, A159–A164 (1945)
19. Lanslots, J., Deblauwe, F., Janssens, K.: Selecting sound source localization techniques for industrial applications. Sound Vib. **44**(6), 6 (2010)
20. NATO: NATO AECTP 200, The Process for the validation of mechanical environmental test methods and severities, Leaflet 2410/1, Edition 3 edn, (2006)
21. Steinberg, D.: Vibration Analysis for Electronic Equipment. Wiley-Interscience, New York (1988)
22. Peeters, B., Van der Auweraer, H., Guillaume, P., Leuridan, J.: The PolyMAX frequency-domain method: a new standard for modal parameter estimation? Shock. Vib. **11**, 395–409 (2004)

Chapter 22
A Multi-View Digital Image Correlation for Extracting Mode Shapes of a Tire

Kiran Patil, Javad Baqersad, and Azadeh Sheidaei

Abstract Modal analysis is used to extract dynamic characteristics of structures for correlation and validation purposes. These characteristics are usually extracted using conventional measurement tools. A known force is imparted to the structure using impact hammers or mechanical shakers and the response is measured using accelerometers. However, accelerometers may induce mass loading effects; thus, the results may not show the true dynamics of the structure. On the other hand, conventional measurement tools can only measure at few discrete locations. Digital Image Correlation and photogrammetry has provided test engineers with a new tool for measuring dynamics of structures. These techniques are non-contacting so they do not induce mass loading and they can provide full-field results. For a DIC measurement to extract mode shapes, operating data of a structure is measured while the cameras are in fixed positions. A stereo camera system has line of sight only on a section of the structure. If the entire dynamics of a structure is desirable, several stereo cameras needs to be used. Another approach is to move a single stereo camera measure dynamics of the structure from multiple field of views; however, the time domain results can only be stitched together if the entire structure is fixed or if the applied force is constant during the entire time of measurement. This assumption is not valid for many dynamic measurements. On the other hand if the DIC system is moved from a view to another view, because the response is measured at different instants of time, operating shapes from each camera view may have a different scaling factor. In the current work, we propose an approach to identify a uniform scaling factor that enables us to stitch these operating shapes extracted from different views of cameras. The new approach is proposed based on conventional modal analysis theory. In the proposed technique, a known force is applied to a structure using a mechanical shaker or an impact hammer. The measured response of the structure in the time domain is transferred to the frequency domain to extract the mode shapes of a section of the structure. A similar procedure is repeated for other sections of the structure to capture the entire area of interest. Mode shapes for all views of the structure are stitched together to extract the mode shape for the entire structure. The proposed technique suggests stitching the views in the frequency domain after being scaled rather than stitching them in the time domain. The proposed method was applied to measure mode shapes of a tire using measured time series from different sections of the tire.

Keywords Digital image correlation • Photogrammetry • Tire dynamics • Modal analysis • Stitching

22.1 Introduction

Validating and updating numerical models are an important aspect of engineering analysis. In the field of dynamics, modal analysis is used to extract resonant frequencies and mode shapes of structures and validating the numerical models. Conventional modal analysis is based on exciting a structure using a mechanical shaker and measuring the response using accelerometers. However, the contact sensors may induce mass loading and can only measure at few discreet locations. Spatial resolution and geometric considerations are other challenges in using conventional sensors. For example, a significant number of sensors are required to fully monitor the dynamics of a tire. Researchers have used roving accelerometer measurements to resolve this issue. However, moving the accelerometers can induce mass loading effects and consequently introduce discrepancy to the data [1, 2]. On the other hand, for conventional modal analysis, an estimate of the geometry of the structure is created that may not necessarily represent the geometry of the structure. Furthermore, the sensor

K. Patil • J. Baqersad (✉)
Experimental Mechanics and NVH Laboratory, Kettering University, 1700 University Avenue, Flint, MI, 48105, USA
e-mail: jbaqersad@kettering.edu

A. Sheidaei
Mechanical Engineering Department, Kettering University, 1700 University Ave, Flint, MI, 48105, USA

J.M. Harvie, J. Baqersad (eds.), *Shock & Vibration, Aircraft/Aerospace, Energy Harvesting, Acoustics & Optics, Volume 9*,
Conference Proceedings of the Society for Experimental Mechanics Series, DOI 10.1007/978-3-319-54735-0_22

locations/orientation is usually identified through many simplifications. Therefore, a novel technique capable of full-field measurements on complicated geometries with adding no mass and stiffness effects is desirable.

Digital Image Correlation is a non-contacting full-field measurement technique that has been introduced to the field of experimental mechanics in 1980s [3, 4]. This approach has been used by many researchers in the field of solid mechanics [5]. Recently, this approach has been applied to the field of vibrations [6]. Researchers have used both point tracking and digital image correlations to measure dynamics of wind turbine blades [7–10], helicopter rotors [11–13], bridges, and infrastructure [14–16].

Most of these applications are based on operational modal analysis. The response of the structure is measured while the input is assumed to be Gaussian noise. Using operational modal analysis tools and calculating auto-power and cross-power spectra, operating shapes can be extracted. However, these shapes need to be scaled to extract mode shapes. Researchers have used the mass-sensitivity technique to scale the modes shapes [17] but this approach may need repeating a single test for several trials and may not lead to very accurate results.

Another difficulty with using digital image correlation is the limitation in the field of view. A stereo camera system can have line of sight only on one section of the structure. Thus, it might not be possible to perform measurement on curved complex structures. In the semi-static configuration, or in a case with steady state vibrations, stitching of views can be performed in the time domain. Using this stitching approach, the views of the camera are stich together using an overlapped view part. However, when this system is used for vibration measurement with a non-steady state loading, the views cannot be easily stitched together because the input is time variant. An approach proposed by Poozesh et al. [18] is to mount several stereo cameras together and perform a measurement by synchronizing all cameras. However, this approach can be very expensive because multiple cameras need to be used in this measurement.

In the current paper, an approach is proposed to measure dynamics of a large complicated structure using a single stereo system looking on the object from multiple-views. In the proposed approach, similar to conventional modal analysis, a mechanical shaker or a modal impact hammer is used to excite the structure. The response of the structure is measured in each view and is processed to extract the mode shapes for a section of structure. The next measurement is performed on another section. The mode shapes of the structure are extracted by assembling the section mode shapes. This approach expands the capabilities of DIC system and enables us to use a single stereo system to measure dynamics of a complicated structure. The merit of the approach is verified in this paper by using time domain data measured using accelerometers.

22.2 Theory

Modal analysis is the process of defining a structure in terms of its natural characteristics such as frequency, damping, and mode shapes. Data measured by sensors can be used for modal data extraction, system identification, and modal updating [19]. The modal parameters can be obtained experimentally by artificially exciting a structure with a known force using an impact hammer or a shaker and then measuring the response (displacement, velocity or acceleration) and post processing the vibration data. This measured data is collected in the time domain and is transferred to the frequency domain using a fast Fourier transform algorithm. Fig. 22.1 shows a schematic of the input and output parameters in the time and frequency domain.

The input-output relationship between two points on a structure can be described by a Frequency Response Function (FRF). The equation to extract the frequency response function *(H)* can be expressed as:

$$H = \frac{S_y \bullet S^*_x}{S_x \bullet S^*_x} \tag{22.1}$$

In this equation, S_x and S_y are the linear Fourier spectra of input and output, respectively. It should be noted that both the input force and motion are vector quantities; hence, direction of excitation and response is important in modal analysis.

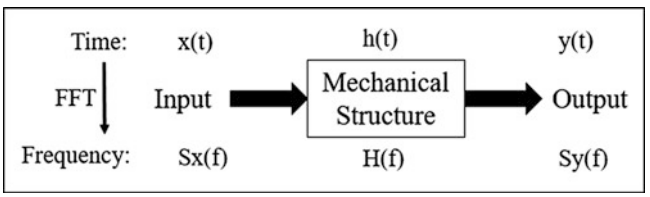

Fig. 22.1 A flowchart showing the input and output measured data in the time and frequency domains

22.3 Methodology

The technique proposed in this paper is to excite the tire with a known force and measure the response using a stereo photogrammetric system. The tire can be excited using a mechanical shaker or an impact hammer. The force applied to the structure is measured using a load cell used in a modal impact hammer or at the connection between the shaker and the structure. The response is measured using a single stereo DIC system. An FRF is obtained based on the measured force and the response. The mode shapes for each section is extracted using the frequency response function shown in Eq. (22.1). The mode shape for another section of the tire can be extracted by moving the cameras to record another view. This process is repeated to extract mode shapes for all sections of the entire structure (see Figs. 22.2 and 22.3). It should be noted that for a 3D DIC measurement, each of these views have three measurement points overlapping with their adjacent view to be able to stitch the views accurately. Further, each individual measurement including the geometries and displacement fields can be converted to a common co-ordinate system. Afterwards, stitching the FRF results in the mode shapes of the entire structure.

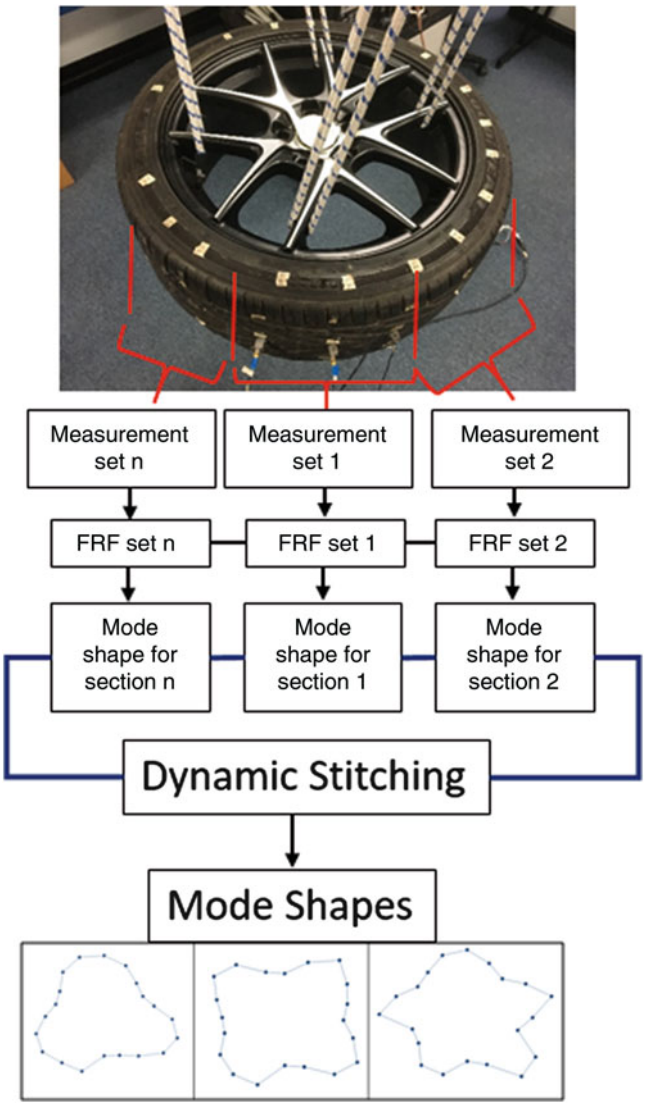

Fig. 22.2 A flowchart showing the process for extracting mode using multi-view

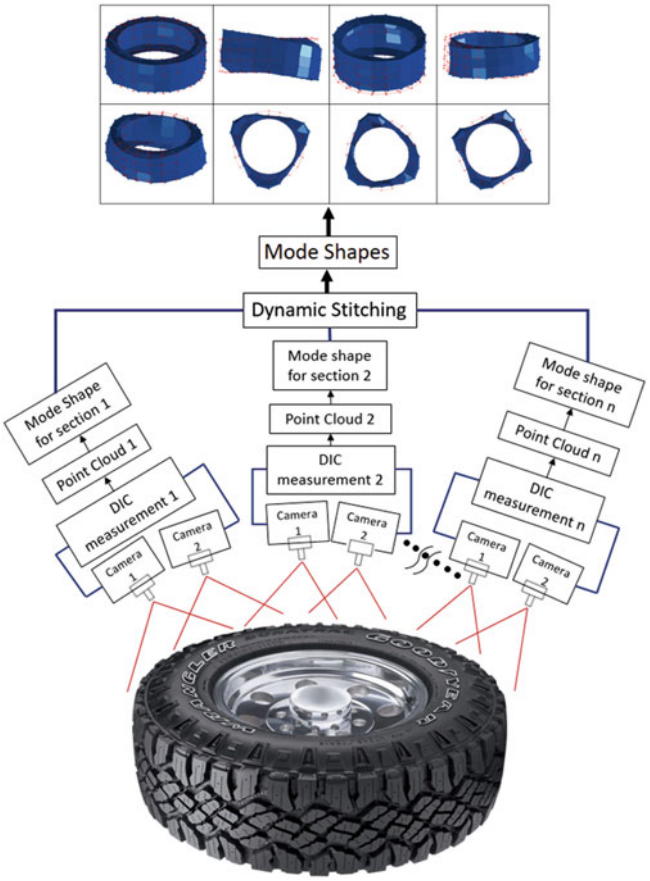

Fig. 22.3 A schematic of the proposed technique to extract mode shapes of the tire using multiple views

22.4 Testing

To show the merit of the proposed approach, the approach was applied to extract mode shapes of a tire. The measured data in a DIC system is time domain trace of displacement for measurement points. Thus, in this paper, the time domain data for three accelerators are used to replicate the data measured using a DIC system.

The experimental setup is shown in the Fig. 22.4. The tire is excited using a mechanical shaker and the response is measured using three Dytran tri-axial accelerometers. However, only 20 points were selected around the belt of the tire to measure the response. These 20 points were further divided into sections of three points each. Burst random signal with 85% of the burst time was used to excite the tire. For every excitation, response was measured at each section. It should be noted that because burst random signal is used for the exaction, the input signal varies with every new set of excitation. The time signals for the input force and the output response were recorded as Throughput data using LMS Test.Lab spectral testing. The input and output response were noted over a period of 129 sec.

In order to obtain the mode shape of the tire, the acquired signals need to be processed. Initially the time domain signals are converted to the frequency domain using the Fast Fourier Transfer function. However, prior performing the FFT, the data needs to be filter using Hanning windows. This filtered time signal over 129s is divided into time signals of 3sec with an overlap of 33% approximately. FFT is performed for every segment to convert the signals from time domain to frequency domain. Following this, a FRF is obtained from the output response and input force for every 3s. Averaging these individual FRF gives the FRF for every response. Fig. 22.5 shows the FRF obtained for a sample point on the tire. It should be noted that while computing the FRF, only the radial direction signals were taken into account.

The next step is stitching of the FRF obtained for every section to obtain the mode shapes of the tire. This is obtained using LMS Test.lab. The obtained FRF was imported to LMS Test.Lab and stitched together along with its geometry to obtain the mode shapes of the tire.

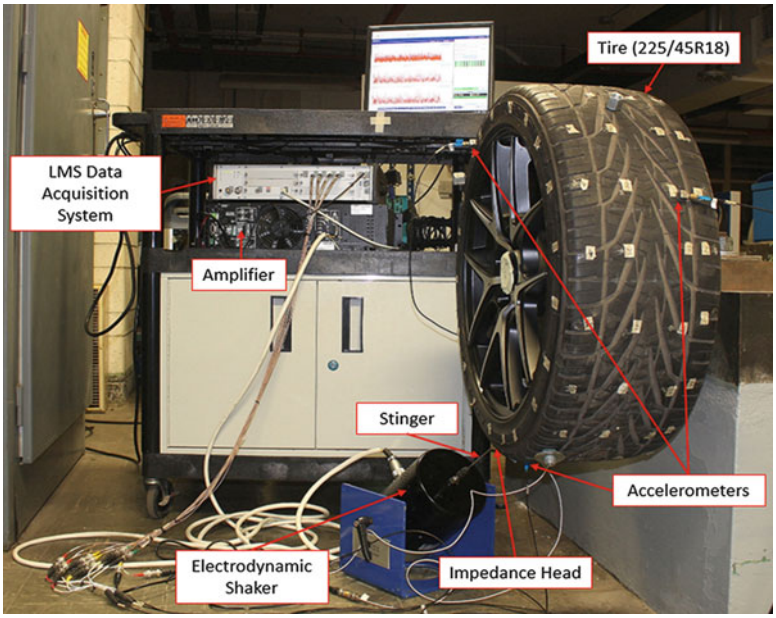

Fig. 22.4 Experimental setup to record the time signals of every section of the tire

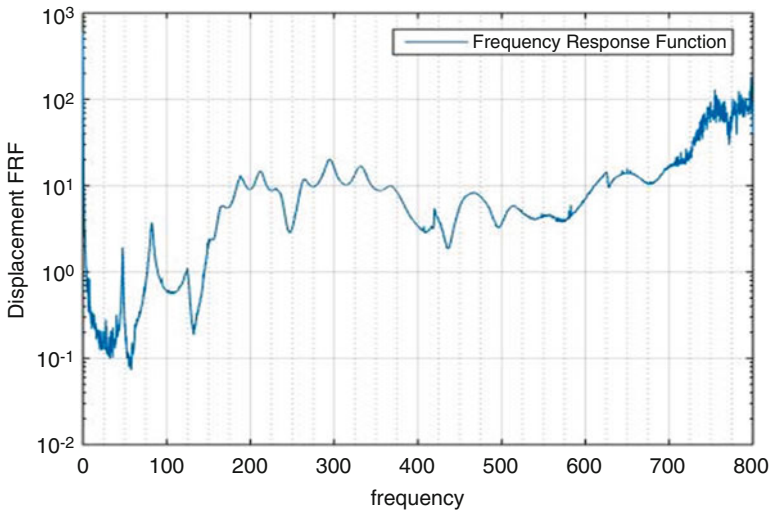

Fig. 22.5 FRF obtained for the response of a sample point on the tire

22.5 Results and Discussion

The FRF obtained for all sections were stitched together using LMS Test.Lab. Furthermore, the mode shapes of the tire were obtained by curve-fitting the FRF using LMS POLYMAX modal analysis. Fig. 22.6 shows the obtained mode shapes of the tire and the corresponding natural frequencies. It should be noted that only the response in radial direction was used to compute the FRF; hence, only the radial mode shapes of the tire could be obtained. Similarly the responses in lateral and tangential direction could be used to compute the respective FRF and the respective mode shapes.

The results of the experiment were validated by comparing the FRFs to the FRFs obtained by conventional modal analysis approach using LMS data acquisition system and LMS Test.Lab. It was observed that the natural frequencies obtained by both the approaches match precisely (refer Fig. 22.7).

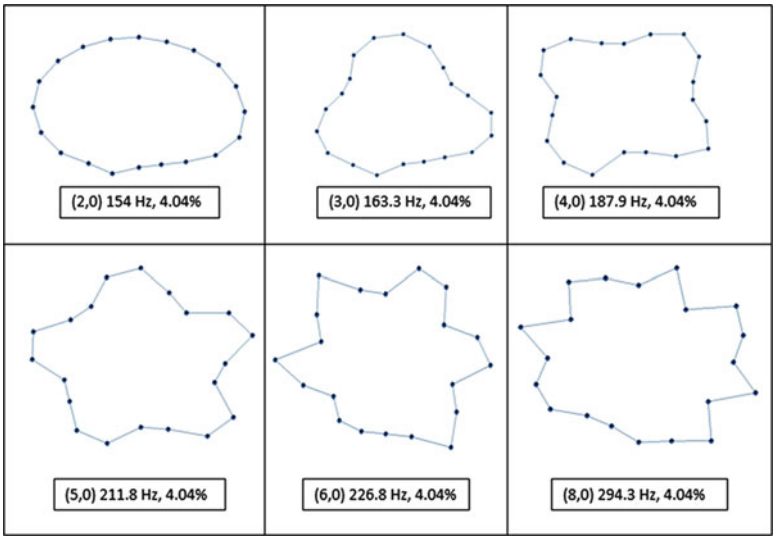

Fig. 22.6 Obtained mode shapes after stitching the mode shapes for each section

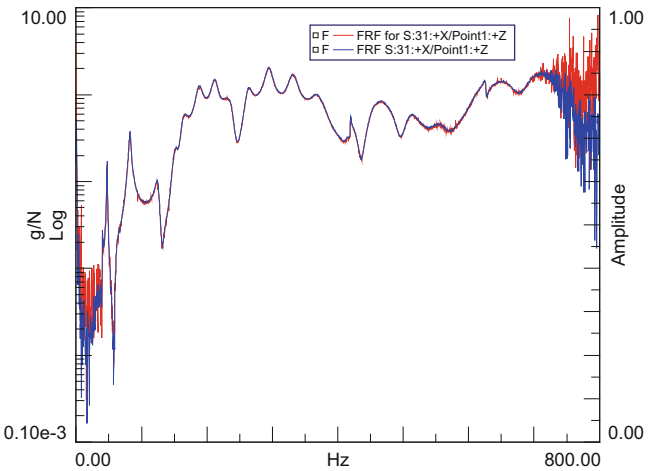

Fig. 22.7 A comparison between the frequency response function extracted using the proposed approach and using LMS frequency response calculation

22.6 Conclusion

This paper proposes a new approach to measure the dynamics of a large complicated structure using a single stereo system looking at the object from multiple views. This approach based on the results obtained from the conventional theory of modal analysis. In the proposed technique, the results from each view is transformed to the frequency domain and mode shape for each view of the structure is extracted. The section mode shapes are stitched together to obtain the mode shapes for the entire structure. Comparing the frequency response functions and the mode shapes obtained with this new approach to that obtained using the LMS Test.Lab spectral analysis, it is shown that the proposed approach can show the mode shapes with very high accuracy. This approach expands the capabilities of DIC system and enables us to use a single stereo system to measure dynamics of a complicated structure.

References

1. Baqersad, J., Niezrecki, C., Avitabile, P., Slattery, M.: Dynamic characterization of a free-free wind turbine blade assembly. In: Allemang, R., De Clerck, J., Niezrecki, C., Wicks, A. (eds.) Special Topics in Structural Dynamics Conference. Proceedings of the Society for Experimental Mechanics Series, vol. 6. Springer, New York (2013)
2. Baqersad, J., Poozesh, P., Niezrecki, C., Avitabile, P.: Comparison of modal parameters extracted using MIMO, SIMO, and impact hammer tests on a three-bladed wind turbine. In: Topics in Modal Analysis II, vol. 8, pp. 185–197. Springer (2014)

3. Peters, W.H., Ranson, W.F.: Digital imaging techniques in experimental stress analysis. Opt. Eng. **21**, 213427 (1982)
4. Sutton, M., Wolters, W., Peters, W., Ranson, W., McNeill, S.: Determination of displacements using an improved digital correlation method. Image Vis. Comput. **1**, 133–139 (1983)
5. Sutton, M.A., Orteu, J.J., Schreier, H.: Image Correlation for Shape, Motion and Deformation Measurements: Basic Concepts, Theory and Applications. Springer, New York (2009). doi:10.1007/978-0-387-78747-3
6. Baqersad, J., Poozesh, P., Niezrecki, C., Avitabile, P.: Photogrammetry and optical methods in structural dynamics – a review. Mech. Syst. Signal Process. **86**, 17–34 (2017)
7. Baqersad, J., Niezrecki, C., Avitabile, P.: Extracting full-field dynamic strain on a wind turbine rotor subjected to arbitrary excitations using 3D point tracking and a modal expansion technique. J. Sound Vib. **352**, 16–29 (2015)
8. Baqersad, J., Niezrecki, C., Avitabile, P.: Full-field dynamic strain prediction on a wind turbine using displacements of optical targets measured by stereophotogrammetry. Mech. Syst. Signal Process. **62**, 284–295 (2015)
9. Poozesh, P., Baqersad, J., Niezrecki, C., Avitabile, P., Harvey, E., Yarala, R.: Large-area photogrammetry based testing of wind turbine blades. Mech. Syst. Signal Process. **86**, 98–115 (2017)
10. Poozesh, P., Baqersad, J., Niezrecki, C., Harvey, E., Yarala, R., Digital Image Correlation Based Testing of Utility-Scale Wind Turbine Blades, MSSP Special Issue: Full-field Vibration Measurement, (2015).
11. Abrego, A.I., Olson, L.E., Romander, E.A., Barrows, D.A., Burner, A.W., Blade displacement measurement technique applied to a full-scale rotor test, In: American Helicopter Society 68th Annual Forum Proceedings, Fort Worth, TX, 1–3 May, 2012
12. Olson, L.E., Abrego, A.I., Barrows, D.A., Burner, A.W., Blade deflection measurements of a full-scale UH-60A rotor system, AHS Aeromechanics Specialists Conference, 2010, pp. 738–747.
13. Lundstrom, T., Baqersad, J., Niezrecki, C., Monitoring the Dynamics of a Helicopter Main Rotor With High-Speed Stereophotogrammetry, Experimental Techniques, (2015).
14. Busca, G., Cigada, A., Mazzoleni, P., Zappa, E.: Vibration monitoring of multiple bridge points by means of a unique vision-based measuring system. Exp. Mech. **54**, 255–271 (2014)
15. Busca, G., Cigada, A., Vanali, M., Zappa, E.: Vision-based vibration monitoring of a large steel structure. In: Experimental Vibration Analysis for Civil Engineering Structures (EVACES). Experimental Vibration Analysis for Civil Engineering Structures Varenna, Italy, pp. 561–568 (2011)
16. Caprioli, A., Manzoni, S., Zappa, E.: People-induced vibrations of civil structures: image-based measurement of crowd motion. Exp. Tech. **35**, 71–79 (2011)
17. Poozesh, P., Sabino, D.D., Baqersad, J., Avitabile, P., Niezrecki, C.: Practical techniques for scaling of optically measured operating deflection shapes. In: De Clerck, J., Epp, D. (eds.) Rotating Machinery, Hybrid Test Methods, Vibro-Acoustics & Laser Vibrometry. Conference Proceedings of the Society for Experimental Mechanics Series, vol. 8. Springer, New York (2016)
18. Poozesh, P., Baqersad, J., Niezrecki, C., Avitabile, P.: A multi-camera stereo dic system for extracting operating mode shapes of large scale structures. In: Advancement of Optical Methods in Experimental Mechanics, vol. 3, pp. 225–238. Springer (2016)
19. Madarshahian, R., Caicedo, J.M., Zárate, B.A.: Using P-box and PiFE to express uncertainty in model updating. In: Simmermacher, T., Cogan, S., Moaveni, B., Papadimitriou, C. (eds.) Topics in Model Validation and Uncertainty Quantification, Volume 5: Proceedings of the 31st IMAC, A Conference on Structural Dynamics, 2013, pp. 81–88. Springer, New York (2013)

Chapter 23
Modal Expansion using Strain Mode Shapes

Javad Baqersad, Kedar Bharadwaj, and Peyman Poozesh

Abstract Reduction/expansion approaches have been conventionally used in correlation and validation studies. Recently, these approaches have also been used to extract full-filed results on structures using limited set of data measured. The expansion techniques are used to expand real-time data measured on components of vehicle chassis, utility scale wind turbines, and helicopter rotors. The resulted full-field data is used to monitor structures and determine their durability. With the advances in Digital Image Correlation (DIC), researchers are able to readily extract strain mode shapes of structures. However, the conventional reduction/expansion techniques are usually limited to displacement, velocity, or acceleration data. This can hinder correlation studies that compare the strain data between two models. Furthermore, this limitation does not allow researchers to expand strain-gage measured data for full-field structural monitoring and durability analysis.

In the current paper, a reduction/expansion technique has been developed to reduce/expand strain data. In this technique, measured strain at limited locations is expanded using strain mode shapes to extract full-field results on the entire surface and within the structure. This technique can also be used to reduce data for correlation studies. In order to demonstrate the merit of the approach, the proposed strain expansion approach was applied to the finite element model of a cantilever beam subjected to sinusoidal and impact excitations. The results show that the proposed approach can effectively expand the strain measured at limited locations. The approach could accurately predict the strain at locations where no sensors were placed.

Keywords Modal expansion • Strain mode shapes • Structural health monitoring • Modal analysis • Expansion methodology

Nomenclature

S_n	Full-space strain vector
$RTOS_a$	Real-time operating strain in reduced-space
V_n	Full-space strain mode shape matrix
U_n	Full-space displacement mode shape matrix
T	Transformation matrix
X_n	Full-space displacement vector
$RTOS_{en}$	Real-time operating strain in full-space
V_a	Reduced-space strain mode shape matrix
P	Mode contribution vector
V_a^g	Generalized inverse of reduced-space mode shape matrix

J. Baqersad (✉) • K. Bharadwaj
Experimental Mechanics and NVH Laboratory, Kettering University, 1700 University Avenue, Flint, MI 48504, USA
e-mail: jbaqersad@kettering.edu

P. Poozesh
Mechanical Engineering Department, University of Massachusetts Lowell, 1 University Ave, Lowell, MA 01854, USA

J.M. Harvie, J. Baqersad (eds.), *Shock & Vibration, Aircraft/Aerospace, Energy Harvesting, Acoustics & Optics, Volume 9*,
Conference Proceedings of the Society for Experimental Mechanics Series, DOI 10.1007/978-3-319-54735-0_23

23.1 Introduction

Health monitoring of structures and durability analysis of mechanical components are currently of particular interest to the industry due to increasing capital investments and maintenance costs for these structures as well as their crucial safety issues. In the wind industry, modern wind turbines continue to grow in size to help reduce the cost of energy capture making wind power competitive with fossil fuels and to meet increasing energy demands. As the size of the wind turbines scales up, the capital investment for these machines is also escalating. Therefore, periodic damage prognosis and condition based monitoring of these structures have become of particular interest. In the automobile industry, the chassis is a critical unit and the durability and fatigue calculations are crucial as any error in the measured values could lead to a malfunctioning of the unit or a safety issue. Pointwise sensors are frequently used to monitor structures during operation. However, the reliability of this method vary with the location of the sensors placed. On the other hand, determining and monitoring the durability of structures experimentally is purely dependent on the sensitivity and the location at which strain is being measured. With the increasing complexity in the geometry of structures, it's very challenging to identify critical locations to place sensors; hence, data collection becomes increasingly complicated. Therefore, developing a full-field monitoring approach that is able to identify the critical locations of structures during operation is very desirable.

Digital Image Correlation (DIC) as a non-contact measurement technique is recently emerging and has been used for structural health monitoring of wind turbine blades [1–4], helicopter rotors [5–8], aircraft fuselages, and bridges [9, 10]. However, for a DIC measurement, a pattern needs to be created on the entire surface of the structure. The large size of some structures (e.g. utility-scale wind turbine blades) may limit the feasibility of patterning the whole surface of large structures. Another approach is to use numerical models to expand limited set of displacement measurements. A technique was proposed by Baqersad et al. [11–13] to expand the limited set of real-time displacement data and apply it to a finite element model to extract full-field strain data. Iliopoulos et al. [14, 15] proposed an approach for expanding accelerometer data for fatigue analysis. Researchers have also used a Confluence Algorithm [16] for full field response prediction. However, all of these approaches work based on expanding displacement, velocity, or acceleration.

In the current paper, a novel approach has been developed to directly expand/reduce strain data. Strain-gages are widely used for monitoring of structures due to their low cost and the valuable information they can provide. In the proposed approach, strain mode shapes of the structure is used to expand the limited set of data measured by strain-gages. The strain mode shapes can be extracted using numerical models. On the other hand, digital image correlation has provided engineers with a robust tool to extract full-field strain mode shapes with no need for numerical modeling. The proposed modal strain expansion technique uses only a limited set of measured strain to predict the full-field strain at all the locations in the structure (i.e. exterior and interior).

23.2 Theory

Modal reduction and expansion approaches have been conventionally used in modal analysis for validation and correlation purposes. Researchers have used Guyan Condensation [17], Dynamic Condensation [18], System Equivalent Reduction Expansion Process [19], and Improved Reduced System (IRS) [20]. System Equivalent Reduction Expansion Process (SEREP) is an approach that uses displacement mode shapes of the structure through a least square minimization to find a transfer matrix that can be used to expand or reduce (the inverse of the matrix) the data. Among the several modal expansion methodologies that can be used to expand any given data, SEREP was used in the current paper because this method is highly efficient in preserving the measured strain results in all the modes of excitation.

To extract the equations for strain mode shapes, we start with displacement mode shapes. Eq. (23.1) shows the basic theory of modal analysis. This theory states that the response of a structure to excitations can be a linear combination of the mode shapes.

$$\{X_n\} = [U_n]\ \{P\} \tag{23.1}$$

In this equation $[U_n\ ]$ and $[X_n]$ represent the displacement mode shapes and displacement response of the structure at full set degrees of freedom (DOFs), respectively. {P} denotes the contribution of each mode in the system's response. A similar equation can be written for strain response.

$$\{S_n\} = [V_n]\{P\} \tag{23.2}$$

where $[V_n]$ denotes the full-space strain mode shapes of the system and $\{S_n\}$ is the full-field strain response of the structure. The full set of DOFs can be shown as a combination of active *(a)* and deleted degrees of freedom *(d)*.

$$\{S_n\} = \begin{Bmatrix} S_a \\ S_d \end{Bmatrix} \tag{23.3}$$

Combining Eq. (23.2) and Eq. (23.3), gives:

$$\begin{Bmatrix} S_a \\ S_d \end{Bmatrix} = [V_n]\{P\} = \begin{bmatrix} V_a \\ V_d \end{bmatrix}\{P\} \tag{23.4}$$

where, V_a and V_d are the strain mode shapes of the structure at the active and deleted degrees of freedom.

$$\{S_a\} = [V_a]\{P\} \tag{23.5}$$

The number of unknowns in Eq. (23.5) is not equal to the number of equations; thus, Eq. (23.5) needs to be solved using the generalized inverse method. The generalized inverse solves these equations using the least squares approach. Pre-multiplying both sides of the Eq. (23.5) by $[V_a]^T$ gives

$$[V_a]^T\{S_a\} = [V_a]^T[V_a]\{P\} \tag{23.6}$$

Pre-multiplying Eq. (23.6) by $([V_a]^T[V_a])^{-1}$, we obtain

$$\left([V_a]^T[V_a]\right)^{-1}[V_a]^T\{S_a\} = \left([V_a]^T[V_a]\right)^{-1}[V_a]^T[V_a]\{P\} \tag{23.7}$$

Equation (23.7) can be written as

$$\{P\} = [V_a]^T[V_a]^{-1}[V_a]^T\{S_a\} \tag{23.8}$$

$$\{P\} = [V_a]^g\{S_a\} \tag{23.9}$$

The superscript g refers to the generalized inverse of the matrix. To find the full-space response, $\{P\}$ from Eq. (23.9) is substituted into Eq. (23.2); that gives

$$\{S_n\} = [V_n][V_a]^g\{S_a\} \tag{23.10}$$

Comparing Eq. (23.10) and Eq. (23.2), transformation matrix for the Strain Expansion Reduction Approach is formed as

$$[T] = [V_n][V_a]^g \tag{23.11}$$

Hence, Eq. (23.11) can be used to expand real-time operating strain data measured by strain-gages $\{RTOS_a\}$ to the expanded expanded (full-(space)) real-time operating data $[RTOS_{en}]$ real-time operating data $[RTOS_{en}]$.

$$[RTOS_{en}] = [T]\{RTOS_a\} \tag{23.12}$$

23.3 Test Model

In order to show the merit of the approach, an analytical study was performed to evaluate the performance of the proposed method in predicting full-field strain on a cantilever beam model. The test model was a hollow aluminum beam with the cross section of 1in x 2 in, a thickness of 1/16 in, and a length of 5 ft. A finite element (FE) model of the beam was developed using Siemens NX 9.0 (see Fig. 23.1) and the simulation was conducted using NX Nastran solver. 3-D Tetrahedral elements (CTETRA 10) with element size of 0.584 were used. The total number of 64,205 nodes (full-space model) were generated.

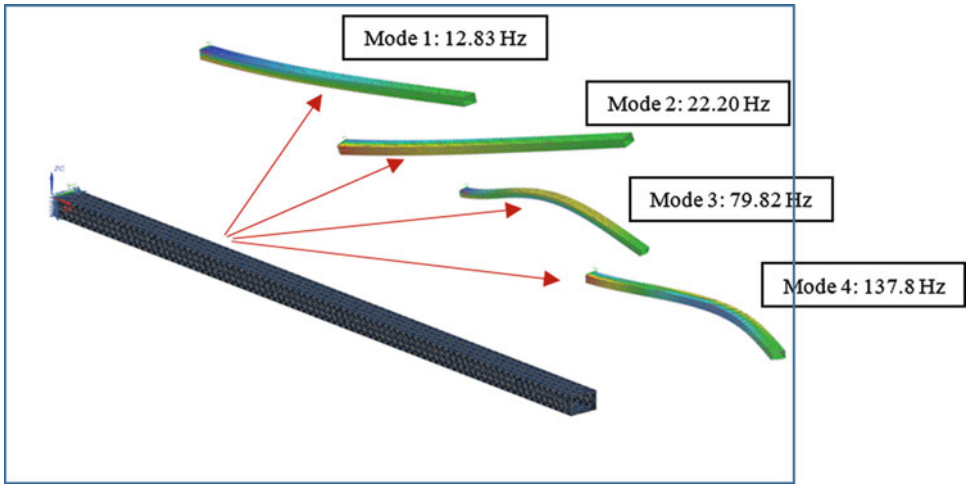

Fig. 23.1 The cantilever beam with its natural frequencies and mode shapes

A cantilever boundary condition was implemented at one end of the beam and an eigensolution was performed to extract the displacement and strain mode shapes of the beam.

23.4 Simulation and Data Processing

After performing an eigensolution on the FE model, the strain values at each mode were exported from the FE software. A full-space strain mode shape matrix was generated in Matlab using these strain values. The strain mode shape matrix for the reduced-space was generated by selecting the mode shape values at five degrees of freedom. Using Eq. (23.12), a transfer matrix for strain expansion was developed. The number of modes involved in the Eq. (23.12) depends on type of excitation applied to the beam.

To verify if this transformation matrix can expand real-time strain results, the beam was excited using two types of excitations. The aluminum beam was subjected a sinusoidal excitation and an impact testing. The load was applied at a node located in the free end of the cantilever. An explicit analysis was performed to extract the transient response of the beam to the excitation. A reduced set of strain values was measured on the beam. This reduced set of data was expanded using the transformation matrix to extract full-field strain over the entire beam. The predicted strain at a degree of freedom that was not initially used in the process was compared to the measured strain. A flowchart of the technique is shown in Fig. 23.2.

23.5 Results and Observation

23.5.1 Sinusoidal Loading

A sinusoidal force with a frequency of 12.8 Hz was applied to the beam to excite the first resonant frequency of the beam. The force was applied to the free end of the cantilever beam, which was simulated for 0.4 s. The real-time longitudinal strain values were extracted in the FE model for all degrees of freedom.

A reduced set strain matrix data was generated by selecting strain values at only four nodes. This limited set of strain data can replicate the real-time strain values measured using strain gages. This reduced set of strain values were expanded using transformation matrix to predict full-field strain at all degrees of freedom (see Eq. (23.12)). To evaluate the accuracy of the approach, the predicted strain value at a random node in the beam was compared to the strain value calculated using the full-space FE model. The results for the sinusoidal excitation is shown in Fig. 23.3. As can be seen, the proposed approach can predict the strain with a very high accuracy.

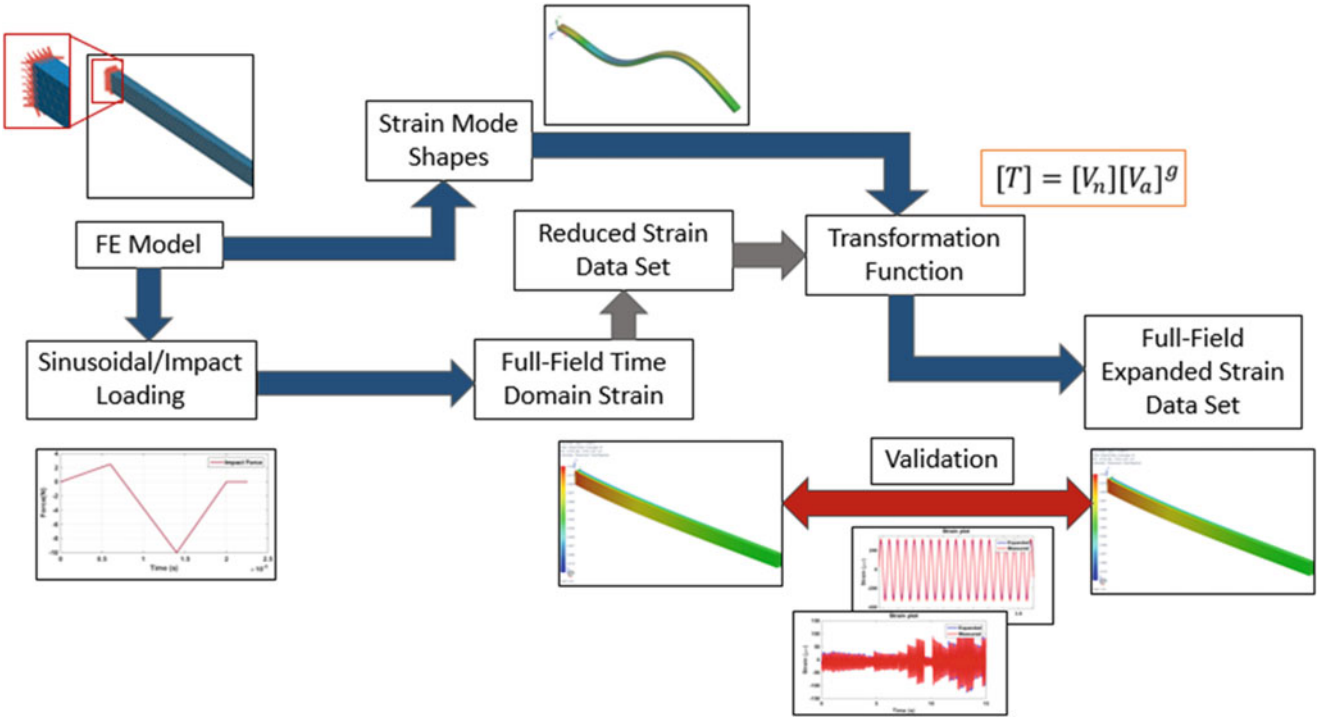

Fig. 23.2 A flowchart showing the process for expansion and comparing the expanded results with original full-field data

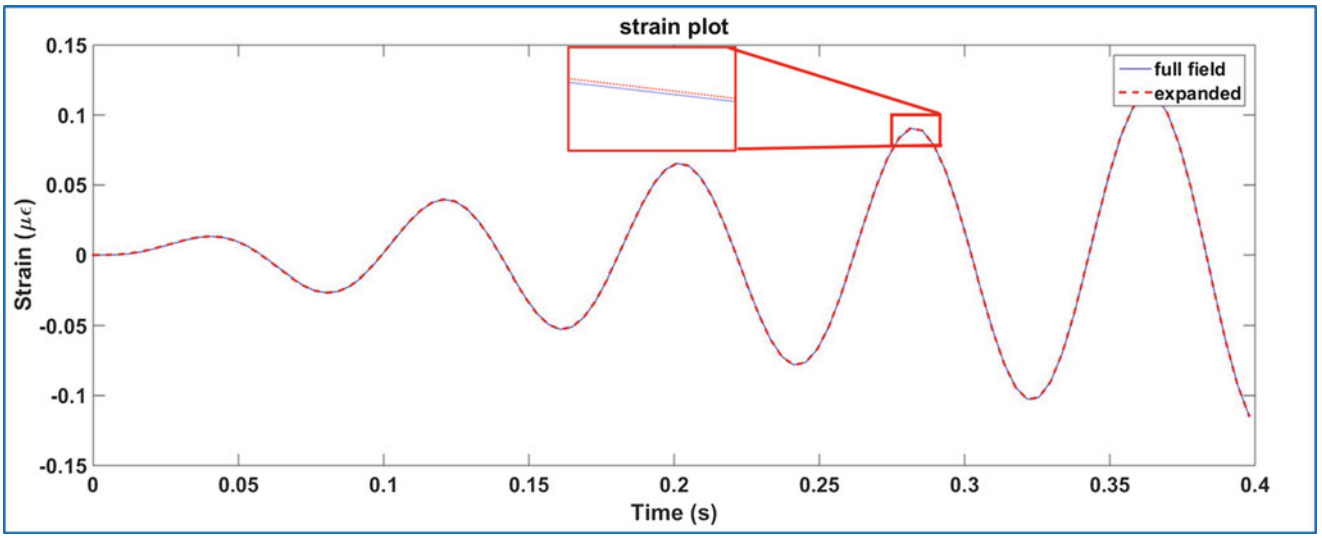

Fig. 23.3 Plot of the resulting strain for sinusoidal loading for a transient condition

23.5.2 Impact Loading

After extracting promising results for the sinusoidal excitation at the first mode, a more complicated case of loading was applied to the beam. An impact loading can excite many modes of the structure. A double sided impact was applied for a time period of 1.7 ms (see Fig. 23.4); then the transient strain values are monitored for 0.1 s. Then the strain data at four nodes of the beam was exported from the FE software.

The limited set of measurement was expanded using the transformation matrix. The number of modes used in the transformation matrix depends on the type of excitation. In the sinusoidal excitation, only one mode was used and very accurate results could be predicted. In this impact test case, when only one mode is used in the excitation, the results were

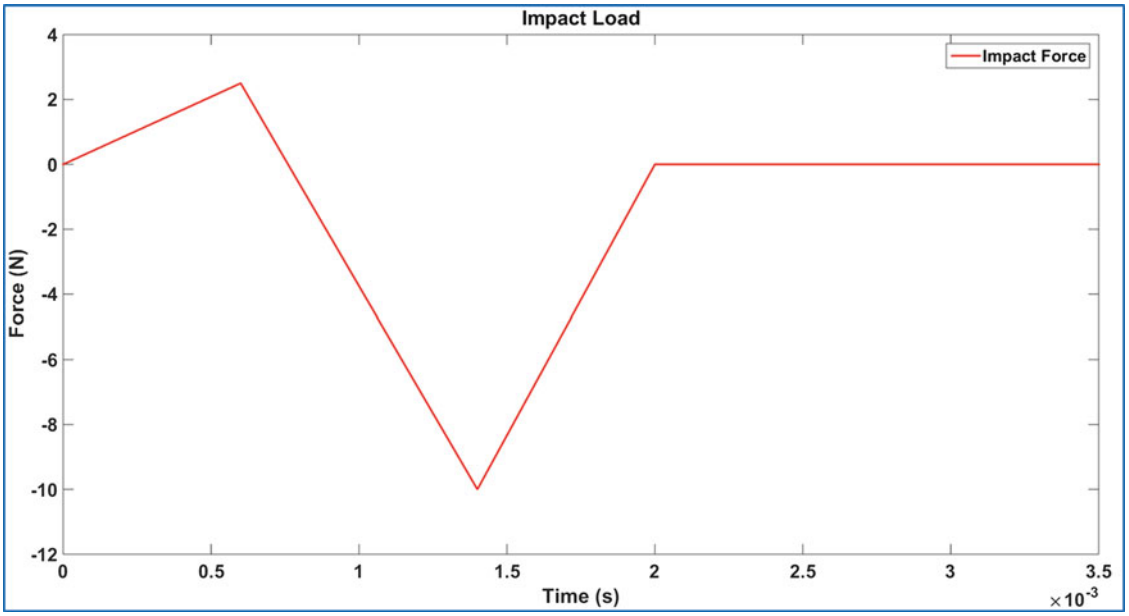

Fig. 23.4 Plot of the impact force being applied on the beam

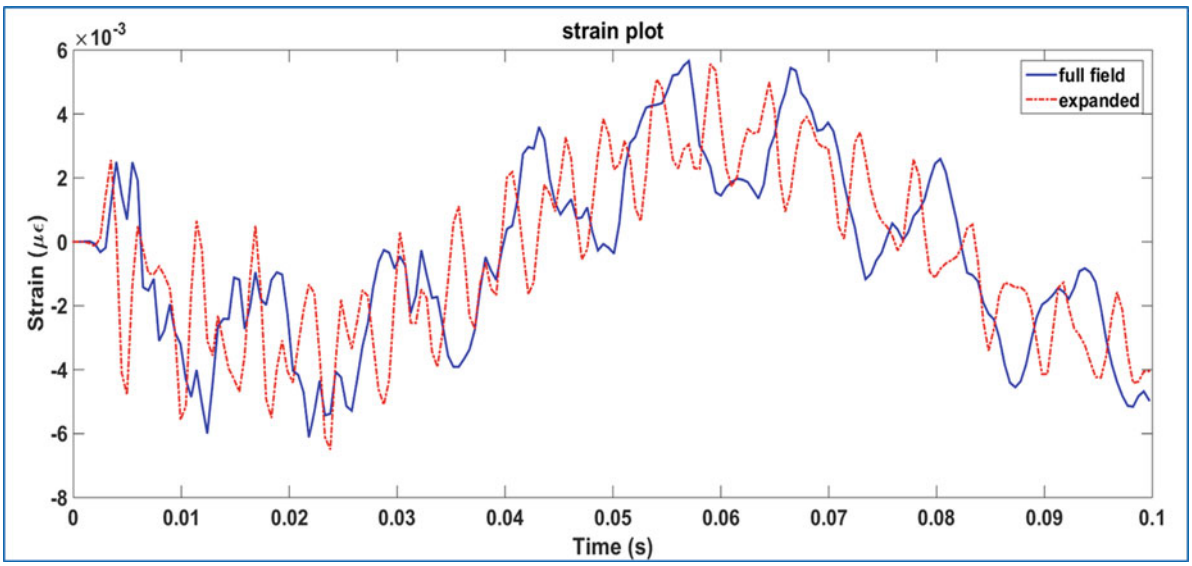

Fig. 23.5 Plot of the resultant strain for impact loading under transient condition considering one mode of excitation

not accurate. A comparison between the predicted results and full-field results is shown in Fig. 23.5. As can be seen the predicted strain values cannot show accurate results. This is because the impact loading can excite many modes and all of these modes need to be used in the expansion process.

In a second trial to generate the transformation matrix, the first three modes of the beam were considered in the process. As can be seen in Fig. 23.6, the predicted strain compares well with the measured strain.

23.6 Conclusion

The current paper proposes a novel approach to predict full-field strain on a structure using a limited strain data set. This technique works based on using strain mode shapes for the expansion process. To verify the merit of the approach, a finite element model of a cantilever beam was used. The beam was excited using sinusoidal and impact loading and the capability

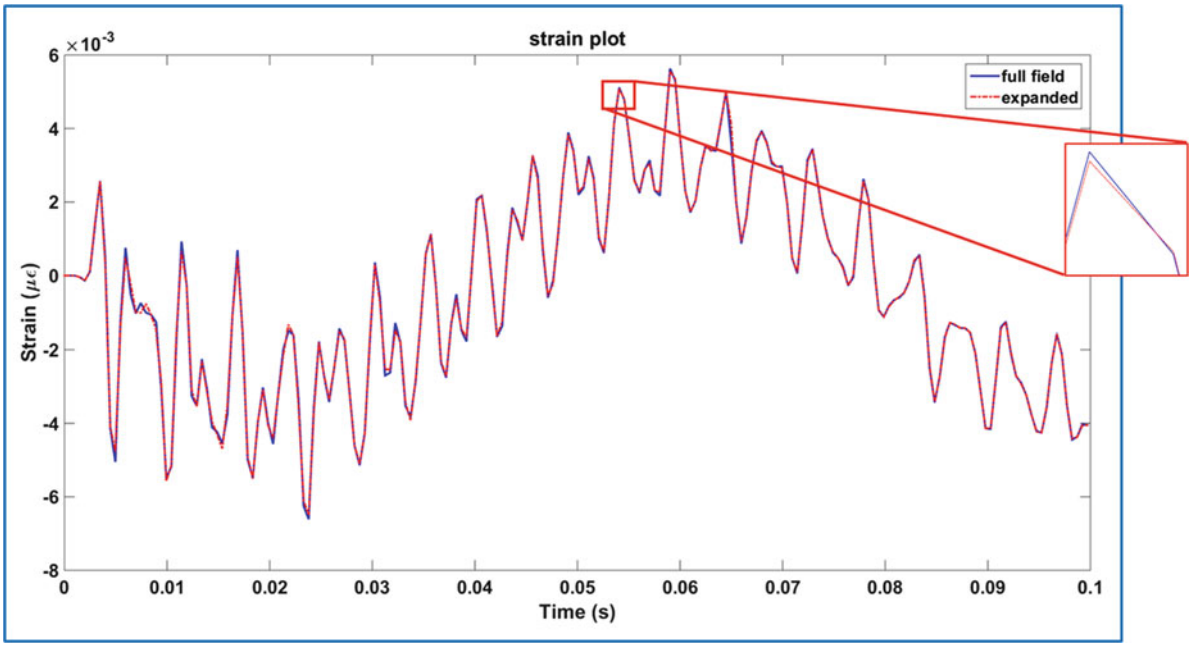

Fig. 23.6 Plot of the resultant strain for impact loading considering three modes of excitation

of the approach in expanding the strain was verified. A comparison between the full-field strain data and expanded strain from a reduced model was conducted. The results obtained suggest that the approach is accurate and demonstrates great potential in determining real-time strain. It was shown that the number of modes of excitation considered plays a vital role in increasing the accuracy of the results depending on the type of loads being applied.

The proposed technique expands the current correlations tools, which are limited to strain data correlation, and enables engineers to use this technique for correlations studies using strain. Furthermore, the results of this study show that real-time operating data at few strain-gages can be expanded to extract full-field strain data for structural health monitoring and durability analysis.

References

1. Carr, J., Baqersad, J., Niezrecki, C., Avitabile, P., Slattery, M.: Dynamic stress–strain on turbine blades using digital image correlation techniques part 2: dynamic measurements. In: Topics in Experimental Dynamics Substructuring and Wind Turbine Dynamics, vol. 2, pp. 221–226. Springer (2012)
2. Poozesh, P., Baqersad, J., Niezrecki, C., Avitabile, P., Harvey, E., Yarala, R.: Large-area photogrammetry based testing of wind turbine blades. Mech. Syst. Signal Process. **86**, 98–115 (2017)
3. Ozbek, M., Rixen, D.J., Erne, O., Sanow, G.: Feasibility of monitoring large wind turbines using photogrammetry. Energy. **35**, 4802–4811 (2010)
4. Poozesh, P., Baqersad, J., Niezrecki, C., Avitabile, P.: A multi-camera stereo dic system for extracting operating mode shapes of large scale structures. In: Advancement of Optical Methods in Experimental Mechanics, vol. 3, pp. 225–238. Springer International Publishing (2016)
5. Abrego, A.I., Olson, L.E., Romander, E.A., Barrows, D.A., Burner, A.W., Blade displacement measurement technique applied to a full-scale rotor test, American Helicopter Society 68th Annual Forum Proceedings, Fort Worth, TX, 1–3 May, 2012
6. Olson, L.E., Abrego, A.I., Barrows, D.A., Burner, A.W., Blade deflection measurements of a full-scale UH-60A rotor system, In: AHS Aeromechanics Specialists Conference, 2010, pp. 738–747.
7. Lundstrom, T., Baqersad, J., Niezrecki, C., Monitoring the Dynamics of a Helicopter Main Rotor With High-Speed Stereophotogrammetry, Experimental Techniques, (2015).
8. Sicard, J., Sirohi, J.: Measurement of the deformation of an extremely flexible rotor blade using digital image correlation. Meas. Sci. Technol. **24**, 065203 (2013)
9. J. Baqersad, P. Poozesh, C. Niezrecki, P. Avitabile, Photogrammetry and optical methods in structural dynamics – A review, Mech. Syst. Signal Process. 86: 17–34 (2017).
10. Busca, G., Cigada, A., Mazzoleni, P., Tarabini, M., Zappa, E.: Static and dynamic monitoring of bridges by means of vision-based measuring system. In: Cunha, A. (ed.) Topics in Dynamics of Bridges, vol. 3, pp. 83–92. Springer, New York (2013)

11. Baqersad, J., Niezrecki, C., Avitabile, P.: Extracting full-field dynamic strain on a wind turbine rotor subjected to arbitrary excitations using 3D point tracking and a modal expansion technique. J. Sound Vib. **352**, 16–29 (2015)
12. Baqersad, J., Niezrecki, C., Avitabile, P.: Full-field dynamic strain prediction on a wind turbine using displacements of optical targets measured by stereophotogrammetry. Mech. Syst. Signal Process. **62**, 284–295 (2015)
13. Baqersad, J., Poozesh, P., Niezrecki, C., Avitabile, P.: A noncontacting approach for full-field strain monitoring of rotating structures. J. Vib. Acoust. **138**, 031008–031008 (2016)
14. Iliopoulos, A., Shirzadeh, R., Weijtjens, W., Guillaume, P., Hemelrijck, D.V., Devriendt, C.: A modal decomposition and expansion approach for prediction of dynamic responses on a monopile offshore wind turbine using a limited number of vibration sensors. Mech. Syst. Signal Process. **68–69**, 84–104 (2016)
15. Maes, K., Iliopoulos, A., Weijtjens, W., Devriendt, C., Lombaert, G.: Dynamic strain estimation for fatigue assessment of an offshore monopile wind turbine using filtering and modal expansion algorithms. Mech. Syst. Signal Process. **76–77**, 592–611 (2016)
16. Rahneshin, V., Chierichetti, M.: An integrated approach for non-periodic dynamic response prediction of complex structures: numerical and experimental analysis. J. Sound Vib. **378**, 38–55 (2016)
17. Guyan, R.J.: Reduction of stiffness and mass matrices. AIAA J. **3**, 380–380 (1965)
18. Kidder, R.L.: Reduction of structural frequency equations. AIAA J. **11**, 892–892 (1973)
19. O'Callahan, J., Avitabile, P., Riemer, R.: System equivalent reduction expansion process (SEREP). In: Proceedings of the 7th International Modal Analysis Conference, pp. 29–37. Union College Schnectady, NY (1989)
20. O'Callahan, J.C., A procedure for an improved reduced system (IRS) model, In: Proceedings of the 7th International Modal Analysis Conference, Las Vegas, 1989, pp. 17–21.

Chapter 24
Vibration Suppression of MR Sandwich Beams Based On Fuzzy Logic

Hasan Malaeke, Hamid Moeenfard, Amir H. Ghasemi, and Javad Baqersad

Abstract In this paper, the vibration suppression capabilities of magnetorheological (MR) layer in smart beams is investigated. A three-layered beam including MR elastomer layer sandwiched between two elastic layers is considered. By assuming the properties of MR layer in the pre-yield region as viscoelastic materials behavior, the governing equations of motion as well as the corresponding boundary conditions are derived using Hamilton's principle. Due to field-dependent shear modulus of MR layer, the stiffness and damping properties of the smart beam can be changed by the application of magnetic field. This feature is utilized to suppress the unwanted vibration of the system. The appropriate magnetic field applied over the beam is chosen through a fuzzy controller for improving the transient response. The designed fuzzy controller uses the modal displacement and modal velocity of the beam as its inputs. Free and forced vibration of smart sandwich beam is investigated using numerical simulations. The results show that the magnetorheological layer along with the designed fuzzy controller can be effectively used to suppress the unwanted vibration of the system. The qualitative and quantitative knowledge resulting from this research is expected to enable the analysis, design and synthesis of smart beams for improving the dynamic performance of smart engineering structures.

Keywords Fuzzy logic • Vibration suppression • Magnetorheological • Smart beams • Fuzzy controller

24.1 Introduction

Vibration absorbers are usually designed to suppress vibration at a specific frequency. Therefore, a conventional vibration absorber is not effective if the spectrum of excitation force consists of many frequencies. A tunable vibration absorber which is capable of being tuned over a range of frequencies can be achieved by incorporating variable stiffness elements. The characteristic behavior of magnetorheological (MR) and electrorheological (ER) materials can change significantly upon application of magnetic/electric field. The change in materials properties (e.g. viscosity and shear modulus) are continuous, reversible fast and easy to control, so MR/ER fluid based devices can provide simple, quiet and rapid response interfaces between electronic control to mechanical systems [1, 2].

In recent years, many research studies have been conducted on the applications of MR elastomer in attenuating vibration in engineering structures [3–8]. Yalcintas and Dai [9] analyzed the dynamic responses of MR fluid in an adaptive structures. They showed that MR fluid based adaptive structures can have higher natural frequencies compare to the ER fluid based adaptive structures. Sung et al. [10] used energy approach to investigate the dynamic response of a MR sandwich beam. They demonstrated the relationship between applied magnetic field and the complex shear modulus. Yeh and Shih [11] analyzed the dynamic behavior and instability of MR structures under buckling loads. Rajamohan et al. [12, 13] derived finite element formulations for a sandwich beam with uniform and partial MR fluid treatment. Lara-Prieto et al. [14] experimentally investigated the dynamic of a MR sandwich cantilever beam subject to uniform and non-uniform magnetic field. They showed that the natural frequencies of the beam decreases as the permanent magnets moved away from the fixed end. While many researchers have studied simple dynamic models of the MR/ER based structures, only some were focused on active vibration tuning of MR/ER beams [15–17]. Wang et al. [15] designed a sliding mode controller for MR fluid based beams. Rahn and

H. Malaeke • H. Moeenfard (✉)
Ferdowsi University of Mashhad, 100 Vakilabad Highway, Mashhad, Iran
e-mail: h.moeenfard@um.ac.ir

A.H. Ghasemi
University of Michigan, 2350 Hayward, Ann Arbor, MI, USA

J. Baqersad
Experimental Mechanics and NVH Laboratory, Kettering University, 1700 University Avenue, Flint, MI 48504, USA

J.M. Harvie, J. Baqersad (eds.), *Shock & Vibration, Aircraft/Aerospace, Energy Harvesting, Acoustics & Optics, Volume 9*,
Conference Proceedings of the Society for Experimental Mechanics Series, DOI 10.1007/978-3-319-54735-0_24

Joshi [16] used Lyapunov theory to ensure stability of all model of the ER beam. Recently, Bajkowski et al. [18] propose a semi-active damping strategy using granular structures sandwiched between elastic beams. The damping properties of the system are controlled pneumatically, by subjecting the granular material to under-pressure at particular moments.

In this paper we demonstrate the effectiveness of the MR beams in reducing unwanted vibration of engineering structures. The governing equations of motion of three-layered beam including MR elastomer sandwiched between two elastic layers is developed using Hamilton's principle. A fuzzy controller is designed to control the intensity of magnetic field applied to the MR layer. The numerical simulation demonstrates the effectiveness of the MR beam along with fuzzy control techniques in attenuating unwanted vibration in engineering structures.

24.2 Mathematical Modeling

Consider the MR sandwich beam shown in Fig. 24.1. The beam consists of an MR elastomer core layer with a thickness of c sandwiched between two elastic layers with a thickness of h. The transverse displacement $w(x,t)$ causes bending of the elastic layer and consequently a shear strain γ is generated in the MR layer. Moreover, the transverse displacement generates the longitudinal displacement $u(x,t)$. In this paper, we assume the beam behaves as an Euler-Bernoulli beam. In specific, we assume that cross sections of the beam do not deform significantly under the application of transverse or axial forces. In addition, deformation of beam's cross section is assumed to remain planar and normal to the deformed axis of the beam [19]. Furthermore, the slippage between the elastic layer and MR fluid is assumed to be negligible. In order to model the characteristic behavior of the MR layer, it is assumed that the MR material is in the pre-yield region. Therefore, the MR layer has the properties of a linear viscoelastic material. In this paper, we assume that the strains are small ($\varepsilon \leq 0.01 \varepsilon \leq 0.01$) and therefore, the assumption of linear viscoelastic model for the MR layer is valid [20, 21].

The relationship between stress and strain of MR material can be expressed based on the linear viscoelastic model as follows

$$\tau = G^* \gamma \tag{24.1}$$

where τ is the shear stress, γ is the shear strain, and G^* is the complex modulus that can be described as

$$G^* = G + i\eta \tag{24.2}$$

In Eq. (24.2), G and η are storage and loss moduli, respectively. The storage Kirchhoff's modulus G and loss modulus η are respectively proportional to the average energy stored and dissipated per unit volume of the material over a cycle of

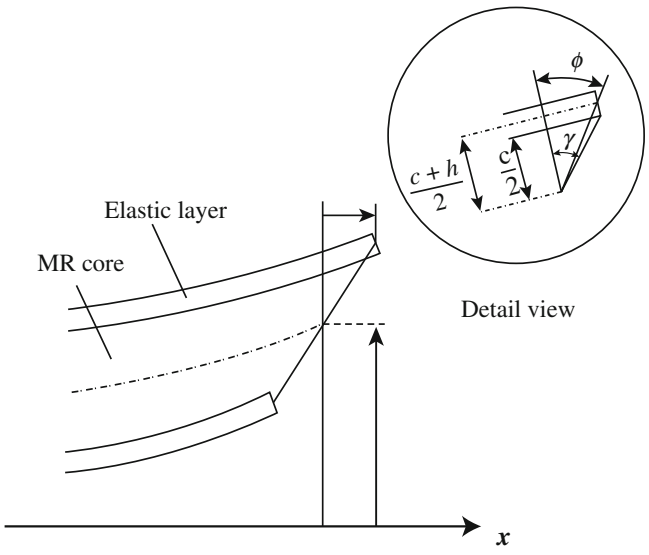

Fig. 24.1 Deformed shape of MR sandwich beam

deformation. The functional dependence of G and η on magnetic field is experimentally determined, and in many cases, a linear approximation is appropriate as

$$\begin{cases} G(B) = m_g B + b_g \\ \eta(B) = m_e E + b_e \end{cases} \tag{24.3}$$

where B is the magnetic field intensity and, m_g, b_g, m_e and b_e are experimentally determined constants [12].

Next, the governing equations of motion are derived using Hamilton's principle. The potential energy of the beam is composed of extensional and bending energy in the elastic layers as well as shear energy in the MR layer. Assuming a uniform shear strain through the thickness of the MR layer, the shear energy in the MR core layer is

$$U_s = \frac{1}{2}\int_0^L GA_s\gamma^2 dx \tag{24.4}$$

where A_s is the cross section of the shear plane and L is the length of the beam. It follows from Fig. 24.1 that the shear strain γ is related to the longitudinal and transverse displacements as follows

$$\gamma = \frac{c+h}{c}\left(\frac{\partial w}{\partial x} + \frac{2u}{c+h}\right) \tag{24.5}$$

The extensional and bending energy in the elastic layers are

$$U = 2\times\left(\frac{1}{2}\int_0^L A\left(\frac{\partial u}{\partial x}\right)^2 dx + \frac{1}{2}\int_0^L EI\left(\frac{\partial^2 w}{\partial x^2}\right)^2 dx\right) \tag{24.6}$$

where A is the elastic layer's cross-section, I is the beam's area moment of inertia, and E is the Young's modulus of the elastic layers.

The kinetic energy associated with transverse and longitudinal displacements is

$$K = \int_0^L \rho A\left(\left(\frac{\partial u}{\partial t}\right)^2 + \left(\frac{\partial w}{\partial t}\right)^2\right) dx \tag{24.7}$$

where ρ is the density of the elastic layers. Finally, the work energy related to the external forces $f(x,t)$ and dissipation in the MR layer can be expressed as

$$\delta W_{ext} = \int_0^L f(x,t)\,\delta w(x,t)\,dx - \int_0^L \eta A_s \dot{\gamma}\,\delta\gamma\,dx \tag{24.8}$$

where $\dot{\gamma}$ is the shear strain rate.

The governing equations of motion are derived by using the Hamilton's principle as

$$2EI\frac{\partial^4 w}{\partial x^4} - \eta A_s\left(\frac{c+h}{c}\right)^2\frac{\partial}{\partial x}\left(\frac{\partial^2 w}{\partial x\partial t} + \frac{2}{c+h}\frac{\partial u}{\partial t}\right) - \left(\frac{c+h}{c}\right)^2\frac{\partial}{\partial x}\left(GA_s\left(\frac{\partial w}{\partial x} + \frac{2u}{c+h}\right)\right) + 2\rho A\frac{\partial^2 w}{\partial t^2} = f(x,t) \tag{24.9}$$

$$-2EA\frac{\partial^2 u}{\partial x^2} + \frac{2\eta A_s}{c+h}\left(\frac{c+h}{c}\right)^2\left(\frac{\partial^2 w}{\partial x\partial t} + \frac{2}{c+h}\frac{\partial u}{\partial t}\right) + \frac{2GA_s}{c+h}\left(\frac{c+h}{c}\right)^2\left(\frac{\partial w}{\partial x} + \frac{2u}{c+h}\right) + 2\rho A\frac{\partial^2 u}{\partial t^2} = 0 \tag{24.10}$$

and the corresponding boundary conditions are derived as

$$\left[-2EI\frac{\partial^3 w}{\partial x^3} + GA_s\left(\frac{c+h}{c}\right)^2\left(\frac{\partial w}{\partial x} + \frac{2u}{c+h}\right) + \eta A_s\left(\frac{c+h}{c}\right)^2\left(\frac{\partial^2 w}{\partial x\partial t} + \frac{2}{c+h}\frac{\partial u}{\partial t}\right)\right]\delta w\Big|_0^L = 0 \tag{24.11}$$

$$EI\frac{\partial^2 w}{\partial x^2}\delta\left(\frac{\partial w}{\partial x}\right)\Big|_0^L = 0 \tag{24.12}$$

$$EA\frac{\partial u}{\partial x}\delta u\Big|_0^L = 0 \tag{24.13}$$

For convenience, the following non-dimensional parameters are defined to simplify the equations of motions:

$$x^* = \frac{x}{L}\ ,\quad w^* = \frac{w}{L}\ ,\quad u^* = \frac{2u}{c+h}\ ,\quad t^* = \frac{t}{L^2}\sqrt{\frac{EI}{\rho A}}\ ,\quad \eta^* = \frac{\eta A_s L^2}{2TEI}\left(\frac{c+h}{c}\right)^2\ ,\quad G^* = \frac{GA_sL^2}{2EI}\left(\frac{c+h}{c}\right)^2,$$
$$f^* = \frac{L^3 f}{2EI}\ ,\quad I^* = \frac{4I}{A(c+h)^2}\ ,\quad D = \frac{I}{AL^2} \tag{24.14}$$

Substituting the non-dimensional parameters Eq. (24.14) into Eqs. (24.9), (24.10), (24.11), (24.12), and (24.13) yields the following non-dimensional equations of motion and boundary conditions:

$$\frac{\partial^4 w}{\partial x^4} - \eta\frac{\partial}{\partial x}\left(\frac{\partial^2 w}{\partial x \partial t} + \frac{\partial u}{\partial t}\right) - \frac{\partial}{\partial x}\left(G\left(\frac{\partial w}{\partial x} + u\right)\right) + \frac{\partial^2 w}{\partial t^2} = f(x,t) \tag{24.15}$$

$$-\frac{\partial^2 u}{\partial x^2} + \eta I\left(\frac{\partial^2 w}{\partial x \partial t} + \frac{\partial u}{\partial t}\right) + GI\left(\frac{\partial w}{\partial x} + u\right) + D\frac{\partial^2 u}{\partial t^2} = 0 \tag{24.16}$$

$$\left[-\frac{\partial^3 w}{\partial x^3} + G\left(\frac{\partial w}{\partial x} + u\right) + \eta\left(\frac{\partial^2 w}{\partial x \partial t} + \frac{\partial u}{\partial t}\right)\right]\delta w\Big|_0^1 \tag{24.17}$$

$$\frac{\partial^2 w}{\partial x^2}\delta\left(\frac{\partial w}{\partial x}\right)\Big|_0^1 = 0 \tag{24.18}$$

$$\frac{\partial u}{\partial x}\delta u\Big|_0^1 = 0 \tag{24.19}$$

where $_*$ have been discarded for notational simplicity.

For a long beam with a small slenderness ratio, the axial inertia can be neglected. Therefore, Eq. (24.15) is simplified as

$$-\frac{\partial^2 u}{\partial x^2} + \eta I\left(\frac{\partial^2 w}{\partial x \partial t} + \frac{\partial u}{\partial t}\right) + GI\left(\frac{\partial w}{\partial x} + u\right) = 0 \tag{24.20}$$

If the system is vibrating at its nth mode, the mode shape of the beam can be expressed as

$$w(x,t) = W_n(x)\exp(i\omega_n t) \quad ,\quad u(x,t) = U_n(x)\exp(i\omega_n t) \tag{24.21}$$

where ω_n is the nth natural frequency.

Substituting Eq. (24.21) into Eqs. (24.14) and (24.15) with $f = 0$ and omitting the damping terms gives us

$$\frac{d^4 W_n}{dx^4} - G_0\left(\frac{d^2 W_n}{dx^2} + \frac{dU_n}{dx}\right) - \omega_n^2 W_n = 0 \tag{24.22}$$

$$\frac{d^2 U_n}{dx^2} - G_0 I\left(\frac{dW_n}{dx} + U_n\right) = 0 \tag{24.23}$$

where G_0 is the storage modulus of the MR layer in absence of a magnetic field. The general solutions of Eq. (24.22) and Eq. (24.23) have the form of

$$W_n(x) = \exp(\lambda x)\ ,\quad U_n(x) = R_n\exp(\lambda x) \tag{24.24}$$

where R_n is the ratio of the longitudinal to transverse displacements. In particular, by substituting Eq. (24.24) into Eq. (24.23), we obtain

$$R_n = -\frac{G_0 I\lambda}{\lambda^2 + G_0 I} \tag{24.25}$$

The characteristic equation results from substitution of Eq. (24.24) into Eq. (24.22) is

$$\lambda^6 + G_0 (I-1)\lambda^4 - \omega_n^2\lambda^2 - G_0 I\omega_n^2 = 0 \tag{24.26}$$

The modal frequencies ω_n and mode shape result from simultaneous solution of Eq. (24.26) and the six boundary conditions. The details are presented in Appendix.

24.3 Fuzzy Controller

In this section, a fuzzy controller is designed to attenuate the vibration of the "smart" beam. The objective is to control the intensity of the magnetic field applies to the MR layer so that by changing the beam's stiffness and damping, unwanted vibration is suppressed. The fuzzy controller consists of four main parts: fuzzier, rules, inference engine, and defuzzifier [22–24]. The model of the fuzzy controller used in this paper is shown in Fig. 24.2. The beam's displacement and velocity are selected as the controller's inputs and the intensity of the magnetic field is selected as the controller's output. The membership functions are selected as seven identical triangles with 50% overlap, illustrated in Fig. 24.3(a) and (b). The labels NL, NM, NS, ZO, PS, PM, PL refer to the linguistic values: negative large, negative medium, negative small, zero, positive small, positive medium, and positive large, respectively. We let the limits of input displacement be from −x to x and the limits of input modal velocity be from −v to v, which can be selected according to the open loop dynamics of the system.

The controller's output is defined on the universe of discourse B and selected as five identical triangles with 50% overlap depicted in Fig. 24.3(c). The labels S, M, L, and VL in Fig. 24.3(c) refer to the linguistic values: small, medium, large and very large. Moreover, B_{max} represents the maximum intensity of the magnetic field applied over the beam.

Based on the physical understanding of the beam dynamics, one can derive some fuzzy IF-THEN rules such that the dynamic behavior of the system using a cause and effects logic can be described. In this paper, we define the logics such that when the beam is moving away from its equilibrium states, the intensity of the magnetic field increases so that with increasing beam's damping, the vibration amplitude reduces. On the other hand, when the beam is moving towards its equilibrium, the magnetic field intensity decreases to reduce the resistance force. The detailed rule-based is presented in Table 24.1. Next, using the combination of the singleton fuzzifier, product inference engine (with the presented rule-based) and center average defuzzifier, the output voltage of the fuzzy controller can be concluded as

$$B = \frac{\sum_{i=1}^{7}\sum_{j=1}^{7}\overline{y}_{ij}\mu_i(q)\mu_j(\dot{q})}{\sum_{i=1}^{7}\sum_{j=1}^{7}\mu_i(q)\mu_j(\dot{q})} \tag{24.27}$$

where q and $\dot{q}$ are respectively modal displacement and modal velocity, μ is the membership function and $\overline{y}_{ij}$ is the center of fuzzy set presented in the ith column and jth row of the Table 24.1.

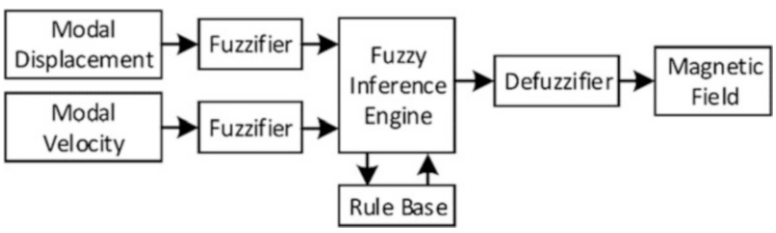

Fig. 24.2 Components of fuzzy system

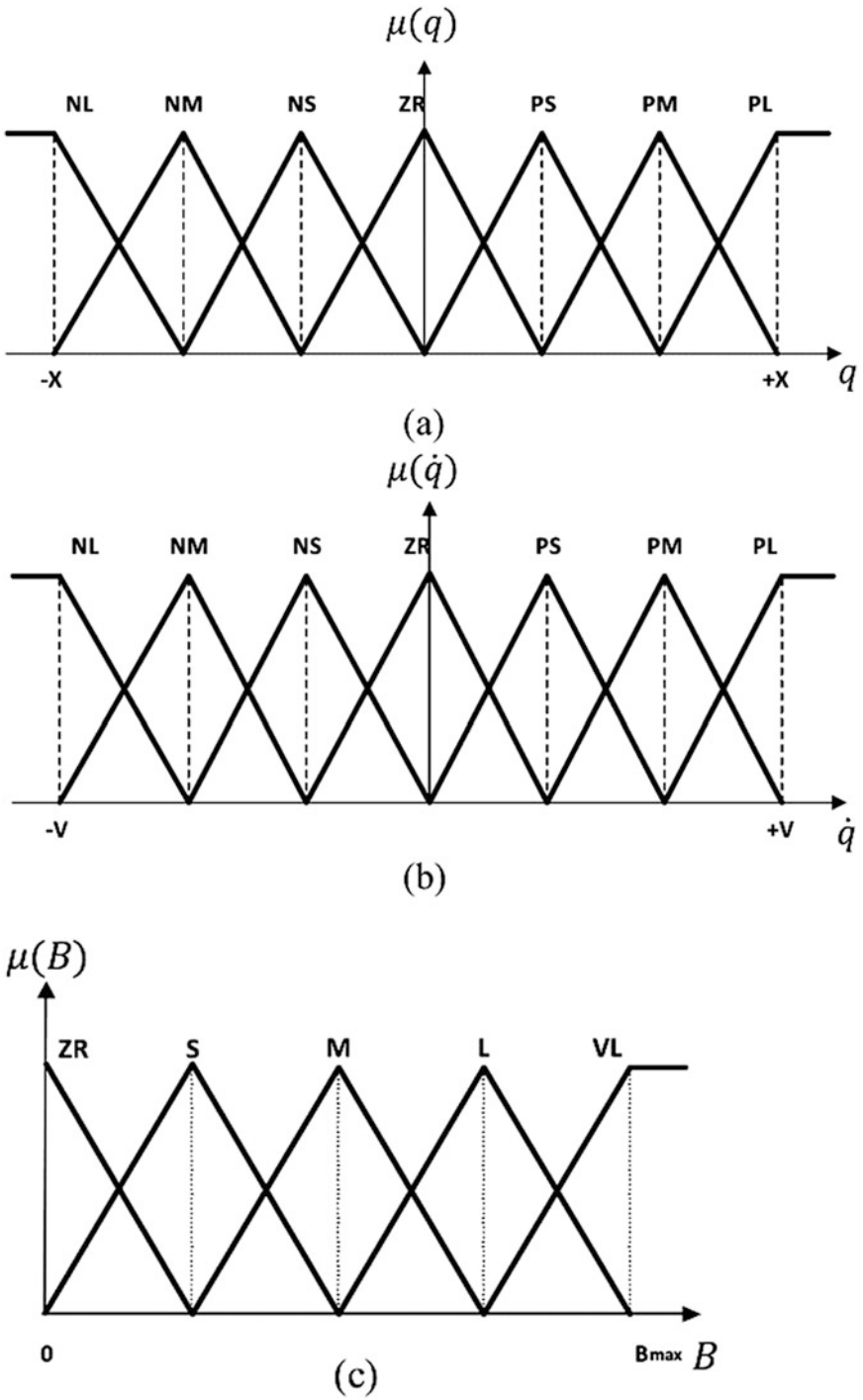

Fig. 24.3 Membership functions of input and output variables of fuzzy controller: (**a**) the first input (Modal Displacement) (**b**) the second input (modal velocity), (**c**) applied magnetic field

24.4 Simulation Results

In this section, we present numerical simulations to demonstrate the effectiveness of using MR layer along with designed fuzzy controller for attenuating beam's vibration. The beam's properties are listed in Table 24.2. We assume the beam is simply-supported. So $\lambda_n = n\pi$ and the mode shapes are

Table 24.1 Rule base of designed fuzzy controller

		Modal displacement						
		NL	*NM*	*NS*	*ZR*	*PS*	*PM*	*PL*
Modal velocity	*NL*	VL	VL	M	L	ZR	ZR	ZR
	NM	VL	L	M	M	ZR	ZR	S
	NS	L	M	S	S	ZR	M	M
	ZR	L	M	S	ZR	S	M	L
	PS	M	M	ZR	S	S	M	L
	PM	S	ZR	ZR	M	M	L	VL
	PL	ZR	ZR	ZR	L	M	VL	VL

Table 24.2 Physical and geometrical properties of sandwich beam

Parameters	'Unit	Value
Elastic modulus of elastic layers	GPa	70
Density of elastic layers	kg/m^3	2710
elastic layers thickness	mm	0.53
MR layer thickness	mm	2
Beam length	mm	25.4
Beam width	mm	254
Initial Magnetic field	T	0.05

$$\begin{cases} w_n(x,t) = q_n(t)\sin(n\pi x) \\ u_n(x,t) = R_n q_n(t)\cos(n\pi x) \end{cases} \tag{24.28}$$

where q_n is the modal displacement of the beam. Furthermore, the natural frequency and damping ration of the beam are

$$\begin{cases} \omega_n = n^2\pi^2\sqrt{1+\frac{G_0 I}{n^2\pi^2+G_0 I}} \\ \zeta_n = \frac{\eta_0}{2\omega_n}\left(\frac{n^4\pi^4}{n^2\pi^2+G_0 I}\right) \end{cases} \tag{24.29}$$

and the beam's dynamic equation can be described as

$$\ddot{q}_n(t) + 2\zeta_n\omega_n\,\dot{q}_n(t) + \omega_n^2 q_n(t) = Q_n(t) \tag{24.30}$$

where Q_n is the generalized force that is defined as

$$Q_n(t) = \int_0^1 f(x,t)\,W_n(x)dx \tag{24.31}$$

Considering one mode for the beam ($n = 1$), Fig. 24.4 shows the transient response of the beam due to a given initial conditions. The initial conditions are $q = 0.05$ and $\dot{q} = 0$. It is shown that using the "smart" MR layer results in a significant reduction in beam's vibration. Fig. 24.5 illustrates the required magnetic field corresponding to the Fig. 24.4. Note, although the magnetic field is nonzero, the amount of the control input can not cause any motion in the system.

Next, a point force with a frequency equal to the beam's first natural frequency is applied to the middle of the beam. It is shown in Fig. 24.6 that with increasing the magnetic fields intensity, the properties of the beam such as its damping and stiffness is increased which consequently reduces beam's vibration. Fig. 24.7 shows the variation of the required control forces in the resonance.

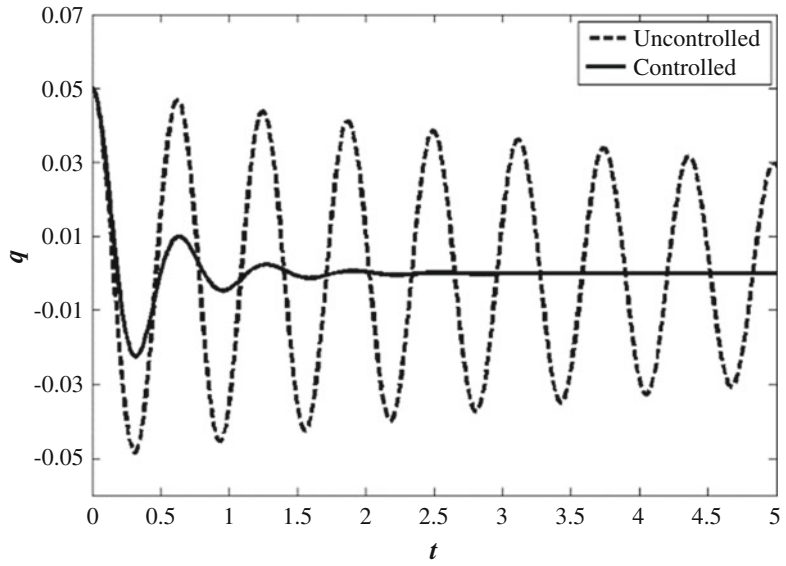

Fig. 24.4 Transient response of the beam due to the initial condition

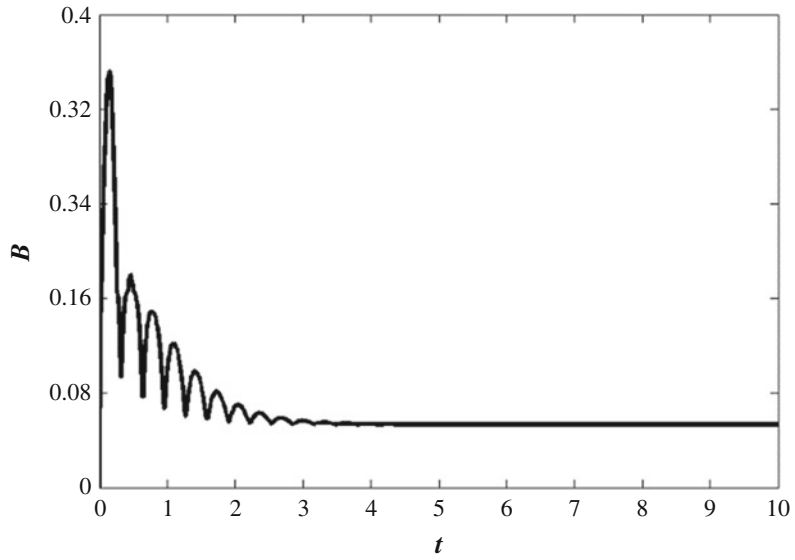

Fig. 24.5 Variation of the applied magnetic field (control effort) due to initial conditions

Finally, the beam's vibration under a shock excitation is shown in Fig. 24.8. The shock excitation is modeled as a half cycle sinusoidal signal with unity integral applied at the center of the beam. It follows from Fig. 24.8 that with changing the characteristic of the MR layer, the beam can significantly reject the effect of the shock excitation (See Fig. 24.9).

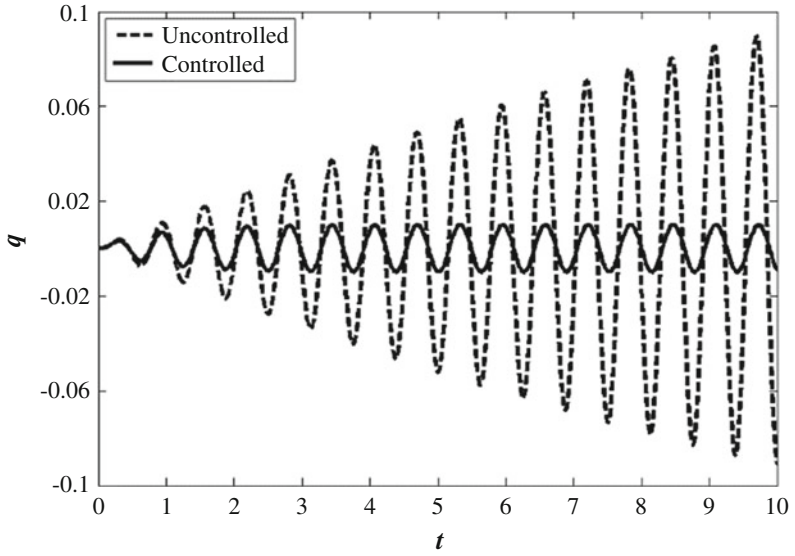

Fig. 24.6 Forced response of the system in resonance

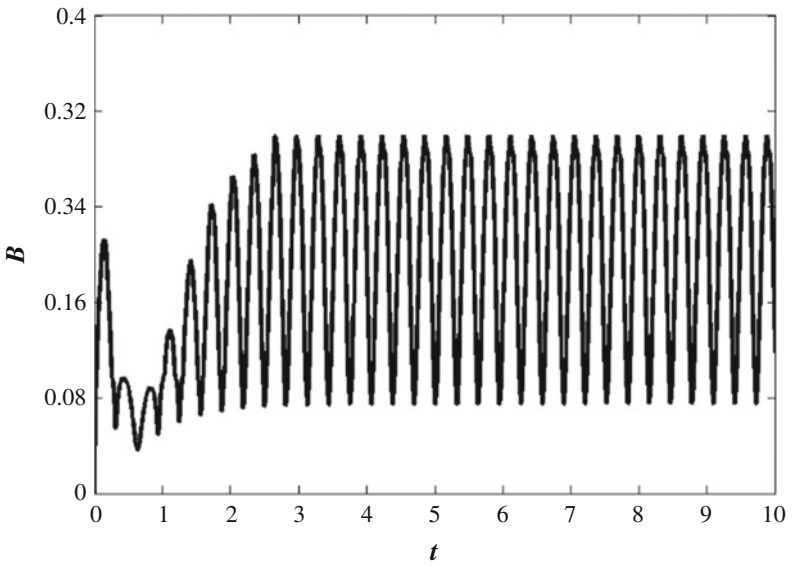

Fig. 24.7 Variation of the applied magnetic field in resonance

24.5 Conclusion

In this paper, we demonstrated that using "smart" beams with MR layers can play a significant role in reducing unwanted vibrations in engineering structures. A three-layered beam consisting of a MR layer sandwiched between two elastic layers was modeled. In order to control the magnetic field applies to the MR layer, a fuzzy controller was designed. It was shown that with changing stiffness and damping of the beam, unwanted vibrations can significantly suppressed.

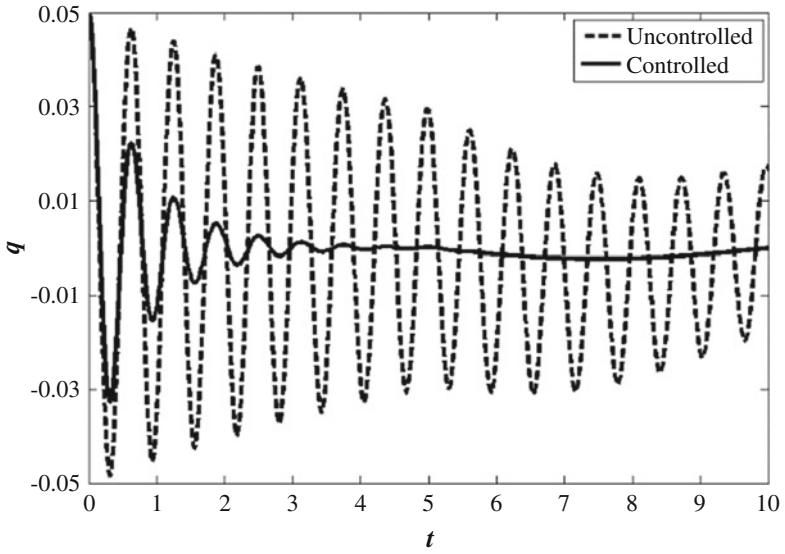

Fig. 24.8 Forced response of the system under sinosoidal shock excitation

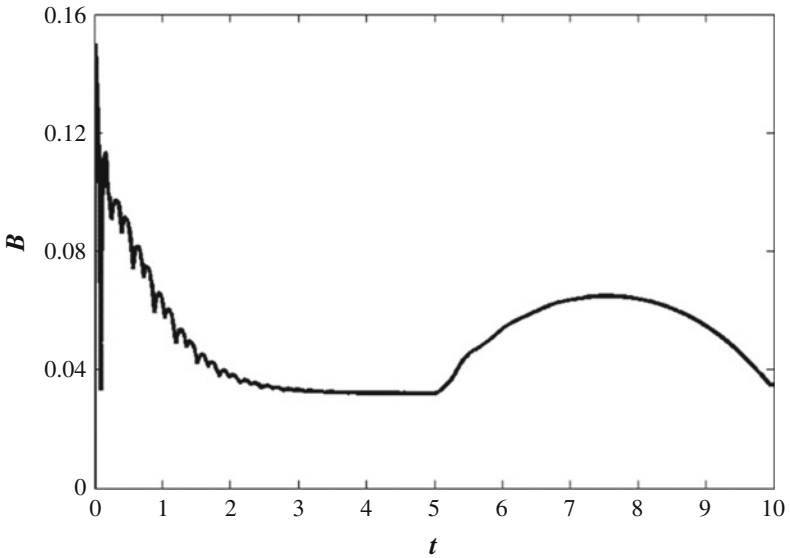

Fig. 24.9 Variation of the applied magnetic field due to sinosoidal shock excitation

Appendix

In this section, we present the free response of a sandwiched beam with arbitrary boundary conditions. The characteristic Eq. (24.26) is a sixth-order polynomial which can be rewritten as

$$\delta^3 + G_0 (I - 1) \delta^2 - \omega_n^2 \delta - G_0 I \omega_n^2 = 0 \tag{24.32}$$

where

$$\delta = \lambda^2 \tag{24.33}$$

The roots of the Eq. (24.32) is described in [25]. The general solution of the system is expressed as

$$\begin{cases} w(x,t) = e^{i\omega_n t} \sum_{i=1}^{6} c_i e^{\lambda_i x} \\ u(x,t) = e^{i\omega_n t} \sum_{i=1}^{6} R_i c_i e^{\lambda_i x} \end{cases} \tag{24.34}$$

where for $i = 1,2,\cdots,6$, λ_i are the roots of the characteristic equation. Substituting Eq. (24.34) into the boundary conditions Eqs. (24.17), (24.18), and (24.19) yields a matrix equation

$$\sum_{j=1}^{6} a_{ij} c_j = 0 \qquad i = 1, \ldots, 6 \tag{24.35}$$

where

$$\begin{aligned} &a_{1j} = 1 \ , \quad a_{2j} = \lambda_j \ , \quad a_{3j} = R_j \ , \quad a_{4j} = \lambda_j^2 e^{\lambda_j}, \\ &a_{5j} = R_j \lambda_j e^{\lambda_j} \ , \quad a_{6j} = G\left(R_j + \lambda_j\right) - \lambda_j^3 \end{aligned} \tag{24.36}$$

for $j = 1, \ldots, 6$, and R_n is given in Eq. (24.25). The natural frequencies ω_n and the solutions of the characteristic equation Eq. (24.26) can be obtained by equating the coefficient matrix zero in Eq. (24.35).

References

1. Carlson, J.D.: Portable controllable fluid rehabilitation devices, Google Patents, 1998
2. Carlson, J.D., Catanzarite, D., Clair, K.S.: Commercial magneto-rheological fluid devices. Int. J. Mod. Phys. B. **10**(23–24), 2857–2865 (1996)
3. Carlson, J.D., Chrzan, M.J., James, F.O.: Magnetorheological fluid devices, Google Patents, 1995
4. Ginder, J.M., Nichols, M.E., Elie, L.D., Tardiff, J.L.: Magnetorheological elastomers: properties and applications. In: Proceeding of International Society for Optics and Photonics 1999, pp. 131–138.
5. Ginder, J.: Rheology controlled by magnetic fields. Encycl. Appl. Phys. **16**, 487–503 (1996)
6. DiTaranto, R.: Theory of vibratory bending for elastic and viscoelastic layered finite-length beams. J. Appl. Mech. **32**(4), 881–886 (1965)
7. A.H. Ghasemi, M.H. Ghaffari Saadat, A.R. Ohadi, Vibration control of a rotor-bearing system with smart bearings using magnetorheologic fluids. In: Proceeding of 15th International Congress on Sound and Vibrations, Daejeon, Korea, 3029–3036, 2008.
8. Mead, D., Markus, S.: The forced vibration of a three-layer, damped sandwich beam with arbitrary boundary conditions. J. Sound Vib. **10**(2), 163–175 (1969)
9. Yalcintas, M., Dai, H.: Magnetorheological and electrorheological materials in adaptive structures and their performance comparison. Smart Mater. Struct. **8**(5), 560 (1999)
10. Sung, Q., Zhou, J.-X., Zhang, L.: An adaptive beam model and dynamic characteristics of magnetorheological materials. J. Sound Vib. **261**(3), 465–481 (2003)
11. Yeh, Z.-F., Shih, Y.-S.: Dynamic characteristics and dynamic instability of magnetorheological material-based adaptive beams. J. Compos. Mater. **40**, 1333–1359 (2006)
12. Rajamohan, V., Rakheja, S., Sedaghati, R.: Vibration analysis of a partially treated multi-layer beam with magnetorheological fluid. J. Sound Vib. **329**, 3451–3469 (2010)
13. Rajamohan, V., Sedaghati, R., Rakheja, S.: Vibration analysis of a multi-layer beam containing magnetorheological fluid. Smart Mater. Struct. **19**, 015013 (2009)
14. Lara-Prieto, V., Parkin, R., Jackson, M., Silberschmidt, V., Zbigniew, K.: Vibration characteristics of MR cantilever sandwich beams: experimental study. Smart Mater. Struct. **19**, 015005 (2009)
15. Rahn, C.D., Joshi, S.: Modeling and control of an electrorheological sandwich beam. J. Vib. Acoust. **120**(1), 221–227 (1998)
16. Wang, K., Kim, Y., Shea, D.: Structural vibration control via electrorheological-fluid-based actuators with adaptive viscous and frictional damping. J. Sound Vib. **177**(2), 227–237 (1994)
17. Chrzan, M.J., Carlson, J.D.: MR fluid sponge devices and their use in vibration control of washing machines. In: Proceeding of SPIE, 370–378, 2001
18. Bajkowski, J.M., Dyniewicz, B., Bajer, C.I.: Semi-active damping strategy for beams system with pneumatically controlled granular structure. Mech. Syst. Signal Process. **70**, 387–396 (2016)
19. Rao, S.S.: Vibration of Continuous Systems, Wiley, New York. (2007)
20. Weiss, K.D., Carlson, J.D., Nixon, D.A.: Viscoelastic properties of magneto-and electro-rheological fluids. J. Intell. Mater. Syst. Struct. **5**(6), 772–775 (1994)
21. Li, W., Du, H., Chen, G., Yeo, S., Guo, N.: Nonlinear rheological behavior of magnetorheological fluids: step-strain experiments. Smart Mater. Struct. **11**(2), 209 (2002)

22. Aliakbari, N., Khadembashi, M., Moeenfard, H., Ghasemi, A.H.: An optimal fuzzy controller stabilizing the rod and controlling the position of single wheeled inverted pendulums, In: Proceeding of Ameircan Control Conference, 2016
23. Khademshai, M., Moeenfard, H., Ghasemi, A.H.: Deflection control of electrostatically actuated mico cantilvers via fuzzy controller. In: Proceeding of Dynamic Systems and Control Conference, 2016
24. Radgolchin, M., Moeenfard, H., Ghasemi, A.H.: A two-level adaptive fuzzy control algorithm for beyond pull-in stabilization of electrostatically actuated microplate. In: Proceeding of Dynamic Systems and Control Conference, 2016
25. Press, W., Teukolsky, S., Vetterling, W., Flannery, B.: Numerical Recipes in Fortran 77: The Art of Scientific Computing, p. 933. Cambridge University Press, New York (1992)

Chapter 25
Logic Analytical Modeling of Piezoelectric Energy Harvesters under Random Base Excitation

Hamid Moeenfard, Mohammad Khadembashi, Amir H. Ghasemi, and Javad Baqersad

Abstract Many of energy harvesting devices use piezoelectric elements to convert mechanical vibrations into usable electrical energy. The input excitation is usually assumed to be a deterministic harmonic wave, while in practical situations; the mechanical excitation of the media is a random signal. The objective of this research is to study the energy harvesting in piezoelectric devices using the random vibration theory. At the first step a lumped parameter physical model of the device is presented. A mathematical model is then developed by obtaining the normalized differential equations governing the voltage induced in the energy harvesting circuit as well as the length of the piezoelectric material. The random vibration theory is then utilized to derive analytical expressions for the statistical properties of the voltage, power and the length of the piezoelectric material in terms of the statistical properties of the excitation which is assumed to be a band limited white noise. It is shown that with proper selection of the system parameters, the expected value of the harvested power can be effectively maximized. The qualitative and quantitative knowledge resulting from this effort is expected to enable the analysis, optimization, and synthesis of piezoelectric energy harvesting devices.

Keywords Energy harvester • Piezoelectric materials • Random vibration • Electrical power

25.1 Introduction

The process of acquiring the energy surrounding a system and converting it into usable electrical energy is termed power harvesting. One driving force behind the search for new energy harvesting devices in recent years is the desire to power sensor networks and mobile devices without batteries. The technology behind this new research field is still being developed. Using energy harvesting technology in small scale electronics, one can power such devices using the vibration energy available in the environment, so the requirement of an external power source or periodic battery replacement can be removed or at least minimized.

A usual approach that is commonly used for harvesting energy from vibrating media is using piezoelectric materials. These materials have a crystalline structure that provides them with the ability to transform mechanical strain energy into electrical charge and, vice versa. The main advantage of piezoelectric devices compared to electromagnetic devices is their high power output for a given device volume [1]. Although not suitable for generating high power levels, they are very suitable for application in small electronic devices [2].

So far researchers have widely modeled piezoelectric based energy harvesters. A brief review of the Energy Harvesting from piezoelectric materials may be found in [3]. Abdelkefi et al. designed [4], modeled and analyzed [5] a piezoaeroelastic energy harvester consisting of a rigid airfoil that is constrained to pitch and plunge. Their device was supported by linear and nonlinear torsional and flexural springs with a piezoelectric coupling attached to the plunge degree of freedom. They [6] parametrically studied the effect of different design parameters to enhance the output harvested power of their piezoaeroelastic energy harvesting system. Li et al. [7] investigated miniature electric generators consisting of piezoelectric benders and elastic bases. Junior et al. [8] presented an electromechanically coupled finite element plate model for predicting

H. Moeenfard (✉) • M. Khadembashi
Ferdowsi University of Mashhad, 100 Vakilabad Highway, Mashhad, Iran
e-mail: h.moeenfard@um.ac.ir

A.H. Ghasemi
University of Michigan, 2350 Hayward, Ann Arbor, MI, USA

J. Baqersad
Experimental Mechanics and NVH Laboratory, Kettering University, 1700 University Avenue, Flint, MI 48504, USA

J.M. Harvie, J. Baqersad (eds.), *Shock & Vibration, Aircraft/Aerospace, Energy Harvesting, Acoustics & Optics, Volume 9*,
Conference Proceedings of the Society for Experimental Mechanics Series, DOI 10.1007/978-3-319-54735-0_25

the electrical power output of piezoelectric energy harvester plates. Abdelkefi et al. [9] proposed the use of a unimorph cantilever beam undergoing bending–torsion vibrations as a new piezoelectric energy harvester design. Ando et al. [1] presented a new strategy for developing broadband, bi-directional, vibration energy harvesters.

As it is observed, design, modeling, optimization and characterization of piezoelectric energy harvesters have been widely presented in the prior art. However most of the related researches have used the theory of deterministic vibration to model the system, while the excitation of the media is practically a broad band one with multiple frequencies. Jackson et al. [10] experimentally compared harvesting power with a piezoelectric vibration powered generator using a full-wave rectifier conditioning circuit for varying sinusoidal, random, and sine on random (SOR) input vibration scenarios. However, as far as the authors know, a detailed random vibration based mathematical approach, for modeling (piezoelectric) energy harvesters has not been presented yet. So here in this paper, a 1D lumped piezoelectric system for harvesting energy from a broad band random excitation is presented. The coupled electromechanical model of the system is then derived in terms of two coupled ODEs. The statistical properties of the output power are derived in terms of the statistical properties of the random input excitation, using random vibration theory. A parametric study is then performed to characterize the effect of different normalized design parameters on the expected value of the harvested power.

25.2 Problem Formulation

25.2.1 Coupled Electromechanical Modeling

The 1-D model of a piezoelectric energy harvester presented in Fig. 25.1 is considered. In this figure, t_e is the thickness of the electrodes which is assumed to be negligible, t_P, $\widehat{z}(\widehat{t})$, R_P and $\widehat{w}_B$ are the initial thickness, the length at time $\widehat{t}$, the internal electrical resistance and the base displacement of the piezoelectric material respectively. Also υ is the produced voltage difference and R_l is the electrical resistance of the consumer.

The system shown in Fig. 25.1 is placed in a moving environment which will force the base of the system to move with an acceleration of $\ddot{\widehat{w}}_B$. Due to the elastic behaviour of the piezoelectric material and also the existence of a proof mass, the piezoelectric will undergo some strain. This strain will induce a voltage difference between two electrodes shown in Fig. 25.1. This voltage can drive some current in the electrical circuit and in this way some energy can be harvested.

Using the proposed 1-D configuration, one can simplify the 3-D linear elastic constitutive relation of the piezoelectric material presented in Eqs. (25.1), (25.2), and (25.3) [11, 12].

$$\begin{Bmatrix} T \\ D \end{Bmatrix} = \begin{bmatrix} c^E & -e^t \\ e & \varepsilon^S \end{bmatrix} \begin{Bmatrix} S \\ E \end{Bmatrix} \tag{25.1}$$

$$\boldsymbol{T}_3 = \boldsymbol{c}_{33}^{\boldsymbol{E}} \boldsymbol{S}_3 - \boldsymbol{e}_{33} \boldsymbol{E}_3 \tag{25.2}$$

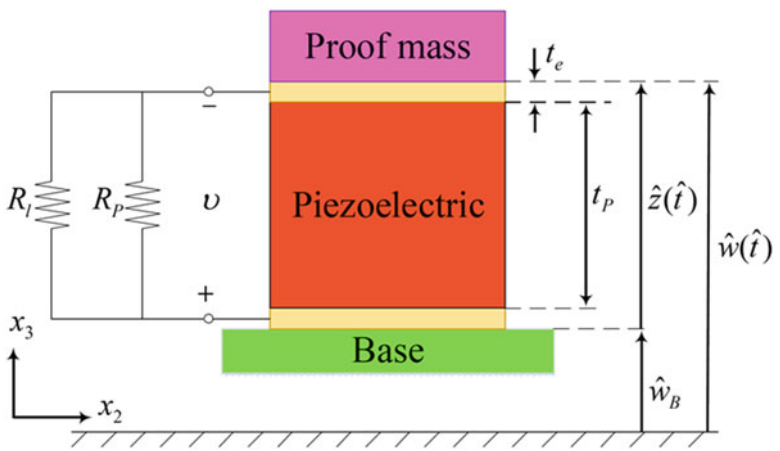

Fig. 25.1 Schematic 1-D model of a piezoelectric energy harvester

$$\boldsymbol{D}_3 = \boldsymbol{e}_{33}\boldsymbol{S}_3 + \boldsymbol{\varepsilon}^{\boldsymbol{S}}_{33}\boldsymbol{E}_3 \tag{25.3}$$

In Eq. (25.1), T, S, E and D are the developed stress tensor, applied strain tensor, applied electric field matrix and the electric displacement matrix respectively. Additionally c, e and ε are defined to be stiffness matrix, piezoelectric constant relating charge density and strain and the permittivity of the piezoelectric element. The superscripts E and S indicate a parameter at constant (typically zero) electric field and strain respectively, while superscript t indicates the transpose of the matrix.

Using the 1-D stress definition along with the newton's second law of motion, the induced stress in the piezoelectric material can be obtained as

$$\boldsymbol{T}_3 = -\frac{\boldsymbol{M_T}\left(\ddot{\widehat{z}}\,(t) + \ddot{\widehat{w}}_B\,(t)\right)}{\boldsymbol{A_P}} \tag{25.4}$$

where A_P is the cross sectional area of the piezoelectric and M_T is the effective mass of the system and can be calculated using the following equation.

$$\boldsymbol{M_T} = \boldsymbol{M} + \frac{1}{3}\boldsymbol{M_P} \tag{25.5}$$

in Eq. (25.5), M_P is the mass of the piezoelectric.

By definition, the engineering strain, the electrical field, the electrical displacement of the piezoelectric can be defined as Eqs. (25.6), (25.7) and (25.8) respectively.

$$S_3 = \frac{\widehat{z}\,(t)}{t_P} \tag{25.6}$$

$$E_3 = -\frac{\widehat{v}\,(t)}{t_P} \tag{25.7}$$

$$\boldsymbol{D}_3 = \frac{\boldsymbol{q}}{\boldsymbol{A_P}} \tag{25.8}$$

By substituting Eqs. (25.4), (25.6), (25.7), and (25.8) into Eqs. (25.2) and (25.3) and doing some algebraic manipulations, Eqs. (25.2) and (25.3) may be simplified to the more practical form presented in Eqs. (25.10) and (25.11) respectively.

$$\boldsymbol{M_T}\ddot{\widehat{z}}\,(t) + \boldsymbol{K}\widehat{z}\,(t) - \boldsymbol{\theta}\,\widehat{v}\,(t) = -\boldsymbol{M_T}\ddot{\widehat{w}}_B\,(t) \tag{25.9}$$

$$\boldsymbol{\theta}\dot{\widehat{z}}\,(t) + \boldsymbol{C_P}\dot{\widehat{v}}\,(t) + \frac{1}{\boldsymbol{R}}\widehat{v}\,(t) = 0 \tag{25.10}$$

Since the internal resistance of the piezoelectric material is usually very high compared to the resistance of the consumer element, i.e. $R_P \gg R_l$, the overall resistance of the circuit, R, can be accurately approximated by the R_l. In other words $R \approx R_l$.

In these equations, the parameters K, C_P and θ are defined as

$$\boldsymbol{K} = \frac{\boldsymbol{c}^{\boldsymbol{E}}_{33}\boldsymbol{A_P}}{\boldsymbol{t_P}} \tag{25.11}$$

$$\boldsymbol{C_P} = \frac{\boldsymbol{\varepsilon}^{\boldsymbol{s}}_{33}\boldsymbol{A_P}}{\boldsymbol{t_P}} \tag{25.12}$$

$$\boldsymbol{\theta} = -\frac{\boldsymbol{e}_{33}\boldsymbol{A_P}}{\boldsymbol{t_P}} \tag{25.13}$$

For convenience purposes, the following normalized variables are defined.

$$z = \frac{\widehat{z}}{t_P} \tag{25.14}$$

$$w_B = \frac{\widehat{w}_B}{t_P} \tag{25.15}$$

$$v = \frac{\widehat{v}}{v_0} \tag{25.16}$$

$$t = \omega_0 \widehat{t} \tag{25.17}$$

where υ_0 and ω_0 are defined to be as follows.

$$v_0 = \frac{\theta\ t_P}{C_P} \tag{25.18}$$

$$\omega_0 = \sqrt{\frac{K}{M_T}} \tag{25.19}$$

Using the normalized variables presented in Eqs. (25.14), (25.15), (25.16), and (25.17), Eqs. (25.9) and (25.10) may be expressed in normalized form as given in Eqs. (25.20) and (25.21) respectively.

$$z''(t) + z(t) - A_1\ v(t) = -w_B''(t) \tag{25.20}$$

$$z'(t) + v'(t) - A_2 v(t) = 0 \tag{25.21}$$

where prime denotes differentiation with respect to t and A_1 and A_2 are two normalized variables defined as

$$A_1 = \frac{\theta^2}{KC_P} \tag{25.22}$$

$$A_2 = -\frac{\theta\sqrt{M_T}}{R_l C_P \sqrt{K}} \tag{25.23}$$

It has to be noted that A_1 and A_2 are both positive parameters.

25.2.2 Random Vibration Modeling

So far researchers have widely modelled piezoelectric based energy harvesters. However, almost all of them have used the theory of deterministic vibration to model the system, while in practice, the excitation of the media is usually a broad band one with multiple frequencies. So here the theory of random vibration will be used to model the statistical properties of the harvested power. To do so, in the first step, the Eqs. (25.20) and (25.21) are re-expressed in matrix form.

$$\left[B^{(1)}\right]\overrightarrow{\Phi}''(t) + \left[B^{(2)}\right]\overrightarrow{\Phi}'(t) + \left[B^{(3)}\right]\overrightarrow{\Phi}(t) = \overrightarrow{Y}(t) \tag{25.24}$$

where

$$\overrightarrow{\Phi}(t) = \begin{Bmatrix} z(t) \\ v(t) \end{Bmatrix} \tag{25.25}$$

$$\overrightarrow{Y}(t) = -\begin{Bmatrix} w_B''(t) \\ 0 \end{Bmatrix} \tag{25.26}$$

$$\left[\boldsymbol{B}^{(1)}\right] = \begin{bmatrix} 1 & 0 \\ 0 & 0 \end{bmatrix} \tag{25.27}$$

$$\left[\boldsymbol{B}^{(2)}\right] = \begin{bmatrix} 0 & 0 \\ 1 & 1 \end{bmatrix} \tag{25.28}$$

$$\left[\boldsymbol{B}^{(3)}\right] = \begin{bmatrix} 1 & -\boldsymbol{A}_1 \\ 0 & -\boldsymbol{A}_2 \end{bmatrix} \tag{25.29}$$

The system of ordinary differential equations given in Eq. (25.24), has a single input and two outputs. The first step in modeling the random vibration in a system is finding the frequency responses of the system. To do so, the input is assumed as

$$\boldsymbol{w_B''}(\boldsymbol{t}) = \boldsymbol{w''_{B_0}} \mathbf{exp}(\boldsymbol{i\omega t}) \tag{25.30}$$

then $\overrightarrow{Y}(t)$ would be as

$$\overrightarrow{\boldsymbol{Y}}(\boldsymbol{t}) = \overrightarrow{\boldsymbol{Y}}_0 \mathbf{exp}(\boldsymbol{i\omega t}) \tag{25.31}$$

where $i = \sqrt{-1}$ and $\overrightarrow{Y}_0$ is defined as

$$\overrightarrow{\boldsymbol{Y}}_0 = -\begin{Bmatrix} \boldsymbol{w''_{B_0}} \\ 0 \end{Bmatrix} \tag{25.32}$$

The output of the system then will be as

$$\overrightarrow{\boldsymbol{\Phi}}(\boldsymbol{t}) = \overrightarrow{\boldsymbol{H}}(\boldsymbol{\omega})\, \boldsymbol{w''_{B_0}} \mathbf{exp}(\boldsymbol{i\omega t}) \tag{25.33}$$

By substituting the Eqs. (25.30) and (25.33) into Eq. (25.24), $\overrightarrow{H}(\omega)$ is obtained as

$$\overrightarrow{\boldsymbol{H}}(\boldsymbol{\omega}) = \begin{Bmatrix} \boldsymbol{H}_1(\boldsymbol{\omega}) \\ \boldsymbol{H}_2(\boldsymbol{\omega}) \end{Bmatrix} \tag{25.34}$$

where

$$\boldsymbol{H}_1(\boldsymbol{\omega}) = \frac{(\boldsymbol{A}_2 - \boldsymbol{i\omega})}{\boldsymbol{A}_2(\boldsymbol{\omega}^2 - 1) + \boldsymbol{i}(\boldsymbol{\omega} + \boldsymbol{A}_1\boldsymbol{\omega} - \boldsymbol{\omega}^3)} \tag{25.35}$$

$$\boldsymbol{H}_2(\boldsymbol{\omega}) = \frac{\boldsymbol{i\omega}}{\boldsymbol{A}_2(\boldsymbol{\omega}^2 - 1) + \boldsymbol{i}(\boldsymbol{\omega} + \boldsymbol{A}_1\boldsymbol{\omega} - \boldsymbol{\omega}^3)} \tag{25.36}$$

Now, the statistical expectation (i.e. average) of the output, i.e. $\overrightarrow{\Phi}(t)$, is obtained as [13]

$$\frac{\boldsymbol{E}\left[\overrightarrow{\boldsymbol{\Phi}}(\boldsymbol{t})\right]}{\boldsymbol{E}\left[\boldsymbol{w_B''}(\boldsymbol{t})\right]} = \overrightarrow{\boldsymbol{H}}(\boldsymbol{\omega})\Big|_{\boldsymbol{\omega}=0} = -\begin{Bmatrix} 1 \\ 0 \end{Bmatrix} \tag{25.37}$$

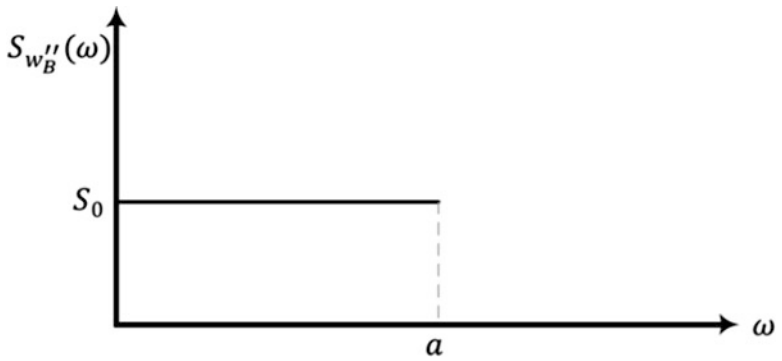

Fig. 25.2 Normalized one-sided Acceleration Spectral density (ASD) of the base of the system which is considered to be a band limited white noise

In other words, the statistical expectation of the $z(t)$ would be minus of the statistical expectation of the acceleration of the base, while the average value of the normalized voltage becomes zero.

The spectral density of the output variables can also be obtained using Eq. (25.38).

$$\vec{S}_{\vec{\Phi}}(\omega) = \begin{Bmatrix} S_z(\omega) \\ S_v(\omega) \end{Bmatrix} \tag{25.38}$$

where

$$S_z(\omega) = |H_1(\omega)|^2 S_{w_B''}(\omega) \tag{25.39}$$

$$S_v(\omega) = |H_2(\omega)|^2 S_{w_B''}(\omega) \tag{25.40}$$

In practical situations, the one sided spectral density of the input base acceleration of the media, is a band limited white noise as shown in Fig. 25.2. So one can assume that

$$S_{w_B''}(\omega) = \begin{cases} S_0 & 0 \le \omega \le a \\ 0 & a < \omega < \infty \end{cases} \tag{25.41}$$

By substituting Eq. (25.41) into Eqs. (25.39) and (25.40) respectively, one can obtain the following equations

$$\frac{S_z(\omega)}{S_0} = \begin{cases} |H_1(\omega)|^2 & 0 \le \omega \le a \\ 0 & a < \omega < \infty \end{cases} \tag{25.42}$$

$$\frac{S_z(\omega)}{S_0} = \begin{cases} |H_2(\omega)|^2 & 0 \le \omega \le a \\ 0 & a < \omega < \infty \end{cases} \tag{25.43}$$

It has been proven in the random vibration theory that the expected square value of a random variable can be obtained by integrating its spectral density over the frequency domain [13]. Using this theorem, the following equations can be presented for finding $E[z^2]$ and $E[v^2]$.

$$\frac{E[z^2]}{S_0} = \int_0^\infty \frac{S_z(\omega)}{S_0} d\omega = \int_0^a |H_1(\omega)|^2 d\omega \tag{25.44}$$

$$\frac{E[v^2]}{S_0} = \int_0^\infty \frac{S_v(\omega)}{S_0} d\omega = \int_0^a |H_2(\omega)|^2 d\omega \tag{25.45}$$

The harvested power of the circuit, $\widehat{P}$, can be obtained from the following famous equation.

$$\widehat{\boldsymbol{P}}\left(\boldsymbol{t}\right) = \frac{\widehat{\boldsymbol{v}}^2}{\boldsymbol{R_l}} \tag{25.46}$$

The normalized power can then be defined as

$$\boldsymbol{P}\left(\boldsymbol{t}\right) = \frac{\widehat{\boldsymbol{P}}\left(\boldsymbol{t}\right)}{\boldsymbol{P}_0} \tag{25.47}$$

where P_0 is defined as

$$\boldsymbol{P}_0 = \frac{\boldsymbol{S}_0 \boldsymbol{v}_0^2}{\boldsymbol{R_l}} \tag{25.48}$$

From Eqs. (25.46), (25.47) and (25.48), it can be easily proven that the expected value of the normalized power is obtained as

$$\boldsymbol{E}\left[\boldsymbol{P}\right] = \frac{\boldsymbol{E}\left[\boldsymbol{v}^2\right]}{\boldsymbol{S}_0} \tag{25.49}$$

In other words Eq. (25.45) can also be used for calculating the expected value of the normalized harvested power.

25.3 Results and Discussion

The geometrical and physical parameters of the system are selected as given in Table 25.1.

In Figs. 25.3 and 25.4, the one sided spectral density $S_v(\omega)/S_0$ is plotted against the normalized frequency ω and the effect of different design prameters, i.e. A_1 and A_2, on these spectral densities are studied. From Fig. 25.3, it is clear that the increasing A_1 at constant value of A_2 can considerably reduce the maximum peak value of the normalized voltage spectral specifically at normalized frequency of unity. However the frequency at which the peak value occurs does not change considerably. In Fig. 25.4, the effects of changing the value of A_2 on the on the voltage spectral density has been studied. It is observed that increasing the value of A_2 would results in decreasing the peak value of the voltage spectral density as well as the frequency at which this peak occurs.

In Figs. 25.5 and 25.6 the effects of changing the values of A_1 and A_2 on the spectral density of z is studied. Clearly with increasing the value of A_1 (at constant value of A_2), $S_z(\omega)/S_0$ is reduced, while with increasing the value of A_2 (at constant value of A_1), $S_z(\omega)/S_0$ is increased. It is also observed that changing the values of A_1 and A_2 does not have appreciable effect on the peak frequency of $S_z(\omega)/S_0$.

Table 25.1 Geometrical and physical parameters of the system shown in Fig. 25.1 [12]

Parameters	Value	Unit	Description
M	0.01	kg	Mass of the proof mass
t_P	0.01	m	Initial thickness
A_P	0.001	m^2	Cross sectional area of the piezoelectric
ω_N	196,570	rad/sec	Natural frequency
M_P	0.0075	kg	Mass of the piezoelectric
e_{33}	28.64	C/m^2	Piezoelectric constant
ε_{33}^s	13.17	$\boldsymbol{nf/m}$	Permittivity of the piezoelectric element
C_{33}^E	48.3	$\boldsymbol{GN/m^2}$	Stiffness matrix
R_P	5	$\boldsymbol{G\Omega}$	Internal electrical resistance

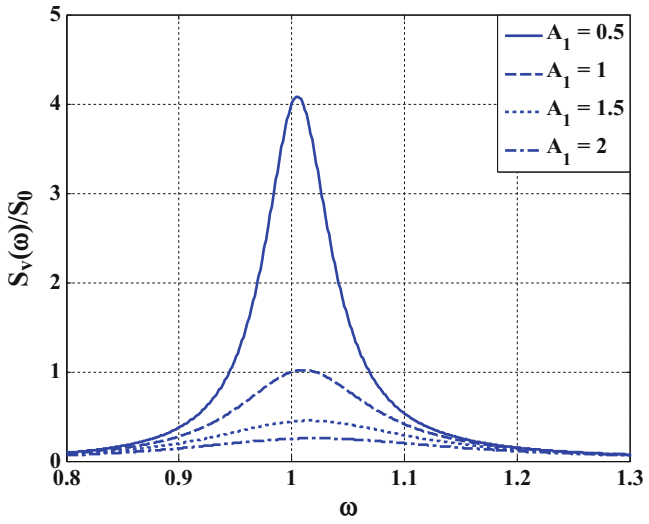

Fig. 25.3 Effect of the normalized parameter A_1 on the normalized voltage spectral density at $A_2 = 7$

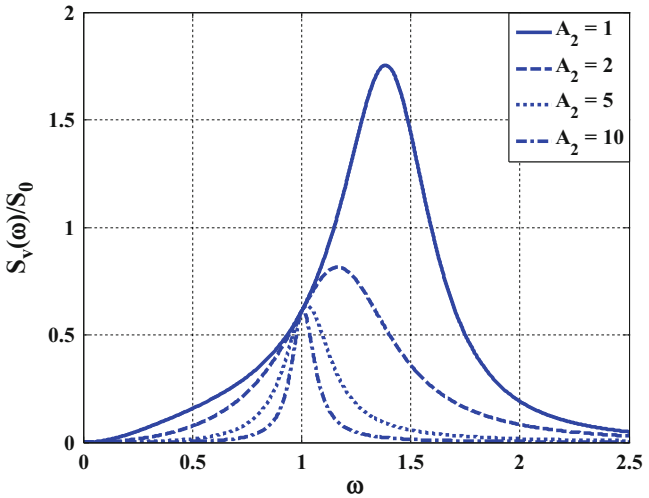

Fig. 25.4 Effect of the normalized parameter A_2 on the normalized voltage spectral density at $A_1 = 1.28$

Using Eq. (25.49), $E[P] = E[v^2]/S_0$ is obtained and the results have been plotted in Figs. 25.7 and 25.8.

These two figures implicitly indicate that the expected value of the harvested normalized power can be maximized by decreasing both design parameters, i.e. A_1 and A_2. Expected square value of any random variable is the area under the curve of the spectral density of that random variable. So the fact that decreasing A_1 and A_2 maximize the expected square voltage, could have also been observed from Figs. 25.3 and 25.4.

In Fig. 25.9, the effects of the design parameters A_1 and A_2 on $E[z^2]$ are presented. It is observed that decreasing the value of A_1 and increasing the value of A_2 would increases $E[z^2]$. It has to be noted that $E[z^2]$ is not as important as $E[P]$ in the energy harvesting mechanism under study and its behavior have been presented here just for the sake of completeness.

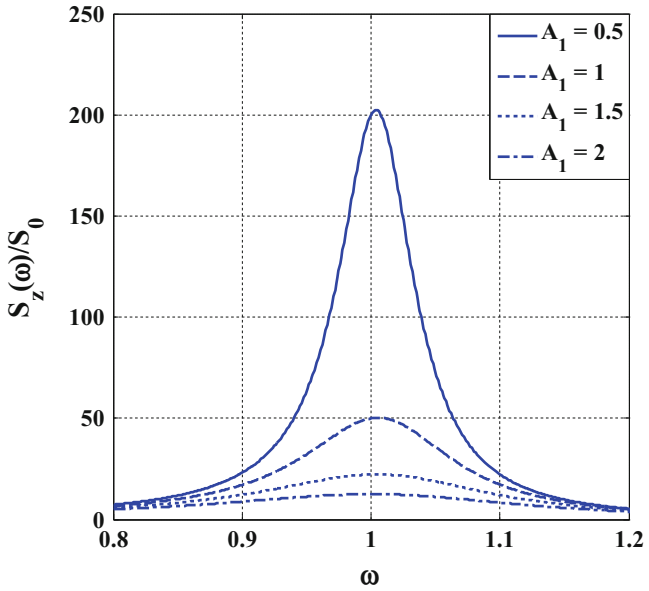

Fig. 25.5 Effect of the normalized parameter A_1 on $S_z(\omega)/S_0$ at $A_2 = 7$

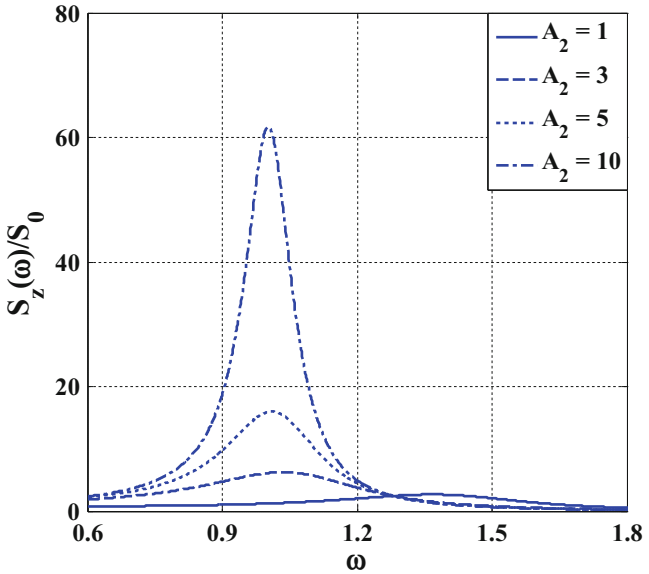

Fig. 25.6 Effect of the normalized parameter A_2 on $S_z(\omega)/S_0$ at $A_1 = 1.28$

25.4 Conclusion

The importance of random based modeling of piezoelectric energy harvesting systems to better inform their design and optimization is well-recognized. However, the presence of effects, such as coupled electromechanical terms in the energy harvesting device, can make this investigation complicated and nontrivial. In this paper, the stochastic dynamic of a piezoelectric energy harvesting device was studied. A lumped parameter physical model representing the devicewas

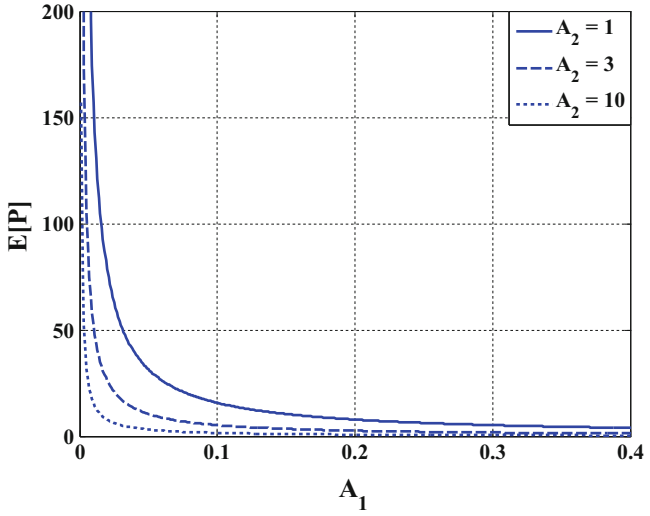

Fig. 25.7 Effect of normalized parameter A_1 on the expected value of the harvested power at different values of A_2

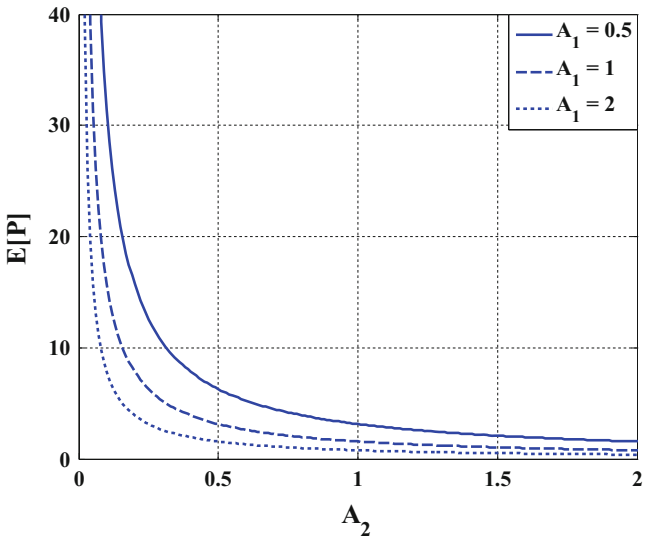

Fig. 25.8 Effect of normalized parameter A_2 on the expected value of the harvested power at different values of A_1

presented and then a normalized mathematical model was developed for simulating the system. Random vibration theory was then applied to characterize the device's output power in terms of the excitation of the surrounding media. Engineering suggestions were proposed for effectively maximizing the expected value of the normalized harvested power. With this clear understanding, one can now make informed decisions regarding the choice of geometrical and physical parameters of energy harvesting systems, which is an essential aspect of design. The procedure suggested in this paper can be used as an effective approach for maximizing all piezoelectric based energy harvesting devices.

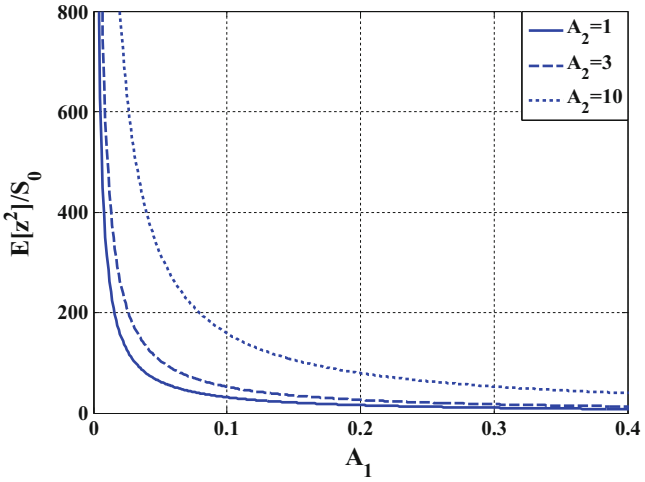

Fig. 25.9 Effect of A_1 and A_2 on $E[z^2]/S_0$

References

1. Ando, B., Baglio, S., Maiorca, F., Trigona, C.: Analysis of two dimensional, wide band, bistable vibration energy harvester. Sensors Actuators. **202**, 176–182 (2013)
2. Abdelkefi, A., Nayfeh, A.H., Hajj, M.R.: Effects of nonlinear piezoelectric coupling on energy harvesters under direct excitation. Nonlinear Dyn. **67**, 1221–1232 (2012)
3. Sodano, H.A., Inman, D.J.: A review of power harvesting from vibration using piezoelectric materials. Shock Vib. Dig. **36**, 197–205 (2004)
4. Abdelkefi, A., Nayfeh, A.H., Hajj, M.R.: Design of piezoaeroelastic energy harvesters. Nonlinear Dyn. **68**, 519–530 (2012)
5. Abdelkefi, A., Nayfeh, A.H., Hajj, M.R.: Modeling and analysis of piezoaeroelastic energy harvesters. Nonlinear Dyn. **67**, 925–939 (2012)
6. Abdelkefi, A., Nayfeh, A.H., Hajj, M.R.: Enhancement of power harvesting from piezoaeroelastic systems. Nonlinear Dyn. **68**, 531–541 (2012)
7. Li, W., Liu, T.S., Hsiao, C.C.: A miniature generator using piezoelectric bender with elastic base. Mechatronics. **21**, 1183–1189 (2011)
8. Junior, C.D.M., Erturk, A., Inman, D.J.: An electromechanical finite element model for piezoelectric energy harvester plates. J. Sound Vib. **327**, 9–25 (2009)
9. Abdelkefi, A., Najar, F., Nayfeh, A.H., Ayed, S.B.: An energy harvester using piezoelectric cantilever beams undergoing coupled bending–torsion vibrations. Smart Mater. Struct. **20**, 1–11 (2011)
10. Cryns, J.W., Hatchell, B.K., Rojas, E.S., Silvers, K.L.: Experimental analysis of a piezoelectric energy harvesting system for harmonic, random, and sine on random vibration. Adv. Acoust. Vib. **2013**, 1–12 (2013)
11. Roundy, S., Wright, P.K., Rabaey, J.: A study of low level vibrations as a power source for wireless sensor nodes. Comput. Commun. **26**, 1131–1144 (2003)
12. duToit, N.E., Wardle, B.L., Kim, S.G.: Design considerations for MEMS-scale piezoelectric mechanical vibration energy harvesters. Integr. Ferroelectr. **71**, 121–160 (2005)
13. Newland, D.E.: An Introduction to Random Vibrations and Spectral Analysis, 2nd edn. Longman Scientific & Technical, New York (1984)

Chapter 26
Driving Point FRF Fixture Evaluation for Shock Testing

David E. Soine and Richard J. Jones Jr.

Abstract Improved testing and modeling capability has provided more accurate environments definition for environmental testing. When those efforts expand the shock testing performance envelope at a production test lab, legacy testing processes may need to be updated to ensure efficient testing and accurate environment reproduction. If new specifications contain reduced shock pulse durations or resonant fixture-type tests, legacy fixtures and legacy fixture designs may no longer be adequate. Failure to properly evaluate legacy fixture designs may lead to increased setup times and dramatically increased testing costs if those designs are carried over into shorter-duration shock tests. This work will examine approaches for fixture evaluation, attempt to evaluate different fixture designs, and investigate the effect of shock machine choice on fixture performance.

Keywords Shock • Testing • Fixture • Environments • Pulse • Natural period

26.1 Introduction

Environmental test specifications sometimes include pulse-type shock events intended to be reproduced on a mechanical drop shock machine or other pulse generating machine. Common aerospace pulse shocks are specified by a pulse acceleration amplitude in g, pulse duration in milliseconds (ms), and a pulse shape. The pulse shape is proscribed by terms like Haversine, Half-Sine, Approximate Half-Sine, etc., which have the basic characteristics of starting with an acceleration value near zero g, rising to some specified peak acceleration value, and returning to near zero acceleration. The ability of an environmental testing lab to provide these types of shock events depends on the performance of the shock machines available, the measurement systems available, and the fixture used to secure the Unit Under Test (UUT). Depending on the duration of the shock pulse, the structural performance of the fixture can lead to unintended effects and shock events applied to the UUT that are quite different from the specified shock.

26.2 Response to Pulse Shock Loads

The nature of the response of a structure due to an approximate haversine pulse shock load applied on a given axis depends primarily on the duration of the pulse and the natural period of the structure that is excited by the shock load. If the duration of the pulse is long compared to the natural period of the structure, the structure appears "stiff" and the acceleration measured anywhere on the structure will be the same as the applied shock pulse. If the duration of the pulse is near or less than the natural period of the structure, the structure will usually respond as a damped single-degree-of-freedom system. Acceleration measurements on the structure now vary depending on measurement location. The initial acceleration of the responding structure (the primary response) can be up to twice the acceleration amplitude applied at the base of the structure,

*The Department of Energy's Kansas City National Security Campus is operated and managed by Honeywell Federal Manufacturing and Technologies, LLC under contract number DE-NA0002839.

D.E. Soine (✉) • R.J. Jones Jr.
Honeywell Federal Manufacturing and Technologies, LLC*, 14520 Botts Road, Kansas City, MO, USA
e-mail: dsoine@kcp.com

J.M. Harvie, J. Baqersad (eds.), *Shock & Vibration, Aircraft/Aerospace, Energy Harvesting, Acoustics & Optics, Volume 9*,
Conference Proceedings of the Society for Experimental Mechanics Series, DOI 10.1007/978-3-319-54735-0_26

and the structure will subsequently exhibit a damped-sine like response (the residual response.) Unfortunately, the applied acceleration pulse and the primary response pulse will also have different durations.

Locations on the structure farthest from the table/fixture interface are most prone to the damped-sine response just described. Unfortunately, those locations are often the most convenient or only possible accelerometer mounting locations, if testing processes specify that the acceleration measurement location should be on the fixture rather than on the shock machine structure (drop table). In this situation the lab technician may have to attempt to adjust the pulse applied by the shock machine so the measured shock pulse looks like a haversine – a difficult if not impossible task since the natural response of the structure is a damped sine.

The shock response spectrum for a single-degree-of-freedom (SDOF) system subject to a haversine base input can be found in the literature [1]. The spectrum predicts the ratio of the primary and residual acceleration response to the peak acceleration input at the base, given the ratio of the base shock duration to the natural period of the SDOF responding system. Although actual fixture structures attached to mechanical shock machines have many dynamic modes, often there is one dynamic mode that dominates the shock response when a pulse shock is applied. The natural period of the dominant mode, therefore, could be used in conjunction with a specified pulse duration and the SDOF shock response spectrum to predict the values of the primary and residual acceleration. The primary and residual response accelerations are important indicators of the suitability of a given fixture structure (and specific measurement point) to perform a specified haversine pulse shock.

26.3 Test Method

A simple experimental method to evaluate the suitability of a shock fixture structure to perform shocks of a given pulse duration was desired. When applied, the method should clearly show whether an approximate haversine response is possible or whether the fixture would have a strong residual response. Since legacy considerations can determine fixture structures and specified measurement locations, it was desired that the method would predict if a residual response could be low enough to be considered "acceptable." For example, a residual response at a level less than 20% of the primary response pulse could be considered acceptable in some situations. It was proposed that a driving point acceleration Frequency Response Function (FRF) measurement could form the basis for the test.

A fixture survey was planned, in which a variety of fixtures would be installed on an appropriate drop shock machine, FRF measurements made, and the ability of the fixture structure to perform a haversine test at the measurement point was assessed. In addition, the expected relative level of the residual acceleration was assessed.

The specific method to predict the response characteristics of the structure is as follows:

1. Perform a driving point acceleration FRF measurement *in situ* at the proposed measurement location.
2. Use the highest peak in the FRF measurement as the indicator of the natural period (T) of the structure. The highest peak is assumed to be the most significant and relevant dynamic response of the structure.
3. Form the ratio of intended haversine pulse duration (D) to the natural period (T).
4. Use a single degree of freedom response model and the duration to natural period ratio (D/T) to predict the character of the shock response at the measurement location. Expected characteristics were:

    a. A ratio greater than 1.8 was expected to produce a residual acceleration response of less than 20%. This expected characteristic was used to form the Low Residual test. The 1.8 value was taken directly from published values for shock response of a single degree of freedom system to a haversine base input.
    b. A ratio greater than 3.2 was expected to produce an approximate haversine shock response (acceleration response at the fixture measurement location less than 105% of the table acceleration.) This expected characteristic was used to form the Stiff Structure test. The 3.2 value is an arbitrary relaxation of alternative ratio values of 4 and 5.36 that can be derived from the shock testing literature.

A series of pulse shocks of varying durations would then be performed to test the predictions. A haversine shock pulse would be developed and measured at the shock machine interface (drop table), and the acceleration at the intended measurement location on the fixture would also be measured. The fixture amplification and residual response are calculated, then compared to the predicted values.

26.4 Fixtures and Driving Point FRFs

Table 26.1 provides a list of test structures evaluated. Figure 26.1 illustrates example test configurations.

FRF and shock testing was performed on a drop shock machine with a ten inch drop table, capable of performing pulsed shock durations down to 0.2 ms. Test structures were secured to the drop table with 3/8"-16 steel cap screws.

Driving point FRF measurements were acquired with an LMS Scadas system, a PCB triaxial accelerometer, and a PCB impact hammer. For the FRF measurements, the table was supported by low stiffness silicone foam rubber, with the table brakes released, to replicate the free falling table environment as closely as possible. In all cases the driving point measurement was made at or as near as possible to the intended measurement point on the fixture, or at an alternate location likely to be used by the a lab technician for the shock measurement. Figure 26.2 contains example driving point FRF measurements.

Table 26.1 List of test structures evaluated

Fixture	Description	Attachment to machine	Measurement location
B	7 × 7 × 4 inch pocket fixture (10 lb.) with no UUT installed	6.5 lb. adapter plate, 1 inch grip length on all bolts	Furthest surface from the table interface
C	5 × 5 × 4 inch pocket fixture (8.9 lb.) with UUT installed	4 bolts, 4.7 inch grip length	Furthest surface from the table interface
D	7 × 5 × 5 inch pocket fixture (10.8 lb.) installed in "Y" Axis direction. UUT installed	4 bolts, 3.25 inch grip length	D(Y) – designed-in location near the machine interface
			D(Y)alt – on the furthest surface from the table interface
	7 × 5 × 5 inch pocket fixture (10.8 lb.) installed in "Z" Axis direction. UUT installed	4 bolts, 3.25 & 1.25 inch grip lengths	D(Z) – designed-in location near the machine interface
			D(Z)alt1 – on the furthest surface from the table interface
			D(Z)alt2 – at another location on the furthest surface from the table interface
E	10 × 11 × 4 inch pocket fixture (34.5 lb.) UUT installed	4 bolts with 2 "straps," 13 inch grip length	Furthest surface from the table interface
F	10 × 10 × 1.5 inch plate fixture (15 lb.) UUT installed	4 bolts with 2 "straps," 11.5 inch grip length	Furthest surface from the table interface

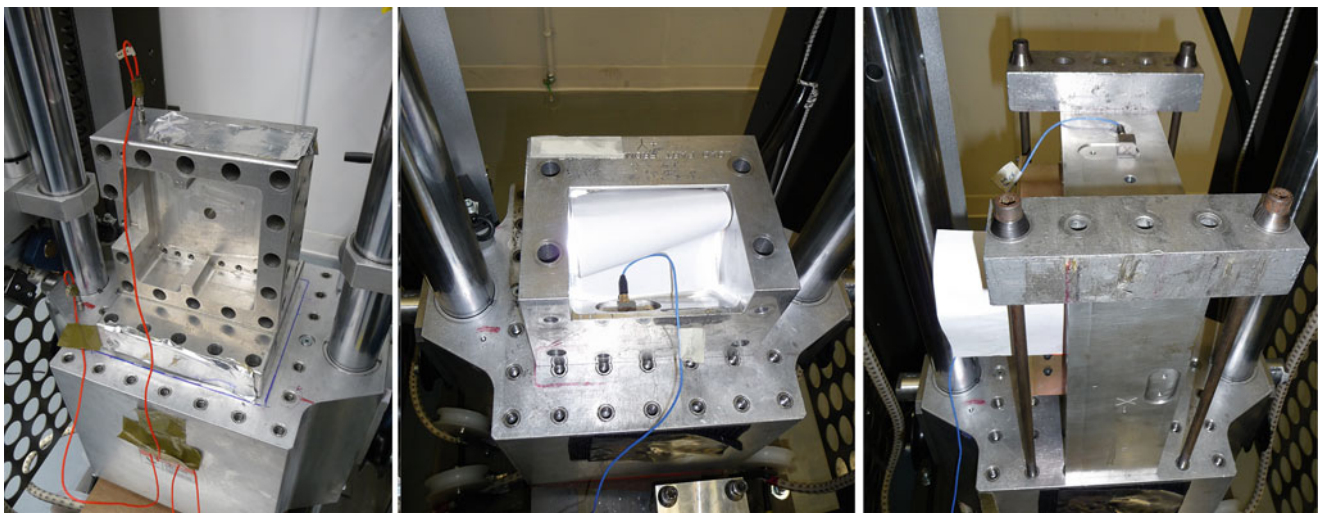

Fig. 26.1 Fixture B with adapter plate, fixture D(Y), fixture E with straps

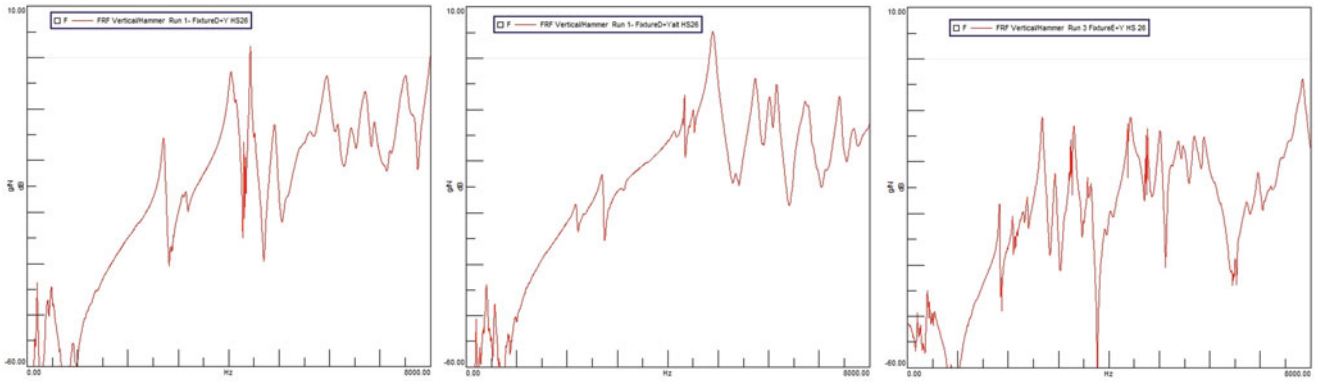

Fig. 26.2 Driving Point FRFs for fixture D(Y), D(Y)alt, and fixture E

Table 26.2 Natural period estimated from Driving Point FRF

Fixture and measurement point	Dominant peak (Hz)	Estimated natural period "T" (ms)
B	2900	0.34
C	4950	0.20
D(Y)	4450	0.22
D(Y) alt	4900	0.20
D(Z)	>8000	<0.13
D(Z) alt1	5150	0.19
D(Z) alt2	5150	0.19
E	7850	0.13
F	7650	0.13

The natural period of the fixture was estimated by using a cursor on the FRF displayed by the measurement system, determining the frequency of the highest peak, and simply inverting the frequency value. The highest or dominant peak in the FRF was usually not the first peak in the measurement. Estimates using this approach for the natural period are summarized in Table 26.2.

26.5 Shock Test Series

For each fixture and measurement configuration, a series of shock pulses was performed. Acceleration was measured at the interface to the shock machine (on top of the drop table) and at the previously described fixture measurement location. The acceleration measurements were made with a Lansmont TestPartner4 measurement system and Kistler 8742 accelerometers. Generally the shock series began with approximately a 2000 g, 0.2–0.3 ms pulse. On a drop shock machine, reducing the drop height will lead to lower peak accelerations levels and correspondingly longer pulse durations. This phenomena was leveraged to form a series of about three or four progressively longer duration (and lower amplitude) shock pulses, out to durations of approximately 0.5 ms.

For each shock measurement, the measured table pulse was assumed to be the "specified" pulse and the duration value "D" was set to the measured 10% pulse duration. (10% pulse duration begins when the primary pulse acceleration reaches 10% of its eventual maximum value on the rising edge of the pulse, and ends when the primary pulse drops below 10% of the maximum on the falling edge of the pulse.) The "amplification" of the pulse is the ratio of the maximum pulse response at the fixture measurement location and the maximum value of the table pulse, reported in percent. The "residual acceleration" value is the ratio of the highest magnitude excursion of the residual response at the fixture measurement location and the maximum primary pulse value at that location, reported in percent. An example of the data collected is shown in Fig. 26.3. Relevant duration and acceleration values, amplification and residual values, and "D/T" ratio are shown for fixture B as an example in Table 26.3.

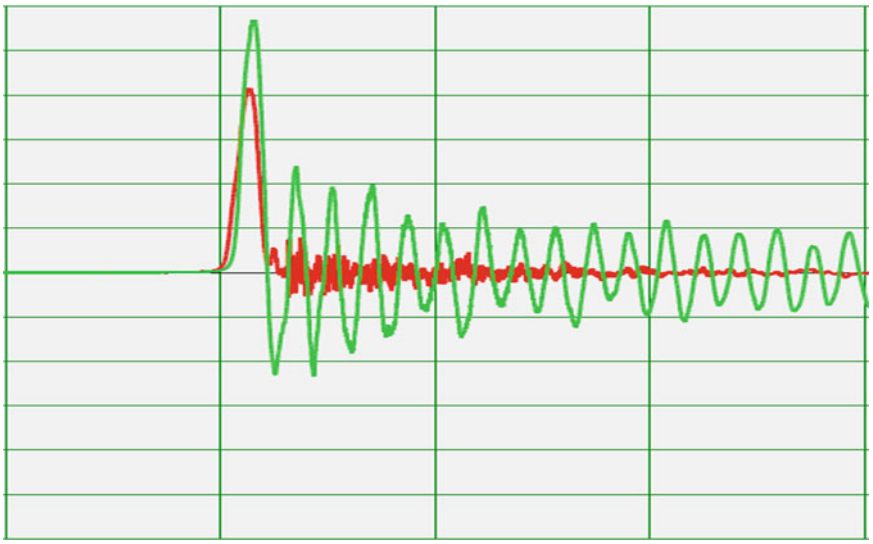

Fig. 26.3 Table (*red*) and Fixture B (*green*) measured acceleration. Duration at the table is 0.37 ms

Table 26.3 Shock series measurements and calculations for fixture B

	Fixture and measurement location B			
Table pulse "D" (ms)	0.19	0.28	0.37	0.53
Table amplitude (g)	2077	1990	2062	1546
Location pulse (ms)	0.21	0.24	0.31	0.43
Location amplitude (g)	3497	3101	2831	1803
Location max residual (g)	2740	1654	1157	420
Location amplification (%)	168%	156%	137%	117%
Location max residual (%)	78%	53%	41%	23%
Natural Period "T" (ms)	0.34 (estimated from FRF)			
"D/T"	0.6	0.8	1.1	1.5

26.6 "D/T" Ratio and the "Stiff Structure" and "Low Residual" Tests

Values for pulse amplification and maximum residual acceleration at the fixture response location were collected and plotted in Figs. 26.4 and 26.5, respectively. For pulse amplification, the "Stiff Structure" test can be shown graphically as a horizontal line on the plot at 105% and bounded on the left by a D/T ratio of 3.2, or alternatively a green box showing data points passing the test, and a red box showing data points failing the test. Similarly for residual acceleration, the "Low Residual" test can be represented by a horizontal line at 20%, bounded on the left by a D/T ratio of 1.8. Box outlines showing passing or failing points are again used.

For both tests, the data shows a dramatic failure of the technique for fixtures E and F. Amplification and residual acceleration are greater than predicted by the technique. A reasonable conclusion is that the value predicted for the natural period of the responding system, obtained from the highest peak in the driving point FRF, was incorrect. Additional work will be required to understand this phenomena. It was observed that the technique failed for the fixtures whose measurement surfaces were the farthest from the table, at 11 and 10 inches. In addition, both fixtures were secured to the table with "straps" and long bolts.

Upon examination, the data also shows unexpectedly low amplification results for fixture configurations D(Y) and D(Y)alt, as well as unexpectedly low residual acceleration for the D(Y) configuration.

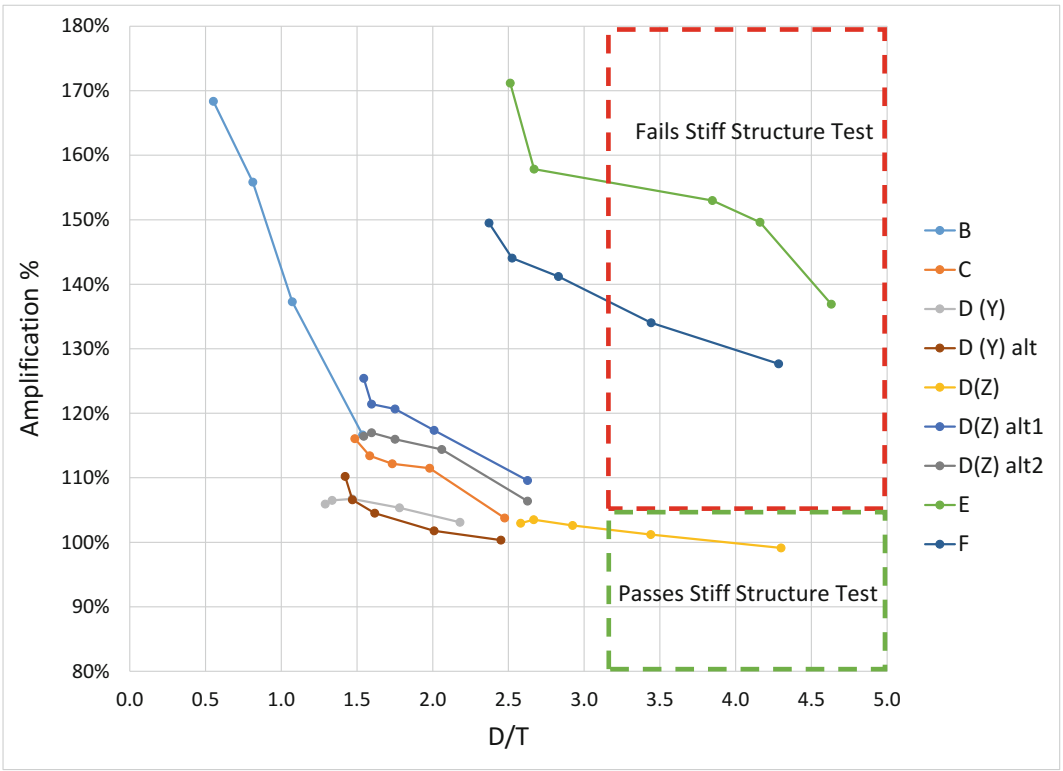

Fig. 26.4 Pulse amplification and the "Stiff Structure" test

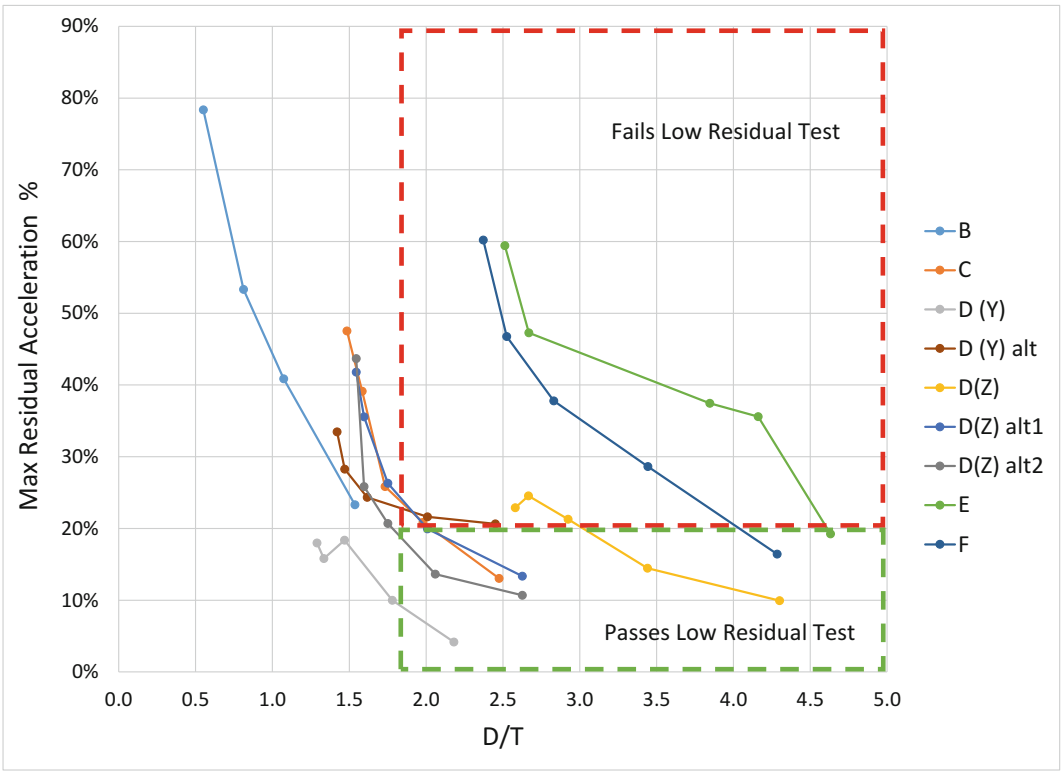

Fig. 26.5 Maximum residual acceleration and the "Low Residual" test

Table 26.4 First Significant Peak estimate for natural period of bolt and strap configuration

Fixture and measurement point	Dominant peak (Hz)	Estimated natural period "T" (ms)	First significant peak (Hz)	Estimated natural period "T" (ms)
B	2900	0.34	–	–
C	4950	0.20	–	–
D(Y)	4450	0.22	–	–
D(Y) alt	4900	0.20	–	–
D(Z)	>8000	<0.13	–	–
D(Z) alt1	5150	0.19	–	–
D(Z) alt2	5150	0.19	–	–
E			2650	0.38
F			3350	0.30

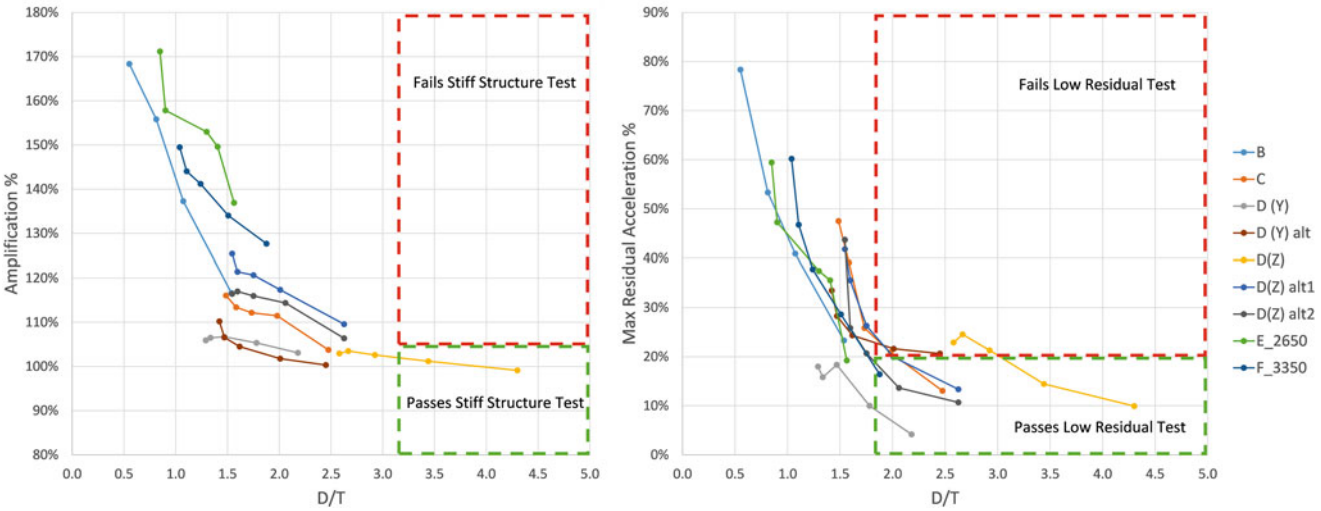

Fig. 26.6 Amplification and residual acceleration with "D/T" adjusted on fixtures D and E

26.7 Potential Correction for "Bolts and Straps"

Alternative values for the natural period of the responding system for the bolt and strap configuration were proposed, since the highest peak in the FRF measurement failed to provide a good prediction of the response. A "first significant peak" approach was attempted, in which the first significant peak in the FRF was used for the value of "T." This approach was only tried for fixtures D and E, and the data and estimated natural period are shown in Table 26.4. The entire data set with "D/T" ratios re-calculated for fixtures E and F (only) are shown in Fig. 26.6.

26.8 Summary

The measured driving point acceleration Frequency Response Function is a fundamental tool of structural dynamics. A driving point FRF, when used in conjunction with the shock response spectrum of single-degree-of-freedom system exposed to a haversine base input, can be used to predict the shock response at a measurement point. Although the technique presented does not work in all situations, the insight provided may help in the selection of appropriate shock test measurement locations and fixture attachment schemes.

Reference

1. Lalanne, C.: Mechanical vibration & shock volume II mechanical shock, p. 43. Taylor and Francis, New York (2002)

Chapter 27
Nonlinear Transverse Vibrations of a Beam with Multiple Breathing Edge Cracks

Ali C. Batihan and Ender Cigeroglu

Abstract One step beyond the studies of transverse vibration of beams with a breathing edge crack is the verification of the theoretical crack beam models with an experimental test set up. Beams with a single breathing edge crack can be used as a specimen for the experimental test. However, there is no assurance against the unexpected additional cracks in the specimens, which may cause unexpected results. Therefore, in this paper nonlinear transverse vibration of a beam with multiple breathing edge cracks is considered as a preliminary study. The breathing effect of the cracks are modeled as piecewise linear stiffness and a harmonic force is applied to the cracked beam. Galerkin's Method is applied with multiple trial functions and nonlinear differential equations obtained are solved by using harmonic balance method with multi harmonics. Utilizing the developed model, effects of crack parameters and crack locations are studied.

Keywords Breathing edge crack • Multiple cracks • Harmonic balance method • Nonlinear vibrations

27.1 Introduction

Vibrations in structures may cause crack propagation which may result in unexpected failure. Therefore, vibration of beams with cracks has been an interesting area of research. Two comprehensive review articles were published by Dimarogonas [1] and Bovsunovsky et al. [2] covering the cracked beam vibration studies that had been done until that time in which studies about linear and nonlinear vibrations, continuous crack beam theories, vibration of cracked plates and beams with breathing edge cracks were considered. Some of the studies available in literature are based on transverse vibration of beams with multiple cracks. Khiem and Lien [3] utilized transfer matrix method and rotational spring model in order to evaluate natural frequencies of a beam with multiple open cracks. In another study, Khiem and Lien [4] formulated natural frequencies in the form of a non-linear optimization problem and proposed a procedure to find the crack depth, crack location and quantity. Mazanoglu et al. [5] used Rayleigh-Ritz approximation method in order to identify the vibrations of non-uniform Euler-Bernoulli beams with multiple open cracks. In the study, the beam model was developed by considering both strain energy change at cracked beam surface and stress field caused by the angular displacement. Caddemi et al. [6] proposed a closed form expression for the modes of an Euler-Bernoulli beam with multiple cracks. The cracks were modeled as open type and a sequence of Dirac's delta generalized functions were utilized in order to express the flexural stiffness. Lee [7] used finite element method to model the beam with multiple open cracks. The author also used Newton-Raphson and singular value decomposition methods to find the crack quantity, depth and location. Xiao et al. [8] applied a method called reverse modal analysis and utilized strain energy density function to evaluate the additional flexibility induced due to the presence of crack. In the study, breathing effect of the crack was considered by defining contact on the colliding surfaces. Using finite element and experimental analysis, natural frequencies and mode shapes of the cracked beam were obtained. In a more recent study, Attar [9] proposed an analytical approach to investigate the natural frequencies and mode shapes of a stepped beam with multiple transverse cracks. Transfer matrix method was utilized as a function of beam properties and crack parameters. The calculated natural frequencies were used for crack identification by the method proposed in the study. Labib et al. [10] carried out a study in order to calculate natural frequencies of beams and frames containing multiple cracks. In the study, dynamic stiffness matrices for beams with multiple cracks were evaluated. The authors represented open cracks by rotational springs and utilized bilinear natural frequency in order to consider the breathing effect.

A.C. Batihan • E. Cigeroglu (✉)
Department of Mechanical Engineering, Middle East Technical University, Ankara 06800, Turkey
e-mail: ender@metu.edu.tr

J.M. Harvie, J. Baqersad (eds.), *Shock & Vibration, Aircraft/Aerospace, Energy Harvesting, Acoustics & Optics, Volume 9*,
Conference Proceedings of the Society for Experimental Mechanics Series, DOI 10.1007/978-3-319-54735-0_27

In this paper, a preliminary study is carried out in order to model the vibration of beams with double breathing edge cracks. An additional breathing edge crack is added to the model proposed by the authors in a previous study [11]. The beam is modeled by Euler-Bernoulli beam theory and a multi degree of freedom (MDOF) representation of the cracked beam is obtained by utilizing Galerkin's method. Three different set of mass normalized eigenfunctions are utilized as trial functions, for instance, the eigenfunctions of a beam with double open cracks and eigenfunctions of a beam with a single open crack at two different locations. Each breathing edge crack is modeled as a piecewise linear stiffness. The state of each crack is determined by checking the slope difference at each crack location. Resulting set of nonlinear differential equations of motion are solved by utilizing harmonic balance method with multi harmonics coupled with a nonlinear equation solver.

27.2 Mathematical Modeling of the Problem

Equation of motion of a uniform continuous beam under the action of an external point force $f(t)$ located at point L_f can be expressed by Euler-Bernoulli beam theory as follows

$$EI\frac{\partial^4 w(x,t)}{\partial x^4} + c\frac{\partial w(x,t)}{\partial t} + m\frac{\partial^2 w(x,t)}{\partial t^2} = f(t)\delta\left(x - L_f\right), \tag{27.1}$$

where $w(x,t)$ is the transverse displacement, EI is the flexural rigidity, m is the mass per unit length of the beam and c is the viscous damping coefficient. Utilizing the expansion theorem, transverse displacement can be expressed as follows

$$w(x,t) = \sum_{j=1} a_j(t)\phi_j(x), \tag{27.2}$$

where $\phi_j(x)$ is the j^{th} trial function and $a_j(t)$ is the corresponding modal coefficient. Substituting Eq. (27.2) into Eq. (27.1), the following expression is obtained

$$\sum_j \left(EIa_j(t)\frac{d^4\phi_j(x)}{dx^4}\right) + \sum_j \left(c\dot{a}_j(t)\phi_j(x)\right) + \sum_j \left(m\ddot{a}_j(t)\phi_j(x)\right) = f(t)\delta\left(x - L_f\right). \tag{27.3}$$

Multiplication of Eq. (27.3) by $\phi_i(x)$ and integration over the spatial domain of the beam results in the following equation

$$\sum_j \left(m_{ij}\right)\ddot{a}_j(t) + \sum_j \left(c_{ij}\right)\dot{a}_j(t) + \sum_j \left(k_{ij}\right)a_j(t) = F_i(t), \tag{27.4}$$

where

$$k_{ij} = \int_0^L EI\phi_i(x)\frac{d^4\phi_j(x)}{dx^4}dx, \tag{27.5}$$

$$c_{ij} = \int_0^L c\phi_i(x)\phi_j(x)dx, \tag{27.6}$$

$$m_{ij} = \int_0^L m\phi_i(x)\phi_j(x)dx, \tag{27.7}$$

$$F_i(t) = \phi_i\left(L_f\right)f(t). \tag{27.8}$$

Rearranging Eq. (27.4), the following matrix equation is obtained.

$$[M]\{\ddot{a}\} + [C]\{\dot{a}\} + [K]\{a\} = \{F\} \tag{27.9}$$

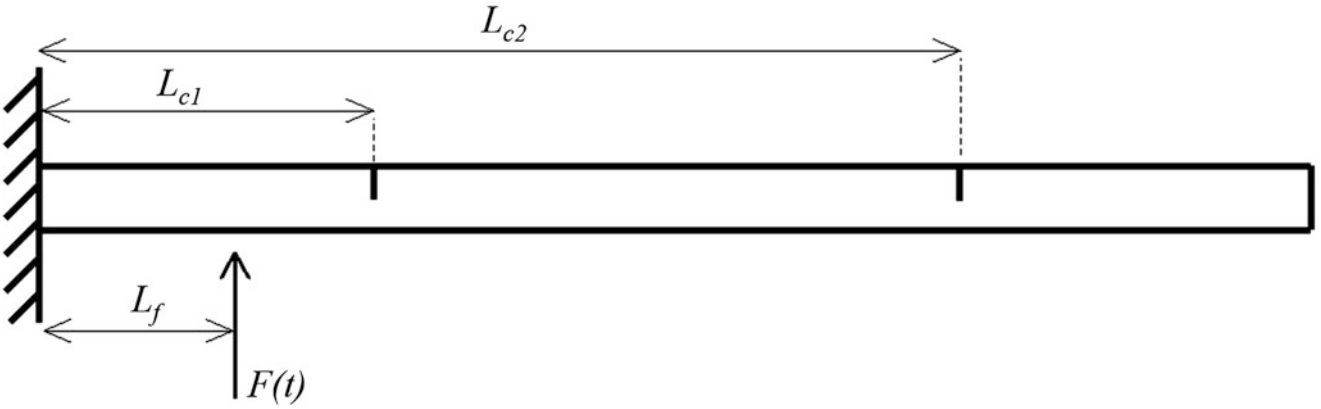

Fig. 27.1 Cantilever beam with double breathing crack

Mass normalized eigenfunctions of the beam with double open cracks are utilized, therefore $[M]$, $[C]$ and $[K]$ are the corresponding mass, damping and stiffness matrices of the beam with double open edge cracks. The details and the derivations of eigenfunctions of a beam with open edge crack can be found in [12].

Fig. 27.1 shows a beam with double cracks under the action of a point force. Depending on the slope difference at the crack locations, each crack may be in open or closed state. Thus, for different time instants of the period, both of the crack at locations L_{c1} and L_{c2} may be closed, only one of the cracks may be closed while the other crack is open or both of them may be open. For the time instants when the cracks are at different states, for instance closed or open, $[M]$ and $[C]$ matrices do not change, however stiffness matrix $[K]$ depends on the state of the cracks. Therefore, in order to consider the breathing effect of each crack, three different sets of eigenfunctions are utilized, i.e. eigenfunctions of a beam with double open edge cracks and eigenfunctions of a beam with a single edge crack for two different crack locations.

For the instant when only the crack at location L_{c1} closes, the stiffness of the double open cracked beam increases. The increase in the stiffness is defined by the following expression,

$$[B_1] = [K_{c2}] - [K]\,, \tag{27.10}$$

where $[K_{c2}]$ is the stiffness matrix of the beam obtained by utilizing the mass normalized eigenfunctions of the beam with a single open edge crack at location L_{c2}. Similarly, the increase in the stiffness at the instant when only the crack at location L_{c2} closes is defined as follows,

$$[B_2] = [K_{c1}] - [K]\,, \tag{27.11}$$

where $[K_{c1}]$ is the stiffness matrix of the beam obtained by utilizing mass normalized eigenfunctions of the beam with a single open edge crack at location L_{c1}. In case both of the cracks are closed, the stiffness of the beam with double cracks becomes equal to the stiffness of the beam with no crack. Therefore, the stiffness matrix of the beam with no crack is taken as follows without introducing any significant errors

$$[K_{nc}] = [K] + [B_1] + [B_2]\,. \tag{27.12}$$

Including the breathing effect of the cracks at different locations, the equation of motion takes the following form,

$$[M]\{\ddot{a}\} + [C]\{\dot{a}\} + [K]\{a\} + \{R_1(\{a\})\} + \{R_2(\{a\})\} = \{F\}\,, \tag{27.13}$$

where $\{R_1(\{a\})\}$ and $\{R_2(\{a\})\}$ are the nonlinear forcing terms that represent the periodic change in the stiffness of the beam due to the breathing effect of each crack and defined as follows

$$\{R_1(\{a\})\} = \begin{cases} [B_1]\{a\} & \text{if } \left.\frac{\partial w(x,t)}{\partial x}\right|_{x=L_{c1}+} - \left.\frac{\partial w(x,t)}{\partial x}\right|_{x=L_{c1}-} \geq 0 \\ \{0\} & \text{if } \left.\frac{\partial w(x,t)}{\partial x}\right|_{x=L_{c1}+} - \left.\frac{\partial w(x,t)}{\partial x}\right|_{x=L_{c1}-} < 0 \end{cases}, \tag{27.14}$$

$$\{R_2(\{a\})\} = \begin{cases} [B_2]\{a\} & if \ \left.\frac{\partial w(x,t)}{\partial x}\right|_{x=L_{c2}+} - \left.\frac{\partial w(x,t)}{\partial x}\right|_{x=L_{c2}-} \geq 0 \\ \{0\} & if \ \left.\frac{\partial w(x,t)}{\partial x}\right|_{x=L_{c2}+} - \left.\frac{\partial w(x,t)}{\partial x}\right|_{x=L_{c2}-} < 0 \end{cases}. \tag{27.15}$$

In order to identify the state of the cracks, the slope difference at each crack location is checked. Positive slope difference at the crack location indicates that the crack is closed and the nonlinear forcing term is nonzero; whereas negative slope difference indicates that the crack is open, thus the nonlinear forcing term is zero.

27.3 Harmonic Balance Method with Multi Harmonics

Nonlinear differential equations of motion obtained is solved by utilizing harmonic balance method with multi harmonics. For periodic forcing, the response can also be assumed periodic. Therefore, modal coefficient of each trial function is expressed as follows

$$a_j(\theta) = a_{j0} + \sum_p a_{jcp}\cos(p\theta) + \sum_p a_{jsp}\sin(p\theta), \tag{27.16}$$

where a_{j0} is the bias term of the j^{th} modal coefficient, a_{jcp} and a_{jsp} are the coefficients of cosine and sine components of the p^{th} harmonic of the j^{th} modal coefficient, respectively and $\theta = \omega t$.

Similarly, the external periodic point force can be written as follows

$$f(\theta) = \sum_p f_{cp}\cos(p\theta) + \sum_p f_{sp}\sin(p\theta). \tag{27.17}$$

In addition, each periodic nonlinear forcing term can be expressed by multi harmonic Fourier series as

$$R_i = R_{i0} + \sum_p R_{icp}\cos(p\theta) + \sum_p R_{isp}\sin(p\theta), \tag{27.18}$$

where $i = 1, 2$ and

$$R_{i0} = \frac{1}{\pi}\int_0^{2\pi} R_i d\theta, \tag{27.19}$$

$$R_{icp} = \frac{1}{\pi}\int_0^{2\pi} R_i\cos(p\theta)\,d\theta, \tag{27.20}$$

$$R_{isp} = \frac{1}{2\pi}\int_0^{2\pi} R_i\sin(p\theta)\,d\theta. \tag{27.21}$$

As given in [11], Eqs. (27.16), (27.17), (27.18), (27.19), (27.20), and (27.21) can be expressed in vector form. Substituting the vector form of the above mentioned equations into Eq. (27.13) and collecting the sine cosine terms leads to the following set of nonlinear equations

$$\left(\begin{bmatrix}[K] & & 0\\ & \ddots & \\ 0 & & [K]\end{bmatrix} - \omega^2 \begin{bmatrix}[M] & & 0\\ & \ddots & \\ 0 & & [M]\end{bmatrix}\begin{bmatrix}[I] & & 0\\ & \ddots & \\ 0 & & p^2\,[I]\end{bmatrix}\right)\begin{Bmatrix}\{a_{c1}\}\\ \vdots \\ \{a_{cp}\}\end{Bmatrix} + \begin{Bmatrix}\{R_{1c1}\}\\ \vdots \\ \{R_{1cp}\}\end{Bmatrix} + \begin{Bmatrix}\{R_{2c1}\}\\ \vdots \\ \{R_{2cp}\}\end{Bmatrix}$$
$$+\omega \begin{bmatrix}[C] & & 0\\ & \ddots & \\ 0 & & [C]\end{bmatrix}\begin{bmatrix}[I] & & 0\\ & \ddots & \\ 0 & & p\,[I]\end{bmatrix}\begin{Bmatrix}\{a_{s1}\}\\ \vdots \\ \{a_{sp}\}\end{Bmatrix} - \begin{bmatrix}[\phi_{L_f}] & & 0\\ & \ddots & \\ 0 & & [\phi_{L_f}]\end{bmatrix}\begin{Bmatrix}f_{c1}\,\{I\}\\ \vdots \\ f_{cp}\,\{I\}\end{Bmatrix} = \begin{Bmatrix}\{0\}\\ \vdots \\ \{0\}\end{Bmatrix}, \tag{27.22}$$

$$\left(\begin{bmatrix}[K] & & 0\\ & \ddots & \\ 0 & & [K]\end{bmatrix} - \omega^2 \begin{bmatrix}[M] & & 0\\ & \ddots & \\ 0 & & [M]\end{bmatrix}\begin{bmatrix}[I] & & 0\\ & \ddots & \\ 0 & & p^2\,[I]\end{bmatrix}\right)\begin{Bmatrix}\{a_{s1}\}\\ \vdots \\ \{a_{sp}\}\end{Bmatrix} + \begin{Bmatrix}\{R_{1s1}\}\\ \vdots \\ \{R_{1sp}\}\end{Bmatrix} + \begin{Bmatrix}\{R_{2s1}\}\\ \vdots \\ \{R_{2sp}\}\end{Bmatrix}$$
$$+\omega \begin{bmatrix}[C] & & 0\\ & \ddots & \\ 0 & & [C]\end{bmatrix}\begin{bmatrix}[I] & & 0\\ & \ddots & \\ 0 & & p\,[I]\end{bmatrix}\begin{Bmatrix}\{a_{c1}\}\\ \vdots \\ \{a_{cp}\}\end{Bmatrix} - \begin{bmatrix}[\phi_{L_f}] & & 0\\ & \ddots & \\ 0 & & [\phi_{L_f}]\end{bmatrix}\begin{Bmatrix}f_{s1}\,\{I\}\\ \vdots \\ f_{sp}\,\{I\}\end{Bmatrix} = \begin{Bmatrix}\{0\}\\ \vdots \\ \{0\}\end{Bmatrix}, \tag{27.23}$$

$$[K]\{a_0\} + \frac{1}{2}\{R_{10}\} + \frac{1}{2}\{R_{20}\} = \{0\}, \tag{27.24}$$

where $[I]$ is the identity matrix, $\{I\}$ is a vector whose elements are all 1, and

$$\left[\phi_{L_f}\right] = \begin{bmatrix}\phi_1\left(L_f\right) & & 0\\ & \ddots & \\ 0 & & \phi_j\left(L_f\right)\end{bmatrix}. \tag{27.25}$$

27.4 Numerical Results

In this study, the concern is the effect of the extra breathing crack that is added to a cantilever beam which already has a breathing edge crack. Therefore, a case study is carried out by using the following beam properties and crack parameters:

$L = 1$ m, $I = 1.6667 \cdot 10^{-9}$ m^4, $A = 2 \cdot 10^{-4}$ m^2, $\rho = 7850$ kg/m^4, $E = 206$ GPa, $\zeta = 0.002$, $L_{c1} = 0.2L$, $L_{c2} = 0.6L$ and crack ratio $\alpha = 0.5$. External point force is applied at location $L_f = 0.3L$ with a magnitude of $f(t) = 100\cos(\omega t)$. Galerkin's method is applied utilizing the first three mass normalized mode shapes of a cantilever beam. Nonlinear equation of motion obtained is solved by utilizing multi harmonic balance method with five harmonics.

In Table 27.1, the first three natural frequencies of intact beam, single crack beam and double crack beam are given and the corresponding mass normalized mode shapes are plotted in Fig. 27.2. If single crack beams are considered, it is seen that the natural frequency is affected by the crack location and an additional crack increases the flexibility of the beam further; therefore, the natural frequencies of the beam with double cracks are the lowest. However, the decrease in the natural frequencies are not significant enough to be used for crack detection purposes, especially considering the effect of measurement noise.

Response of the beam is obtained for three different cases, i.e., a beam with a single breathing crack at location $0.2L$, a beam with a single breathing crack at location $0.6L$ and a beam with double breathing cracks at locations $0.2L$ and $0.6L$. In Fig. 27.3a, b total transverse displacement and acceleration amplitudes of the free end point are plotted as functions of frequency. It is observed that the change in amplitudes is not significant for each case. In both plots, especially in acceleration amplitude plot, there are additional local peaks at frequencies other than the natural frequencies of the beams.

Table 27.1 First three natural frequencies of beams with no crack, single crack and double crack

(Hz)	Intact beam	Single crack (0.2 L)	Single crack (0.6 L)	Double crack (0.2 L and 0.6 L)
1st	8.28	8.10	8.25	7.99
2nd	51.86	51.84	50.39	50.37
3rd	145.21	143.85	142.87	141.52

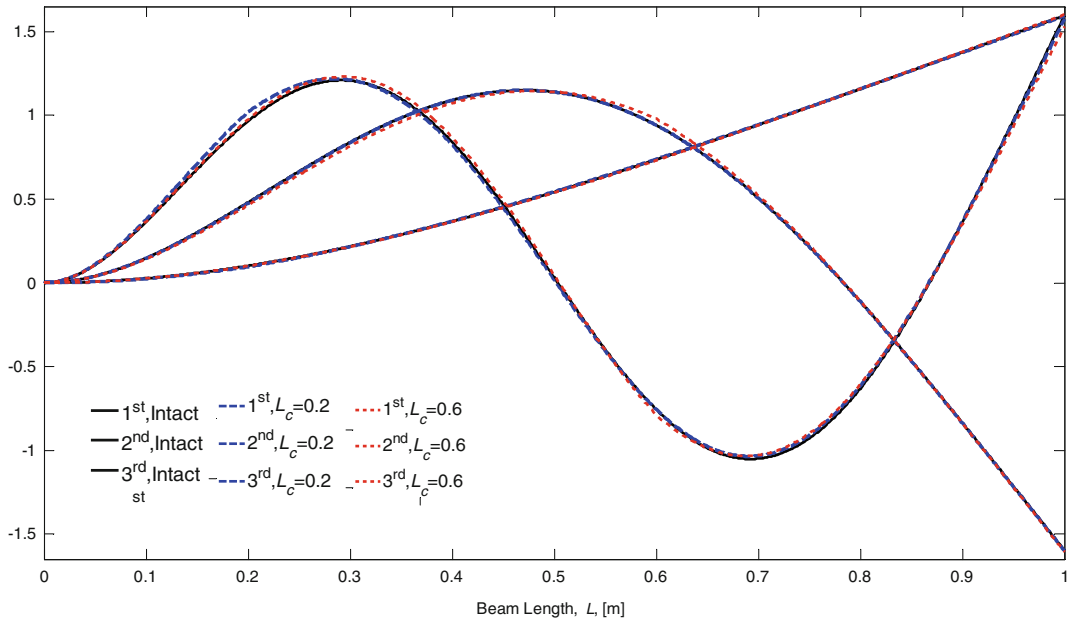

Fig. 27.2 First Three Mass Normalized Mode Shapes of Intact Beam, Beam with Open Crack at $L_c = 0.2$ L and Beam with Open Crack at $L_c = 0.6$ L

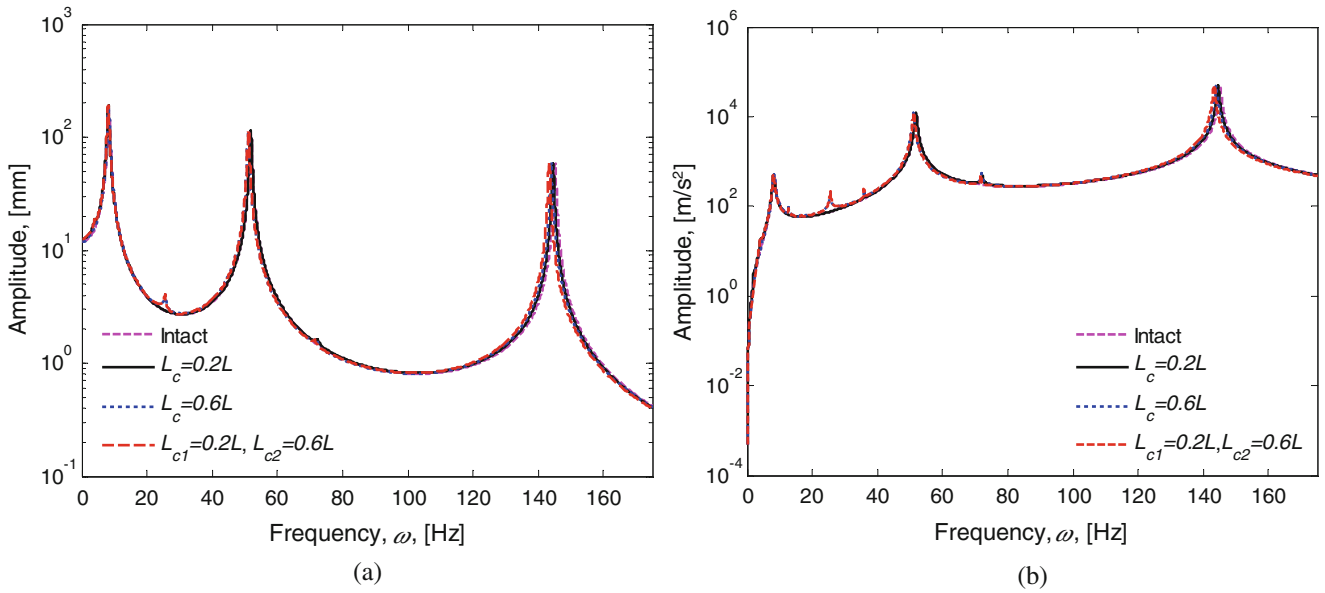

Fig. 27.3 Beams with single crack at $L_c = 0.2$ L, at $L_c = 0.6$ L and beam with double cracks at $L_{c1} = 0.2$ L, $L_{c2} = 0.6$ L (**a**) tip point displacement amplitude, (**b**) tip point acceleration amplitude

These additional local peaks are related to the nonlinearity due to the breathing crack. However, by observing the amplitude plots, it is not possible to get information about the additional breathing crack. Therefore, higher harmonics of the response are also plotted for the same frequency range to in order to see the effect of the additional breathing crack.

In Fig. 27.4a, the first harmonic is given as a function of frequency which is the most dominant harmonic in the total response. It is slightly influenced by the crack parameters; therefore, it is not possible to perform crack identification by observing the first harmonic. However, from Fig. 27.4b, it is seen that the bias term is significantly affected by the crack parameters. Magnitude of the bias term of the beam with double breathing crack is similar to the magnitude of the bias term of the beam with a single crack at $L_c = 0.2L$ up to 20 Hz. Starting from about 40 Hz, up to about 100 Hz, the beam with double cracks has a magnitude of bias term similar to the magnitude of the bias term of a beam with single crack at location $L_c = 0.6L$.

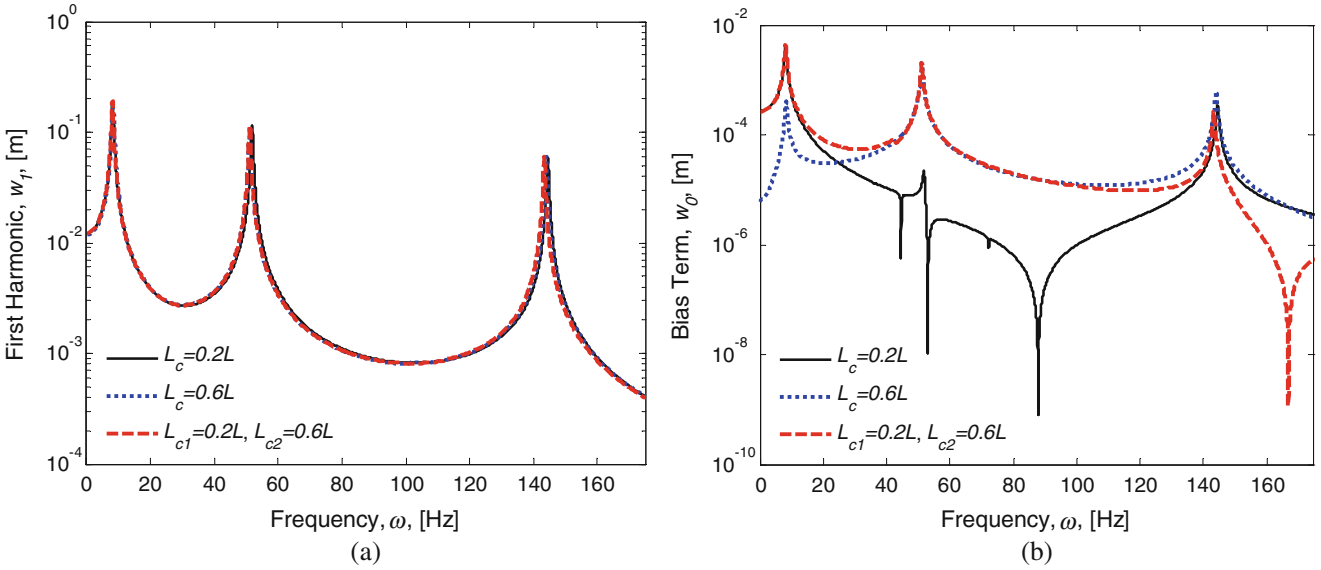

Fig. 27.4 (**a**) First harmonic, (**b**) Bias term

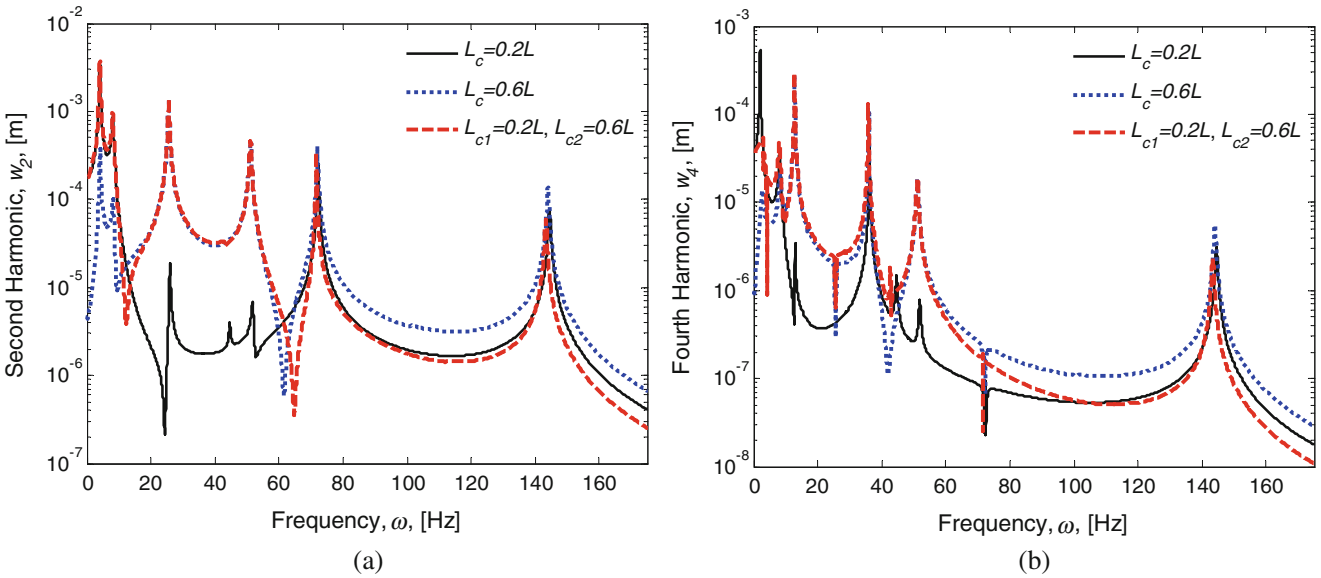

Fig. 27.5 Even numbered harmonics (**a**) second harmonic, (**b**) fourth harmonic

In Fig. 27.5 even numbered harmonics are presented as a function of frequency. At different frequency ranges, the beam with double breathing crack follows a pattern similar to the pattern of the beam with a single breathing crack at location $L_c = 0.2L$ or at location $L_c = 0.6L$.

Odd numbered harmonics are shown in Fig. 27.6. Studying these figures, similar behavior of the double crack as in the odd numbered harmonics is observed. However, at higher frequencies the order magnitude gets smaller for the odd numbered harmonics. Therefore, when the crack detection is the concern, odd harmonics may not be as useful as the even harmonics.

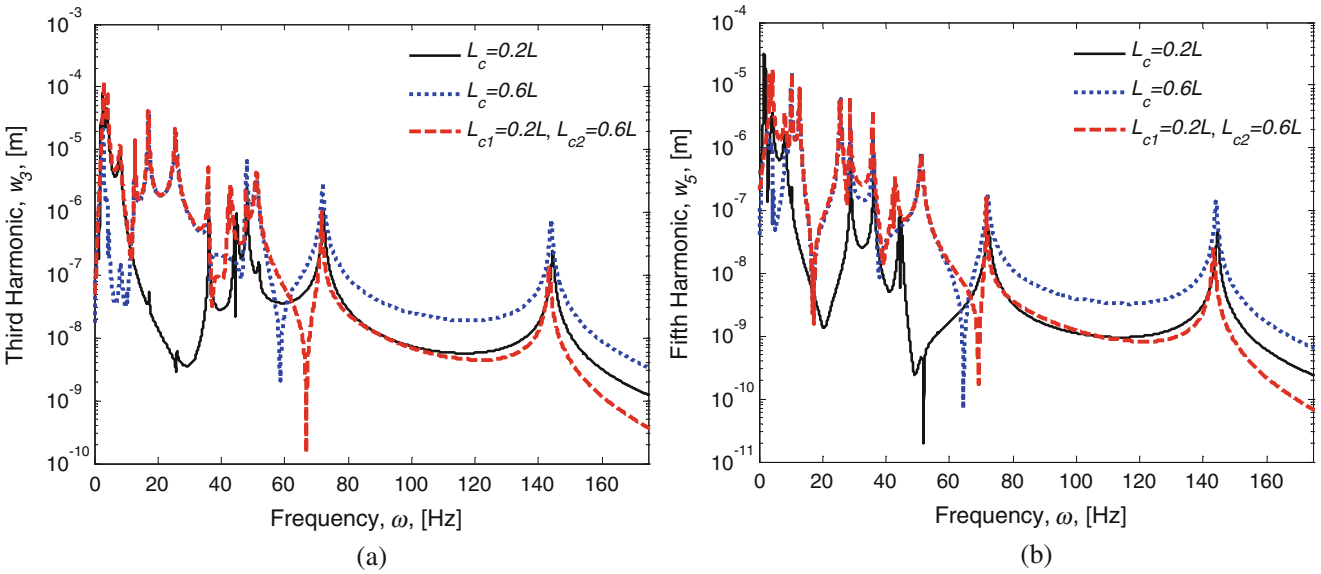

Fig. 27.6 Odd numbered harmonics (**a**) third harmonic, (**b**) fifth harmonic

27.5 Conclusion

In this paper, a preliminary study is carried out in order to observe the effects of the additional breathing crack. The beam which is under the action of a harmonic point forcing is modeled by Euler-Bernoulli beam theory and the breathing effect is modeled in terms of bi-linear stiffness. Utilizing Galerkin's method, a nonlinear system of differential equations is obtained for a beam with double cracks at locations L_{c1} and L_{c2}. By the application of harmonic balance method with multi harmonics, a nonlinear set of algebraic equations is obtained and solved by utilizing Newton's method. Higher harmonics of the total displacement of the tip point is plotted as a function of excitation frequency. The results obtained showed that, at different frequency ranges, the harmonics of the beam with double breathing edge crack is similar to the harmonics of the beam with a single breathing crack at locations L_{c1} or L_{c2}. It is also shown that as the frequency increases, the order of magnitude of the odd numbered harmonics decreases, therefore even numbered harmonics might have more significance for detection purposes.

References

1. Dimarogonas, A.D.: Vibration of cracked structures: a state of the art review. Eng. Fract. Mech. **55**(5), 831–857 (1996)
2. Bovsunovsky, A., Surace, C.: Non linearities in the vibrations of elastic structures with a closing crack: a state of the art review. Mech. Syst. Signal Process. **62-63**, 129–148 (2015)
3. Khiem, N.T., Lien, T.V.: A simplified method for natural frequency analysis of multiple cracked beam. J. Sound Vib. **254**(4), 737–751 (2001)
4. Khiem, N.T., Lien, T.V.: Multi crack detection for beam by the natural frequencies. J. Sound Vib. **273**, 175–184 (2004)
5. Mazanoglu, K., Yesilyurt, I., Sabuncu, M.: Vibration analysis of multiple cracked non-uniform beams. J. Sound Vib. **320**, 977–989 (2009)
6. Caddemi, S., Calio, I.: Exact closed-form solution for the vibration modes of the Euler-Bernoulli beam with multiple open cracks. J. Sound Vib. **327**, 473–480 (2009)
7. Lee, J.: Identification of multiple cracks in a beam using vibration amplitudes. J. Sound Vib. **326**, 205–212 (2009)
8. Xiao, C., Lingling, X.: Vibration analysis of a beam with multiple cracks. Appl. Mech. Mater. **178–181**, 2505–2508 (2012)
9. Attar, M.: A transfer matrix method for free vibration analysis and crack identification of stepped beams with multiple edge cracks and different boundary conditions. Int. J. Mech. Sci. **57**, 19–33 (2012)
10. Labib, A., Kennedy, C., Featherston, C.: Free vibration analysis of beams and frames with multiple cracks for damage detection. J. Sound Vib. **333**, 4991–5003 (2014)
11. Batihan, A.C., Cigeroglu, E., Nonlinear vibrations of a beam with a breathing edge crack using multiple trial functions, IMAC XXXIV, (2016).
12. Batihan, A.C.: Vibration analysis of cracked beams on elastic foundation using timoshenko beam theory. Middle East Technical University, Master Thesis (2011)

Chapter 28
TESS Lens-Bezel Assembly Modal Testing

Brandon J. Dilworth and Alexandra Karlicek

Abstract The Transiting Exoplanet Survey Satellite (TESS) program, led by the Kavli Institute for Astrophysics and Space Research at the Massachusetts Institute of Technology (MIT) will be the first-ever spaceborne all-sky transit survey. MIT Lincoln Laboratory is responsible for the cameras, including the lens assemblies, detector assemblies, lens hoods, and camera mounts. TESS is scheduled to be launched in August of 2017 with the primary goal to detect small planets with bright host starts in the solar neighborhood, so that detailed characterizations of the planets and their atmospheres can be performed.

The TESS payload consists of four identical cameras and a data handling unit. Each camera consists of a lens assembly with seven optical elements and a detector assembly with four charge-coupled devices (CCDs) including their associated electronics. The optical prescription requires that several of the lenses are in close proximity to a neighboring element. A finite element model (FEM) was developed to estimate the relative deflections between each lens-bezel assembly under launch loads to predict that there are adequate clearances preventing the lenses from making contact. Modal tests using non-contact response measurements were conducted to experimentally estimate the modal parameters of the lens-bezel assembly, and used to validate the initial FEM assumptions.

Keywords Non-contact measurements • Modal analysis • Model validation • Optics • Opto-mechanical

Nomenclature

AR	Anti-reflective
CCD	Charge-coupled device
EDU	Engineering development unit
FEA	Finite element analysis
FEM	Finite element model
FRF	Frequency response function
HeNe	Helium-NEON
MDOF	Multiple degree of freedom
MIT	Massachusetts Institute of Technology
RTV	Room temperature vulcanization
TESS	Transiting exoplanet survey satellite
α_E	Coefficient of thermal expansion of elastomer
α_G	Coefficient of thermal expansion of glass
α_M	Coefficient of thermal expansion of metal
D_G	Diameter of glass
t_E	Thickness of elastomer

B.J. Dilworth (✉) • A. Karlicek
MIT Lincoln Laboratory, 244 Wood Street, Lexington, MA 02420, USA
e-mail: brandon.dilworth@ll.mit.edu

J.M. Harvie, J. Baqersad (eds.), *Shock & Vibration, Aircraft/Aerospace, Energy Harvesting, Acoustics & Optics, Volume 9*,
Conference Proceedings of the Society for Experimental Mechanics Series, DOI 10.1007/978-3-319-54735-0_28

28.1 Background and Motivation

The TESS instrument is a 7-element optical system with several of the lenses in close axial proximity to each other. The optical system is configured to function in the visible spectrum. A cross-section view of the 7-element system is shown in Fig. 28.1.

The lenses are bonded to their associated aluminum bezels using a low-outgassing RTV (room temperature vulcanization) Silicone. The thickness of the RTV bonds is tailored to enable an athermal optical prescription. A common method to calculate necessary bond thicknesses to achieve this behavior follows Eq. (28.1) [1].

$$t_E = \frac{D_G\left(\alpha_M - \alpha_G\right)}{2\left(\alpha_E - \alpha_M\right)} \tag{28.1}$$

The thickness of the RTV bond and the cured RTV mechanical properties are the drivers to the effective stiffness of the lens-bezel interface. It is typical for elastomer materials, such as RTV, to not have handbook values for properties such as modulus which makes it difficult to estimate the joint stiffness with hand calculations. As-built cured RTV properties will vary from unit-to-unit due to factors such as mix ratios, mixing methods, cure temperature, and bakeout schedules. Because of this variation, it was desired to obtain measured results to inform the model of the estimated stiffness of the RTV joint.

A key interest early in the program was to determine if the RTV bonds, effectively relatively compliant springs, would be adequate to prevent the lenses from impacting each other during a launch environment. Early finite element analysis (FEA) models were used to perform the initial calculations of the sway-space of each lens during a launch loads analysis; sway-space being the total range of expected axial displacement of each lens. A 5-sigma factor and a factor a safety of 1.2 were applied to the displacement results from the launch loads FEA. The target metric (i.e. positive margin) was to ensure that each lens would remain within its allotted sway-space. The program desired to validate their FEA model with experiments, but the lens assemblies do not lend themselves to 'classical' dynamic measurement methods (i.e. one would not mount accelerometers to an optical element's surface). Multiple non-contact measurement methods were explored to accomplish model validation.

It should be noted that a complimentary need for the program was to not just validate the FEA model, but to also develop a test that would enable an in-situ estimate of the effective bond area relative to its nominal. If model validation was the only desire of the program, then one could imagine using mass mock-ups to analyze the dynamic stiffness of each bond thickness which could easily be accomplished with traditional measurement methods. However, this complimentary desire of the program led to explore other measurement options that could be executed with the actual optical elements as part of the test.

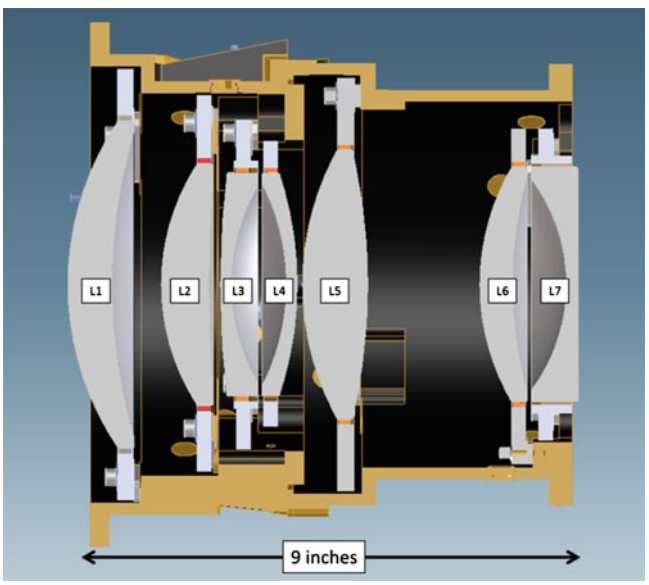

Fig. 28.1 Cross-section view of TESS lens barrel assembly

28.2 Technical Approach

As a baseline approach, a measurement method that could provide insight to the modal parameters of the first three modes of the lens-bezel assembly was desired. For all of the lens-bezel assemblies, it was expected that the first mode would be a piston mode (the lens moving planar in the axial direction) and the second and third modes would be tip and tilt. As the lens-bezel assemblies are nominally a symmetric geometry, the tip and tilt modes were expected to be very closely spaced modes. Analytically, the tip and tilt modes are double modes, but the expectation was that minor asymmetries as a result of fabrication tolerances would prevent these from being true double modes in the measurements. As with all systems with expected closely spaced modes, the experimental setup to include multiple reference locations in order to distinguish these modes [2].

As noted earlier, the desire to measure lens-bezel assemblies in-situ drove the need to explore non-contact measurement techniques. The first non-contact dynamic measurement method explored was laser Doppler vibrometry. Laser Doppler vibrometers measure Doppler shift using an interferometric technique which provides a direct measurand of relative surface velocity between the laser head and the target surface of the device under test [3]. A draw-back to laser vibrometry is the need to have a diffuse reflective surface at the target measurement locations. This is a difficult metric for lenses coated in the visible spectrum which include anti-reflective (AR) coatings (i.e. the HeNe red visible laser passes straight through the lens with a minimal return) without some kind of surface preparation. However, even with the need of a surface treatment, a significant advantage to the results of the laser vibrometer is to be able to scale the mode shape vectors relative to the physical structure during parameter estimation.

To demonstrate the feasibility of using a laser vibrometer for this type of test article, a modal impact test was conducted. An EDU lens-bezel assembly with representative RTV bonds was selected for testing. The lens-bezel assembly was mounted in a relatively massive fixture and the fixture was mounted to soft foam to estimate free-free boundary conditions. Two impact locations were selected, located at mounting bolt interfaces of the bezel (i.e. at the load path of the interface of the bezel), providing suitable results for reliably extracting the [expected] closely spaced tip-tilt modes. To prepare the optic such that it had a diffuse reflective surface, a developer was used which resulted in a flat white surface. The developer wasalso chosen as it was believed (and later proven) to be able to be cleaned from the optic. A photograph of the initial test setup is shown in Fig. 28.2.

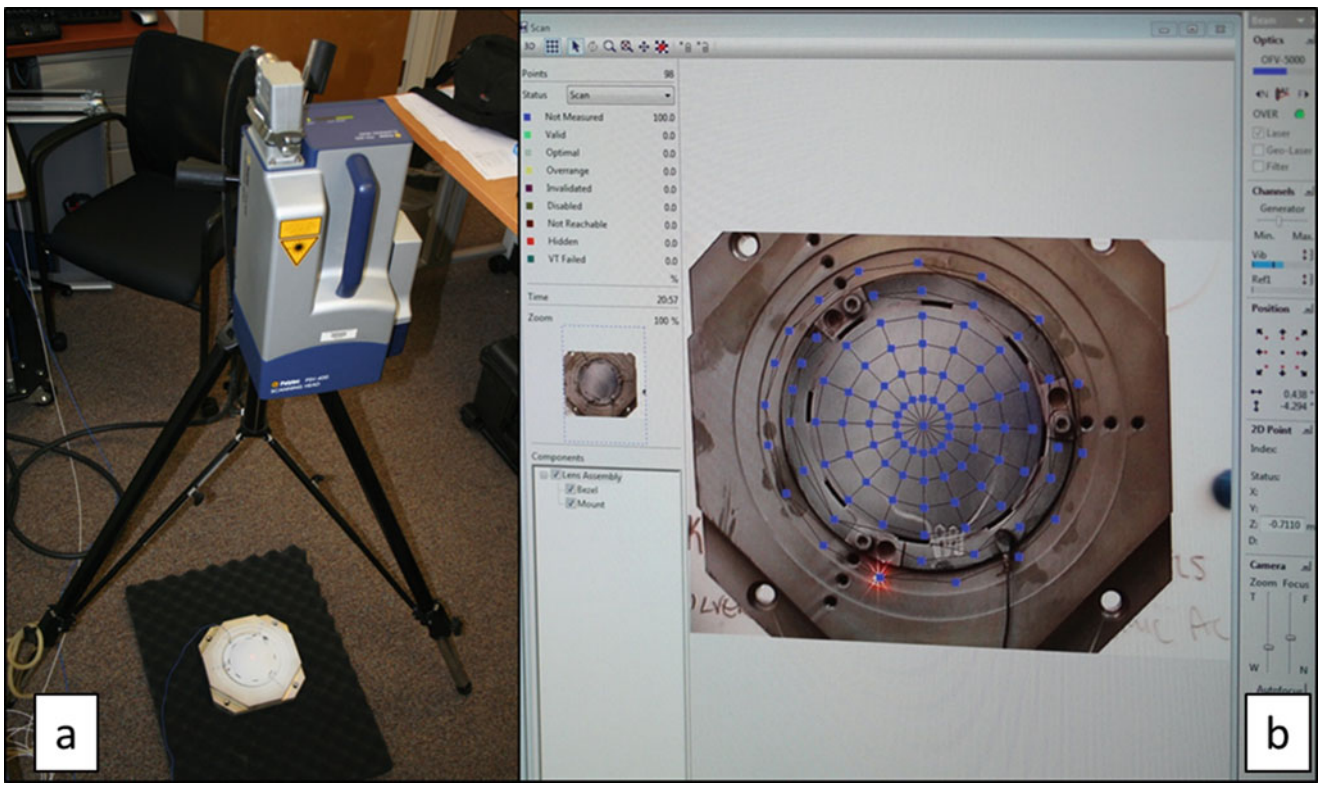

Fig. 28.2 Initial laser vibrometer setup (**a**) and initial measurement grid (**b**)

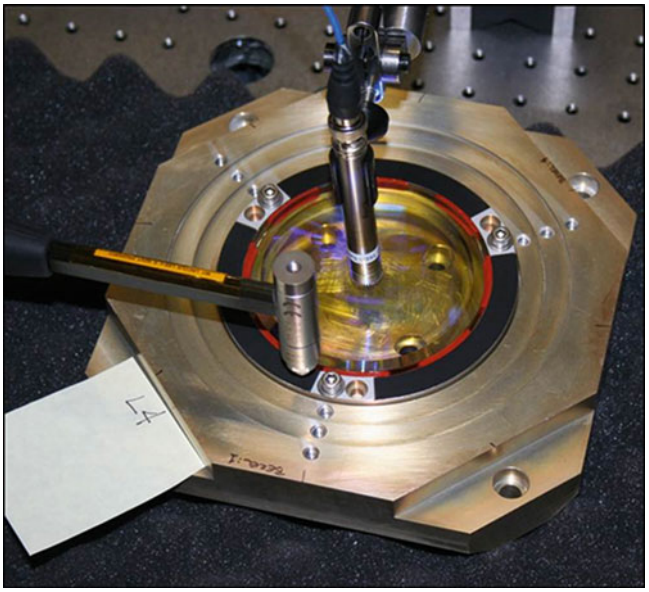

Fig. 28.3 Initial microphone setup

The laser vibrometer response measurement geometry was defined across the optic and around the bezel to provide confidence that the lens modes were separable from the fixture modes. For the initial measurements, a single axis accelerometer was also mounted on the bezel at the impact/input locations to validate driving point frequency response functions (FRF's). Detailed results will be presented in the following section, but the conclusion of the laser vibrometer testing was that the lens modes were readily separable from the fixture modes.

With the successful results of the laser vibrometer measurements, the program desired to develop a measurement technique where modifying the surface of the optic was not required. A couple of key considerations were made to evaluate a different approach. First, a non-contact method that did not require modifying the surface of the optic and still allowed modal parameter estimation was the primary interest. Second, scaled mode shapes were not considered necessary for evaluating the as-built condition of all the lens assemblies. Since the surface of the glass was considered to be very rigid and the glass would move as a rigid body relative to the bezel, a measurement method using microphones was considered. Using the microphones in the near-field, it was presumed that the pressure wave due to the motion of the glass would provide sufficient signal-to-noise to estimate the modal parameters of the lens-bezel assemblies. A subset of the response measurement locations used during laser vibrometer testing was selected for microphone tests. A photo of the initial measurement with a single microphone is shown in Fig. 28.3. Detailed results are discussed in the next section.

28.3 Results

Initial calculations indicated that the first three modes of the lens-bezel assemblies were expected to be in the frequency range of 150–600 Hz. To ensure that this entire frequency range was excited by the modal hammer, a Teflon tip was selected which resulted in an excitation bandwidth of ~1600 Hz. Softer tips were found not to excite the structure at a high enough frequency. Sampling parameters of the acquisition system were selected to match the excitation bandwidth, which is standard practice for any modal tests. Rectangular windowing was selected and a relatively unconventional excitation approached was used with a 2.5 s measurement window. Rather than a single impact, several impacts in a non-repeatable pattern were used to excite the structure. This method allowed an improved signal-to-noise ratio to be achieved in the measurement compared to a single impact. Initial measurements which justified this approach are shown in Fig. 28.4. Note that the FRF's have about half of the variance with the multiple impact method compared to a single impact for a given measurement average.

For the laser vibrometer measurements, an engineering unit (i.e. non-Flight) L4 lens-bezel assembly was used. Because it was a non-Flight lens, the program was willing to consider the use of a developer on the surface of the lens to provide a diffuse reflective surface for the vibrometer. It took several iterations to obtain a reliable return on the lens. Several coats of the developer were applied, and a beam dump (i.e. flat black paper) was placed behind the lens to limit the return of the laser

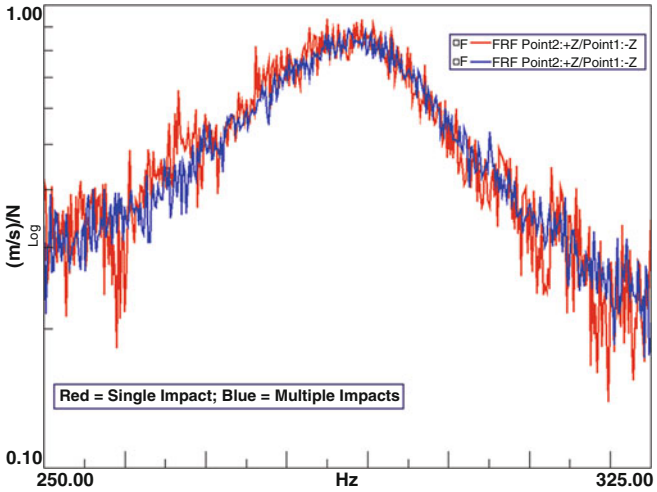

Fig. 28.4 FRF comparison of single impact versus multiple impacts

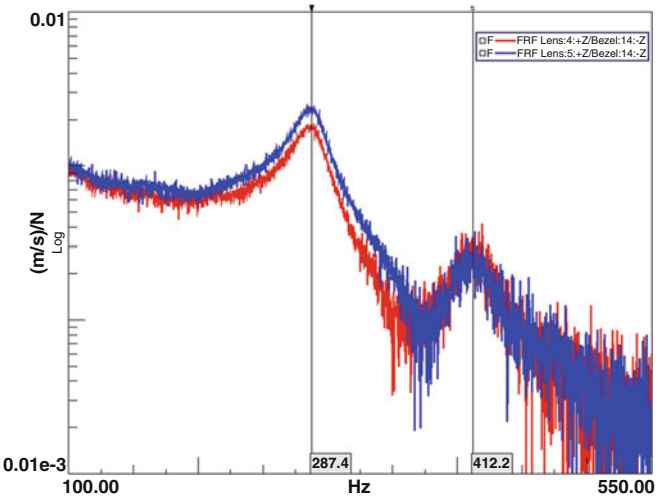

Fig. 28.5 Representative FRF's from vibrometer measurements

light from the fixture. It was discovered that the back reflection from the fixture behind the lens interfered with the reflection of the front surface of the lens; the front surface of the lens being the measurand of interest. The beam dump measurably improved the signal-to-noise on the return beam.

Representative FRF's from the laser vibrometer measurements are shown in Fig. 28.5. These FRF's were used with a Time MDOF (multi-degree of freedom) curve fitter to estimate the modal parameters. The piston mode was readily observed as shown in Fig. 28.6a, and the tip/tilt modes were also readily extracted as shown in Fig. 28.6b. The curve fitted results were used to inform and update the stiffness calculation of the RTV in the lens-bezel assembly.

Testing of the engineering unit L4 lens-bezel assembly proved insightful enough that the program desired to perform insitu testing of all of the lenses (L1, L2, L3, L4, L5, L6, and L7). For these Flight-qualified lens-bezel assemblies, the microphone measurement technique was used. The same excitation method and sampling parameters used for the laser vibrometer tests was used for the microphone tests. Representative FRF's from the microphone approach are shown in Fig. 28.7. Although the FRF's are notably noisier than the results from the vibrometer measurements, the curve fitting was still able to successfully extract the modes of interest as shown in Fig. 28.8a, b. These results compared very favorable to the updated calculations predicted by analysis.

These results showed that a reliable measurement method was demonstrated to perform an insitu estimate of the first three modes by using microphones. The microphones successfully accomplished this task without the need of modifying the surface of the lens in any way. The insight gained with this measurement prompted the program to desire to execute this measurement for all of the Flight lens-bezel assemblies as a means to verify the RTV bond. To prepare for testing five

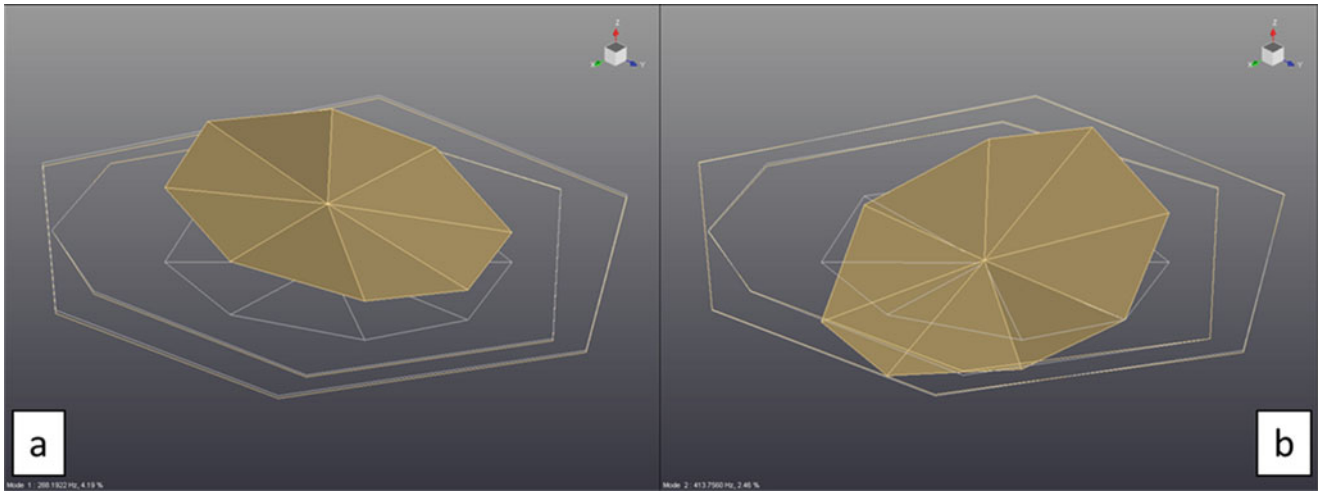

Fig. 28.6 Piston mode (**a**) tip/tilt mode (**b**)

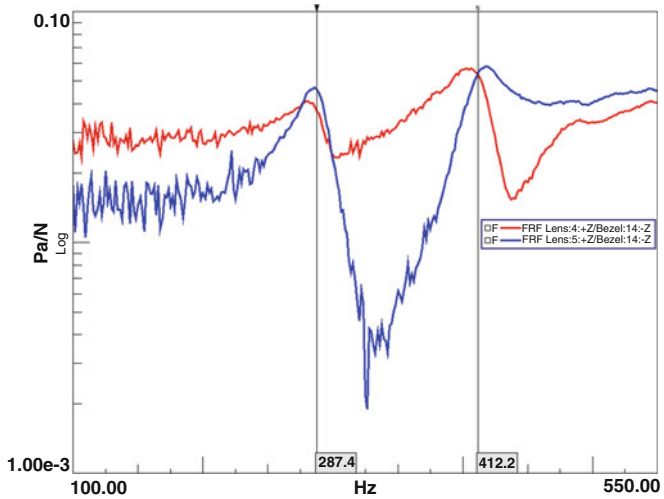

Fig. 28.7 Representative FRF's from microphone measurements

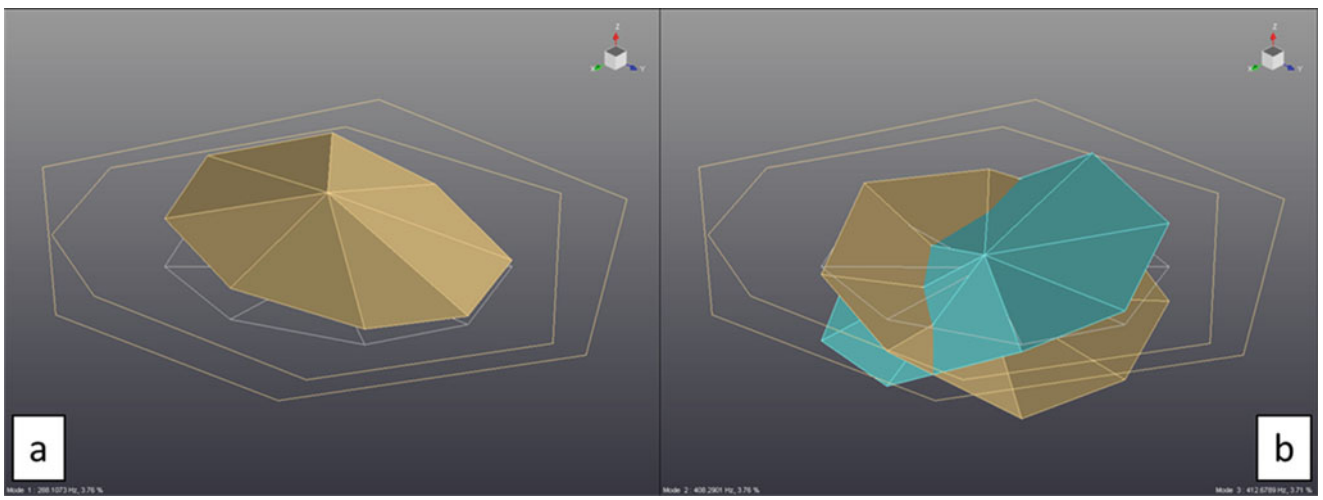

Fig. 28.8 piston mode (**a**); tip/tilt mode (**b**)

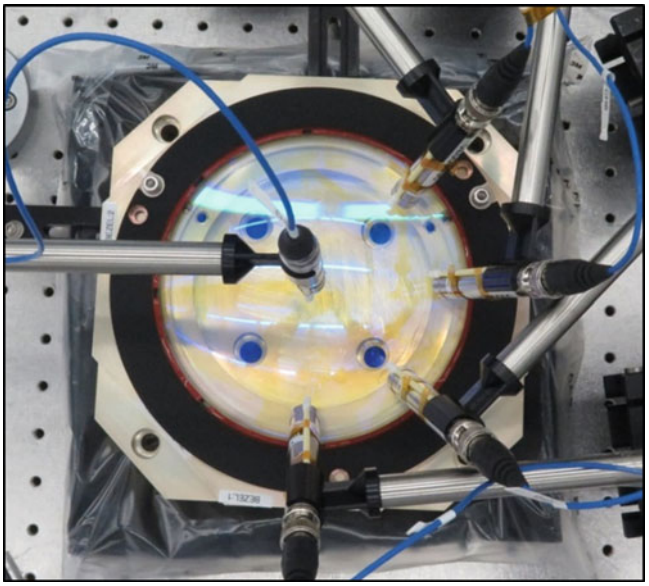

Fig. 28.9 Flight lens testing setup

sets (4 sets of Flight and 1 set of spare) of lens assemblies (28 lens-bezel assemblies in total), multiple microphones and associated fixtures were used to shorten the test duration for each lens. A photo of the test setup for the Flight lens-bezel assemblies is shown in Fig. 28.9.

Testing of the Flight lens-bezel assemblies identified an unanticipated result. The first three modes were higher in frequency than predicted for RTV pads with 100% coverage. It was noted after some investigation that the Flight lens-bezel assemblies had been exposed to a vacuum bake at elevated temperatures where the non-Flight lens-bezel assemblies had not. With independent measurements of baked out RTV samples, it was found that the RTV stiffness did increase; validating the results of the modal testing. The results of the Flight lens-bezel assemblies were fed back into the FEA of the barrel assemblies and was determined that the sway space of each lens was reduced, as one would expect for modes at higher frequencies for a given load input.

28.4 Conclusion

A non-contact measurement method using microphones was developed to successfully determine the first three modes of the lens-bezel assemblies within the TESS barrel assembly. The microphone measurement method was proven on engineering unit assemblies and was readily transferrable to Flight unit assemblies. The developed measurement has been used on all Flight lens-bezel to prove the quality of the RTV bonds prior to final assembly.

Acknowledgement This work is sponsored by the National Aeronautics and Space Administration under Air Force Contract #FA8721-05-C-0002. Opinions, interpretations, conclusions and recommendations are those of the author and are not necessarily endorsed by the United States Government.

References

1. Yoder, P. Jr.: Opto-mechanical systems design. In: Optical Engineering, vol. 9, p. 104. Marcel Dekker, Inc., New York (1986)
2. Heylen, W., Lammens, S., Sas, P.: Modal Analysis Theory and Testing, p. B.2.9. Katholieke Universiteit Leuven, Leuven (1997)
3. Polytec, “Theory Manual”, As of Software 8.8, 2011.

Chapter 29
Vibration Suppression in Metastructures Using Zigzag Inserts Optimized by Genetic Algorithms

Onur Avci, Osama Abdeljaber, Serkan Kiranyaz, and Daniel Inman

Abstract Metastructures are known to provide considerable vibration attenuation for mechanical systems. With the optimization of the internal geometry of metastructures, the suppression performance of the host structure increases. While the zigzag inserts have been shown to be efficient for vibration attenuation, the geometric properties of the inserts affect the suppression performance in a complex manner when attached to the host structure. This paper presents a genetic algorithm based optimization study conducted to come up with the most efficient geometric properties of the zigzag inserts. The inserts studied in this paper are simply cantilever zigzag structures with a mass attached to the unsupported tips. Numerical simulations are run to show the efficiency of the optimization process.

Keywords Structural vibration control • Passive control • Metastructures • Zigzag inserts • Genetic algorithms

29.1 Introduction

Vibrations generated by machines, human activities, traffic or environmental factors result in serviceability, malfunctioning or even structural health issues, especially in flexible structures [1–4]. Therefore, a large body of research have been devoted to investigate various structural vibration control systems. Metastructures (i.e. metamaterial-based structures) are a class of passively controlled structural members that have been recently investigated by researchers.

Metastructures are composed of a main structure referred to as the host structure attached to a number of substructures which are called resonators or inserts. These inserts, which are periodically or non-periodically distributed along the host structure, resonate locally when the metastructure vibrates. It was found that the local resonance of the inserts induces significant frequency bandgaps in the response of the metastructure resulting in significant passive vibration suppression. Also, previous studies suggest that the locations and the sizes of these bandgaps can be easily adjusted by manipulating the geometry and distribution of the resonators [5].

Civil structures are usually subjected to periodic and non-periodic low-frequency excitations; therefore, researchers are looking for structural inserts that are capable of providing wide bandgaps at very low frequencies. For this purpose, a new class of resonators referred to as zigzag inserts have been recently developed. Zigzag inserts have been found to have natural frequencies that are significantly lower than other types of structural inserts. In addition, attaching a mass at the unsupported tip of a zigzag insert as shown in Fig. 29.1 reduces its natural frequency remarkably. Therefore, using such inserts within a metastructure will definitely create low-frequency bandgaps which result in efficient vibration suppression at low frequencies. Zigzag inserts were firstly utilized for energy harvesting applications under low-frequency vibrations [6]. Afterwards, in a preliminary study, Hobeck and Inman [7] utilized zigzag inserts for passive vibration suppression. The findings of their study suggested that attaching these resonators to a cantilever beam results in an efficient vibration attenuation performance.

The study presented in this paper attempts to enhance the vibration suppression capability of zigzag inserts by developing an automated method for optimizing the dimensions and distribution of these inserts. This optimization method is based on genetic algorithms (GAs) which are known for their ability to solve challenging optimization problems. The goal of the

O. Avci (✉) • O. Abdeljaber
Department of Civil and Architectural Engineering, Qatar University, Doha, Qatar
e-mail: oavci@vt.edu

S. Kiranyaz
Department of Electrical Engineering, Qatar University, Doha, Qatar

D. Inman
Department of Aerospace Engineering, University of Michigan, Ann Arbor, MI, USA

J.M. Harvie, J. Baqersad (eds.), *Shock & Vibration, Aircraft/Aerospace, Energy Harvesting, Acoustics & Optics, Volume 9*,
Conference Proceedings of the Society for Experimental Mechanics Series, DOI 10.1007/978-3-319-54735-0_29

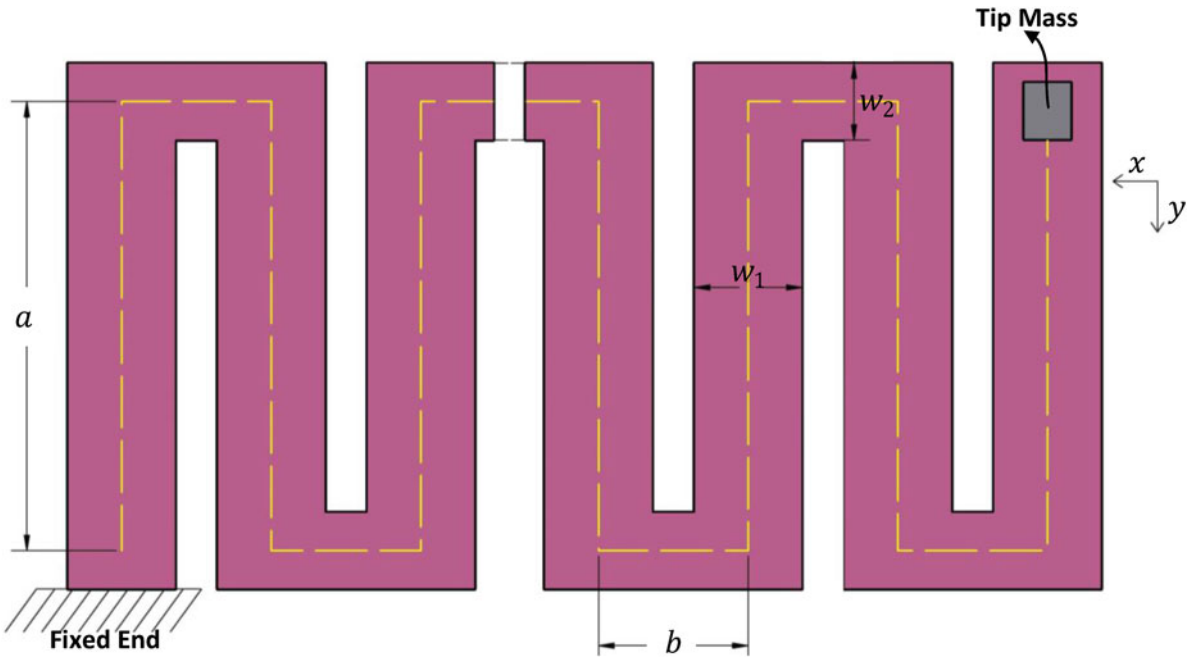

Fig. 29.1 Description of the zigzag geometry

optimization is to explore the optimal geometry and distribution of zigzag inserts that would produce wide bandgaps at low frequencies when attached to a specific host structure.

The remaining sections of the paper are organized as the follows. Section 29.2 discusses the use of Rayleigh's Quotient for modeling of zigzag inserts. Section 29.3 presents an analytical model of the metastructure (i.e. a cantilever beam coupled with zigzags) based on Rayleigh-Ritz technique. Section 29.4 explains the parameters, linear and nonlinear constraints, and the fitness function of the zigzag optimization problem. In Section 29.5, the proposed optimization process is demonstrated through numerical simulations. Finally, the results are discussed in Sect. 29.6, and the conclusions are presented in Sect. 29.7.

29.2 Modeling of Zigzag Inserts

For the study presented herein, Rayleigh's Quotient has been used in order to approximate the first natural frequency, equivalent stiffness, and equivalent mass of a zigzag resonator with a given geometry and tip mass. The analytical formulation is based on the assumption that the zigzag insert consists of a number of beams experiencing small and linear deflections. As illustrated in Fig. 29.1, a zigzag insert is composed of a total of N beam segments. The beams along x-direction are called b-beams, while ones along the y-directions are called a-beams. All beams within the zigzag have a rectangular cross-section with a uniform thickness. The beams are numbered starting from the beam at which the tip mass is placed. Based on Rayleigh's Quotient, the fundamental frequency along with the equivalent mass and stiffness of the zigzag estimated by the following equation.

$$\omega^2 = \frac{\widehat{k} z_1^2(a)}{\widehat{m} z_1^2(a)} = \frac{\sum_{i=1}^{N} \int_0^{L_i} \left[\frac{1}{EI_i} M_i^2 + \frac{1}{GJ_i} T_i^2 \right] dz_i}{\sum_{i=1}^{N} \left[m_i \int_0^{L_i} D_i^2 dz_i + \delta_{i,1} m_t D_i^2 (L_i) \right]} \tag{29.1}$$

where ω is the fundamental zigzag frequency in Rad/s, $\widehat{k}$ and $\widehat{m}$ are the equivalent stiffness and mass, respectively, $z_1(a)$ is the deflection at the zigzag's tip, and m_t is the tip mass. As it is clear from the equation, computing the aforementioned quantities requires obtaining the moment M_i, torsion T_i, and deflection D_i distributions along the N beams segments as well as their

flexural rigidities EI_i. These computations are omitted from this paper for brevity. The reader is referred to [8] for more details. Equation (29.1) was coded as a Matlab function that directly computes ω, $\widehat{k}$ and $\widehat{m}$ according to the given dimensions and tip mass m_t.

29.3 Modeling of the Metastructure

As mentioned earlier, a metastructure consists of a host structure coupled with a number of inserts. The host structure in this study was assumed as a cantilever u-channel. As shown in Figs. 29.2 and 29.3, voids are cut out from the flange to allow for the insertion of zigzags.

Due to the presence of voids, the mass and stiffness along the structure are not uniform. Therefore, it is required to define a formulation that would compute the linear mass and stiffness along the channel. As shown in Figs. 29.2 and 29.3, depending on the location with respect to the voids, the distribution of linear mass $m(x)$ and linear stiffness $EI(x)$ can be computed as:

$$m(x) = m_{AA}\left[H\left(x_{1,1}\right) - H\left(x - x_{1,1}\right)\right] + m_{BB}\left[H\left(x - x_{1,1}\right) - H\left(x - x_{2,1}\right)\right] + m_{CC}\left[H\left(x - x_{2,1}\right) - H\left(x - x_{3,1}\right)\right] + \cdots$$
$$+ m_{AA}\left[H\left(x - x_{3,N_v-1}\right) - H\left(x - x_{1,N_v}\right)\right] + m_{BB}\left[H\left(x - x_{1,N_v}\right) - H\left(x - x_{2,N_v}\right)\right] + m_{CC}\left[H\left(x - x_{2,N_v}\right) - H\left(x - x_{3,N_v}\right)\right] \tag{29.1}$$

$$EI(x) = EI_{AA}\left[H\left(x_{1,1}\right) - H\left(x - x_{1,1}\right)\right] + EI_{BB}\left[H\left(x - x_{1,1}\right) - H\left(x - x_{2,1}\right)\right] + EI_{CC}\left[H\left(x - x_{2,1}\right) - H\left(x - x_{3,1}\right)\right] + \cdots$$
$$+ EI_{AA}\left[H\left(x - x_{3,N_v-1}\right) - H\left(x - x_{1,N_v}\right)\right] + EI_{BB}\left[H\left(x - x_{1,N_v}\right) - H\left(x - x_{2,N_v}\right)\right] + EI_{CC}\left[H\left(x - x_{2,N_v}\right) - H\left(x - x_{3,N_v}\right)\right] \tag{29.2}$$

where $H(\bullet)$ is the Heaviside function, N_v is the number of voids, m_{AA}, m_{BB}, and m_{CC} are the linear masses of Section A-A, Section B-B, and Section C-C, respectively, and EI_{AA}, EI_{BB}, and EI_{CC} are the linear bending stifnesses of Section A-A, Section B-B, and Section C-C, respectively. Also, the dimensions $x_{1,i}$, $x_{2,i}$, and $x_{3,i}$ $(1 \leq i \leq N_v)$ are explained in Fig. 29.2.

The next step toward the analytical modeling of the metastructure is to convert the N_v zigzags to 1-DOF resonators using the method explained in Sect. 29.2. After that, Rayleigh-Ritz technique is used to define the analytical model of the

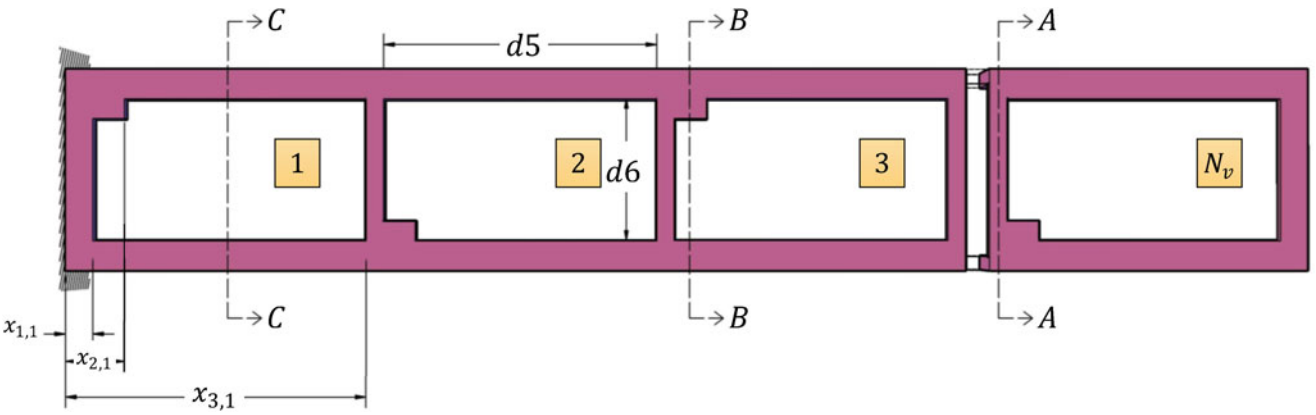

Fig. 29.2 The U-channel after cutting the voids (i.e. the host structure)

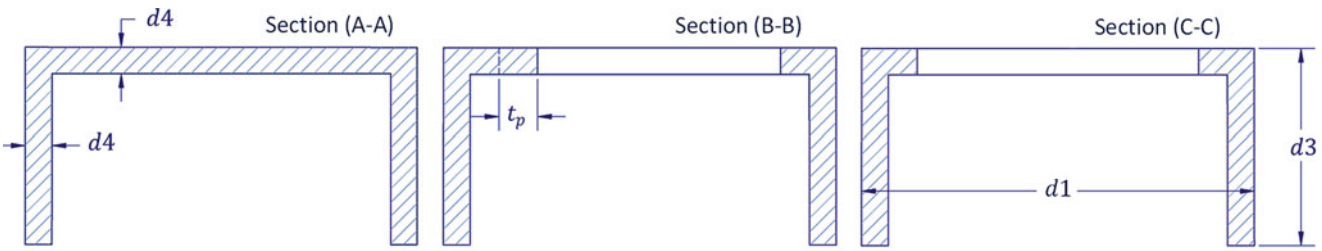

Fig. 29.3 The three cross-sections of the cut channel

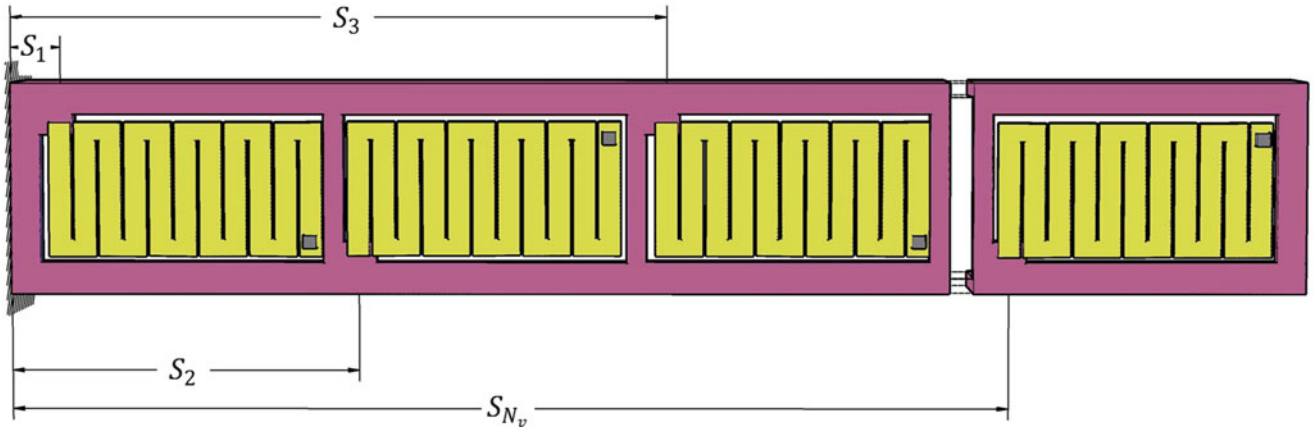

Fig. 29.4 A cut channel coupled with zigzag resonators

metastructure (i.e. the cut channel with the 1-DOF resonators). This model can be derived from the maximum total potential energy U and kinetic energy T of the metastructure which are given as

$$U = \frac{1}{2}\int_0^l EI(x)u''(x)^2 dx + \frac{1}{2}\sum_{j=1}^{N_v} \widehat{k}_j \left[u\left(s_j\right) - y_j\right]^2 \tag{29.4}$$

$$T = \frac{1}{2}\int_0^l m(x)\dot{u}(x)^2 dx + \frac{1}{2}\sum_{j=1}^{N_v} \widehat{m}_j \dot{y}_j^2 \tag{29.5}$$

where $u(x)$ is the deflection distribution of the cantilever channel, l is the length of the channel, y_j is the deflection of the j^{th} insert, $\widehat{m}_j$ and $\widehat{k}_j$ are the equivalent stiffness and mass of the j^{th} resonator, respectively, and s_j denotes the coordinate of the point at which the j^{th} resonator is connected to the cut channel as shown in Fig. 29.4.

Assuming that the deflection of the cut channel can be expressed as

$$u(x) = \sum_{c=1}^{N_m} p_c U_c(x) \tag{29.6}$$

where $U_c(x)$ are orthonormal twice differentiable admissible shape functions that meet the geometric boundary conditions of the u-channel, and p_c are the weights corresponding to each shape function. Substituting Eq. (29.6) into Eq. (29.4) and Eq. (29.5), the mass matrix of the metastructure can be written as

$$\mathbf{M} = \begin{bmatrix} \mathbf{M_B} & 0 \\ 0 & \mathbf{M_Z} \end{bmatrix} \tag{29.7}$$

where $\mathbf{M_B}$ is a matrix of size $N_m \times N_m$ including the quantities corresponding to the cut channel, and $\mathbf{M_Z}$ is a matrix of size $N_w \times N_v$ of size that contains the terms associated with the inserts. Each term in the matrix $\mathbf{M_B}$ is expressed as

$$\boldsymbol{M}_{\boldsymbol{B}(c,r)} = \int_0^l m(x)U_c(x)U_r(x)dx \tag{29.8}$$

where c and r are integers representing the indices of $\mathbf{M_B}$, while the matrix $\mathbf{M_Z}$ can be written as

$$\mathbf{M_Z} = \text{diag}\ [\widehat{m}_1\ \ \widehat{m}_2\ \ \cdots\ \ \widehat{m}_{N_v}] \tag{29.9}$$

In addition, the stiffness matrix of the metastructure system is given as

$$\mathbf{K} = \begin{bmatrix} \mathbf{K_A} & \mathbf{K_C} \\ [\mathbf{K_C}]^{\mathbf{T}} & \mathbf{K_B} \end{bmatrix} \tag{29.10}$$

where $\mathbf{K_A}$ is a matrix of size $N_m \times N_m$ that expresses the stiffness of the beam and the zigzag resonators, $\mathbf{K_B}$ is a matrix of size $N_v \times N_v$ that includes the stifnesses of the inserts, and $\mathbf{K_C}$ is a matrix of size $N_m \times N_v$ that defines coupled channel-zigzag deformations. The matrix $\boldsymbol{K_B}$ is given as

$$\mathbf{K_B} = \text{diag}\left[\widehat{k}_1\ \widehat{k}_2 \cdots \widehat{k}_{N_v}\right] \tag{29.11}$$

Please note, the terms of $\mathbf{K_A}$ and $\mathbf{K_C}$ can be computed as follows

$$\boldsymbol{K}_{\boldsymbol{A}(c,r)} = \int_0^l EI(x)U_c''(x)U_r''(x)dx + \sum_{j=1}^{N_v} \widehat{k}_j U_c\left(s_j\right) U_r\left(s_j\right) \tag{29.12}$$

$$\boldsymbol{K}_{\boldsymbol{C}(c,j)} = -\widehat{k}_j U_c\left(s_j\right) \tag{29.13}$$

As a result, the response of the channel-zigzag metastructure can be computed using the following state space system

$$\begin{aligned} \dot{\mathbf{R}} &= \begin{bmatrix} 0 & \boldsymbol{I} \\ -\boldsymbol{K}\boldsymbol{M}^{-1} & 0 \end{bmatrix} \mathbf{R} + \begin{bmatrix} 0 \\ \boldsymbol{M}^{-1} \end{bmatrix} \mathbf{P} \\ \mathbf{V} &= \begin{bmatrix} 0\ \boldsymbol{I} \end{bmatrix} \mathbf{R} + [0]\,\mathbf{P} \end{aligned} \tag{29.14}$$

where $\mathbf{I}$ is the identity matrix, $\mathbf{P}$ is the input vector, and $\mathbf{V}$ is the output vector that can be used to calculate the velocity of the inserts and the channel, and the state vector $\mathbf{R}$ is given as

$$\mathbf{R} = \left[p_1 \cdots p_{N_M}\ y_1 \cdots y_{N_v}\ \dot{p}_1 \cdots \dot{p}_{N_M}\ \dot{y}_1 \cdots \dot{y}_{N_v}\right]^T \tag{29.15}$$

29.4 The Optimization Process

The optimization process is explained in this section. It should be noted that the metastructure considered in this study consists of a cut channel coupled with a total N_v zigzag inserts that have a unified geometry. Please note that, a tip mass is placed at the unsupported end of each zigzag along the channel. As mentioned earlier, the natural frequencies of the zigzags are affected by their geometry as well as the distribution of the tip masses along the metastructure. In this study, a GA-based optimization process is developed to automatically determine the optimal geometry of the zigzag inserts and the best distribution of the tip masses such that the vibration response of the metastructure is minimized. The geometry of the zigzag is governed by the length of the a-beams a, the length of the b-beam b, the width of the a-beams w_1, the width of the b-beams w_2, the zigzag thickness h, and the number of a-beams in the zigzag assembly N_a. These four parameters are called geometry parameters.

For enabling the zigzag optimization process to explore different tip mass distributions, another set of parameters referred to as mass grading parameters is introduced. It is obvious that grading the masses along the metastructure results in zigzag inserts with graded natural frequencies. Previous studies conducted using other types of inserts suggest that grading the frequencies of the inserts results in better vibration suppression performance than the case with unified frequency resonators [9, 10]. The mass grading parameters are displayed in Fig. 29.5. As shown in this Figure, these parameters are: the mass placed on the first zigzag M_s, the mass placed on the middle zigzag M_m, and the mass placed on the last zigzag M_f. The tip masses of the remaining zigzags can be interpolated according to a second order polynomial.

After defining the optimization parameters, the next step is to define the upper and lower bounds of each parameter along with a number of linear and nonlinear constraints. These bounds and constraints are imposed to ensure that the optimization process will result in feasible zigzag designs which would fit inside the designated voids in the cut channel. The reader is referred to [8] for a detailed explanation of the linear and nonlinear constraints considered in the optimization process.

Finally, as in any GA-based optimization process, it is required to define a fitness function that measures the optimality of each individual solution in the population [11]. In this study, the inputs to the fitness function are simply the values of the six geometry parameters and the three mass grading parameters. The output of the fitness function should be a single score that reflects the degree of the vibration attenuation achieved when attaching the zigzag configuration defined by the input values to a certain u-channel. Therefore, a Matlab function is written and used as the fitness function of the optimization process. This function works as follows:

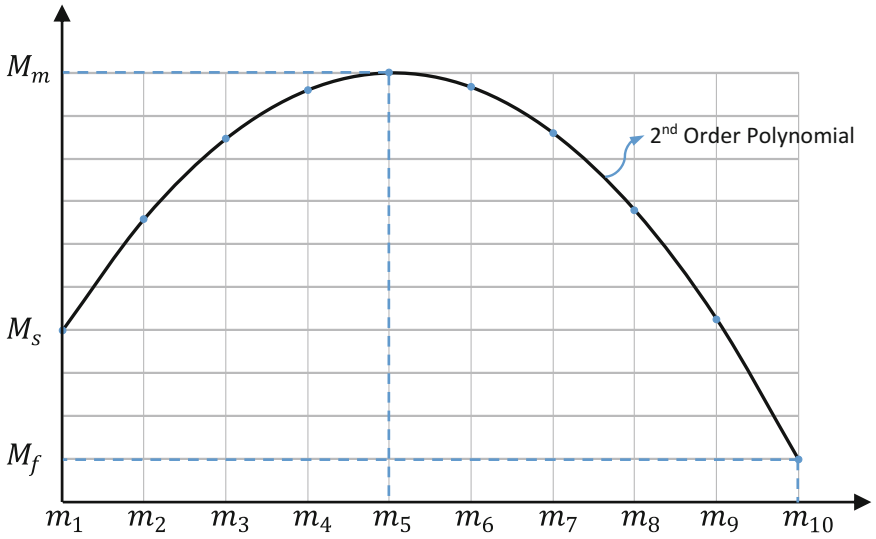

Fig. 29.5 Description of the mass grading parameters for a metastructure with ten zigzag inserts

Table 29.1 Dimensions of the cut channel

Dimension	Symbol	Value	Unit
Length	L	74.61	cm
Base width	$d1$	5.080	cm
Leg length	$d3$	2.540	cm
Thickness	$d4$	3.429	mm
Cutout length	$d5$	6.922	cm
Cutout width	$d6$	3.594	cm

1. The function takes certain values of the nine zigzag parameters as an input. These values represent a feasible zigzag configuration that satisfy a set of predefined upper and lower bounds and linear and nonlinear constraints.
2. The function asks the user to define the material properties and the geometry of the host structure (i.e. the cut channel) including its length, width, thickness, and the number and dimensions of voids.
3. The function converts the zigzag inserts defined in Step 1 to equivalent 1-DOF resonators using the analytical model explained in Sect. 29.2.
4. The function creates a dynamic model of the metastructure using Rayleigh-Ritz technique as explained in Sect. 29.3.
5. The function uses the abovementioned model to simulate the acceleration response at the tip of the cantilever channel under a swept-sine base excitation that varies within the frequency range of interest. For example, if the goal is to minimize the vibration response between 0 and 50 Hz, the frequency range of the excitation should be 0–50 Hz.
6. As a last step, the fitness score (i.e. the output of the fitness function) is calculated as the RMS value of the acceleration signal obtained in Step 5.

29.5 Numerical Demonstration

In this section, the efficiency of the proposed zigzag optimization process is demonstrated analytically by a numerical example. The objective in this example is to obtain the optimal zigzag design for a cut channel with the geometry specified in Table 29.1. Note that the material properties of the zigzags and the cut channel are listed in Table 29.2. Using the analytical model introduced in Sect. 29.3, the first natural frequency of the plain cut channel (i.e. without zigzag inserts) was found to be 40.42 Hz.

The GA solver under Matlab Genetic Algorithms Toolbox [12] was used to launch the optimization process. This toolbox requires defining the fitness function, upper and lower bounds, linear and nonlinear constraints, and the GA properties such as creation, selection, and scaling functions. The Matlab function explained in Sect. 29.4 was used as the fitness function, while the lower and upper bounds of the optimization parameters are shown in Table 29.3. Also, linear and nonlinear constraints were imposed as discussed in [8].

Table 29.2 Material properties of the zigzags and the cut channel

Property	Symbol	Value	Unit
Modulus of elasticity	E	72.00	GPa
Shear modulus	G	25.90	GPa
Density	ρ	2700	kg/m^3

Table 29.3 Lower and upper bounds of the optimization parameters

Variable	N_a	a	b	w_1	w_2	h	M_s	M_m	M_f
Unit	–	mm	mm	mm	mm	mm	gm	gm	gm
Lower bound	3	5	1	1	1	0.5	0	0	0
Upper bound	20	29.94	20	10	10	3	2	2	2

Table 29.4 Optimal zigzag design found using the optimization process

Variable	N_a	a	b	w_1	w_2	h	M_s	M_m	M_f
Unit	–	mm	mm	mm	mm	mm	gm	gm	gm
Optimal design	9	24.5	12.1	4.01	6.70	1.05	1.58	1.36	0.412

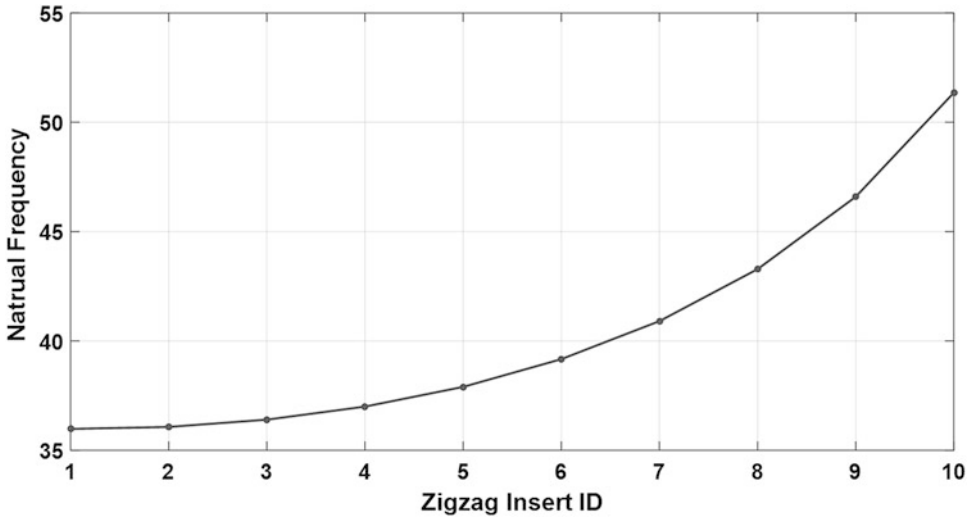

Fig. 29.6 Frequency grading of the optimized zigzag inserts

As mentioned earlier, the fitness function requires defining the frequency range of interest. Since the objective of this study is to minimize the low-frequency response, the frequency of the swept-sine excitation was selected as 0–100 Hz. Using the toolbox, the zigzag optimization process was conducted until it converged to the optimal zigzag designs given in Table 29.4. As anticipated, the process yielded a zigzag configuration with a graded (i.e. non-uniform) tip mass distribution along the metastructure as shown in Fig. 29.6.

In order to quantify the vibration attenuation performance of the optimal zigzag configuration, the acceleration response of the channel with the optimal inserts was compared to the response of the plain channel under a 0–70 Hz band-limited white noise base excitation. This comparison is presented in Fig. 29.7.

29.6 Discussions

The results shown in Sect. 29.5 highlight the efficiency of the optimal zigzag designs obtained by the proposed method in terms of vibration attenuation. As shown in Fig. 29.7, the optimal zigzags resulted in considerable vibration suppression over the entire frequency range of interest. The maximum acceleration response was reduced by 37% compared to the plain channel, while the RMS value was reduced by 35%.

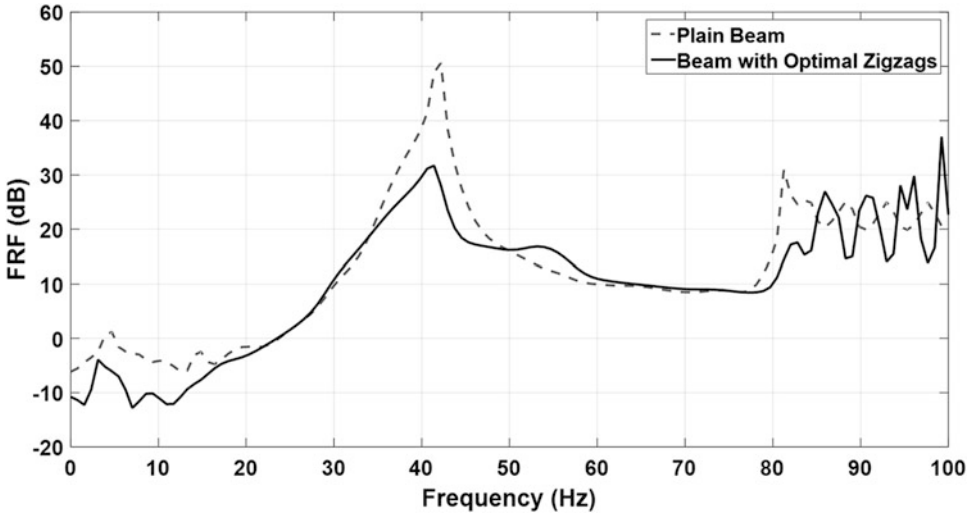

Fig. 29.7 Comparison between the acceleration response of the plain channel and the response of the channel with optimized zigzag inserts under 0–70 Hz band-limited white noise signal base excitation

Interestingly, the proposed zigzag optimization process resulted in zigzag designs with graded tip masses as shown in Fig. 29.6. The frequencies of the optimal zigzag inserts are distributed around the fundamental frequency of the plain channel (40.42 Hz). These results are consistent with findings of previous studies on metastructures which suggested that grading the frequencies of the inserts around the modal frequencies of the host structures results in broadband vibration suppression.

29.7 Conclusions

This study proposed a GA-based method for optimization of linear zigzag inserts. The objective of this method is to automatically determine optimal zigzag configuration that will result in low-frequency vibration attenuation. Two sets of parameters have been considered in the optimization process. The first set determines the geometry of the inserts, while the second set governs the grading of the tip masses along the metastructure. A numerical simulation was carried out to demonstrate the efficiency of the proposed zigzag optimization approach. The analytical results showed that the optimal zigzag design obtained using the proposed method resulted in a significant vibration suppression at low frequencies.

References

1. Avci, O.: Amplitude-dependent damping in vibration serviceability: case of a laboratory footbridge. J. Archit. Eng. **22**(3), (2016). doi:10.1061/(ASCE)AE.1943-5568.0000211
2. Davis, B., Avci, O.: Simplified Vibration Serviceability Evaluation of Slender Monumental Stairs. J. Struct. Eng. **141**, 4015017 (2015). doi:10.1061/(ASCE)ST.1943-541X.0001256
3. Barrett, A., Avci, O., Setareh, M., Murray, T.M.: Observations from vibration testing of in-situ structures. In: Proceedings of Structures Congress and Exposition, ASCE Structures Congress—2006, pp. 1–10. ASCE Reston, Va (2006)
4. Bhargava, A., Al-Smadi, Y., Avci, O.: Vibrations assessment of a hospital floor for a magnetic resonance imaging unit (MRI) replacement. In: Structures Congress 2013: Bridging Your Passion with Your Profession, ASCE, pp. 2433–2444 (2013)
5. Baravelli, E., Ruzzene, M.: Internally resonating lattices for bandgap generation and low-frequency vibration control. J. Sound Vib. **332**, 6562–6579 (2013). doi:10.1016/j.jsv.2013.08.014
6. Karami, M.A., Inman, D.J.: Analytical modeling and experimental verification of the vibrations of the zigzag microstructure for energy harvesting. J. Vib. Acoust. **133**, 11002 (2011). doi:10.1115/1.4002783
7. Hobeck, J.D., Inman, D.J.: Magnetoelastic metastructures for passive broadband vibration suppression. SPIE Smart Struct Integr Syst\. **9431**, 1–9 (2015). doi:10.1117/12.2083887
8. Abdeljaber, O., Avci, O., Kiranyaz, S., Inman, D.J.: Optimization of linear zigzag insert metastructures for low-frequency vibration attenuation using genetic algorithms. Mech. Syst. Signal Process. **84**, 625–641 (2017)
9. Pai, P.F.: Metamaterial-based broadband elastic wave absorber. J. Intell. Mater. Syst. Struct. **21**, 517–528 (2010). doi:10.1177/1045389X09359436

10. Abdeljaber, O., Avci, O., Inman, D.J.: Optimization of chiral lattice based metastructures for broadband vibration suppression using genetic algorithms. J. Sound Vib. (2015). doi:10.1016/j.jsv.2015.11.048
11. Deepa, S.N., Sivanandam, S.N.: Introduction to Genetic Algorithms (2008). doi:10.1007/978-3-540-73190-0
12. Matlab version 8.1.0.604. Natick, Massachusetts: The MathWorks Inc., (2013).

Chapter 30
Experimental Modal Analysis on Vibration Data Measured by Digital Image Correlation

P. Castellini, P. Chiariotti, M. Martarelli, E. Zappa, and A. Lavatelli

Abstract This paper discusses the application of 3D vision-based techniques to recover the Operational Deflection Shapes of a reference specimen consisting in a rectangular section cantilever beam. The research work focuses on the analysis of the accuracy of this measuring approach and discusses the strong points and the limitation of the photogrammetric approaches to experimental modal analysis. Two different types of area-based matching techniques are considered here: the former is based on incremental displacement estimation of subsets of subsequent images. This technique works the approach of Particle Image Velocimetry (PIV), with an Eulerian approach. The second technique considered here is on the contrary based on the estimation of the absolute displacement, considering the first acquired image as the reference for all the subsequent ones. In this last case a Lagrangian approach is used and the applied algorithm is the Digital Image Correlation (DIC). The main advantage of Eulerian (i.e. PIV) approach is that it is possible to analyse also the vibration of a moving object (like in belt dynamic characterization), where the reference region imaged in the first acquired picture, comes out of the field of view much before the end of the test. On the other hand, the Lagrangian approach shows some accuracy problems in the applications where the estimation of the displacement is request instead of velocity. In these cases, the incremental displacement estimated at each new image has to be composed with all the previously estimated ones to obtain the overall motion. Experimental tests were done using a cantilever beam as a case study. The excitation of the beam is done by means of an electromagnetic shaker, while the reference transducer used to validate the output of vision-based techniques is a Scanning Laser Doppler Vibrometry. Results show that the two image-based methodologies have similar performances when estimating natural frequencies, loss factors and ODSs.

Keywords Digital image correlation • Particle image velocimetry • Laser doppler vibrometry • Experimental modal analysis • Folded optics

30.1 Introduction

Vibration measurement plays an essential role in the operative monitoring and characterization of mechanical systems. During the last two decades, it has been possible to develop several non-contact methodologies able to measure vibration remotely, thanks to the continuous improvement of the hardware, in terms of calculation power and size. For instance, with reference to the problem of characterizing the dynamics of timing belt, non-contact approaches (mainly Scanning Laser Doppler Vibrometry [1–4]) have proven their efficacy. This dissertation will focus onto the application of imaging techniques to analyse the modal behaviour of a test specimen.

The use of imaging devices as displacement transducers was firstly proposed in almost-static applications, where the effect of target motion during the exposure time can be neglected. Thanks to technology improvements, the applications of vision-based measurement to dynamic applications have been increasing in the last years. The available image resolutions and the high grabbing frequencies allow to acquire high-speed moving object and to perform dynamic analysis of vibrating objects. Consequently, the scientific community is exploiting imaging methods to perform more and more challenging tasks.

P. Castellini • P. Chiariotti
Università Politecnica delle Marche, via Brecce Bianche, 60131 Ancona, Italy

M. Martarelli (✉)
Università degli Studi e-Campus, via Isimbardi, Novedrate, Italy
e-mail: milena.martarelli@uniecampus.it

E. Zappa • A. Lavatelli
Politecnico di Milano, via La Masa, 1, Milan, Italy

J.M. Harvie, J. Baqersad (eds.), *Shock & Vibration, Aircraft/Aerospace, Energy Harvesting, Acoustics & Optics, Volume 9*,
Conference Proceedings of the Society for Experimental Mechanics Series, DOI 10.1007/978-3-319-54735-0_30

The application of vision-based measuring techniques in dynamic applications requires an accurate estimation of the uncertainty, mainly due to the motion blur on images [5, 6]. For what concerns vibration measurements, several image processing techniques may be suitable. Among all the image processing methods developed in the last 20 years, Digital Image Correlation (DIC) [7, 8], is one of the most interesting and accurate for measuring 2D and 3D displacements (and from that recover velocity, deformation and strain). Compared to other photogrammetry based techniques, DIC has proven to be characterized by very high accuracy, so that it is possible to measure strain down to the microscale with good repeatability. Furthermore, the growth and diffusion of DIC is due to the relative ease to measure full field displacement for both large scale mechanical systems [9] and micro scale/nano structure mechanical system [10]. To sum up, DIC is a valuable measurement technology to solve complex problems in the field of experimental mechanics, but in the context of dynamic measurements uncertainty is still hard to manage. More in details, the sources of uncertainty are related both to static factors [8] and dynamic phenomena [11, 12].

The early applications of DIC in dynamic contexts [13, 14] were focused on pure displacement measurement, without any issue on recovering modal parameters. During the last decade several researchers succeeded in using DIC as a measurement source to perform modal analysis, especially for the reconstruction of Operational Deflection Shapes (ODSs) and Frequency Response Functions (FRFs). Baqersad et al. [15] recently provided a broad review of the most successful application of DIC in modal analysis. The first experiences saw the application of DIC to extract mode shapes of mechanical system using monomodal excitation: for instance, in [16–18] the authors compared DIC results (in terms of ODSs and FRFs) with data gathered from standard acceleration and LDV-based measurements. The more recent developments saw the application of DIC in the field of Operational Modal Analysis, with Poozesh et al. [19, 20] successfully recovering operating mode shapes on large structures. A 3D DIC system was also exploited in [21] to determine shape-descriptor frequency response functions of the field response of a complex-shaped object as a car bonnet. Dynamic point tracking using DIC has also been successfully demonstrated in [22] where operational modal analysis of helicopter rotors was conducted. In [23] a further step forward has been made by applying three dimensional point tracking (3DPT) and stereo photogrammetry to the rotor of a Robinson R44 helicopter.

This paper represents a feasibility study to understand the potentials and the critical aspects of using DIC for measuring span vibration, with particular focus in the analysis of out-of-plane ODSs. The paper is organised as follows: the test bench and its experimental characterisation in controlled conditions (impact hammer test) are presented in Sect. 30.2; Sect. 30.3 will describe the DIC experimental set-up used and the processing approach adopted; Sect. 30.4 will discuss the main results obtained. The main conclusions of the work are reported in Sect. 30.5.

30.2 Test Bench

30.2.1 Experimental Test Bench

The object under test is an aluminium cantilever beam of 320 × 50 × 5 mm dimension, see Fig. 30.1 forced into vibration by a shaker fed with a random noise in the frequency range of the first four modes of the beam, i.e. 0–800 Hz. The shaker was connected to the beam via a force cell measuring the input force inferred to the structure.

30.2.2 Beam Dynamic Characterization

A modal test has been performed to estimate natural frequencies and relative mode shapes of the beam under analysis by measuring the beam Frequency Response Functions by means a Scanning Laser Doppler Vibrometer (SLDV) in terms of Mobility. This test was intended to provide a baseline for validating and comparing results of discrete SLDV and 3D DIC. The Laser Doppler Vibrometer was placed 1.5 m far from the target beam, aligned in such a way to have the laser beam orthogonal to the target surface when the scanning mirrors are in their rest position.

In order to compare modal parameters extracted from the reference test and the ones obtained from the vibration response of the beam measured by the video camera, the vibration responses acquired by the SLDV have been taken into account. Because the response obtained from the camera by applying the DIC Lagrangian processing is proportional to the structure displacement, the response spectra measured by the SLDV have been transformed in displacement too, by integrating them in the frequency domain. The modal parameters extracted from the SLDV displacement responses are reported in Table 30.1. The mode shapes are shown in Fig. 30.2.

Fig. 30.1 Cantilever beam

Table 30.1 Mode shapes, natural frequencies and loss factor of the first four modes of the beam estimated from SLDV displacement responses

Mode shape	Natural frequency (Hz)	Loss factor (dimensionless)
I flexural	37.9	0.008
II flexural	233.6	0.038
I torsional	468.8	0.005
III flexural	627.3	0.027

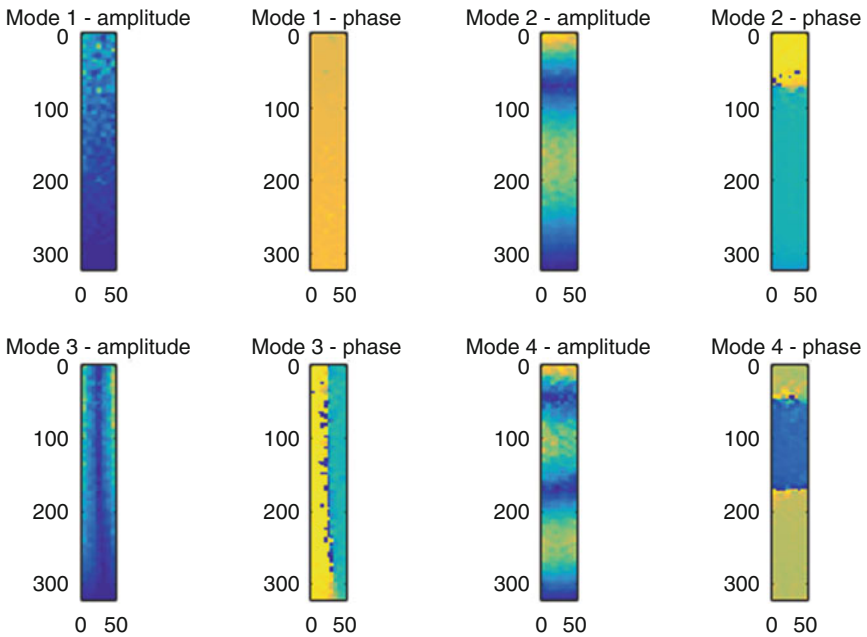

Fig. 30.2 Mode shapes amplitude and phase

30.3 Digital Image Correlation Measurement

DIC is based on the observation of a random pattern characterizing the surface of a structure as the latter vibrates. Typically, the pattern is a black and white speckle randomly distributed all over the target surface in order to ensure high contrast in the grayscale image formed in the digital camera (higher grey level intensity variations). Speckle pattern can be critical whenever a quantitative analysis is wanted in a DIC measurement. Pan demonstrated in [24] that indeed measurement error is strictly

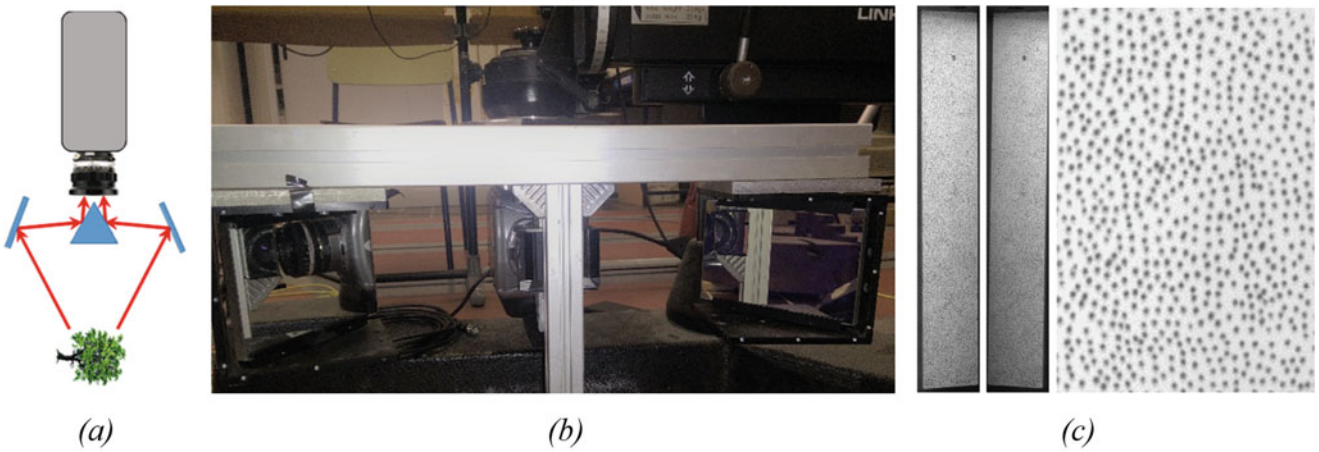

Fig. 30.3 DIC experimental set-up: folded optics scheme adopted for 3D motion measurement (**a**); real implementation (**b**) and example of stereo images with speckle pattern detail (**c**)

Fig. 30.4 Calibration images for the VIC-3D software. (**a**) left camera. (**b**) right camera

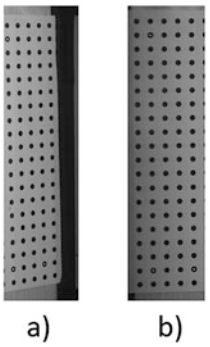

related to the speckle pattern morphology. Therefore, particular attention should be put in preparing the target surface, in order to ease the following pattern recognition step.

A black and white speckle pattern was created on the surface of a cantilever beam as reported in Fig. 30.3c. In order to estimate the out-of-plane vibration component, a 3D DIC approach is needed. A stereo set-up based on fast cameras is very expensive, due to the cost of high performance cameras. Moreover, cameras need to be synchronized, therefore the complexity of the whole measurement system increases. In order to obtain stereo images by means of a unique high-speed camera, a folded optic solution was applied, as shown in Fig. 30.3a, b. This solution is realised by splitting the field of view of the camera into two projections by means of a set of mirrors. An example of folded image of the cantilever beam is given in Fig. 30.3c.

The hardware used in this experimental analysis is composed by a high speed Phantom V10 camera equipped with a 50 mm Nikon Nikkor f 1.8 series E lens and the fore mentioned folded optic. It was placed 1 m far from the target surface. A proper lightning system was also set-up in order to allow the reduction of exposure time down to 620 μs: in this way it was possible to reduce the motion blur phenomenon as much as possible and to reach a frame rate of 1600 fps. The size of both left and right images is 277 $\times$ 1704 pixels. From the software side, DIC has been performed with the Correlated Solutions VIC 3D software. A proper calibration of the whole DIC measurement system was done prior to perform any measurement. Calibration, as usual in vision based techniques, makes it possible to extract the intrinsic and the extrinsic parameters of the cameras. Such operation is fundamental for properly combining two images acquired from different lines of sight. Lens distortions were evaluated as well. Different calibration target, having different calibration patterns, can be adopted. Correlated Solutions software uses its own proprietary calibration algorithm that requires the experimenter to acquire a coded target composed by an equally spaced point grid. The calibration target used in this experimentation was a 20 $\times$ 6 grid with 10 mm spacing, as shown in Fig. 30.4.

As for any DIC task, it is necessary to configure the correlation process. This require the experimenter to select an area of interest (AOI) and specify values for the subset size, the subset step and the subset weights. Then it is necessary to select the image interpolation method and the image correlation criterion. The optimal selection of these values in order to reduce

Table 30.2 Configuration parameters chosen for the DIC analysis

Property	Value	Description
Subset size	33 px	Size of each subset used in the correlation
Subset step	16 px	Size of subset overlap (both in vertical and horizontal direction)
Subset weights	Gaussian	These parameters refer to the correlation calculation procedure. An extensive description of their meaning can be found in [8]
Interpolation method	Optimized 8 tap	
Correlation criterion	Zero normalized squared differences	

Table 30.3 Mode shapes, natural frequencies and loss factor of the first four modes of the beam estimated from PIV and DIC displacement responses

	PIV		DIC	
Mode shape	Natural frequency (Hz)	Loss factor (dimensionless)	Natural frequency (Hz)	Loss factor (dimensionless)
I flexural	37.3	0.105	36.3	0.003
II flexural	234.2	0.036	231.5	0.020
I torsional	471.8	0.005	469.3	0.002
III flexural	617.5	0.014	611.4	0.012

measurement errors and uncertainty has been broadly discussed in literature [8, 25]. For what concerns the DIC application presented in this paper, the values for the configured parameters are listed in Table 30.2.

30.4 Results and Discussion

The modal parameters extracted by the Eulerian PIV method and the Lagrangian DIC one are compared in this section with the reference parameters obtained from the SLDV displacement responses. The Eulerian PIV responses are given in terms of velocity and therefore, before the modal parameters extraction, the PIV responses have been integrated in frequency domain to obtain displacement spectra. The frequency and loss factor estimated from DIC and PIV responses are listed in Table 30.3. The comparison between PIV and DIC with respect to the reference parameters obtained by SLDV are illustrated in Figs. 30.5 and 30.6, in terms of natural frequencies and loss factors, respectively.

It is evident that the natural frequencies are properly estimated from both the datasets; a maximum frequency discrepancy of 4.1% occurs between the SLDV and PIV first natural frequency. The maximum error between SLDV and DIC is of 1.5% at the fourth natural frequency. Concerning the loss factor a larger spread is noticeable, as expected. It is evident an important overestimation of the loss factor from the data obtained by the PIV processing for the first mode. This can be due also to the integration of the velocity data coming from the DIC processing.

Finally, a comparison of the mode shapes extracted can be performed by calculating the degree of consistency between them thanks to the statistical indicator called Modal Assurance Criterion (MAC). When mode shapes of different sets (DIC and PIV with respect to the reference SLDV) are correlated, the MAC value, given in %, should be close to 100%. The MAC values for mode shapes extracted from DIC data with respect to the SLDV data are given in Fig. 30.7, left, while the MAC values for mode shapes obtained from PIV data with respect to SLDV are reported in Fig. 30.7, right. Except for the first mode shape where the correlation is low (78%) due to the fact the first mode is always more spoiled by noise since it is the most affected by external factors, as constraint and shaker connection, the other modes are highly correlated. The second mode exhibit the maximum consistency with a MAC value of 99% between modes extracted from PIV data and SLDV and of 98% between modes extracted from DIC data and SLDV.

30.5 Conclusions

This paper demonstrated the applicability of 3D vision-based techniques to measure dynamic responses of mechanical structures that can be processed with conventional modal analysis algorithm to recover modal parameters (natural frequencies, modal damping and mode shapes). The two different methods based on area-based matching techniques for the displacement (the so-called DIC approach) and velocity (the so-called PIV approach) reconstruction gave good results in

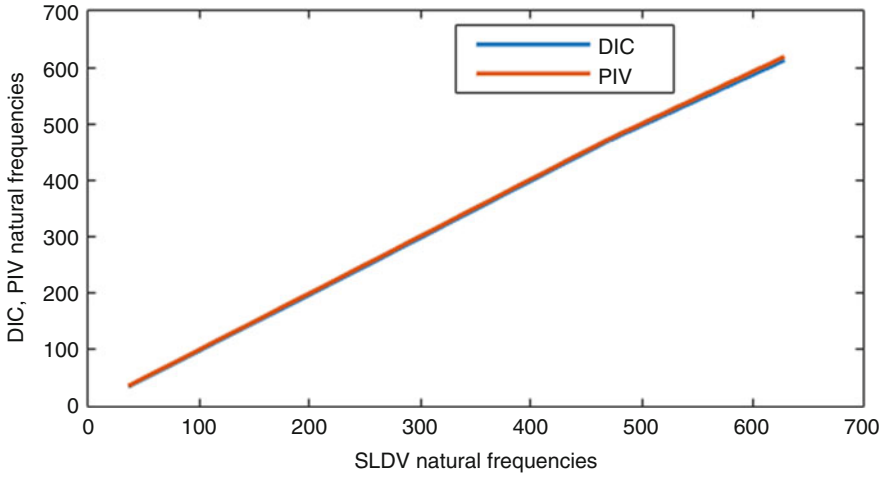

Fig. 30.5 DIC, PIV natural frequencies vs SLDV ones

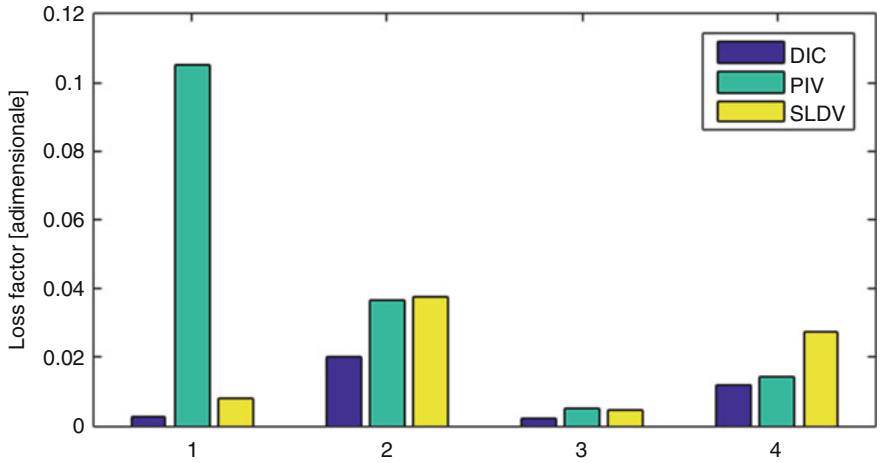

Fig. 30.6 DIC, PIV and SLDV loss factors

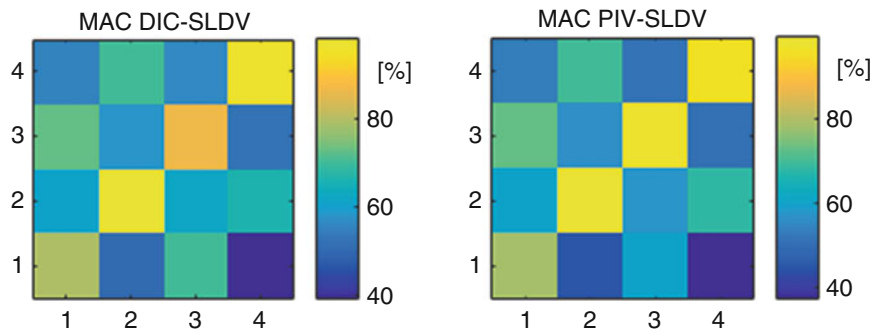

Fig. 30.7 MAC between DIC and SLDV, top, and PIV and SLDV, bottom

comparison with the reference data-set measured by SLDV. The experimental tests on a vibrating cantilever beam evidenced that modal parameter can be recovered with sufficient accuracy by both the methods. Natural frequencies are estimated with a maximum discrepancy of 4% by the PIV method on the first mode and 1.5% by the DIC method on the fourth mode. The loss factor is always underestimated except for the first mode where the PIV method largely overestimates this parameter. The correlation between mode shapes recovered from DIC and PIV data is good (higher than 96%) except for the first mode where the MAC value is about 78%. The low correlation of the first mode is justified by the fact that the frequency range

where the mode is acting is the one more spoiled by noise due to the interference of constraints and shaker connection. Therefore, omitting the first mode, the correlation between modal parameters with respect to the reference ones can be considered more than satisfactory.

References

1. Di Sante, R., Rossi, G.L.: A new approach to the measurement of transverse vibration and acoustic radiation of automotive belts using laser Doppler vibrometry and acoustic intensity techniques. Meas. Sci. Technol. **12**(4), 525–533 (2001)
2. Di Sante, R., Revel, G.M., Rossi, G.L.: Measurement techniques for the acoustic analysis of synchronous belts. Meas. Sci. Technol. **11**(10), 1463 (2000)
3. Martin, P., Rothberg, S.: Methods for the quantification of pseudo-vibration sensitivities in laser vibrometry. Meas. Sci. Technol. **22**(3), 035302 (2011). doi:10.1088/0957-0233/22/3/035302
4. Rothberg, S.J., Baker, J.R., Halliwell, N.A.: Laser vibrometry: pseudo-vibrations. J. Sound Vib. **135**(3), 516–522 (1989)
5. Wang, Y., Lava, P., Reu, P., Debruyne, D.: Theoretical analysis on the measurement errors of local 2D DIC: part I temporal and spatial uncertainty quantification of displacement measurements. Strain. **52**(2), 110–128 (2015)
6. Busca, G., Ghislanzoni, G., Zappa, E.: Indexes for performance evaluation of cameras applied to dynamic measurements. Measurement. **51**(1), 182–196 (2014)
7. Keating, T.J., Wolf, P.R., Scarpace, F.L.: An improved method of digital image correlation. Photogramm. Eng. Remote Sens. **41**(8), 993–1002 (1975)
8. Sutton, M.A., Orteu, J.-J., Schreier, H.W.: Book-Image Correlation for Shape, Motion and Deformation Measurements. Springer, New York (2009). isbn:978-0-387-78746-6
9. Nansteel, M.W., Chen, C.C.T.: Digital image correlation: a measurement tool for the study of explosive effects. In: IEEE Conference on Technologies for Homeland Security, 2009, HST '09, pp. 234–241 (2009)
10. Li, X., Xu, W., Sutton, M.A., Mello, M.: In situ nanoscale inplane deformation studies of ultrathin polymeric films during tensile deformation using atomic force microscopy and digital image correlation techniques. IEEE Trans. Nanotechnol. **6**, 4–12 (2007)
11. Lavatelli, A., Zappa, E.: Modeling uncertainty for a vision system applied to vibration measurements. IEEE Trans. Instrum. Meas. **65**, 1818–1826 (2016)
12. Zappa, E., Matinmanesh, A., Mazzoleni, P.: Evaluation and improvement of digital image correlation uncertainty in dynamic conditions. Opt. Lasers Eng. **59**, 82–92 (2014)
13. Schmidt, T., Tyson, J., Galanulis, K.: Full-field dynamic displacement and strain measurement using advanced 3D image correlation photogrammetry: part I. Exp. Tech. **27**(3), 47–50 (2003)
14. Schmidt, T., Tyson, J., Galanulis, K.: Full-field dynamic displacement and strain measurement—specific examples using advanced 3D image correlation photogrammetry: part II. Exp. Tech. **27**(4), 22–26 (2003)
15. Baqersad, J., Poozesh, P., Niezrecki, C., Avitabile, P.: Photogrammetry and optical methods in structural dynamics—a review. Mech. Syst. Sig. Process. **86**(Part B), 17–34 (2016)
16. Helfrick, M.N., Niezrecki, C., Avitabile, P., Schmidt, T.: 3d digital image correlation methods for full-field vibration measurement. Mech. Syst. Signal Process. **25**(3), 917–927 (2011)
17. Warren, C., Niezrecki, C., Avitabile, P., Pingle, P.: Comparison of FRF measurements and mode shapes determined using optically image based, laser, and accelerometer measurements. Mech. Syst. Signal Process. **25**, 2191–2202 (2011)
18. Helfrick, M.N., Pingle, P., Niezrecki, C., Avitabile, P.: Optical non-contacting vibration measurement of rotating turbine blades. In: Proceedings of the IMAC-XXVII, pp. 1–5 (2009)
19. Poozesh, P., Baqersad, J., Niezrecki, C., Avitabile, P., Harvey, E., Yarala, R.: Large-area photogrammetry based testing of wind turbine blades. Mech. Syst. Signal Process. (2016)
20. Poozesh, P., Baqersad, J., Niezrecki, C., Avitabile, P.: Advancement of optical methods in experimental mechanics. In: Proceedings of the 2015 Annual Conference on Experimental and Applied Mechanics, ch. A Multi-camera Stereo DIC System for Extracting Operating Mode Shapes of Large Scale Structures, vol. 3, pp. 225–238. Springer International Publishing, Cham (2016)
21. Wang, W., Mottershead, J.E., Siebert, T., Pipino, A.: Frequency response functions of shape features from full-field vibration measurements using digital image correlation. Mech. Syst. Signal Process. **28**, 333–347 (2012)
22. Javad, J.B., Lundstrom, T., Niezrecki, C., Avitabile, P: Measuring the dynamics of operating helicopter rotors and wind turbines using 3D digital stereophotogrammetry. In: Annual Forum Proceedings, AHS International, vol. 3, pp. 2250–2256 (2013)
23. Lundstrom, T., Baqersad, J., Niezrecki, C.: Using high-speed stereo-photogrammetry to collect operating data on a Robinson R44 helicopter. In: Conference Proceedings of the Society for Experimental Mechanics Series, vol. 6 (2013)
24. Pan, B.: Recent progress in digital image correlation. Exp. Mech. **51**(7), 1223–1235 (2010)
25. Bornert, M., Brémand, F., Doumalin, P., Dupré, J.-C., Fazzini, M., Grédiac, M., Hild, F., Mistou, S., Molimard, J., Orteu, J.-J., Robert, L., Surrel, Y., Vacher, P., Wattrisse, B.: Assessment of digital image correlation measurement errors: methodology and results. Exp. Mech. **49**(3), 353–370 (2009)

Chapter 31
Rolling Bearing Diagnostics by Means of EMD-Based Independent Component Analysis on Vibration and Acoustic Data

G. Tollis, P. Chiariotti, and M. Martarelli

Abstract Independent Component Analysis (ICA) is used for recovering the various independent sources exciting a system and to separate their contributions. In this paper, ICA is applied to vibrational and acoustic data measured on undamaged and damaged rolling bearings, where those data contains information about the vibration frequencies related to the defect, if present, to the rotation of the bearing, to its dynamic behaviour (resonance frequencies) and to random noise. The aim of the method is to separate those different contributions and to enhance only the one related to the vibration frequency associated to the defect in order to diagnose its presence. To improve the power of the method to identify the contribution of the bearing fault characteristic frequency, a pre-processing step is introduced based on Empirical Mode Decomposition (EMD), allowing to reconstruct multiple sets of time series from a single sensor data, called multiple intrinsic mode functions, which are then given as input to the ICA.

Keywords Bearing diagnostics • Localized faults • Empirical mode decomposition • Independent component analysis • Vibro-acoustic data

31.1 Introduction

This paper claims that the ICA can be satisfactorily used as a non destructive method, starting from a paper by Qiang Miao [1] that set the stage to developing an algorithm that, using the EMD of a signal, deduces a certain number of Intrinsic Mode Functions (IMF), in other words zero time mean functions, that represent several vibration phenomena that are typical of the system of interest. Some of that IMFs are strictly connected to the defect vibration signal. The IMFs classification is carried out using a signal frequency energy based method; then we are going on isolating the Independent Components via FastICA algorithm. After that, the following examination of an Independent Component evaluation index (C_i) can lead to the statement of a positive or negative diagnosis about the existence of a defect, and about its position in the bearing. EMD and ICA are both two method already used for signal analysis in diverse areas of interest, like mechanical components diagnostics, medical sciences, statistics.

The EMD is an iterative method that allows to isolate and recognize some different component of an input signal. For example, when a defect affected bearing is operating, a pulse string is generated. It puts on vibration the system, but in the vibrational signal captured with an accelerometer are blended several signals linked to the same amount of system characteristics, like noise, vibrational modes, shaft rotation, etc. So, the EMD, by means of a procedure substantially based on signal envelopes maximum and minimum interpolation, allows to recognize the frequencies linked to the above mentioned characteristics.

The ICA, in its first formulation at least, bore to solve the "cocktail party problem", that is to determinate from two vectors of sources $[s_1(t), s_2(t)]$ and acoustic signal $[x_1(t), x_2(t)]$, with the second obtained by a sensor, of a coefficient matrix [2]

$$\begin{pmatrix} a_{11} & a_{12} \\ a_{21} & a_{22} \end{pmatrix} \tag{31.1}$$

G. Tollis • M. Martarelli (✉)
Università degli Studi e-Campus, via Isimbardi, Novedrate, Italy
e-mail: milena.martarelli@uniecampus.it

P. Chiariotti
Università Politecnica delle Marche, via Brecce Bianche, 60131, Ancona, Italy

J.M. Harvie, J. Baqersad (eds.), *Shock & Vibration, Aircraft/Aerospace, Energy Harvesting, Acoustics & Optics, Volume 9*,
Conference Proceedings of the Society for Experimental Mechanics Series, DOI 10.1007/978-3-319-54735-0_31

so that we have:

$$\begin{cases} x_1(t) = a_{11}s_1 + a_{12}s_2 \\ x_2(t) = a_{21}s_1 + a_{22}s_2 \end{cases}. \tag{31.2}$$

The fundamental assumption is that s_1 and s_2, rather than two time functions, are two random variables instead. The same states for x_1 and x_2. In order to meet this condition, the gaussianity of the signal must be minimised. This operation is the real cornerstone of the entire method and the more extensively used algorithm for this aim is FastICA: it provides for the maximization of a peculiar function called Negentropy J, that can be efficiently described by this proportionality relation [2]:

$$J(\boldsymbol{y}) \propto [E\{G(\boldsymbol{y})\} - E\{G(\boldsymbol{v})\}]^2 \tag{31.3}$$

where E is the probability function, $\boldsymbol{v}$ is the standard gaussian zero-mean unitary-variance variable. y can be defined like this:

$$\boldsymbol{y} = \boldsymbol{w}^T\boldsymbol{x} \tag{31.4}$$

with $\boldsymbol{x}$ the input array and $\boldsymbol{w}$ the direction maximizing the non-gaussianity.

G is a specific non-quadratic non-linear function, which has a crucial role in FastICA effectiveness. It is the primitive function of a $g(y)$ definable like following:

- "pow3" (power 3) $\rightarrow g(y) = y^3$
- "gauss" (gaussian distribution function) $\rightarrow g(y) = y \bullet e^{-\frac{y^2}{2}}$
- "tanh" (hyperbolic tangent) $\rightarrow g(y) = tanh(y)$
- "skew" (skewness) $\rightarrow g(y) = y^2$

In this paper it is proposed a strategy to recognize the most important component in the full spectrum obtained by the combined application of EMD and FastICA. Then we will prove the strength of the method, either for artificial and experimental signals, into revealing not only the presence, but even the position of a possible defect in the tested bearing.

In Sect. 31.2 this diagnostic methodology is described, in Sect. 31.3 its validation is assessed by using synthesised signal and in Sect. 31.4 its application to a real case study is reported.

31.2 Method Theoretical Description

The main concern in the using of the combination of EMD and ICA to recognize mechanical component defects is the need of an incontrovertible evaluation index that highlight the defect frequency. So this description is mainly directed to this point of interest.

As the measured signal is acquired from an accelerometer, or a microphone, the EMD process extracts the wanted number of zero time mean components, called IMFs, and given by Eq. (31.5). These time signals, I_i, are then processed with Fast Fourier Transform and reorganized depending on an energetic criterion:

$$I_i = \frac{ESS_i}{\sum_i ESS_i} \tag{31.5}$$

$$ESS_i = \sum_f (ES_i(f))^2 \tag{31.6}$$

$$ES_i = \left| \int_{-\infty}^{+\infty} c_i(t) e^{-2\pi ift} dt \right| \tag{31.7}$$

where i goes from 1 to n, with n being the number of IMFs extracted. Equation (31.6) is the representation of the spectrum energy for the i-th component and Eq. (31.7) is the Fourier Transform magnitude of the signal $c_i(t)$.

The IMF can be processed by FastICA, after having been centered and whitened. The Independent Components IC_s can be considered the components of the vector of sources mentioned in Sect. 31.1, where s is the number of significant IC:

$$\boldsymbol{s} = [IC_1(t), IC_2(t), \ldots, IC_8(t)] \tag{31.8}$$

One of the *n ICs* is correlated with the defect: therefore exists the need of a criterion to recognize that. The defect position in a rolling bearing can be recognised from the vibro-acoustic spectrum measured on the bearing proximity on the basis of the frequency excited during vibration. If the defect is located in the outer or inner race the main vibration frequency is given by Eq. (31.8′) or (31.9′). If the defect is located in the rolling element the main vibration frequency is given by Eq. (31.10′); the fundamental train frequency is given by Eq. (31.11′) [3].

- Ball pass frequency on outer race: $BPFO = f_{rO} = \frac{nf_r}{2}\left(1 - \frac{d}{D}\cos\beta\right)$ (31.8′)
- Ball pass frequency on inner race: $BPFI = f_{rI} = \frac{nf_r}{2}\left(1 + \frac{d}{D}\cos\beta\right)$ (31.9′)
- Single ball frequency: $BSF = f_{rR} = \frac{Df_r}{2d}\left[1 - \left(\frac{d}{D}\cos\beta\right)^2\right]$ (31.10′)
- Fundamental train frequency: $FTF = f_{rC} = \frac{f_r}{2}\left(1 - \frac{d}{D}\cos\beta\right)$ (31.11′)

with n number of balls, f_r shaft revolution frequency in Hz, d balls diameter in mm, D balls center trajectory diameter in mm, β contact angle in deg. An IC boasting a frequency among the above mentioned, together with some of its harmonics, is a clear symptom of the defect presence in the corresponding position.

By considering the Fourier Transform magnitude of each *IC* Eq. (31.9), it is possible to calculate the energy at the specific frequency f and its harmonics Eq. (31.10):

$$IES_i(f) = \left| \int_{-\infty}^{+\infty} IC_i(t) e^{-2\pi i f t} dt \right| \tag{31.9}$$

$$ICI_i = \sqrt{\left(IES_i\left(f^*\right)\right)^2 + \left(IES_i\left(2f^*\right)\right)^2 + \left(IES_i\left(3f^*\right)\right)^2 + \cdots + \left(IES_i\left(kf^*\right)\right)^2}/k \tag{31.10}$$

being k the number of significant harmonics.

Definitively, the dominant frequency highlighting indicator, called C_i is:

$$C_i = ICI_i^2 \tag{31.11}$$

The highest C_i pertains to the frequency of interest.

31.3 Application to a Synthesised Signal

In the first phase of the experimentation the algorithm has been applied to a synthesised signal created to simulate the vibration signal originated from a bearing in the following working conditions:

- Shaft angular velocity: 1772 rpm
- Outer race diameter: 45,6 mm
- Inner race diameter: 33,3 mm
- Balls number: 13
- Defect on outer race with a frequency of 162 Hz, according to Eq. (31.9)

The sampling parameter for the synthesis of the signal are the ensuing:

- Sampling frequency: 12 kHz
- Acquisition time: 1 s

Gaussian noise with 20 dB SNR (Signal to Noise Ratio) has then be added to the simulated signal.

In Fig. 31.1 is reported the part of the synthesised signal, in Fig. 31.2 the IMFs obtained by considering the non linear function g as "tanh" and in Fig. 31.3 the Independent Components (IC_S) spectra.

The final results reported in Fig. 31.4 correspond with the outcome of Eq. (31.11), in which the preponderance of C_3 is clear both in the (a) plot, representing the spectral energy of each IC at the defect frequency (162 Hz) and its harmonics with respect to the noise energy, and in the plot (b), representing the spectral energy at the defect frequency as a bar plot. Paying more attention to the IC3 spectrum (plot 3 in Fig. 31.3), indeed, we can easily detect the peak that can be reported to 162 Hz, otherwise the defect characteristic frequency.

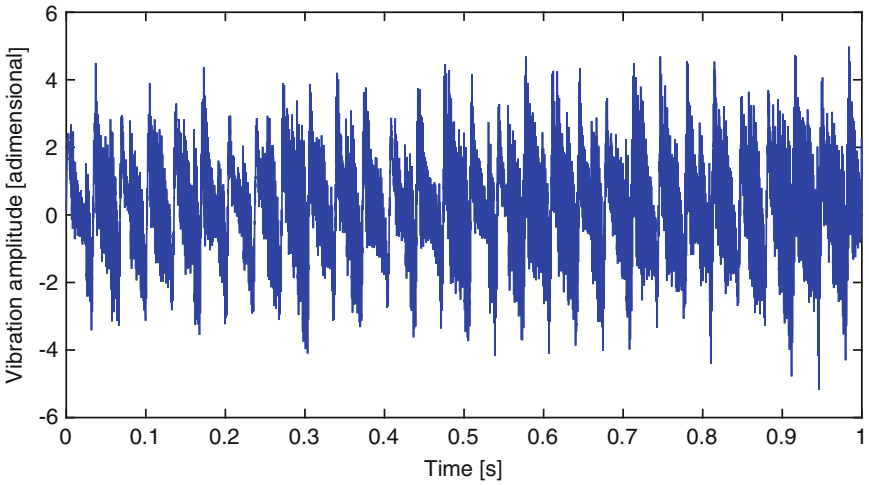

Fig. 31.1 Synthetized time signal

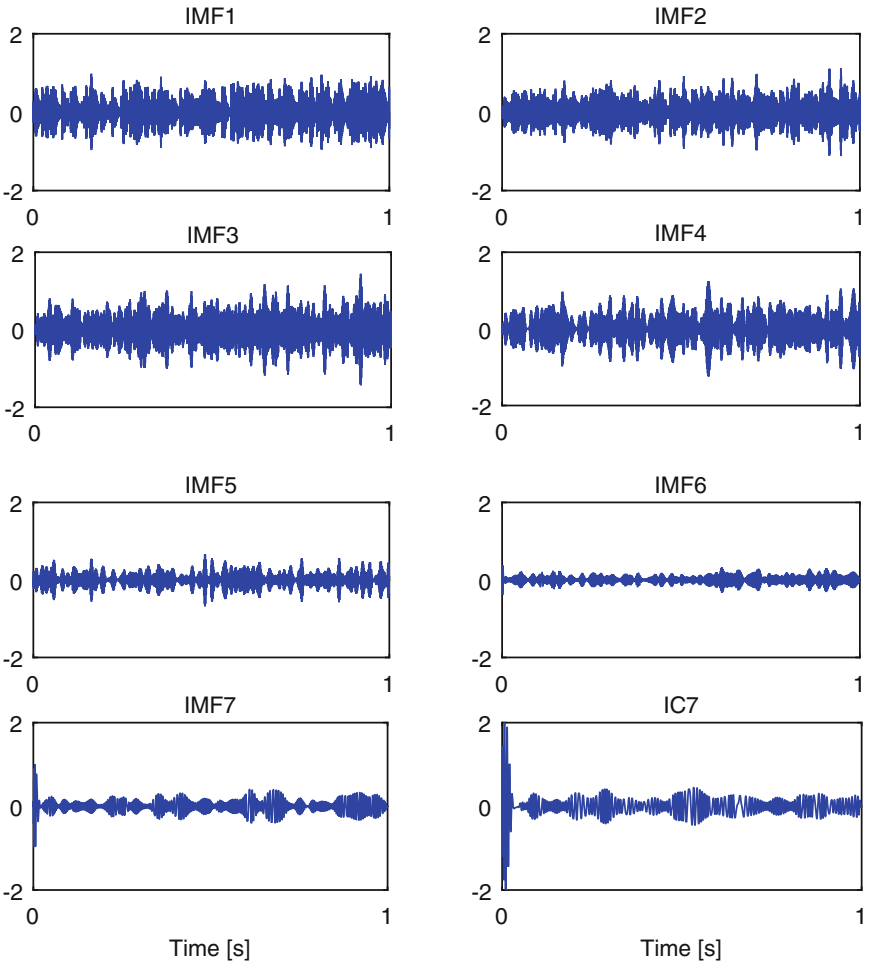

Fig. 31.2 Independent mode functions time history extracted via EMD

This section can be ended, specifying that the best results are obtained, for the sort of application object of this paper, by using, for FFT algorithm, the non linear functions “Gauss” and “Tanh”. Non linear function “Pow3” gives good outputs for high SNR values only.

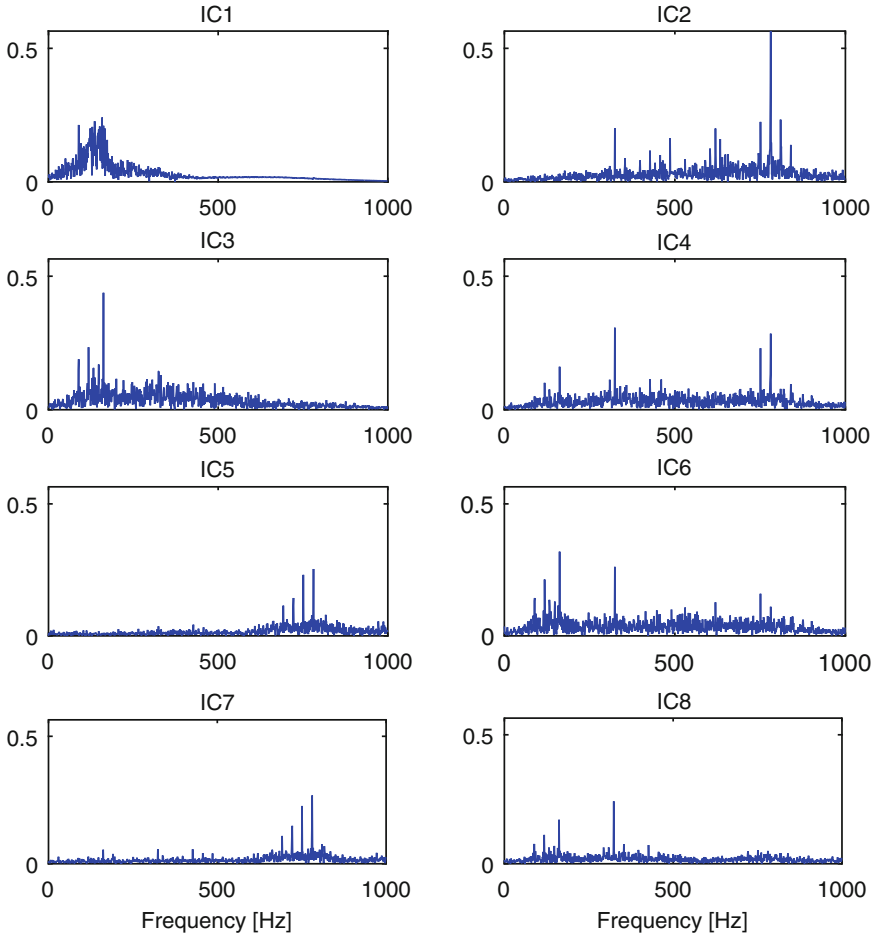

Fig. 31.3 Independent Component spectra extracted via FastICA

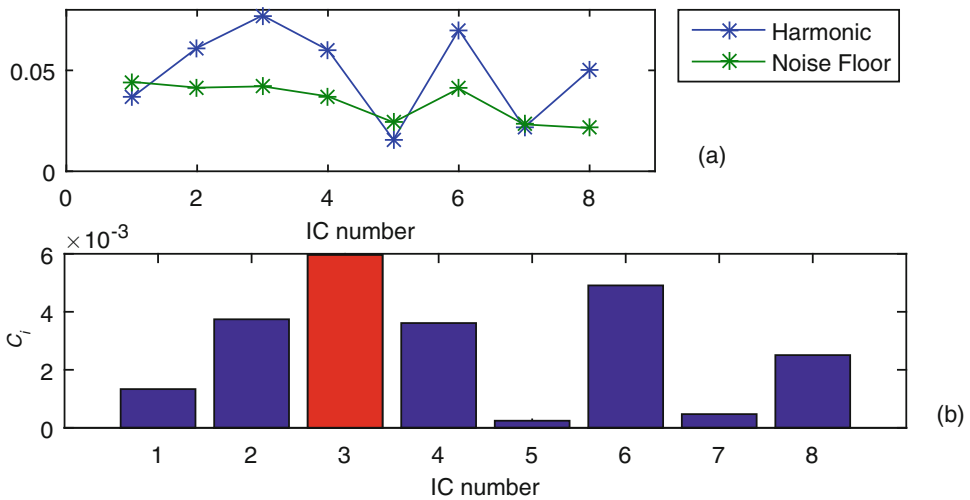

Fig. 31.4 Independent Components extracted via FastICA

31.4 Experimental Validation

In this section, the application of the diagnostic processing method to a real experimental dataset is reported. The vibration and acoustic emission of damaged bearing on its inner race have been acquired by an accelerometer placed on the bearing support and an omnidirectional microphone located 20 mm far from the bearing case. The bearing is an SFK 1205 ETN9,

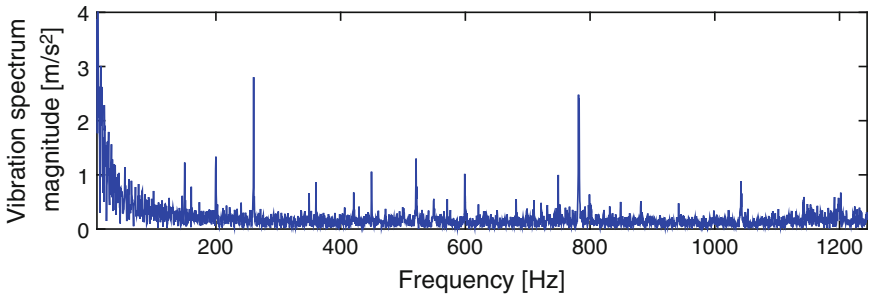

Fig. 31.5 Vibration, top, and acoustic, bottom, spectra measured during the rotation of the shaft

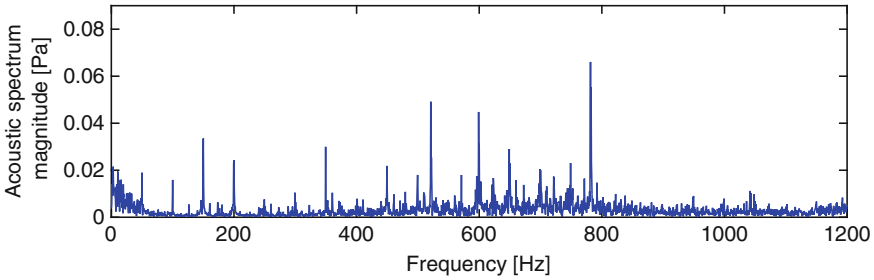

Fig. 31.6 Independent Component spectra extracted via FastICA from the vibration data

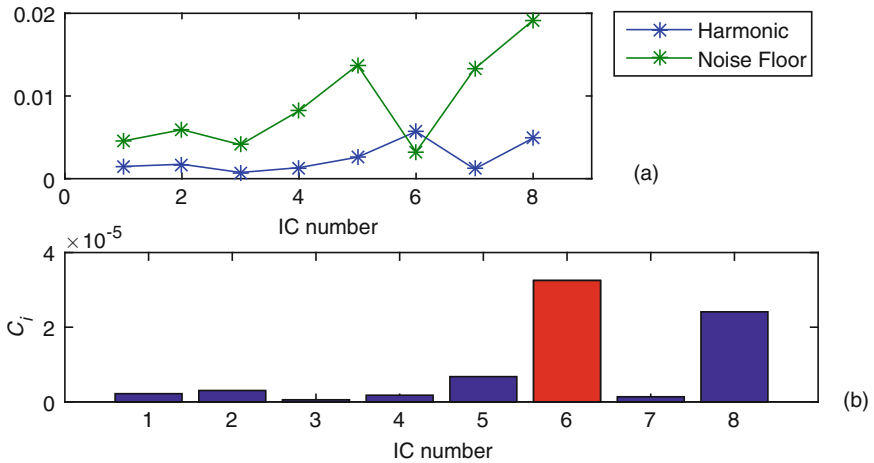

Fig. 31.7 Independent Components extracted via FastICA for the vibration data

with outer and inner race diameter of 52 mm and 25 mm respectively, mounted on a rotating shaft at the angular velocity of 2940 rpm. The defect characteristic frequency is given by Eq. (31.10) and it is 260.5 Hz. The acquisition parameters were 51,200 Hz of sampling frequency and 20 s of acquisition time.

Figure 31.5 shows the spectra measured by the accelerometer and the microphone; it is quite evident the presence of a peak at the defect characteristic frequency in the vibration spectrum, while that frequency is completely spoiled by the noise in the acoustic spectrum.

By applying the FastICA process to the IMFs obtained from the vibration data, using "Pow3" as non-linear function $g(t)$, the independent components are estimated. The ICs spectra are shown in Fig. 31.6. The indicator *Ci*, expressing the energy of the ICs at specific frequencies, has been calculated and reported in Fig. 31.7. According to the last histogram, IC_6 should be the most energetic component at the defect characteristic frequency, and it can be observed indeed that it contains the characteristic defect frequency and its harmonics (sixth IC spectrum in Fig. 31.6).

The same processing has been applied to the acoustic data: the ICs spectra and the indicator *Ci* plot are given in Figs. 31.8 and 31.9. In this case, the IC presenting more energy in the defect characteristic frequency is IC_5, as evidenced in Fig. 31.9 but also in the IC5 spectrum, (the fifth plot in Fig. 31.8), where the defect frequency and its harmonics are emerging clearly

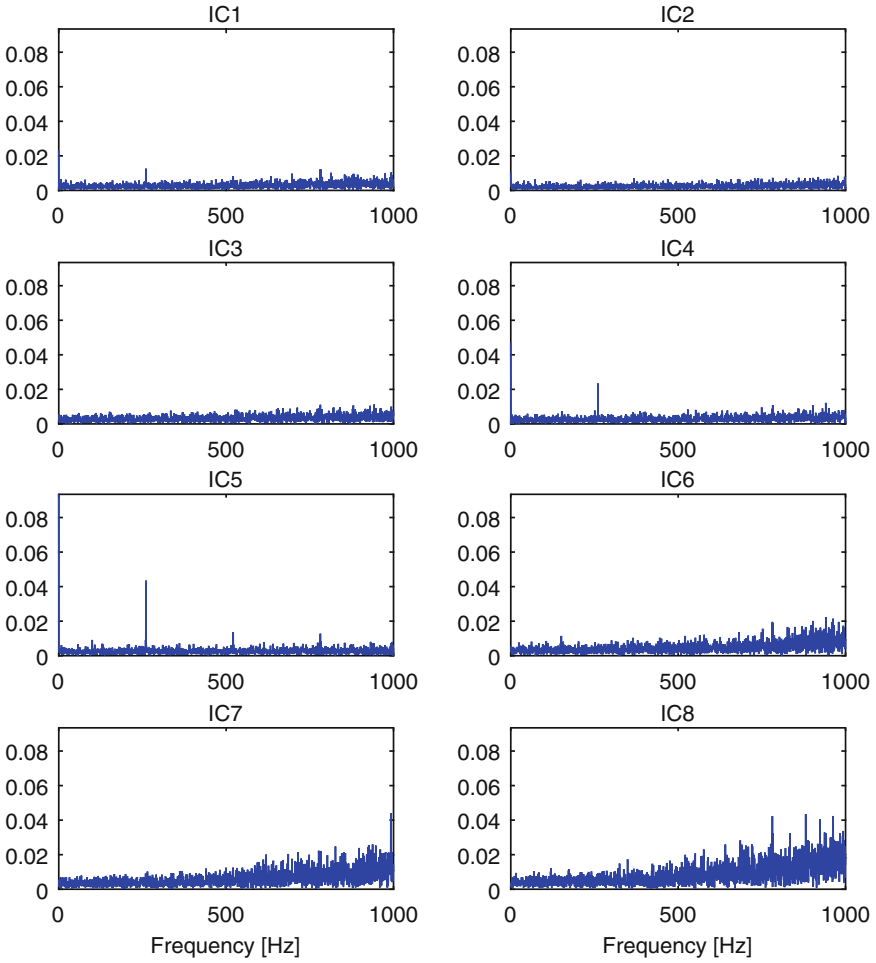

Fig. 31.8 Independent Component spectra extracted via FastICA from the acoustic data

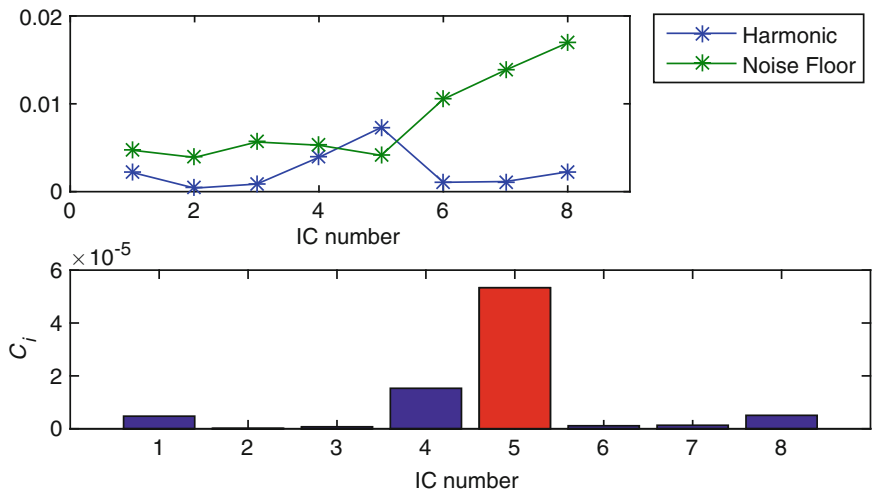

Fig. 31.9 Independent Components extracted via FastICA for the acoustic data

from the noise floor. This indicates that the process (EMD plus FastICA) is very well indicated for working with low SNR signals as the acoustic ones that are highly spoiled by the environmental noise, if thinking to a production line, for instance.

31.5 Conclusions

This paper shows the strength of the EMD-ICA diagnostic method when it is combined with a suitable evaluation tool, like C_i index able to identify the extracted independent component more correlated with a certain frequency. The EMD-based ICA method has been applied to a synthesised signal in order to validate its performance and to a set of experimental data obtained from a damaged rolling bearing.

It has been demonstrated that the method is able to separate different contributions, as random noise, vibration related to the bench structural dynamics, rotation frequency and damage characteristic freqeuncy. By means of the Ci indicator it was possible to identify the IC with the strongest energy at the defect frequency and its harmonics.

The most important result of this paper is to have proved the good performances of the diagnostic method presented also when applied to low SNR data as the ones coming form an acoustic measurement, which are heavily spoiled by environmental noise. Due to this fact, microphones are usually discarded as potential sensors for industrial diagnostic, especially if they have been applied for quality control in production line. By using the EMD-ICA diagnostic method indeed the application of microphones in production line becomes feasible.

References

1. Miao, Q., Wang, D., Pecht, M.: Rolling element bearing fault feature extraction using EMD-based independent component analysis. In: 2011 IEEE Conference on Prognostics and Health Management (PHM), pp. 1–6 (2011)
2. Hyvärinen, A., Oja, E.: Independent component analysis: algorithms and application. Neural Netw. **13**(4–5), 411–430 (2000)
3. Randall, R.B., Antoni, J.: Rolling element bearing diagnostic—a tutorial. Mech. Syst. Signal Process. **25**(2), 485–520 (2011)

Chapter 32
Flutter and Limit Cycle Oscillation Suppression Using Linear and Nonlinear Tuned Vibration Absorbers

E. Verstraelen, G. Kerschen, and G. Dimitriadis

Abstract Aircraft are more than ever pushed to their limits for performance reasons. Consequently, they become increasingly nonlinear and they are more prone to undergo aeroelastic limit cycle oscillations. Structural nonlinearities affect aircraft such as the F-16, which can undergo store-induced limit cycle oscillations (LCOs). Furthermore, transonic buzz can lead to LCOs because of moving shock waves in transonic flight conditions on many aircraft.

This study presents a numerical investigation of passive LCO suppression on a typical aeroelastic system with pitch and plunge degrees of freedom and a hardening stiffness nonlinearity. The absorber used is made of a piezoelectric patch glued to the plunge springs and connected to a resistor and an inductance forming a RLC circuit. A mechanical tuned mass damper absorber of similar configuration is also considered. The piezoelectric absorber features significant advantages in terms of size, weight and tuning convenience.

The results show that both types of absorber increase the linear flutter speed of the system in a similar fashion but, when optimal, they lead to a sub-critical bifurcation while a super-critical bifurcation was observed without absorber. Finally, it is shown that the addition of a properly tuned nonlinear spring (mechanical absorber) or capacitor (piezoelectric absorber) can restore the super-criticality of the bifurcation. The tuning of the nonlinearity is carried out using numerical continuation.

Keywords Aeroelasticity • Limit cycle oscillation • Bifurcation • Piezoelectric • Nonlinear tuned vibration absorber

32.1 Introduction

Flutter is a dangerous aeroelastic mechanism arising from the coalescence of two or more system modes in the presence of an airflow. The phenomenon can lead to a reduction of the aircraft's flight envelope or even necessitate a re-design of the structure. In some cases, nonlinearities present in the aircraft's structure or in the airflow can cause limit cycle oscillations (LCOs) at airspeeds much lower the flutter speed. Among these nonlinearities, freeplay, transonic buzz and store-induced limit cycle oscillations are the most common.

An alternative to aircraft re-design could be the use of mitigation techniques. Active control using control surface or piezoelectric patches can significantly delay these oscillations [1–5]. Alternatively, passive methods such as the nonlinear energy sink [6–9] or the linear tuned vibration absorber (LTVA) [10–12] and its nonlinear version, the nonlinear tuned vibration absorber (NLTVA) [11, 13], can also have a substantial beneficial effect.

In this paper, we study mechanical and electromechanical linear and nonlinear passive vibration absorbers in order to increase a nonlinear aeroelastic system's linear flutter speed and LCO onset speed. The linear flutter speed, which is the linear equivalent of the Hopf bifurcation speed and is defined as the airspeed where the damping of one of the linearised system modes becomes negative, can be increased by means of a properly tuned linear absorber. Conversely, the LCO onset speed, defined as the first airspeed where LCOs can be observed, is equal to the flutter speed in a linear system but can be significantly smaller in the presence of nonlinearities. The LCO onset speed can be increased by means of properly tuned nonlinearities in the absorbers.

The mechanical linear and nonlinear tuned vibration absorbers (MLTVA and MNLTVA) are made of a mass-spring-dashpot subsystem that is attached to the primary structure. Previous studies showed that such a mechanical linear absorber can drastically increase the linear flutter speed of the system but can also lead to an area of bi-stability that would be

E. Verstraelen (✉) • G. Kerschen • G. Dimitriadis
Department of Aerospace and Mechanical Engineering, University of Liège, Liège, Belgium
e-mail: everstraelen@uig.ac.de

J.M. Harvie, J. Baqersad (eds.), *Shock & Vibration, Aircraft/Aerospace, Energy Harvesting, Acoustics & Optics, Volume 9*,
Conference Proceedings of the Society for Experimental Mechanics Series, DOI 10.1007/978-3-319-54735-0_32

dangerous in real life applications [10–13]. In this work, we demonstrate that adding nonlinearity to the absorber's stiffness can suppress bi-stable phenomena. Malher et al. already demonstrated this beneficial effect of the nonlinear absorber however, they did not investigate the possible presence of isolated solutions [13].

The electrical linear and nonlinear tuned vibration absorbers (ELTVA and ENLTVA) are made of piezoelectric (PZT) patches glued to the primary system and connected to a circuit with an inductance and a resistance, forming a RLC circuit. The potential of these passive absorbers has been demonstrated for forced vibration mitigation [14, 15] (PZT shunting) but to the authors' knowledge, none of the studies considered the case of flutter. Again, we demonstrate that the addition of a nonlinear capacitor to the absorber can suppress bi-stable phenomena caused by the linear absorber and the primary system's nonlinearity.

The effect of these linear and nonlinear, mechanical and electrical tuned vibration absorbers is assessed numerically on a classical wing with pitch and plunge degrees-of-freedom (DOFs) and a hardening nonlinearity in the pitch DOF. The model used and all the parameter values are based on an experiment that is currently being built at the wind tunnel lab of the university of Liège (Belgium). The study is conducted in three parts. First, the optimal linear flutter speed of the aeroelastic system coupled to both types of linear absorbers is considered. Then, the effect of the optimal absorbers on the pre-critical response of the linearised system is assessed. Finally, nonlinear analysis is performed using linear and nonlinear absorbers in order to analyse their effect on the LCO onset speed of the system.

32.2 Aeroelastic System

Figure 32.1 depicts the typical aeroelastic system, called the primary system, considered in this study. It consists of a rigid symmetric wing with chord $c = 200\,\text{mm}$ and span $s = 1000\,\text{mm}$ attached to springs and dashpots that provide elastic degrees of freedom in pitch (θ) and plunge (h). The system respectively features rotational and translational inertia I_θ & m_h, stiffness k_θ & k_h, damping c_θ & c_h and a static imbalance S. The flexural axis is located at a distance $x_f = 0.35c$ from the leading edge. All the system parameters are linear apart from the stiffness in pitch which follows a cubic hardening curve of coefficient $k_{\theta,3}$ so that the total stiffness in pitch is given by $k_\theta\theta + k_{\theta,3}\theta^3$. This system, whose parameters values are given in Table 32.1, is an approximation of an experimental apparatus that is being built at the University of Liège. Without any mitigation device the flutter speed of the wing is $U_0^* = 17.5$ m/s.

The first vibration absorber considered is the mechanical absorber (Fig. 32.1a), which serves as a reference as its capabilities have already been demonstrated [10–12]. It consists of a mass m_{ltva} attached to the wing at a distance x_{ltva} from the flexural axis by means of a spring and a dashpot of stiffness and damping k_{ltva} and c_{ltva} respectively. The mass ratio $\overline{m}_{ltva}$ of this absorber is varied from 1 to 8% of the mass of the primary system while the only position considered is $x_{ltva} = 0$ i.e. the absorber is located on the flexural axis of the wing and therefore only affects the plunge. This absorber configuration adds a DOF y that measures the displacement of the absorber's mass. A nonlinear version of this absorber with a cubic stiffness of coefficient $k_{nl,3}$ is also considered so that the total absorber stiffness force is given by $(y-h)k_{ltva} + k_{nl,3}(y-h)^3$. Throughout the paper, the mechanical absorber is called MLTVA when the nonlinear coefficient $k_{nl,3}$ is equal to zero and MNLTVA when it is different from zero.

Alternatively, the electromechanical absorber (Fig. 32.1b) consists of a RL electrical circuit with resistance R and inductance L coupled to the plunge springs by up to eight PI255 piezoelectric patches of capacitance $C_{pzt} = 87.5\,\text{nF}$ and coupling coefficient $\beta_{pzt} = 7500\,\text{C/m}$ per PZT patch. In this configuration, the LTVA capacitance $C_{ltva} = N_{pzt} \times C_{pzt}$ and the

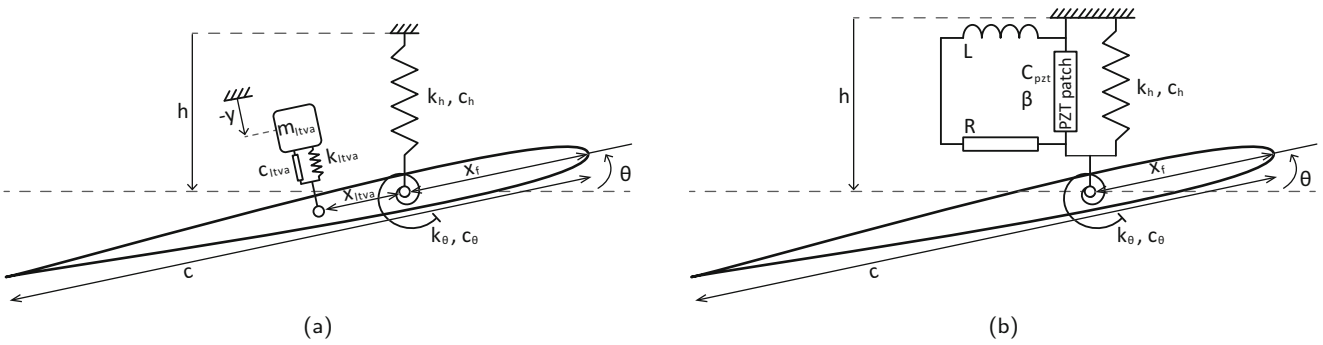

Fig. 32.1 Aeroelastic system with different absorbers. (**a**) Mechanical LTVA. (**b**) Electrical LTVA

Table 32.1 Characteristics of the system

Primary system		
Wing chord	c	200 mm
Wing span	s	1000 mm
Flexural axis position	x_f	0.35c
Pitch inertia	I_θ	0.005 kg m^2
Pitch stiffness	k_θ	20 Nm/rad
Pitch damping	c_θ	0.019 Mm s/rad
Pitch nonlinear stiffness	$k_{3,\theta}$	600 Nm/rad^3
Static imbalance	S	0.028 kg m
Plunge inertia	m_h	2.8910 kg
Plunge stiffness	k_h	6000 N/m
Plunge damping	c_h	2.63 N s/m
Mechanical NLTVA		
Mass ratio	$\overline{m}_{ltva}$	1–8%
Absorber position	x_{ltva}	0
Stiffness	k_{ltva}	Optimised for each $\overline{m}_{ltva}$
Damping	c_{ltva}	Optimised for each $\overline{m}_{ltva}$
Frequency	f_{ltva}	$\frac{1}{2\pi}\sqrt{\frac{k_{ltva}}{m_{ltva}}}$
Damping ratio	ζ_{ltva}	$\frac{c_{ltva}}{2\sqrt{k_{ltva}m_{ltva}}}$
Nonlinear coefficient	$k_{nl,3}$	$[0–800]\times k_{ltva}$ N/m^3
Electrical NLTVA		
Amount of patches	N_{pzt}	1 - 8
Coupling factor	β_{ltva}	$N_{pzt} \times 7500$ C/m
Capacitance	C_{ltva}	$N_{pzt} \times 87.5$ nF
Inductance	L	Optimised for each N_{pzt}
Resistance	R	Optimised for each N_{pzt}
Frequency	f_{ltva}	$\frac{1}{2\pi}\sqrt{\frac{1}{LC}}$
Damping ratio	ζ_{ltva}	$\frac{R}{2\sqrt{L/C}}$
Nonlinear coefficient	$C_{nl,3}$	$[0–8 \times 10^6] \times 1/C_{ltva}$ V/C^3

LTVA coupling coefficient $\beta_{ltva} = N_{pzt} \times \beta_{pzt}$ of the absorber are the product of the number of patches N_{pzt} and the individual capacitance and coupling coefficient of the patches. This absorber configuration adds a DOF q, the charge in the electrical circuit, to the system. A nonlinear version of this absorber with a cubic capacitive term $C_{nl,3}$ is also considered so that the capacitive tension in the circuit is given by $\frac{1}{C_{ltva}}q + C_{nl,3}q^3$. Throughout the paper, the electromechanical absorber is called ELTVA when the nonlinear coefficient $C_{nl,3}$ is equal to zero and ENLTVA when it is different from zero.

Assuming small displacements, the structural equations of motion of the system coupled to a MNLTVA at $x_{ltva} = 0$ are given by

$$\begin{cases} m\ddot{h} + S\ddot{\theta} + c_h\dot{h} + c_{ltva}(\dot{h}-\dot{y}) + k_h h + k_{ltva}(h-y) + k_{nl,3}(h-y)^3 = F_{ext,h} \\ S\ddot{h} + I_\theta\ddot{\theta} + c_\theta\dot{\theta} + k_\theta\theta + k_{\theta,3}\theta^3 = F_{ext,\theta} \\ m_{ltva}\ddot{y} + c_{ltva}(\dot{y}-\dot{h}) + k_{ltva}(y-h) + k_{nl,3}(y-h)^3 = 0 \end{cases} \tag{32.1}$$

and the equations of motion of the system coupled to a ENLTVA are written as

$$\begin{cases} m\ddot{h} + S\ddot{\theta} + c_h\dot{h} + k_h h + \beta_{ltva}q = F_{ext,h} \\ I_\theta\ddot{\theta} + S\ddot{h} + c_\theta\dot{\theta} + k_\theta\theta + k_{\theta,3}\theta^3 = F_{ext,\theta} \\ L\ddot{q} + R\dot{q} + \frac{1}{C_{ltva}}q + \beta_{ltva}h + C_{nl,3}q^3 = 0 \end{cases} \tag{32.2}$$

where $F_{ext,h}$ and $F_{ext,\theta}$ correspond to plunge and pitch aerodynamic loads that can be computed using any unsteady aerodynamic formulation. In both cases, the linear absorber is recovered by setting $C_{nl,3}$ or $k_{nl,3}$ to zero. The equations of motion of the system with a mechanical and an electrical absorber are very similar as the inductance plays the role of the inertia, the resistance of the damping and the capacitance of the stiffness. The only difference between the two absorbers lies in their coupling to the primary system.

Assuming a linear attached airflow and unsteady aerodynamics based on the Wagner function [16], the aeroelastic equations of motion of the coupled system subject to an air stream of density ρ and airspeed U are given by

$$\dot{\mathbf{x}} = \mathbf{Q}\mathbf{x} + \mathbf{f}_{nl} = \begin{pmatrix} -\mathbf{M}^{-1}(\mathbf{C} + \rho U\mathbf{D}) & -\mathbf{M}^{-1}(\mathbf{E} + \rho U^2\mathbf{F}) & -\rho U^3\mathbf{M}^{-1}\mathbf{W} \\ \mathbf{I}_{3\times3} & \mathbf{0}_{3\times3} & \mathbf{0}_{4\times3} \\ \mathbf{0}_{4\times3} & \mathbf{W_1} & U\mathbf{W_2} \end{pmatrix} \mathbf{x} + k_{\theta,3}\theta^3 \times \begin{pmatrix} -\mathbf{M}^{-1} \begin{pmatrix} 0 \\ 1 \\ 0 \end{pmatrix} \\ \mathbf{0}_{7\times1} \end{pmatrix}$$

where $\mathbf{x} = [\dot{\mathbf{z}}\ \mathbf{z}\ \mathbf{w}]^T$ is the state vector that comprises $\mathbf{z}$, the structural DOFs of the system with an absorber, and $\mathbf{w} = [w_1\ w_2\ w_3\ w_4]$, the aerodynamic state vector that models the memory effect of the wake. The structural DOFs of the system are written $\mathbf{z} = [h\,\theta\,y]$ when a mechanical absorber is considered and $\mathbf{z} = [h\,\theta\,q]$ when an electrical absorber is used. Matrix $\mathbf{C}$ is the structural damping matrix, $\rho U\mathbf{D}$ is the aerodynamic damping matrix, $\mathbf{E}$ is the structural stiffness matrix, $\rho U^2\mathbf{F}$ is the aerodynamic stiffness matrix, $\mathbf{W}$ is the aerodynamic state matrix, $\mathbf{W_1}$ and $\mathbf{W_2}$ are the aerodynamic state matrices, $\mathbf{A}$ is the structural mass matrix, $\rho\mathbf{B}$ is the aerodynamic mass matrix and $\mathbf{M}$ is defined as $\mathbf{M} = \mathbf{A} + \rho\mathbf{B}$. All those matrices are given in Appendix.

32.3 Effect of the Absorber on the Flutter Speed

Figure 32.2a plots the relative flutter speed of the system defined as U^*/U_0^*, the ratio between U^*, the linear flutter speed of the system with an optimally tuned LTVA and $U_0^* = 17.5$ m/s, the flutter speed of the primary system alone. The mechanical absorber (blue) increases the flutter speed by 10 to 35% depending on the mass ratio while the electrical absorber (black) is ineffective if too few PZT patches are used but can increase the flutter speed by up to 80% with 8 patches. Figure 32.2a, b depict the optimal absorber frequency and damping as a function of the mass ratio or amount of PZT patches. The mechanical absorber's optimal frequency decreases and its optimal damping increases as the absorber becomes heavier; the behaviour resembles Den Hartoog's criterion for LTVA tuning in forced systems [17]. Conversely, with a ELTVA the optimum frequency increases while $N_{pzt} \leq 4$ then decreases, while the damping increases monotonously. Absorbers with $\overline{m}_{ltva} = 4.2\%$ and $N_{pzt} = 4$ are studied in detail in the rest of the study. In these configurations, both absorbers increase the flutter speed by 25% when optimally tuned.

Figure 32.3a plots the linear relative flutter speed of the system as a function of the absorber damping and frequency with a MLTVA with $\overline{m}_{ltva} = 4.2\%$. Figure 32.3b depicts the same quantities for a ELTVA with $N_{pzt} = 4$. In this case, both absorbers increase the flutter speed by up to 25%. They lose their effectiveness smoothly as their damping is modified or when their frequency is increased but very abruptly when their frequency is decreased. This phenomenon, due to the damping variation with airspeed, is investigated in Sect. 32.4. The white line separates the area where the absorber has a detrimental effect on the system. Mechanical absorbers with small frequency and damping reduce the frequency gap between the system's modes without providing any damping to the system, which reduces the flutter speed. Electrical absorbers without sufficient damping have a similar effect.

In the rest of this work, only the optimal absorbers are studied in detail. The optimal mechanical absorber with $\overline{m}_{ltva} = 4.2\%$ is tuned at $f_{ltva} = 8.0732$ Hz and $\zeta_{ltva} = 7.9145\%$ and the optimal electrical absorber with $N_{pzt} = 4$ is tuned at $f_{ltva} = 8.1878$ Hz and $\zeta_{ltva} = 7.8085\%$. These parameters are very finely tuned in order to study the optimal absorber but a detuning of 0.1 Hz in the absorber still leads to a significant increase in flutter speed and to detuning phenomena similar to those observed in the rest of this work. A fine frequency tuning of the absorber should be possible in the wind tunnel by slightly modifying the mass of the MLTVA or the inductance of the ELTVA.

32.4 Linear System Frequency and Damping Variation with Airspeed

Figure 32.4 depicts the frequency and damping variation with relative airspeed in the case where no LTVA is attached to the system (grey), with an optimally tuned MLTVA (blue) and with an optimally tuned ELTVA (black). Figure 32.4a corresponds to the frequency variation with airspeed, Fig. 32.4b plots the damping variation with airspeed while Fig. 32.4c is a zoom in the purple rectangle of Fig. 32.4b. These figures are computed from linear stability analysis after linearizing the system around the fixed point at the origin. The modes are named M_{0i} for the reference system, M_{ei} for the system with the ELTVA and M_{mi} for the system with the MLTVA. The wind-off mode shapes and frequencies are described in Table 32.2.

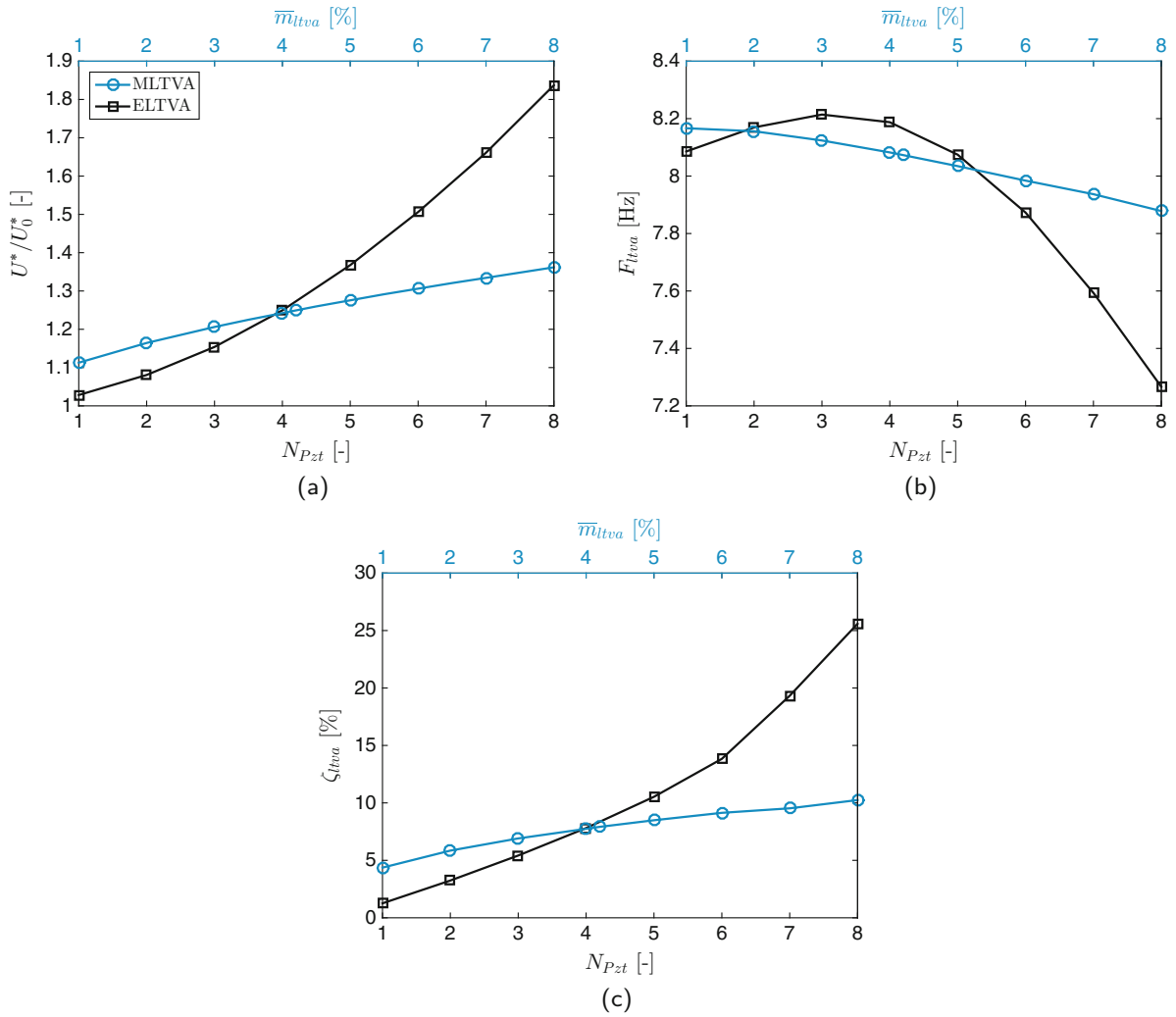

Fig. 32.2 Performance of different absorbers and their optimal tuning. The legend of subfigure (**c**) applies to all three subfigures. (**a**) Optimum flutter speed. (**b**) Optimum absorber frequency. (**c**) Optimum absorber damping

The primary system features two modes, M_{01} and M_{02}. As the airspeed increases, the system frequencies approach each other while the damping of mode M_{01} increases then decreases to cause flutter and the damping of mode M_{02} increases monotonously. The addition of a MLTVA introduces a new mode with an intermediate wind-off frequency. In that case, the damping of mode M_{m3} increases monotonously, the damping of mode M_{m2} increases, decreases, becomes almost zero at point B then increases again while the damping of mode M_{m1} increases at first then decreases to cause flutter. Any small decrease in absorber frequency would make the mode M_{m2} flutter at point B, hence the abrupt detuning observed in Fig. 32.3a, while any small increase in absorber frequency would just reduce the flutter speed of mode M_{m1} (point C) and increase the damping of mode M_{m2} at point B. The behaviour of the system with a ELTVA is very similar to that of the system with a MLTVA. When optimally tuned, the coupled system has a mode M_{e2} whose damping nearly causes flutter at point A then increases and a mode M_{e1} whose damping becomes negative at point C. Again, any small decrease in ELTVA frequency would cause the system to flutter at point A, which explains the sensitivity of the system to a decrease in absorber frequency.

32.5 Bifurcation Analysis of the System with Linear Tuned Vibration Absorbers

The bifurcation diagrams in pitch amplitude of the system without absorber (grey), with an optimal MLTVA (blue) and with an optimal ELTVA (black) are depicted in Fig. 32.5. These diagrams plot limit cycle amplitude in pitch against relative airspeed and are computed using a numerical continuation technique based on finite differences [18]. Without absorber, the

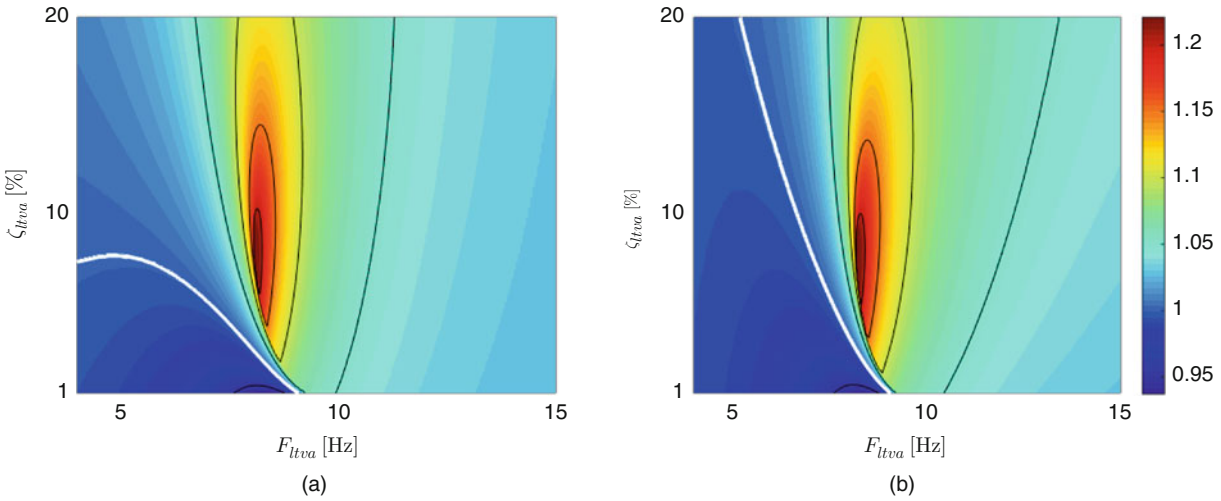

Fig. 32.3 Flutter speed of the system as a function of the LTVA frequency and damping. The *colorbar* or subfigure (**b**) applies to subfigures (**a**) and (**b**). (**a**) MLTVA with $\overline{m}_{ltva} = 4.2\%$. (**b**) ELTVA with $N_{pzt} = 4$

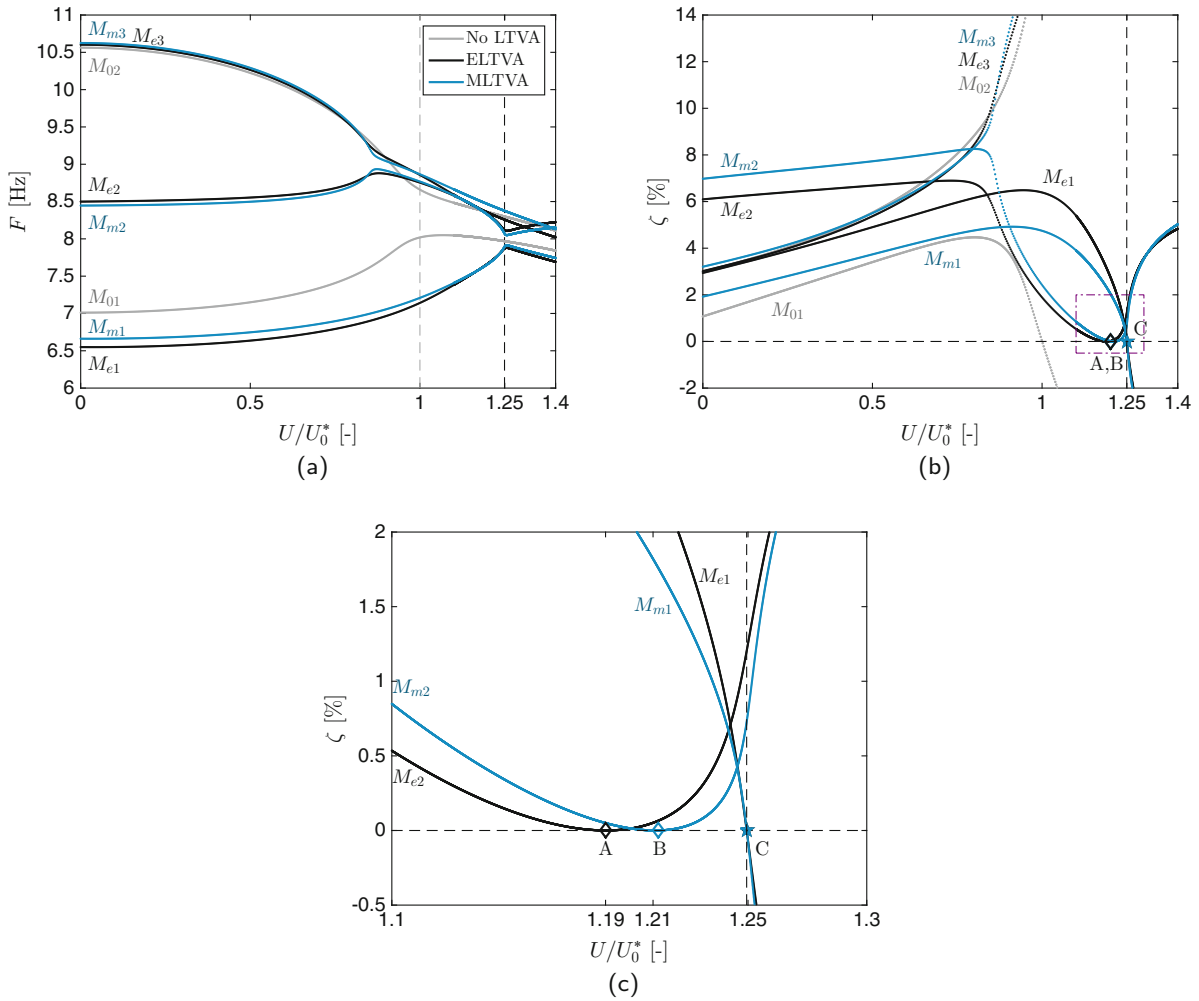

Fig. 32.4 Frequency and damping variation with airspeed of the system without absorber and with mechanical and electrical linear tuned vibration absorbers. The *legend* in subfigure (**a**) applies to all three subfigures. (**a**) Frequency. (**b**) Damping. (**c**) Damping (zoom on the *purple square*)

Table 32.2 Wind-off mode shapes of the system with and without absorber

Mode	Wind-off frequency (Hz)	Wind-off mode description
M_{01}	7.01	In-phase mode, plunge dominated
M_{02}	10.56	Out-of-phase mode, pitch dominated
M_{e1}	6.55	All in-phase, plunge dominated
M_{e2}	8.49	LTVA out-of-phase, LTVA dominated
M_{e3}	10.60	Plunge out-of-phase, pitch dominated
M_{m1}	6.66	LTVA out-of-phase, plunge and LTVA dominated
M_{m2}	8.45	All in-phase, pitch and LTVA dominated
M_{m3}	10.63	Pitch out-of-phase, pitch dominated

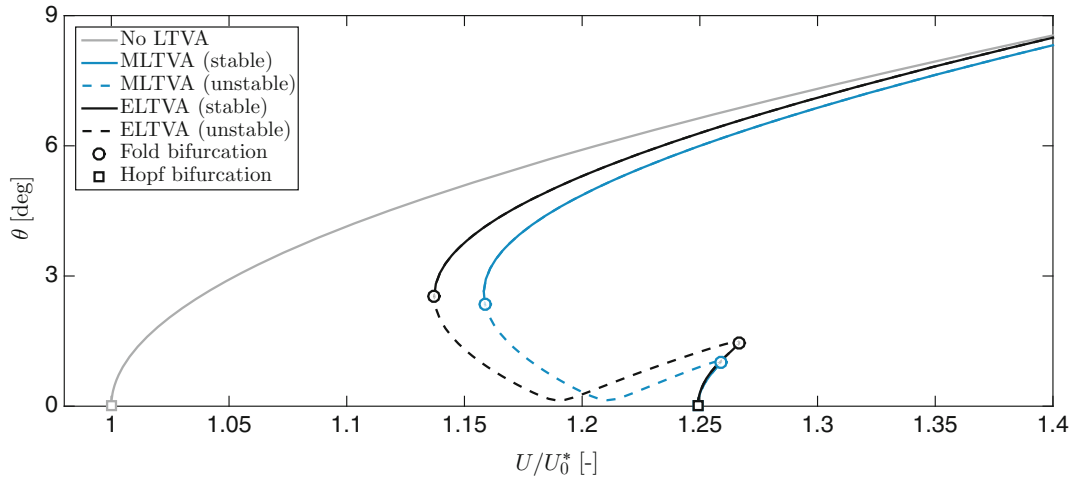

Fig. 32.5 Bifurcation diagram of the system with and without linear absorbers

system undergoes a supercritical Hopf bifurcation at relative airspeed 1, then the LCO amplitude increases monotonously with airspeed. In this case, the linear flutter speed coincides with the LCO onset speed (smallest airspeed at which a LCO can be observed) and the pitch nonlinearity has a beneficial effect because it prevents the oscillation amplitude from becoming infinite at the flutter airspeed.

The bifurcation branch with a MTLVA (blue) is significantly different than that without absorber. The coupled system undergoes a supercritical Hopf bifurcation at an airspeed of 1.25, then the amplitude increases with airspeed until 1.26 where the branch folds back and becomes unstable. At $U/U_0^* = 1.16$, a second fold occurs, the branch becomes stable again and its amplitude increases monotonously with airspeed. As a result, the relative LCO onset speed is only 1.16 and it no longer coincides with the linear flutter speed of the system. The bifurcation branch of the system with a ELTVA is very similar. The Hopf airspeed lies again at 1.25 but the two folds occur at 1.27 and 1.14. In this case, the LCO onset speed is only 1.14. For both absorbers, the region between the Hopf and first fold is bi-stable, as there are two possible stable limit cycle oscillations, one of low and of high amplitude. The region between the Hopf and the second fold is also bi-stable, as the system's response trajectories can be attracted by either the stable fixed point or the stable limit cycle.

The bi-stability and the reduction in LCO onset speed are due to the detuning of the absorbers. The linear absorbers are only effective when the amplitude is small, i.e. when the effects of the structural nonlinearity can be neglected. In that case, they increase the relative Hopf speed of the coupled system to 1.25. If the oscillation amplitude is increased, the equivalent linear stiffness of the primary system increases, which detunes the absorbers. The detuning of the absorbers due to the structural nonlinearity in the primary system can cause limit cycle oscillations at airspeeds lower than the linear flutter speed, which leads to a bi-stable region where LCOs or static solutions can exist depending on the initial conditions. In many real-life applications, LCOs can not be tolerated. As a consequence, the performance of the systems with absorbers is determined by the LCO onset speed rather than the linear flutter speed. With that in mind, the MLTVA increases the performance of the system by only 16% while the ELTVA provides an improvement of only 14% while linear analysis predicted a performance gain of 25%.

32.6 Bifurcation Analysis of the System with Nonlinear Tuned Vibration Absorbers

The detuning of the linear absorbers that is causing the large bi-stable area can be countered by introducing a nonlinear stiffness (MNLTVA) or capacitance (ENLTVA) to the respective LTVAs. This nonlinearity added to the absorbers allows them to increase their equivalent stiffness to cancel the detuning. For the mechanical absorber, the stiffness force is given by $F_{nl} = k_{ltva}\,(y-h) + k_{nl,3}\,(y-h)^3$ with values of $k_{nl,3}$ ranging from 0 (linear absorber) to $800 \times k_{ltva}$.

Figure 32.6 depicts bifurcation diagrams of the system with MNLTVAs of nonlinear coefficient between 0 and $800 \times k_{ltva}$. These diagrams, computed using a numerical continuation algorithm based on a shooting method [18], are described as follows.

- Figure 32.6a: $k_{nl,3} = 0 \times k_{ltva}$. This figure plots the bifurcation behaviour of the linear absorber that was studied in detail in Sect. 32.5. The Hopf relative speed is increased to 1.25 however a large bi-stable area arises from the detuning of the absorber. As a result, the LCO onset speed is equal to only 1.16, the relative airspeed of the fold B.
- Figure 32.6b: $k_{nl,3} = 20 \times k_{ltva}$. This absorber increases the relative LCO onset speed (fold B) to 1.161 because its nonlinearity mitigates the detuning of the absorber to a certain extent but is not sufficiently large. At higher airspeeds, two new fold bifurcations C and D arise at high amplitudes.
- Figure 32.6c: $k_{nl,3} = 60 \times k_{ltva}$. Increasing the NLTVA nonlinear coefficient delays the LCO onset speed slightly further as the fold B is now located at an airspeed of 1.171. More importantly, the increased nonlinearity in the absorber reduces the airspeed and amplitude of the folds C and D and therefore the airspeed at which the lower amplitude LCO branch arises.
- Figure 32.6d: $k_{nl,3} = 70 \times k_{ltva}$. When the nonlinear coefficient reaches approximately 70 times the linear coefficient, the folds at points D and A merge and disappear. There are now two separate limit cycle branches, one that appears at the supercritical Hopf point and an isolated branch that closes in on itself. The folds B and C now lie on the isolated solution branch and the LCO onset speed reaches 1.175.
- Figure 32.6e: $k_{nl,3} = 120 \times k_{ltva}$. Increasing the nonlinear coefficient further has very little effect on the main branch however it reduces the span of the isolated solution branch. At this point, the relative LCO onset speed is equal to 1.201. This isolated solution is dangerous because it is rather narrow and can easily be missed when performing continuation without bifurcation tracking.
- Figure 32.6f: $k_{nl,3} = 130 \times k_{ltva}$. This nonlinear coefficient is sufficient to totally suppress the isolated solution branch. As a result, the system now features a smooth super-critical bifurcation diagram with a nonlinear LCO onset speed that coincides with the Hopf point and without any bi-stable regions. This is the optimal tuning of the nonlinear absorber.
- Figure 32.6g: $k_{nl,3} = 400 \times k_{ltva}$. Nonlinear absorber coefficients larger than the optimal turn the super-critical Hopf bifurcation into sub-critical, which reduces the LCO onset speed but also increases the LCO onset amplitude. The higher the nonlinear coefficient, the lower the LCO onset speed. Nevertheless, even at three times the optimal value, the relative LCO onset speed is equal to 1.230 for this absorber which is much better than a LTVA.
- Figure 32.6h: $k_{nl,3} = 800 \times k_{ltva}$. Even at about six times the optimal value, this nonlinear absorber still features a relative LCO onset speed of 1.203 which further proves the robustness of this absorber.

Similar phenomena are observed with an electromechanical vibration absorber. In this case, the capacitive tension is given by $V_C = \frac{1}{C_{ltva}} q + C_{nl,3} q^3$. The values of the nonlinear coefficient $C_{nl,3}$ are varied from 0 to $80 \times 10^5 \times \frac{1}{C_{ltva}}$. Theses values of the nonlinear coefficient may seem extreme but in fact, they are not because the charge q in the absorber is very small. Figure 32.7 depicts mostly the same phenomena as Fig. 32.6 for an electromechanical nonlinear absorber.

- Figure 32.7a–e: for nonlinear coefficients smaller than $7 \times 10^5 \times \frac{1}{C_{ltva}}$, the absorber's nonlinearity causes the appearance of two additional folds at points C and D. As the nonlinear coefficient increases, the folds at points A and D merge, creating an isolated branch when the nonlinear coefficient is sufficiently large. Increasing the nonlinear coefficient increases the LCO onset speed and reduces the span of the isolated branch. Note that in Fig. 32.7e, the fold C has an airspeed smaller than that of the Hopf point which means that between relative airspeeds of 1.219 and 1.248, only static solutions exist.
- Figure 32.7f corresponds to a nonlinear coefficient of $13 \times 10^5 \times \frac{1}{C_{ltva}}$, which is the optimal value for this system. This nonlinearity is just sufficient to suppress the isola and the LCO onset speed coincides with the Hopf speed.
- Figure 32.7g, h: when the nonlinear capacity is higher than the optimal, the super-critical Hopf bifurcation is turned into sub-critical, which leads to a large LCO onset amplitude. The system is not sensitive to the exact value of $C_{nl,3}$ as a nonlinear coefficient about six times higher than the optimal one leads to a relative LCO onset speed of 1.195, which is still much higher than the onset speed of the system with a linear absorber.

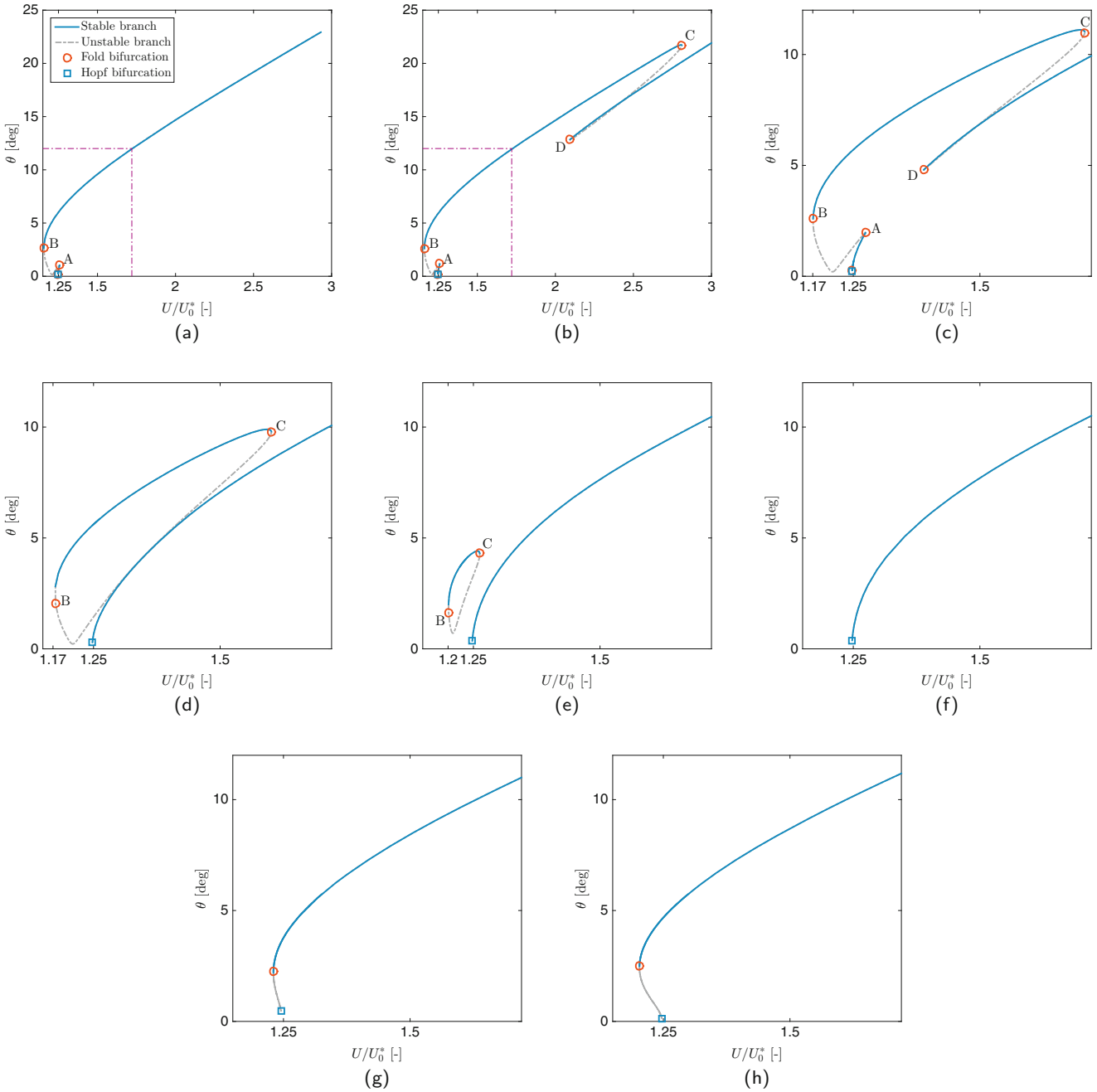

Fig. 32.6 Bifurcation diagrams of the system with linear and nonlinear mechanical vibration absorbers. The *legend* in subfigure (**a**) applies to all eight subfigures. (**a**) $k_{nl,3} = 0 \times k_{ltva}$. (**b**) $k_{nl,3} = 20 \times k_{ltva}$. (**c**) $k_{nl,3} = 60 \times k_{ltva}$. (**d**) $k_{nl,3} = 70 \times k_{ltva}$. (**e**) $k_{nl,3} = 120 \times k_{ltva}$. (**f**) $k_{nl,3} = 130 \times k_{ltva}$. (**g**) $k_{nl,3} = 400 \times k_{ltva}$. (**h**) $k_{nl,3} = 800 \times k_{ltva}$

In summary, the addition of a properly tuned nonlinear stiffness term to the MLTVA or of a properly tuned nonlinear capacitive term to the ELTVA increases the LCO onset speed to the linear flutter speed of the system and suppresses a potentially dangerous bi-stable area. The LCO onset speed is quite sensitive to the absorber's nonlinearity when it is smaller than the optimal value, i.e. when the absorber is not capable of suppressing the isolated branch, but not so sensitive when it is larger than the optimal value, which is encouraging for practical implementations.

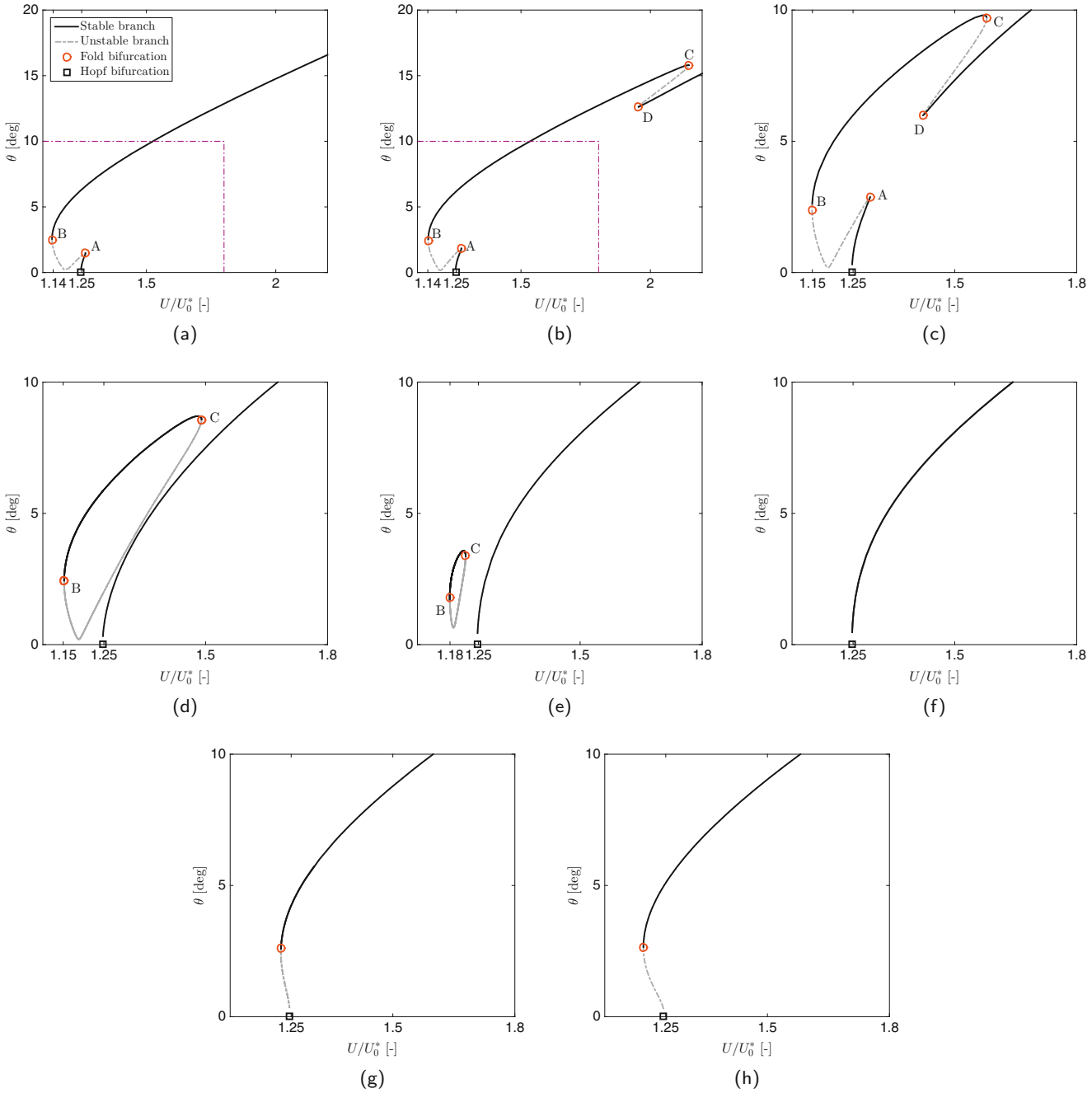

Fig. 32.7 Bifurcation diagrams of the system with linear and nonlinear electromechanical vibration absorbers. The legend in subfigure (*a*) applies to all eight subfigures. (**a**) $C_{nl,3} = 0 \times \frac{1}{C_{ltva}}$. (**b**) $C_{nl,3} = 3 \times 10^5 \times \frac{1}{C_{ltva}}$. (**c**) $C_{nl,3} = 6 \times 10^5 \times \frac{1}{C_{ltva}}$. (**d**) $C_{nl,3} = 7 \times 10^5 \times \frac{1}{C_{ltva}}$. (**e**) $C_{nl,3} = 12 \times 10^5 \times \frac{1}{C_{ltva}}$. (**f**) $(C_{nl,3} = 13 \times 10^5 \times \frac{1}{C_{ltva}}$. **g**) $(C_{nl,3} = 40 \times 10^5 \times \frac{1}{C_{ltva}}$. **h**) $C_{nl,3} = 80 \times 10^5 \times \frac{1}{C_{ltva}}$

32.7 Conclusions

This work shows numerically that an electrical linear tuned vibration absorber made of a RL circuit and PZT patches can perform at least as well as a mechanical linear tuned vibration absorber. Both linear absorbers have a similar effect on the system and lead to a substantial increase in linear flutter speed. On the other hand, a large bi-stable region, due to the structural nonlinearity of the primary system, greatly reduces the nonlinear LCO onset speed of the system.

The addition of a properly tuned nonlinear stiffness or capacity on the mechanical or electrical absorbers respectively totally suppresses the bi-stable area. Finally, it must be noted that unlike the linear absorber parameters that require a very fine tuning, the nonlinear parameters do not have a significant impact on the absorber performance provided they are sufficiently large.

Acknowledgements E. Verstraelen, G. Kerschen, and G. Dimitriadis would like to acknowledge the financial support of the European Union (ERC Starting Grant NoVib 307265).

Appendix: Structural and Aerodynamic Matrices of the System

Structural Matrices

The system structural matrices based on Eqs. (32.1) and (32.2), with parameters values from Table 32.1, are given by

$$\mathbf{A} = \begin{pmatrix} m & S & 0 \\ S & I_\theta & 0 \\ 0 & 0 & 0 \end{pmatrix} + \mathbf{A}_{ltva} \tag{32.3}$$

$$\mathbf{C} = \begin{pmatrix} c_h & 0 & 0 \\ 0 & c_\theta & 0 \\ 0 & 0 & 0 \end{pmatrix} + \mathbf{C}_{ltva} \tag{32.4}$$

$$\mathbf{E} = \begin{pmatrix} k_h & 0 & 0 \\ 0 & k_\theta & 0 \\ 0 & 0 & 0 \end{pmatrix} + \mathbf{E}_{ltva} \tag{32.5}$$

assuming small displacements and linear electromechanical coupling, the MLTVA and ELTVA equations are written as

	MLTVA	*ELTVA*
$\mathbf{A}_{ltva}$	$m_{ltva}\begin{pmatrix} 0 & 0 & 0 \\ 0 & 0 & 0 \\ 0 & 0 & 1 \end{pmatrix}$	$L\begin{pmatrix} 0 & 0 & 0 \\ 0 & 0 & 0 \\ 0 & 0 & 1 \end{pmatrix}$
$\mathbf{C}_{ltva}$	$c_{ltva}\begin{pmatrix} 1 & r_{ltva} & -1 \\ r_{ltva} & r_{ltva}^2 & r_{ltva} \\ -1 & r_{ltva} & 1 \end{pmatrix}$	$R\begin{pmatrix} 0 & 0 & 0 \\ 0 & 0 & 0 \\ 0 & 0 & 1 \end{pmatrix}$
$\mathbf{E}_{ltva}$	$k_{ltva}\begin{pmatrix} 1 & r_{ltva} & -1 \\ r_{ltva} & r_{ltva}^2 & r_{ltva} \\ -1 & r_{ltva} & 1 \end{pmatrix}$	$\begin{pmatrix} 0 & 0 & \beta_{ltva} \\ 0 & 0 & 0 \\ \beta_{ltva} & 0 & \frac{1}{C_{ltva}} \end{pmatrix}$

(32.6)

with $r_{ltva} = 0$ in this study.

Aerodynamic Matrices

The aerodynamic matrices that are used in Eq. (32.2) have been computed using linear unsteady aerodynamics based on Wagner's theory. The Wagner function is given by

$$\Phi(t) = 1 - \Psi_1 e^{-\varepsilon_1 Ut/b} - \Psi_2 e^{-\varepsilon_2 Ut/b} \tag{32.7}$$

with $\Psi_1 = 0.165$, $\Psi_2 = 0.335$, $\varepsilon_1 = 0.0455$ and $\varepsilon_2 = 0.3$. The aerodynamic mass matrix is written as

$$\mathbf{B} = b^2 \begin{pmatrix} \pi & -\pi ab \\ -\pi ab & \pi b^2(1/8 + a^2) \end{pmatrix} \tag{32.8}$$

with $a = x_f/b$. Then, the aerodynamic damping matrix is given by

$$\mathbf{D} = \pi b^2 \begin{pmatrix} 0 & 1 \\ 0 & -b(a - 1/2) \end{pmatrix} + 2\pi b\Phi(0) \begin{pmatrix} 1 & -b(a - 1/2) \\ -b(a + 1/2) & b^2(a + 1/2)(a - 1/2) \end{pmatrix} \tag{32.9}$$

and the stiffness matrix is written as

$$\mathbf{F} = 2\pi b\Phi(0) \begin{pmatrix} 0 & 1 \\ 0 & -b(a + 1/2) \end{pmatrix} + 2\pi b\dot{\Phi}(0) \begin{pmatrix} 1 & -b(a - 1/2) \\ -b(a + 1/2) & b^2(a + 1/2)(a - 1/2) \end{pmatrix} \tag{32.10}$$

The aerodynamic state matrix is given by

$$\mathbf{W} = 2\pi b \begin{pmatrix} \Theta \\ -b(a + 1/2)\Theta \\ \mathbf{0}_{1\times 4} \end{pmatrix} \tag{32.11}$$

with

$$\mathbf{\Theta} = \begin{pmatrix} -\Psi_1(\varepsilon_1/b)^2 \\ -\Psi_2(\varepsilon_2/b)^2 \\ \Psi_1\varepsilon_1/b[1 + \varepsilon_1(a - 1/2)] \\ \Psi_2\varepsilon_2/b[1 + \varepsilon_2(a - 1/2)] \end{pmatrix}^T \tag{32.12}$$

Finally, the aerodynamic state equations are given by

$$\mathbf{W}_1 = \begin{pmatrix} 1 & 0 & 0 \\ 1 & 0 & 0 \\ 0 & 1 & 0 \\ 0 & 1 & 0 \end{pmatrix} \tag{32.13}$$

$$\mathbf{W_2} = \begin{pmatrix} -\varepsilon_1/b & 0 & 0 & 0 \\ 0 & -\varepsilon_2/b & 0 & 0 \\ 0 & 0 & -\varepsilon_1/b & 0 \\ 0 & 0 & 0 & -\varepsilon_2/b \end{pmatrix} \tag{32.14}$$

References

1. Dowell, E., Clark, R., Cox, D., et al.: In: G.M.L. Gladwell (ed.) A Modern Course in Aeroelasticity. Solid Mechanics and its Applications. Kluwer, Dordrecht (2005)
2. Borglund, D., Kuttenkeuler, J.: Active wing flutter suppression using a trailing edge flap. J. Fluids Struct. **16**(3), 271–294 (2002). ISSN 0889-9746. doi:http://dx.doi.org/10.1006/jfls.2001.0426
3. Yu, M., Hu, H.: Flutter control based on ultrasonic motor for a two-dimensional airfoil section. J. Fluids Struct. **28**, 89–102 (2012). ISSN 0889-9746. doi:http://dx.doi.org/10.1016/j.jfluidstructs.2011.08.015
4. Huang, R., Qian, W., Hu, H., et al.: Design of active flutter suppression and wind-tunnel tests of a wing model involving a control delay. J. Fluids Struct. **55**, 409–427 (2015). ISSN 0889-9746. doi:http://dx.doi.org/10.1016/j.jfluidstructs.2015.03.014
5. Han, J.-H., Tani, J., Qiu, J.: Active flutter suppression of a lifting surface using piezoelectric actuation and modern control theory. J. Sound Vib. **291**(3–5), 706–722 (2006). ISSN 0022-460X. doi:http://dx.doi.org/10.1016/j.jsv.2005.06.029
6. Lee, Y., Vakakis, A., Bergman, L., et al.: Suppression aeroelastic instability using broadband passive targeted energy transfers, part 1: theory. AIAA J. **45**(3), 693–711 (2007). doi:10.2514/1.24062

7. Lee, Y.S., Kerschen, G., McFarland, D.M., et al.: Suppressing aeroelastic instability using broadband passive targeted energy transfers, part 2: experiments. AIAA J. **45**(10), 2391–2400 (2007). doi:10.2514/1.28300
8. Lee, Y.S., Vakakis, A.F., Bergman, L.A., et al.: Enhancing the robustness of aeroelastic instability suppression using multi-degree-of-freedom nonlinear energy sinks. AIAA J. **46**(6), 1371–1394 (2008). doi:10.2514/1.30302
9. Hubbard, S.A., Fontenot, R.L., McFarland, D.M., et al.: Transonic aeroelastic instability suppression for a swept wing by targeted energy transfer. J. Aircr. **51**(5), 1467–1482 (2014). doi:10.2514/1.C032339
10. Karpel, M.: Design for Active and Passive Flutter Suppression and Gust Alleviation, vol. 3482. National Aeronautics and Space Administration, Scientific and Technical Information Branch (1981)
11. Habib, G., Kerschen, G.: Passive Flutter Suppression Using a Nonlinear Tuned Vibration Absorber, chap. 11. Springer International Publishing, Cham (2016). ISBN 978-3-319-15221-9, pp. 133–144. doi:10.1007/978-3-319-15221-9_11
12. Verstraelen, E., Habib, G., Kerschen, G., et al.: Experimental Passive Flutter Mitigation Using a Linear Tuned Vibrations Absorber, chap. 35. Springer International Publishing, Cham (2016). ISBN 978-3-319-29739-2, pp. 389–403. doi:10.1007/978-3-319-29739-2_35
13. Malher, A., Touzé, C., Doaré, O., et al.: Passive control of airfoil flutter using a nonlinear tuned vibration absorber. In: 11th International Conference on Flow-induced vibrations, FIV2016. La Haye, Netherlands (2016)
14. Thomas, O., Ducarne, J., Deü, J.-F.: Performance of piezoelectric shunts for vibration reduction. Smart Mater. Struct. **21**(1), 015008 (2012)
15. Soltani, P., Kerschen, G., Tondreau, G., et al.: Piezoelectric vibration damping using resonant shunt circuits: an exact solution. Smart Mater. Struct. **23**(12), 125014 (2014)
16. Fung, Y.: An Introduction to the Theory of Aeroelasticity. Dover, New York (1993)
17. Hartog, J.D.: Mechanical Vibrations. Courier Corporation, North Chelmsford, MA (1985)
18. Dimitriadis, G.: Numerical continuation of aeroelastic systems: shooting vs finite difference approach. In: RTO-MP-AVT-152 Limit Cycle Oscillations and Other Amplitude-Limited Self-Excited Vibrations, AVT-152-025, Loen (2008)

Chapter 33
A Montecarlo Approach to Test the Modes of Vibration of a 6-DoF Parallel Kinematic Simulator

E. Fiore and H. Giberti

Abstract Parallel kinematic manipulator are for sure the best choice to fulfill the need of high accuracy and high stiffness. By the way due to the always increasing required performances, poor decisions during the early design stages might lead to the arising of vibration phenomena during the operating phase of the machine. Due to the intrinsic nonlinearities that characterize this kind of machines the modes of vibration of the structure strongly depend on the pose of the robot. In addition in many applications as the one presented in this paper the tasks the machine is required to perform are not known in advance. Usually the technical specification for a PKM in terms of workspace dimensions and maximum excitation frequencies are related to the end-effector. By the way the kinematics that links the motion of the mobile platform to the joints motion is highly nonlinear, and thus might produce the insurgence of higher frequencies excitations. This paper presents an approach to test the modes of vibration of a 6-DoF parallel kinematic simulator that relies on a statistical method to investigate different possible motions of the end-effector that involve a combination of translations and rotations on the basis of their probability density functions (PDF).

Keywords Parallel Kinematic Machines • Robot • Monte Carlo Method • Flexible multibody systems • Frequency mapping

33.1 Introduction

In general parallel kinematic manipulators (PKMs) represent the best solution for those applications in which a complex motion of a large payload has to be simulated. As a matter of fact parallel architecture robots are characterized by higher stiffness and dynamic performances with respect to serial robots thanks to a fair distribution of the loads among the links connecting the platform to the base and to a reduced overall inertia. For sure the workspace of these machines is quite low compared to their size and so a optimization process like the one presented in [1, 2] is required in order to achieve the desired performances. The performances of these machines strictly depend on their dimensions and so making a comparison between different architectures is a difficult task as stated by Merlet in [3]. Very often the motion laws these robots have to reproduce are computed in real-time by means of a mathematical model whose inputs are the actual position and orientation of the payload as well as the forces and moments exchanged between payload and the robot itself. It is evident how finding a suitable set of simulations for sizing the actuating system and testing the mechanical components during the design phase could be a very hard task due to the randomness of the actual operating conditions. In addition, in most of the cases, the technical specifications for the machines in terms of maximum displacements/rotations and motion frequencies are provided in the workspace; by the way, due to the non-linear kinematic relationships between robot pose (position and orientation of the end effector) and the actuating system displacements, higher order harmonics components are likely to arise which may lead to the machine approaching resonance conditions, consequently affecting the accuracy. This paper presents a statistical approach based on the Monte Carlo Method to generate a set of simulations to the test the validity of the design a PKM provided that the probability density functions of a set of parameters describing the end effector motion are known. In order to illustrate this method its application to a specific problem is described. In particular the problem under investigation regards a 6-DoF PKM whose aim is to simulate the motion of a floater of a floating offshore wind turbine scale model during HIL simulations within the wind tunnel of Politecnico di Milano [4] as part of the Horizon 2020 project LIFES50+ [5]. The workspace and the first machine design are shown in Fig. 33.1. The maximum excitation frequency is set to 3 Hz.

E. Fiore (✉) • H. Giberti
Mechanical Engineering Department, Politecnico di Milano, Via La Masa 1, 20156 Milano, Italy
e-mail: enrico.fiore@polimi.it

J.M. Harvie, J. Baqersad (eds.), *Shock & Vibration, Aircraft/Aerospace, Energy Harvesting, Acoustics & Optics, Volume 9*,
Conference Proceedings of the Society for Experimental Mechanics Series, DOI 10.1007/978-3-319-54735-0_33

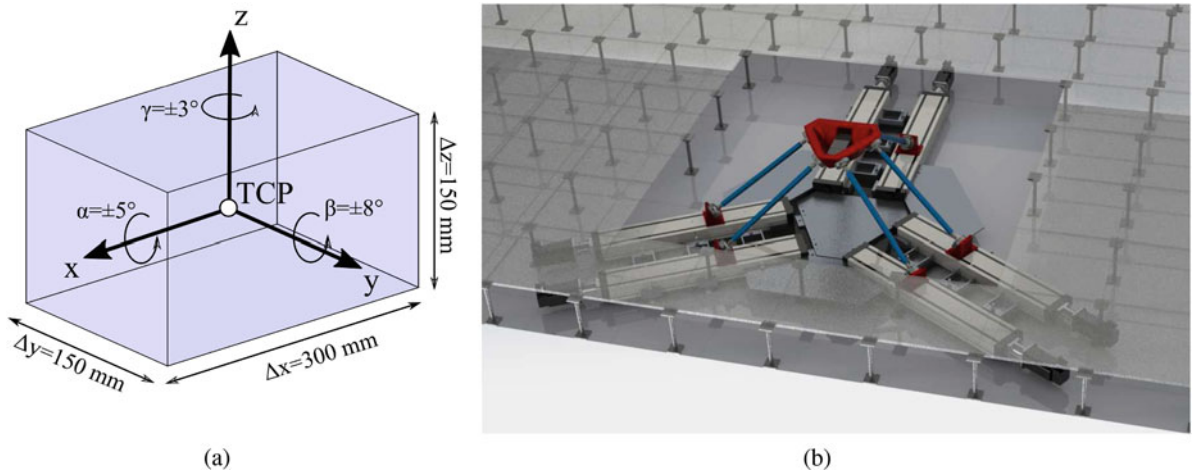

Fig. 33.1 Desired workspace and first machine design. (**a**) Workspace. (**b**) First machine design

The chosen parallel architecture is called Hexaslide, and belongs to the 6-PUS family. In order to test the stiffness of the robot a flexible multibody model has been realized using the software ADAMS. In particular, the components that are considered to be flexible are: the links, which are modeled as discrete flexible elements; the transmission units, which are modeled as elastic forces, neglecting their inertial contribution.

The following sections are organized as follow: Sect. 33.2 describes the inverse kinematics of the machine; Sect. 33.3 defines how the TCP motion are generated and how they are translated into the motions to be provided to the sliders during the dynamic analyses; Sect. 33.4 presents the flexible multibody model describing how all elements are modeled. Results are given in Sect. 33.5.

33.2 Hexaslide Kinematics

The Hexaslide robot is made of a mobile platform connected to six linear guides by means of six links of fixed length, so that six independent kinematic chains can be identified belonging to the PUS family. A detailed description of 6-DoF PUS PKMs is provided by Bonev in [6, 7]. The six linear guides are organized into three couples of parallel transmission units, each one out of phase by 120° with respect to the z axis.

Given the TCP position and the mobile platform orientation, $\Theta = \{\alpha, \beta, \gamma\}$, it is possible to find each slider position, q_i, by performing the inverse kinematics analysis. With reference to Fig. 33.2, for the ith kinematic chain it is possible to write:

$$\mathbf{l}_i = \mathbf{d}_i + q_i \hat{\mathbf{u}}_i \qquad \text{with} \qquad \mathbf{d}_i = \mathbf{p} + [R]\mathbf{b}'_i - \mathbf{s}_i \tag{33.1}$$

The [R] matrix is the rotational matrix used to switch from the mobile frame to the fixed one, and it is function of the platform orientation Θ. After some simple mathematical passages one gets:

$$q_i = \mathbf{d}_i^T \hat{\mathbf{u}}_i \pm \sqrt{\mathbf{d}_i^T (\hat{\mathbf{u}}_i \hat{\mathbf{u}}_i^T - [I])\mathbf{d}_i + l_i^2} \tag{33.2}$$

Once solved the inverse kinematics it is possible to find the relationship between the slider velocity and the velocity of the TCP. It can be shown that for the ith kinematic chain the following expression holds:

$$\hat{\mathbf{n}}_i^T \hat{\mathbf{u}}_i \dot{q}_i - [\hat{\mathbf{n}}_i^T \quad (\mathbf{b}_i \times \hat{\mathbf{n}}_i)^T]\mathbf{W} = 0 \tag{33.3}$$

where $\mathbf{W} = [\dot{x}, \dot{y}, \dot{z}, \omega_x, \omega_y, \omega_z]^T$ is a vector containing both the translational and angular components of TCP velocity. Considering all the six links the previous relationship can be expressed through the Jacobian matrix $[J]$ as:

$$\mathbf{W} = [J]\dot{\mathbf{q}} \tag{33.4}$$

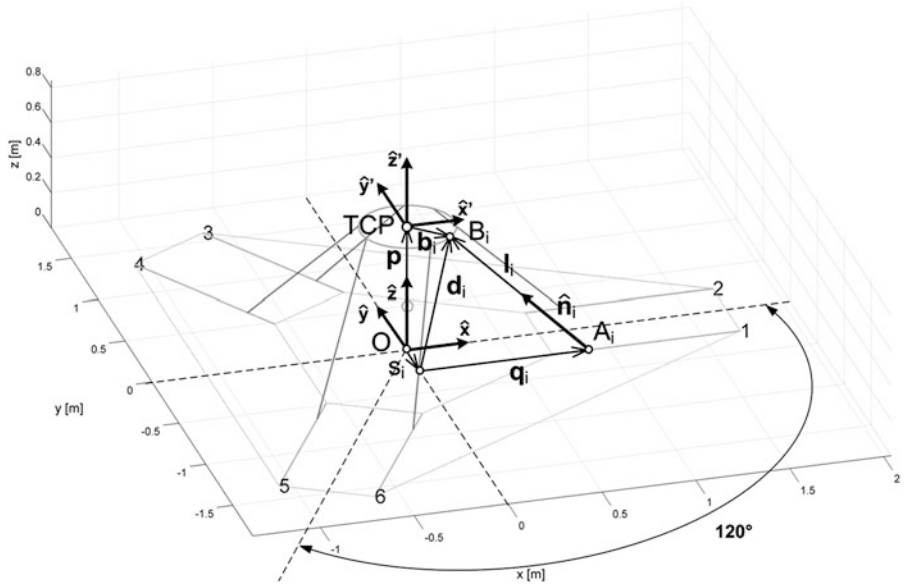

Fig. 33.2 Hexaslide kinematics

The Jacobian matrix represents the relationship between the sliders velocity and the TCP velocity. Under the hypothesis of small displacements it is possible to use the Jacobian matrix to relate the small variations of the sliders position to the variation of the robot pose as follows:

$$\Delta \mathbf{X} = [J]\Delta \mathbf{q} \tag{33.5}$$

This relationship allows to compute the TCP positioning error due to the linear units accuracy.

33.3 Motion Generation

According to [8–10] the wave motion can be expressed as a combination of six cosinusoidal motions, one for each displacement and angle describing the robot pose. The jth DoF of the machine can thus be described by the following equation:

$$j(t) = A_{0,j} + A_j \cos(2\pi f_j t + \phi_j) \qquad (\text{with } j = x, y, z, \alpha, \beta, \gamma) \tag{33.6}$$

where A_j is the amplitude of the cosinusoid, and f_j and ϕ_j the associated frequency and phase. It is important to notice that the characteristics of the machine strongly depend on its pose, and so it is necessary to consider the fact that the motion may not be centered around the center of the workspace; for this reason for each of the six DoFs the term $A_{0,j}$ is added, which represents an initial shift with respect to the workspace center. Thus each DoF is completely described by four parameters, for a total of 24 characterizing the overall TCP motion. In order to extract a statistical sample of possible simulations, it is first necessary to establish which are the PDFs of the four parameters. The adopted approach tends to be as general as possible, with only constraint of having a motion that is inscribed within the dimensions of the workspace. The four PDFs are:

- Initial position $A_{0,j}$: uniform distribution in the range between $-L_{wsd,j}$ and $+L_{wsd,j}$;
- Frequency f_j: uniform distribution in the range between 0 and 3 Hz;
- Phase ϕ_j: uniform distribution in the range between 0 and 2π rad;
- Amplitude A_j: the value associated with the amplitude must satisfy the relation $|A_{0,j} \pm A_j| < L_{wsd,j}$, where $L_{wsd,j}$ represents half of the total range of the jth DoF. The distribution of the amplitude is assumed to follow the Rayleigh distribution; there is no guarantee that the constraint on the limits of the workspace are respected, and thus all the simulations for which $|A_{0,j} \pm A_j|$ is greater than $L_{wsd,j}$ for at least one DoF are automatically excluded.

Once the PDFs are defined the 24 parameters are sampled and a set 1000 simulations is generated. Next step is the translation of the sinusoidal motions in correspondence of the TCP into the six time histories of the sliders displacements, which can be easily done solving the inverse kinematics problem. In this way, during the dynamic analyses it is possible to impose the motion directly the sliders motions and to measure the actual TCP position and orientation as a function of time to be compared with the ideal ones.

33.4 Multibody Model

Figure 33.3 shows the flexible multibody model of the robot. The model has been realized using ADAMS®. It is important to highlight that in order to handle the processes of importing the sliders time histories generated with the MCM and of exporting the resulting TCP measured motions, the model has been created using a macro. In addition macros are very useful when it comes to build models with a great amount of markers (triads) and with a particular orientation with respect to each other. Indeed by using it is possible to easily parametrize markers used to describe inertial properties of a body, to characterize a constraint, to apply a specific force, etc. For the model described here all markers are parametrized directly or indirectly with respect to the one in correspondence of the TCP. In this way by changing the pose of this marker, all elements belonging to the model are automatically rearranged in the new configuration. This process is important in order to avoid discontinuities at the first time step of each of the 1000 simulations.

Even if the platform has not been designed yet it is reasonable to assume that it can be regarded as a rigid structure. As a matter of fact it is possible to realize a very stiff element by means of a reticular structure. At the moment the platform is represented through a cylindrical shaped rigid body. The links are modeled using discrete beam elements, that is a sequence of rigid segments, each of them with its inertia properties, connected by means of force fields that simulate the sectional stresses arising in the beam section due to external loads. The relationship between the forces arising between two adjacent segments and their relative displacements is expressed as follows:

$$\begin{Bmatrix} F_x \\ F_y \\ F_z \\ T_x \\ T_y \\ T_z \end{Bmatrix} = - \begin{bmatrix} \frac{EA}{L} & 0 & 0 & 0 & 0 & 0 \\ 0 & 12\frac{EI_{zz}}{L^3} & 0 & 0 & 0 & -6\frac{EI_{zz}}{L^2} \\ 0 & 0 & 12\frac{EI_{yy}}{L^3} & 0 & 6\frac{EI_{yy}}{L^2} & 0 \\ 0 & 0 & 0 & \frac{GI_{xx}}{L} & 0 & 0 \\ 0 & 0 & 6\frac{EI_{yy}}{L^2} & 0 & 4\frac{EI_{yy}}{L} & 0 \\ 0 & -6\frac{EI_{zz}}{L^2} & 0 & 0 & 0 & 4\frac{EI_{zz}}{L} \end{bmatrix} \begin{Bmatrix} \Delta x \\ \Delta y \\ \Delta z \\ \Delta \phi_x \\ \Delta \phi_y \\ \Delta \phi_z \end{Bmatrix} \tag{33.7}$$

For each segment three different markers are created: one *center of mass marker* that defines the location of the center of mass of the corresponding marker and the orientation of its principal axes of inertia; two *force markers* whose aim is to define the position and orientation of their corresponding segment with respect to the previous and next ones. It's worth to

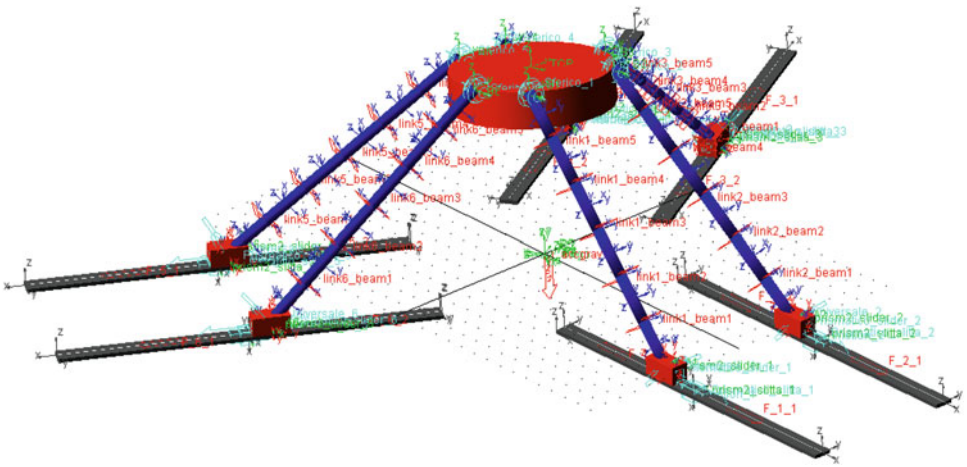

Fig. 33.3 Multibody model

notice that all these markers are parametrized with respect to those positioned at the two ends of each link. In turns these markers are parametrized with respect to the one representing the TCP so that by changing its location and orientation every single element in model is brought to the new configuration respecting the kinematics constraints.

As mentioned before the actuation of the Hexaslide is achieved through six linear transmission units. The choice is restricted to two different kinds of transmission unit: (1) belt-driven transmission units which are relatively cheap and present a quite low additional inertia but whose elasticity contributes to worsen the overall performances of the machine; (2) ball-screw transmission units that for sure are stiffer with respect to the previous mentioned belt-driven ones and moreover allow precise positioning and ensure a great efficiency; the main drawback of this kind of transmission unit is their great rotational inertia which means having bigger and so more expensive drive systems. The effect of the transmission unit is taken into account by means of 12 forces (2 for each slider) which are formulated as:

$$\begin{aligned} F_{belt,iA} &= -k_{eq,A}(\Delta\xi_{i,A} - \Delta\xi_{i,A0}) \\ F_{belt,iB} &= k_{eq,B}(\Delta\xi_{i,B} - \Delta\xi_{i,B0}) \end{aligned} \tag{33.8}$$

where $\Delta\xi_{i,A0}$ and $\Delta\xi_{i,B0}$ are the distance computed before each simulation between the ith slider and two points placed respectively 0.5 m ahead and 0.5 m behind it along its axis when the robot is in the home position configuration. $\Delta\xi_{i,A}$ and $\Delta\xi_{i,B}$ instead represent the instantaneous values of these quantities. Finally k_{eq} is an equivalent stiffness defined as:

$$k_{eq,A} = \frac{c_{spec}}{\Delta\xi_{i,A0}} \quad \text{and} \quad k_{eq,B} = \frac{c_{spec}}{\Delta\xi_{i,B0}} \tag{33.9}$$

The c_{spec} constant represents the product of an equivalent Young's modulus, which takes into account the various materials transmission unit is made of, and an equivalent section area. The goal of this paper is not to consider effects like friction and backlashes, for this reason the model presented here takes into account only the effect related to the flexibility. More informations about non ideal transmission units and about control system aimed at reducing their effect can be found in [11].

33.5 Results

Figure 33.4 shows the distribution of the mean error recorded for each of the six DoFs along the 1000 simulations. It is evident that the BDTU causes a worsening of the behavior of the robot. In particular the most affected DoFs are the roll α and pitch β. In Fig. 33.5 are reported the two spectra of the α and β for the two simulations in which the maximum mean error is recorded. In both figures, for the case with belt driven transmission units, it is evident a peak around 12–13 Hz which is supposed to be associated to the first mode of vibration of the structure. Following the approach described in [12], the frequency associated to the first mode of vibration is mapped in order to see how its value changes according to the pose of the robot. Maps are shown in Fig. 33.6, and in particular those related to the ball-screw transmission units show that the value of the frequency associated to the first mode of vibration is comparable to the one found in Fig. 33.5, demonstrating that the distortion in the signals is related to the first mode of vibration of the robot.

33.6 Conclusions

This paper presents a new methodology to assess the behavior of a 6-DoF PKM. The multibody model of the robot is presented and the results of the analyses performed on the model are shown. The obtained results put in evidence the validity of the method and the ability to forecast the presence of critical areas within the workspace. The described method can be easily generalized and applied to any complex system characterized by non linear kinematic relationships, provided the PDFs of the characteristic parameters describing the motion of the system are known. The statistical approach can also be used to size the motor-reducer group using the approach described in [13–16].

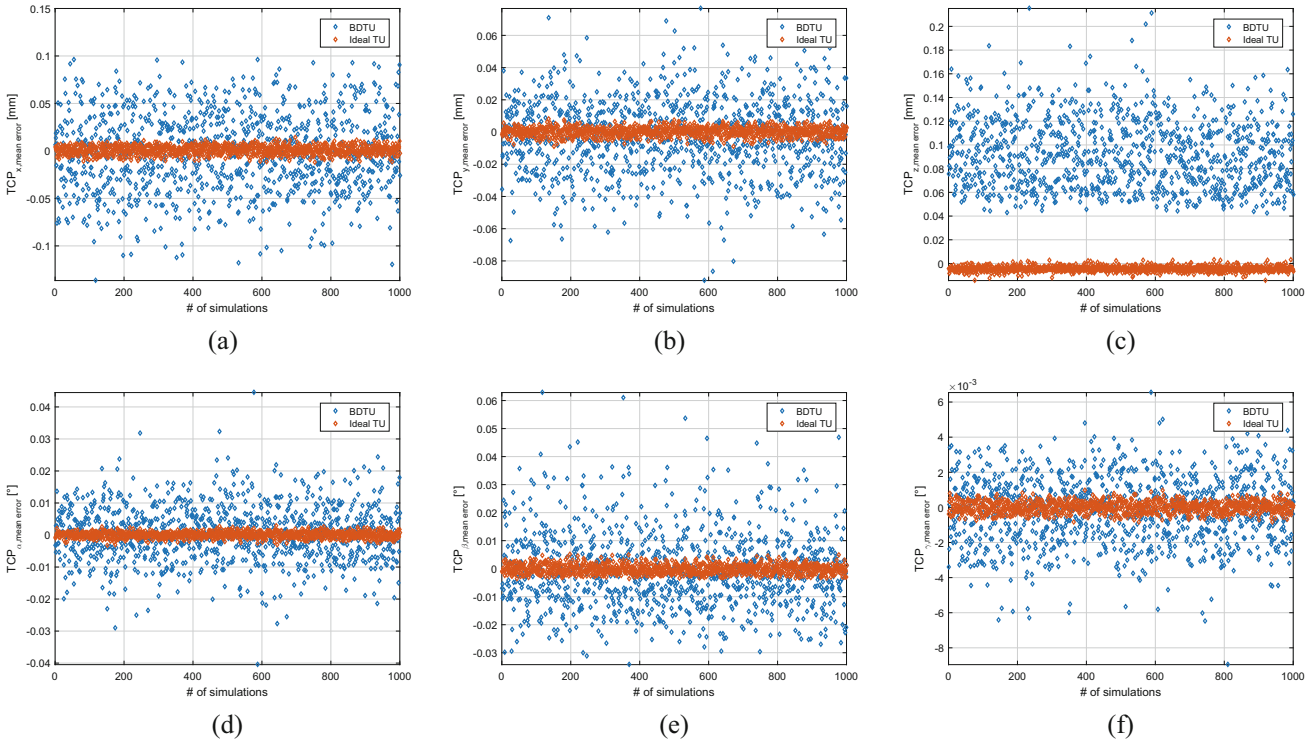

Fig. 33.4 Mean error distribution along all 1000 simulation for the BDTUs (*blue*) and BSTUs (*red*). (**a**) TCP x displacement mean error. (**b**) TCP y displacement mean error. (**c**) TCP z displacement mean error. (**d**) TCP α mean error. (**e**) TCP β mean error. (**f**) TCP γ mean error

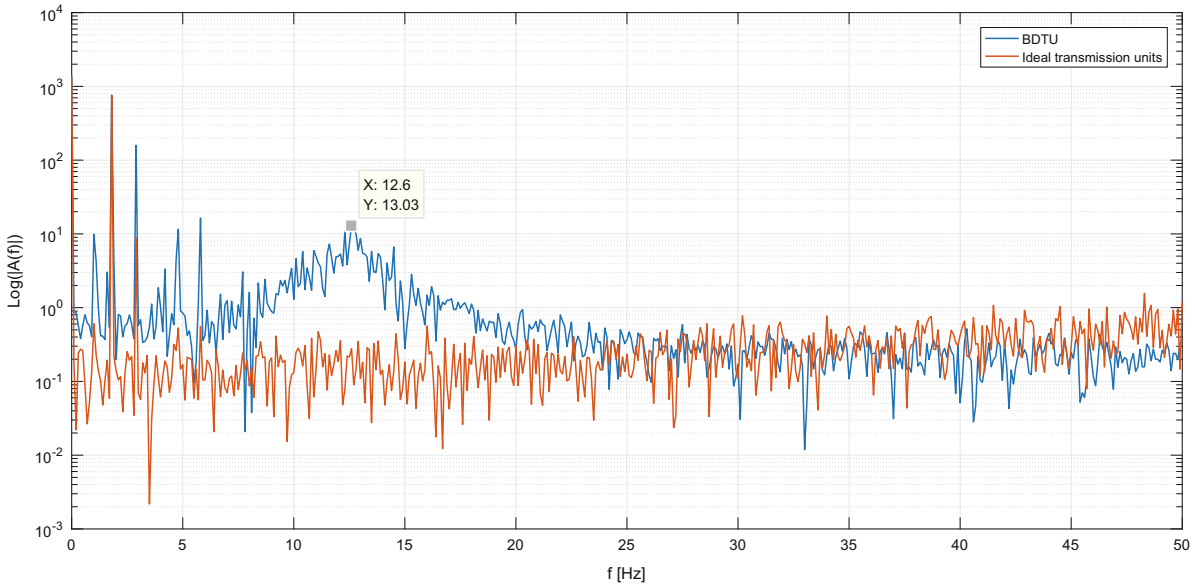

(a)

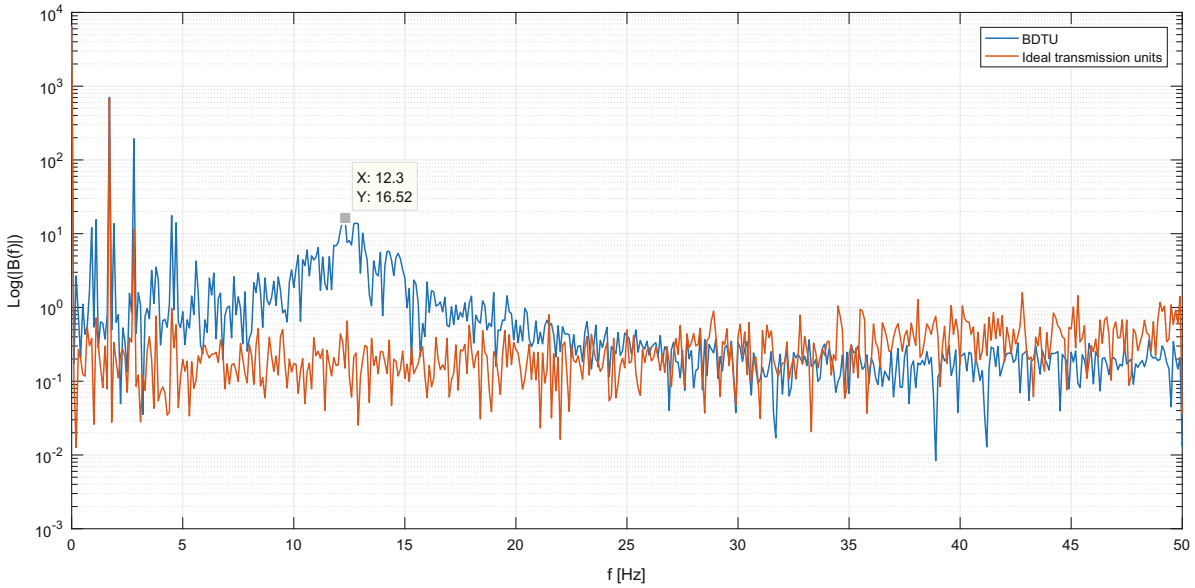

(b)

Fig. 33.5 Spectra of α and β during the two simulations in which their mean error is maximum: BDTU in *blue* and BSTU in *red*. (**a**) α spectrum during the simulation in which its maximum mean error is recorded. (**b**) β spectrum during the simulation in which its maximum mean error is recorded

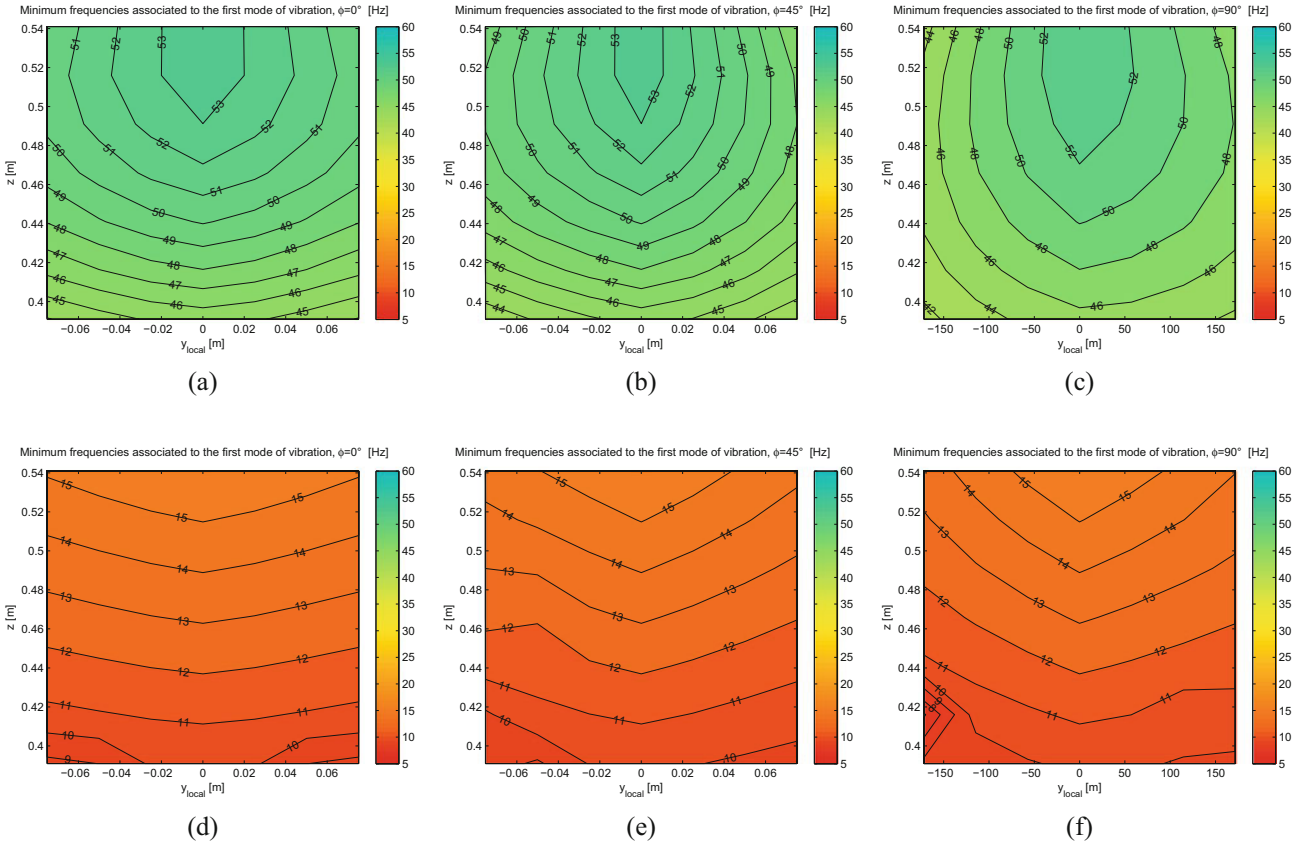

Fig. 33.6 Maps of the frequency associated to the first mode of vibration of the system expressed in [Hz] for ideal transmission units (*left column*) and for belt-driven transmission units (*right column*). (**a**) $\varphi = 0°$ plane, with ball-screw transmission units. (**b**) $\varphi = 0°$ plane, with ball-screw transmission units. (**c**) $\varphi = 45°$ plane, with ball-screw transmission units. (**d**) $\varphi = 45°$ plane, with belt-driven transmission units. (**e**) $\varphi = 90°$ plane, with belt-driven transmission units. (**f**) $\varphi = 90°$ plane, with belt-driven transmission units

References

1. Ferrari, D., Giberti, H.: A genetic algorithm approach to the kinematic synthesis of a 6-DoF parallel manipulator. In: IEEE Multi-Conference on Systems and Control, Antibes, 8–10 October 2014
2. Cinquemani, S., Ferrari, D.: A genetic algorithm optimization for independent modal space control technique. In: IEEE Multi-Conference on Systems and Control, Antibes, 8–10 October 2014
3. Merlet, J.P.: Parallel Robots, 2nd edn. Springer, Berlin (2006)
4. Bayati, I., Belloli, M., Ferrari, D., Fossati, F., Giberti, H.: Design of a 6-DoF robotic platform for wind tunnel tests of floating wind turbines. Energy Procedia J. **53**, 313–323 (2014)
5. H2020 LIFES50+ project: http://lifes50plus.eu/
6. Bonev, I.A.: Analysis and design of a 6-DOF 6-PRRS parallel manipulators? M.Sc. thesis, GIST (1998)
7. Bonev, I.A.: A geometrical method for computing the constant-orientation workspace of 6-PRRS parallel manipulators? Mech. Mach. Theory **36**, 1–13 (2001)
8. Longuet-Higgins, M.S.: On the statistical distribution of the height of sea waves. J. Mar. Res. **11**(3), 245–266 (1952)
9. Longuet-Higgins, M.S.: The statistical analysis of a random moving surface. Philos. Trans. R. Soc. Lond. A **249**, 321–387 (1957)
10. Xu, D., Li, X., Zhang, L., Hu, N., Lu, H.: On the distributions of wave periods, wavelengths, and amplitudes in a random wave field. J. Geophys. Res. **109**, C05016 (2004). doi:10.1029/2003JC002073
11. Negahbani, N., Giberti, H., Fiore, E.: Error analysis and adaptive-robust control of a 6-DoF parallel robot with ball-screw drive actuators. J. Robot. **2016**, 15 (2016). doi:10.1155/2016/4938562
12. Fiore, E., Giberti, H., Ferrari, D.: Dynamics modeling and accuracy evaluation of a 6-DoF hexaslide robot. In: Proceedings of the 33rd IMAC, pp. 473–479 (2015)
13. Giberti H., Ferrari D.: Drive system sizing of a 6-DoF parallel robotic platform. In: Proceedings of ASME 12th Biennial Conference on Engineering Systems Design and Analysis, ESDA2014, Copenhagen, 25–27 June 2014

14. Giberti, H., Cinquemani, S., Legnani, G.: A practical approach to the selection of the motor-reducer unit in electric drive systems. Mech. Based Des. Struct. Mach. **39**(3), 303–319 (2011)
15. Giberti, H., Cinquemani, S., Legnani, G.: Effects of transmission mechanical characteristics on the choice of a motor-reducer. Mechatronics **20**, 604–610 (2010)
16. Giberti, H., Clerici, A., Cinquemani, S.: Specific accelerating factor: one more tool in motor sizing projects. Mechatronics **24**(7), 898–905 (2014)

Chapter 34
Equating Severity in Qualification Testing

M. Prisbrey, J. Senecal, M. Sethi, C. Haynes, and S. Taylor

Abstract Understanding how damage progresses in engineering materials is of the utmost importance for ensuring safety and reliability. Mechanical components and structures must often perform safely and reliably for much longer than can be reasonably tested, or the components must operate in severe environments that are difficult to reproduce. The capability to perform real-time, real-scenario testing is not always present or attainable however, and failure to adequately test components can lead to catastrophic consequences or high preventative-maintenance costs resulting from the use of weaker presumptive models. As a solution, a criterion for ductile metals for equating high-stress single shock damage, to periodic, low-stress, multiple shock damage is presented. The correspondence in damage, exhibited as an equivalency in deformation, is derived and experimentally validated. To accomplish this process, we relate the plastic deformation a test coupon experiences under a shock input, to the shock parameters under both single shock and multiple shock regimes. We then compare the proposed theoretical damage model against the experimental data.

Keywords Qualification • Testing • Severity • Shock • Damage

34.1 Introduction

Many times in system qualification testing, it is necessary to perform testing under conditions that either do not reproduce the stress or the duration of the service environment. When the time available for testing is much less than the service lifetime, often the stress level of the test is increased in order to achieve an equivalence in damage. When it is not possible to reach the level of stress that a system will experience in service, a common approach is to use a shock response spectrum to generate an alternative shock waveform that the test apparatus is capable of producing. However, the SRS approach is a demonstrably inadequate means of equating the severity of shock environments, and there is no widely accepted alternative.

In this work we develop a model to equate high mechanical input, single-shock damage, to lower mechanical input, multiple shock damage, for 18-8 stainless steel test coupons. The relationship between single-shock and multiple shock damage is based on the concept of damage accumulation, originally developed by Palmgren and Miner [1]. Miner's rule states that a number of cycles at a given stress level consumes a proportion of the life of a mechanical component [2]. In keeping with the Palmgren-Miner damage accumulation theory, a large number of shocks at a low input level should accumulate until a mechanical component fails. It follows then, that a certain, smaller number of shocks at a high input level should accumulate damage and be equivalent to a larger number of shocks at a low input level.

We developed the damage equivalence model using damped sine acceleration inputs, with varied peak amplitudes. We then tested acceleration inputs with added random frequency content at two different severity levels, to demonstrate that the model developed using damped sine acceleration inputs is capable of withstanding a degree of randomness and uncertainty in shock inputs.

M. Prisbrey
Department of Mechanical Engineering, University of Utah, 201 Presidents Cir, Salt Lake City, UT 84119, USA

J. Senecal
Department of Mechanical Engineering, Montana State University, 211 Montana Hall, Bozeman, MT 59717, USA

M. Sethi
Department of Mechanical Engineering, Olin College of Engineering, 1000 Olin Way, Needham, MA 02492, USA

C. Haynes (✉) • S. Taylor
Los Alamos National Laboratory, PO Box 1663, Los Alamos, NM 87545, USA
e-mail: cmhaynes@lanl.gov

J.M. Harvie, J. Baqersad (eds.), *Shock & Vibration, Aircraft/Aerospace, Energy Harvesting, Acoustics & Optics, Volume 9*,
Conference Proceedings of the Society for Experimental Mechanics Series, DOI 10.1007/978-3-319-54735-0_34

34.2 Methodology

Shocks are applied to a cantilever beam with a tip mass, by way of a base acceleration produced by an electrodynamic shaker. An illustration of the experimental set-up can be found in Fig. 34.1. In this study, consumer-off-the-shelf key stock with a 0.16 cm^2 cross sectional area, and a length of 13.5 cm was used for the cantilever beam. Post-machining of the standard part was required to produce the required test coupon length, and to create a notch in the test coupon to seed failure.

In order to relate a number of shocks at a given severity level, we must first define the severity level seen by the test coupon.

The known value is the base excitation, a_{base}, delivered to the electrodynamic shaker. The acceleration of the tip of the beam, $a_{beam\ tip}$ can then be calculated through the transfer function,

$$a_{beam\ tip} = a_{base} * \sqrt{\frac{1 + (2\varsigma\rho)^2}{(1-\rho^2)^2 + (2\varsigma\rho)^2}}, \tag{34.1}$$

where $\rho = \frac{f}{f_n}$, is the ratio between input frequency, f and natural frequency, f_n of the beam, and ς is the damping ratio of the beam. Force at the tip of the beam can then be calculated as

$$F_{tip} = ma_{coupon\ tip}, \tag{34.2}$$

where m is the tip mass on the beam. The moment produced at the notch in the test coupon is equal to

$$\tau_{notch} = F_{tip}L_{beam}, \tag{34.3}$$

where L_{beam} is the length from the notch to the tip mass. Now bending stress can be calculated as

$$\sigma_{notch} = \frac{\tau_{notch}c}{I}, \tag{34.4}$$

where $c = h_{notch}/2$ and I is the moment of inertia of the test coupon cross-section, at the notch. Severity, S is then defined as

$$S = \frac{\sigma_{notch}}{\sigma_Y}, \tag{34.5}$$

where σ_Y is the material yield stress.

We derived the relationship between severity and number of shocks required to achieve an equivalent level of damage using damped sine inputs with constant frequency content. Shock profiles observed during previous testing procedures provided the basis for this choice. The previous test consisted of striking a portal frame structure with an impact hammer, using four hammer tips of different hardness levels and then recording the acceleration response due to striking the portal frame in six different locations. In one case where the base of the portal frame was clamped to a rigid structure, and in another case where the portal frame was resting unclamped, making for 48 unique cases. The acceleration response of the portal frame from 100 strikes were recorded at two different locations resulting in 200 acceleration response time histories.

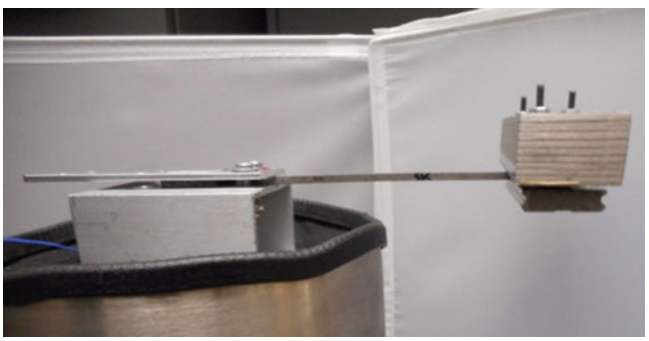

Fig. 34.1 Cantilever beam experimental setup. The electrodynamic shaker produces base accelerations

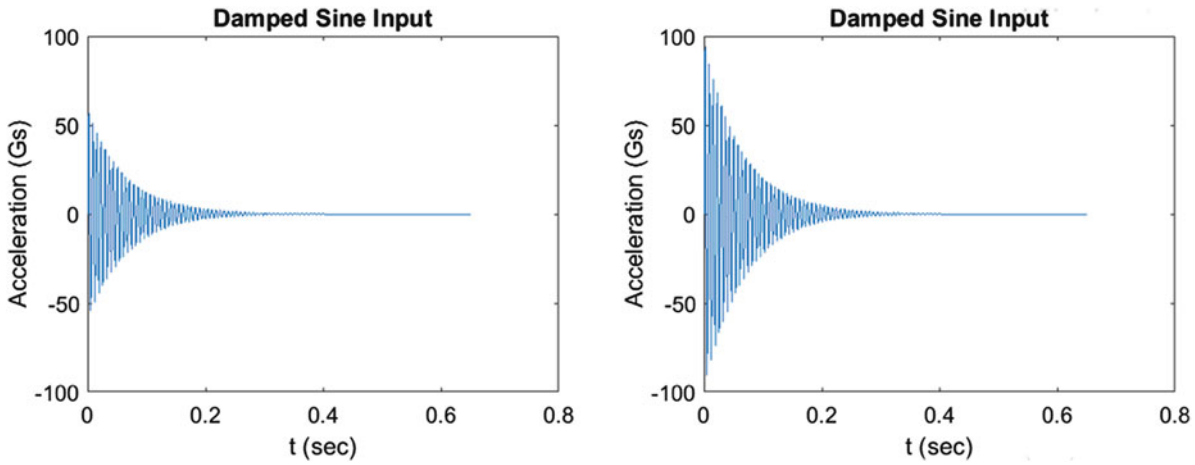

Fig. 34.2 Damped sine inputs at two different severity levels

The findings from that study, showed that the resultant response of the structure took on the general appearance of a damped sine wave with randomized frequency content. In an effort to ensure consistency in the shocks applied to the test coupons, we subjected each test coupon to a damped sine wave with known peak acceleration and constant frequency content.

To determine if an equivalent damage model—developed using the derived severity criteria, and consistent damped sine waves—is capable of being extended to shocks with random frequency content, we tested additional components using the same experimental procedure. However, the damped sine wave shock input was replaced with a more realistic shock input that is derived from the empirical data collected from the response of the aforementioned portal frame.

We created these realistic shock inputs using a Karhunen-Loeve Expansion (KLE) which uses a centered, mean-square, continuous stochastic process to condense the time samples of the collected acceleration response from the frame into a single signal, with the introduction of random frequency content to each signal created. Henceforth, these inputs will be referred to as KLE realizations. In order to isolate the randomness of the signal as the only discrepancy between the KLE realizations and classic damped sine, each KLE realization was standardized to have identical peak acceleration, time duration, and bulk frequency content as its classic damped sine input counterpart.

We kept the characteristics of the input excitation constant across the frequency domain, as well as the damping ratio, leaving only maximum amplitude as the independent metric for adjusting the severity of the input shock. Figure 34.2 displays damped sine inputs at two different severity levels. While Fig. 34.3 illustrates the difference in frequency content between the damped sine and KLE waveforms.

34.3 Procedure

Using an electrodynamic shaker, we input a shock to the base of the cantilever beam test coupon and record the resultant deflection as an angle relative to the horizontal plane (i.e. parallel with the ground). This process was repeated with the same coupon until the cumulative deflection reached 15°, as seen in Fig. 34.4, measured using a protractor held on the top surface of the electrodynamic shaker table. We chose a maximum deflection of 15° because the physical constraints of the experimental setup did not allow for further deflection. We tested ten specimens in this fashion, keeping the amplitude and frequency of the shock constant. We continued with this testing procedure while adjusting the peak acceleration of the input shocks, in order to vary the severity level of the tests. We performed a sweep across peak accelerations from 30 Gs to 100 Gs in intervals of 5 Gs. In total, we tested 76 specimens under the damped sine shock regime.

After the completion of these tests we conducted additional tests in the same fashion using KLE realizations as the shock input for two severity levels, 1.43 and 2.00, as defined in Eq. (34.5).

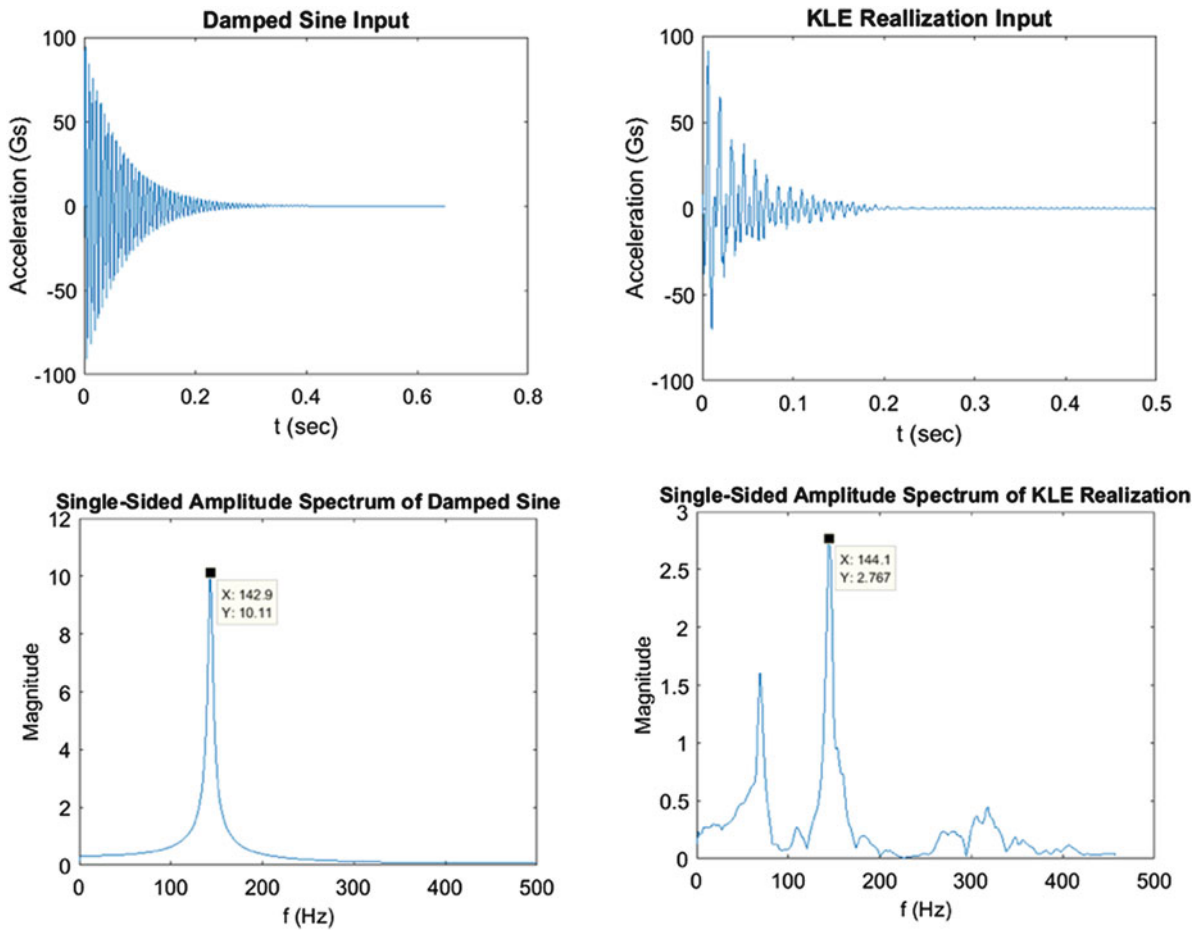

Fig. 34.3 Comparison of the frequency content present in the damped sine and KLE waveforms

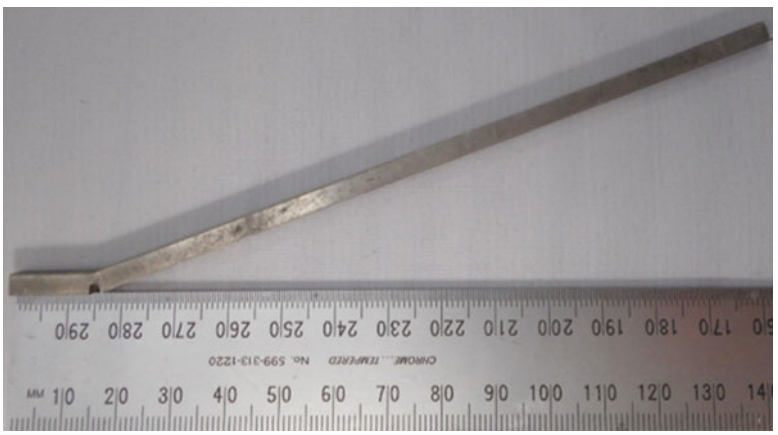

Fig. 34.4 Test coupon post-testing showing angle of deflection used as metric for damage

34.4 Results

Figure 34.5 shows the average severity S, on the x-axis versus average number of shocks N, on the y-axis to achieve 15 degrees of deflection. The trend line (red) is fit to the damped sine data points (blue circles) as an inverse power law, using a least squares fit. The 90% LCL (yellow) gives the number of shocks required at a given severity level in order to be 90% confident that a component has accumulated the same amount of damage as a component subjected to a different severity level.

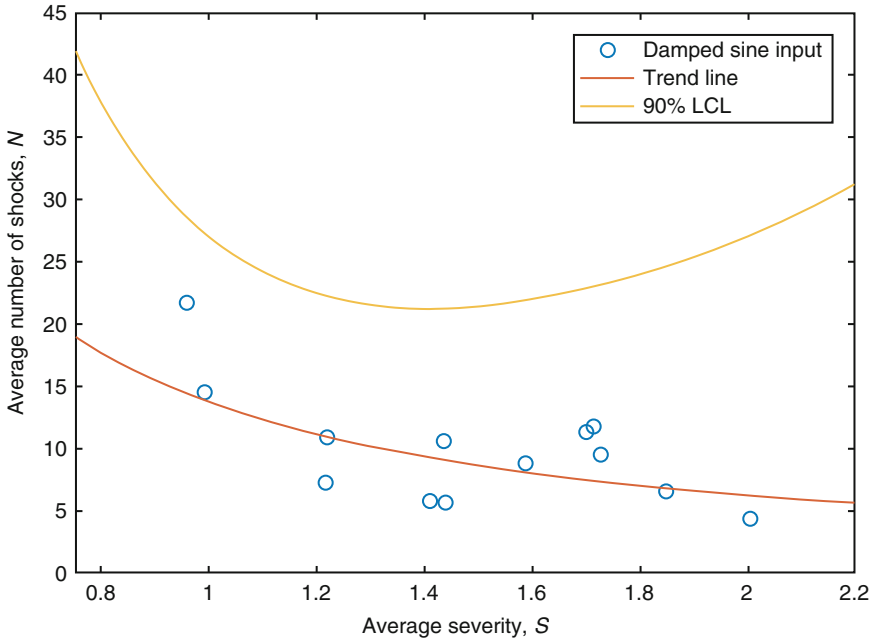

Fig. 34.5 Showing average severity, S vs. average number of shocks, N to reach 15 degrees of deflection consisting of the damped sine input (*blue circles*), trend line (*red*) of the damped sine input, and the 90% lower confidence line (LCL) (*yellow*)

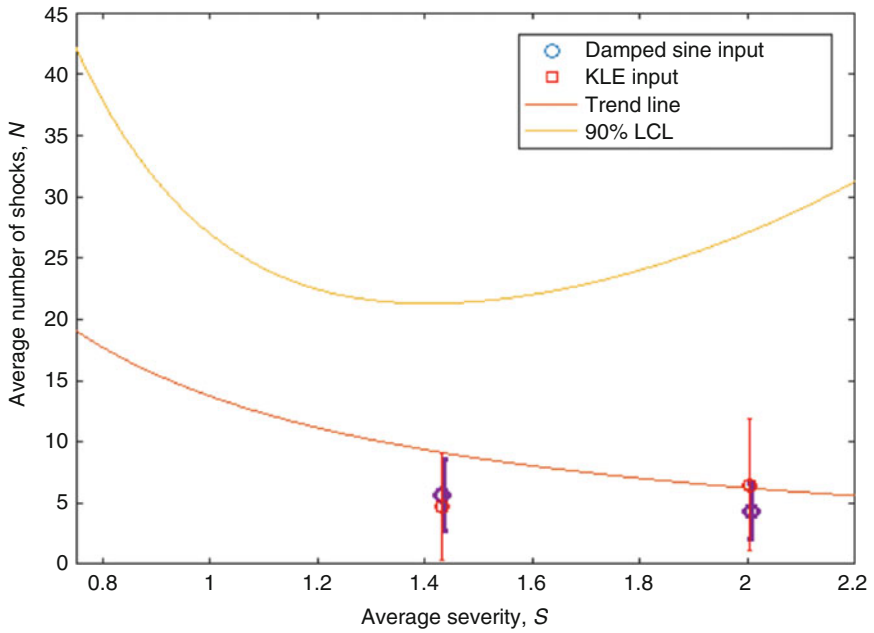

Fig. 34.6 Showing average severity, S vs. average number of shocks, N to reach 15 degrees of deflection consisting of the damped sine input (blue circles) and KLE input (red squares) with symmetric error bars, trend line, and 90% LCL

Figure 34.6 shows the average severity, S on the x-axis vs. average number of shocks, N on the y-axis to achieve 15 degrees of deflection at two severity levels, 1.43 and 2.00, consisting of the damped sine input (blue circles) and KLE input (red squares), with blue and red symmetric error bars respectively. The error bars represent one standard deviation away from the mean number of shocks. We qualitatively observe good agreement between the damped sine and KLE inputs. Additionally, we conducted a mean comparison, two-tailed t-test, to determine the significance of the difference between the two data sets with a null and alternative hypothesis for both severity levels:

$$\mathrm{H_o} : \mu_{KLE} = \mu_{DS} \tag{34.6}$$

$$H_1 : \mu_{KLE} \neq \mu_{DS} \tag{34.7}$$

where μ_{KLE} and μ_{DS} are the mean number of shocks to reach 15 degrees of deflection at the two tested severity levels for the KLE and damped sine inputs, respectively. At $S = 1.43$ and $S = 2.00$ we observe p-values of 0.354 and 0.141, respectively. With a significance level of $\alpha = 0.05$ we reject our alternative hypothesis and conclude that the difference between the mean number of shocks using a KLE and a damped sine input to achieve 15 degrees of deflection is statistically insignificant. Limitations come in the form of high margins for a 90% confidence interval largely resulting from uncertainty caused by small sample sizes. Although nearly 100 coupons were tested, the results suggest that additional test points will be needed to tighten the confidence interval margin. Additionally, variations in the coupon length, notch depth, and cross-sectional area were not taken into consideration in this study, which could lead to inaccuracies in the calculations for severity, based on Eq. (34.5). The widening margin between the trend line and the 90% LCL at lower and higher severity levels is a result of the lower number of samples tested at these levels. Furthermore, the coupons were machined using hand tools, contributing to a higher than desired level of variance of the test coupon length and notch depth.

34.5 Conclusion

The current state of test engineering does not use a standard for equating damage across parameters, and much of the emerging work in this field is limited to studies in cyclical continuous damage. This look at discrete shock damage accumulation provides a viable approach to creating a cumulative damage equivalency model. Using simplified shock profiles, i.e. using damped sine accelerations in place of more realistic shock profiles, we demonstrated that a damage equivalency model can be developed which can then be applied to more realistic shock profiles with reasonable accuracy.

34.6 Future Work

In order to overcome the limitation of the large confidence interval margin, future iterations of this study would include testing a larger number of coupons across the spectrum of severity levels. Additionally, to ensure a more accurate calculation of the severity, S, the test coupons used would need to be manufactured using more precise machining methods and any variation in coupon dimensions would need to be accounted for.

Alternate perspectives on this study may focus on observing the differences in equating severity between coupons prepared through traditional manufacturing methods, as was the case in this study, and those prepared using additive manufacturing due to the unexplored differences in material properties.

Acknowledgments This work is approved for public release and distribution is unlimited under LA-UR-16-28258. This project was funded through the Los Alamos Dynamics Summer School program of the Los Alamos National Laboratory under the direction of Charles Farrar.

References

1. Fatemi, A., Yang, L.: Cumulative fatigue damage and life prediction theories: a survey of the state of the art for homogeneous materials. Int. J. Fatigue. **20**(1), 9–34 (1998)
2. Miner, M.A.: Cumulative damage in fatigue. J. Appl. Mech. **67**, AI59–AI64 (1945)

Chapter 35
Design of an Assembly for Nonlinear Vibration Reduction

P. Butaud and G. Chevallier

Abstract The lightness of the space and aerospace structures causes their vulnerability to vibrations. The cold temperatures do not allow using polymer materials. Active and semi-active control using piezos embedded on the structure can be used efficiently instead of polymers but they induce energy consumption. Friction damping is less efficient but it does not depend on temperature and it is energetically passive. Unfortunately its efficiency depends on the vibration amplitude as well as on the tightening force. The damping is very low for the lowest amplitudes and the largest tightening loads and increase up to an optimal value. This optimum damping is adjustable thanks to the tightening force. The purpose of our work is to evaluate the efficiency of the control of the tightening force in bolted joints to reduce the vibration of the assembled structure. In the first part, we present a original setup and a very detailed design of experiments that highlights the optimal sets of parameter in order to get a good control of the vibrations according to the frequency and the magnitude of the load. To conclude, we propose to share experimental data with the attendees for further discussions.

Keywords Assembly • Lapjoint • Nonlinear • Experimental • Dynamic

35.1 Introduction

The modeling and the prediction of vibration damping remains a great challenge because the physical phenomena involved in energy dissipation are not very well known. The damping might be induced through several common ways such as viscoelastic materials, pressure loss in fluids or solid friction. The latter remains badly modeled, whereas the joints, such as welded points, bolted joints or rivets, are widely used to link the parts of the mechanisms and the structures.

Among all the studies that focus on friction-damping, it is commonplace to separate the works that highlight energy dissipations coming from macro-sliding, and micro-sliding. In the first category, the damping is due to long-scale friction zones, see Berthillier et al. [3] or Poudou et al. [16] for instance. In this case, simulations and tests are easy to perform because the contact region is generally well-localized and the slipping occurs all over the contact area. In the second case, the damping comes from partial sliding between the parts. Thus the effective contact region is generally badly known and stick-slip-separation in the interfaces is commonplace. It was shown experimentally by many authors (Goodman et al. [9], Beards et al. [2], Pian [15], Ungar [20]) that, in turn, the modal damping and the eigenfrequencies are strongly dependent to the vibration amplitudes. This is due to the pressure and the shear stress variations. This leads to difficulties in modelling this case, see Festjens et al. [7] and Caignot et al. [4]. In simulations, geometrical defects and loading trajectories have to be carefully taken into account. To avoid this difficulty, it is also possible to measure and identify meta-models, see Festjens et al. [8], on specifically designed test-benches. Several testing devices have been designed in order to achieve this goal Fig. 35.1. The advantages of most of the experimental setups, according to their design properties and their experimental process, were exposed in Dion et al. [5]. Special attention has been payed to the coupling between tangential and normal loads in the joints because this coupling makes the experiments quite hard to perform, as the limit of sliding is depending on the normal load dynamics. Each of these experimental configurations had been tested with specific excitation devices and excitation signals. There are several experimental ways to highlight non-linear effects such as amplitude-dependent eigenfrequencies and damping, which are very commonplace for friction dampers. Many works are based on steady-state analysis in order to build Frequency Response Functions (FRF), [1, 2, 6] to estimate the Energy Loss (EL), through the frequency bandwidth or the quality factor of each modes. EL can also be estimated through quasi-static analysis [1, 9, 12]. In this case, the

P. Butaud (✉) • G. Chevallier
Department of Applied Mechanics, Univ. Bourgogne Franche-Comté, FEMTO-ST Institute, CNRS/UFC/ENSMM/UTBM, 25000 Besancon, France
e-mail: pauline.butaud@univ-fcomte.fr

J.M. Harvie, J. Baqersad (eds.), *Shock & Vibration, Aircraft/Aerospace, Energy Harvesting, Acoustics & Optics, Volume 9*, Conference Proceedings of the Society for Experimental Mechanics Series, DOI 10.1007/978-3-319-54735-0_35

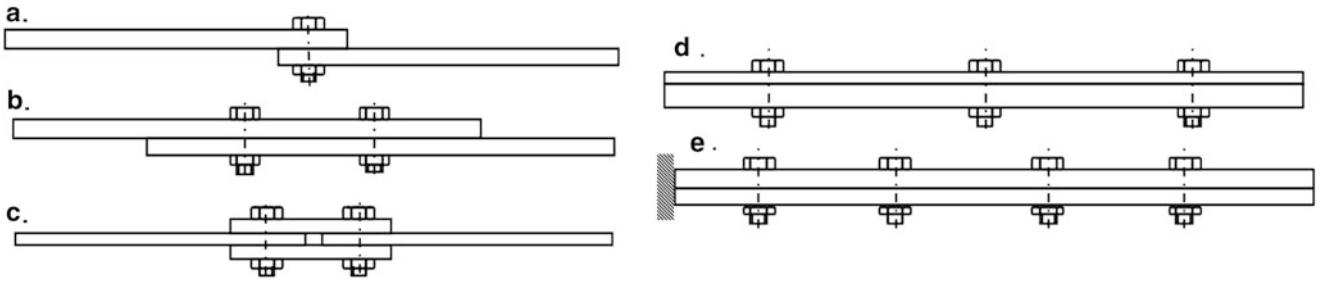

Fig. 35.1 Examples of testing devices developed to highlight friction induced damping in joints. (**a**) Beam assembly with a single bolted joint from Ahmadian et al. [1]. (**b**) Beam assembly with two bolted joints from Metherell et al. [12] or Esteban et al. [6]. (**c**) Beam assembly symmetrically screwed with two bolted joints from Song et al. [19]. (**d**) beam assembly with distributed bolted joints in free conditions from Heller et al. [10, 11]. (**e**) beam assembly with distributed bolted joints in clamped-free conditions from Goodman et al. [9], Nanda et al. [13, 14]

objective is to build energy ratios for various loading trajectories. This experimental procedure is very close to the procedure performed with Dynamic Mechanical Analyzer (DMA) for viscoelastic properties identification. Transient analysis can also be performed: the classical approach is to excite the structure with an impact hammer [17]. A more original approach is to obtain free-decay response by disconnecting the sine-excitation device to the structure since a steady-state response very close to the modal response was obtained [10, 19]. This procedure is called *stop-sine*. It allows to get the so-called *backbones* of the system; that is to say, the amplitude-dependence of the natural frequency and the modal damping.

The new setup presented in this paper is composed of two thin beams linked by three bolted joints. Contact patches have been added to each contact area in order to ensure the contact localization. This make this experience robust compared to previous ones. Among the three bolted connexions, one is dedicated to the stiffness function, the two others are dedicated to energy dissipation. Thus, this new setup is a functionalized assembly that allows to manage these two important parameters of a dynamic device. Few years ago, Sandia Institute proposed a benchmark that involves two thick beams also linked by three bolted joints [18]. Compared with Sandia's one, this new setup aims to complete the knowledge on assembly dynamics with a new academic configuration. The paper is organized as follow: we first present the setup, then we present results under random and harmonic excitation.

35.2 Experimental Setup

The benchmark designed in this work is an assembly of two beams with the following dimensions $200 \times 30 \times 1.7$ mm. The beams are linked together by three M4 screws spaced of 15 mm. In order to avoid uncertainties on the contact area, there are contact patches under each screw with an extra thickness of 0.3 mm and a square of 12 mm^2 for external screws and 18 mm^2 for the central screw (Fig. 35.2a). A washer is placed under each screw and nut each. The tightness applied on the external screws is 10, 40 or 80 cNm, to observe its influence on the structure response. The tightness of the central screw is constant during the tests, this screw ensures the stiffness of the assembly, the tightening torque applied is 80 cNm. The tightening torque is obtained with a torque wrench and is checked during the experiment thanks to the instrumentation of the screw (strain gauges in the screw head).

The structure is clamped on one side (Fig. 35.2b). In order to be as close as possible to a perfect clamp, a length 30 mm is screwed into a heavy steel block. The assembly is excited next to the clamp by a electromagnetic shaker model K2004E01 from the modalshop. Two excitations signals have been used: a frequency-controlled white noise between 20 and 2000 Hz and a step-sine varying between 900 and 1100 Hz. In order to highlight the non-linear behavior of the structure, the excitation amplitude varies between [100–500] mV in white noise and [10–500] mV for harmonic test.

The measurement are made using PSV-500 scanning laser 3D vibrometer from Polytec, its working distance is between 125 mm and 100 m, its minimum resolution is of 10 nm per second per square root of frequency. The structure is scanned on 118 points during the random excitation and on 92 points for the harmonic tests. The acquisition is repeated six times and averaged in order to build the H1 estimator of the Frequency Response Function between the excitation signal and the measured velocity. The results presented in next sections are the FRF RMS velocity.

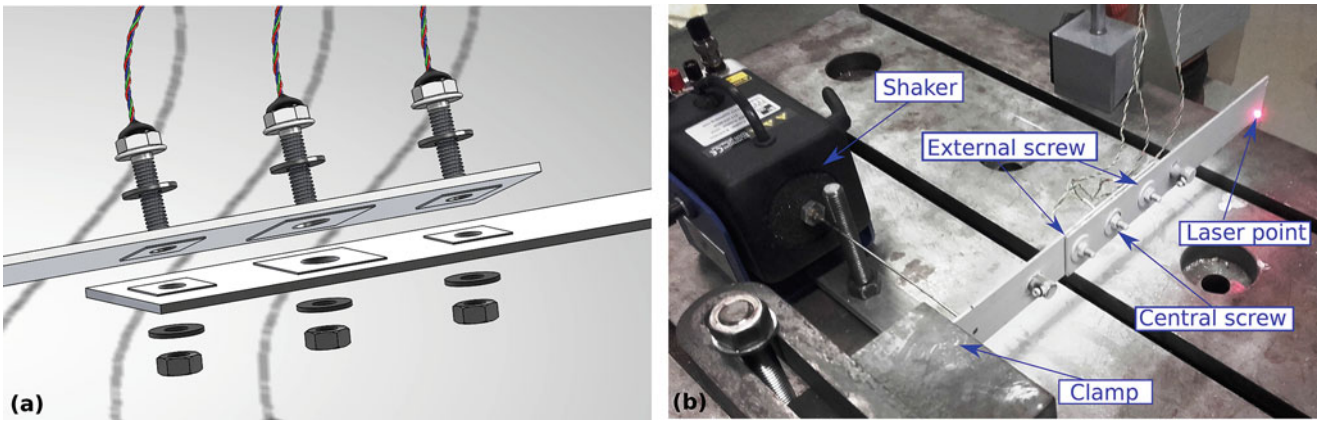

Fig. 35.2 (**a**) Lapjoint CAO. (**b**) Experimental setup

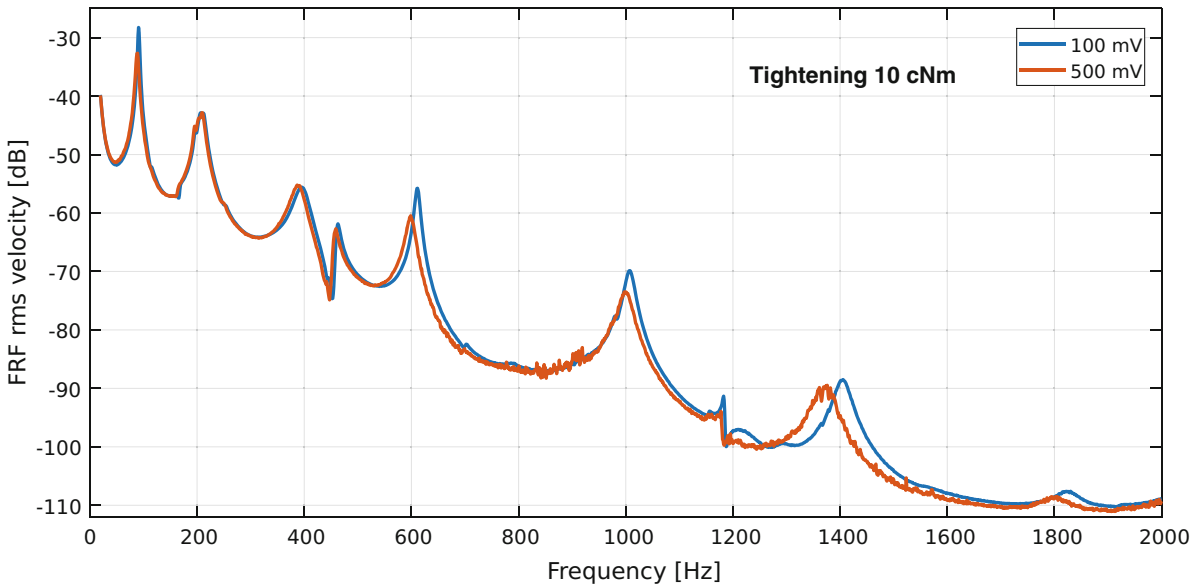

Fig. 35.3 Influence of the excitation amplitude, at 10 cNm of tightness degree, for a random excitation of white noise type between [20–2000] Hz

35.3 Results

35.3.1 Random Excitation Results

The first analysis is conducted to observe the influence of the excitation amplitude. The three tightening torques are tested, the result at 10 cNm is presented on Fig. 35.3). For this degree of tightness, as for the others, a nonlinear behavior is noticed: the increase of the excitation amplitude induces a shift of the resonance frequency near the low frequencies and leads to an increase of the damping.

The second analysis is conducted to observe the influence of the tightening torque, only the external screws are impacted. This test is done for two excitation amplitudes (100 and 500 mV). The FRF RMS velocity for the three tightness is presented at 100 mV on Fig. 35.4. For this excitation amplitude, as for the other, a nonlinear behavior is observed: the decrease of the tightness induces a shift of the resonance frequency near the low frequencies and leads to a decrease of the damping.

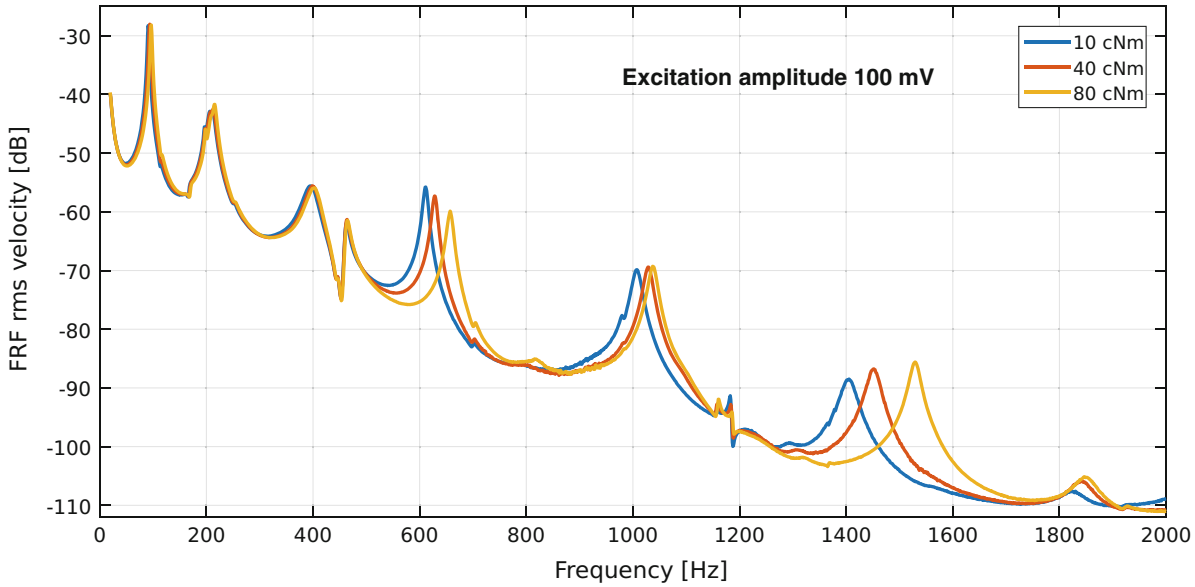

Fig. 35.4 Influence of the tightening torque, at 100 mV for excitation amplitude, for a random excitation of white noise type between [20–2000] Hz

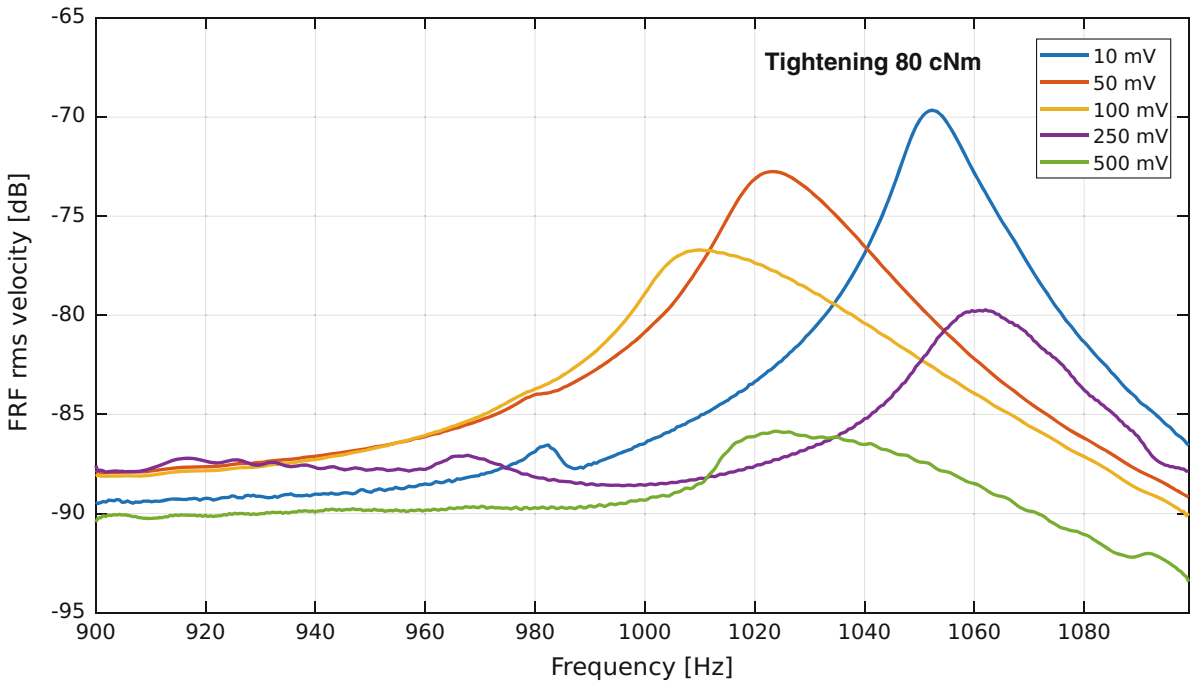

Fig. 35.5 Influence of the excitation amplitude for harmonic excitation between [900–1000] Hz and for one tightening torque of 80 cNm

35.3.2 Harmonic Results

Figure 35.5 shows the influence of the excitation amplitude on the structure behavior between 900 Hz and 1100 Hz. The curves presented here are obtained for a degree of tightness of 80 cNm and for five excitation amplitudes between 10 and 500 mV. It can be noticed that more the excitation is important, more the resonance is damped. The effect of the excitation amplitude is quite impressive. The mode almost disappears in this observed frequency window. From 100 mV, the non-linearity of the peak is clear, and from 250 mV, the higher order mode is observed.

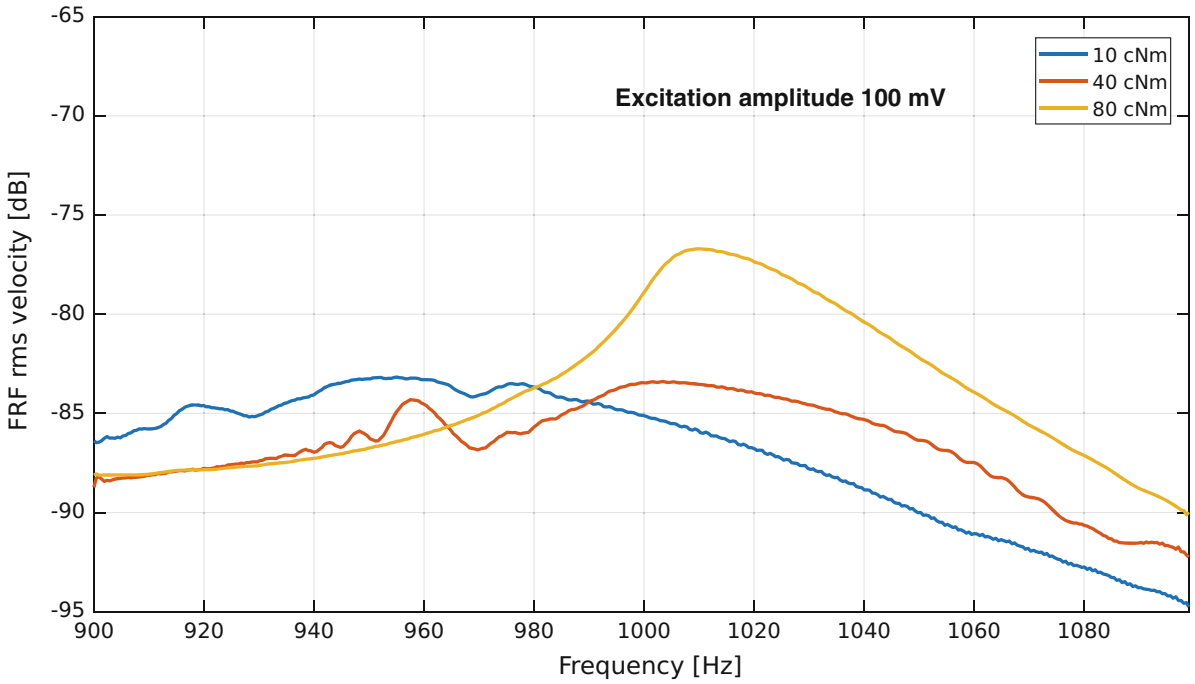

Fig. 35.6 Influence of the tightening, sine excitation [900–1000] Hz

In a second time, the excitation amplitude is fixed at 100 mV and the tightening torque varies between 10 cNm and 80 cNm. The FRF RMS velocity observed is given in Fig. 35.6. The results are very interesting, with the loosening of the screws the damping is drastically increased. The wavelets observed comes from a chirp experimental issue but do not question the conclusions.

35.4 Conclusions

This work aims to provide detailed datas to anyone who want to improve its simulation tools. All the experimental datas can be asked to the authors and will be sent in a "unv" file. Numerical datas, such as meshes and geometry, material properties, loadings amplitude can also be sent. Moreover, this work highlight the fact that this kind of functionalized connexion can be used for vibration control as it can be used to get damping and to tune the natural frequencies.

Acknowledgements P. Butaud and G. Chevallier would like to acknowledge the "Fond Interministeriel Unique" that funds the project CLIMA and the "Bourse-Oréal UNESCO Pour les Femmes et la Science" that encourage women to make sciences.

References

1. Ahmadian, H., Jalali, H.: Identification of bolted lap joints parameters in assembled structures. Mech. Syst. Signal Process. **21**(2), 1041–1050 (2007)
2. Beards, C.F., Williams, J.L.: The damping of structural vibration by rotational slip in joints. J. Sound Vib. **53**(3), 333–340 (1977)
3. Berthillier, M., Dupont, C., Mondal, R., Barrau, J.J.: Blades forced response analysis with friction dampers. Trans. Am. Soc. Mech. Eng. **120**, 468–474 (1998)
4. Caignot, A., Ladeveze, P., Neron, D., Durand, J.-F.: Virtual testing for the prediction of damping in joints. Eng. Comput. **27**(5), 621–644 (2010)
5. Dion, J.-L., Chevallier, G., Peyret, N.: Improvement of measurement techniques for damping induced by micro-sliding. Mech. Syst. Signal Process. **34**(1–2), 106–115 (2012)
6. Esteban, J., Rogers, C.A.: Energy dissipation through joints: theory and experiments. Comput. Struct. **75**(4), 347–359 (2000)

7. Festjens, H., Chevallier, G., Dion, J.S-L.: A numerical tool for the design of assembled structures under dynamic loads. Int. J. Mech. Sci. **75**, 170–177 (2013)
8. Festjens, H., Chevallier, G., Dion, J.L.: Nonlinear model order reduction of jointed structures for dynamic analysis. J. Sound Vib. **333**(7), 2100–2113 (2014)
9. Goodman, L.E., Klumpp, J.H.: Analysis of slip damping with reference to turbine blade vibration. ASME Appl. Mech. Div. **23**(3), 421–429 (1956)
10. Heller, L.: Damping in assemblies structures. Ph.D. thesis, Universite de Franche-Comte (2005)
11. Heller, L., Foltete, E., Piranda, J.: Experimental identification of nonlinear dynamic properties of built-up structures. J. Sound Vib. **327**(1), 183–196 (2009)
12. Metherell, A.F., Diller, S.V.: Instantaneous energy dissipation rate in a lap joint—uniform clamping pressure. J. Appl. Mech. **35**(1), 123–128 (1968)
13. Nanda, B.K.: Study of the effect of bolt diameter and washer on damping in layered and jointed structures. J. Sound Vib. **290**(3–5), 1286–1314 (2006)
14. Nanda, B.K., Behera, A.K.: Study on damping in layered and jointed structures with uniform pressure distribution at the interfaces. J. Sound Vib. **226**(4), 607–624 (1999)
15. Pian, T.H.H.: Structural damping of a simple built-up beam with riveted joints in bending. ASME J. Appl. Mech. **24**, 35–38 (1957)
16. Poudou, O., Pierre, C.: Blades forced response analysis with friction dampers. Ph.D. thesis, University of Michigan (2007)
17. Ren, Y., Beards, C.: Identification of joint properties of a structure using frf data. J. Sound Vib. **186**(4), 567–587 (1995)
18. Salles, L., Swacek, C., Lacayo, R.M., Reuss, P., Brake, M.R.W., Schwingshackl, C.W.: Numerical round robin for prediction of dissipation in lap joints. In: Nonlinear Dynamics, vol. 1, pp. 53–64. Springer, Berlin (2016)
19. Song, Y.: Simulation of dynamics of beam structures with bolted joints using adjusted iwan beam elements. J. Sound Vib. **273**(1–2), 249–276 (2004)
20. Ungar, E.E.: The status of engineering knowledge concerning the damping of built-up structures. J. Sound Vib. **26**(1), 141–154 (1973)

Chapter 36
A Numerical Approach to System Model Identification of Random Vibration Test

Washington J. DeLima, Richard Jones, Eric Dodgen, and Melanie N. Ambrose

Abstract A closed-loop random vibration test is a common test used to qualify systems that will be submitted to similar vibration loads during their life. Numerical modeling of this type of test is an important tool to provide insight about the robustness and success of the tests. In this paper the response of an electro-dynamic shaker will be modeled and validated with experimental data.

Keywords Virtual test • Electro-dynamic shaker • Simulation • Characterization

36.1 Introduction

Computational models which simulate random vibration tests can reduce time and cost by evaluating the robustness of the test procedure. Random vibration tests are widely used to qualify components. Evaluating the robustness of a test procedure experimentally can be time consuming, creating delays and adding cost. Some factors that affect the test robustness include the: weight of the Device Under Test (DUT), weight of adapter, closed loop vibration control system, frequency range, and vibration levels in the test specification. Ricci et al. [1, 2] presented a virtual shaker simulation model that would represent the actual vibration test. A lumped parameter electro-mechanical model of the shaker was used following similar work [3–5] together with a model of the vibration controller. Klenke et al. [6] developed VETO (Vibration Virtual Environment for Test Optimization) to help test engineers to select the optimal test parameters needed in the design test. Xiang et al. [7, 8] presented a sequential process to simulate vibration tests with application to satellite tests. DeLima and Ambrose [10–12] presented an experimental characterization of the systems used in random vibration tests and a simplified model of the system to simulate the test.

Creating a calibrated shaker model allows the opportunity to design test fixtures that are robust and well-behaved under the testing frequencies. A complete model that captures the interactions and cumulative response of the shaker, adapter, and fixture assembly provides the basis for predictive design of the test setup. This paper is a continuation of what was presented in the work by DeLima and Ambrose [10–12]. It presents a Finite Element Analysis (FEA) model of a shaker based on actual shaker characteristic.

36.2 Closed Loop Randon Vibration Test

A schematic diagram of a closed-loop vibration test is presented in Fig. 36.1. In a closed-loop vibration test, the controller sends a signal (driver voltage) to an amplifier that sends the amplified signal to the shaker [9]. The shaker sends the signal to the DUT that is attached to the shaker through a shaker-adapter and fixture. A feedback response is sent back to the vibration controller that compensates the signal to adjust it to the test specification.

The Department of Energy's Kansas City National Security Campus is operated and managed by Honeywell Federal Manufacturing & Technologies, LLC under contract number DE-NA0002839.

W.J. DeLima (✉) • R. Jones • E. Dodgen • M.N. Ambrose
KCNSC – Kansas City National Security Campus, Honeywell Federal Manufacturing and Technologies, Kansas City, MO, USA
e-mail: wdelima@kcp.com

J.M. Harvie, J. Baqersad (eds.), *Shock & Vibration, Aircraft/Aerospace, Energy Harvesting, Acoustics & Optics, Volume 9*,
Conference Proceedings of the Society for Experimental Mechanics Series, DOI 10.1007/978-3-319-54735-0_36

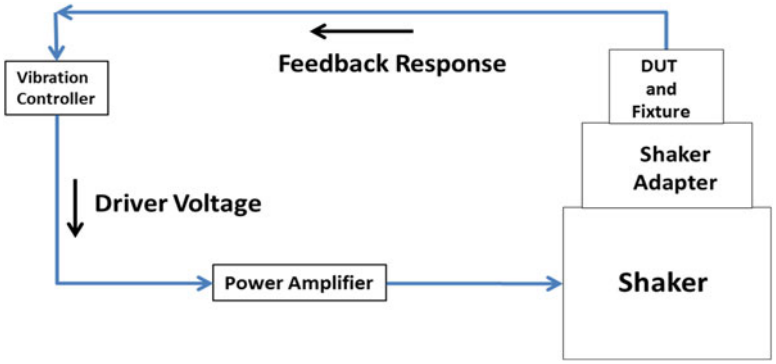

Fig. 36.1 A schematic diagram of closed-loop vibration test

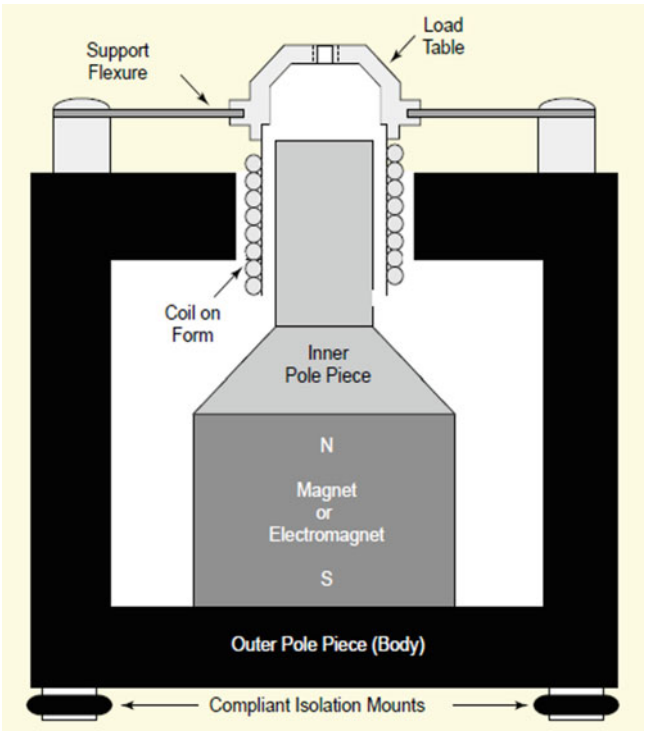

Fig. 36.2 A schematic diagram of electrodynamic shaker

The efficacy of the test simulation tool depends greatly on how accurate the elements on Fig. 36.1 are represented. One of the most import elements is the shaker (Fig. 36.2). Electro-mechanical shakers [9] are widely used in vibration testing. The structure of a conventional shaker resembles a loudspeaker where an AC electrical current passes through a coil wire that is in a fixed magnetic field [3–5]. The fixed magnetic field is create in the body of the shaker where a magnetic permeable circuit transmits flux from both poles of an axially magnetized permanent magnet (small shakers) or electromagnet (large shakers); this is accomplished, as shown, by means of an inner pole piece and a back circuit conducting flux to an outer pole piece with a hole in its center surrounding the coil. Interaction between the current in the coil and the magnet field creates a dynamic axial force in the coil proportional to the current. The motion of the coil is transmitted to the table that is attached to the coil. The coil and table combination is called an armature assembly, where the bottom of the armature is the coil and the top is the table. On top of the table is attached the DUT, fixture, and the shaker adapter.

36.3 Numerical Simulations

Predictive modeling is an integral piece of successful environmental testing. To obtain a predictive model, verification and validation of the assumptions and results of the model are critical. In this paper the vibration response of an electrodynamic shaker will be modeled. The response of the shaker will be represented by the response of its armature. This approach assumes that the body of the shaker is a rigid body with mass much bigger than the mass of the armature. The connection between the armature and the shaker body (soft elastic suspension, shear mount, and flex mount) will be represented as lumped springs. The electromagnetic force is represented as a body-force applied to the coil of the armature (Fig. 36.3).

An experimental test was performed on two shakers (UD T2000) to obtain the uncontrolled axial response of their armature when submitted to constant current in the frequency range from 20 Hz to 4000 Hz (Fig. 36.4). Since the force is linearly related to the current, a constant current produces a constant force. Two resonances appear below 3000 Hz. The low frequency resonance (300 Hz) is due to interaction of the armature and body of the shaker. The high frequency resonance (2300 Hz) is the resonance that defines the shaker. As expected, above 3000 Hz other resonances appear and the response of the shaker is more complex. It is also important to note the above the shaker resonance and in particular above 3000 Hz, there is a shaker to shaker variation. This variation is most likely due to the manufacturing variability; which is likely the reason the manufacturer does not guarantee shaker performance above this frequency.

The spring constants are tuned to make the simulation model match the resonance frequency at 300 Hz. The first mode is a symmetric axial mode where the coil and the table move in phase as one part. The shaker mode at 2300 Hz is an antisymmetric axial mode where the coil and the table move out of phase (Fig. 36.5).

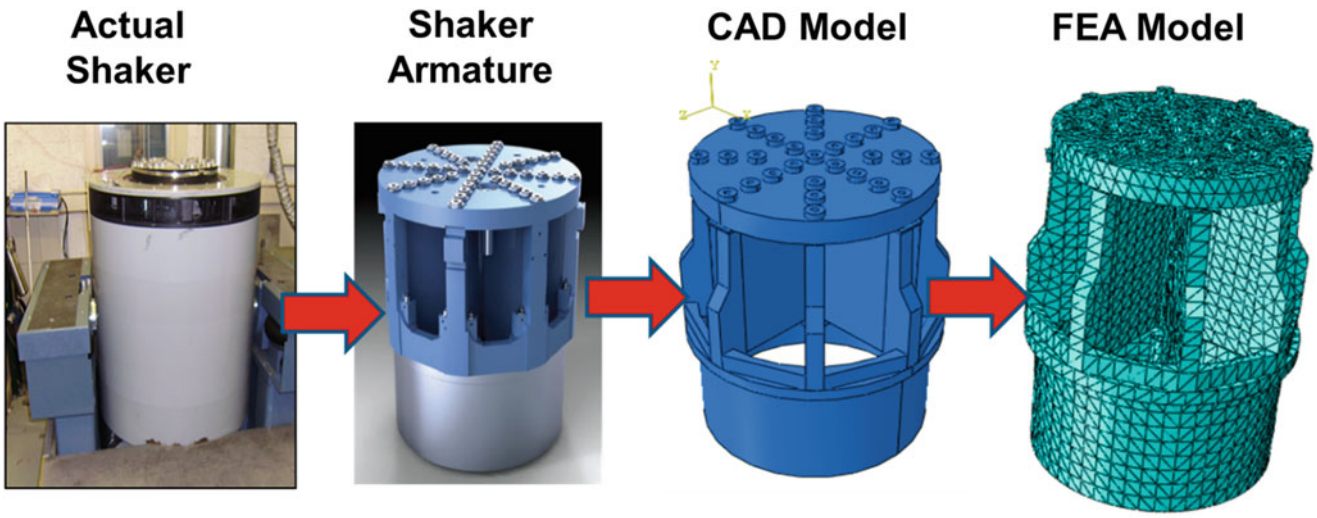

Fig. 36.3 Approach to model a shaker

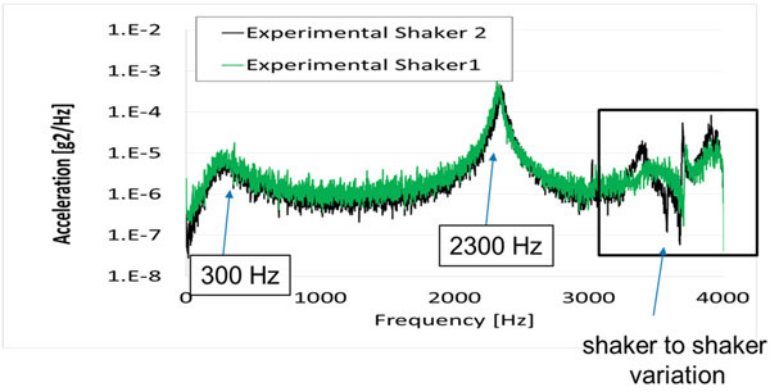

Fig. 36.4 Experimental response of a shaker submitted to constant current

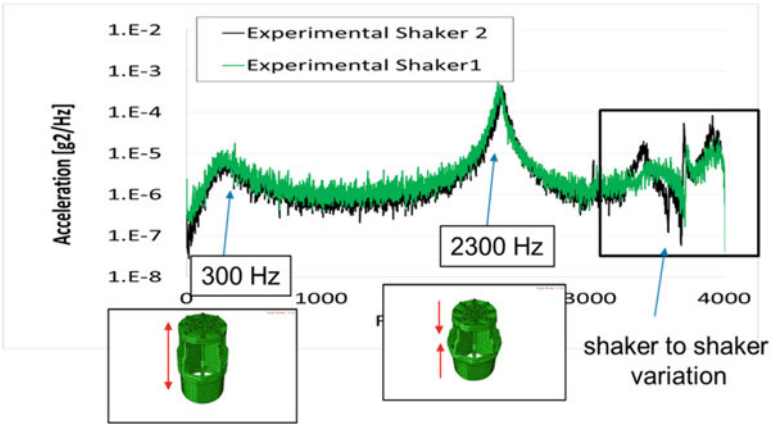

Fig. 36.5 Experimental response of a shaker submitted to constant current. Resonance at 300 Hz and 2300 Hz are presented

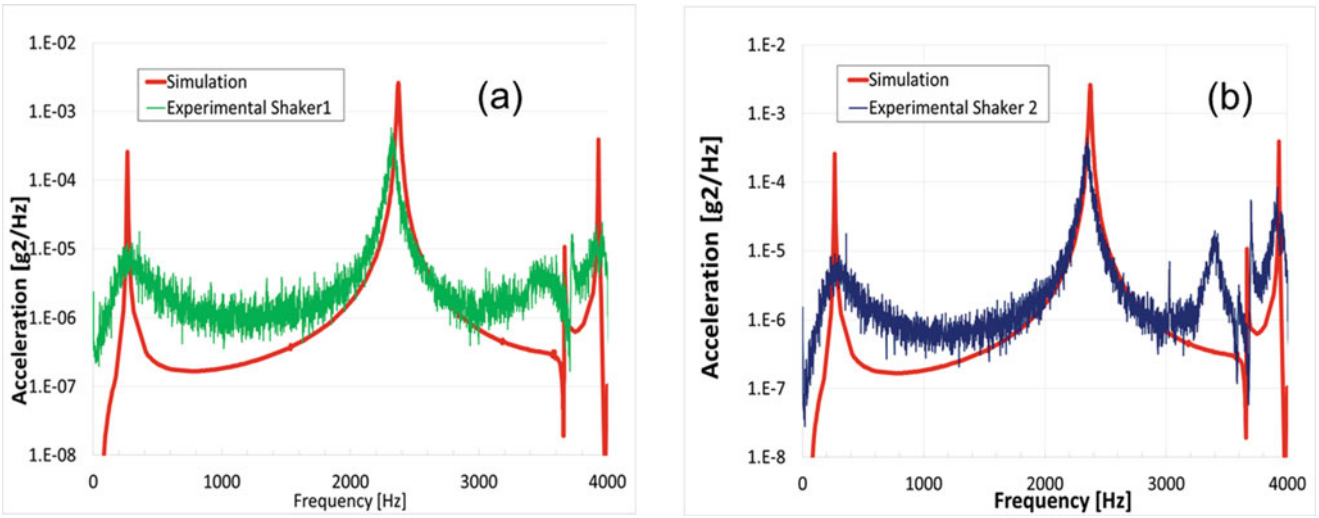

Fig. 36.6 Comparison between the simulation and the experiment. (**a**) Shaker 1; (**b**) Shaker 2

Since the constant that relates the force to current is not know for this shaker, the amplitude of the force was chosen such that the model matches the experiment. Figure 36.6 shows a comparison between the simulation and the experiment. It is noted that there is a reasonable agreement between simulation and experimental response for shaker 1 (Fig. 36.6a). However, shaker 2 presents an additional resonance that the current numerical model could not predict.

36.4 Conclusion

A FEA model of a shaker was able to reproduce the response of the armature. The interaction between the armature and shaker body was represented by lumped springs with stiffness values tuned to match the low frequency resonance in the response. Due to shaker variation at high frequencies each shaker requires its own numerical model.

References

1. Ricci, S., Peeters, B., Debille, J., Britte, L., Faignet, E.: Virtual shaker testing: a novel approach for improving vibration test performance. In: Proceedings of the ISMA 2008 International Conference on Noise and Vibration Engineering, Leuven, Belgium, 15–17 September 2008
2. Ricci, S., Peeters, B., Debille, J., Britte, L., Faignet, E.: Virtual shaker testing for predicting and improving vibration test performance. In: Proceedings of the 27th International Modal Analysis Conference, IMAC-XXVII, Orlando, Florida USA, 9–12 Feb 2009

3. Varoto, P.S., de Oliveira, L.P.R.: Interaction between a vibration exciter and the structure under test. Sound Vib. **36**(10), 20–26 (2002)
4. Lang, G.F., Snyder, D.: Understanding the physics of electrodynamic shaker performance. Sound Vib. **35**(10), 24–33 (2001)
5. Lang, G.F.: Electrodynamic shaker fundamentals. Sound Vib. **31**(4), 14–23 (1997)
6. Klenke, S.E., Lauffer, J.P., Gregory, D.L., Togami, T.C.: The Vibration Virtual Environment for Test Optimization (VETO), SAND-96-2217C. Sandia National Labs, Albuquerque, NM (1996)
7. Chuang, L., Xiang, S.-H., Feng, Y.-Q.: Research on virtual test system for the satellite. In: Proceedings of the 17th International Congress on Sound and Vibration, ICSV 17, Cairo, 18–22 July 2010
8. Xiang, S.-H., Liu, C., Yan, T.-F.: Virtual vibration test and verification for the satellite. In: Proceedings of the 14th International Congress on Sound and Vibration, ICSV 13, Cairns, Australia, 9–12 July 2007
9. Rogers, P., Garofalo, M.: What is an Induct-A-Ring shaker? Sound Vib. **43**(3), 7 (2009)
10. Delima, W.J., Ambrose, M.A. : Experimental characterization and simulation of vibration environmental test. In: Conference Proceedings of the Society for Experimental Mechanics Series. IMAC-33rd, Topics in Modal Analysis, Chapter 6, vol. 10, pp. 45–55, Springer, Cham (2015)
11. Delima, W.J., Ambrose, M.A.: Characterization of Shaker test for environmental test. In: Conference Proceedings of 2015 Spacecraft and Launch Vehicle Dynamic Environments Workshop, Los Angelis, CA.
12. Delima, W. J., Ambrose, M. N., Jones, R.: Modeling of high frequency shock tests. In: Conference Proceedings of the Society for Experimental Mechanics Series, IMAC-34th, Shock & Vibration, Aircraft/Aerospace, Energy harvesting, Acoustic & Optics, Chapter 13, vol. 9, pp. 145–155. Springer, Cham (2016)